UNIVERSITAT POLITÈCNICA DE CATALUNYA
BARCELONATECH
Escola Tècnica Superior d'Enginyeria Industrial de Barcelona
ETSEIB

STUDY OF THE MONOFILAR SUTURE BASED ON THE SEGMENTED COPOLYMER GL-*b*-(GL-*co*-TMC-*co*-CL-)-*b*-GL THERMAL BEHAVIOR, DEGRADABILITY AND INCORPORATION OF ACTIVE AGENTS

Polymers and Biopolymers

Yolanda Márquez Lobato

Advisors: Jordi Puiggalí Bellalta and M. Lourdes Franco García

Departament d'Enginyeria Química
Escola Tècnica Superior d'Enginyeria Industrial de Barcelona
Universitat Politècnica de Catalunya

Barcelona, 2016

A vosotros,
Valientes

ABSTRACT

Biomaterials based on block segmented copolymers constituted by *hard* and *soft segments* have attracted much attention for biomedical applications in the last decades, specifically as absorbable monofilament sutures. Polyglycolide has demonstrated to be a good candidate to constitute the *hard segment* due to its biodegradability and high stiffness, whereas the incorporation of different monomers (e.g., ε-caprolactone, trimethylene carbonate or glycolide) in a random distribution as *soft segment* promotes material flexibility and enhances *in vitro* degradation rates. Resulting material properties can be tailored by the combination of different ratios of *hard* and *soft segments* and the specific monomer composition.

In this Thesis the study of a tricomponent segmented copolymer commercially marketed as Monosyn® by B. Braun Surgical as an absorbable monofilament suture is presented. The main goals of the work concern to: a) the complete physical characterization that involves the study of the crystallization kinetics and thermal stability, b) the study of the degradation behavior and the associated microstructural changes, c) the evaluation of the capability to improve the performance of Monosyn® by adding compounds with pharmacological activity and d) the production of nanofibers to be employed as reinforcing agents.

Isothermal and non-isothermal crystallizations were followed by different techniques (e.g., optical microscopy, differential scanning calorimetry and time-resolved SAXS experiments in a synchrotron radiation facility). The composition of the *soft segment* influenced in the crystallization of the segmented copolymer as could be deduced by comparison with reported data on similar bicomponent systems.

Hydrolytic degradation was carried out at different temperatures and in buffered media of a continuous range of pH. Surface morphology of hydrolyzed sutures showed the formation of longitudinal and circumferential cracks in the outer and inner part of the suture, respectively. These fractures were associated to the existence of interfibrillar and interlamellar amorphous domains as was revealed by SAXS experiments.

To explore the potential applications of Monosyn® as an absorbable monofilament suture with pharmacological activity, different drugs were incorporated. Moreover, the use of an amorphous copolymer coating was also evaluated. The first group of drugs selected were

biguanide compounds (i.e., chlorhexidine and polyhexametilen biguanide), which have a well-recognized bactericide activity. Specifically, the effectiveness of using a coating was proved as well as the influence of drug molecular size in the activity. The study of the loading process, release behavior and pharmacological activity was completed considering an antibiotic (chloramphenicol) and a healing agent (captopril).

Finally, nanofibers of the selected copolymer were prepared by means of the electrospinning technique. These nanofibers were also loaded with pharmacological drugs and used as reinforcing agent of biodegradable polymer matrices. In order to obtain appropriate fabrics different fiber compositions and electrospun set up configurations were tested.

ACKNOWLEDGEMENTS

Me gustaría aprovechar esta oportunidad para expresar mi más sincero agradecimiento a mis directores, Prof. Dr Jordi Puiggalí Bellalta y la Dr. M. Lourdes Franco García. Gracias por brindarme la oportunidad de realizar este proyecto en el grupo y por vuestra supervisión, dedicación y paciencia a lo largo de este periodo. Sin lugar a dudas, la buena disposición a enseñar y compartir vuestros conocimientos y cada uno de vuestros consejos ha hecho posible que este día llegue.

Quiero extender mis agradecimientos al Dr. Luis Javier del Valle, dispuesto siempre a enseñar y resolver cualquier duda sobre temas biológicos. Gracias también al Dr. Alfonso Rodríguez, a la Dr. M. Teresa Casas y al Dr. Francesc Estrany, por el análisis de espectros de RMN, la realización de micrografías mediante microscopía electrónica y AFM, respectivamente.

Agradecer también al Dr. Trifon Trifonov por enseñarme la técnica de microscopía electrónica de barrido y su amable disposición a resolver cualquier duda en el centro de Nano, y a Juan Carlos Martínez por su ayuda y colaboración en las jornadas intensivas en el Sincrotrón.

Gracias a los compañeros del grupo y del departamento que durante estos años hemos compartido laboratorio, horas en el UV-Vis, debates, comidas, cafés, e incluso piso. Angélica, Sara, Elena, Gustavo, Tània, Alice, Josep, Hussein, Manolo, Georgina, Dani, Esther, Mar, Silvana, Neudys, Enric, Mayka, Ana, Elena, Ernesto, Cinthia (y seguro que sin querer me olvido a alguien), la lista es larga pero de todos me llevo algo. Y lo mejor, lo que nos queda por compartir.

Quiero expresar mi enorme gratitud a quién ha sido una parte fundamental en el desarrollo de esta Tesis, la compañía B.Braun Surgical, en particular al Dr. Pau Turon. No sólo nos ha facilitado todas las muestras que hemos necesitado, además se ha implicado desde el principio con un continuo seguimiento y asesoramiento. Gracias por confiar en el grupo y el proyecto, y darme la oportunidad de formar parte del equipo de I+D.

Agradecer también al Dr. Lutz Funk, Marta González, Dr. Elena Díaz, Jordi Ardèvol e Irene Prieto, que a lo largo de este período y más ahora al final, he necesitado resolver algunas

dudas y cuestiones, y no habéis dudado ni un momento en dedicarme el tiempo necesario en ayudarme.

Extiendo los agradecimientos a todos y cada uno de los compañeros de I+D, que me habéis preguntado sobre el estado de mi tesis y animado a lo largo de estos casi dos años.

A Mònica, con la que he compartido la aventura ETSEIB, y quién nos lo hubiera dicho que nos quedaríamos a hacer el doctorado.., una aventura más y muchas más que nos faltan. Ánimo que también te queda poquito!. A Alba y Maixa, casi toda una vida juntas y aunque no nos veamos tanto como quisiéramos, siempre habéis tenido palabras de ánimo.

Y por último, a mis constantes, a mi familia. Muchísimas gracias. Os lo debo todo, y sin vosotros no estaría escribiendo estos agradecimientos ahora. Gracias David, mención particular como bien mereces, que no has dudado en echarme una mano siempre que lo he necesitado. Y a ti Alex, santa paciència has tingut! Gracias por escucharme y animarme en todo momento.

En definitiva, la culminación de este trabajo no habría sido posible sin la ayuda y apoyo de todos y cada uno de vosotros.

Gracias

SCIENTIFIC PUBLICATIONS

Scientific production derived from this thesis:

- Márquez, Y., Franco, L. & Puiggalí, J. Thermal degradation of poly(trimethylene carbonate) blends with either polylactide or polycaprolactone. *Thermochim. Acta* **550**, 65-75 (2012).
- Márquez, Y., Franco, L., Turon P., Rodríguez-Galán, A. & Puiggalí, J. Study on the hydrolytic degradation of the segmented GL-*b*-(GL-*co*-TMC-*co*-CL)-*b*-GL copolymer with application as monofilar surgical suture. *Polym. Degrad. Stabil.* **98**, 2709-2721 (2013).
- Márquez, Y., Franco, L., Turon P. & Puiggalí, J. Isothermal and non-isothermal crystallization kinetics of a polyglycolide copolymer having a tricomponent middle soft segment. *Thermochim. Acta* **585**, 71-80 (2014).
- Márquez, Y., Martínez, J. C., Turon, P., Franco, L. & Puiggalí, J. Influence of pH on morphology and structure during hydrolytic degradation of the segmented GL-*b*-(GL-*co*-TMC-*co*-CL)-*b*-GL copolymer. *Fibers* **3**, 348-372 (2015).
- Márquez, Y., Franco, L., Martínez, J. C., Estrany, F., Turon P. & Puiggalí, J. Spherulitic morphologies of the triblock poly(GL)-*b*-poly(GL-*co*-TMC-*co*-CL)-*b*-poly(GL) copolymer: Isothermal and non-isothermal crystallization studies. *Eur. Polym. J.* **73**, 222-236 (2015).
- Márquez, Y., Graupera, J., del Valle, L. J., Turon, P., Franco, L. & Puiggalí, J. Poly(ε-caprolactone) films reinforced with chlorhexidine loaded electrospun polylactide microfibers. *Submitted.* (2016).
- Márquez, Y., Franco, L., Turon, P., Martínez, J. C. & Puiggalí, J. Study of non-isothermal crystallization of polydioxanone and analysis of morphological changes occurring during heating and cooling processes. *Accepted. In Press* (2016).
- Márquez, Y., Cabral, T., Lorenzetti, A., Franco, L., Turon, P., del Valle, L. J. & Puiggalí, J. Incorporation of biguanide compounds into poly(GL)-*b*-poly(GL-*co*-TMC-*co*-CL)-*b*-poly(GL) monofilar surgical sutures. *Submitted. Revision process* (2016).
- Márquez, Y., Cabral, T., Lorenzetti, A., Franco, L., Turon, P., del Valle, L. J. & Puiggalí, J. Incorporation of chloramphenicol and captopril into poly(GL)-*b*-poly(GL-*co*-TMC-*co*-CL)-*b*-poly(GL) monofilar surgical sutures. *Submitted. Revision process* (2016).

- Díaz Celorio, E., Franco, L., Márquez, Y., Rodríguez-Galán, A. & Puiggalí, J. Thermal degradation studies on homopolymers and copolymers based on trimethylene carbonate. *Thermochim. Acta* **528**, 23-31 (2012).

CONFERENCE PROCEEDINGS

- Márquez, Y., Franco, L. & Puiggalí, J. Study on the crystallization of segmented copolymers constituted by polyglycolide hard segments and poly(glycolide-*co*-trimethylene carbonate-*co*-caprolactone) soft segments. Poster at *Frontiers in Polymer Science*, 21th-23th May 2013, Sitges, Barcelona, Spain.
- Márquez, Y., Franco, L., Rodríguez-Galán, A. & Puiggalí, J. Study on the hydrolytic degradation of segmented copolymers constituted by hard segment and a middle poly(glycolide-*co*-trimethylene carbonate-*co*-caprolactone) soft segment. Poster at *Frontiers in Polymer Science*, 21th-23th May 2013, Sitges, Barcelona, Spain.
- Márquez, Y., Cabral, T., del Valle, L., Rodríguez-Galán, A., Turon, P., Franco, L. & Puiggalí, J. Monofilament bioabsorbable surgical sutures: Incorporation of compounds with pharmacological activity. Oral communication at *XIII Meeting of the Group of Polymers (GEP) of the Spanish Royal Chemistry and Royal Physics Society,* 7th–10th September 2014, Girona, Spain.
- Márquez, Y., del Valle, L. J., Franco, L., Turon, P. & Puiggalí, J. Non-isothermal crystallization of polydioxanone and morphological changes occurring during heating and cooling processes. Poster at *XIV Meeting of the Group of Polymers (GEP) of the Spanish Royal Chemistry and Royal Physics Society,* 5th–8th September 2016, Burgos, Spain.

GLOSSARY OF ACRONYMS

AFM	Atomic Force Microscopy
ATR	Attenuated Total Reflection
BGA	Brilliant Green Agar
CABG	Coronary Artery Bypass Grafting
CAP	Captopril
Cap	Caproyl unit
CFU	Colony Forming Unit
CHO	Chloramphenicol
CHX	Chlorhexidine
CL	Caprolactone
DEG	Diethylene glycol
DMEM	Dulbecco's Modified Eagle Medium
DMSO	Dimethyl sulfoxide
DNA	Deoxyribonucleic Acid
DSC	Differential Scanning Calorimetry
DTGA	Derivative Thermogravimetric Analysis
EtOH	Ethanol
FDA	Food and Drug Administration
FTIR	Fourier Transform Infrared (Spectrometer/Spectroscopy)
G	Glycolyl unit
GL	Glycolide
GPC	Gel Permeation Chromatography
HFIP	1,1,1,3,3,3-Hexafluoroisopropanol
HS	Hard segment
IKP	Invariant Kinetic Parameters
IR	Infrared
KAS	Kissinger-Akahira-Sunose
LA	Lactide
LH	Lauritzen Hoffman
MTT	3-(4,5-dimethylthiazol-2-yl)-2,5-diphenyl-2H-tetrazolium bromide
M_n	Number-average molecular weight
M_w	Weight-average molecular weight
NCD	Non Crystalline Diffraction
NMR	Nuclear Magnetic Resonance

PAA	Poly(acrylic acid)
PBS	Phosphate Buffered Saline
PCL	Poly(ε-caprolactone)
PDLA	Poly(D-lactide)
PDLLA	Poly(D,L-lactide)
PDO	Poly(*p*-dioxanone)
PDX	Poly(*p*-dioxanone)
PE	Polyethylene
PGL/PGA	Polyglycolide
PGLA	Poly(glycolide-*co*-lactide)
PHMB	Poly(hexamethylene biguanide)
PI	Polydispersity Index
PLA	Polylactide
PLLA	Poly(L-lactide)
PLGA	Poly(lactide-*co*-glycolide)
PP	Polypropylene
PTMC	Poly(trimethylene carbonate)
RCS	Refrigerated Cooling System
RCT	Randomized Controlling Trial
RNA	Ribonucleic Acid
ROP	Ring Opening Polymerization
SAXS	Small Angle X-ray Scattering
SEM	Scanning Electron Microscopy
SRC	Self-Reinforced Composite
SS	Soft Segment
SSI	Surgical Site Infection
T	Trimethylene carbonyl unit
TCS	Triclosan
TGA	Thermogravimetric Analysis
TMC	Trimethylene carbonate
USP	United States Pharmacopoeia
UV-Vis	Ultraviolet Visible (spectroscopy)
WAXD	Wide Angle X-ray Diffraction
WC	Wound Closure
ε-CL	ε-Caprolactone

TABLE OF CONTENTS

STRUCTURE OF THE THESIS

This Thesis consists of seven chapters followed by a summary of the conclusions drawn from the whole work.

Chapter 1 is a general introduction of the Thesis which includes a brief review of common polymeric materials used in biomedical applications. Among all the biomaterials, surgical sutures have had the longest historical contribution. Since an absorbable monofilament suture plays a key role in this Thesis, a detailed explanation about characteristics, physical configuration, degradation phenomena and absorption is included in this chapter. Furthermore, the use of antibacterial coating for multifilament as well as monofilament sutures is also reviewed. Finally, a short review of polymeric scaffolding materials for tissue engineering is given. Electrospinning technique is presented as an easy method to obtain reinforced polymeric scaffolds with micro- and nanofibers which can work as drug delivery systems.

Chapter 2 includes the general and specific objectives of this Thesis

Chapter 3 presents kinetic studies of isothermal and non-isothermal crystallization studies of the GL-*b*-(GL-*co*-TMC-*co*-CL)-*b*-GL monofilament suture have been undertaken by means of calorimetric methods. Crystallization has also been studied by means of optical microscopy, atomic force microscopy and time resolved X-ray diffraction techniques. The results obtained from both, isothermal and non-isothermal crystallizations allowed to obtain bell shaped curves that defined the temperature dependence of the crystal growth rate. Polyglycolide segments were able to crystallize giving rise to peculiar positive birefringent spherulites with a morphology, which depends on crystallization temperature (i.e., flat-on and edge-on crystals) as verified by AFM.

Chapter 4 describes degradation process of the GL-*b*-(GL-*co*-TMC-*co*-CL)-*b*-GL monofilament suture in terms of thermal stability and hydrolytic degradation. First of all, thermal stability and degradation kinetics of blends based on the homopolymers which constituted the segmented copolymer were evaluated by thermogravimetric analysis as a basis for future studies. On the other hand, hydrolytic degradation of GL-*b*-(GL-*co*-TMC-*co*-CL)-*b*-GL monofilar suture in media having a continuous variation of pH from 2 to 12 was studied. Results reflected the different hydrolytic mechanism that took place in acid and basic media and the different solubilization of the degradation

products. Heating processes performed with degraded samples were fundamental to reveal the changes on microstructure that occurred during degradation and even the initial lamellar arrangement. In particular, the presence of interfibrillar domains and the disposition of lamellar domains at different levels along the fiber axis for a determined cross-section were evidenced.

Chapter 5 presents the non-isothermal crystallization kinetics of poly(*p*-dioxanone) (PDO), a polymer with a well-established applications as bioabsorbable monofilar suture, investigated by means of calorimetric methods. Results showed two secondary nucleation constants derived from calorimetric data, and were corroborated by typical non-isothermal crystallization analysis based on the determination of crystal growth by optical microscopy. Microstructure were characterized by time resolved X-ray diffraction techniques. Also, degraded samples under distinct pH media revealed differences in evolution of lamellar microstructure during subsequent heating processes as well as in macroscopic morphologies.

In **Chapter 6**, monofilament sutures of GL-*b*-(GL-*co*-TMC-*co*-CL)-*b*-GL were loaded with chlorhexidine (CHX) and poly(hexamethylene biguanide) (PHMB) to explore the possibility to achieve antimicrobial activity without adverse cytotoxic effects. Also, incorporation of chloramphenicol and captopril to coated and uncoated monofilament sutures was evaluated as well as the derived bactericide and wound healing effects.

Chapter 7 presents reinforced polymeric matrix with electrospun micro- and nanofibers. On the one hand, poly(*ε*-caprolactone) (PCL) films reinforced with polylactide (PLA) microfibers were prepared by using two different methodologies: a) melt pressing of an electrospun PLA mat between two PCL films and b) melt pressing of a co-electrospun mat composed of PLA microfibers and PCL nanofibers. From both configurations, antimicrobial activity was also evaluated when chlorhexidine was incorporated in the different elements of the resulting matrices. On the other hand, multilayer matrices with antibacterial activity were also performed. In this case, reinforced fibers were formed of segmented copolymer which are alternated with poly(*ε*-caprolactone) films. Corresponding biological assays were carried out to analyzed the effects of an antibacterial drug such as chlorhexidine when it was incorporated at different layers.

1.

INTRODUCTION

1.1 Biomaterials

1.1.1 INTRODUCTION

Originally, the term of biomaterial was defined as "non-viable material used in a medical device, intended to interact with biological systems".[1] Over the years, this definition has evolved to more general meaning, which can encompass the wide variety of applications. Therefore, biomaterial definition is presented as a "substance that has been engineered to take a form which, alone or as part of a complex system, is used to direct, by control of interactions with components of living systems, the course of any therapeutic or diagnostic procedure, in human or veterinary medicine".[2] The most important factor attributable to a biomaterial is the biocompatibility, defined in 2008 as "the ability to perform its desired function without eliciting any undesirable local or systemic effect in the recipient or beneficiary of that medical treatment, but generating the most appropriate beneficial cellular or tissue response in that specific situation, and optimizing the clinically relevant performance of that therapy".[3] To meet the specific requirements of the biomedical community, materials constituted from metals and ceramics to glasses and polymers have been thoroughly investigated.[4]

1.1.2 POLYMERIC BIOMATERIALS

Polymers are a well-suited materials for biomedical applications because their physical and mechanical properties, and their relatively simple processability.[5,6] The latest advancement in polymeric biomaterials is focused on the design of more specific biological response materials. This new generation, with tailored controlled properties, includes drug and cell carriers, biologically inspired materials that mimic natural processes and three-dimensional architectures to obtain well-defined patterns for diagnostics and tissue engineering.[7]

In general terms, medical application of polymers (Figure 1.1) can be classified into three main categories: (i) extracorporeal uses (e.g., catheters, tubing, dialysis membranes, ocular devices, wound dressing and artificial skin), (ii) permanent implanted devices (e.g., sensory, cardiovascular, orthopedic and dental devices), and (iii) temporary implants (e.g., wound closure devices, implantable drug delivery systems, polymeric scaffolds, temporary vascular grafts and arterial stent, and temporary bone fixation devices).[8]

Figure 1.1. Examples of applications of polymeric biomaterials: **(a)** connection tubing with safeflow, **(b)** gastric tubes, naso-gastric and naso-intestinal PVC tubes for short term use only, **(c)** single use trocar system, **(d)** CranioFix® absorbable, absorbable cranial fixation system, **(e)** TSPACE® PEEK, implant for stabilization of the lumbar and thoracic spine, **(f)** Uni-graft® W Aortic Arch, impregnated woven polyester vascular prosthesis, **(g)** Neuro-Patch®, substitute for the repair of the dura mater in neurosurgery, **(h)** Optilene® Mesh, universal-light mesh for inguinal and incisional hernia repair and **(i)** Optilene® surgical suture**.** (Courtesy of B. Braun, from official website [9])

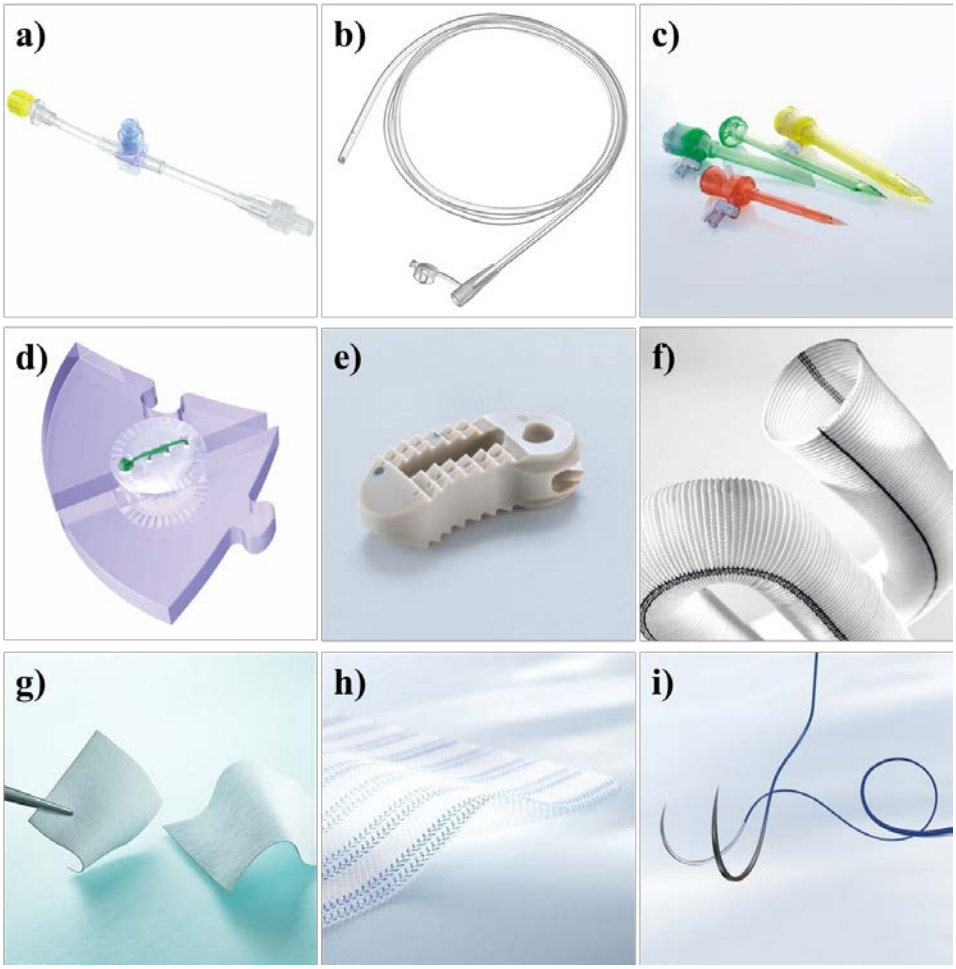

1.1.2.1 Biodegradable polymers

In recent years, the use of biodegradable polymers has been increasing, specifically toward biomedical applications as temporary devices, because these materials are able to be broken down and excreted or resorbed without removal or surgical revision. By definition, biodegradable polymers degrade as a result of the action of microorganism and/or enzymes.[10] In addition, the most important criteria for a biodegradable polymer is the non-toxicity of the generated products from degradation (i.e., degradation product should not invoke any unacceptable toxicity and immune response).[11]

Polymeric biomaterials can be distinguished in two main categories depending on their source: non synthetic polymers which include natural and microbial, or synthetic polymers. A more detailed classification is shown in Figure 1.2.

Figure 1.2. Classification of biodegradable polymers.[4]

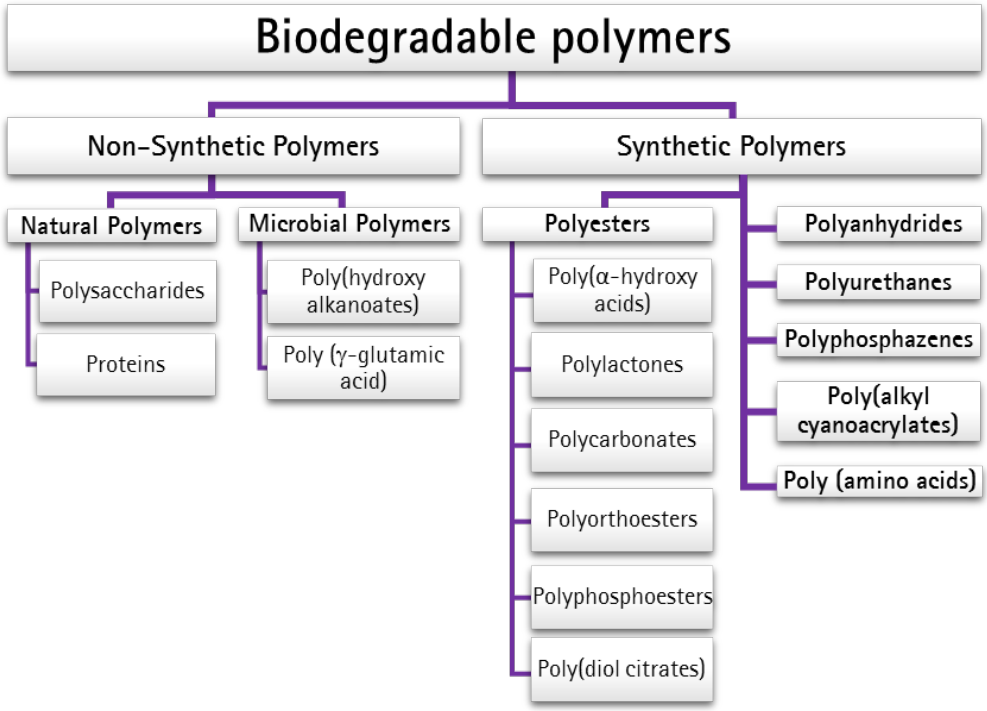

Even though the high biocompatibility is the main interest of natural polymers, the antigenicity and batch to batch variation are undesirable properties. In contrast, synthetic polymers allow to match degradation rate and mechanical properties to fit with the specific application. Normally, enzymatic degradation routes are present in natural polymers, whereas synthetic polymers use to be hydrolytically degradable, because they have hydrolytically labile chemical bonds in the backbone (e.g., ester, anhydride, carbonate, amide, urethane functional groups).[11–13]

1.1.2.2 Biodegradation phenomena

The biodegradation phenomena of a polymer is strictly defined as the deterioration of its physical and chemical properties and a decrease of its molecular mass to the formation of CO_2, H_2O, CH_4 and other low molecular-weight products under the influence of microorganisms in both, aerobic and anaerobic conditions aided by abiotic chemical reactions like photodegradation, oxidation and hydrolysis.[14] Basically, it includes a first step based on the chain cleavage into lower molecular mass species and a second step, where the microbial assimilation and mineralization of the resulting products occur (**Figure 1.3**).

Then, degradation of a polymer is greatly influenced by its backbone structure, being the most relevant requirement the presence of hydrolytic or/and oxidizable linkages.[15] There are two main ways by which polymer chains can be hydrolyzed, i.e., passively, by chemical hydrolysis, or actively, by enzymatic reaction.

There are many other factors which largely affect the rate of biodegradation. They can be intrinsic material properties such as the type of repetitive unit, composition, sequence length, molecular geometry, molecular weight, morphology (e.g., crystallinity, size of the spherulites, orientation), hydrophilicity, surface area, and additives,[16] but also external environmental factors, like pH, temperature and presence or concentration of enzymes.[17] Among the various polymers susceptible to hydrolysis including esters, ortho-esters, anhydrides, carbonates, acetals, amides, urethanes, phosphates and phosphazenes, degradation rates can vary from very hydrolytically unstable (polyphosphazenes) to extremely hydrolytically stable (polyamides).[18]

The mass loss mechanism of the polymeric matrix is influenced by degradation rates as well as hydrophilicity and crystallinity, which define the water diffusion and monomer

solubility. Normally, the homogeneous hydrolytic degradation of these polymers is divided in two cases, the bulk erosion and the surface erosion, or a combination of both (Figure 1.3). Bulk erosion is characterized by water diffusion much faster than degradation, leading to degradation and subsequent mass loss occurring throughout the bulk of the material. On the contrary, in surface erosion, the rate of polymer degradation and mass relief at the water-device interface is much greater than the rate at which water diffuses into the bulk, leading to a device that degrades almost entirely at its outermost parts of the sample.[19]

Determining the degradation mechanism is important to choose the best material for a desired application. For example, a material that can undergo surface erosion may be useful in sustained drug delivery, because stable near zeroth-order release can be maintained and release kinetics can be more easily tailored.[20] On the other hand, for application as permeable membrane in tissue engineering, bulk eroding materials would allow for necessary hydrolytic diffusion.[21]

Figure 1.3. Scheme of biodegradation phenomena and erosion process.

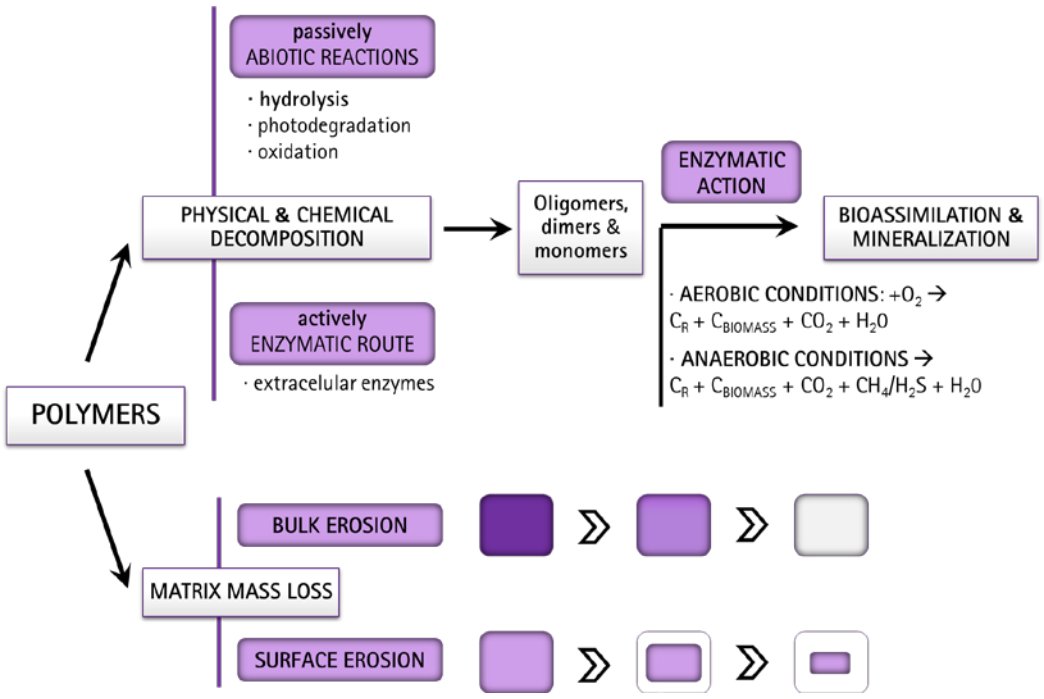

1.2 Polyesters for biomedical applications

1.2.1 INTRODUCTION

Specially, poly(α-esters) are thermoplastic polymers with hydrolytically labile aliphatic ester linkages in their backbone. As esterification is a chemically reversible process, all polyesters are theoretically degradable, but only aliphatic polyesters with reasonably short aliphatic chains between ester bonds can degrade over the time frame required for the majority of biomedical applications. The singularity of this group of polymers lies in the relative ease and versatility of their synthesis, via ring-opening or condensation polymerization, depending on the monomeric units.[4]

Due to the variety of applications in the biomedical field and the commercial availability, poly(α-esters) have been the most extensively investigated class of biodegradable polymers.

1.2.2 POLY(α-ESTERS) APPLIED AS BIOMATERIALS

Among the group of poly(α-esters) used for biomedical applications, the common chosen polymers are belonged to poly(α-hydroxy acids), polylactones and polycarbonates categories.

However, polyorthoesters, polyphosphoesters and poly(diol citrates) are also used in biomedical field. Polyorthoesthers are considered a surface eroding polymer. Their hydrophobic nature combined with hydrolytically labile bond on the surface makes them an excellent material for drug delivery systems. In gene therapy and delivery of chemotherapeutic devices, novel prodrugs are developed using the pentavalency of phosphorous atoms from polyphosphosesters, which helps in linkage of drugs or proteins. And poly(diol citrates) have been investigated for ligament reconstruction and vascular engineering, due to their excellent mechanical properties (related to diols units) and hemocompatibility.[22]

In the present work, specific polymers from common poly(α-esters) groups are mentioned as homopolymers form as well as copolymer or blend compositions. Thus, these specific examples from each category are briefly introduced in the following sections.

1.2.2.1 Poly(α-hydroxy acids)

The risen development of these polymers from the first absorbable suture into most preferred materials for controlled drug delivery systems makes them the representative class of biodegradable polymers.

Poly(α-hydroxy acids) includes poly(glycolic acid), poly(lactic acid) and a range of their copolymers poly(lactic-*co*-glycolic acid) (Figure 1.4). These polymers undergo degradation by non-enzymatic hydrolysis of ester linkages along the backbone into lactic and glycolic acids which are reabsorbed through metabolic pathways.[22]

Figure 1.4. Chemical structure of representative poly(α-hydroxy acids).

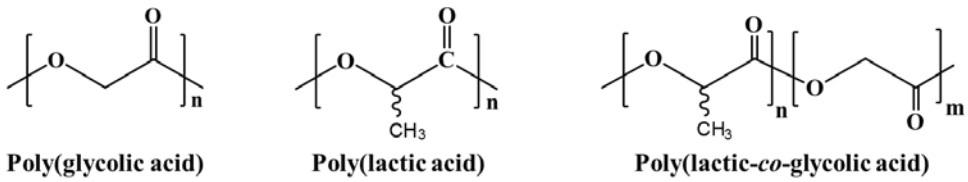

Poly(glycolic acid) (PGA) or polyglycolide (PGL)

Polyglycolide is the simplest linear aliphatic polyester with a highly crystalline nature (around 45–55%), leading to a high tensile modulus. It has a melting point ranging between 220 and 225 ºC and its glass transition temperature ranges between 35 and 40 ºC.[23,24]

Due to its excellent fiber-forming ability and biodegradability, polyglycolide was the first suture approved by FDA (Food and Drug Administration), commercially known as *Dexon*™ and developed in 1969. Normally, PGA filaments are used as multifilament because the obtained filament is rigid and less flexible. In spite of having many advantages, its application is limited in terms of degradation, it presents a higher rate of degradation, low solubility in organic solvent, and accumulation of acidic degradation products,[25–27] and also in terms of stiffness, which can be compensated copolymerizing it with other monomers.[28]

Poly(lactic acid) (PLA) or polylactide

Poly(lactic acid) is a rigid thermoplastic polymer that can be semicrystalline or totally amorphous, depending on the stereoregularity of the polymer backbone, because there are two optically active forms which are L-lactide and D-lactide (Figure 1.5). Whereas the polymerization of these monomers leads to the formation of semicrystalline polymers, the polymerization of racemic (D,L-lactide) and mesolactide results in amorphous polymers with lower mechanical strength. However, among these monomers, L-lactide is the naturally occurring isomer.[29,30]

Figure 1.5. Stereoisomer chemical structures of polylactide.

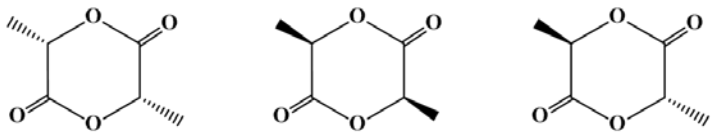

Poly(L-lactic acid) (PLLA) is also a crystalline polymer (around 37%) and the degree of crystallinity is related to the molecular weight and polymer processing parameters. It has a glass transition temperature around 60 and 65 ºC and a melting point of approximatively 175 ºC.[23]

PLA type polymers are characterized by their inherent biodegradability, biocompatibility with high mechanical strength and can be made from renewable resources. Basically, they may be the polymers with the broadest range of applications because of their capacity to be stress crystallized, thermally crystallized, impact modified, filled, copolymerized and processed in most polymer processing equipment. Moreover, they have excellent organoleptic characteristics, being excellent for food contact and related packaging applications.[31] However, in clinical applications, PLLA is sometimes affected by the high hydrophobic behavior and consequent poor water uptake, which leads to slow hydrolytic degradation rate.[32]

Poly(lactic-*co*-glycolic acid) (PLGA) or poly(lactide-*co*-glycolide)

Copolymers of lactide and glycolide were developed to overcome the disadvantages of individual polymers and for better property modulation. The properties of these copolymers

like mechanical strength, swelling behavior and rate of degradation are defined by the degree of crystallinity of the PLGA, which is further dependent on the type and proportion of each of the monomer components. Regarding biodegradation rate, crystalline PGA, when copolymerized with PLA, reduces the degree of crystallinity of PLGA and as a result increase the rate of hydration and hydrolysis. As a rule, higher content of PGA leads to quicker rates of degradation with an exception of 50:50 ratio of PLA/PGA, which exhibits the fastest degradation, with higher PGA content leading to increased degradation interval below 50%.[22,33]

Normally, copolymers of lactide and glycolide are amorphous rather than crystalline and show a glass transition temperature in the range between 40 and 60 ºC. Unlike the homopolymers of lactic and glycolic acids which are characterized by poor solubility, PLGA can be dissolved by a wide range of common solvents.[28]

Since last two decades, PLGA has been among the most attractive polymeric material used to develop devices for controlled drug delivery and tissue engineering applications, due to the wide controllable range of erosion time, tunable mechanical properties and more importantly, for its approval by the FDA for use in humans.[4,33]

1.2.2.2 Polylactones

Poly(ε-caprolactone) (PCL)

Poly(ε-caprolactone) (Figure 1.6) is a semicrystalline polymer with great solubility in common organic solvents, a melting temperature ranging between 55 and 60 ºC, and a glass transition temperature approximately of -54 ºC.[34] PCL, also approved by FDA, has a low tensile strength but an extremely high elongation at break, making it a good elastic material.

Due to the very slow *in vivo* degradation rate (on the order of two –three years) and the high drug permeability, it has found as a proper candidate for a long-term implant delivery device and as a vehicle for cell-based therapies.[4,22,28]

Poly(ρ-dioxanone) (PDO)

Poly(ρ-dioxanone) (Figure 1.6) was developed specifically for wound closure sutures, commercially named *PDS*™ in 1980s. It exhibits a crystalline fraction of 55% and a very low glass transition temperature ranging from -10 ºC to 0 ºC.[22,28]

As a monofilament suture, PDO shows high flexibility, because of the incorporation of an ether oxygen group in the backbone structure, and higher strength retention.[35] Compared to other sutures based on PLGA and PGA, it has slower absorption rates, due to the high crystallinity and hydrophobicity, and lower inflammatory response. Thus, although it can be considered a slow to moderately degrading polymer, it is faster than PCL.

One of the most important disadvantages of PDO suture is its shape memory effect, but this property, as well as its compatibility, its degradation rate and its flexibility make it suitable when the design of current tissue engineering scaffolds is considered.[36] Moreover, apart from its initial use as a suture, it may be employed as orthopedics, plastic surgery, drug delivery, cardiovascular indication and bone repair applications.

Figure 1.6. Chemical structure of representative polylactones.

Poly(ε-caprolactone) Poly(p-dioxanone)

1.2.2.3 Polycarbonates

Polycarbonates are linear polymers with two geminal ether bonds and a carbonyl bond. Although this bond is extremely hydrolytically stable, research has shown that *in vivo* degradation proceeds faster due to enzymatic degradation which causes these polymers to be surface eroding.[4] The most extensively studied polycarbonate is poly(trimethylene carbonate) (Figure 1.7).

Figure 1.7. Chemical structure of the main representative polycarbonate.

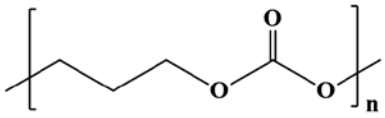

Poly(trimethylene carbonate)

Poly(trimethylene carbonate) (PTMC)

PTMC is an elastomeric aliphatic polymer with a glass transition temperature around -17 ºC.[37] It shows a great flexibility and a slow degradation profile, but poor mechanical strength, which is an advantageous characteristic for soft tissue regeneration.[22]

To enhance the potential application of PTMC, the monomer is often copolymerized with LA, CL, or GL for the fabrication of biomaterials with higher mechanical strength, to be used as a suture materials or bone fixation devices, and with superior degradation properties, to be used as a drug delivery system.[4]

1.2.2.4 Blends and copolymers

The majority of the biomedical devices are formed by blending or copolymerization of aforementioned monomers, to overcome the drawbacks of single components. In fact, the extensive number of current publications are a worthy proof of the interest in this field.

Polymer blending has attracted much attention as an easy and cost-effective method of developing polymeric biomaterials with tailored characteristics by mixing the different components.[38,39] The desired properties and degradation rates of the resulting blend can be controlled by adjusting the blending ratio, preparation conditions and morphology of blends.[40,41] Polymer blends are classified into miscible (homogeneous) or immiscible (heterogeneous). Miscibility of components is an important feature to determine the physicochemical and mechanical properties of the corresponding polymeric blend. Miscible or immiscible characteristics also impact on biological response, a relevant aspect for tissue engineering application. Normally, blends of biodegradable and bioresorbable polyesters are mostly immiscible and only in a few cases they are miscible/compatible. Immiscibility in polymer blends generally translates into good cells adhesion and

proliferation. In contrast, compatible blends compared to immiscible blends have better cellular infiltration.[42,43]

On the other hand, copolymerization is a versatile synthetic tool, which implies a covalent chemical bond connection amongst different constituents (repeating structural units), for controlling the functionality and tailoring of the physical and mechanical properties of macromolecules. Specifically, the increasing interest in block copolymers for technological applications arises mainly from its microphase separation,[44] leading amphiphilic properties in solution and microdomains formations in solid state.[45]

The polyesters can be tailored by block copolymerization with various architectures (Figure 1.8) to achieve a wide range of properties from brittle glass plastics to elastomers.

Figure 1.8. Schematic drawings of various linear block copolymers architecture: **(a)** AB di-block, **(b)** (AB)n multiblocks, **(c)** ABA tri-block copolymer; and non-linear structures: **(d)** graft, **(e)** dendrimer-like and **(f)** star block.

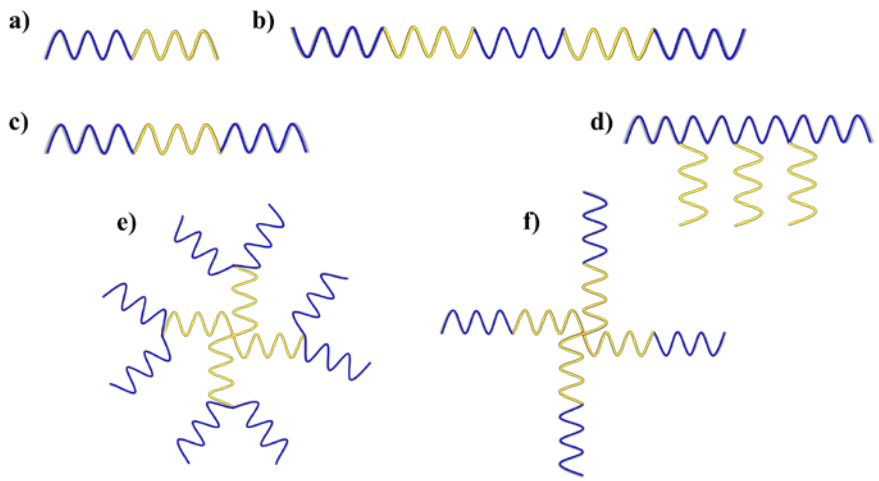

In fact, typically block segmented copolymers have been developed for absorbable monofilament sutures in order to enhance flexibility and degradation rates. They are prepared as A-B-A block copolymer, where A is a *hard segment*, which is usually made with glycolide (GL), and B is a *soft segment* of statistical copolymers, normally with trimethylene carbonate (TMC) monomer, but also can be ε–caprolactone. The *soft segment* provides elastomeric characteristics to the whole and compensates the high stiffness of polyglycolide. For example, Maxon™ is probably one of the simplest bioabsorbable

monofilament derived from block copolymerization based on glycolide and trimethylene carbonate. Regarding *soft segment* block, glycolide and trimethylene carbonate have also been copolymerized with *p*-dioxanone (PDO) to form a terpolymer suture, commercially known as Biosyn™ or with *ε*-caprolactone (*ε*-CL) commercially called as Monosyn®.

The present work is mainly focused on Monosyn®, absorbable monofilament suture kindly supplied by B. Braun Surgical. In order to guarantee the segmented nature of the copolymer, Monosyn® is synthesized following a procedure involving two steps (Figure 1.9). This segmented copolymer is constituted by a middle *soft segment* which represents a 43 wt-% of the sample, and it is based on three aforementioned components (35 wt-% of glycolyl, 32.5 wt-% of trimethylene carbonyl and 32.5 wt-% of *ε*-caproyl units).

Figure 1.9. Schematic two steps synthesis of Monosyn® segmented copolymer and image of Monosyn® absorbable monofilament suture. (Courtesy of B. Braun Surgical from official website [9]).

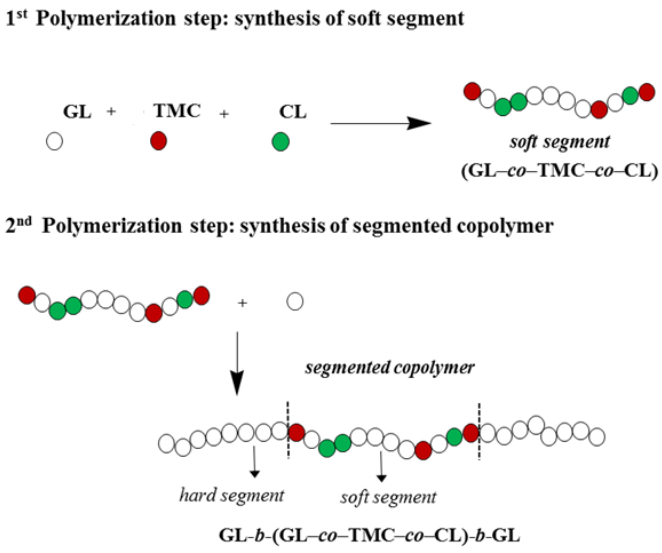

1.2.3 BIOMEDICAL APPLICATIONS

There are a wide range of biodegradable polymers that have been proved to be versatile materials with a great potential use in the biomedical field, due to the tailored properties according to the application requirements. The biomedical applications can be classified into different areas:

- **Medical devices,** includes a huge variety of elements, from temporary vascular grafts and arterial stents, commonly used in cardiovascular diseases or orthopedic devices[23] to disposable devices such as syringes, catheters, surgical gloves, amongst others.
- **Wound dressing,** an important group for developing surgical practice. Sutures are the most well-known example for wound closure device.
- **Tissue engineering,** also called regenerative medicine. It develops biological substitutes or reconstructs tissues in order to restore, maintain, or improve tissue functions.[46]
- **Drug delivery systems,** focused on controlling drug release and developing smart polymers that lead a more accurate and programmable drug delivery.[47]

And the newest applications:

- **Control release and gene delivery,** synthetic polymer vectors in gene therapy provide an improved safety, greater flexibility and more facile manufacturing for treating various humans diseases, avoiding the use of viral vectors.[48]
- **Patterned biomaterial for diagnostics,** able to amplify and transmit signals and have to be sensitive to screening in a reduced size. Patterning has enabled researchers to create diagnostic tools by miniaturizing and combining laboratory procedures onto a single device.[49]

Amongst the different areas, biomedical applications of the main polyesters are generally included in former categories (Table 1.1).

Table 1.1. Biomedical applications of main polyesters.[4,22]

Polyester family	Biomedical Application
Poly(α-hydroxy acids)	
PGL	wound closure, orthopaedics
PLLA	wound closure, bone fixation device, tissue engineering
PDLLA	drug delivery, tissue engineering
PGLA	wound closure, tissue regeneration, drug and protein delivery
Polylactones	
PCL	long-term drug/vaccines delivery, cell-based therapy, tissue engineering
PDO	wound closure, orthopaedics, bone fixation screws, tissue engineering
Polycarbonates	
PTMC	soft tissue regeneration
Polyorthoesters	drug delivery
Polyphosphoesters	drug and protein delivery, gene therapy, tissue engineering
Poly(diol citrates)	ligament reconstruction, vascular engineering

Furthermore, combination of different polyesters are not only used in the same biomedical application than related homopolymer, but they are also employed as filler material and in short-term tissue engineering (e.g., copolymers of PGL).

1.3 Surgical sutures

1.3.1 INTRODUCTION

Wound closure biomaterials and devices have been an important key in the development of surgical practice. In fact, they have the longest historical contribution among all the biomaterials. Generally, wound closure biomaterials and devices can be categorized into sutures, ligating clips/staplers, tissue adhesives, strips and surgical meshes. The former mentioned, sutures, have received the most attention since they have been the most widely used in wound closure for many centuries.[50]

A suture is defined as a strand of material, either natural or synthetic, used to ligate blood vessels and to approximate tissues together.[50] Hence, its major functions are to bring and hold tissues together after an injury or trauma. The objectives of wound closure comprise

obliteration of dead space, distribution of tension along deep suture lines, maintenance of tensile strength across the wound until tissue tensile strength is adequate, as well as, approximation of the epithelial portion of the closure.[28]

Despite the existence of other biomaterials and devices for mechanical wound closure, sutures are the most frequent materials and the ones with the earliest history. Indeed, the first documentation about sutures dates back to 2000 B.C., and describes the employment of linen to close wounds.[51] Since the beginning, many natural materials were used, reaching an extensively use of silk, cotton and catgut at the 1800s and early 1900s. The introduction of synthetic materials in the 1940s, expanded the diversity of sutures. Consequently, the development of the first absorbable synthetic suture based on polyglycolide (Dexon™) was in the 1970 and led a new trend in synthetic absorbable suture materials and devices.[28,50,52]

Nowadays, a new approach in developing novel concepts and designs of suture materials has been required by the increasing complexity and technical needs of internal surgical application. Since knotting induces a decrease in mechanical properties and it is considered a critical point in the suturing technique, new physical configurations have been designed, such as knotless suture materials and 'smart sutures'. For example, this smart suture possesses thermal properties that allow to seal difficult wounds where access is limited, reacting with temperature and provoking self-knotting action.[53] On the other hand, the attention of researchers is also directed to a complex biological behavior, not only antimicrobial activity, but also bioactive, anesthetic and antineoplastic functions.[28]

1.3.2 CHARACTERISTICS OF SUTURE MATERIALS

Suture materials are characterized and evaluated involving physical/mechanical properties, handling characteristics, biological and biodegradation behavior. Figure 1.10 summarizes the broad variety of properties.[50]

Figure 1.10. Properties of suture materials.

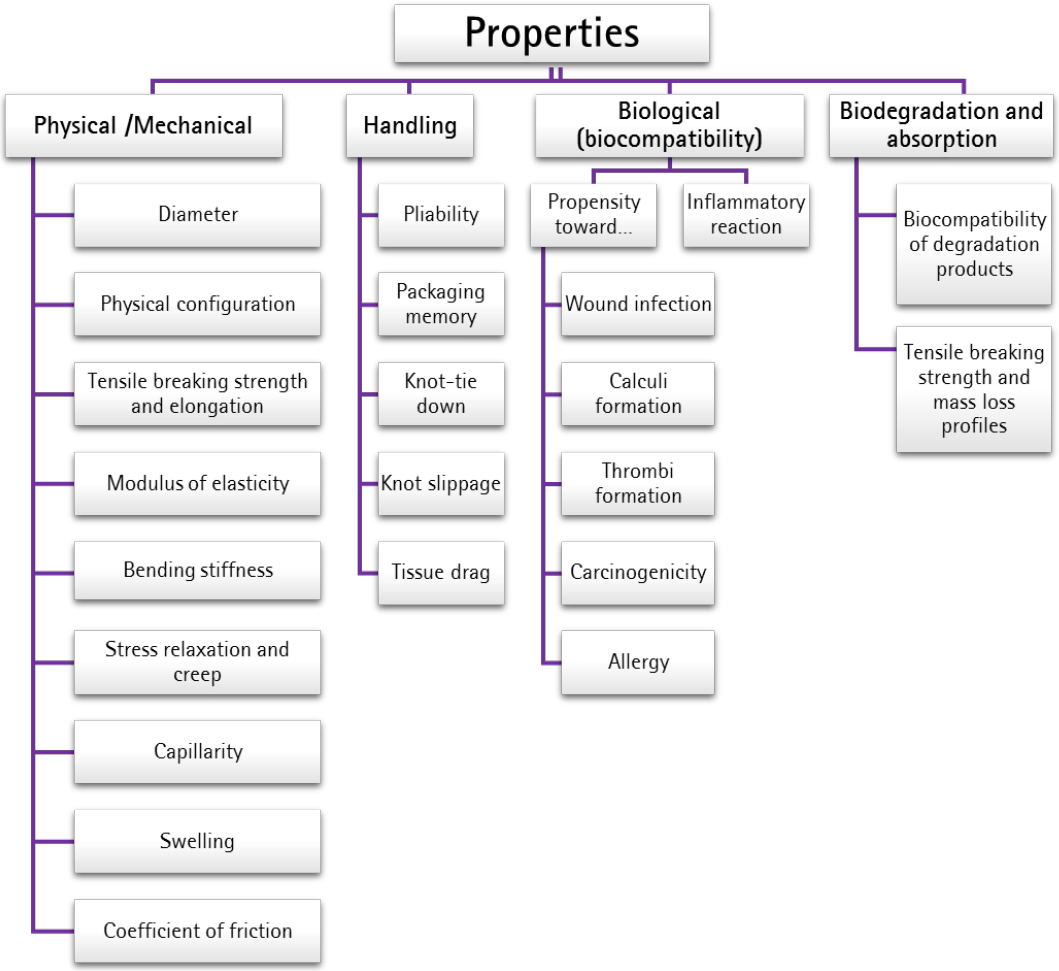

The good performance of the suture materials depends on their physical properties as well as tissue compatibility and surgical handling. Furthermore, the degree of tissue reaction is directly influenced by the mass of the suture and the time it remains in the tissue, clearly associated with the biodegradation / absorption rate.[50]

The ideal suture should be easy to tie, form secure knots, having excellent tensile strength, not produce adverse effects on wound healing or promote infection, and be easily visible in the surgical intervention. It should be able to stretch, accommodate wound edema and recoil to its original length with wound contraction. In addition, the ideal suture would be easily sterilized, readily available and with a reasonable cost. In most applications, surgical sutures are not permanently required. The longer suture mass stays in the human body, the more likely it is to produce undesirable tissue reactions. Thus, an ideal suture should retain enough tensile strength during the wound healing period, and its mass should be absorbed as soon as possible without overloading the metabolic capacity of the surrounding tissues once the sutures is no longer functional.[52,54,55]

Obviously, the perfect suture is unobtainable because no single material can fulfill all the above mentioned criteria. Surgeons must choose the most appropriate suture for the specific type of surgery, depending on the characteristics of the tissue involved and various patient factors, such as debility, respiratory problems, obesity, *etc.*, which affect directly the healing rate of tissues, and the potential post-operative complications.[56–59] Since a universal suture does not exist, surgeons and medical designers have focused on developing custom sutures with tailored properties, in order to fulfill the requirements of the specific surgical intervention. Therefore, the task of suture selection has become challenging by the wide variety of suturing materials available.

1.3.3 CLASSIFICATION OF SUTURE MATERIALS

In general, sutures may be made from naturally source or synthetic fibers, and are classified as non-absorbable or absorbable. The following tables (Tables 1.2 and 1.3) listed some current non-absorbable and absorbable surgical sutures that are available in the market. Although only few companies share the leadership in the market, there are a lot of commercial brands and manufacturers (not included in the tables but cited in references).[9,60–85]

In all cases, most of suture materials are based on the same raw polymers which hinder the incorporation of innovative polymeric materials in this competitive market.

Table 1.2. Representative non-absorbable surgical sutures commercially available of B. Braun Surgical.[9]

Brand name	Material	Physical configuration	Indications
		Natural Sutures	
Linatrix®	Linen	Multifilament (twisted) Coated	Ligatures in gastrointestinal surgery
Silkam®	Silk	Multifilament (braided) Coated	General surgery, skin closure, oral surgery, neurosurgery, ligatures
Virgin silk	Silk	Multifilament (twisted)	Ophthalmic surgery
		Synthetic Sutures	
Dafilon®	Nylon 6 / 6.6 (dyed blue or undyed) Nylon 6.6 (dyed black)	Monofilament	Skin closure, plastic and reconstructive surgery, microsurgery, ophthalmic surgery
Dagrofil®	Polyester	Multifilament (braided)	General surgery, orthopaedics, ligatures
Optilene®	PP/PE	Monofilament	Cardiovascular surgery, neurosurgery, ophthalmology, microsurgery, general soft tissue approximation
PremiCron®	Polyester	Multifilament (braided) Coated	Cardiac surgery (valve surgery), general surgery
Supramid®	Nylon 6.6 Nylon 6	Multifilament (core) Monofilament (shell)	Skin closure
Steelex®	Stainless Steel	Monofilament Multifilament (twisted)	Orthopaedics, sternal closure
Trelon®	Nylon 6.6	Multifilament (braided) Coated	General surgery, neurosurgery

Table 1.3. Representative absorbable synthetic surgical sutures commercially available of B. Braun Surgical.[9]

Brand name	Material	Physical configuration	Indications
		Synthetic Sutures	
MonoMax®	Poly-4 hydroxybutyrate	Monofilament	Closure of abdominal wall
MonoPlus®	Polydioxanone	Monofilament	Orthopaedics, paediatric cardiovascular surgery, general surgery, abdominal wall closure
Monosyn®	Copolymer of glycolide, trimethylene carbonate and ε-caprolactone	Monofilament	Gastrointestinal surgery, gyneacology and obstetrics, urology, skin closure, paediatrics, ligatures
Monosyn Quick®	Copolymer of glycolide, trimethylene carbonate and ε-caprolactone	Monofilament	Plastic surgery, gyneacology and obstetrics, urology and paediatrics, odontology, maxilofacial
Novosyn®	Poly(glycolide-*co*-*L*-lactid) 90/10	Multifilament (braided) Coated	Gastrointestinal surgery, gyneacology and obstetrics, orthopaedics, ophthalmic surgery, urology, skin closure, ligatures
Safil®	Polyglycolic acid	Multifilament (braided) Coated	Gastrointestinal surgery, gyneacology and obstetrics, ophthalmic surgery, urology, skin closure, neurosurgery, ligatures
Safil Quick®	Polyglycolic acid	Multifilament (braided) Coated	Gyneacology and obstetrics, urology, ophthalmic surgery, odontology, paediatric surgery, skin closure, ligatures

Specifically, a suture is considered absorbable when it loses most of its breaking strength within 60 days after placement. By this definition, poly(glycolide-*co*-L-lactide) 90/10, polyglycolic acid, catgut, and poly(*p*-dioxanone) are all included in absorbable sutures. Silk and nylon, although they are considered as non-absorbable, are actually also absorbed, but more slowly over many months.[52] Amongst absorbable sutures, synthetic ones are preferred because hydrolysis is more stable, reproducible and predictable mechanism, minimizing chronic undesirable tissue reactions when the sutures have lost their function.[28,86]

In terms of physical configuration, the thread itself may also be multifilament or monofilament (Figure 1.11).

Multifilament conformation consists of several filaments or strands being braided or twisted together, resulting in a strong suture that is flexible and easy to handle.[28] Normally, multifilament suture are known as braided suture because it is the common configuration for multifilament threads. The first absorbable sutures belong to multifilament (braided) category. They were based on polyglycolic acid and poly(glycolide-*co*-L-lactide) 90/10 and commercialized as Dexon™ and Vicryl™, respectively. However, there are some inconvenient related to multifilament sutures. As a consequence of their physical structure, the surface is less smooth resulting in a less easily pass through the tissue, which could cause tissue trauma. In addition, braided and twisted sutures possess a high degree of capillarity, which is correlated with a tendency to absorb and retain fluid and to harbor bacteria. This may promote the risk of infection if bacterial contamination occurs during or shortly after surgery.[87] Both problems, tissue drag and capillarity, associated with multifilament, are significantly reduced by coating the braided material.[28]

In contrast, the surface of a monofilament is very smooth and passes easily through tissue, minimizing the tissue drag and reducing infections. In addition, the lack of capillarity on the surface prevents the penetration and migration of pathogens agents, avoiding the infection risk along the wound closure. The first absorbable monofilament was based on poly(*p*-dioxanone) and was commercialized as PDS™ at 1980s. However, monofilament threads are less flexible than multifilament, meaning a difficult handle and tie. Moreover, most of monofilament constructions also have a memory effect, a bad trait, because they hold the shape they had in the package, making more difficult to work with.[86,88]

Figure 1.11. SEM micrographs of different physical configuration of thread sutures: **(a)** multifilament (braided) thread and **(b)** monofilament thread.

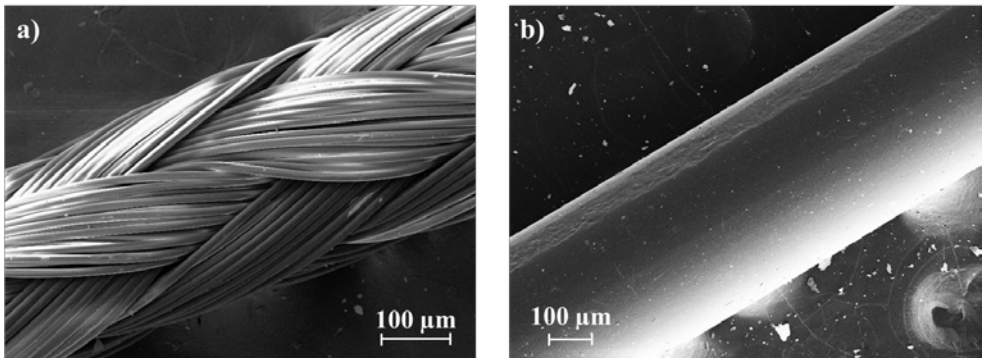

Even though the mentioned drawbacks from monofilament sutures, an increasing number of surgeons believe that monofilament products will play an important role in the future.[89] Therefore, the investigations are focused on providing monofilament sutures with similar physical and mechanical properties of braided ones.

1.3.4 DEGRADATION PHENOMENA AND ABSORPTION

On suture materials, the degradation takes place mainly through hydrolysis, with or without enzymes, that leads a breakage of the backbone macromolecules and a decrease of their chain length during the process. As a result, their physical, mechanical, thermal, and morphological properties change.

There are three most important properties used to describe degradation phenomena [90]:

(i) The loss of tensile strength profile
(ii) The loss of mass profile
(iii) The type of degradation products released into surrounding tissues.

Ideally, mass loss and strength loss profile should be synchronized, but in practice, the profile of strength loss always occurs much earlier than the profile of mass loss. This fact is due to both, the inherent dependence of fiber strength on tie-chain segments in the noncrystalline domains of fibers and the two-step hydrolytic degradation observed in all semicrystalline fibers.

The hydrolytic degradation is known to start in the amorphous regions and then extend to the crystalline domains due to the inability of water molecules to penetrate into the

tightly packed crystalline domains. This two-step hydrolytic degradation mechanism results in distinctive patterns of changes in molecular weight, strength, mass, diameter, level of crystallinity, crystallite size, fiber orientation, and surface and interior morphology. Namely, the hydrolytic scissions of tie-chain segment in the amorphous regions would be reflected in the observed loss of tensile properties, while the mass loss must come from the destructions of the crystalline domains.

For absorbable suture, degradation is an inherent property which leads to absorption phenomena. Thus, the ability of water to penetrate into the suture determines whether the degradation follows a bulk, surface, or both modes. In general, evidence available indicates that absorbable sutures degrade hydrolytically through the bulk mode, whereas the non-absorbable sutures degrade through the surface mode. Bulk hydrolytic degradation would result in a fast loss of tensile strength within a short period of time, while the surface mode of degradation would retain tensile strength for a longer period than the bulk mode.

The biocompatibility of degradation products is usually not a problem because all existing absorbable sutures are made from the well-known biocompatible glycolide, lactide, and their derivatives. However, biocompatibility of degradation products also depends on the rate of their accumulation in the surrounding tissues. This implies that the ability of the surrounding tissues to actively metabolize degradation products is essential.[91]

The rate of absorption is commonly determined as a percentage of the remaining breaking strain and it can vary. Depending on the time required for reabsorption, wound closure devices can be grouped into four categories (Table 1.4).

Table 1.4. Examples of applications according to absorption time. [92]

Absorbable suture	Absorption time	Examples of applications
Short-term	aprox. 50 days	Fast-healing tissues (skin, mucosa), episiotomy
Mid-term	60 – 90 days	Soft tissue approximation: general surgery, orthopedics, urology, ophthalmology, gynecology, maxillofacial, plastic, neurosurgery
Long-term	180 – 210 days	Vascular surgery, abdominal wall closure, orthopedics
Extra-long-term	390 days	Abdominal wall closure, difficult healing

1.4 Coating materials for surgical suture

1.4.1 INTRODUCTION

Suture materials are frequently coated, especially most braided or twisted sutures to homogenize the surface[93] as well as to facilitate their handling properties, particularly a reduction of tissue drag effect when passing through the needle tract, precise knot placement and smooth tie-down. Although coating of suture materials facilitates easy passage through tissue and handling properties, it frequently results in poor knot security.[91]

Traditionally, coating materials were bees wax, paraffin wax, silicone, poly(tetrafluoroethylene), *etc*. The current trend is going toward a coating material with chemical properties similar to the selected suture. Thus, the coatings depend upon whether the suture is absorbable or non-absorbable. Furthermore, absorbable coating materials should have better tissue biocompatibility because of the lack of chronic tissue reaction. Absorbable coatings integrate calcium stearate with poly(ε-caprolactone), copolymer of glycolic acid and lactic acid (*PGLA 30:70)*, and/or copolymer of glycolic acid and poly(ε-caprolactone).[28]

There are mainly two types of absorbable coatings materials: water insoluble and water soluble. Water insoluble coatings have similar chemical constituents to the suture, and they are broken down by hydrolysis, so they remain on the suture surface longer than water soluble coating. On the contrary, water soluble coatings dissolve promptly to reveal the underlying uncoated suture after wound closure, which have better knot security.[91,94]

Although, initially coatings were applied on multifilament suture, it has been extended to monofilament suture. A novel copolymer constituted by lactic acid and ε-caprolactone was designed to solve the poor handling. Even though that new copolymer reached enough handling characteristics, the tenacity of the strand was not sufficient due to the nature of the components. In order to overcome those shortcomings of monofilament sutures, coating material comprising an ε-caprolactone homopolymer or its copolymer with another absorbable monomer and calcium stearate was patented.[95] Moreover, it was reported that water soluble coatings based on poly(ε-caprolactone) or copolymer of at least 90% by weight of ε-caprolactone and almost 10% of other biodegradable monomers like glycolide, lactide and their derivatives improve knot tie-down and knot security.[96–98]

Following the same purpose of improving knot security, a patented random copolymer of 25-75% by weight of glycolide and trimethylene carbonate was suggested to have the advantages of not flaking off from the substrate sutures because of its high molecular weight and low glass transition temperature and to retain its lubricant property even when the coated suture was wet.[99]

The recent approaches are focused on developing an antibacterial coating material for multifilament surface as well as monofilament suture, in order to avoid and prevent the potential wound infection.

1.4.2 SURGICAL SITE INFECTIONS (SSIs)

Surgical site infections (SSIs), formerly called surgical wound infections, are defined as infection occurring at, or near the site of surgery within 30 days after the operation or within 1 year if implant is in place.[100]

Roughly, risk factors of having SSIs can be classified into patient-related (e.g., age, severity of illness, obesity, malnutrition, smoking, *etc.*), operation-related (Table 1.5) and operation room environment-related, mainly considering ventilation and number of people and traffic.[101,102]

Table 1.5. Operation-related factors that may influence the risk of SSIs development. [100,102,103]

	Operation-related characteristics
Preoperative	Preparation of the patient
	Hand/forearm antisepsis for surgical team member
	Management of infected or colonized surgical personnel
	Antimicrobial prophylaxis
Intraoperative	Cleaning and disinfection of environmental surface
	Microbiologic sampling
	Sterilization of surgical instrument
	Surgical attire and drapes
	Surgical duration
	Asepsis and surgical technique
Postoperative	Incision care
	Discharge planning

SSI has a high cost associated, since it leads a prolonged hospitalization, more dressing materials and longer antibiotic treatment. Also, depending on the surgical intervention, the SSI may follow by infectious complications, which may require a second surgery.[104]

The most surgical site infections are related to many different factors. One of them is also the surgical suture, since the presence of foreign materials in wound has been known to enhance the risk of infection of the surrounding tissues. The susceptibility of suture materials to produce bacterial infection in surgical wounds vary depending on physical configuration, specific microbial species and chemical composition of the device.[105,106]

Multifilament form results in higher affinity for microbial colonization than the same sutures in monofilament form. Twisted sutures produce more infection than braided ones, due to the rather loose arrangement of the fibers in the twisted form.[107]

Capillarity is also an important feature related to wound infection. It is an inherent physical property of multifilament suture because of the available interstitial space and hence, it is related to the ability of a suture to transport or spread microorganisms.[91]

Any suture material based on natural or synthetic composition and mono- or multifilament structure is susceptible to bacterial attachment and colonization. Furthermore, bacterial species are capable of forming biofilms which potentiate the infection. Once stablished, biofilms bacteria are difficult to treat because, shielded within the matrix, they have a much higher resistance to conventional antibiotics and antiseptics [108] and may lead to chronic microbial infection and tissue necrosis.[109]

The use of antibacterial sutures is expected to provide protection from wound infection, not only in multifilament forms but also in monofilament configuration.[110]

1.4.3 ANTIBACTERIAL SUTURES

In 1965 it was reported a recommendation that all suture materials should be steeped in a 1/2000 solution of chlorhexidine before suturing in order to reduce SSI.[111] Since the early 1980s, development of an antibacterial surgical suture has been under consideration. Although experimental research and findings have been interesting, the development of a FDA-approved surgical suture has been slow, in part due to the technical issues involving product safety, stability and standardization.[112]

There are few major antibacterial strategies applied to suture and biomaterials in general (Figure 1.12):

- **passive coatings** based on cationic biopolymer and 'intelligent' surface that prevent bacterial attachment and have antimicrobial properties. An example of passive coating employs thermal nanoparticles which show surface plasmon resonance effect. In this case, coated substrate is converted into a bacteriostatic and bactericidal surface when it is light irradiated.[113]
- **active coatings** that release active compounds in the tissue and kill suspended bacteria.
- **nanostructured surface** that have the capacity of preventing bacterial attachment and biofilm formation, reducing contact area available between bacteria and surface and without affecting the macroscopic degradation properties.[114,115]

Although, the interest in nano-patterning has increased in recent years, effectiveness of passive and active strategies has been the main topic to investigate and evaluate in terms of antibacterial suture materials.

Figure 1.12. Surface modification methods for different antibacterial strategies. Passive coating includes **(a)** hydrophilic surface, **(b)** hydrophobic surface, **(c)** zwitterionic surface, **(d)** cationic antimicrobial surface and **(e)** biomolecule functionalized surface. **(f)** Active coating as drug eluting surface. **(g)** Nanostructured surface.

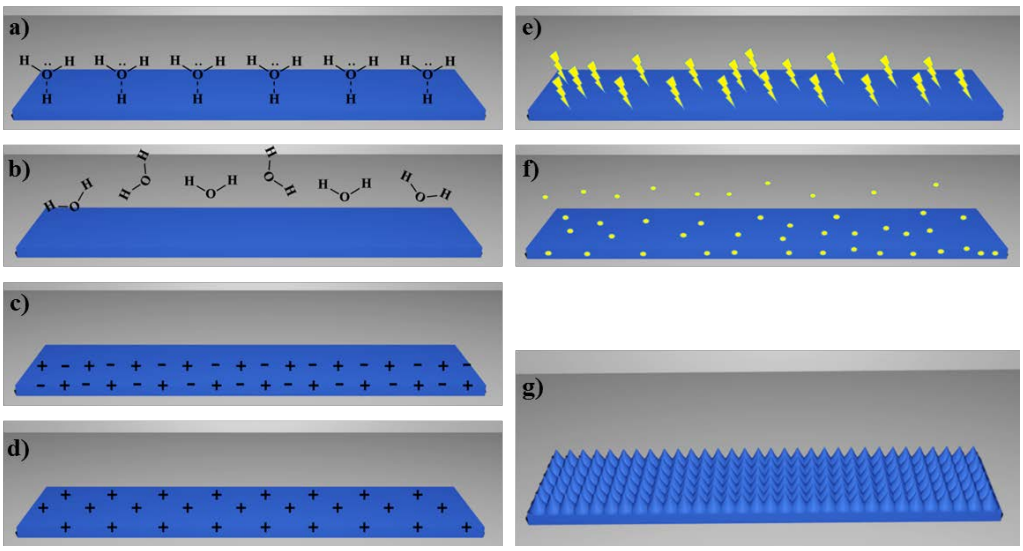

In terms of biocompatibility passive strategies are preferred, though active strategies are often more effective in spite of toxicity issue and the development of resistant microbial strains compromise their application.[114] Commonly, active strategies are related to preventive approaches which include antimicrobial ion (e.g., silver-ion), prophylactic antibiotics before the biofilm can form and potential antiseptics (e.g., chlorhexidine, polyhexamethylene biguanide, nitrofurazone,[116] octenidine,[117] and triclosan).[118]

The antimicrobial properties of the silver ion have been exploited for a long time. When metallic silver reacts with moisture on the skin surface or with wound fluids, silver ions are released, damaging bacterial RNA and DNA, hence inhibiting replication. In recent years, silk and poly(glycolide-*co*-L-lactide) 90/10 sutures were coated with silver-doped bioactive glass by dipping process. The resulting coated sutures showed both antibacterial and bioactive properties through *in vitro* assays.[119] Other formulation of silver has also been employed for antibacterial purpose. In this case, silver nanoparticles were sequentially deposited layer-by-layer, leading to the growth of an onion shell type of coating.[120]

On the other side, antibiotics generally have single pharmacological target, whereas antiseptics have several or multiple targets. The first antibacterial suture commercially available was Coated Vicryl Plus® Antibacterial suture, a poly(glycolide-*co*-L-lactide) 90/10 multifilament impregnated with triclosan, which is a broad-spectrum antiseptic. Triclosan coated sutures have not been only limited to multifilament threads. Monofilament sutures constituted by glycolide and ε-caprolactone copolymer and poly(p-dioxanone) have been introduced in the market, commercially known as Monocryl™ Plus and PDS™ Plus, respectively. The efficiency of antibacterial sutures has been evaluated in several studies, including *in vitro* and *in vivo* assays, as well as clinical trials.

In vitro assays demonstrated that triclosan coated sutures were highly effective in reducing the adherence of selective Gram-positive, Gram-negative, drug-resistant, and biofilm-forming strain to the surface.[112,121–123] When comparing monofilaments with Coated Vicryl Plus® Antibacterial suture, the excellent performance of the monofilaments makes questionable whether the additional cost associated with antimicrobial forms are justified.[124]

In vivo experiments showed that Coated Vicryl Plus® Antibacterial suture prevents bacterial colonization and modulates the inflammatory response allowing tissue healing.[125]

Whereas, under simulated conditions of severe intraoperative contamination, the antibacterial suture reduced the number of positive cultures after orthopedic surgery.[126]

The sutures with triclosan were compared clinically to non-impregnated suture materials. The former sutures were shown to perform as well or better than traditional sutures with respect to intraoperative handling and wound healing in pediatric general surgery,[127] pediatric neurosurgery,[128] thoracic[129] and abdominal surgery.[130–132] However, other studies suggest that Coated Vicryl Plus® Antibacterial suture do not show any efficacy in the bacterial inhibition, even more, it seems to have adverse effects on wound healing.[104,133,134]

Recently, some studies in breast surgery showed that multifilament and monofilament threads coated with triclosan presented better cosmetic outcomes and efficiency in reducing SSI,[135,136] particularly in the high-risk group.[137] Also in dentistry, the use of this antibacterial suture, instead of silk suture, provided little safety in the control of SSI.[138] Other current study has concluded that triclosan coated suture does not reduce the incidence of sternal SSI after a coronary artery bypass grafting (CABG) [139] or have some local side effect in colorectal surgery.[140]

Over these years, since the first antibacterial suture was launched into a commercial market, the study of effectiveness has been continued and the results are still unclear. Given the conflicting results in the literature on the benefit and harm of triclosan-impregnated materials on incision healing, further large randomized controlled trials are needed before introducing it in a routine clinical use.

Consequently, many research lines are focused on developing new antiseptic coating strategies, as the addition of a coating after the impregnation of triclosan,[141] or incorporating other antiseptics instead of triclosan, for example chlorhexidine. Actually, commercial sutures with chlorhexidine are available exclusively for veterinarian field (e.g., Visorb® Plus, Monoswift® Plus and Mono-Dox® Plus from CP Medical). Furthermore, researchers also include this antiseptic in new strategies for coating methods. For instance, using layer-by-layer self-assembly technique, chlorhexidine-functionalized polyelectrolyte films were developed to inhibit bacterial proliferation[109] or synthesis of chlorhexidine coating based on fatty acids to achieve a slow release for suture materials.[142]

Other alternatives refer to the incorporation of different kind of drugs, not only antiseptic, but pain-relief. The incorporation of ibuprofen on coated multi- and monofilaments by immersion of the suture in the solution with certain concentration of drug and coating was evaluated by means of *in vitro* release.[110] The main inconvenient of dipping, grafting or encasing drug in the suture thread is the possibility to damage or adversely influence the mechanical strength of the suture. For this reason, the incorporation of pain-relief drug in a polymeric sheet which was braided around the multifilament suture has recently been evaluated.[143] Also, melt spun bioactive sutures containing nanohybrid for local delivery of anti-inflammatory drugs were also developed.[144] The effectiveness of ibuprofen in the polymeric sheet and diclofenac in the melt spun bioactive suture was also proved in *in vivo* experiments.[143,144]

1.5 Tissue engineering

1.5.1 INTRODUCTION

Tissue engineering, also called regenerative medicine, is an interdisciplinary field which uses three basic components (cells, scaffolds and biomolecules) to develop biofunctional substitutes for restore and maintenance of tissue function which has been destroyed by disease, injury or congenital defects without stimulating any immune response.[145]

Ideally, a tissue engineering scaffold must have the following characteristics: (i) three-dimensional and highly porous with an interconnected pore network for cell growth and flow transport of nutrient and metabolic waste; (ii) biocompatible and bioresorbable with controllable degradation and resorption rate to match cell/tissue growth; (iii) suitable surface chemistry for cell attachment, proliferation and differentiation and (iv) mechanical properties to match those of the tissues at the site of implantation.[146] However, requirements of scaffold are directly dependent of the kind of tissue where it will be implanted. Thus, flexibility and stiffness have to be within the same order of magnitude as the surrounding tissues in order to prevent either breaking, collapsing or stress shielding the adjacent tissues.

Targeted tissue dictates the optimum scaffold design because a universal scaffold with all the requirements of various tissues do not exist. Versatility of bioabsorbable polymers make them the best candidates as scaffolding materials, because they can be employed to

provide a temporary function for newly-forming tissue. Bioabsorbable polymers can be subsequently replaced by native tissue with the polymer material getting removed by natural and metabolic processes of the body, without generating any residual material that can act as focus of irritation.

The most widely used synthetic biopolymer to prepare scaffolds are PLLA, PCL, PGL and lactide-*co*-glycolide copolymer, which have an outstanding biocompatibility, biodegradability and mechanical properties.[147,148]

Over the last decade, electrospinning technique has enable the development of scaffolds and multifunctional fibers that are capable of releasing drugs, such as antibiotics, anticancer drugs, polypeptides or polynucleotides, *etc.*

1.5.2 PREPARATION OF SCAFFOLDS: ELECTROSPINNING TECHNIQUE

The renewest interest in electrospinning as a potential processing technique for application in tissue engineering can be attributed to its ease of use, adaptability, and the ability to fabricate continuous fibers with diameters on nanometer size scale. Moreover, fibers can be obtained with using very small amounts of polymeric solution. Electrospinning process affords the opportunity to engineer scaffolds from micro to nanoscale topography and high porosity similar to the natural extracellular matrix. The inherently high surface / volume ratio of electrospun scaffolds can enhance cell attachment, drug loading and mass transfer properties.[149]

Electrospinning equipment is manly constituted by three components: a syringe as a reservoir for polymer solution, a needle, a high-voltage power supply and a metallic collector. The electrospinning process consists in the application of a high voltage on the polymer solution between the needle and the collector. At the needle tip, the polymer solution deforms from a spherical pendant droplet to a conical shape (Taylor cone) (**Figure 1.13**).

Figure 1.13. Schematic illustration of the formation of the Taylor cone.

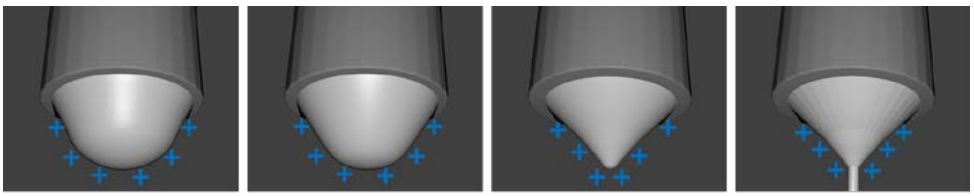

As the electrostatic forces of repulsion are stronger than the surface tension of the polymer droplet, the charged jet is ejected from the cone surface and is deformed uniaxially through the electric field toward the collector. The solvent is evaporated and the polymer jet is accelerated, leading to the ultrathin polymer fibers of non-woven mat on the collector (Figure 1.14).[149,150] The process may occur either at room temperature or inside a fume chamber, depending on the used polymer and solvent type. Electrospinning is also possible without solvent, by using melt polymers in a vacuum chamber.[147]

Figure 1.14. Schematic illustration of a typical basic electrospinning setup.

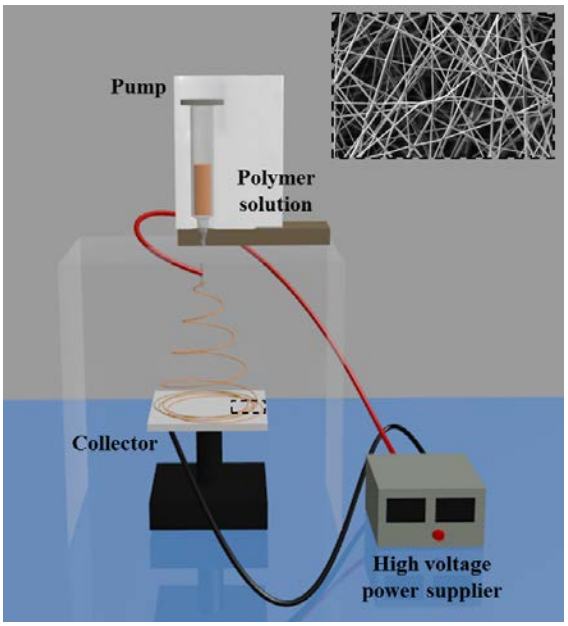

The morphologies and sizes of the electrospun fibers depend on the adjustment of several parameters (Table 1.6).[151]

Table 1.6. Parameters of electrospinning and their common effects on fiber morphology.

Parameters	Effect on fiber morphology
Viscosity / concentration	Low values → defects in form of beads and junctions High values → reduction of defects / Increase of fiber diameters
Conductivity / Solution charge density	High conductivity → production of uniform bead-free fibers / smaller fibers in general (except PAA and polyamide-6)
Surface tension	No conclusive relation
Polymer molecular weight	High values → reduction the number of beads and droplets
Dipole moment and dielectric constant	High dielectric constant → successful spinning occurred in solvent
Flow rate	Low values → fibers with smaller diameters High values → not dried fibers upon reaching the collector
Field strength / Voltage	High voltage → beading effect Relation of voltage with fiber diameter is ambiguous
Distance between tip and collector	Minimum distance is required to obtain dried fibers Too far / too close → beading effect
Needle tip design	Coaxial → hollow fibers Multiple needle tips → increase throughput
Collector composition and geometry	Metal collector → smoother fibers Porous collector → more porous fiber structure Conductive frame, rotating drum or wheel-like bobbin collector → aligned fibers* Yarns and braided fibers
Ambient parameters	High temperature → decrease in solution viscosity → smaller fibers High humidity → appearance of circular pores on the fibers

**Aligned fibers are important to guide regeneration of tissue like neural, ligamentous, etc.*

These parameters can be classified into three categories:

(i) **Solution properties**, i.e., viscosity, conductivity, surface tension, polymer molecular weight, dipole moment, and dielectric constant.

(ii) **Processing variables**, i.e., flow rate, electric field strength, distance between tip and collector, needle tip design, and collector composition and geometry.

(iii) **Ambient conditions**, i.e., temperature, humidity, and air velocity.

1.5.3 MULTIFUNCTIONAL SCAFFOLDS

Functionalization of fibers can be achieved through different approaches. For example, by the incorporation of drug in the fiber scaffold itself or by a post-electrospinning coating with loaded drug substance (Figure 1.15a).

In general, drug incorporation can be understood as drug included in surrounding substance, in this case, polymeric fibers, *embedded drug*, or as a drug enclosed like a capsule in the polymeric fibers, *encapsulated drug*.

(i) **Embedded drug.**

The procedure consists in mixing the bioactive agent with the biodegradable polymer solution to prepare bioactive composite fibers by means of electrospinning technique (Figure 1.15b).

Drug characteristics and its interactions with the appropriate polymer in the mixture can affect drug incorporation. The favorable case is when agent/drug is included inside the fibers, leading a sustainable release. However, it is also possible the superficial deposition of drug on fibers. In this case, a worse situation takes place when almost all drug is placed in the fiber surface since a high burst release in the initial stages can occur.

Other disadvantage for embedded drug is due to its dissolution in an aggressive solvent. The exposure of some bioactive molecules such as growth factor, to harsh solvent could lead to their loss of bioactivity. Consequently, several nanoscale carriers are employed to immobilize and encapsulate the therapeutic drug.

(ii) **Encapsulated drug:**

Capsule-like devices into fibers can be obtained by a specific electrospinning procedure:

a. **Coaxial electrospinning** (Figure 1.15c). This method produces fibers with a core-shell structure. The loaded agent can be included in the core, and shell may work as a control mechanism over the release. It is an easier process and has a higher efficiency.

b. **Emulsion electrospinning** (Figure 1.15d). The technique consists in the emulsification of core materials in a solvent (including agent or drug), dissolution of fiber forming polymer in the continuous phase and afterwards, electrospinning the resulting mixture.[152]

The release profiles of bioactive compound can be designed as rapid, immediate and delayed manner, depending on the nature of polymer, properties of drug, initial drug load, drug–matrix interaction, fabrication method and the resulting fiber geometry.

(i) **Nature of polymer:** drug release from semi-crystalline polymer fibers exhibits a rapid burst release and a subsequent relatively slower sustained release.
(ii) **Properties of drug:** high crystalline drug tends to move onto the fiber surface during electrospinning and trigger burst release, while drug in amorphous state can be easily encapsulated inside of the fibers and be released in a sustained manner.
(iii) **Initial drug loading:** higher initial drug loading results in a faster drug release.
(iv) **Drug–matrix interaction:** compatibility of drug and polymer solution as well as the interaction between them is relevant to determine the drug release kinetic in a nanofiber based drug delivery system.

The main purpose of bioactive multifunctional scaffolds is to achieve a controlled drug delivery system. In general, drug can be released by means of three mechanism: diffusion, chemical reaction and solvent activation. Most of the current nanofibers-based drug delivery systems are classified as diffusion-controlled system, which can be divided into matrix-type and/or reservoir-type.[153]

- **Matrix-type** is associated to the embedded drug incorporation method, where the drug is homogeneously distributed into the polymeric matrix. This method can provide diffusion-mediate biphasic drug release by a slow controlled release after a burst effect.
- **Reservoir-type** normally includes coaxial electrospinning method, where drug is surrounded by a polymer shell. It forms a core-shell structure which allows a constant and prolonged release.

Figure 1.15. Examples of drug incorporation in electrospun fibers: (a) post-electrospinning coating with bioactive agent, (b) embedded drug, (c) coaxial electrospinning and (d) emulsion electrospinning.

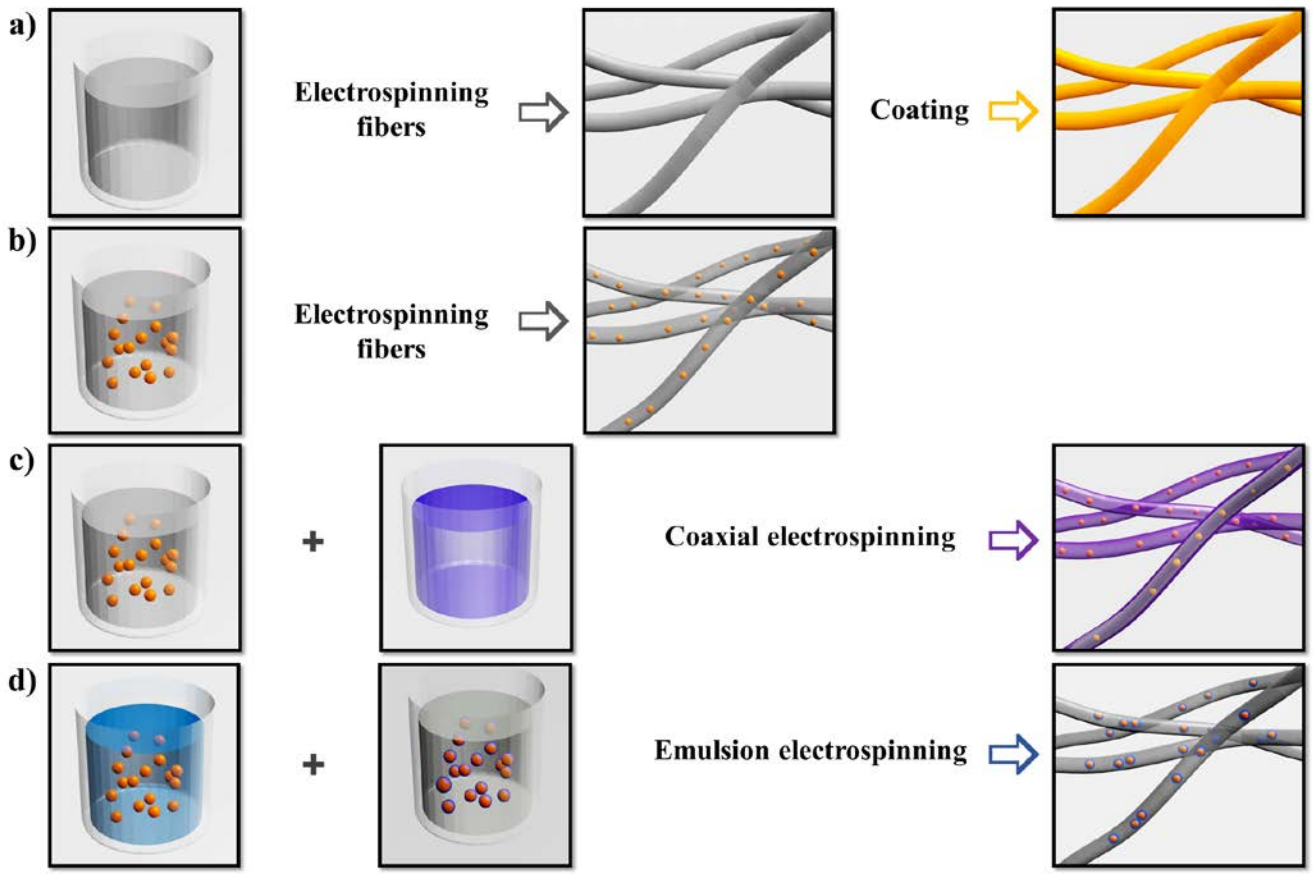

Furthermore, degradable characteristic of polymeric materials is an extra factor to take into account in the drug release profile. In biodegradable systems, scaffold degradation contributes to drug release. Thus, tailoring biodegradation rate in relation diffusion release rate is quite important. For example, if polymeric matrix starts to biodegrade by bulk erosion, before the drug is continuously released, a burst effect or high concentration of delivered drug may occur with a potential toxic level for the tissue.

1.5.4 REINFORCED SCAFFOLDS

The increasing interest in electrospinning technique to produce multifunctional scaffolds and its versatility to be employed in certain applications has favored the use of continuous or short nanofibers[154] for reinforcement.

Generally, reinforcing action requires that the generated structure possesses a higher stiffness and strength than the matrix. In addition, the reinforcement should be well "bonded" to the matrix polymer and consequently, the stress can be transferred from the weak matrix to the strong reinforcing structure.[155]

There are two main approaches to prepare reinforced scaffolds in terms of variety of components: self-reinforced composites (SRC) or heterogeneous composite (Figure 1.16).

Figure 1.16. Examples of reinforced scaffolds: **(a)** self-reinforced composite and **(b)** heterogeneous composite.

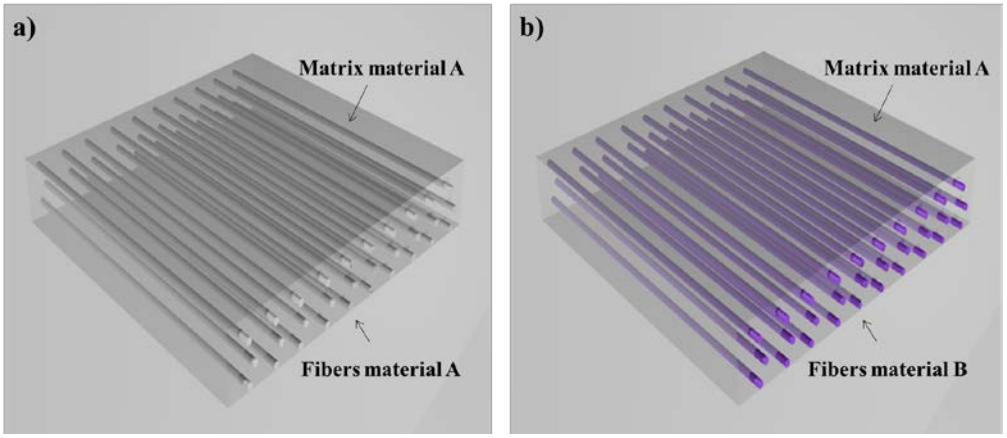

Strictly, the former refers to a composite comprising polymeric oriented reinforcing elements (usually fibers or tapes) or rigid particles in a matrix of the same polymer. However, there are other kinds of SRCs based on molecular orientation. They comprise homogeneous polymers or polymer blends that have a level of preferred molecular orientation to work as reinforcement[156] (e.g., self-reinforced PLLA suture[157]). On the other hand, heterogeneous composite is based on the combination of different materials or distinct polymers belonging at the same family, to enhance the reinforcement action (e.g., amorphous polymer sheets and highly crystalline polymeric fibers).

Preparation of reinforced scaffolds is commonly made by film stacking and compression molding, in which the chosen film generally has a lower melting point than the fibers.

Since reinforcing fibers can incorporate bioactive agents, the huge possibilities of combined scaffolds have been a new strategy to enhance mechanical properties as well as controlled drug release.

1.6 References

1. Williams, D. F. In *Definitions in biomaterials, in Proceedings of a Consensus Conference of the European Society for Biomaterials* (ed. ESB) (Elsevier, 1987).
2. Williams, D. F. On the nature of biomaterials. *Biomaterials* **30,** 5897–5909 (2009).
3. Williams, D. F. On the mechanisms of biocompatibility. *Biomaterials* **29,** 2941–2953 (2008).
4. Ulery, B. D., Nair, L. S. & Laurencin, C. T. Biomedical applications of biodegradable polymers. *J. Polym. Sci. B. Polym. Phys.* **49,** 832–864 (2011).
5. Kuhn, L. T. In *Introduction to Biomedical Engineering* 278–335 (2005).
6. Jandt, K. D. Evolutions, revolutions and trends in biomaterials science - A perspective. *Adv. Eng. Mater.* **9,** 1035–1050 (2007).
7. Tathe, A., Ghodke, M. & Nikalje, A. A brief review: biomaterials and their application. *Int. J. Pharm. Pharm. Sci.* **2,** 19–23 (2010).
8. *Polymeric biomaterials.* (Ed. Severian Dumitriu) (2002).
9. B. Braun Sharing Expertise. at <https://www.bbraun.com/en/products/>
10. Karlsson, S. & Albertsson, A. Biodegradable polymers and environmental interaction. *Polym. Eng. Sci.* **38,** 1251–1253 (1998).
11. Jain, J. P., Ayen, W. Y., Domb, A. J. & Kumar, N. Biodegradable polymers in drug delivery. In *Biodegradable Polymers in Clinical Use and Clinical Development* (eds. Domb, A. J. & Kumar, N.) 1–58 (Wiley & Sons, 2011).
12. Nair, L. S. & Laurencin, C. T. Polymers as biomaterials for tissue engineering and controlled drug delivery. *Adv. Biochem. Eng. Biotechnol.* **102,** 47–90 (2006).
13. Domb, A. J. & Khan, W. Biodegradable polymers as drug carrier systems. In *Polymeric Biomaterials* (ed. Severian Dumitriu) 135–175 (2012).
14. Wang, X. L., Yang, K. K. & Wang, Y. Z. Properties of starch blends with biodegradable polymers. *J. Macromol. Sci. Part C Polym. Rev.* **43,** 385–409 (2003).
15. Albertsson, A. C. Degradable polymers. *J. Macromol. Sci. Part A. Pure Appl. Chem.* **A30,** 757–765 (1993).
16. Holland, S. J. & Tighe, B. J. Biodegradable polymers. *Adv. Pharm. Sci.* **6,** 101–164 (1992).
17. Chen, G. Degradation behavior of aliphatic biodegradable polyesters. *Soc. Plast. Eng.* (2010).
18. Von Burkersroda, F., Schedl, L. & Göpferich, A. Why degradable polymers undergo surface erosion or bulk erosion. *Biomaterials* **23,** 4221–4231 (2002).
19. Albertsson, A. C. & Varma, I. K. Aliphatic polyesters: synthesis, properties and applications. In *Degradable Aliphatic Polyesters* **157,** 1–40 (Springer-Verlag, 2002).
20. Determan, A. S., Trewyn, B. G., Lin, V. S.-Y., Nilsen-Hamilton, M. & Narasimhan, B. Encapsulation, stabilization and release of BSA-FITC from polyanhydride microspheres. *J. Control. Release* **100,** 97–109 (2004).

21. Wen, X. & Tresco, P. A. Fabrication and characterization of permeable degradable poly(DL-lactide-*co*-glycolide)(PLGA) hollow fiber phase inversion membranes for use as nerve tract guidance channels. *Bionaterials* **27,** 3800–3809 (2006).

22. Doppalapudi, S., Jain, A., Khan, W. & Domb, A. J. Biodegradable polymers - an overview. *Polym. Adv. Technol.* **25,** 427–435 (2014).

23. Middleton, J. C. & Tipton, A. J. Synthetic biodegradable polymers as orthopedic devices. *Biomaterials* **21,** 2335–2346 (2000).

24. Gunatillake, P., Mayadunne, R. & Adhikari, R. Recent developments in biodegradable synthetic polymers. *Biotechnol. Annu. Rev.* **12,** 301–347 (2006).

25. Jain, J. P., Ayen, W. Y., Domb, A. J. & Kumar, N. *Biodegradable polymers in clinical use and clinical development*. (2011).

26. Edlund, U. & Albertsson, A. C. Degradable polymer microspheres for controlled drug delivery. In *Degradable Aliphatic Polyesters* **157,** 67–112 (Springer, 2002).

27. Pillai, O. & Panchagnula, R. Polymers in drug delivery. *Curr. Opin. Chem. Biol.* **5,** 447–451 (2001).

28. Pillai, C. K. S. & Sharma, C. P. Review paper: absorbable polymeric surgical sutures: chemistry, production, properties, biodegradability, and performance. *J. Biomater. Appl.* **25,** 291–366 (2010).

29. Garlotta, D. A literature review of poly(lactic acid). *J. Polym. Environ.* **9,** 63–83 (2001).

30. Avérous, L. & Pollet, E. Biodegradable polymers. In *Environmental Silicate Nano-Biocomposites, Green Energy and Technology* 13–39 (Springer-Verlag, 2012).

31. Henton, D. E., Gruber, P., Lunt, J. & Randall, J. Polylactic acid technology. In *Natural Fibers, Biopolymers and Biocomposites* 527–577 (2005).

32. Bergsma, J. E. *et al. In vivo* degradation and biocompatibility study of *in vitro* pre-degraded as polymerized polylactide particles. *Biomaterials* **16,** 267–274 (1995).

33. Makadia, H. K. & Siegel, S. J. Poly lactic-*co*-glycolic acid (PLGA) as biodegradable controlled drug delivery carrier. *Polymers.* **3,** 1377–1397 (2011).

34. Patlolla, A., Collins, G. & Arinzeh, T. L. Solvent-dependent properties of electrospun fibrous composites for bone tissue regeneration. *Acta Biomater.* **6,** 90–101 (2010).

35. Ray, J. A., Doddi, N., Regula, D., Williams, J. A. & Melveger, A. Polydioxanone (PDS), a novel monofilament synthetic absorbable suture. *Surgery, Gynecol. Obstet.* **153,** 497–507 (1981).

36. Boland, E. D. *et al.* Electrospinning polydioxanone for biomedical applications. *Acta Biomater.* **1,** 115–123 (2005).

37. Pêgo, A. P. *et al. In vivo* behaviour of poly(1,3-trimethylene carbonate) and copolymers of 1,3-trimethylene carbonate with D,L lactide or epsilon-caprolactone: Degradation and tissue response. *J. Biomed. Mater. Res. A* **67,** 1044–1054 (2003).

38. Meaurio, E., Hernandez-Montero, N., Zuza, E. & Sarasua, J. R. Miscible blends based on biodegradable polymers. In *Characterization of polymer blends: Miscibility, Morphology and Interfaces* (ed. S. Thomas, Y. Grohens, P. J.) (Wiley-VCH Verlag GmbH & Co. KGaA, 2014).

39. Parameswarapillai, J., Tomas, S. & Grohens, Y. Polymer blends state of art, new challenges and opportunities. In *Characterization of Polymer Blends: Miscibility, Morphology and Interfaces* (Wiley-VCH Verlag GmbH & Co. KGaA, 2015).

40. Chavalitpanya, K. & Phattanarudee, S. Poly(lactic acid)/polycaprolactone blends compatibilized with block copolymer. *Energy Procedia* **34,** 542–548 (2013).

41. Datta, S. & Lohse, D. J. Graft copolymer compatibilizers for blends of isotactic polypropylene and ethene-propene copolymers. 2. Functional polymers approach. *Macromolecules* **26,** 2064–2076 (1993).

42. Amass, W., Amass, A. & Tighe, B. A review of biodegradable polymers: uses, current developments in the synthesis and characterization of biodegradable polyesters, blends of biodegradable polymers and recent advances in biodegradation studies. *Polym. Int.* **47,** 89–144 (1998).

43. Goonoo, N., Bhaw-Luximon, A. & Jhurry, D. Biodegradable polymer blends: miscibility, physicochemical properties and biological response of scaffolds. *Polym. Int. Soc. Chem. Ind.* **64,** 1289–1302 (2015).

44. Lodge, T. P. Block copolymers: past successes and future challenges. *Macromol. Chem. Phys.* **204,** 265–273 (2003).

45. Arslan, H. Block and graft copolymerization by controlled/living radical polymerization methods. In *Polymerization* (ed. Gomes, A. de S.) 279–320 (2012).

46. Dhandayuthapani, B., Yoshida, Y., Maekawa, T. & Kumar, D. S. Polymeric scaffolds in tissue engineering application: A review. *Int. J. Polym. Sci.* (2011).

47. Kim, S., Kim, J.-H., Jeon, O., Kwon, I. C. & Park, K. Engineered polymers for advanced drug delivery. *Eur. J. Pharm. Biopharm.* **71,** 420–430 (2008).

48. Kundu, P. P. & Sharma, V. Synthetic polymeric vectors in gene therapy. *Curr. Opin. Solid State Mater. Sci.* **12,** 89–102 (2008).

49. Ratner, B. D. & Bryant, S. J. Biomaterials: where we have been and where we are going. *Anu. Rev. Biomed. Eng.* **6,** 41–75 (2004).

50. Chu, C. C. *Wound closure biomaterials and devices.* (CRC Press, 1997).

51. Goldenberg, I. Catgut, silk and silver - the story of surgical sutures. *Surgery* **46,** 908–912 (1959).

52. Harloff, J. *Application of polymers for surgical sutures.* (1995).

53. Lendlein, A. & Langer, R. Biodegradable, elastic shape memory polymers for potential biomedical applications. *Science (80-.).* **296,** 1673–1676 (2002).

54. Barrows, T. H., Johnson, J. D., Gibson, S. J. & Grussing, D. M. The design and synthesis of bioabsorbable poly(ester-amides). In *Polymers in Medicine II . Biomedical and Pharmaceutical Applications* (eds. Chielleni, E., Giusti, P., Migliaresi, C. & Nicolais, L.) (Plenum Press, 1985).

55. Zhang, L., Chu, C. C. & Loh, I. H. Effect of a combined gamma irradiation and parylene plasma treatment on the hydrolytic degradation of synthetic biodegradable sutures. *J. Biomed. Mater. Res.* **27,** 1425–1441 (1993).

56. Brissot, H. Current suture materials in surgery [Les sutures chirurgicales aujourd'hui]. *Prat. médicale Chir. l'animal Cie.* **37,** 469–474 (2002).

57. Heyl, V. Plastic and reconstructive surgery: suture tecnique and scar issues [Nahttechnik and Narbenprobleme bei plastischen und rekonstrucktiven Operationen]. *Gynakol. Prax.* **31,** 701–706 (2007).

58. Grisham, J. E. & Zukin, D. D. Suture selection for the pediatrician. *Pediatr. Emerg. Care* **6,** 301–314 (1990).

59. O'Neal, R. B. & Alleyn, C. D. Suture materials and techniques. *Curr. Opin. Periodontol.* **4,** 89–95 (1997).

60. Wego Sutures. at <http://www.wegosuture.com/>

61. Unik Surgical Sutures MFG. Co. at <http://www.taiwantrade.com.tw/>

62. SMB Corporation of India. at <http://www.smbcorpn.com/>

63. Vital Sutures. at <http://www.vitalsutures.com/>

64. Suru International Pvt. Ltd. at <http://www.suru.com/>

65. Sutures, Quality is our strength. at <http://www.sutures.co.uk/>

66. Starmedix. at <http://www.starmedix.com/>

67. aurolab. at <http://www.aurolab.com/>

68. Footberg saving life. at <http://footberg.com/>

69. Sutcon Sutures. at <http://www.sutcon.net/>

70. MCO Hospital Aids. at <http://www.mcoh.co.in/>

71. SMI suture materials. at <http://www.sutures.be/>

72. DYNEK surgical excellence. at <http://www.dynek.com/>

73. Coreflon PTFE sutures. at <http://www.coreflon.pl/>

74. Teleflex(R) Medical OEM. at <http://www.teleflexmedicaloem.com/>

75. DemeTECH. at <http://www.demetech.us/>

76. Centenial Surgical Suture Ltd. at <http://www.centenialindia.com/>

77. Dolphin Sutures. at <http://www.dolphinsutures.com/>

78. Lorca Marín. at <http://www.lorcamarin.es/>

79. Laboratorio Aragó. at <http://www.laboratorioarago.com/>

80. Covidien. at <http://www.covidien.com/>

81. Ethicon. at <http://www.ethicon.com/>

82. CP Medical. at <http://www.cpmedical.com/>

83. Lotus-Surgicals. at <http://www.lotus-surgicals.com/>

84. Assut Europe. at <http://www.assuteurope.com/>

85. Merillife. at <http://www.merillife.com/>

86. Patel, K. A. & Thomas, W. E. G. Sutures, ligatures and staples. *Surgery* **26,** 48–53 (2007).

87. Suzuki, S. & Ikada, Y. Sutures for wound closure. In *Biomaterials for Surgical Operation* 189–197 (Springer Science + Business Media, LLC, 2012).

88. Skilbeck, C. J. Sutures, ligatures and knots. *Surgery* **29,** 63–66 (2010).

89. Sutures, B. B. 100 years of industrially manufactured sterile suture from B. Braun. *B. Braun Shar. Expert. Aesculap, Inc.* **6,** (2007).

90. Chu, C. C. In *Wound Closure Biomaterials and Devices* (ed. C.C. Chu, J.A. von Fraunhofer, H. . G.) (CRC Press LLC, 1997).

91. Chu, C. C. Textile-based biomaterials for surgical applications. In *Polymeric Biomaterials* (ed. Dumitriu, S.) 491–544 (Marcel Dekker Inc., 2002).

92. Braun, A.-B. Suture Glossary.

93. Rodeheaver, G. T. *et al.* Knotting and handling characteristics of coated synthetic absorbable sutures. *J. Surg. Res.* **35,** 525–530 (1983).

94. Rodeheaver, G. T., Thacker, J. G. & Edlich, R. F. Mechanical performance of polyglycolic acid and polyglactin 910 synthetic absorbable sutures. *Surg. Gynecol. Obstet.* **153,** 835–841 (1981).

95. Tomihata, K., Suzuki, M. & Sasaki, I. Coating for surgical suture comprising calcium stearate and caprolactone polymer. 1–13 (2010).

96. Kawai, T., Matsuda, T. & Yoshimoto, M. Coated sutures exhibiting improved knot security. (1991).

97. Messier, K. A. & Rhum, J. D. Caprolactone polymers for suture coating. (1986).

98. Bezwada, R. S., Hunter, A. W. & Shalaby, S. W. Copolymers of e-caprolactone, glycolide and glycolic acid for suture coatings. (1991).

99. Wang, D. W., Casey, D. J. & Lehmann, L. T. Surgical suture coating. (1987).

100. Mangram, A. J., Horan, T. C., Pearson, M. L., Silver, L. C. & Jarvis, W. R. Guideline for prevention of surgical site infection. Hospital Infection Control Practices Advisory Committee. *Infect. Control Hosp. Epidemiol.* **20,** 250–278 (1999).

101. Consensus paper on the surveillance of surgical wound infections. *Am. J. Infect. Control* **20,** 263–270 (1992).

102. Borens, O., Yusuf, E. & Trampuz, A. Surgical site infections (SSIs): risk factors and prevention strategies. *Eur. Instr. Lect.* 15–24 (2013).

103. Leaper, D. J. Risk factors for surgical infection. *J. Hosp. Infect.* **30,** 127–139 (1995).

104. Baracs, J., Huszár, O., Sajjadi, S. G. & Horváth, Ö. P. Surgical site infections after abdominal closure in colorectal surgey using triclosan-coated absorbable suture (PDS Plus) vs. uncoated sutures (PDS II): a randomized multicenter study. *Surg. Infect.*. **12,** 483–489 (2011).

105. Ostenberg, B. & Blomstedt, B. Effect of suture materials on bacterial survival in infected wounds: an experimental study. *Acta Chir. Scand.* **145,** 431–434 (1979).

106. Chu, C. C. & Williams, D. F. Effect of physical configuration and chemical structure of suture material on bacterial adherence. *Am. J. Surg.* **147,** 197–204 (1984).

107. Alexander, J. W., Kaplan, J. Z. & Altemeier, W. A. Role of suture materials in the development of wound infection. *Ann. Surg.* **165,** 192 (1967).

108. Kathju, S., Nistico, L., Lasko, L.-A. & Stoodley, P. Bacterial biofilm on monofilament suture and porcine xenograft after inguinal herniorrhaphy. *FEMS Immunol. Med. Microbiol.* **59,** 405–409 (2010).

109. Harnet, J. C. *et al.* Antibacterial protection of suture material by chlorhexidine-functionalized polyelectrolyte multilayer films. *J. Mater. Sci. Mater. Med.* **20,** (2009).

110. Zurita, R., Puiggalí, J. & Rodríguez-Galán, A. Loading and release of ibuprofen in multi- and monofilament surgical sutures. *Macromol. Biosci.* **6,** 767–75 (2006).

111. Howell, J. J. Chlorhexidine and suture materials. *Br. Med. J.* **1,** 449–450 (1965).

112. Edmiston, C. E. *et al.* Bacterial adherence to surgical sutures: Can antibacterial-coated sutures reduce the risk of microbial contamination? *J. Am. Coll. Surg.* **203,** 481–489 (2006).

113. Quidant, R. *et al.* A modified surface capable of having bacteriostatic and bactericide activity, the method for obtaining it and use thereof. (2015).

114. Serrano, C. *et al.* Nanostructured medical sutures with antibacterial properties. *Biomaterials* **52,** 291–300 (2015).

115. Hasan, J., Crawford, R. J. & Ivanova, E. P. Antibacterial surfaces: the quest for a new generation of biomaterials. *Trends Biotechnol.* **31,** 295–304 (2013).

116. Boybeyi, O. *et al.* Bacterial adhesion to braided surgical sutures: an *in vitro* study. *Eur. J. Plast. Surg.* **39,** 1–6 (2016).

117. Obermeier, A. *et al. In vitro* evaluation of novel antimicrobial coatings for surgical sutures using octenidine. *BMC Microbiol.* **15,** 186–193 (2015).

118. Mingmalairak, C. Antimicrobial sutures: New strategy in surgical site infections. *Sci. against Microb. Pathog. Commun. Curr. Res. Technol. Adv.* 313–323 (2011).

119. Blaker, J. J., Nazhar, S. N. & Boccaccini, A. R. Development and characterization of silver-doped bioactive glass-coated sutures for tissue engineering and wound healing applications. *Biomaterials* **25,** 1319–1329 (2004).

120. Dubas, S. T., Wacharanad, S. & Potiyaraj, P. Tunning of the antimicrobial activity of surgical sutures coated with silver nanoparticles. *Colloids Surfaces A. Physicochem. Eng. Asp.* **380,** 25–28 (2011).

121. Rothenburger, S., Spangler, D., Bhende, S. & Burkley, D. *In vitro* antimicrobial evaluation of Coated VICRYL Plus® Antibacterial Suture (coated polyglactin 910 with Triclosan) using zone of inhibition assays. *Surg. Infect.* **3,** 79–87 (2002).

122. Matalon, S. *et al.* The effect of commonly used sutures on inflammation inducing pathogens - An *in vitro* study. *J. Cranio-Maxillo-Facial Surg.* **41,** 593–597 (2013).

123. Marzo, G. *et al. In vitro* antibacterial efficacy of Vicryl Plus suture (coated polyglactin 910 with triclosan) using zone of inhibition assays. *Oral Implantol.* **1,** 43–48 (2008).

124. Masini, B. D., Stinner, D. J., Waterman, S. M. & Wenke, J. C. Bacterial adherence to suture materials. *J. Surg. Educ.* **68,** 101–104 (2011).

125. Gómez-Alonso, A. *et al.* Study of the efficacy of Coated VICRYL Plus® Antibacterial suture (coated Polyglactin 910 suture with Triclosan) in two animal models of general surgery. *J. Infect.* **54,** 82–88 (2007).

126. Marco, F. *et al.* Study of the efficacy of Coated Vicryl Plus® Antibacterial suture in an animal model of orthopedic surgery. *Surg. Infect.* **8,** 359–365 (2007).

127. Ford, H. R., Jones, P., Gaines, B., Reblock, K. & Simpkins, D. L. Intraoperative handling and wound healing: Controlled clinical trial comparing Coated Vicryl® Plus Antibacterial suture (coated polyglactin 910 suture with triclosan) with Coated Vicryl® suture (coated polyglactin 910 suture). *Surg. Infect.* **6,** 313–321 (2005).

128. Rozzelle, C. J., Leonardo, J. & Li, V. Antimicrobial suture wound closure for cerebrospinal fluid shunt surgery: a prospective, double-blinded, randomized controlled trial. *J. Neurosurg. Pediatr.* **2,** 111–117 (2008).

129. Fleck, T. *et al.* Triclosan-coated sutures for the reduction of sternal wound infections: economic considerations. *Ann. Thorac. Surg.* **84,** 232–236 (2007).

130. Justinger, C. *et al.* Antibiotic coating of abdominal closure sutures and wound infection. *Surgery* **145,** 330–334 (2009).

131. Mingmalairak, C., Ungbhakorn, P. & Paocharoen, V. Efficacy of antimicrobial coating suture coated polyglactin 91 with triclosan (Vicryl Plus) compared with polyglactin 910 (Vicryl) in reduced surgical site infection of appendicitis, double blind randomized control trial, preliminary safety report. *J. Med. Assoc. Thail.* **92,** 770–775 (2009).

132. Justinger, C. *et al.* Surgical-site infection after abdominal wall closure with triclosan-impregnated polydioxanone sutures: Results of randomized clinical pathway facilitated trial (NCT00998907). *Surgery* **154,** 589–595 (2013).

133. Deliaert, A. E. *et al.* The effect of triclosan-coated sutures in wound healing. A double blind randomised prospective pilot study. *J. Plast. Reconstr. Aesthetic Surg.* **62,** 771–773 (2009).

134. Chen, S. Y. *et al.* Do antibacterial-coated sutures reduce wound infection in head and neck cancer reconstruction? *Eur. J. Surg. Oncol.* **37,** 300–304 (2011).

135. William, N., Sweetland, H., Goyal, S., Ivins, N. & Leaper, D. J. Randomized trial of antimicrobial-coated sutures to prevent surgical site infection after breast cancer surgery. *Surg. Infect.* **12,** 469–474 (2011).

136. Zhang, Z. T. *et al.* Cosmetic outcome and surgical site infection rates of antibacterial absorbable (polyglactin 910) suture compared to Chinese silk suture in breast cancer surgery: a randomized pilot research. *Chin. Med. J. (Engl).* **124,** 719–724 (2011).

137. Laas, E. *et al.* Antibacterial-Coated suture in reducing surgical site infection in breast surgery: A prospective study. *Int. J. Breast Cancer* (2012).

138. Sala-Pérez, S., López-Ramírez, M., Quinteros-Borgarello, M., Valmaseda-Castellón, E. & Gay-Escoda, C. Antibacterial suture vs silk for the surgical removal of impacted lower third molars. A randomized clinical study. *Med Oral Patol Oral Cir Bucal.* **21,** 95–102 (2016).

139. Steingrimsson, S. *et al.* Triclosan-coated sutures and sternal wound infections: a prospective randomized clinical trial. *Eur. J. Clin. Microbiol. Infect. Dis.* **34,** 2331–2338 (2015).

140. Mattavelli, I. *et al.* Multi-center randomized controlled trial on the effect of triclosan-coated sutures on surgical site infection after colorectar surgery. *Surg. Infect.* **16,** 226–235 (2015).

141. Blanco, M. G., Franco, L., Puiggalí, J. & Rodríguez-Galán, A. Incorporation of triclosan into polydioxanone monofilaments and evaluation of the corresponding release. *J. Appl. Polym. Sci.* **114,** 3440–3451 (2009).

142. Obermeier, A. *et al.* Novel high efficient coatings for anti-microbial surgical sutures using chlorhexidine in fatty acid slow-release carrier systems. *PLoS One* **9,** (2014).

143. Lee, J. E. *et al.* Surgical suture assembled with polymeric drug-delivery sheet for sustained, local pain relief. *Acta Biomater.* **9,** 8318–8327 (2013).

144. Catanzano, O. *et al.* Melt-spun bioactive sutures containing nanohybrids for local delivery of anti-inflammatory drugs. *Mater. Sci. Eng. C* **43,** 300–309 (2014).

145. Agarwal, S., Wendorff, J. H. & Greiner, A. Use of electrospinning tecnique for biomedical applications. *Polymer.* **49,** 5603–5621 (2008).

146. Hutmacher, D. W. Scaffolds in tissue engineering bone and cartilage. *Biomaterials* **21,** 2529–2543 (2000).

147. Ashammakhi, N. *et al.* Biodegradable nanomats produced by electrospinning. *J. Nanosci. Nanotechnol.* **6,** 2693–2711 (2006).

148. Ramakrishna, S. Textile scaffolds in tissue engineering. In *Smart fibres, fabrics, and clothing* 291 (2001).

149. Sill, T. J. & von Racum, H. A. Electrospinning: Applications in drug delivery and tissue engineering. *Biomaterials* **29,** 1989–2006 (2008).

150. Kai, D., Liow, S. S. & Loh, X. J. Biodegradable polymers for electrospinning. Towards biomedical applications. *Mater. Sci. Eng. C* **45,** 659–670 (2014).

151. Pham, Q. P., Sharma, U. & Mikos, A. G. Electrospinning of polymeric nanofibers for tissue engineering applications: A review. *Tissue Eng.* **12,** 1197–1211 (2006).

152. Qi, H., Hu, P., Xu, J. & Wang, A. Encapsulation of drug reservoirs in fibers by emulsion electrospinning: Morphology characterization and preliminary release assessment. *Biomacromolecules* **7,** 2327–2330 (2006).

153. He, C., Nie, W. & Feng, W. Engineering of biomimetic nanofibrous matrices for drug delivery and tissue engineering. *J. Mater. Chem. B* **2,** 7828–7848 (2014).

154. Jiang, S., Duan, G., Schöbel, J., Agarwal, S. & Greiner, A. Short electrospun polymeric reinforced polyimide nanocomposite. *Compos. Sci. Technol.* **88,** 57–61 (2013).

155. Kmetty, A., Bárány, T. & Karger-Kocsis, J. Self-reinforced polymeric materials: A review. *Prog. Polym. Sci.* **35,** 1288–1310 (2010).

156. Gao, C., Yu, L., Liu, H. & Chen, L. Development of self-reinforced polymer composites. *Prog. Polym. Sci.* **37,** 767–780 (2012).

157. Mäkelä, P., Pohjonen, T., Törmalä, P., Waris, T. & Ashammakhi, N. Strength retention properties of self-reinforced poly L-lactide (SR-PLLA) sutures compared with polyglyconate (Maxon®) and polydioxanone (PDS) sutures. An in vitro study. *Biomaterials* **23,** 2587–2592 (2002).

2.

OBJECTIVES

This work has been carried out under the collaborative research project established between PSEP (Polímeros Sintéticos. Estructura y Propiedades) group of Universitat Politècnica de Catalunya and B. Braun Surgical S.A. (Center of Excellence for Closure Technologies) with the main purpose of developing and studying polymeric systems with specific biomedical applications. The University and the Company have been joining in different projects since 2002, and their results have been reported in many publications and two Doctoral Thesis.

Thus, the first Doctoral Thesis entitled "Microestructura, propiedades y aplicaciones médicas de materiales poliméricos biodegradables" provided the bases for the future research. The aim of the first part of the research was the study of the ring opening copolymerization of lactones performed on a laboratory scale, the influence of reactions conditions and catalysts, and the analysis of the microstructure. On the other hand, the incorporation and release of antibacterial agents onto from polyglycolide multifilament threads and poly(*p*-dioxanone) monofilament threads (e.g., triclosan, chlorhexidine digluconate and ibuprofen) were also evaluated.

The second Doctoral Thesis entitled "Influence of composition and microstructure on properties of new trimethylene carbonate/glycolide copolymers with biomedical applications" was focused on the influence of both, the molecular architecture and composition on the final properties of the copolymers based on trimethylene carbonate and glycolide units. These copolymers play a fundamental role as absorbable surgical suture. In fact, commercial absorbable suture with segmented nature and constituted by trimethylene carbonate and glycolide units, Maxon™, was selected as an ideal suture to start the physical characterization since it represented a good reference for further studies.

The main goal of the present work corresponds to the study of segmented nature copolymer constituted in this case by trimethylene carbonate, glycolide and ε-caprolactone units and commercialized as a monofilament absorbable surgical suture (Monosyn®) by B. Braun Surgical, S. A. Specifically, the three following points are considered:

i) Physico-chemical characterization and determination of thermal and mechanical properties. The influence of a third component in the soft segment will be analyze taking into account the previous results reported for the

bicomponent system (Maxon™) This general approach involves several specific objectives:

a. Crystallization studies under isothermal and non-isothermal conditions and using both, calorimetry an optical microscopy techniques.

b. Degradation studies which comprise:

i. Study of the thermal degradation kinetics and thermal stability of blends constituted by homopolymers related to segmented copolymers (i.e., poly(trimethylene carbonate) and poly(ε-caprolactone)). In order to complete other studies concerning the effect of the addition of poly(trimethylene carbonate) in thermal degradation of polylactones, the combination of poly(trimethylene carbonate) and poly(lactide) has also been considered. Results and methodologies of this study would be the basis for future thermal degradation evaluation.

ii. Study of hydrolytic degradation of monofilament absorbable suture Monosyn® in different media, varying pH and temperature. Analysis of degradation effects on thermal and mechanical properties, as well as composition and morphological changes.

c. Non-isothermal crystallization study of the monofilament suture constituted by homopolymer, poly(*p*-dioxanone), as a complementary crystallization work of the monofilament suture based on a segmented nature. Hydrolytic degradation study in different media of the monofilament poly(*p*-dioxanone) has also been performed and analyzed.

ii) Incorporation of different pharmacological agents onto monofilament surgical sutures. Selected drugs have different effects such as antimicrobial, antibiotic and wound healing activity. The specific aims derived from this study are the followings:

a. Synthesis of a coating copolymer with required characteristics of solubility, glass transition temperature and affinity with the drug selected. Random copolymers derived from trimethylene carbonate and different lactones like lactide, ε-caprolactone and glycolide have been considered as possible coating copolymers.

b. Evaluation of the drug incorporation, with and without a coating copolymer onto the monofilament suture. Analysis of the release profile in media with different hydrophobicity. The corresponding biological assays of each pharmacological agent have also been examined.

iii) Development of reinforced polymeric matrices derived from segmented copolymers (e.g., Monosyn®) in order to obtain matrices with antibacterial activity and maintain or improve its mechanical properties. Reinforcing fibers produced by means of electrospinning method are incorporated in different configurations. Specific aims are derived from this objective:

a. Preparation of poly(ε-caprolactone) matrices reinforced with poly(lactide) fibers. As a first step to learn the electrospinning method, current well-known polymers are selected. A first approach is the evaluation of different methodologies to prepare a reinforced matrix, and also the characterization of the antibacterial effect when appropriate drugs are incorporated in different elements of the matrices. The disposition of the reinforcing polylactide fibers are placed between two layers of poly(ε-caprolactone) with the purpose to achieve a sustainable release when antibacterial drug is into the fibers. Release and antibacterial activity have been analyzed for different configurations.

b. Reinforcing fibers of Monosyn® will be incorporated on PCL as a polymer matrix. Incorporation of antibacterial agents is carried out while the release profile and the corresponding activity are evaluated.

3.

CRYSTALLIZATION STUDIES OF GL–*b*–(GL–*co*–TMC–*co*–CL)–*b*–GL MONOFILAR SURGICAL SUTURE

3.1 Isothermal and non-isothermal crystallization kinetics by means of Differential Scanning Calorimetry

Kinetics of isothermal and non-isothermal crystallization studies of a biodegradable monofilament suture constituted by polyglycolide *hard blocks* and *soft segments* derived from glycolide, ε-caprolactone and trimethylene carbonate have been undertaken by means of calorimetric methods. This segmented polymer was semicrystalline with melting and crystallization characteristics defined by the polyglycolide *hard segments*. The amorphous phase had a glass transition temperature highly influenced by thermal processing and the random microstructure of the *soft segment*. Melting process was complex due to the occurrence of lamellae with different degree of perfection. Equilibrium melting point, determined by the Hoffman-Weeks methodology, became slightly lower than reported for polyglycolide and segmented copolymers having a lower *soft segment* content.

A heterogeneous nucleation and a three-dimensional crystal growth were characteristic for isothermal crystallizations performed from the melt state, being the Avrami exponent very close to 3 for all experiments. Secondary nucleation constant was evaluated from the overall crystallization rates and by assuming the validity of Lauritzen-Hofmann approach. Results point out a maximum rate for a crystallization temperature of 131 ºC and probably an underestimated nucleation constant.

Kinetic parameters for non-isothermal crystallization were deduced by Avrami, Ozawa and Cazé methods. A good agreement with isothermal parameters was only attained with the last methodology, although results from the other ones were appropriate to simulate the crystallization process. Isoconversional analysis was a good methodology to estimate the secondary nucleation constant from a non-isothermal crystallization.

3.1.1 INTRODUCTION

Polyglycolide is one of the first biodegradable synthetic polymers investigated for biomedical applications, with the development of bioabsorbable surgical sutures being one of the main achievements.[1,2] Its biodegradable and biocompatible character, fiber forming ability and excellent mechanical properties associated with its high crystallinity were fundamental for this purpose. Furthermore, polyglycolide has unusual properties compared to the related series of linear and unsubstituted polyhydroxyalkanoates. Thus, this polymer has a melting temperature higher than 200 ºC and a glass transition temperature in the 35-40 °C range, in contrast with the low values found for the other members of the series (e.g., melting point of 55–60 °C and glass transition temperature close to –60 °C for poly(ε-caprolactone) [3]).

Monofilament sutures have clear advantages over conventional braided threads (e.g., high resistance to harbor microorganisms and low tissue damage).[4–6] Unfortunately, the high stiffness of polyglycolide makes its processing in a monofilament form impossible. Hence, copolymers having two polyglycolide *hard segments* and a middle *soft segment* derived from glycolide and other monomers (e.g., trimethylene carbonate, ε-caprolactone or *p*-dioxanone) have been prepared to impart flexibility.[7–9] Maxon™ (Syneture) is one of the first and most simple monofilament synthetic suture based on polyglycolide ever commercialized. Specifically, *hard segments* represent a 62 wt-% and the middle *soft segment* is produced by random copolymerization of 85 wt-% of trimethylene carbonate and 15 wt-% of glycolide.[10,11]

Final properties of semicrystalline polymers are highly dependent on processing conditions since the degree of crystallinity can be well controlled within a delimited range. In this sense, the kinetic study of the crystallization process under both isothermal and non-isothermal conditions is an essential tool. These kinetic data have been reported for Maxon™.[12,13] It has also been indicated that small changes in the *soft segment* composition, even keeping a bicomponent system, and in the *hard segment* content may have a great influence on properties, degradation rate and even crystalline morphology and primary nucleation.[14–16]

Monosyn® (B. Braun Surgical S.A.) is another monofilament suture synthesized following the classical two step procedure in Figure 3.1.1 which guarantees a segmented molecular architecture. In this case, the middle *soft segment* is based on three components (35 wt-%

of glycolyl, 32.5 wt-% of trimethylene carbonyl and 32.5 wt-% of ε-caproyl units) and constitutes a 43 wt-% of the sample.[8] With regard to Maxon™, percentages are slightly different, i.e., glycolyl (72 as opposed to 67.5 wt-%) and *hard segment* (57 as opposed to 62 wt-%). Data about the crystallization process of this commercial suture are scarce despite its wide commercial use. Furthermore, the kinetic study seems interesting to complement previous observations on Maxon™ and also to determine the possible influence of *soft segment* composition (e.g., a tricomponent as opposed to a bicomponent system) on the crystallization process. Finally, it is worth noting that the selected sample is a simple system to study the crystallization of block copolymers since it is constituted by two crystallizable *hard segments* and a middle one that remains amorphous. Crystallization is expected to take place from the mixed melt, and microphase separation driven by crystallization should lead to a lamellar morphology.[17]

Figure 3.1.1. Two step synthesis of GL-*b*-(GL-*co*-TMC-*co*-CL)-*b*-GL.

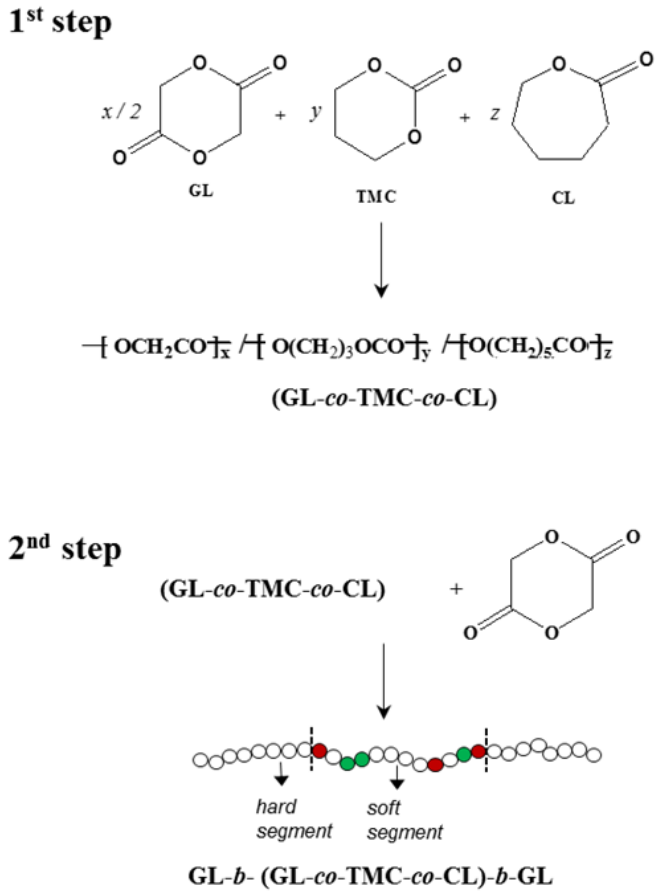

3.1.2 EXPERIMENTAL SECTION

3.1.2.1 Materials

Commercially available sutures of GL-*b*-(GL-*co*-TMC-*co*-CL)-*b*-GL (Monosyn®, USP 1) were kindly supplied by B. Braun Surgical S.A. Weight and number average molecular weights of Monosyn® samples were 71,000 and 41,000 g/mol, as determined by GPC.

3.1.2.2 Measurements

Molecular weight was estimated by size exclusion chromatography (GPC) using a liquid chromatograph (Shimadzu, model LC-8A) equipped with an Empower computer program (Waters). A PL HFIP gel column (Polymer Lab) and a refractive index detector (Shimadzu RID-10A) were employed. The polymer was dissolved and eluted in 1,1,1,3,3,3-hexafluoroisopropanol containing CF_3COONa (0.05 M) at a flow rate of 1 mL/min (injected volume 100 µL, sample concentration 2.0 mg/mL). Number and weight average molecular weights were calculated using polymethyl methacrylate standards.

Calorimetric data were obtained by differential scanning calorimetry with a TA Instruments Q100 series equipped with a refrigerated cooling system (RCS) operating at temperatures from -90 ºC to 550 ºC. Experiments were conducted under a flow of dry nitrogen with a sample weight of approximately 5 mg and calibration was performed with indium. T_{zero} technology requires a calibration based on two experiments: the first was performed without samples while sapphire disks were used in the second. Thermal characterization was performed following a four run protocol consisting on a heating run (20 ºC/min) of the segmented GL-*b*-(GL-*co*-TMC-*co*-CL)-*b*-GL commercial suture, a cooling run (10 ºC/min) after keeping the sample in the melt state for one minute, a subsequent heating run (20 ºC/min) of the hot crystallized sample and finally a heating run (20 ºC/min) of a sample quenched from the melt state by immersion in liquid nitrogen. Related to isothermal crystallization studies, the sample was heated to melt state, in this case to 225 ºC, which is a temperature 25 ºC above the melting peak, at a heating rate of 20 ºC/min. It was held for 5 min at 225 ºC and after, the sample was cooled to the selected temperature at 50 ºC/min. The sample was kept at the isothermal temperature until baseline was attained. For non-isothermal crystallization experiments, the molten samples were cooled at different rates from 20 to 5 ºC/min.

3.1.3 RESULTS AND DISCUSSION

3.1.3.1 Thermal properties

Thermal properties of the Monosyn® commercial suture were analyzed from the DSC traces given in Figure 3.1.2. Three points can be emphasized:

a) All heating runs showed a predominant melting peak near 200 ºC which is associated with crystalline domains constituted by polyglycolide *hard segments*. This peak became more complex when the sample was slowly crystallized from the melt, leading to the appearance of a new small peak at a slightly lower temperature. This peak may be attributed to the fusion of lamellar crystals with a smaller thickness or alternatively to the incorporation of a larger number of comonomer units into the crystalline phase. In addition, the as-processed sample exhibited a very small endothermic peak (4.1 J/g) near 100 ºC that could be associated with highly defective crystalline domains formed from small glycolide blocks of the *soft segment*, as previously reported for Maxon™.[13] The annealing conditions to which the fiber was submitted during processing make this defective arrangement feasible.

b) Samples easily crystallized from the melt and the glass state, as revealed by the corresponding, well defined hot and cold exothermic peaks.

c) The occurrence of a clear glass transition indicated that the amorphous content was significant, even for the hot crystallized sample. It merits attention that *soft* and *hard segments* were compatible/miscible, as can be deduced from the single glass transition observed in the heating scan of a fully amorphous sample obtained after quenching the melted sample in liquid nitrogen. The glass transition temperature was highly variable depending on the processing conditions (i.e., -3 and 14 ºC for melt crystallized and quenched samples, respectively). Logically this temperature increased when the amorphous phase was richer in stiff glycolide units, as expected when the sample was quenched and the crystallization of polyglycolide *hard segments* hindered. In the same way the presence of comonomers with higher flexibility than glycolide caused a decrease on the glass transition temperature as observed when the *soft segment* was predominant in the amorphous phase (i.e., sample slowly crystallized from the melt).

Figure 3.1.2. DSC traces obtained during the heating run of the segmented GL-*b*-(GL-*co*-TMC-*co*-CL)-*b*-GL commercial suture **(a)**, the cooling run from the melt state **(b)**, the heating run of a hot crystallized sample **(c)** and the heating run of a sample quenched from the melt state **(d)**.

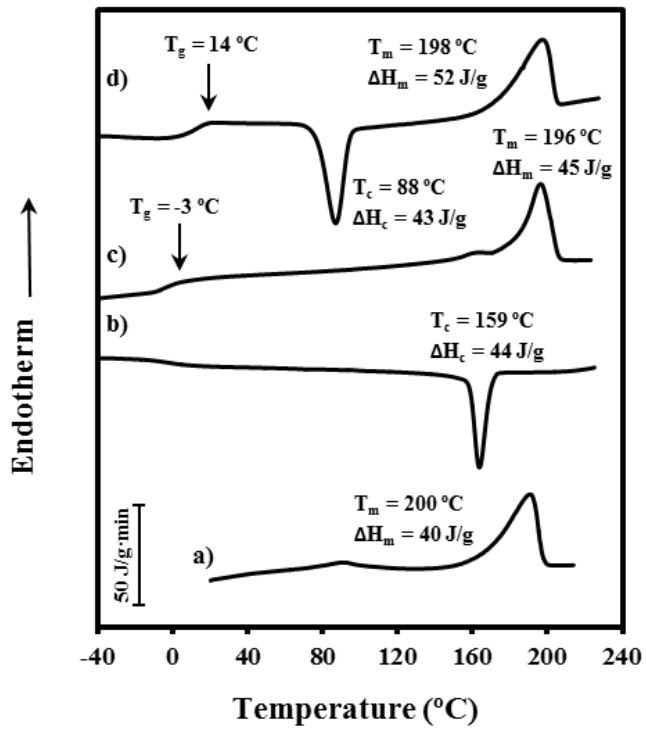

3.1.3.2 Equilibrium melting temperature

Equilibrium melting temperature (T_m^0) is a crucial parameter for determining crystal growth rate and specifically degree of supercooling ($T_m^0 - T_c$). The Hoffman-Weeks extrapolation[18] is a commonly accepted method of estimating the equilibrium temperature due to its simplicity and straightforward implementation, although it is subject to criticism[19] and improvements have been proposed.[20] The method is based on **equation 1**, which was deduced from a combination of the well-known Gibbs-Thomson equation and secondary nucleation theory.[21] This equation relates the melting temperature, T_m, of a crystal formed at a temperature T_c, the equilibrium melting temperature and the thickening coefficient, γ, defined as the ratio between the thickness of the grown crystal and the initial thickness of a "virgin lamella":

$$T_m = T_m^0 (1 - 1/\gamma) + T_c/\gamma \quad (1)$$

A straight line is obtained by plotting T_m as a function of T_c , with the equilibrium temperature corresponding to the intersection of this line with the $T_m = T_c$ line. The validity of equation 1 implies that lamellar crystals thicken at a specific crystallization temperature which also influences the thickening parameter.

Figure 3.1.3a shows the complex melting behavior of the segmented copolymer crystallized at different temperatures. The predominant melting peak (peak I) shifts to higher temperatures with the crystallization temperature and allows the unambiguous estimation of an equilibrium melting temperature of 219 ºC from the Hoffman-Weeks plot (Figure 3.1.3b). This temperature is in close agreement with the values of 229 and 225 ºC reported for polyglycolide[22] and Maxon™ [12], respectively, and logically decreases for higher *soft segment* contents (i.e., 38 and 43 wt-% corresponds to Maxon™ and Monosyn®, respectively). The DSC thermograms show a broad endotherm at a lower temperature that, in fact, seems to be constituted by two different peaks (II and III), as revealed by traces obtained at the lower and higher crystallization temperatures (Figure 3.1.3a). The temperature evolution of these two peaks also led to the above equilibrium melting temperature, although the higher inaccuracy caused by the imprecise peak temperature and scarce experimental data available to perform the Hoffman-Weeks extrapolation is worth mentioning. These low temperature peaks correspond to more defective lamellae, whose reorganization/recrystallization process became more significant (i.e., the peak had a smaller relative area) for crystals formed at lower temperatures. It is worth emphasizing that the temperature of the predominant peak also depends on the crystallization temperature, and consequently the initial crystalline state seems to determine the characteristics of reorganized lamellae.

Figure 3.1.3. (a) DSC heating runs (20 ºC/min) of GL-b-(GL-*co*-TMC-*co*-CL)-*b*-GL isothermally crystallized at temperatures from 166 to 182 ºC. **(b)** Hoffman-Weeks plot of temperatures corresponding to the three observed endothermic melting peaks versus hot crystallization temperature. An equilibrium melting temperature close to 219 ºC can be deduced.

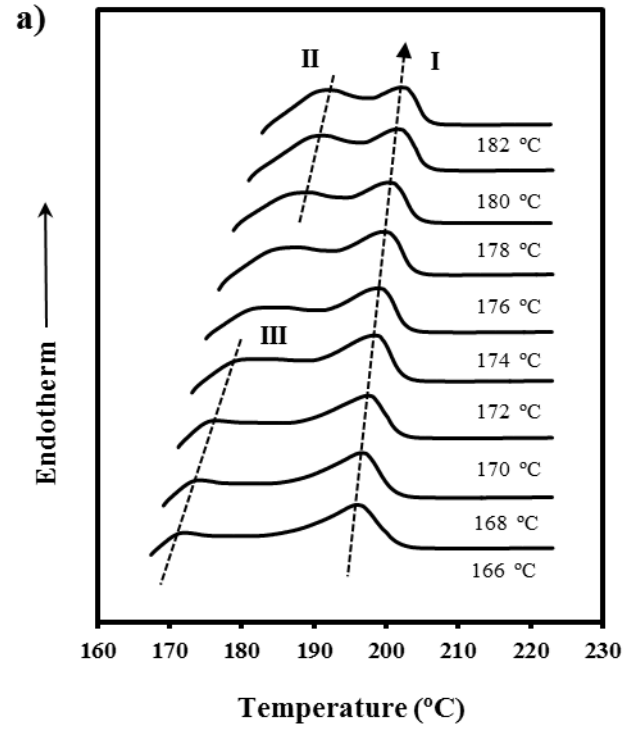

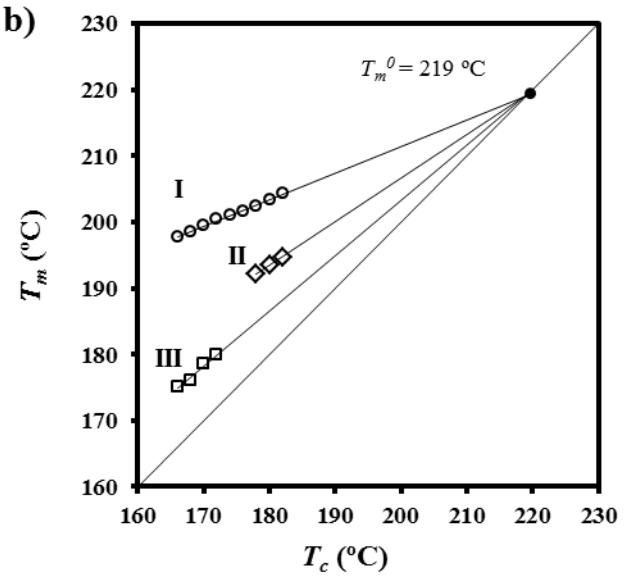

3.1.3.3 Isothermal crystallization analysis from calorimetric data

Kinetic analysis of GL-*b*-(GL-*co*-TMC-*co*-CL)-*b*-GL could only be performed for the hot crystallization process because of the impossibility to obtain amorphous samples by cooling the melted polymer at the maximum rate allowed by the equipment. This behavior is clearly different to that observed for Maxon™ and reflects a remarkable increase on the primary nucleation.

Hot crystallization experiments were therefore carried out in the narrow 166-182 ºC temperature interval due to experimental limitations. The time evolution of the relative degree of crystallinity, $\chi(t)$, was determined from hot crystallization exotherms (Figure 3.1.4a) through the ratio area of the exotherm up to time t divided by the total exotherm area, i.e.,

$$\chi(t) = \int_{t_0}^{t} (dH/dt)dt \;/\; \int_{t_0}^{\infty} (dH/dt)dt \qquad (2)$$

where dH/dt is the heat flow rate and t_0 the induction time. The development of crystallinity always showed a characteristic sigmoidal dependence on time, as plotted in Figure 3.1.4b for nine hot crystallization experiments. These data were analyzed assuming the well-known Avrami equation [23,24] for primary crystallization:

$$1 - \chi(t-t_0) = \exp[-Z(t-t_0)^n] \qquad (3)$$

where Z is the temperature-dependent rate constant and n the Avrami exponent whose value varies according to the crystallization mechanism. A normalized rate constant, $k = Z^{1/n}$, is usually evaluated for comparison purposes since its dimension (time^{-1}) is independent of the value of the Avrami exponent.

Figure 3.1.4. **(a)** Exothermic DSC peaks corresponding to isothermal hot crystallizations performed between 166 and 182 ºC of GL-*b*-(GL-*co*-TMC-*co*-CL)-*b*-GL. **(b)** Time evolution of relative crystallinity for isothermal crystallizations between 166 and 182 ºC.

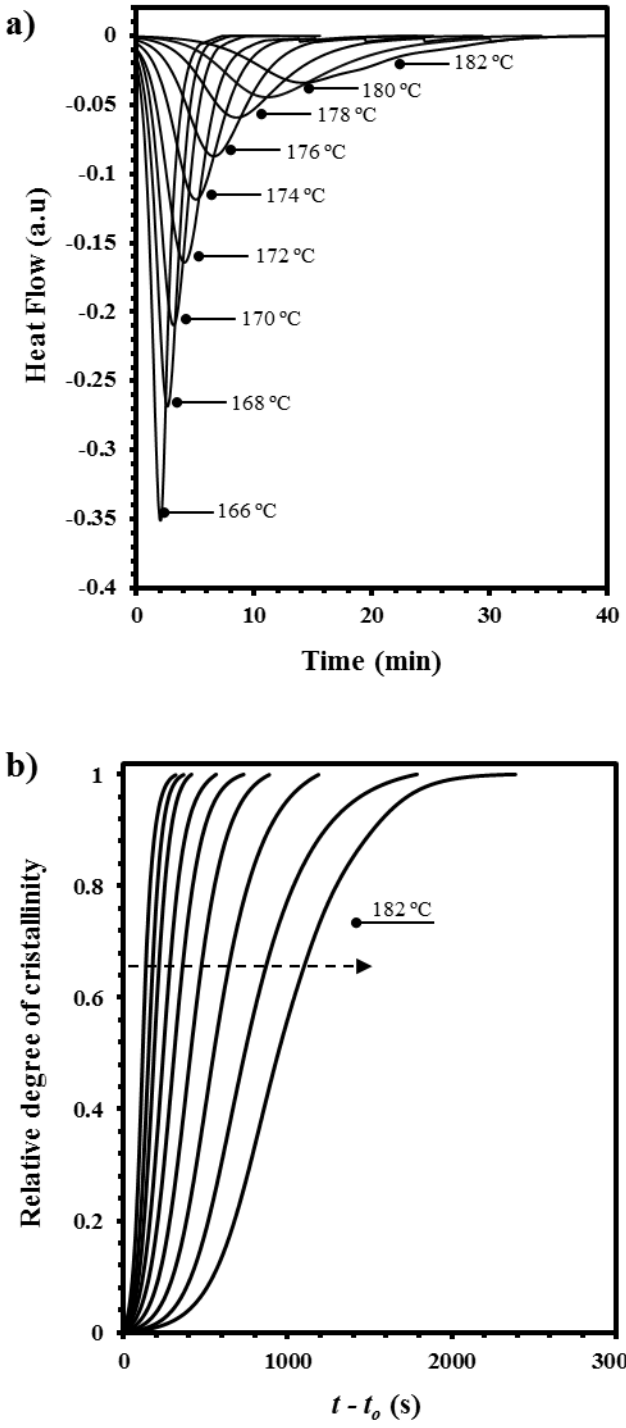

Table 3.1.1 summarizes the main kinetic parameters of the primary crystallization process, as deduced from the plots of $\log\{-\ln[1-\chi(t-t_0)]\}$ against $\log(t-t_0)$ (Figure 3.1.5a). The values of the Avrami exponent lie in a narrow range, from 2.72 to 3.00, 2.86 being the average value. This suggests the occurrence of predetermined (heterogeneous) nucleation with spherical growth under geometric constraints since the theoretical value should be equal to 3. Both sporadic (heterogeneous) and homogeneous nucleation can be clearly discarded as a higher exponent, close to 4, should be derived. Furthermore, homogeneous nucleation usually requires high undercooling, which is not the case. It is interesting to note that the Avrami exponents tend to decrease with increasing the crystallization temperature. Specifically, at temperatures higher than 180 ºC crystallization approaches two-dimensional growth.

Table 3.1.1. Main isothermal crystallization kinetic parameters of GL-*b*-(GL-*co*-TMC-*co*-CL)-*b*-GL determined by DSC.

T_c (ºC)	n	Z (s^{-n})	$k \times 10^3$ (s^{-1})	$\tau_{1/2}$ (s)	$(1/\tau_{1/2}) \times 10^3$ (s^{-1})	$(Z/\ln 2)^{1/n} \times 10^3$ (s^{-1})
166	2.69	1.91×10^{-6}	7.44	117	8.55	8.53
168	2.77	6.09×10^{-7}	5.73	153	6.54	6.54
170	2.82	2.70×10^{-7}	4.72	186	5.38	5.38
172	2.72	2.34×10^{-7}	3.61	242	4.13	4.13
174	2.82	6.52×10^{-8}	2.83	309	3.24	3.23
176	2.95	1.37×10^{-8}	2.15	408	2.45	2.43
178	2.98	4.44×10^{-9}	1.59	549	1.82	1.80
180	2.95	2.19×10^{-9}	1.17	738	1.36	1.33
182	3.00	7.75×10^{-10}	0.93	942	1.06	1.05

The values of the corresponding reciprocal crystallization half-times ($1/\tau_{1/2}$), calculated as the inverse of the difference between crystallization start time and half-crystallization time, are also given in Table 3.1.1. This parameter is a direct measure of the crystallization process, and was therefore used to check the accuracy of Avrami analysis by comparison with the theoretical kinetic value (i.e., $1/\tau_{1/2} = (Z/\ln 2)^{1/n}$). Figure 3.1.5b demonstrated

also the accuracy of the Avrami analysis since temperature evolution of the overall crystallization rate, k, was very similar to that found for the experimental $1/\tau_{1/2}$values.

Figure 3.1.5. (a) Avrami analyses for isothermal crystallization of GL-*b*-(GL-*co*-TMC-*co*-CL)-*b*-GL. **(b)** Comparison between the temperature evolution of the overall crystallization rate (□) and the reciprocal of the crystallization half-time (○).

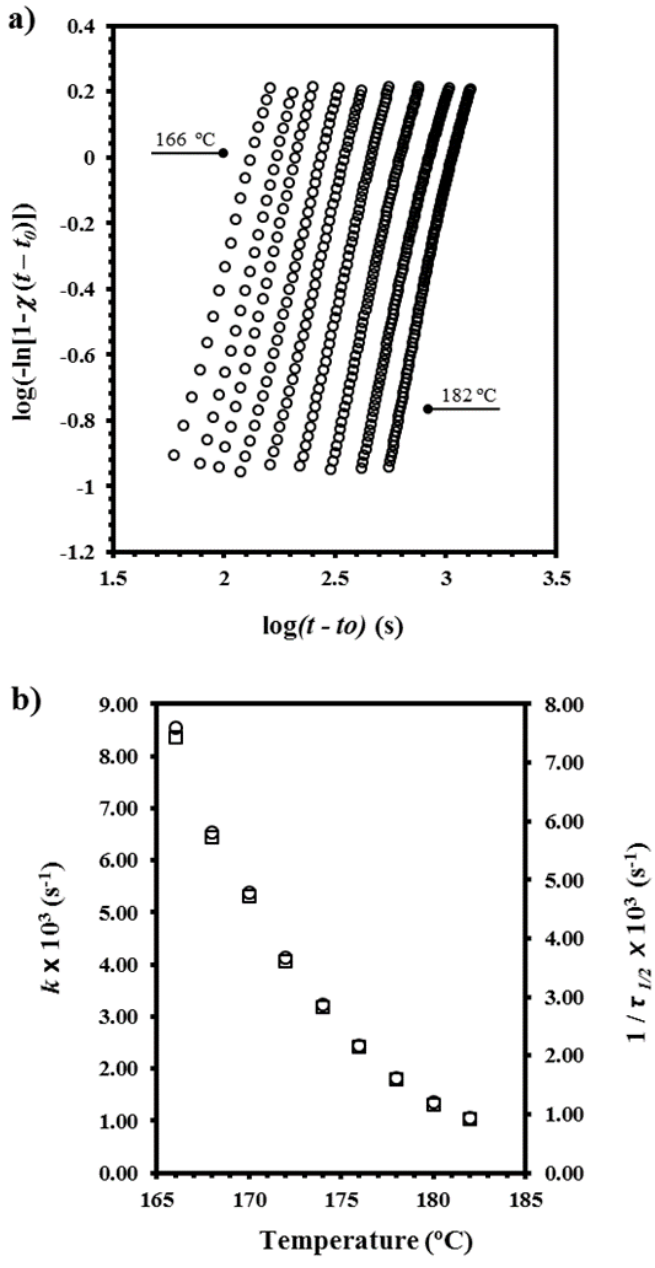

3.1.3.4 Secondary nucleation constant for the isothermal crystallization

The radial growth rate (G) of polymer crystals is usually described by the Lauritzen and Hoffman equation,[25] which is based on the Turnbull–Fisher expression[26] suitable for the crystallization process of homopolymers. Some authors[27,28] have proposed a proportionality between the normalized rate constant (k) and the radial growth rate when an heterogeneous nucleation is assumed. Therefore, the original Lauritzen and Hoffman equation was reformulated as:

$$k = k_0 \exp[-U^*/(R(T_c - T_\infty))]\exp[-K_g/(T_c(\Delta T)f)] \quad (4)$$

where k_0 is a constant preexponential factor, U^* represents the activation energy characteristic of the transport of the crystallizing segments across the liquid–crystal interface, T_∞ is the temperature below which such motion ceases, T_c is the crystallization temperature, R is the gas constant, K_g is a nucleation parameter, ΔT is the degree of supercooling measured as $T_m^0 - T_c$, and f is a correction factor accounting for the variation in the bulk melting enthalpy per unit volume with temperature ($f = 2T_c/(T_m^0 + T_c)$).

It is advisable to rearrange Eq. (4) in a logarithmic form:

$$\ln k + U^*/R(T_c - T_\infty) = \ln k_0 - K_g/[T_c(\Delta T) f] \quad (5)$$

and plot the left-hand side of the equation versus $1/[T_c(\Delta T) f]$. Straight lines with slopes equal to $-K_g$ should be obtained.

The Lauritzen-Hoffman plot was fitted with a straight line (r^2 = 0.994) when the "universal" values reported by Suzuki and Kovacs[29] (i.e., U^* = 1500 cal/mol and $T_\infty = T_g$ - 30 K) were used in the calculation (Figure 3.1.6). Kinetic features at low supercoolings are basically governed by the nucleation term, and consequently crystallization rates could become relatively insensitive to the U^* and T_∞ parameters. The plot was used to estimate a secondary nucleation constant of 1.51×10^5 K^2 which became close to the value of 1.86×10^5 K^2 reported for Maxon.[12] This observation suggests a lower difficulty for crystal growth which is not an expected result taking into account the higher content of non-crystallizable *soft segments* with a more statistical monomer distribution. Therefore, a complementary analysis from optical microscopy observations seems

necessary in order to corroborate if the proportionality between G and k can be in this case assumed.

Figure 3.1.6. Plot of ln $k + U^*/R(T_c-T_\infty)$ versus $1/T_c(\Delta T)f$ to determine the K_g secondary nucleation parameter of GL-*b*-(GL-*co*-TMC-*co*-CL)-*b*-GL.

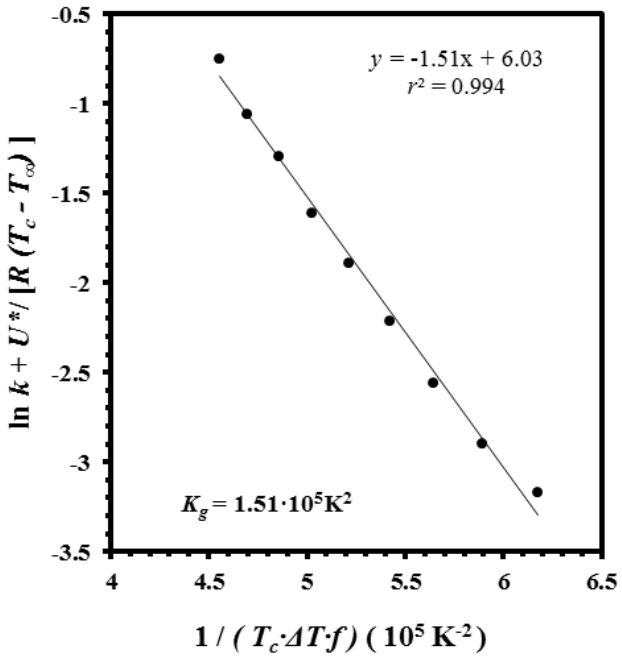

LH parameters were used to evaluate the temperature dependence of the overall crystallization rate (equation 4), which followed a typical bell-shaped curve as depicted in Figure 3.1.7. The interplay between secondary nucleation and segmental mobility gives rise to a maximum crystallization rate, which for the studied copolymer corresponded to a temperature of 131 ºC. This became close to the value of 132 ºC previously determined for Maxon™ from optical microscopy observations.[12] Nevertheless, it must be indicated the impossibility to perform a cold crystallization study for GL-*b*-(GL-*co*-TMC-*co*-CL)-*b*-GL and consequently that the available experimental data for the present analysis covered only a narrow temperature range.

Figure 3.1.7. Temperature dependence of overall crystallization rate (○ symbols) determined by equation 4 and using the best fit parameters in the text and experimental values (♦ symbols).

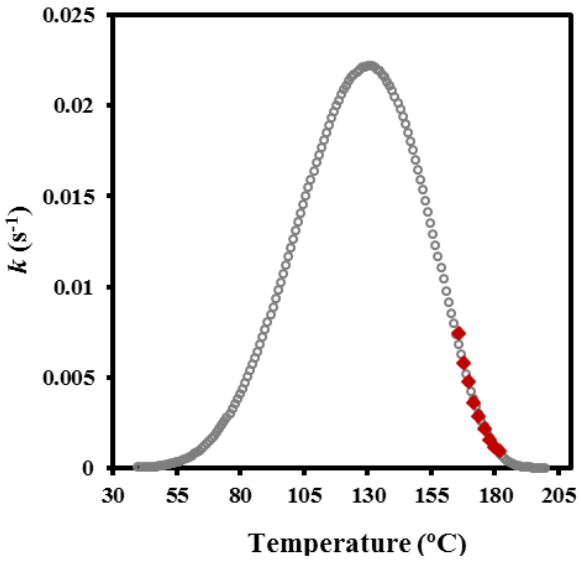

3.1.3.5 Kinetic studies for the non-isothermal crystallization

Figure 3.1.8 shows the dynamic DSC curves obtained from melted samples at different cooling rates. Crystallization peaks become sharper and their temperature (T_p) progressively shifts to lower values with increasing the cooling rate. They are relatively narrow and asymmetrical since a long tail is observed as consequence of a restricted secondary crystallization that needs a high supercooling to be completed.

Calorimetric data were used to determine the relative degree of crystallinity at any temperature, χ(T), for all cooling rates by the expression

$$\chi(T) = \frac{\int_{T_0}^{T_c} (dH_c/dT)dT}{\int_{T_0}^{T_\infty} (dH_c/dT)dT} \qquad (6)$$

where dH_c is the enthalpy of crystallization released within an infinitesimal temperature range dT, T_0 denotes the initial crystallization temperature and T_c and T_∞ are the crystallization temperature at time t and after completion of the crystallization process, respectively. Thus, the denominator corresponds to the overall enthalpy of crystallization for specific heating/cooling conditions.

Figure 3.1.8. Dynamic DSC curves obtained at the indicated rates for hot crystallization experiments with GL-*b*-(GL-*co*-TMC-*co*-CL)-*b*-GL.

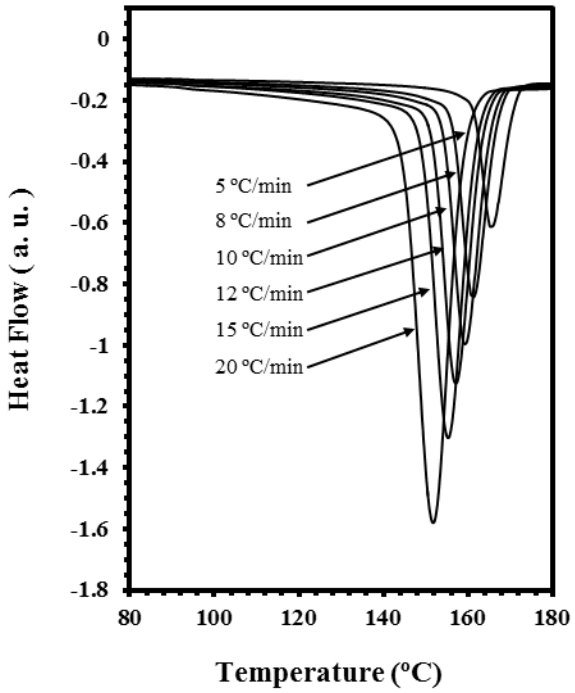

The relative degree of crystallinity can be calculated as a function of time by the relationship:

$$(t - t_0) = (T_0 - T) / \phi \qquad (7)$$

where T_0 is the temperature at which crystallization begins ($t = t_0$) and ϕ is the value of the cooling rate, respectively.

Figure 3.1.9a also illustrates the variation of the time-dependent degree of crystallinity, $\chi(t)$, at different cooling rates. The characteristic Avrami analysis [23,24] can thus be applied to these non-isothermal experiments by using the equation (3).

Figure 3.1.9b shows the plots of $\log\{-\ln[1-\chi(t-t_0)]\}$ versus $\log(t-t_0)$ for different cooling rates. It is remarkable that deviation of linearity is only observed at high values of the relative degree of crystallinity when secondary crystallization caused by the impingement of spherulites. Thus, primary crystallization can be well characterized until a relative degree of crystallinity of 0.80.

Figure 3.1.9. Time evolution of relative crystallinity **(a)** and Avrami plots **(b)** at the indicated cooling rates for the non-isothermal crystallization of GL-*b*-(GL-*co*-TMC-*co*-CL)-*b*-GL.

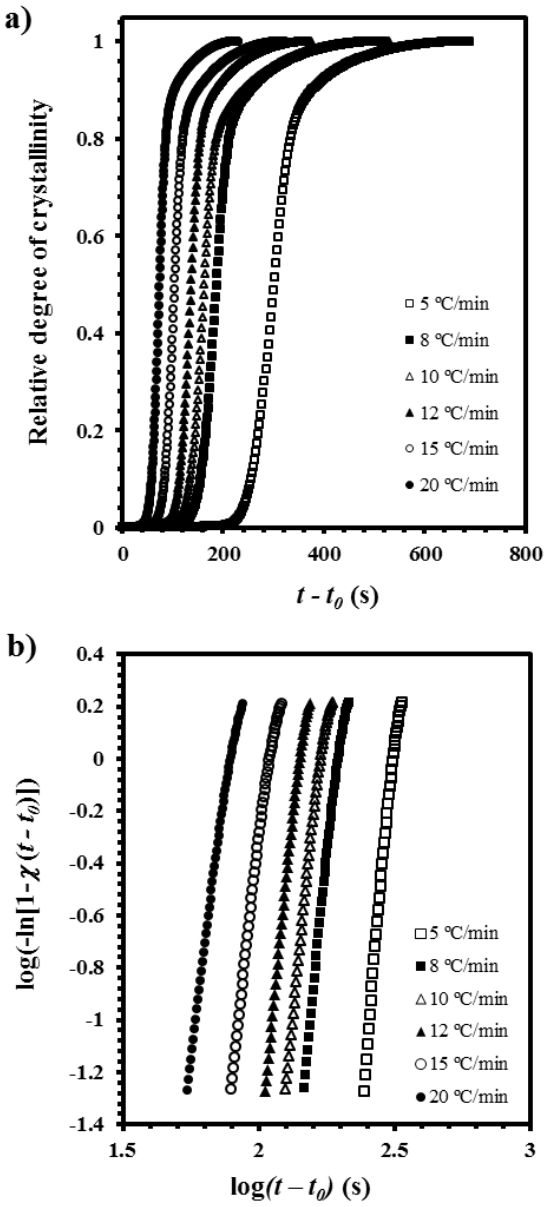

Table 3.1.2 summarizes the main kinetic parameters deduced by the Avrami analysis. As presumable, the normalized rate constant increased when cooling rate also did. The deduced rate constants are in a relative good agreement with those previously derived from isothermal studies that covered a restricted crystallization temperature range of 166-182 ºC. Thus for example, crystallization rates of 3.18×10^{-3} and 5.79×10^{-3} s^{-1} were determined for crystallizations performed at cooling rates of 5 and 10 ºC/min, respectively.

Table 3.1.2. Main non-isothermal crystallization kinetic parameters of GL-*b*-(GL-*co*-TMC-*co*-CL)-*b*-GL determined by DSC.

ϕ (ºC/min)	n	Z (s^{-n})	$k \times 10^3$ (s^{-1})	$\tau_{1/2}$ (s)	$(1/\tau_{1/2}) \times 10^3$ (s^{-1})	$(Z/\ln 2)^{1/n} \times 10^3$ (s^{-1})
5	10.95	4.67×10^{-28}	3.18	301	3.32	3.29
8	9.24	6.27×10^{-22}	5.06	188	5.33	5.27
10	9.04	5.89×10^{-21}	5.79	163	6.13	6.03
12	9.37	5.65×10^{-21}	6.92	138	7.27	7.19
15	8.18	1.89×10^{-17}	9.02	104	9.58	9.44
20	7.40	8.77×10^{-15}	12.58	75	13.41	13.22

Note that the corresponding peak temperatures (165 and 159 ºC) were similar but always slightly lower than the temperatures (Table 3.1.1) at which isothermal crystallization proceeded at a similar rate (i.e., 3.61×10^{-3} and 5.73×10^{-3} s^{-1} for 172 and 168 ºC, respectively).

Avrami exponents took average values of 9.09 which is very far from those deduced by isothermal crystallization experiments (i.e., 2.86). In fact, it is well stated that application of the Avrami equation under non-isothermal conditions merely corresponds to a mathematical fitting that allows to derive appropriate values of the rate constant but has not a reliable physical sense in terms of the corresponding exponent.[30–32] Table 3.1.2 precisely shows the good agreement between the reciprocal crystallization half-times directly determined from the experimental data and those deduced from the Avrami parameters. Therefore, these parameters are at least appropriated to simulate the non-isothermal crystallization process.

Crystallization under non-isothermal conditions is a process rather complicated to be analyzed since for example the crystallization from the melt takes place under different degrees of supercoolings. This feature is clear when the methodology proposed by Ozawa is applied.[33] In this case, it was formulated an equation that considers the effect of the cooling rate (ϕ):

$$1-\chi(T) = \exp(-R(T) / \phi^m) \quad (8)$$

where m is the so-called Ozawa exponent that depends on the growth geometry of the crystalline entities and $R(T)$ is a cooling function that only varies with temperature and indicates how fast crystallization proceed. A plot of log $\{-\ln[1-\chi(T)]\}$ versus log ϕ may allow to determine the Ozawa exponent if linearity is accomplished. Note that the Ozawa exponent is expected to be similar to that deduced from Avrami analysis under isothermal conditions.

Figure 3.1.10 clearly demonstrates that for each crystallization temperature, a substantial departure from linearity exists and that exponents similar to the isothermal Avrami exponent (2.86) are only found in a very narrow range of cooling rates. This non-isothermal analysis reveals the limitations associated with the superposition of different crystallization processes, i.e., crystallinity values at a given temperature may correspond to primary processes at certain cooling rates and to secondary processes at lower cooling rates. In this way, exponents must reflect the impingement occurring at high degrees of crystallinity[31] and should be affected, at the beginning of crystallization, by an inaccurate measurement of the temperature at which crystallization starts.[32]

A kinetic equation that combines the Avrami and Ozawa expressions (i.e., equations 2 and 4) has been derived and applied in different non-isothermal studies [34]:

$$\log \phi = \log F(T) - a \log(t-t_0) \quad (9)$$

where $F(T)$ is a kinetic parameter referring to the cooling rate which must be chosen at a unit crystallization time when the system reaches a certain crystallinity, and a is the ratio of apparent Avrami and Ozawa exponents.

Figure 3.1.10. Plots of log{-ln[1- χ (T)]} versus log ϕ for non-isothermal crystallizations of GL-*b*-(GL-*co*-TMC-*co*-CL)-*b*-GL at the indicated temperatures. Straight segments with slopes of 2.86 are drawn.

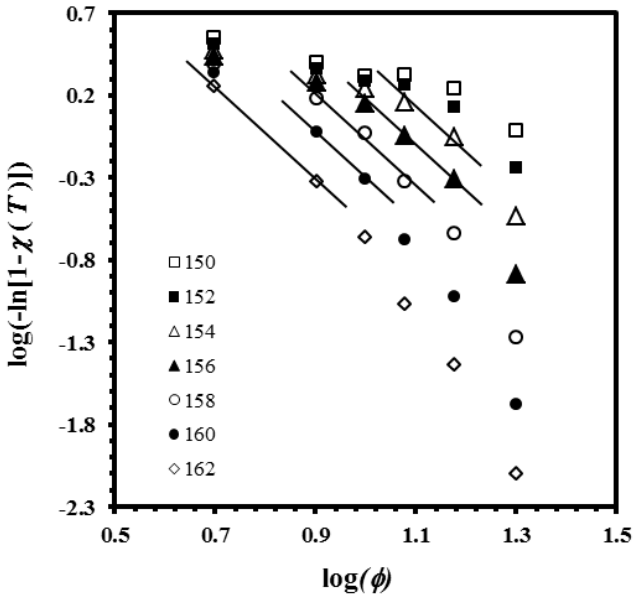

A plot of log ϕ versus log $(t - t_0)$ yields a series of straight lines at a given value of $\chi(T)$ (Figure 3.1.11) that suggests the validity of the combined equation for this system, and where kinetic parameters could be estimated by the intercept and slope of these lines. The $F(T)$ values increased with crystallinity (Table 3.1.3) since the motion of molecular chains was slower as the material crystallized and the formation of new crystals became hindered. The values of *a* were almost constant between 0.96 and 1.07 and slightly increased with the relative degree of crystallinity. However, the deduced values were again inadequate to get exponents such as Ozawa (i.e., n/a) with a physical meaning.

Figure 3.1.11. Plots of log ϕ versus log ($t-t_0$) for non-isothermal crystallization of GL-*b*-(GL-*co*-TMC-*co*-CL)-*b*-GL performed at the indicated crystallinities.

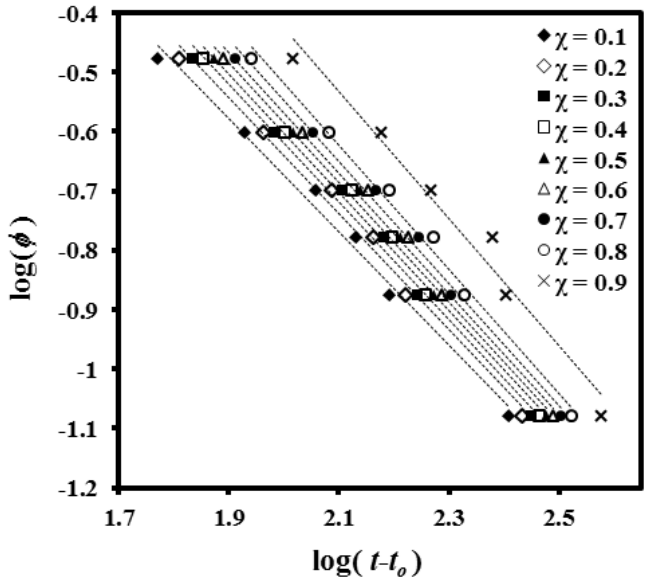

Table 3.1.3. Values of kinetic parameters at a given crystallinity estimated from the combined model [34] for non-isothermal crystallization of GL-*b*-(GL-*co*-TMC-*co*-CL)-*b*-GL.

$\chi(T)$	a	$F(T)$	r^2
0.1	0.96	17.27	0.990
0.2	0.97	20.30	0.990
0.3	0.99	22.46	0.991
0.4	0.99	24.41	0.991
0.5	1.00	26.45	0.992
0.6	1.01	28.87	0.992
0.7	1.03	32.01	0.992
0.8	1.04	36.92	0.992
0.9	1.07	52.13	0.974

The method reported by Cazé is a relatively simple analysis by which an average value for the Avrami exponent, n, can be determined based on experimental measurements from DSC cooling curves.[35] Cazé method assumes that crystallization exotherms have a Gaussian shape and thus only the maximum and inflexion point of the curves need to be considered to work with transformation rates at which impingement remains low. A theoretical peak temperature T_p' and a new constant a' are estimated by the following equation:

$$\ln\{-\ln[1-\chi(T)]\} = a'(T - T_p') \quad (10)$$

The plots of $\ln[-\ln(1-\chi(T)]$ versus T at different cooling rates (Figure 3.1.12a) are linear and are used to calculate the above parameters (Table 3.1.4). The range of application of equation 6 starts at a relative crystallinity of about 2% to ensure precision and ends when the regression coefficient is greater than 0.99. Thus, only primary crystallization is considered.

The theoretical peak temperature can be related to the value of the cooling rate by the expression:

$$T_p' = (m / a') \ln \phi - b'/a' \quad (11)$$

where b' is a new constant and m the new estimate of the exponent related to nucleation and crystal growth geometry. This exponent can be easily derived from the slope of the straight line obtained by plotting T_p' against $(\ln \phi) / a'$, as shown in Figure 3.1.12b.

An exponent of 2.98 was deduced from the non-isothermal hot crystallization experiments, which is in full agreement with a crystallization defined by predetermined (heterogeneous) nucleation and spherical growth. Note that the exponent is also in full concordance with that found for isothermal crystallization (i.e., 2.86) and therefore the physical sense is not lost.

Figure 3.1.12. (a) Plots of ln{-ln[1- χ (T)]} against temperature for non-isothermal crystallization of GL-*b*-(GL-*co*-TMC-*co*-CL)-*b*-GL with cooling rate as a parameter. **(b)** Determination of the Avrami exponent using linear plots of T_p' against (ln ϕ) / a'.

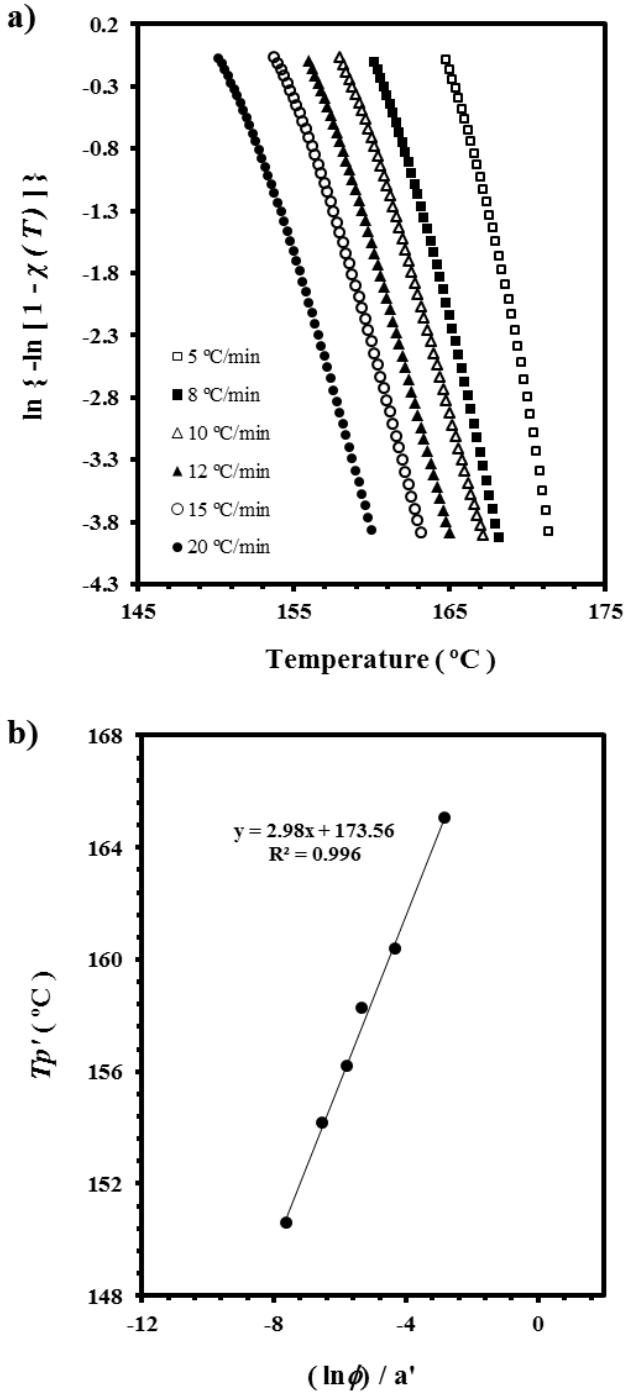

Table 3.1.4. Characteristic hot and cold crystallization parameters obtained for the segmented GL-*b*- (GL-*co*-TMC-*co*-CL)-*b*-GL sample by using the methodology developed by Cazé *et al*.[35]

ϕ (ºC/min)	a'	Tp' (ºC)	Tp^a (ºC)
5	-0.57	165.03	165.46
8	-0.48	160.39	161.15
10	-0.43	158.27	159.30
12	-0.43	156.19	157.11
15	-0.41	154.17	155.23
20	-0.39	150.60	151.76

[a] *Temperature determined for the exothermic peak observed in the cooling scans*

A methodology based on isoconversional analysis of calorimetric data was developed to estimate crystallization parameters (i.e., activation energy and secondary nucleation constant) from non-isothermal processes.[36–38] The kinetics of these crystallizations have a non-Arrheniusian behavior and therefore, a temperature-dependent effective activation energy of the growth rate was defined and derived from Lauritzen-Hoffman equation [25] by Vyazovkin and Sbirrazzuoli [36]:

$$E(T) = -R\, d\ln G / d T^{-1} = U^*[T^2/(T-T_\infty)^2] + K_g R[(2\Delta T - T_m^0 f)/(\Delta T)^2 f] \qquad (12)$$

The isoconversional method of Friedman[39] can be used to determine *effective activation energy* for a given degree of crystallinity as:

$$[d\chi / dt]_\chi = A \exp(-E_\chi / RT)\, f[\chi] \qquad (13)$$

where A is a preexponential factor and $f[\chi]$ is the crystallization model. Values of $\ln [d\chi/dt]_\chi$ at different temperatures and degrees of crystallization can be obtained from the above indicated crystallization experiments performed at different cooling rates. In this way, it is possible to determine E_χ from the slopes of the linear plots of $\ln [d\chi/dt]_\chi$ versus $1/T$ (Figure 3.1.13).

Figure 3.1.13. Plots of ln $[d\chi/dt]_\chi$ versus $1/T$ for non-isothermal crystallization of GL-*b*-(GL-*co*-TMC-*co*-CL)-*b*-GL at the indicated cooling rates. Data corresponding to relative degrees of crystallinity of 0.8, 0.5 and 0.1 are represented by blue, green and red symbols, respectively.

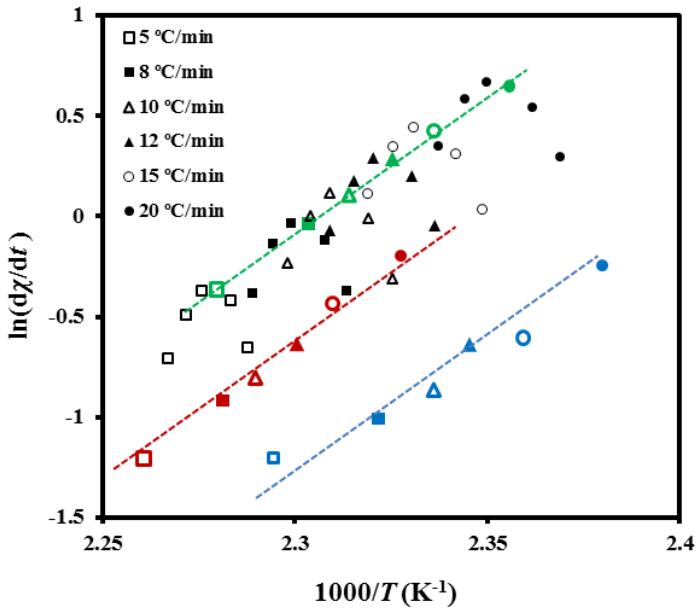

Finally, the temperature dependence of the *effective activation energy* can be derived by considering also the average temperature associated with a given conversion (Figure 3.1.14a).

Figure 3.1.14b displays the deduced E_χ-T plot from experimental data and also those simulated considering equation 12, the universal U^* and T_∞ values reported by Suzuki and Kovacs[29] and representative K_g values. In fact U^* and T_∞ have little influence on a temperature range that is far from the glass transition temperature. The best fit between experimental and theoretical data was obtained with a K_g parameter of 1.90×10^5 K^2, which makes more sense that the above deduced value from isothermal experiments. Nevertheless, the constant was again lower that the valued deduced for Maxon™ from the isoconversional analysis (2.30×10^5 K^2).[13]

The *effective activation energy* was negative at high crystallization temperatures (i.e., the zone controlled by secondary nucleation) and progressively increased with decreasing the temperature. This feature means that the crystallization rate increased with decreasing

temperatures as discussed at length by Vyazovkin and Dranca.[37] The plot shows that the maximum crystallization rate is expected for a temperature of 124.7 ºC, which is in agreement with the value deduced from the isothermal study (131 ºC).

Figure 3.1.14. (a) Dependence of the activation energy of crystallization (●) and the average temperature (○) on crystallinity. **(b)** Experimental E_χ on T data and simulated curves according to equation 12 and different values for the secondary nucleation constant. Arrow indicates the expected temperature for the maximum crystallization rate (i.e., *effective activation energy* equal to zero).

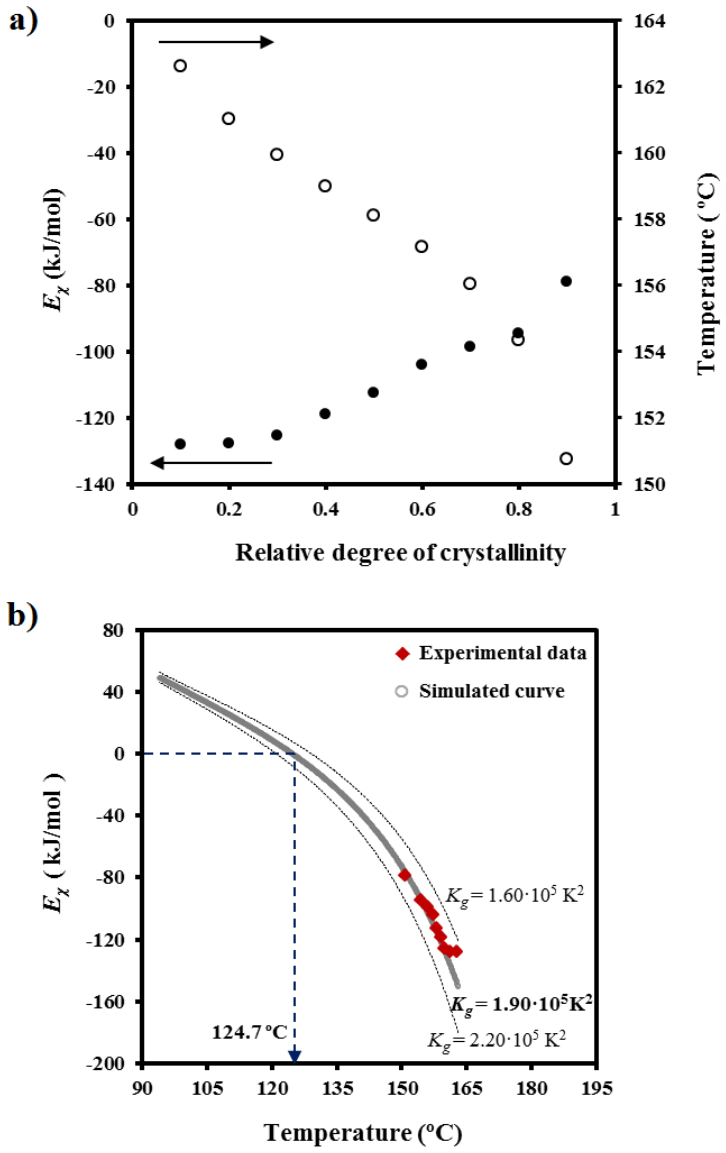

3.1.4 CONCLUSIONS

Incorporation of a 43 wt-% of amorphous GL-*co*-TMC-*co*-CL *soft segment* into the polyglycolide molecular chain caused a small depression on the melting point and had a major influence on the glass transition temperature. This mainly depended on the composition of the *soft segment* when the sample was slowly cooled from the melt state.

The melting process was complex and was characterized by a predominant melting peak that was always observed at the highest temperature and varied with the temperature at which the sample was previously crystallized. This dependence allowed determining the equilibrium melting temperature of the sample (219 ºC), which became lower than that reported for the polyglycolide homopolymer and segmented polyglycolide copolymers having a lower *soft segment* content.

Isothermal crystallization of GL-*b*-(GL-*co*-TMC-*co*-CL)-*b*-GL from the melt state took place according to a heterogeneous nucleation and a spherulitic growth, being minimum the change on the Avrami exponent with crystallization temperature. Maximum overall crystallization rate was estimated to occur at 131 ºC according to the Lauritzen-Hoffman treatment. This allowed estimating a secondary nucleation constant that resulted lower than expected and consequently a lack of proportionality between the overall crystallization rate and the crystal growth rate seems to exist.

Non-isothermal crystallization from the melt state could be well simulated by considering high Avrami exponents (i.e., higher than 7) that had not physical meaning. Ozawa analysis revealed the limitations associated with the superposition of different crystallization processes, whereas the Ozawa and Avrami combined analysis pointed out that the motion of molecular chains became slower as the material crystallized. The simple method reported by Cazé gave an average value for the Avrami exponent that was in close agreement with that deduced from isothermal experiments and consequently was the only method that rendered values with a physical meaning. Secondary nucleation constant could be estimated from non-isothermal experiments following an isoconversional analysis. This allowed deducing a constant close to 1.90×10^5 K^2 and temperature for the maximum crystallization rate of 127.5 ºC.

3.1.5 REFERENCES

1. Schmitt, E. E. & Polistina, R. A. Surgical sutures. U. S. Patent 3.297.033. American Cyanamid (1967).
2. Schmitt, E. E. & Polistina, R. A. Polyglycolic acid prosthetic devices. U. S. Patent 3.463.158. American Cyanamid (1969).
3. Brandrup, J., Immergut, E. H. & Grulke, E. A. Solid state properties (Chapter 6). In *Polymer Handbook* (Interscience Publishers, 1999).
4. Homsy, C. A., McDonald, E. R. & Akers, W. W. Surgical suture-canine tissue interaction for six common suture types. *J. Biomed. Mater. Res.* **2,** 215–230 (1968).
5. Blomstedt, B. & Ostenberg, B. Suture materials and wound infection. An experimental study. *Acta Chir. Scand.* **144,** 269–274 (1978).
6. Rodeheaver, G. T. *et al.* Knotting and handling characteristics of coated synthetic absorbable sutures. *J. Surg. Res.* **35,** 525–530 (1983).
7. Katz, A. R., Mukherjee, D. P., Kaganov, A. L. & Gordon, S. A new synthetic monofilament absorbable suture made from polytrimethylene carbonate. *Surgery, Gynecol. Obstet.* **161,** 213–222 (1985).
8. Oberhoffner, S. & Planck, H. Surgical suture material from triblockterpolymer, its use in surgery and process for its preparation. EP 0835895. (2003).
9. Roby, M. S., Bennet, S. L. & Liu, E. K. Absorbable block copolymers and surgical articles fabricated thereform. U.S.Patent 5.403.347. (1995).
10. Bezwada, R. S. *et al.* Monocryl suture, a new ultra-pliable absorbable monofilament suture. *Biomaterials* **16,** 1141–1148 (1995).
11. Noorsal, K., Mantle, M. D., Gladden, L. F. & Cameron, R. E. Degradation and drug-release studies of a poly(glycolide-*co*-trimethylene carbonate) copolymer (Maxon). *J. Appl. Polym. Sci.* **95,** 475–486 (2005).
12. Díaz-Celorio, E., Franco, L. & Puiggalí, J. Isothermal crystallization study on a biodegradable segmented copolymer constituted by glycolide and trimethylene carbonate units. *J. Appl. Polym. Sci.* **116,** 577–589 (2010).
13. Díaz-Celorio, E., Franco, L. & Puiggalí, J. Nonisothermal crystallization behavior of a biodegradable segmented copolymer constituted by glycolide and trimethylene carbonate units. *J. Appl. Polym. Sci.* **119,** 1548–1559 (2011).
14. Díaz-Celorio, E., Franco, L., Rodríguez-Galán, A. & Puiggalí, J. Synthesis of glycolide/trimethylene carbonate copolymers: Influence of microstructure on properties. *Eur. Polym. J.* **48,** 60–73 (2012).
15. Díaz-Celorio, E., Franco, L., Rodríguez-Galán, A. & Puiggalí, J. Study on the hydrolytic degradation of glycolide/trimethylene carbonate copolymers having different microstructure and composition. *Polym. Degrad. Stab.* **98,** 133–143 (2013).
16. Díaz-Celorio, E., Franco, L. & Puiggalí, J. Influence of microstructure on the crystallization of segmented copolymers constituted by glycolide and trimethylene carbonate units. *Express Polym. Lett.* **7,** 186–198 (2013).
17. Castillo, R. V. & Müller, A. J. Crystallization and morphology of biodegradable or biostable single and double crystalline block copolymers. *Prog. Polym. Sci.* **34,** 516–560 (2009).

18. Hoffman, J. D. & Weeks, J. J. Melting process and the equilibrium melting temperature of polychlorotrifluoroethylene. *J. Res. Natl. Bur. Stand. A Phys. Chem.* **66A,** 13–28 (1962).

19. Strobl, G. From the melt via mesomorphic and granular crystalline layers to lamellar crystallites: a major route followed in polymer crystallization? *Eur. Polym. J.* **E3,** 165–183 (2000).

20. Marand, H., Xu, S. & Srinivas, S. Determination of the equilibrium melting temperature of polymer crystals: linear an nonlinear Hoffman-Weeks extrapolations. *Macromolecules* **31,** 8219–8229 (1998).

21. Hoffman, J. D., Davies, G. T. & Lauritzen, J. D. The rate of crystallization of linear polymers with chain folding (Chapter 7) In *Treatise on solid state chemistry* (ed. Hannay, N. B.) (1976).

22. Lebedev, B. V., Yepstropov, A. A., Kiparisova, V. G. & Belov, V. I. The thermodynamics of glycolide, polyglycolide and of polymerization of glycolide in the temperature range of 0 - 550K. *Polym. Sci. U.S.S.R* **20,** 32–42 (1978).

23. Avrami, M. Kinetics of phase change. I General theory. *J. Chem. Phys.* **7,** 1103–1112 (1939).

24. Avrami, M. Kinetics of phase change. II Transformation time relations for random distribution of nuclei. *J. Chem. Phys.* **8,** 212–224 (1940).

25. Lauritzen, J. I. & Hoffman, J. D. Extension of theory of growth of chain-folded polymer crystals to large undercoolings. *J. Appl. Phys.* **44,** 4340-4352 (1973).

26. Turnbull, D. & Fisher, J. C. Rate of nucleation in condensed systems. *J. Chem. Phys.* **17,** 71–73 (1949).

27. Kenny, J. M., Maffezzoli, A. & Nicolais, R. A new kinetic model for polymer crystallization by calorimetric analysis. *Thermochim. Acta* **227,** 83–95 (1993).

28. Urbanovici, E., Schneider, H. A. & Cantow, H. J. Some considerations concerning the temperature dependence of the bulk crystallization rate constants of polymer materials. *J. Polym. Sci. Part B Polym. Phys.* **35,** 359–369 (1997).

29. Suzuki, T. & Kovacs, A. J. Temperature dependence of spherulitic growth rate of isotactic polystryrene. A critical comparison with the kinetic theory of surface nucleation. *Polym. J.* **1,** 82–100 (1970).

30. Schultz, J. M. *Polymer crystallization the development of crystalline order in thermoplastic polymers.* (ACS/Oxford University Press, 2001).

31. López, L. C. & Wilkes, G. L. Non-isothermal crystallization kinetics of poly(*p*-phenylene suphide). *Polymer.* **30,** 882–887 (1989).

32. Privalko, V. P., Kawai, T. & Lipatov, Y. S. Crystallization of filled Nylon 6. III Non-isothermal crystallization. *Colloid. Polym. Sci.* **257,** 1042–1048 (1979).

33. Ozawa, T. A new method of analyzing thermogravimetric data. *Bull. Chem. Soc. Jpn.* **38,** 1881–1886 (1965).

34. Liu, T. X., Mo, Z. S., Wang, S. G. & Zhang, H. F. Nonisothermal melt and cold crystallization kinetics of poly(aryl ether ether ketone ketone). *Polym. Eng. Sci.* **37,** 568–575 (1997).

35. Cazé, C., Devaux, E., Crespy, A. & Cavrot, J. P. A new method to determine the Avrami exponent by DSC studies of non-isothermal crystallization from the molten state. *Polymer*. **38,** 497–502 (1997).

36. Vyazovkin, S. & Sbirrazzouli, N. Isoconversional approach to evaluating the Hoffman-Lauritzen parameters (U^* and K_g) from overall rates of nonisothermal melt crystallization. *Macromol. Rapid Commun.* **25 (6),** 733–738 (2004).

37. Vyazovkin, S. & Dranca, I. Isoconversional analysis of combined melt and glass crystallization data. *Macromol. Chem. Phys.* **207,** 20–25 (2006).

38. Vyazovkin, S., Stone, J. & Sbirrazzouli, N. Hoffman-Lauritzen parameters for non-isothermal crystallization of poly(ethylene terephthalate) and poly(ethylene oxide) melts. *J. Therm. Anal. Calorim.* **80,** 177–180 (2005).

39. Friedman, H. J. Kinetics of thermal degradation of char-forming plastics from thermogravimetry. *J. Polym. Sci. Part C Polym. Symp.* **6,** 183–195 (1964).

3.2. Spherulitic morphologies: Isothermal and non-isothermal crystallization studies

Crystallization of a biodegradable segmented copolymer constituted by polyglycolide *hard segments* and a middle *soft segment* constituted by a random disposition of glycolyl, ε-caproyl and trimethylene carbonyl units has been studied by means of optical microscopy, atomic force microscopy and time resolved X-ray diffraction techniques. This GL-*b*-(GL-*co*-TMC-*co*-CL)-*b*-GL copolymer is widely employed as surgical suture and has similar characteristics than previously studied copolymers having a middle *soft segment* constituted by only two monomers (i.e., glycolide and trimethylene carbonate).

FTIR and NMR spectroscopies demonstrated that the middle segment had an amorphous character and a random microstructure as consequence of transesterification reactions that took place during synthesis. Nevertheless, polyglycolide segments were able to crystallize giving rise to peculiar positive birefringent spherulites with a morphology, which depends on crystallization temperature (i.e., flat-on and edge-on crystals) as verified by AFM and electron diffraction patterns.

Complete bell shaped curves that defined the temperature dependence of the crystal growth rate could be experimentally obtained from both, isothermal and non-isothermal crystallizations. Data from both analyses were in close agreement and pointed out a secondary nucleation constant (2.42-2.88 $\times$ 10^5 K^2) which was clearly higher than that determined for the related system with two components. Lamellar morphologic parameters were similar for samples crystallized from the melt state and after the reordering process that took place on heating. Comparing to the bicomponent system, significant differences were again observed highlighting the influence of the *soft segment* on the crystallization behavior.

3.2.1. INTRODUCTION

Polyglycolide is a biodegradable polyester widely employed for biomedical applications, being specifically the development of bioabsorbable surgical sutures one of its first applications.[1–8] Polyglycolide has a distinctive crystalline structure that renders differentiated properties respect to similar aliphatic polyesters.[9] Thus, for example it has a melting temperature higher than 200 ºC and a glass transition temperature in the 35-40 °C range that contrast with the low values found for the other members of the series (e.g., melting point of 55–60 °C and glass transition temperature close to –60 °C for poly(ε-caprolactone)[10]). In addition, polyglycolide is relatively hygroscopic and therefore exhibits a high degradation rate, shows a good biocompatibility and excellent fiber forming properties. These good properties can be extended to a wide range of copolymers differing on components and composition, being specifically degradation behavior and mechanical properties intensively investigated.[11–15]

Bioabsorbable surgical sutures can be processed in monofilament and multifilament forms, being the former preferred due to advantages like more resistance to harbor microorganisms and higher facility to passage through tissue than conventional braided threads.[16–18] The high stiffness of polyglycolide makes its processing as a monofilament suture impossible, being therefore different formulations developed to get flexible materials while glycolide is kept as a predominant component. In this way, different segmented copolymers having two polyglycolide *hard segments* and a middle *soft segment* derived from glycolide and other monomers (e.g., trimethylene carbonate, ε-caprolactone or *p*-dioxanone) have been prepared to provide flexibility.[19–21]

Maxon™ (Syneture) is one of the most simple monofilament synthetic sutures based on glycolide copolymers that has been employed. This copolymer is characterized by a 62 wt-% of polyglycolide *hard segments* and a middle *soft segment* constituted by a random disposition of 85 wt-% of trimethylene carbonate and 15 wt-% of glycolide.[22] The design of this GL-*b*-(GL-*co*-TMC)-*b*-GL copolymer is relevant to meet the requirements of a bioresorbable suture. It should be also considered that processing affects crystallinity and hence mechanical properties and degradability. In this way, comprehension of the crystallization process in a polymeric system where amorphous (*soft segments*) and crystalline domains (*hard segments*) coexist is a highly interesting topic.

The crystallization process of GL-*b*-(GL-*co*-TMC)-*b*-GL has been extensively evaluated under both isothermal and non-isothermal conditions for the commercial sample[23,24] as well as for copolymers with slightly different microstructure. Results demonstrated that small variations on the *hard segment* length and the *soft segment* content had a high influence on melting temperature, degree of crystallinity, degradation rate, crystallization kinetics and crystalline morphology.[25–27] For example, the crystalline lamellar thickness is higher for samples with a low polyglycolide *hard segment* content as a consequence of the incorporation of *soft segments* into the crystalline phase in such a way that imperfect crystals with a low melting point are developed.[27]

GL-*b*-(GL-*co*-TMC-*co*-CL)-*b*-GL has also been employed as a monofilament suture with properties (e.g., *in vitro* degradation) that covers a similar range than Maxon™. This segmented copolymer is synthesized following the two step procedure (**Figure 3.1.1**), which renders a middle *soft segment* based on three components and two polyglycolide *hard blocks*.[20] With regard to Maxon™, it is significant the different constitution of the *soft segment* (three components instead of two), the lower *hard segment* percentage (57 versus 62 wt-%) and the slightly higher glycolyl content (72 versus 67.5 wt-%).

Studies about the crystallization process of the commercial GL-*b*-(GL-*co*-TMC-*co*-CL)-*b*-GL suture are scarce and basically concern to isothermal and non-isothermal analyses from DSC calorimetric data.[28] These indicated a maximum overall crystallization rate around 131 °C and a secondary nucleation constant of 1.51×10^5 K^2 that became lower than reported for Maxon™ (1.86×10^5 K^2). This is an expected result taking into account the higher content of non-crystallizable *soft segments* with greater statistical monomer distribution. Therefore, a complementary study using optical microscopy data appears necessary. Furthermore, morphological data concerning the lamellar structure are also interesting in order to improve comprehension of how small changes on the polymer architecture can affect microphase separation. In fact, fiber properties are governed by physical structures of different scales, including amorphous and crystalline domains as well as lamellar structures.

3.2.2. EXPERIMENTAL SECTION

3.2.2.1. Materials

Commercially available sutures of GL-*b*-(GL-*co*-TMC-*co*-CL)-*b*-GL (Monosyn®, USP 1) were kindly supplied by B. Braun Surgical, S.A. This triblock copolymer has a middle *soft segment* that constitutes a 43 wt-% of the sample and that is composed of 35 wt-%, 32.5 wt-% and 32.5 wt-% of glycolyl, trimethylene carbonyl and ε-caproyl units, respectively.[20] Diethylene glycol was used as a bifunctional initiator for the ring opening polymerization that leads to the *soft segment* (see the first synthesis step of Figure 3.1.1). Therefore, a prepolymer having two hydroxyl terminal groups was obtained and consequently, polyglycolide hard blocks could be incorporated at both ends in the second polymerization step (Figure 3.1.1).Weight and number average molecular weights of GL-*b*-(GL-*co*-TMC-*co*-CL)-*b*-GL samples were 71,000 and 41,000 g/mol, as previously reported.[28]

3.2.2.2. Measurements

^{1}H-NMR spectra were acquired with a Bruker AMX-300 spectrometer operating at 300.1 MHz and 75.7 MHz, respectively. Chemical shifts were calibrated using tetramethylsilane as an internal standard. Dried dimethyl sulfoxide-d_6 (DMSO) was used as the solvent at a temperature of 90-95 ºC to enhance solubility and resolution.

Infrared absorption spectra were recorded with a Fourier Transform FTIR 4100 Jasco spectrometer in the 4000-600 cm^{-1} range. A Specac model MKII Golden Gate attenuated total reflection (ATR) cell with a heated Diamond ATR Top-Plate which can be used at up to 200 ºC, and a Series 4000 High Stability Temperature Controler were also employed.

Calorimetric data were obtained by differential scanning calorimetry with a TA Instruments Q100 series. Experiments were conducted under a flow of dry nitrogen with a sample weight of approximately 5 mg and at a heating rate of 20 ºC/min.

The spherulite growth rate was determined by optical microscopy using a Zeiss Axioskop 40 Pol light polarizing microscope equipped with a Linkam temperature control system configured by a THMS 600 heating and freezing stage connected to a LNP 94 liquid nitrogen cooling system. Spherulites were grown from homogeneous thin films prepared by evaporation of dilute solutions of the polymer in 1,1,1,3,3,3-hexafluoroisopropanol (0.5

mg/mL). Next, small sections of these films were pressed or smeared between two cover slides and inserted into the hot stage, with thicknesses of close to 10 μm in all cases. Samples were kept at 220 ºC (approximately 20 ºC above the polymer melting point of 200 ºC) for 5 minutes to eliminate sample history effects. For hot crystallization experiments, samples were quickly cooled to the selected crystallization temperature, whereas for cold crystallization experiments, they were quickly cooled to room temperature and then quickly heated to the selected crystallization temperature. The radius of growing spherulites was monitored during crystallization with micrographs taken with a Zeiss AxiosCam MRC5 digital camera at appropriate time intervals. A first-order red tint plate was employed to determine the sign of spherulite birefringence under crossed polarizers. For non-isothermal experiments, the radius of growing spherulites was also monitored during crystallization with micrographs taken at appropriate time intervals.

A Philips TECNAI 10 electron microscope was used and operated at 100 kV for bright field and electron diffraction modes, respectively. Selected area electron diffraction patterns were taken with a SIS MegaView II digital camera and internally calibrated with gold (d_{111} = 0.235 nm). Spherulites were grown at 80 and 150 ºC from melted thin films which had previously been prepared by solvent casting from a dilute solution of the polymer in 1,1,1,3,3,3-hexafluoroisopropanol. Nucleation density was determined from low magnification micrographs (i.e., ×100 due to the great size of spherulites) by counting the number of spherulites developed in representative areas.

For AFM studies, thin films were prepared by solvent casting of a dilute solution in 1,1,1,3,3,3-hexafluoroisopropanol and placed between cover slides. Samples were subsequently heated above the melting point to perform cold (after quenching) and hot crystallization experiments at the selected temperatures. After crystallization cover slides were manually separated to perform AFM observations. This feature caused some limitations on the image quality and especially for the thinnest spherulites characterized by a planar lamellar disposition as then will be shown. Height and amplitude images of spherulites were obtained with a Molecular Imaging PicoSPM using a NanoScope IV controller in ambient conditions and a scan window size of 10 x 10 μm^2. The tapping mode AFM was operated at constant deflections (i.e., vertical constant force with triangular gold-coated silicon nitride). Row scanning frequency was set to 1 Hz and physical tip-sample motion speed was 10 μm/s.

Time resolved SAXS experiments were carried out at the NCD beamline (BL11) of the Alba synchrotron radiation light facility of Cerdanyola del Vallès (Catalunya). The beam was monochromatized to a wavelength of 0.100 nm. Polymer samples were confined in capillaries and then held on a Linkam HFSX-350-CAP hot stage with temperature control within ±0.1 ºC. SAXS profiles were acquired during heating and cooling runs in time frames of 20 s and rates of 10 ºC/min. The detector was calibrated with different orders of diffraction from silver behenate. The diffraction profiles were normalized to the beam intensity and corrected considering the empty sample background. The correlation function and corresponding parameters were calculated with the CORFUNC program for Fibre Diffraction / Non-Crystalline Diffraction provided by the Collaborative Computational Project 13. The WAXD detector was calibrated with diffractions of a standard of a Cr_2O_3 sample. The diffraction profiles were normalized to the beam intensity and corrected considering the empty sample background. Deconvolution of WAXD peaks was performed with the PeakFit v4 program by Jandel Scientific Software using a mathematical function known as "Gaussian area".

3.2.3. RESULTS AND DISCUSSION

3.2.3.1. Characterization

Figure 3.2.1 shows the ^{1}H-NMR spectra of the GL-*b*-(GL-*co*-TMC-*co*-CL)-*b*-GL sample with an assignment of the characteristic signals based on previous works on bicomponent systems (i.e., poly(glycolide-*co*-trimethylene carbonate)[29] and poly(glycolide-*co*-caprolactone) [30]). A sequence sensitivity is observed, especially for signals corresponding to glycolyl protons, which extends over the 4.83-4.57 ppm range (Table 3.2.1 and inset of Figure 3.2.1).

It is interesting to remark that the signal of the middle glycolyl protons of a GGG sequence (G, glycolyl unit) appears at 4.83 ppm whereas the four signals at 4.64-4.57 ppm correspond to the glycolyl protons of transesterification sequences that cannot be produced by direct ring opening polymerization. Note that glycolide should lead to sequences having at least two consecutive glycolyl units. Transesterification reactions should mainly occur during the first polymerization step where trimethylene carbonate and ε-caprolactone rings are at the highest ratio.[25] The spectra indicate that the four transesterification sequences (i.e., TGT, TGCap, CapGT and CapGCap listed from downfield to upfield) appeared with similar intensity, and therefore all possible thermally induced

transesterification reactions were practically equiprobable. ^{1}H-NMR spectra support an amorphous character of the *soft segment* due to the multiple sequences produced by practically random copolymerization of the three involved monomers and the occurrence of subsequent transesterification reactions. In fact, the areas of NMR signals indicate that 7.8 molar-% of glycolyl units was incorporated into the transesterification sequences.

Figure 3.2.1. ^{1}H-NMR spectra of GL-*b*-(GL-*co*-TMC-*co*-CL)-*b*-GL with labelling of the most distinctive sequences. Inset shows a detail of glycolyl signals and characteristic transesterification sequences

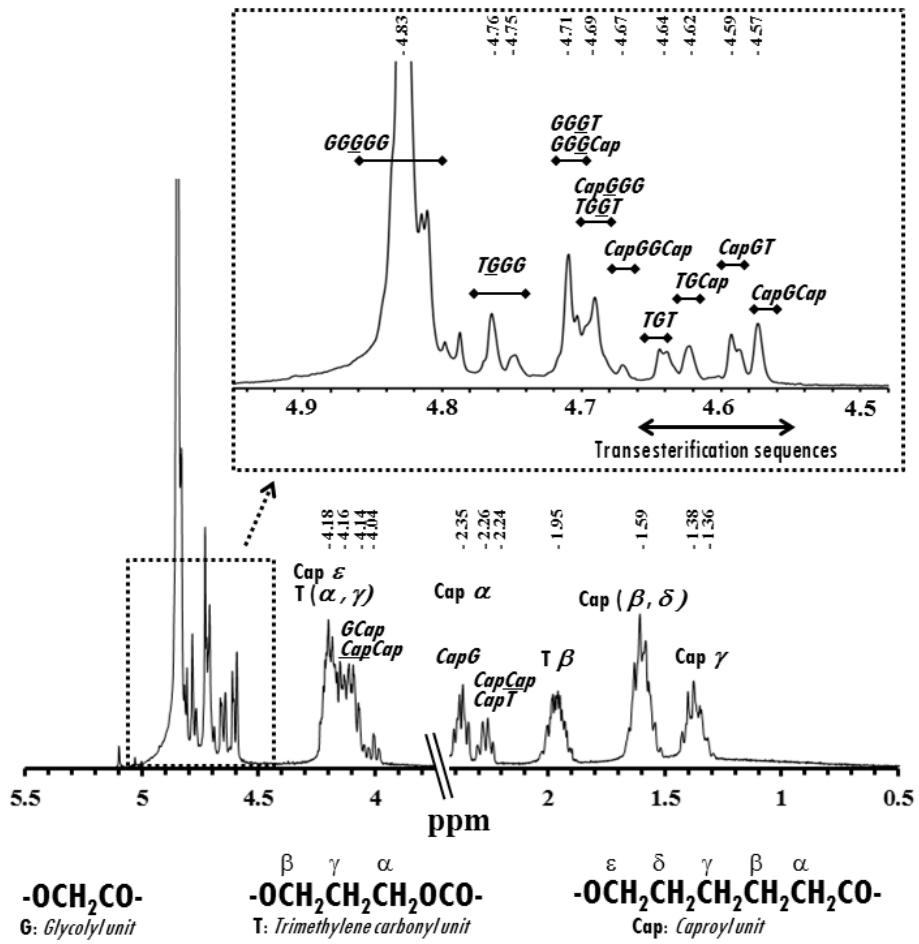

Table 3.2.1. Main distinctive signals observed in the ^{1}H-NMR spectra of GL-*b*-(GL-*co*-TMC-*co*-CL)-*b*-GL.

Sequence	δ (ppm)
Glycolide methylene protons	
GGGGG	4.83
TGGG	4.76 - 4.75
GGGT + GGGCap	4.70
CapGGG + TGGT	4.69
CapGGCap	4.67
TGT	4.64
TGCap	4.62
CapGT	4.59
CapGCap	4.57
CH_2 (ε) protons of the ε-oxycaproyl unit	
GCap	4.14
CapCap	4.04
CH_2 (α) protons of the ε-oxycaproyl unit	
CapG	2.35
CapCap + CapT	2.26 – 2.24

The infrared absorption spectrum in the 1800-750 cm^{-1} wavenumber region is highly sensitive to the amorphous and crystalline character of samples, and therefore useful to complete their characterization. **Figure 3.2.2** compares the FTIR spectra of the three homopolymers and the triblock copolymer. The presence of bands typically reported for the crystalline homopolymer, [25,31,32] such as those at 1414, 972 and 902 cm^{-1}, indicates that polyglycolide crystalline domains were abundant in the as-processed suture. The spectra changed when the sample was melted and became highly similar to that corresponding to amorphous polyglycolide with characteristic bands at 1425 and 1399 cm^{-1}. Despite the low trimethylene carbonate unit content, some typical bands of PTMC (e.g., 1030 and 788 cm^{-1}) could still be detected in both amorphous and crystalline copolymer samples.[32]

In addition, the presence of crystalline caproyl units can be discarded since their characteristic and well defined bands were not detected (e.g., 960 and 933 cm^{-1}).

Figure 3.2.2. Transmission FTIR spectra (1800-750 cm^{-1}) of semicrystalline (black traces) and/or amorphous (red traces) of PGL, PCL, PTMC and GL-*b*-(GL-*co*-TMC-*co*-CL)-*b*-GL samples. Characteristic amorphous (G_{am}) and crystalline (G_{cr}) bands associated with PGL and amorphous PTMC bands are indicated by arrows in the spectra of the suture. Note also the absence of PCL crystalline bands at 960 and 933 cm^{-1} in the spectrum of the semicrystalline copolymer samples.

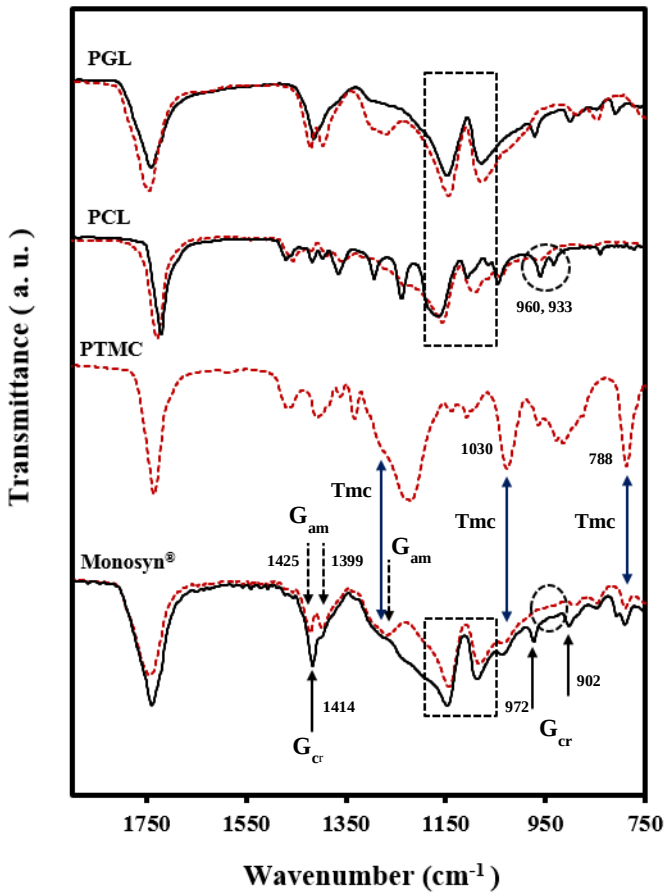

DSC heating traces of polyglycolide and the triblock copolymers (Figure 3.2.3) showed clear differences concerning to the melting temperature and enthalpy that logically decreased for the copolymer (i.e., from 213-222 ºC to 200 ºC and from 80 J/g to 40 J/g). The clear decrease on the melting enthalpy corroborated the high amorphous content, being nevertheless the value comparable with that found for the homopolymer when the energy was referred to the *hard segment* content (i.e., 70 J/g).

Figure 3.2.3. DSC heating traces of polyglycolide (up) and the triblock copolymer (down).

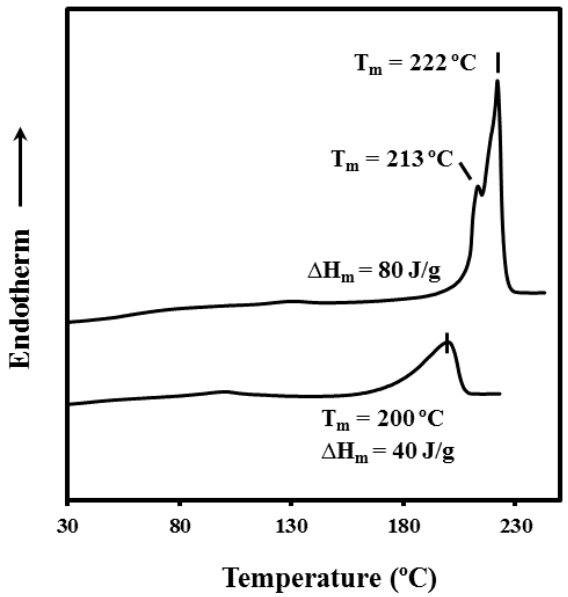

WAXD diffraction profile of the copolymer (Figure 3.2.4) allowed estimating a degree of crystallinity close to 25%, which was significantly lower than found for PGL and coherent with the hard block content.

Figure 3.2.4. X-ray diffraction profile of the triblock copolymer showing two amorphous halos (dashed lines) and the main Bragg reflections (red lines).

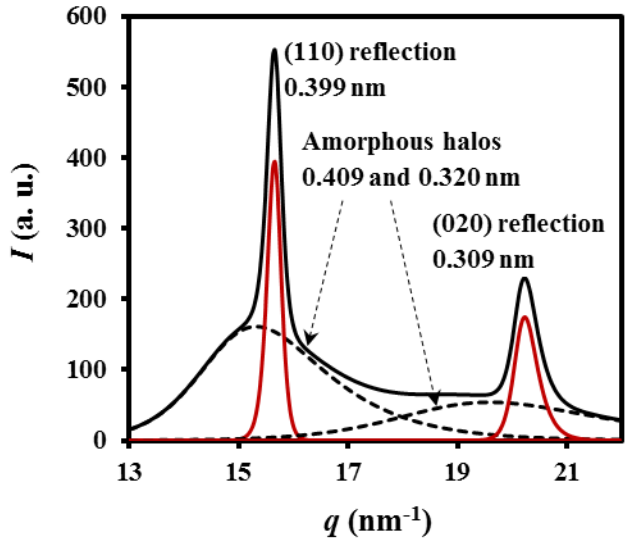

3.2.3.2. Spherulitic morphologies developed during isothermal crystallization

GL-*b*-(GL-*co*-TMC-*co*-CL)-*b*-GL spherulites were obtained from hot and cold crystallization experiments. In all cases, a positive birefringence was observed (Figure 3.2.5) because of the peculiar crystalline structure of polyglycolide. In fact, the structure of polyglycolide is defined by an orthorhombic unit cell with a = 0.522 nm, b = 0.619 nm, and c = 0.702 nm and a $P2_12_12_1$ space group where molecules with a fully extended zigzag conformation form sheets parallel to the *ac* crystallographic plane.[9] The setting angle of the molecular segments is 0º or 180º, values clearly different from typical angles of ±45º determined for other aliphatic polyesters with a planar zigzag conformation. Unlike conventional polyesters that rendered spherulites with a negative birefringence,[33–35] polyglycolide has a perfect alignment of ester groups along the *a* crystallographic direction. This feature can explain the peculiar positive birefringence when this direction becomes parallel to the spherulitic radi.

Slight differences in spherulitic morphology were detected with the crystallization temperature. Specifically, spherulites grown at the higher temperatures had a flower-like

appearance (e.g., crystallization performed at 160 ºC in Figure 3.2.5a) characterized by the development of multiple sectors. This morphology may suggest confined crystallization of flat-on lamellae instead of formation of edge-on or even twisted lamellae going round the spherulite, as is characteristic of typical fibrilar or ringed spherulites. Irregular boundaries derived from this morphology were still evident at 145 ºC (arrows in Figure 3.2.5b), but perfectly round morphologies formed at even lower temperatures (e.g., Figure 3.2.5c for crystallization at 80 ºC). Logically, spherulites obtained from cold crystallization (Figure 3.2.5d) showed similar characteristics to those observed at low temperature crystallizations from the melt state. It is also clear that the latter had a fibrilar morphology whereas at the highest temperature greater crystalline domains that could correspond to flat-on lamellae were detected within the spherulites. It is also interesting to note that amorphous domains associated with the *soft segments* should be inside the spherulites since these covered all the available space when they grew until impingement (Figures 3.2.5e and 3.2.5f).

Figure 3.2.5. Polarized optical micrographs of GL-*b*-(GL-*co*-TMC-*co*-CL)-*b*-GL spherulites crystallized from the melt **(a, b, c, e)** and cold crystallized **(d, f)**. Black and white micrographs correspond to samples crystallized at 160 ºC **(a)**, 145 ºC **(b)**, 80 ºC **(c)**, 70 ºC **(d)**, whereas color micrographs were taken at the end of crystallizations performed at 155 ºC **(e)** and 70 ºC **(f)** using a first-order red tint plate. Arrows point to irregular edges detected during high temperature crystallizations.

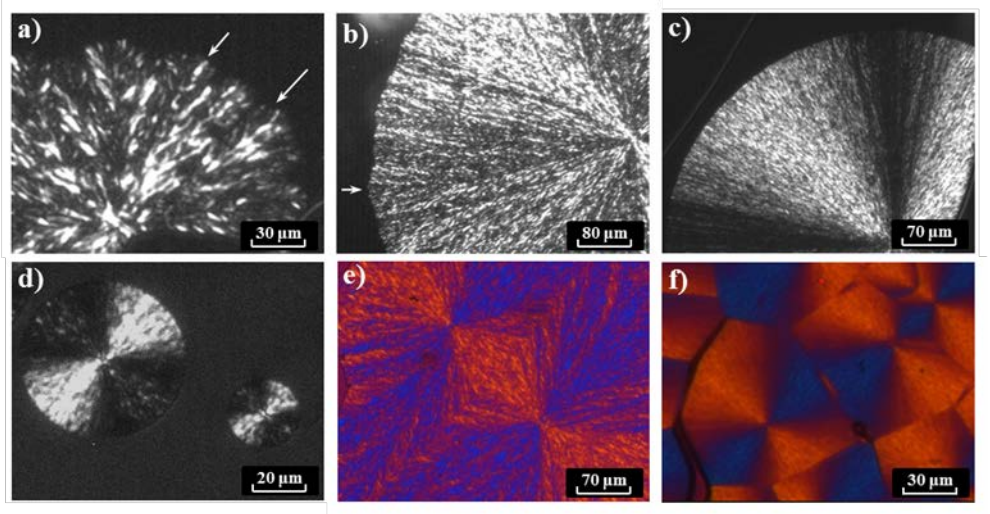

The intensity of birefringence of spherulites grown following several isothermal steps decreased at lower temperatures for samples crystallized from the melt (Figure 3.2.6a) and the glass state (Figure 3.2.6b). Micrographs showed that inner crystalline domains were similar in zones formed at different temperatures, although their size clearly decreased with decreasing temperature. In fact, flat-on crystals with lateral dimensions of up to 1 μm were envisaged in the AFM micrographs of spherulites grown at high temperature (blue arrows in Figure 3.2.7a), whereas microcrystals had a more acicular, often even twisted (red arrows), form at lower crystallization temperatures (Figure 3.2.7b).

Figure 3.2.6. Polarized optical micrographs of GL-*b*-(GL-*co*-TMC-*co*-CL)-*b*-GL spherulites isothermally grown at three temperature starting at 150 ºC **(a)** and 85 ºC **(b)**.

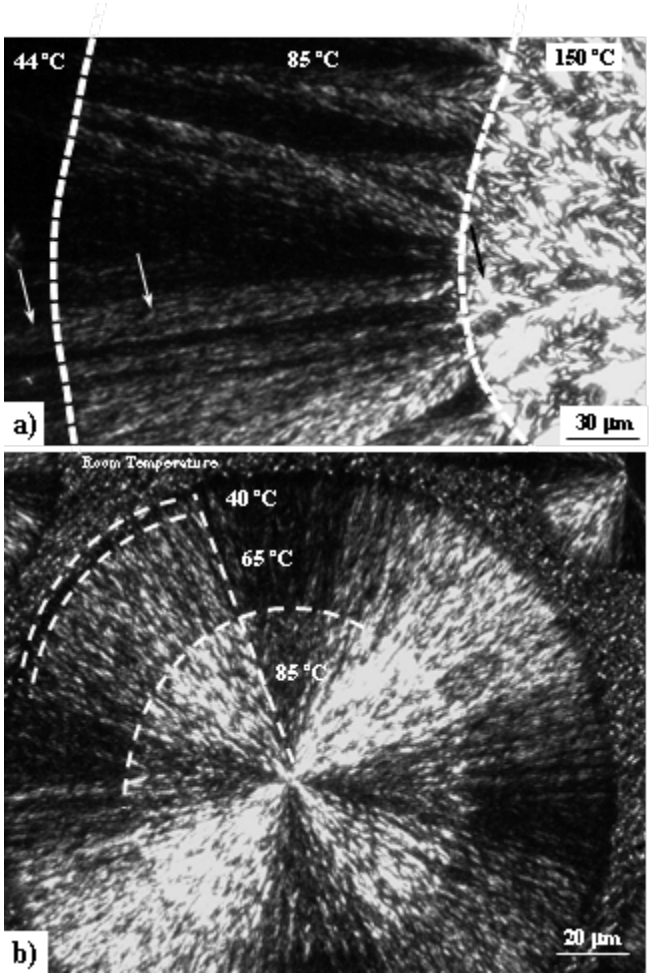

Figure 3.2.7. Atomic force microscopy 3D height images of GL-*b*-(GL-*co*-TMC-*co*-CL)-*b*-GL spherulites isothermally crystallized from the melt and the glass state at 150 ºC **(a)** and 80 ºC **(b)**, respectively. Insets show amplitude and low magnification 3D height images.

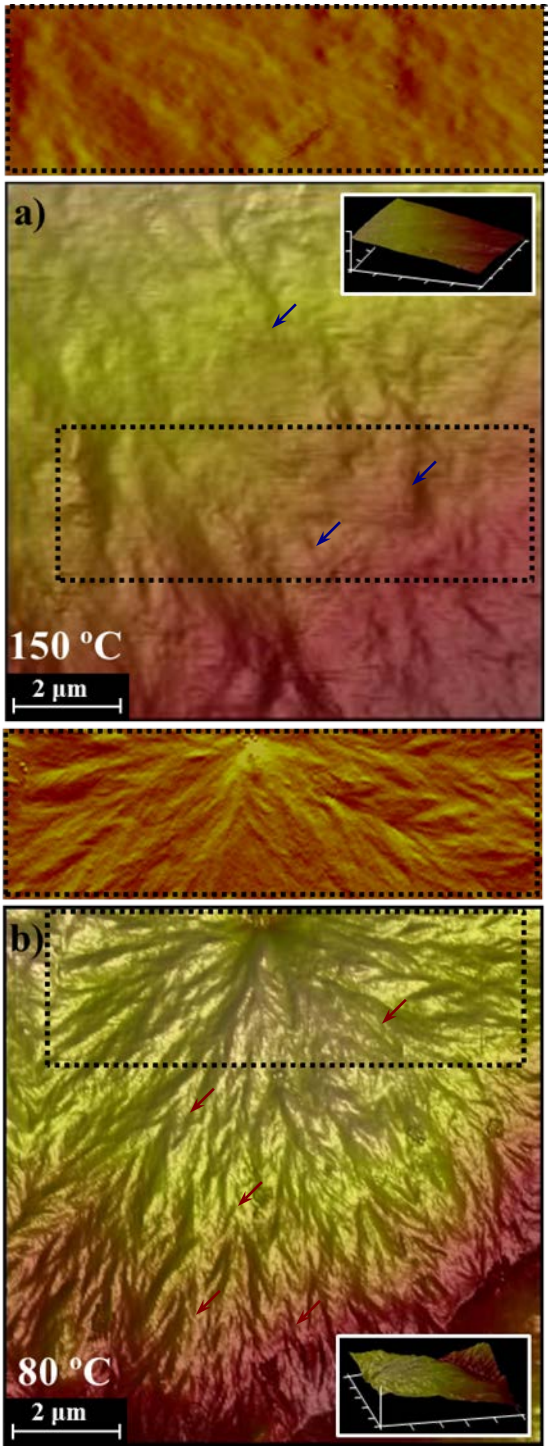

These observations were confirmed by electron diffraction patterns recorded from the different spherulites. Thus, typical polyglycolide *hk*0 diffraction pattern with strong 110 (0.399 nm) and 020 (0.309 nm) reflections were easily obtained from high temperature crystallized spherulites (Figure 3.2.8a), whereas this pattern was hardly observed in low temperature crystallized samples. In this case, the intensity of reflections was low (Figure 3.2.8b) and even asymmetric patterns (Figure 3.2.8c) indicative of lamellar twisting were more frequently recorded. The *hk*0 pattern was always oriented with its *a** reciprocal axis parallel to the spherulite radius, justifying the peculiar positive birefringence sign of the spherulite as above indicated.

Figure 3.2.8. Electron diffraction patterns of GL-*b*-(GL-*co*-TMC-*co*-CL)-*b*-GL spherulites crystallized from the melt and the glass state at 150 ºC **(a)** and 80 ºC **(b,c)**, respectively. In all cases, the *a** reciprocal axis is parallel to the spherulite radius.

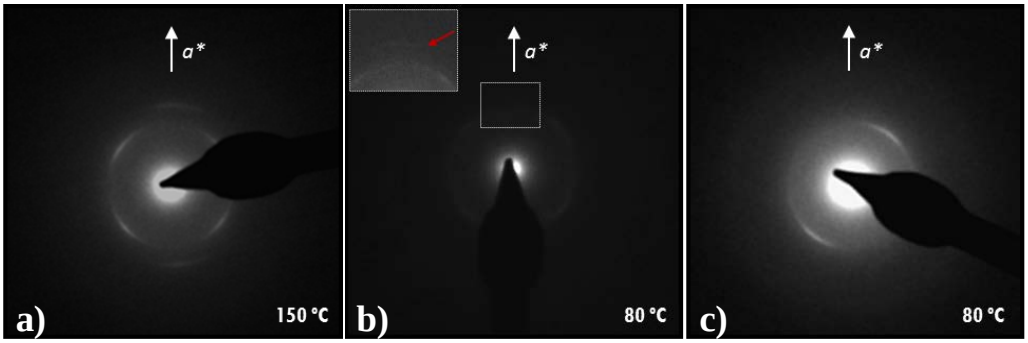

3.2.3.3. Secondary nucleation constant for the isothermal crystallization

Kinetics of crystallization of GL-*b*-(GL-*co*-TMC-*co*-CL)-*b*-GL from the melt and the glass state was studied by optical microscopy. Spherulite radii grew linearly with time until impingement, as shown in Figure 3.2.9 for cold crystallization experiments performed in the temperature range from 60 ºC to 90 ºC. Final radii varied in this case between 28 and 65 μm and logically decreased at higher primary nucleation densities (i.e., at lower crystallization temperatures).

Figure 3.2.9. Plots of the radius of GL-*b*-(GL-*co*-TMC-*co*-CL)-*b*-GL spherulites versus crystallization time for isothermal cold crystallizations performed between 60-90 ºC.

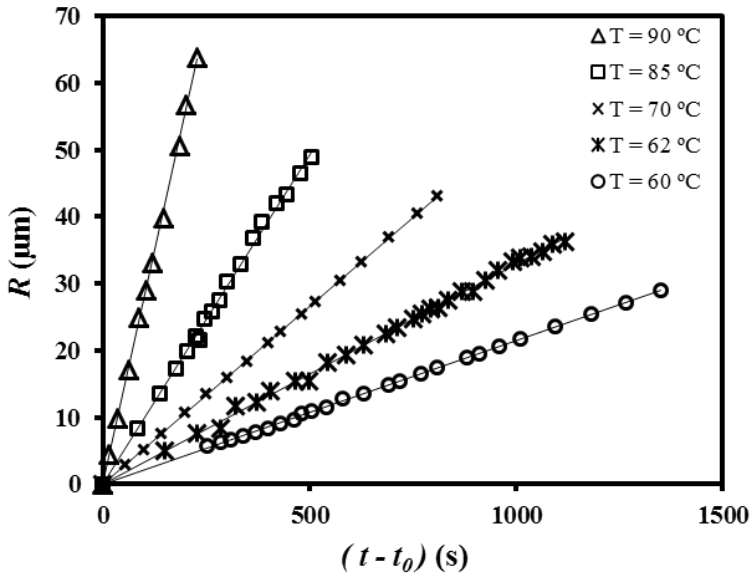

Nucleation was very low at the higher temperatures of crystallization experiments carried out from the melt state where spherulites with diameters larger than 500 µm could be obtained. The number of nuclei slightly varied during isothermal crystallization at a given temperature (not shown) and consequently a deviation from a perfect athermal nucleation was detected. As can be seen in Figure 3.2.10, the temperature evolution of primary nucleation reveals a single exponential dependence. It is remarkable that the number of active nuclei is very low (e.g., 335 nuclei/mm^2 at such a low temperature as 70 ºC), even lower than that determined for Maxon™ (e.g., 600 nuclei/mm^2 at 80 ºC).[23] Crystallization of GL-*b*-(GL-*co*-TMC-*co*-CL)-*b*-GL seems more hindered because of its higher content in non-crystallizable *soft segments* (i.e., 43 versus 38 wt-%) with a more statistical monomer distribution (i.e., three as opposed to two components).

Figure 3.2.10. Change in the nucleation density with isothermal crystallization temperature.

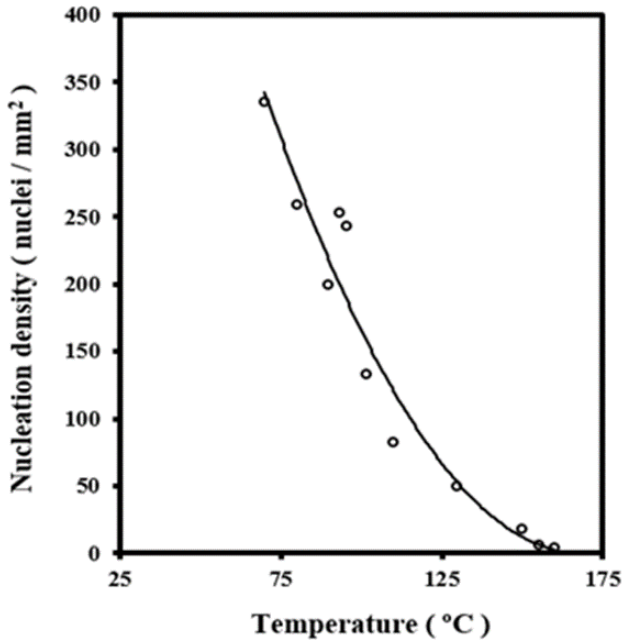

Figure 3.2.11a is the typical bell-shaped curve that defines the temperature dependence of the crystal growth rate. The low nucleation and growth rate allowed the collection of experimental data over the whole temperature range for crystallizations performed from the melt state. Namely, measurements could be taken even when crystallization began during the cooling run from the melt to the selected temperature due to inability of formed spherulites to collapse.

Crystal growth rates determined from cold crystallization experiments fitted also with the same curve (Figure 3.2.11a). Data from these cold crystallization experiments could also be achieved for slightly high temperatures despite some crystallization took place during the heating step. For the sake of completeness, the curve previously reported for Maxon™ is also given in Figure 3.2.11a.[23] The GL-*b*-(GL-*co*-TMC-*co*-CL)-*b*-GL plot has significant differences concerning a higher supercooling to initiate crystallization and the shift of the curve to lower temperatures. Namely, a greater difficulty for primary nuclei to begin the crystallization process was detected. It should also be pointed out the higher growth rate determined at the maximum of the curve, which may be related to a lower molecular

weight (i.e., M_w of 71,000 g/mol as opposed to the value of 95,000 g/mol reported for Maxon™, [23]).

The crystal growth rate was analyzed by the Lauritzen-Hoffman equation[36]:

$$G = G_0 \exp\left[-U^*/\left(R\left(T_c - T_\infty\right)\right)\right] \times \exp\left[-K_g/\left(T_c\left(\Delta T\right) f\right)\right] \quad (1)$$

where G_0 is a constant preexponential factor, U^* represents the activation energy characteristic of the transport of crystallizing segments across the liquid–crystal interface, T_∞ is the temperature below which such motion ceases, T_c is the crystallization temperature, R is the gas constant, K_g is the secondary nucleation constant, ΔT is the degree of supercooling measured as $T_m^0 - Tc$; and f is a correction factor accounting for the variation in the bulk melting enthalpy per unit volume with temperature ($f = 2T_c/(T_m^0 + T_c)$).

The Lauritzen-Hoffman plot was fitted with a straight line (r^2 = 0.989) when the "universal" values reported by Suzuki and Kovacs[37] (i.e., U^* = 1500 cal/mol and $T_\infty = T_g$ - 30 K) were used in the calculation. A slight variation was introduced (**Figure 3.2.11b**) to improve the fit (i.e., r^2 = 0.991 using U^* = 1740 cal/mol and $T_\infty = T_g$ - 32 K). Nevertheless, kinetic features at low supercoolings are basically governed by the nucleation term, and consequently crystallization rates could become relatively insensitive to the U^* and T_∞ parameters. The plot was used to estimate a secondary nucleation constant of 2.88 × 10^5 K^2, which is significantly higher than the value reported for Maxon™,[23] (i.e., 1.82 × 10^5 K^2) and reveals greater difficulty in the crystal growth process. This is probably because proper arrangement of *hard blocks* becomes hindered again at higher contents of non-crystallizable *soft segments* with a more statistical monomer distribution. Results appear more consistent than those attained from calorimetric analyses since in the case of GL-*b*-(GL-*co*-TMC-*co*-CL)-*b*-GL a lack of proportionality between the overall crystallization rate and the crystal growth rate seems to exist.

Figure 3.2.11. (a) Temperature dependence of crystal growth rate (○ symbols) determined by equation 1 and using the best fit parameters. Experimental crystal growth rates (green and red symbols for crystallizations from the glass and the melt state, respectively) as well as the theoretical curve from isothermal crystallization of GL-*b*-(GL-*co*-TMC)-*b*-GL (□ symbols)[23] are also shown for comparison. **(b)** Plot of ln $G + U^*/R(T_c - T_\infty)$ versus $1 / T_c(\Delta T)f$ to determine the K_g secondary nucleation parameter of GL-*b*-(GL-*co*-TMC-*co*-CL)-*b*-GL.

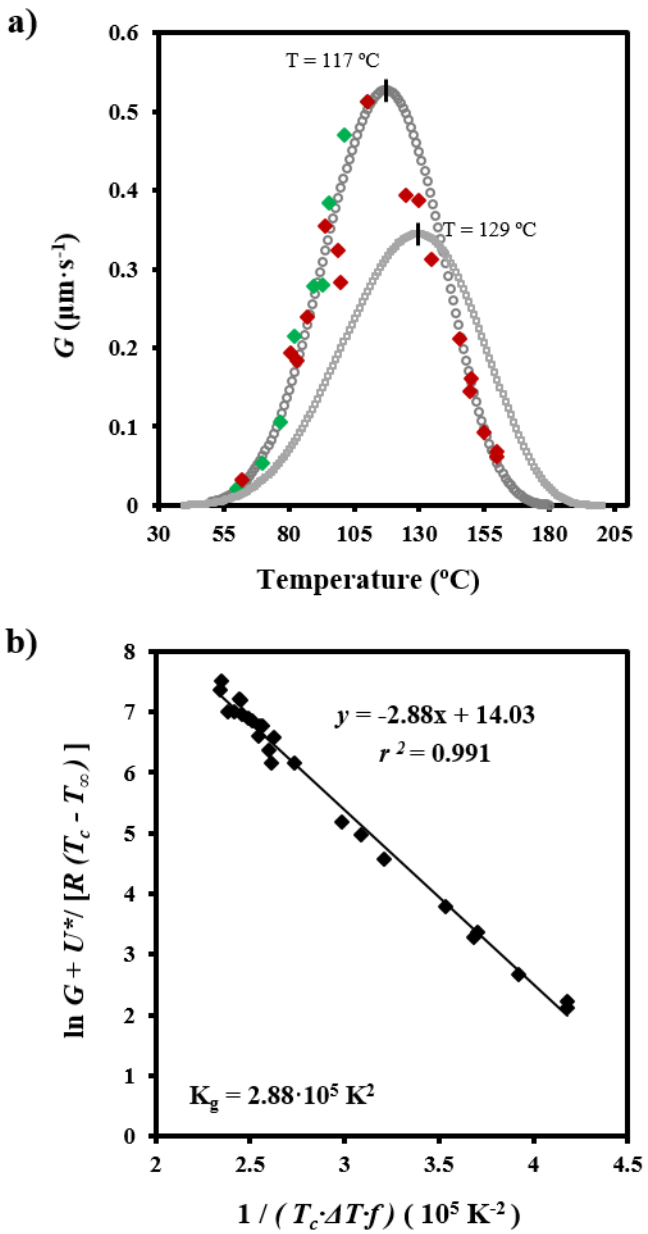

3.2.3.4. Kinetic studies for the non-isothermal crystallization

Non-isothermal procedures can also be applied to study the temperature dependence of the spherulite growth rate during crystallization from both the melt and the glass states.[38–40] Thus, this rate (G) can be estimated by measuring the change of the spherulite radius (R) with temperature (T) at a constant cooling/heating rate (dT/dt):

$$G = dR/dt = (dR/dT)(dT/dt) \quad (2)$$

The plot of the radius versus experimental temperature data can be adjusted to a polynomial equation with a good regression coefficient (r) to calculate the value of its first derivative (dR/dT) as a function of the crystallization temperature for all cooling/heating rates. Experimental problems lie in the choice of the cooling/heating rate required to maximize the crystallization temperature range where radii can be well measured. To this end, the use of various rates can be highly effective.

The change in the radius of a typical GL-*b*-(GL-*co*-TMC-*co*-CL)-*b*-GL spherulite during the temperature ramp at different cooling/heating rates is shown in Figure 3.2.12a. A polynomial fitting with a high regression coefficient was obtained in all crystallizations. Third-order equations were always chosen (Table 3.2.2) since regression coefficients ($\geq$ 0.979) were slightly better than those calculated for lower order equations and remained constant for higher orders.

Relationships between spherulite growth rate and crystallization temperature were obtained by differentiating third-order equations based on temperature and considering the cooling/heating rate (Equation 2). Figure 3.2.12b plots the G values, deduced for several cooling/heating rates as a function of temperature. A bell-shaped curve with a maximum of 122 ºC was derived with data from all crystallization temperatures. It is remarkable that spherulite growth rates could be measured in the low temperature range (48-117 ºC) from crystallization experiments from both the glass and the melt state. Relatively good agreement was found between data obtained from isothermal and non-isothermal crystallization, as also shown in Figure 3.2.12b.

Figure 3.2.12. (a) Variation in spherulite radius with temperature during heating and cooling at the indicated rates. **(b)** Spherulite growth rates determined by the equations deduced for cooling and heating runs. Theoretical curves for non-isothermal (○) and isothermal (-) crystallization of GL-*b*-(GL-*co*-TMC-*co*-CL)-*b*-GL are also drawn for comparative purposes. For the sake of completeness, insets show representative spherulites non-isothermally crystallized from the melt and the glass state that had irregular and rounded edges, respectively.

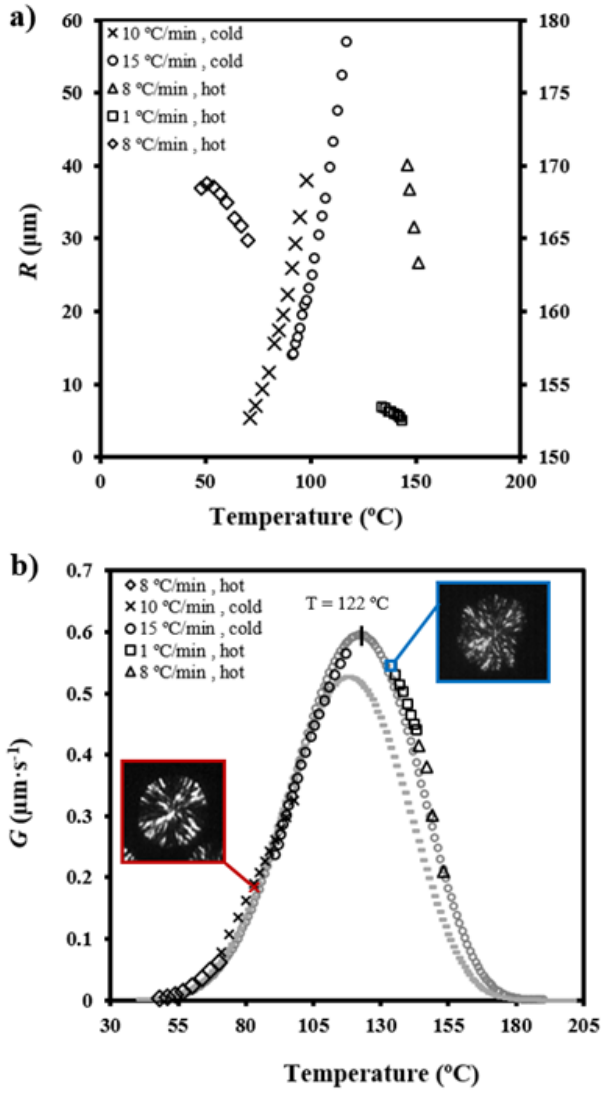

Table 3.2.2. Third order equations that fit the temperature dependence of GL-*b*-(GL-*co*-TMC-*co*-CL)-*b*-GL spherulitic radius during hot and cold non-isothermal crystallizations.

Crystallization from the melt		
Cooling rate (°C/min)	**Equation**	r^2
1[a]	$-0.00386\ T^3 + 1.59973\ T^2 - 220.9300\ T + 10181.50$	0.9793
8	$0.00042\ T^3 - 0.08243\ T^2 + 5.16050\ T + 64.5514$	0.9961
Cold crystallization		
Heating rate (°C/min)	**Equation**	r^2
10	$-0.00001\ T^3 + 0.02892\ T^2 - 3.54359\ T + 113.3528$	0.9992
15	$0.00026\ T^3 - 0.05358\ T^2 + 4.26076\ T - 128.2495$	0.9996

[a] *Sample was previously cooled at the maximum rate allowed by the equipment up to 190°C and then the experiment was carried out at the indicated cooling rate.*

Lauritzen-Hoffman (equation 1) was also used to deduce the value of the secondary nucleation constant for non-isothermal crystallization. Figure 3.2.13 shows the linear plot obtained using U^* and T_∞ parameters of 1780 cal·mol^{-1} and T_g – 33 K, respectively. It is clear that a single crystallization regime defined by a secondary nucleation constant of 2.42×10^5 K^2 fits all the experimental data. The good agreement between experimental and theoretical data (i.e., those obtained from equation 1 and the deduced parameters) is also shown in Figure 3.2.12b. The deduced secondary nucleation constant is similar to, although slightly lower than, that determined from isothermal analysis (i.e., 2.42×10^5 K^2 respect to 2.88×10^5 K^2). Note that the average constant (2.65×10^5 K^2) is clearly higher than the value determined from DSC experiments and becomes higher than the average constant deduced from isothermal and non-isothermal crystallizations of the GL-*b*-(GL-*co*-TMC)-*b*-GL bicomponent system (2.13×10^5 K^2).[24] Therefore, analyses from optical microscopy observations render reliable values of the secondary nucleation

constant that justify a greater difficulty to crystallize for samples having a more disordered *soft segment* despite having a lower molecular weight.

Figure 3.2.13. Plot of ln $G + U^* / R(T_c - T_\infty)$ versus $1 / T_c(\Delta T) f$ to determine the K_g secondary nucleation parameter of GL-*b*-(GL-*co*-TMC-*co*-CL)-*b*-GL.

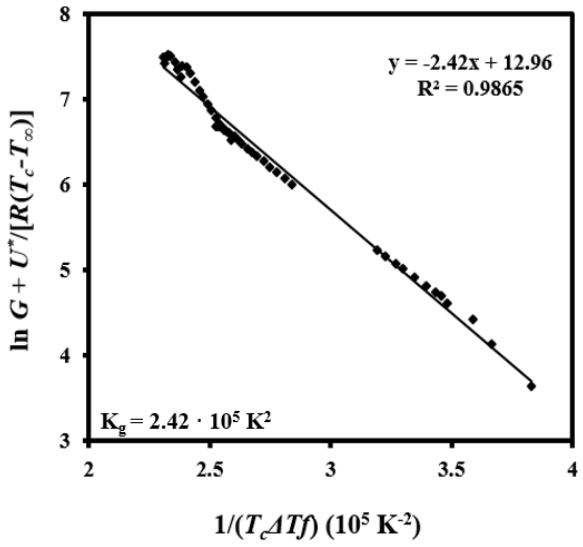

3.2.3.5. Changes on lamellar morphology during cooling and heating processes

Figure 3.2.14 shows representative time-resolved SAXS profiles of GL-*b*-(GL-*co*-TMC-*co*-CL)-*b*-GL obtained during a non-isothermal hot crystallization performed at 10 ºC/min. A SAXS long period peak is clearly seen at a value of the scattering vector, $q = [4\pi/\lambda] \sin(\theta)$, close to 0.45 nm^{-1} after subtraction of the empty sample background observed near the beam stop. This peak can be attributed to the lamellar structure of the spherulites and starts to appear at temperature close to 147 ºC (a value which slightly increases with decreasing the crystallization cooling rate). Subsequently, the peak intensity increases significantly with decreasing temperature until reaching a plateau value at a temperature close to 126 ºC at which crystallization can be considered completely finished. The high intensity of the final SAXS peaks, suggests a large difference between the electronic density of the amorphous and the crystalline phases, which is in agreement with the tight packing of polyglycolide.[9] During crystallization the SAXS peak slightly shifts to higher q values and the change is more pronounced at the initial stages.

Figure 3.2.14. Time-resolved SAXS three-dimensional profiles of GL-*b*-(GL-*co*-TMC-*co*-CL)-*b*-GL during non-isothermal crystallization from the melt. Cooling rate was 10 ºC/min. SAXS curves are shown after subtraction of empty sample background and Lorentz correction.

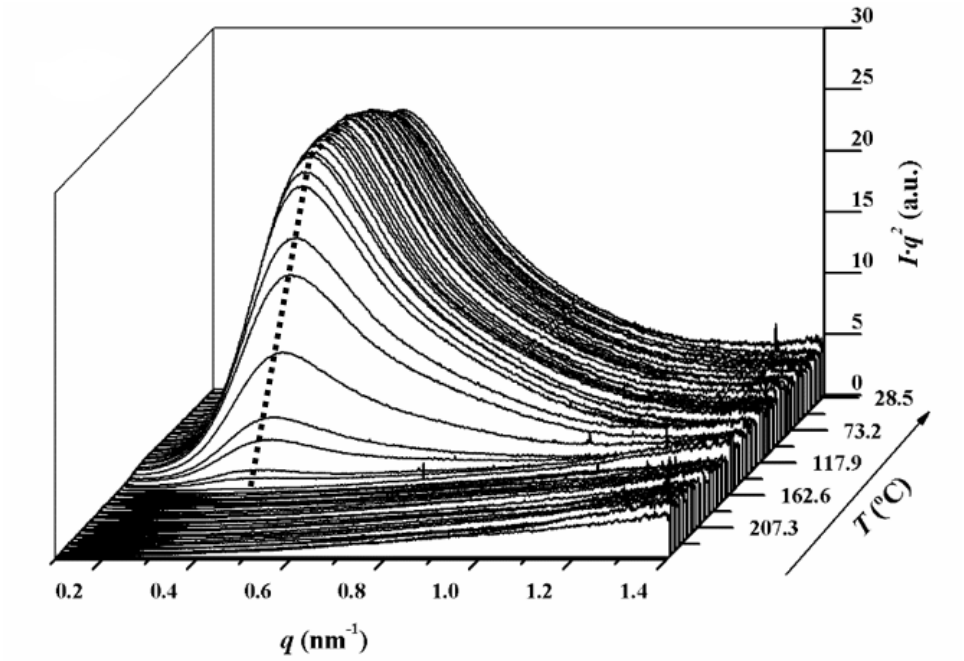

Characteristic lamellar parameters (i.e., long period, L_γ, amorphous layer thickness, l_a, and crystalline lamellar thickness, l_c) and crystallinity (i.e., crystallinity within the lamellar stacks, $X_c^{SAXS} = l_c / L_\gamma$, and scattering invariant, Q) were determined by means of the normalized one-dimensional correlation function[41], $\gamma(r)$:

$$\gamma(r) = \int_0^\infty q^2 I(q) \cos(qr) dq \; / \; \int_0^\infty q^2 I(q) dq \qquad (3)$$

SAXS data were collected within a limited angular range and consequently Vonk's model [42] and Porod's law were applied to perform extrapolations to low and high q values.

Representative correlation functions (i.e., at the beginning and at the end of the crystallization process) are displayed in Figure 3.2.15 whereas the evolution of morphologic parameter and the invariant are shown in Figure 3.2.16. Main conclusions

that can be deduced for the crystallization process are the followings: a) L_γ was clearly higher than the long period determined from twice the value of the first minimum of the correlation function (i.e., 10.6 nm respect to 8.0 nm), which suggests a broad distribution of the layer widths of the crystal phase. b) l_a remained practically constant during crystallization since only a decrease from 2.2 to 1.9 nm was detected, whereas l_c significantly decreased (i.e., from 9.8 to 8.6 nm) as a consequence of a typical lamellar insertion mechanism. c) Scattering invariant logically increased during non-isothermal crystallization but at low temperature (e.g., close to 51 ºC) it starts to decrease as a consequence of an increase on the electronic density of the interlamellar amorphous phase. d) Crystallinity within the lamellar stacks was very high (0.82) as a consequence of the reduced amorphous thickness. In fact, this is a distinctive feature with respect to Maxon™ samples crystallized under identical experimental conditions and a clear evidence of the influence of microstructure on morphology. In the case of Maxon™ the final l_a and l_c parameters were 10.0 and 3.5 nm, respectively, whereas X_c^{SAXS} was only 0.74.

Figure 3.2.15. Comparison between correlation functions of GL-*b*-(GL-*co*-TMC-*co*-CL)-*b*-GL for: initial sample **(a)**, after heating up to 180 ºC **(b)**, at the first stages of crystallization from the melt **(c)** and after finishing the non-isothermal crystallization **(d)**. Heating and cooling rates were 10 ºC/min.

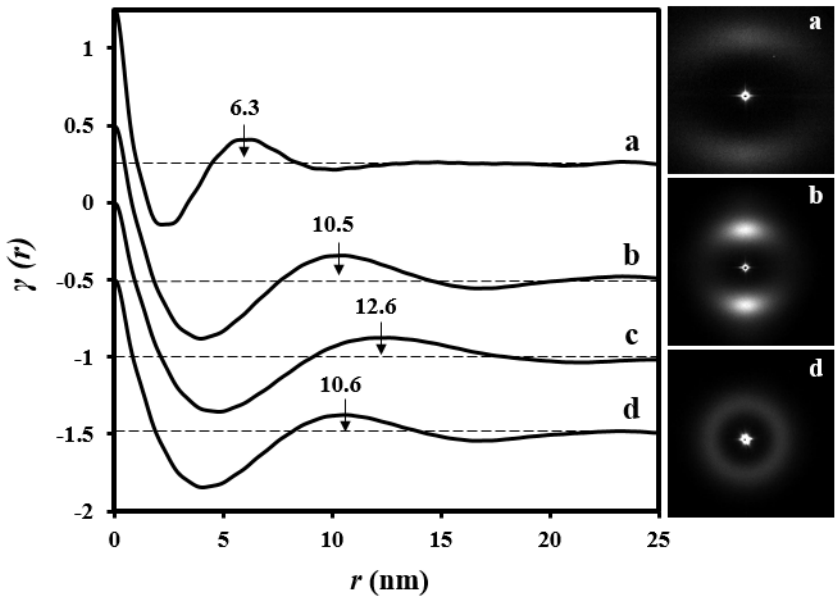

Figure 3.2.16. Evolution of the long period from correlation function (●), L_γ, crystal thickness (■), l_a amorphous thickness (▲), l_a, and scattering invariant (♦), Q, during non-isothermal crystallization performed at 10 ºC/min with GL-*b*-(GL-*co*-TMC-*co*-CL)-*b*-GL sample. Evolution of spacing parameters during a heating scan (10 ºC/min) of the initial sample is also shown (empty symbols).

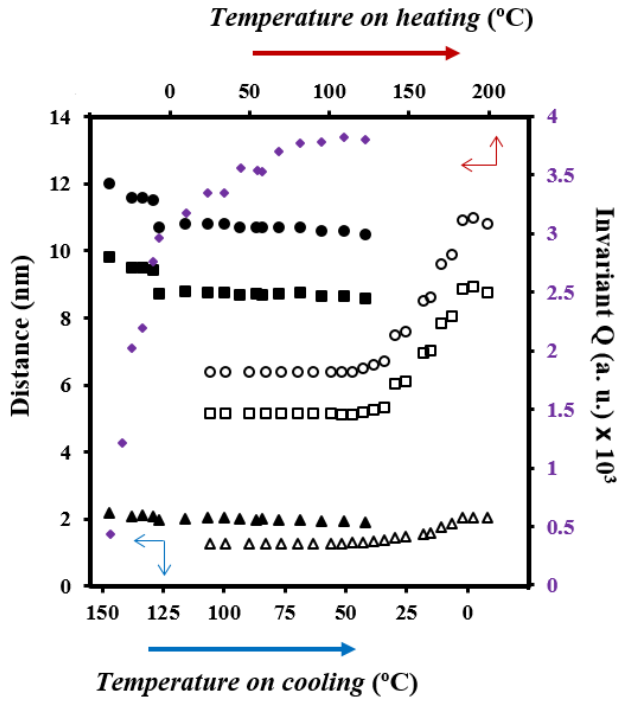

Lamellar structure is clearly different for the as-processed sutures, which display a typical fiber pattern with oriented WAXD reflections (not shown) and an intense meridional SAXS reflection (Figure 3.2.15). Lamellar structure is defined by l_a and l_c parameters of 5.1 and 1.3 nm, respectively, and a X_c^{SAXS} value of 0.80. Thus, processing characterized by a rapid cooling from spinneret and a subsequent annealing process render a well differentiated structure from melt crystallized spherulites as can be deduced by comparison of correlation functions (Figures 3.2.15a and 3.2.15c). Again a broad distribution of the layer widths of the crystal phase can be deduced for the as-processed sample (i.e., 6.3 nm and 4.8 nm are measured for the first maximum and the double value of the first minima, respectively). Despite the great difference on the lamellar morphology it should be indicated that X_c^{SAXS} was very close to the value determined for melt crystallization (i.e., 0.80 with respect to 0.82). Morphology drastically changed during a subsequent

heating process since the SAXS peak increased in intensity (probably as consequence of the decrease of the electronic density of the interlamellar amorphous phase) and moved towards lower *q* values (Figure 3.2.17). This lamellar reordering process was initiated at a temperature close to 101 ºC and ended at 202 ºC just when melting process began. It should be pointed out that any endothermic event was observed in previous DSC experiments[28] and consequently diffraction data are essential to demonstrate the thickening process of GL-*b*-(GL-*co*-TMC-*co*-CL)-*b*-GL.

Figure 3.2.17. Time-resolved SAXS three-dimensional profiles of GL-*b*-(GL-*co*-TMC-*co*-CL)-*b*-GL during heating from room temperature. Heating rate was 10 ºC/min. SAXS curves are shown after subtraction of empty sample background and Lorentz correction.

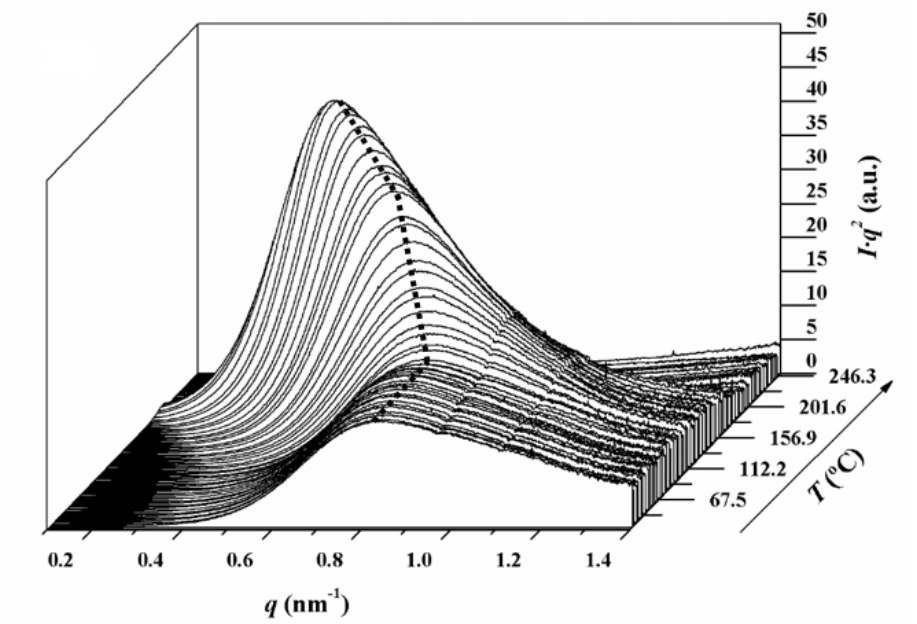

Figures 3.2.15b and 3.2.16 shows the correlation function at the end of lamellar reordering process and the temperature evolution of morphologic parameters. Note that they were practically constant up to 115 ºC, increased between 115 and 190 ºC and decreased at higher temperatures than 190 ºC. The evolution of the amorphous and crystalline lamellar thicknesses was proportional and consequently X_c^{SAXS} remained practically constant (increased only from 0.80 to 0.82). It is remarkable that the lamellar structure became practically identical to that attained after crystallization from the melt (Figures 3.2.15b and 3.2.15d), being l_a and l_c parameters 9.0 and 2.0 nm, respectively (i.e., close to the previously reported values of 8.6 and 1.9 nm).

3.2.4. CONCLUSIONS

Crystallization of segmented copolymers having polyglycolide *hard segments* is influenced by the constitution of the amorphous *soft segment*. Thus, significant differences on secondary nucleation constant and lamellar morphology were found between copolymers displaying similar properties but having *soft segments* with three (i.e., glycolide, trimethylene carbonate and ε-caprolactone) or two components (i.e., glycolide and trimethylene carbonate).

Hard and *soft segments* of GL-*b*-(GL-*co*-TMC-*co*-CL)-*b*-GL were compatible/miscible and on crystallization gave rise to spherulites with a positive birefringence from the melt and the glass state. These spherulites included the non-crystallizable *soft segments* and showed morphological features that varied with the crystallization temperature. Specifically, spherulites obtained under low supercoolings had a flower-like appearance and were mainly constituted by flat-on lamellae. Isothermal and non-isothermal kinetic analyses indicated heterogeneous nucleation and three-dimensional growth which tended to be two-dimensional for isothermal crystallizations under low supercooling.

Crystallization was characterized by a rather low primary nucleation density and crystal growth rate. A typical bell-shaped curve defined the dependence of crystal growth rate on temperature, with small differences between isothermal and non-isothermal crystallization data. Lauritzen and Hoffman analysis demonstrated a single crystallization regime defined by a secondary nucleation constant (K_g = 2.88×10^5 K^2 - 2.42×10^5 K^2) higher than that determined for related segmented copolymers with a slightly lower *soft segment* content. Statistical blocks constituted by three repeat units played a significant role in hindering primary nucleation and proper arrangement of polyglycolide *hard segments* over crystal growth surfaces.

Similar lamellar morphologies were attained by crystallization from the melt state or from thermal treatment of oriented fibers, being characteristic lamellar insertion and lamellar thickening processes, respectively. Final morphologies are defined by a crystallinity within the lamellar stacks of 0.82 and a crystalline thickness of 8.6-9.0 nm that contrast with values of 0.74-0.83 and 10.0 nm found for the bicomponent system when was processed in a similar form.

3.2.5. REFERENCES

1. Schmitt, E. E. & Polistina, R. A. Surgical sutures. U.S. Patent 3.297.033. American Cyanamid (1967).

2. Schmitt, E. E. & Polistina, R. A. Polyglycolic acid prosthetic devices. U.S. Patent 3.463.158. American Cyanamid (1969).

3. Cameron, R. E. & Kamvari-Moghadam, A. Synthetic bioresorbable polymers. In *Durability and reliability of medical polymers* 96–118 (2012).

4. Pillai, C. K. S. & Sharma, C. P. Review paper: absorbable polymeric surgical sutures: chemistry, production, properties, biodegradability, and performance. *J. Biomater. Appl.* **25**, 291–366 (2010).

5. Kundra, R. K. *et al.* Absorbable or non-absorbable sutures? A prospective, randomised evaluation of aesthetic outcomes in patients undergoing elective day-case hand and wrist surgery. *Ann. R. Coll. Surg. Engl.* **92**, 665–667 (2010).

6. Nair, L. S. & Laurencin, C. T. Biodegradable polymers as biomaterials. *Prog. Polym. Sci.* **32**, 762–798 (2007).

7. Ulery, B. D., Nair, L. S. & Laurencin, C. T. Biomedical applications of biodegradable polymers. *J. Polym. Sci. B. Polym. Phys.* **49**, 832–864 (2011).

8. Gunatillake, P., Mayadunne, R. & Adhikari, R. Recent developments in biodegradable synthetic polymers. *Biotechnol. Annu. Rev.* **12**, 301–347 (2006).

9. Chatani, Y., Suehiro, K., Okita, Y., Tadokoro, H. & Chujo, K. Structural studies of polyesters. I Crystal structure of polyglycolide. *Die Makromolekulare Chemie* **113**, 215–229 (1968).

10. Brandrup, J., Immergut, E. H. & Grulke, E. A. Solid state properties (Chapter 6). In *Polymer Handbook* (Interscience Publishers, 1999).

11. Farrar, D. Modelling of the degradation process of bioresorbable polymers. In *Durability and reliability of medical polymer* 186–206 (2008).

12. Noorsal, K., Mantle, M. D., Gladden, L. F. & Cameron, R. E. Degradation and drug-release studies of a poly(glycolide-*co*-trimethylene carbonate) copolymer (Maxon). *J. Appl. Polym. Sci.* **95**, 475–486 (2005).

13. Freudenberg, S. *et al.* Biodegradation of absorbable sutures in body fluids and pH buffers. *Eur. Surg. Res.* **36**, 376–385 (2004).

14. Sun, L., Wanasekara, N., Chalivendra, V. & Calvert, P. Nano-mechanical studies on polyglactin sutures subjected to *in vitro* hydrolytic and enzymatic degradation. *J. Nanosci. Nanotechnol.* **15**, 93–99 (2005).

15. Haghighat, F. & Ravandi, S. A. H. Mechanical properties and *in vitro* degradation of PLGA suture manufactured via electrospinning. *Fibers Polym.* **15**, 71–77 (2014).

16. Homsy, C. A., Mcdonald, E. R. & Akers, W. W. Surgical suture-canine tissue interaction for six common suture types. *J. Biomed. Mater. Res.* **2**, 215–230 (1968).

17. Blomstedt, B. & Ostenberg, B. Suture materials and wound infection. An experimental study. *Acta Chir. Scand.* **144**, 269–274 (1978).

18. Rodeheaver, G. T. *et al.* Knotting and handling characteristics of coated synthetic absorbable sutures. *J. Surg. Res.* **35**, 525–530 (1983).

19. Katz, A. R., Mukherjee, D. P., Kaganov, A. L. & Gordon, S. A new synthetic monofilament absorbable suture made from polytrimethylene carbonate. *Surgery, Gynecol. Obstet.* **161**, 213–222 (1985).

20. Oberhoffner, S. & Planck, H. Surgical suture material from triblockterpolymer, its use in surgery and process for its preparation. EP 0835895. (1996).

21. Roby, M. S., Bennet, S. L. & Liu, E. K. Absorbable block copolymers and surgical articles fabricated thereform. U.S.Patent 5.403.347. (1995).

22. Bezwada, R. S. *et al.* Monocryl suture , a new ultra-pliable absorbable monofilament suture. *Biomaterials* **16**, 1141–1148 (1995).

23. Díaz-Celorio, E., Franco, L. & Puiggalí, J. Isothermal crystallization study on a biodegradable segmented copolymer constituted by glycolide and trimethylene carbonate units. *J. Appl. Polym. Sci.* **116**, 577–589 (2010).

24. Díaz-Celorio, E., Franco, L. & Puiggalí, J. Nonisothermal crystallization behavior of a biodegradable segmented copolymer constituted by glycolide and trimethylene carbonate units. *J. Appl. Polym. Sci.* **119**, 1548–1559 (2011).

25. Díaz-Celorio, E., Franco, L., Rodríguez-Galán, A. & Puiggalí, J. Synthesis of glycolide/trimethylene carbonate copolymers: Influence of microstructure on properties. *Eur. Polym. J.* **48**, 60–73 (2012).

26. Díaz-Celorio, E., Franco, L., Rodríguez-Galán, A. & Puiggalí, J. Study on the hydrolytic degradation of glycolide/trimethylene carbonate copolymers having different microstructure and composition. *Polym. Degrad. Stab.* **98**, 133–143 (2013).

27. Díaz-Celorio, E., Franco, L. & Puiggalí, J. Influence of microstructure on the crystallization of segmented copolymers constituted by glycolide and trimethylene carbonate units. *Express Polym. Lett.* **7**, 186–198 (2013).

28. Márquez, Y., Franco, L., Turon, P. & Puiggalí, J. Isothermal and non-isothermal crystallization kinetics of a polyglycolide copolymer having a tricomponent middle soft segment. *Thermochim. Acta* **585**, 71–80 (2014).

29. Zurita, R., Puiggalí, J., Franco, L. & Rodríguez-Galán, A. Copolymerization of glycolide and trimethylene carbonate. *J. Polym. Sci. Part A Polym. Chem.* 44, 993–1013 (2006).

30. Kasperczyk, J. Copolymerization of glycolide and ε-caprolactone, 1 Analysis of the copolymer microstructure by means of ^{1}H and ^{13}C NMR spectroscopy. *Macromol. Chem. Phys.* **910**, 903–910 (1999).

31. Kister, G., Cassanas, G. & Vert, M. Morphology of poly (glycolic acid) by IR and Raman spectroscopies. *Spectrochim. Acta Part* A **53**, 1399–1403 (1997).

32. Wang, H., Dong, J. H. U. A. & Qiu, K. U. N. Y. Synthesis and characterization of ABA-type block copolymer of poly (trimethylene carbonate) with poly (ethylene glycol): Bioerodible copolymer. *J. Polym. Sci. A Polym. Chem.* **36**, 695–702 (1998).

33. Xu, J. *et al.* Observation of banded spherulites in pure poly(L-lactide) and its miscible blends with amorphous polymer. *Polymer.* **46**, 9176–9185 (2005).

34. Nikolova, L. & Ramanujam, P. S. Azobenzene and azobenzene-containing polymers (Chapter 4). In *Polarization Holography.* First Ed. Cambridge University Press, UK (2009).

35. Magill, J. H. Review spherulites: A personal perspective. *J. Mater. Sci.* **36**, 3134–3164 (2001).

36. Lauritzen, J. I. & Hoffman, J. D. Extension of theory of growth of chain-folded polymer crystals to large undercoolings. *J. Appl. Phys.* **44**, 4340–4352 (1973).

37. Suzuki, T. & Kovacs, A. J. Temperature dependence of spherulitic growth rate of isotactic polystryrene. A critical comparison with the kinetic theory of surface nucleation. *Polym. J.* **1**, 82–100 (1970).

38. Chen, M. & Chung, C. Analysis of crystallization kinetics of poly (ether ether ketone) by a nonisothermal method. *J. Polym. Sci. Part B Polym. Phys.* **36**, 2393–2399 (1998).

39. Di Lorenzo, M. L., Cimmino, S. & Silvestre, C. Nonisothermal crystallization of isotactic polypropylene blended with poly (R -pinene). 2 . Growth rates. *Macromolecules* **33**, 3828–3832 (2000).

40. Di Lorenzo, L. M. Determination of spherulite growth rates of poly (L-lactic acid) using combined isothermal and non-isothermal procedures. *Polymer.* **42**, 9441–9446 (2001).

41. Vonk, C. G. & Kortleve, G. X-ray small-angle scattering of bulk polyethylene. *Kolloid Z Z Polym* **220**, 19–24 (1967).

42. Vonk, C. G. A general computer program for the processing of small-angle X-ray scattering data. *J. Appl. Crystallogr.* **8**, 340–341 (1975).

4.

DEGRADATION STUDIES OF GL-*b*-(GL-*co*-TMC-*co*-CL)-*b*-GL MONOFILAR SURGICAL SUTURES

4.1. Thermal degradation studies of poly(trimethylene carbonate) blends with poly(ε-caprolactone) and others polyesters

The thermal stability and degradation kinetics of poly(trimethylene carbonate) (PTMC) blends with different ratios of polylactide (PLA) and alternatively poly(ε-caprolactone) (PCL) were investigated by thermogravimetric analysis under a nitrogen atmosphere. These studies were extended to the single components (i.e., PCL and PLA). In all cases, the derivative thermogravimetric curves indicated a complex decomposition process with at least two degradation steps. The kinetic parameters of the main step, including activation energy, reaction model and pre-exponential factor, were evaluated by the Kissinger, isoconversional (Friedman and KAS) and Coats-Redfern methods. Data of the main decomposition process were obtained by mathematical deconvolution of experimental DTG curves acquired at heating rates ranging from 2 to 40 ^{o}C/min.

It was demonstrated that degradation of blends did not correspond to a mere superposition of the characteristic decomposition processes of the two involved polymers. Furthermore, PCL and PLA influenced the decomposition of the less thermally stable PTMC component in a different way. Thus, PLA modified the degradation of PTMC, and specifically led to thermal stabilization and a new decomposition process characterized by a higher activation energy. On the other hand, PCL favored the degradation of PTMC by enhancing a typical minor decomposition process that occurred in the single component at a lower temperature.

The main decomposition step of PTMC, PLA, PCL and the studied blends always followed an Avrami model but with significant differences in their exponents (i.e., from 2 to 7).

4.1.1. INTRODUCTION

The use of biodegradable polyesters derived from lactones (e.g., polyglycolide (PGL), polylactide (PLA) and poly(ε-caprolactone) (PCL)) in temporary biomedical applications has increased significantly over the past decade.[1–4] These materials can be used in various forms (films, fibers, foams…) to cover a wide set of applications that range from bioabsorbable sutures, implantable medical devices or tissue engineering scaffolds to controlled drug delivery systems.[5–9] However, a constant effort to develop materials with improved properties is required due to the complex requirements of clinical applications.

In this way, poly(trimethylene carbonate) (PTMC) and its derivatives are currently receiving great attention due to their high flexibility[10] and potential applications as biomaterials, in particular in soft tissue engineering,[11–13] and even as monofilament surgical sutures.[14–16]

Evaluation of thermal stability and the degradation mechanism is crucial because materials are usually melt-processed. Hence, it is necessary to take precautions when polymers have high melting temperatures, as is the case of glycolide and lactide derivatives. Thermal degradation behavior of polymers can be modified by incorporation of different chemical units in the main chain and even by blending. For example, it has been reported that degradation behavior of copolymers constituted by glycolide and trimethylene carbonate units as well as blends of PTMC and PGL was significantly different from that determined for the corresponding homopolymers.[17] Specifically, the main degradation step of blends of PTMC and PGL had activation energies and frequency factors between those calculated for the homopolymers. Furthermore, degradation proceeded according to a well differentiated mechanism. The main goal of the present work is to provide insight into the thermal stability of physical mixtures based on PTMC and commercial polylactones such as PLA and PCL, complementing previous data obtained with PGL.

Degradation studies on PTMC indicated that two processes were involved in its decomposition: a non-radical ester interchange reaction leading to the corresponding cyclic monomer, and a random decarboxylation reaction (Figure 4.1.1).[18] The latter was the main decomposition process and occurred at the highest temperature. The kinetics of this step was recently evaluated by the KAS, Friedman and Coats-Redfern methodologies,[17] which gave an activation energy between 79 and 85 kJ/mol. An A_3 mechanism and a frequency factor ln (A / min^{-1}) of 14.6 were also deduced.

Figure 4.1.1. (a) Unzipping depolymerization and decarboxylation reactions postulated for the degradation of poly(trimethylene carbonate).[18] **(b)** Decarboxylation and backbiting reactions postulated for poly(ε-caprolactone).[24]

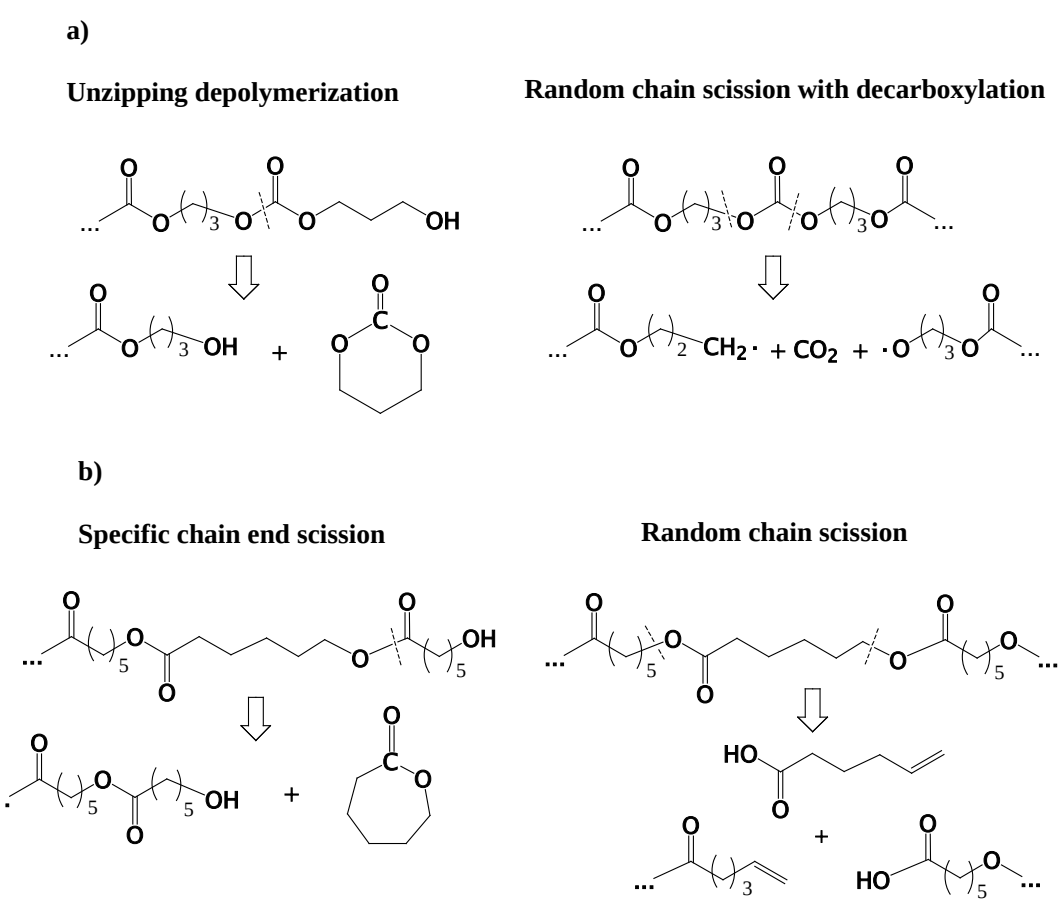

Studies on the thermal degradation of PLA have provided different interpretations ranging between a first-order reaction model and a complex decomposition process.[19,20] Moreover, highly controversial results are still given in the most recent works. For example, it has been postulated a complex reaction process with the participation of at least two different mechanisms: an *n*th-order with an activation energy of 116-117 kJ/mol for the first process (F_n), and an *n*th-order with autocatalysis (C_n) and an activation energy of 161-162 kJ/mol for the second mechanism.[21] On the other hand, thermal degradation for conversion degrees between 0.2 and 0.7 has also been described by a nucleation model (A_2) [22] which suggests the presence of active zones (nuclei) favoring the formation and

growth of gas bubbles in the polymer melt.[23] In this case, the activation energy calculated by the Friedman and Kissinger methods was close to 207 kJ/mol [22].

Thermal degradation studies concerning poly(ε-caprolactone) have revealed the existence of two well differentiated steps through analysis of evolved products: chain cleavages randomly distributed along the chain with formation of H_2O, CO_2 and 5-hexenoic acid for the low temperature decomposition process and depolymerization via an unzipping polymerization process for the high temperature step (Figure 4.1.1).[24] The Friedman and Chang methods of analysis showed a 3-fold change (from 75 to 230–259 kJ/mol) in the activation energy from low to high temperatures during degradation.[25]

4.1.2. EXPERIMENTAL SECTION

4.1.2.1. Materials

Trimethylene carbonate, initiator (diethylene glycol, DEG) and catalyst ($Sn(Oct)_2$) were purchased from Boehringer Ingelheim, Panreac and Sigma-Aldrich, respectively. Polymerization of trimethylene carbonate was performed under a nitrogen atmosphere in a stainless steel jacketed batch reactor at 0.2 MPa and 180 ºC. PTMC was obtained with a weight average molecular weight of 83,000 g/mol. PTMC was amorphous with a glass transition temperature of -15 ºC.

Polylactide, a product of Natureworks® (polymer 2002D), was kindly supplied by Nupik International (Polinyà, Spain). According to the manufacturer, this PLA has a D content of 4.25%, a residual monomer content of 0.3%, a density of 1.24 g/cc, a glass transition temperature (T_g) of 58 °C and a melting point of 153 °C. Poly(ε-caprolactone) (M_w: 65,000 g/mol) was purchased from Sigma-Aldrich.

Blends of PTMC with either PLA or PCL were prepared by melting and mixing the appropriate amount of each homopolymer in the sample pan. Mixtures are named as PLA/PTMC-*x* and PCL/PTMC-*x* where *x* indicates the weight percentage of PLA or PCL in the blend.

4.1.2.2. Measurements

^{1}H-NMR spectra were obtained with a Bruker AMX-300 spectrometer operating at 300.1 MHz. Chemical shifts were calibrated using tetramethylsilane as an internal standard and deuterated chloroform was used as the solvent.

Thermal degradation was determined at heating rates of 2, 5, 10, 20 and 40 ºC/min with around 5 mg samples in a Q50 thermogravimetric analyzer of TA Instruments under a flow of dry nitrogen and in the temperature range from 50 to 600 ºC. Deconvolution of the derivative thermogravimetric analysis (DTG) curve was performed with the PeakFit v4 program by Jandel Scientific Software using an asymmetric function known as "asymmetric double sigmoidal".

4.1.2.3. Evaluation of the activation energy for thermal degradation processes

According to non-isothermal kinetic theory, thermal degradation of a sample can be expressed by the following function:

$$\frac{d\alpha}{dT} = \frac{1}{\beta} A \exp\left(-\frac{E}{RT}\right) f(\alpha) \qquad (1)$$

where β is the heating rate, T is the absolute temperature, R is the gas constant, $f(\alpha)$ is the differential conversion function, and A and E are the pre-exponential factor and the activation energy for the decomposition reaction step, respectively.

Activation energies can be determined by the Kissinger method[26] and advanced isoconversional methods such as Kissinger-Akahira-Sunose (KAS) [26,27] and Friedman [28,29], which do not require the knowledge of the exact thermodegradation mechanism. Integral (KAS) and differential (Friedman) isoconversional methods use the isoconversional principle, which states that at a constant extent of conversion the reaction rate is a function of the temperature only.

The Kissinger method,[26] which gives the associated activation energy, E, only at the maximum of the DTG curve for each degradation step, is based on the following equation:

$$\ln\frac{\beta}{T_{max}^2}=\ln\frac{AR}{E}+\ln\left[n(1-\alpha_{max})^{n-1}\right]-\frac{E}{RT_{max}} \quad (2)$$

where β is the heating rate, T_{max} is the temperature at the maximum reaction rate, α_{max} is the conversion at this T_{max} temperature, n is the reaction order and A the frequency factor. From a plot of ln (β/ T_{max}^2) versus 1/T_{max} and fitting the data to a straight line, the activation energy of the degradation step could be determined from the slope.

It should be pointed out that Kissinger is not an isoconversional method since the peak temperature is obtained at different heating rates and the extent of conversion related to the peak is known to change with the heating rate.[30,31] Moreover, the activation energy value determined may lose its meaning if it varies throughout the degradation process.

The activation energy during the whole process can be calculated by the KAS method.[26,27] This methodology is based on the integration of equation 1, which after reordering, becomes

$$\ln\frac{\beta}{T^2}=\ln\left[\frac{AR}{g(\alpha)E}\right]-\frac{E}{RT} \quad (3)$$

where $g(\alpha)$ is the integral conversion function (i.e., $g(\alpha)=\int_0^{\alpha}\frac{d\alpha}{f(\alpha)}$).

For each degree of conversion and each step of the degradation process the activation energy is obtained from the slope of the linear representation of ln (β/ T^2) versus 1/T.

The Friedman method [28,29] (equation 4) derives from the logarithmic form of the rate (equation 1) and is used to obtain the values of activation energies over a wide range of conversions by plotting ln (β dα / dT) versus 1/T from thermogravimetric curves recorded at several heating rates:

$$\ln\frac{\beta d\alpha}{dT}=\ln A+\ln f(\alpha)-\frac{E}{RT} \quad (4)$$

4.1.2.4. Determination of thermal degradation mechanisms

The Coats-Redfern method [32] calculates the activation energy using conventional $g(\alpha)$ functions [33,34] according to equation 5, which was derived considering an asymptotic approximation ($2RT/E<<1$) and using conventional $g(\alpha)$ functions [33,34]:

$$\ln\frac{g(\alpha)}{T^2}=\ln\left(\frac{AR}{\beta E}\right)-\frac{E}{RT} \qquad (5)$$

Caution must be taken as this equation was obtained assuming that the activation energy was independent of the degree of conversion.

The slope of the linear plot of $\ln g(\alpha)/T^2$ versus $1/T$ allowed the activation energy to be determined for each possible model and the model to be selected by considering the agreement with the previously calculated activation energy and the achievement of a good regression coefficient. With the Coats-Redfern method, it is also possible to determine the frequency factor from the intercept at the origin, and therefore the complete kinetic triplet (E, A and $f(\alpha)$), which defines the variation of the degree of conversion with the temperature (equation 1).

The master curve procedure [35] is an alternative method to discriminate the most suitable kinetic model for a degradation process. A differential master equation can be easily derived from equation 1 using the conversion α = 0.5 as a reference and assuming constant values for the activation energy and the pre-exponential factor:

$$\frac{f(\alpha)}{f(0.5)}=\frac{\mathrm{d}\alpha/\mathrm{d}t}{(\mathrm{d}\alpha/\mathrm{d}t)_{0.5}}\frac{\exp(-E/RT_{0.5})}{\exp(-E/RT)} \qquad (6)$$

where $(\mathrm{d}\alpha/\mathrm{d}t)_{0.5}$, $T_{0.5}$ and $f(0.5)$ are the reaction rate, temperature and differential conversion function at α = 0.5, respectively.

The left hand side of this equation is a reduced theoretical curve which is characteristic of each kinetic model. The activation energy of the right hand side is chosen as the most representative of the overall process. By comparing both sides of the equation, it is possible to discern the kinetic model that best describes the experimental reaction process.

4.1.3. RESULTS AND DISCUSSION

4.1.3.1. Thermal degradation mechanism of polylactide

Polylactide decomposes in a nitrogen atmosphere at temperatures between 240 and 420 ºC depending on the heating rate. Logically, thermogravimetric traces shift to higher temperatures with increasing the heating rate, and this dependence makes it possible to determine the activation energy associated with the decomposition process.

In all cases, the degree of degradation or conversion, α, at a given temperature was calculated from the thermogravimetric traces as

$$\alpha = \frac{W_0 - W}{W_0 - W_\infty} \qquad (7)$$

where W_0, W and W_∞ are the initial weight, the weight at the selected temperature and the final weight at the end of the degradation process, respectively.

Figure 4.1.2 plots the degree of conversion versus temperature curves of polylactide at all heating rates tested, together with the corresponding DTG derivative curves. These suggested a complex degradation process since the peak was highly asymmetric, and furthermore a shoulder was clearly envisaged at a lower temperature, when the lower heating rates were used (see blue arrows in Figure 4.1.2). The activation energy from the experimental degradation profiles showed a steady increase when calculated by the KAS or Friedman methods (Figure 4.1.3), as expected for a complex decomposition process where the second step has the higher activation energy. The lower value, which is associated with the first process, justified that this step was enhanced by decreasing the heating rate, as observed in the DTG curves, since in this case degradation occurred at lower temperatures.

PLA degradation kinetics can be studied by analyzing the different decomposition processes separately. A first approach consists of the treatment of the two single curves obtained after mathematical deconvolution of the experimental DTG traces, as shown in Figure 4.1.2 for a representative heating rate. We also paid special attention to the predominant decomposition step because it was expected to lead to less experimental error.

Figure 4.1.2. Degree of conversion (□) versus temperature and derivative curves for the decomposition of polylactide. Curves are drawn from left to right in increasing order of heating rates (2, 5, 10, 20 and 40 ºC/min). The two-peak deconvolution (red curves) is only shown for a representative DTG curve (2 ºC/min). Blue arrows point to the shoulder in DTG curves obtained at low heating rates.

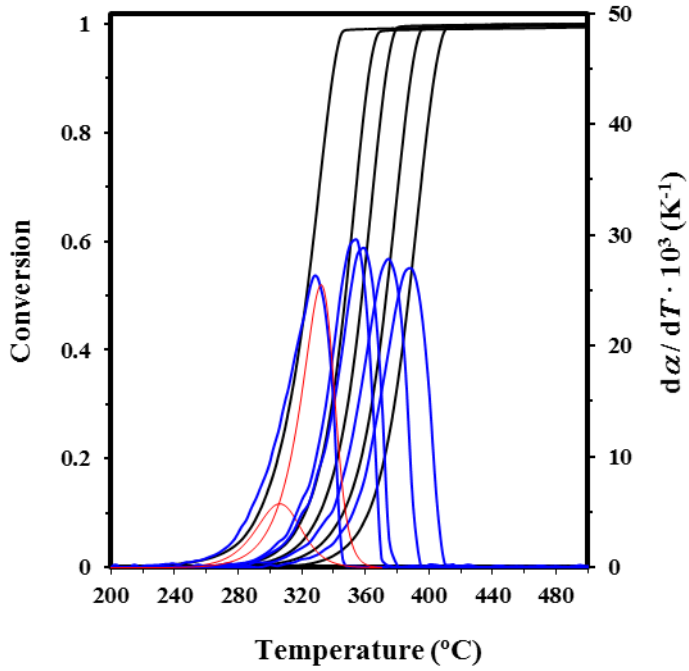

The KAS and Friedman methods gave rise to linear plots for all conversion degrees, with correlation coefficients not less than 0.9910 and 0.9966, respectively. In both cases, the worst agreement was detected for the lowest degree of conversion (0.1). This was probably due to the intrinsic error associated with the mathematical treatment since the overlapping of deconvoluted profiles was highly significant at low conversions.

Figure 4.1.3 shows that the activation energy determined by the Friedman method was practically constant for conversions higher than 0.1 (i.e., 155-159 kJ/mol), which should result in the lowest experimental error, as indicated above. Deconvolution of DTG curves appears as a good approach for analyzing the main decomposition process as the calculated energy was rather constant (average value of 156 kJ/mol) and in close agreement with the value previously reported in the literature[21] (161-162 kJ/mol). The KAS method gave slightly worse results. Thus, greater fluctuation in energy was observed,

conversions needed to be higher than 0.2 to obtain a practically constant energy and the average value was slightly underestimated (i.e., 149 ± 7 kJ/mol), as typically found when comparing results from the Friedman and KAS methods. In fact, the former solves the differential kinetic form (equation 1) without approximations whereas the latter uses a close-form approximation [36] to derive the integral equation 3, thus providing a less accurate activation energy value.

Figure 4.1.3. Plots of the activation energy calculated by the KAS (■,●) and Friedman (□,○) methods for the main degradation step of polylactide (■,□) and polytrimethylene carbonate (●,○).[17] Activation energies calculated by applying the KAS and Friedman methods to the non deconvoluted DTG curve are also plotted (gray symbols). Blue (PLA) and red (PTMC) dashed lines indicate the average activation energy over the conversion range where it can be considered practically constant.

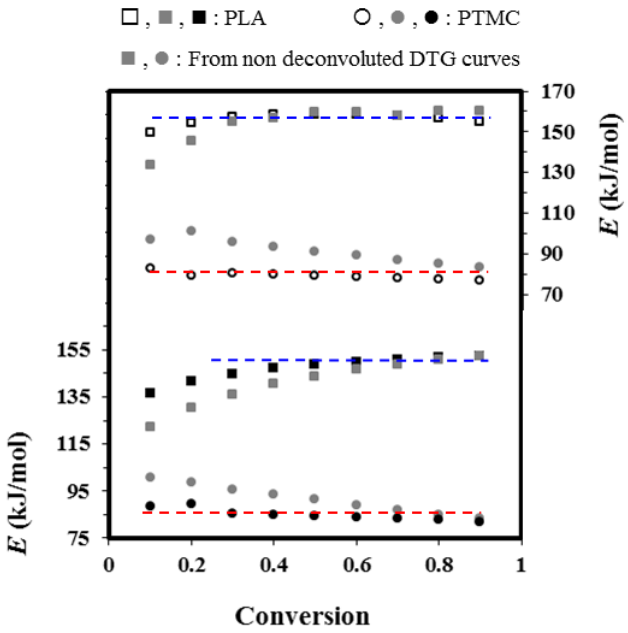

The Coats-Redfern method was applied to determine the degradation mechanism associated with the decomposition step. Specifically, Table 4.1.1 summarizes the values determined for an intermediate heating rate (10 ºC/min) at which the experimental data basically corresponded to the main step because of its higher activation energy.

Table 4.1.1. Activation energies obtained by the Coats-Redfern method for the main degradation step of PLA (10 °C/min) and PLA/PTMC-*x* blends for a heating rate of (10 °C/min).[a]

	PLA		PLA/PTMC-0.8		PLA/PTMC-0.5		PLA/PTMC-0.2	
	E (kJ/mol)	*r*	*E* (kJ/mol)	*r*	*E* (kJ/mol)	*r*	*E* (kJ/mol)	*r*
Power	115.0	0.9896	104.5	0.9952	263.6	0.9807	138.9	0.9708
F_1	336.0	0.9998	302.4	0.9992	755.8	0.9981	414.0	0.9950
$A_{3/2}$	220.5	0.9998	198.4	0.9992	500.6	0.9981	272.8	0.9949
A_2	**162.7**	**0.9998**	146.3	0.9992	373.0	0.9980	202.2	0.9947
A_3	105.0	0.9998	**94.3**	**0.9991**	245.4	0.9980	**131.6**	**0.9945**
A_4	76.1	0.9998	68.3	0.9991	181.6	0.9979	96.3	0.9942
A_5	58.8	0.9998	52.7	0.9990	143.4	0.9979	75.1	0.9939
A_6	47.2	0.9998	42.3	0.9989	117.9	0.9978	61.0	0.9935
A_7	39.0	0.9998	34.8	0.9989	**99.6**	**0.9977**	50.9	0.9932
R_2	283.9	0.9972	256.8	0.9995	635.7	0.9918	344.4	0.9860
R_3	300.2	0.9985	271.2	0.9998	673.2	0.9944	366.2	0.9895
D_1	491.4	0.9909	447.2	0.9958	1083.7	0.9817	584.2	0.9735
D_2	554.2	0.9954	502.9	0.9985	1211.6	0.9884	662.1	0.9822
D_3	611.0	0.9986	552.1	0.9998	1356.2	0.9945	741.9	0.9898
D_4	566.3	0.9966	513.0	0.9992	1253.7	0.9907	682.5	0.9848
n=1.5	397.2	0.9985	355.8	0.9950	898.5	0.9999	496.7	0.9993
n=2	467.1	0.9941	416.8	0.9880	1062.7	0.9981	591.9	0.9998
n=3	628.9	0.9812	557.4	0.9710	1443.7	0.9888	813.3	0.9944
n=1.5 m=0.5	228.3	0.9938	203.5	0.9874	526.5	0.9980	291.2	0.9998
n=1.9 m=0.1	419.4	0.9940	374.1	0.9879	955.4	0.9981	531.8	0.9998

[a] *Selected activation energies are written in bold*

Good correlation coefficients were generally found for all models. However, it is clear that only the A_2 nucleation model gave an activation energy (162.7 kJ/mol) that was in agreement with the values computed by the KAS and Friedman methods. Furthermore, rather similar activation energies were calculated at all heating rates, the average value (151 kJ/mol) being intermediate between those determined by Friedman and KAS. After selection of the kinetic model, it is possible to calculate the frequency factor ($\ln (A / min^{-1})$ = 27.46), and therefore determine the complete kinetic triplet (E, A and $f(\alpha)$) for the considered degradation step (Table 4.1.2).

Table 4.1.2. Kinetic parameters determined for poly(trimethylene carbonate),[17] polylactide and PLA/PTMC-*x* blends.

Sample	Activation energy (kJ/mol)				Model	Frequency factor
	Kissinger	KAS	Friedman	Coats-Redfern[a]		$\ln (A / min^{-1})$[a]
PTMC	83	85	75	72	A_3	14.60
PLA	153	147	156	151	A_2	27.46
PLA/PTMC-0.2	119	117	127	125	A_3	25.05
PLA/PTMC-0.5	99	98	100	100	A_7	19.35
PLA/PTMC-0.8	97	98	96	102	A_3	19.62

[a] *Values determined by considering all heating rates (i.e., 2, 5, 10, 20 and 40°C/min).*

4.1.3.2. Thermal degradation of polylactide and poly(trimethylene carbonate) blends

Thermogravimetric and derivative thermogravimetric curves of PTMC, PLA and selected PLA/PTMC blends are compared in Figure 4.1.4. Blends clearly have a rather similar degradation behavior despite significant differences in the PLA/PTMC polymer ratio (i.e., the polytrimethylene carbonate content ranged from 20 to 80 wt-%). In addition, blends decomposed at an intermediate temperature interval between those of the corresponding PLA and PTMC samples and showed a degradation profile that could not be associated with a simple combination of the characteristic degradation curves of the two constituent homopolymers.

The DTG curve of PTMC pointed to a complex mechanism as a peak and a shoulder were envisaged. In fact, KAS and Friedman analyses were previously performed [17] in a similar way as for PLA. It was shown that the activation energy decreased with conversion when considering non deconvoluted profiles and that the energy value was constant (close to 85 kJ/mol) when considering only the deconvoluted curve associated with the predominant degradation step (i.e., the second one) (Figure 4.1.3).[17] Unlike in the case of PLA, the first degradation step of PTMC had the higher activation energy and justified the higher value determined for the predominant step at low conversions.

Degradation behavior of PLA/PTMC-0.20 was surprisingly significantly different from that observed for its major component (i.e., PTMC). Specifically, a shift towards higher temperatures was clearly detected. Experiments carried out at a representative heating rate of 10 ºC/min (Figure 4.1.4) showed that: a) Degradation of the blend started at a temperature more than 40 ºC higher than PTMC; b) The char yield was clearly higher for the blend (values close to 4% and 0% were found at 330 ºC for the blend and PTMC samples, respectively) and c) The mass loss of the blend was only 30% at the temperature corresponding to the complete degradation of PTMC. Note that this value is in full disagreement with the PTMC content (i.e., 80%), and therefore a physical or a chemical change (e.g., occurrence of transesterification reactions) should be considered.

A complex degradation mechanism for the blend could also be inferred from its DTG curve, where a main peak associated to PTMC degradation is observed together with a shoulder at a lower temperature that could be related to the decomposition of the polymer that is in less proportion (PLA). The incorporation of PTMC in the blend may cause a catalytic effect over the degradation of the second component.

DTG curves of PLA/PTMC-0.80 were again complex and showed a major peak, which should be associated in this case to the PLA decomposition, and a small shoulder a lower temperature that may correspond to PTMC decomposition. Degradation behavior of PLA/PTMC-0.80 seems easier to understand since the initial decomposition process of PTMC could generate some products that accelerate the decomposition of the theoretically most stable component (i.e., PLA). Note that the peak associated with PLA decomposition moved to lower temperatures as compared to pure PLA when the blend had an increasing ratio of PTMC (i.e., PLA, PLA/PTMC-0.20 and PLA/PTMC-0.80 samples) demonstrating a destabilizing effect. On the contrary, the PTMC decomposition moved to higher temperatures with increasing PLA ratios.

Finally, PLA/PTMC-0.50 exhibited a behavior intermediate between those of the other two blends since two peaks that could be related to the decomposition of each sample were clearly observed. Note that both peaks appeared at a lower temperature than the predominant peak observed for the PLA/PTMC-0.80 sample, indicating again an enhanced decomposition process of PLA. NMR spectra of a sample that experimented a weight loss close to 30% showed a clear decrease on the PLA ratio, as will be discussed below, and consequently it could be inferred that the first decomposition peak could be unambiguously associated to the decomposition of PLA.

Figure 4.1.4. Thermogravimetric and derivative curves obtained at a heating rate of 10 ºC/min for PTMC (black), PLA (black) and PLA/PTMC-*x* blends with *x* = 0.20 (green), 0.50 (blue) and 0.80 (red).

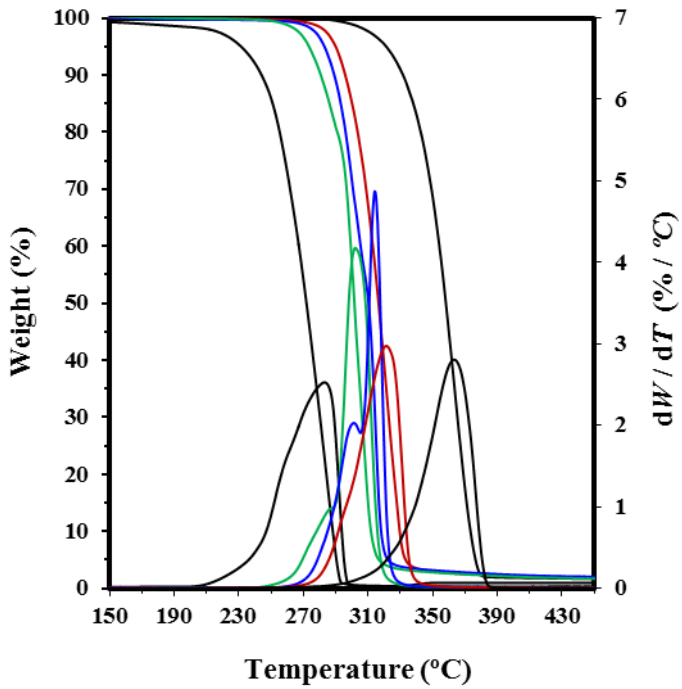

Figure 4.1.5 plots the degree of conversion versus temperature curves of the three blends at all heating rates, together with the corresponding DTG derivative curves. The activation energies of the main degradation step can be well compared for all samples by the Kissinger method which, despite being an approximation, has the advantage of using only well-defined peak temperatures. Thus, results are not dependent on mathematical deconvolution accuracy.

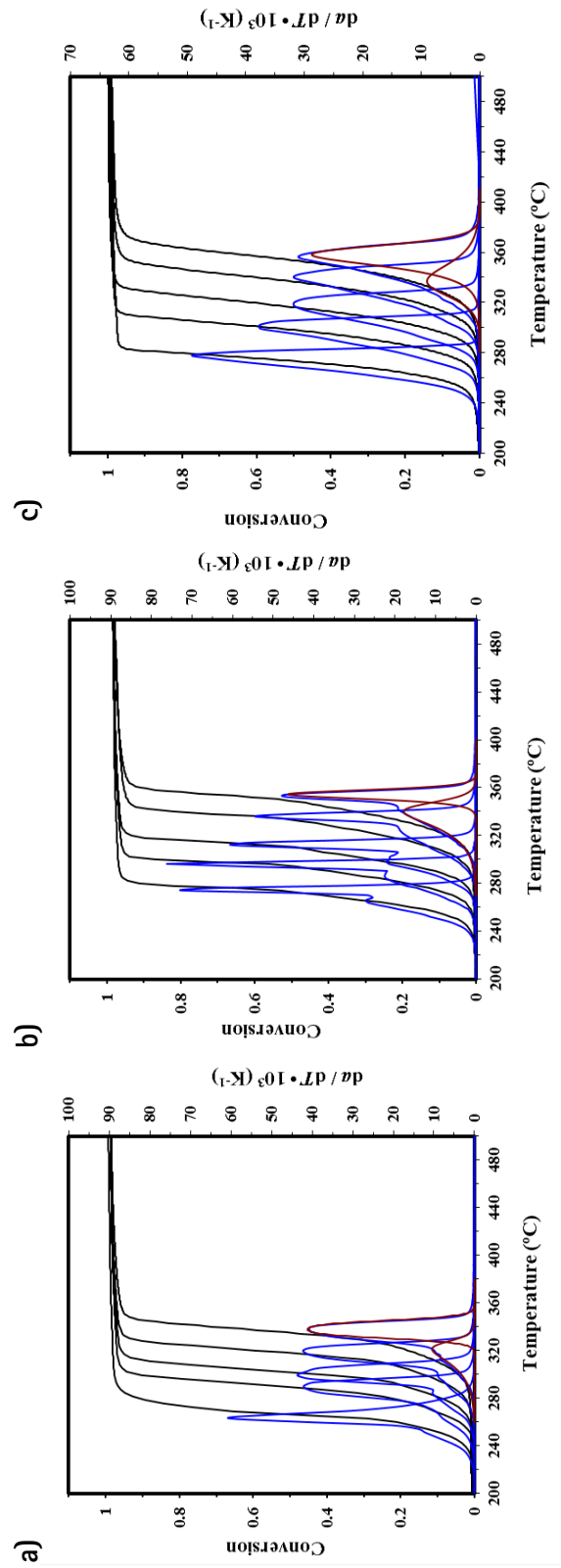

Figure 4.1.5. Degree of conversion (α) versus temperature and derivative curves for the decomposition of PLA/PTMC-x blends with x = 0.20 (**a**), 0.50 (**b**) and 0.80 (**c**). Curves are drawn from left to right in increasing order of heating rates (2, 5, 10, 20 and 40 °C/min). In all cases, the two-peak deconvolution (red curves) is only shown for the representative DTG curve obtained at the highest heating rate.

Figure 4.1.6 shows that the slopes corresponding to the three blends are highly similar although a slightly higher slope was found for the PLA/PTMC-0.20 blend. Specifically, activation energies of 97, 99 and 119 kJ/mol were determined for the peaks that should correspond, as explained above, to the decomposition of PLA, PTMC and PTMC, respectively. These values are clearly different from those calculated for PTMC (83 kJ/mol) and PLA (153 kJ/mol) samples as summarized in Table 4.1.2. It merits attention the clear decrease and increase detected for PLA and PTMC, respectively, when they are blended.

Figure 4.1.6. Kissinger plots of the main degradation step of PTMC (◊),[17] PLA (□) and PLA/PTMC-*x* blends with *x* = 0.20 (x), 0.50 (Δ) and 0.80 (○).

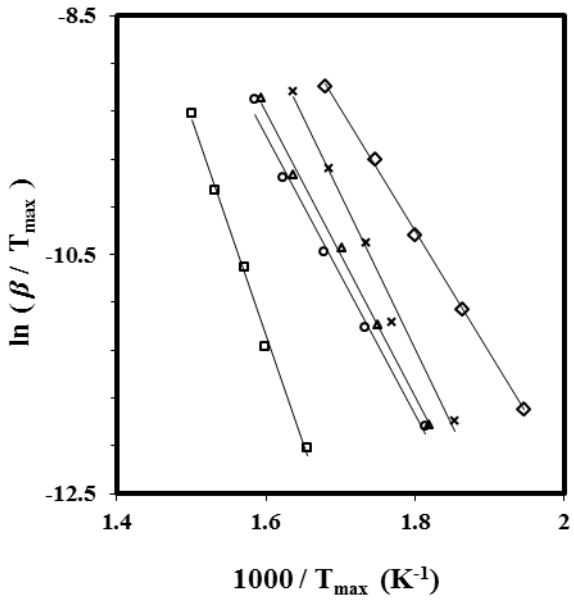

A more detailed study of the main decomposition process was conducted for each sample by considering the representative single peak obtained after mathematical deconvolution, as also shown in Figure 4.1.5 for a representative heating rate. The Friedman and KAS methods always led to linear plots with correlation coefficients not less than 0.9982, which were attained at a conversion of 0.2 with the PLA/PTMC-0.20 sample. Figure 4.1.7 shows that the calculated activation energies were almost constant for conversions higher than 0.2, i.e., they were not significantly affected by inaccuracies associated with mathematical deconvolution. Note that slightly higher or lower values were found at low conversions depending on the energy associated with the first degradation step (i.e., higher or lower energy, respectively). Thus, the first step of decomposition of PLA/PTMC-

0.20 corresponds to the PLA component which should have lower activation energy in the mixture. On the contrary, the first step of PLA/PTMC-0.80 corresponds to PTMC which should have the higher activation energy. It should be pointed out that the activation energy of PLA/PTMC-0.50 remained practically constant since DTG peaks were well defined and the mathematical deconvolution had a lower error associated.

Figure 4.1.7. Plots of the activation energy calculated by the KAS (full symbols) and Friedman (empty symbols) methods for the main degradation step of poly(trimethylene carbonate) (◊),[17] polylactide (□) and the PLA/PTMC-*x* blends with *x* = 0.20 (x), 0.50 (Δ) and 0.80 (○). Blue (PTMC and PLA) and red (PLA/PTMC-*x*) dashed lines indicate the average activation energy over the conversion range where it can be considered practically constant.

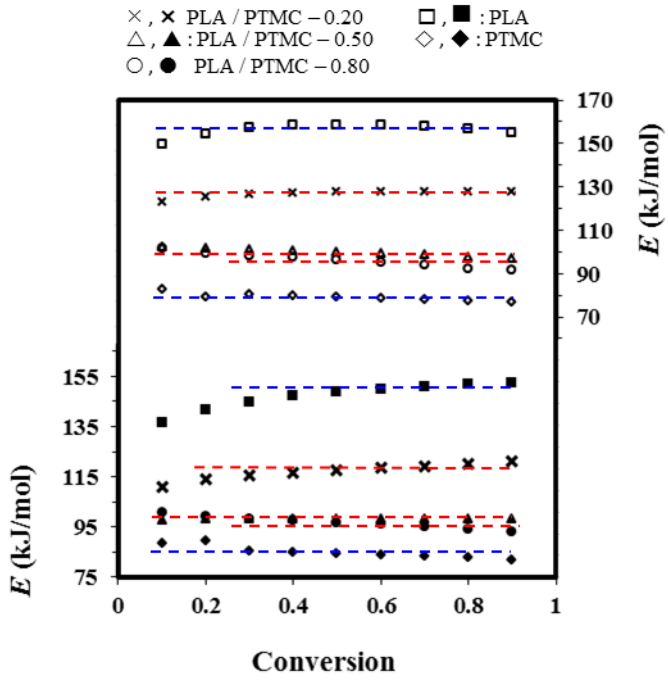

Energies deduced from both methods were comparable, as summarized in Table 4.1.2. The following points are worth noting: a) The activation energy associated to the main degradation step of blends was intermediate between those of the two constituent polymers, suggesting the occurrence of well differentiated decomposition processes; b) The incorporation of a smaller amount of PLA strongly affects the degradation behavior since the activation energy of PLA/PTMC-0.20 samples becomes clearly greater than that

of PTMC and even than that of the other two blends; c) The incorporation of a smaller amount of PTMC strongly affects also the degradation behavior. In this case, the blend with 80 wt-% of PLA has a lower activation energy than that found for PLA.

According to the Coats-Redfern methodology, the A_3 model was the only one to render activation energies close to the experimental ones for blends with 20 or 80 wt-% of PLA (see Table 4.1.1 for a representative heating rate). Thus, average values of 125 and 102 kJ/mol were respectively determined for all heating rates. Note that these values were comparable to those calculated by Friedman and even KAS (Table 4.1.2).

Furthermore, the A_3 model was confirmed by comparing the $f(\alpha)$ functions normalized at $\alpha = 0.5$ for all the kinetic models with the right hand side of equation 6, as calculated for selected conversions and assuming the average activation energies determined for both blends (Figure 4.1.8).

Figure 4.1.8. Comparison of the $f(\alpha)$ functions (solid lines) normalized at $\alpha = 0.5$ corresponding to ideal kinetic models with the right hand side of equation 6 applied to selected conversions and data corresponding to a heating rate of 20 ºC/min for PLA/PTMC-x blends with $x = 0.20$ (red) and 0.80 (green) (dots). Bold line emphasizes the A_3 and A_2 kinetic models. Data corresponding to the PLA sample are also plotted for the sake of completeness (blue).

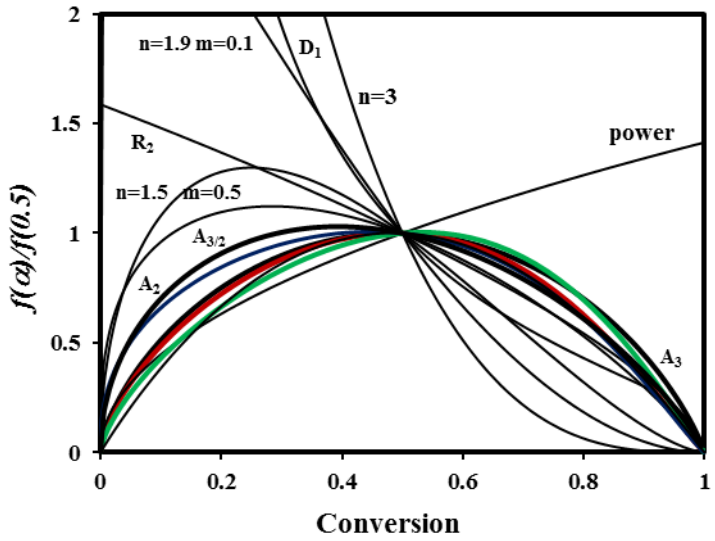

Despite having a similar activation energy, the main degradation step of PLA/PTMC-0.50 was clearly different from that observed in the related PLA/PTMC-0.80 sample since weight was lost in a narrower range and the corresponding DTG peak became larger. In fact, the peak can be associated to the decomposition of PTMC or PLA, respectively. The abrupt decomposition observed for PLA/PTMC-0.50 was well explained by Coats-Redfern assuming an A_7 kinetic model (Table 4.1.1). This mechanism suggests an increase in active zones (nuclei) because of the previous decomposition, which is mainly associated with PLA. It should be pointed out that the PTMC degradation process becomes faster in blends when increasing the PLA content (i.e., 50 with respect to 20 wt-%).

Pre-exponential factors corresponding to the main degradation step of blends were easily calculated after selection of the degradation mechanism (see Table 4.1.2, which also includes other data of the kinetic triplet).

4.1.3.3. Thermal degradation of blends of poly(ε-caprolactone) and poly(trimethylene carbonate)

Figure 4.1.9 compares thermogravimetric and derivative thermogravimetric curves of PTMC, PCL and PTMC/PCL blends at a representative heating rate (10 ºC/min). It is clear that the thermal degradation of both polymers drastically changed after mixing, leading to a highly complex decomposition process. The degradation behavior of these PTMC/PCL blends was completely different from that of the related PTMC/PLA blends.

Surprisingly, the first characteristic decomposition step of PTMC was enhanced to the detriment of the second, i.e., after mixing the polymer with PCL. On the contrary, this step was either not detected when PLA blends were degraded or was minor when only the PTMC sample was degraded (Figure 4.1.4). It should also be pointed out that the DTG curves of the three studied blends (i.e., those with 80, 50 and 20 wt-% of PTMC) showed a well-defined peak at practically the same temperature as the shoulder observed in the DTG curve of PTMC (Figure 4.1.9), and obviously at a lower temperature than that corresponding to its predominant peak (second step). Unlike PLA, the presence of PCL somehow seems to favor the first decomposition process.

A second but more logical observation is that the degradation of the PCL component occurred faster in the blend, probably because of the generation of decomposition by-products during the decomposition of the less stable component of the mixture (i.e.,

PTMC) or even a change in the microstructure caused by transesterification reactions. Thus, the PCL/PTMC-0.50 sample became practically fully degraded (weight loss close to 98%) when the temperature at which the PCL sample had a 5% weight loss was reached (i.e., 367 ºC for the heating rate of 10 ºC/min). The PCL rich sample exhibited the most complex behavior since more than four peaks were observed in the corresponding DTG curve. In this case, some amount of the PCL component (less than 20 wt-%) degraded at the characteristic temperature range observed for the single polymer (i.e., 370-430 ºC for the heating rate used).

Because of the complexity of the degradation of PTMC/PCL blends, we paid attention to the first decomposition step, which is associated with the PTMC component. Also for the sake of completeness we focused to the degradation of the PCL sample. The analyses were performed considering the DTG derivative curves of PCL/PTMC-*x* and PCL samples obtained at heating rates of 2, 5, 10, 20 and 40 ºC/min (not shown).

Figure 4.1.9. Thermogravimetric and derivative curves obtained at a heating rate of 10 ºC/min for PTMC (black), PCL (black) and PCL/PTMC-*x* blends with *x* = 0.20 (green), 0.50 (blue) and 0.80 (red).

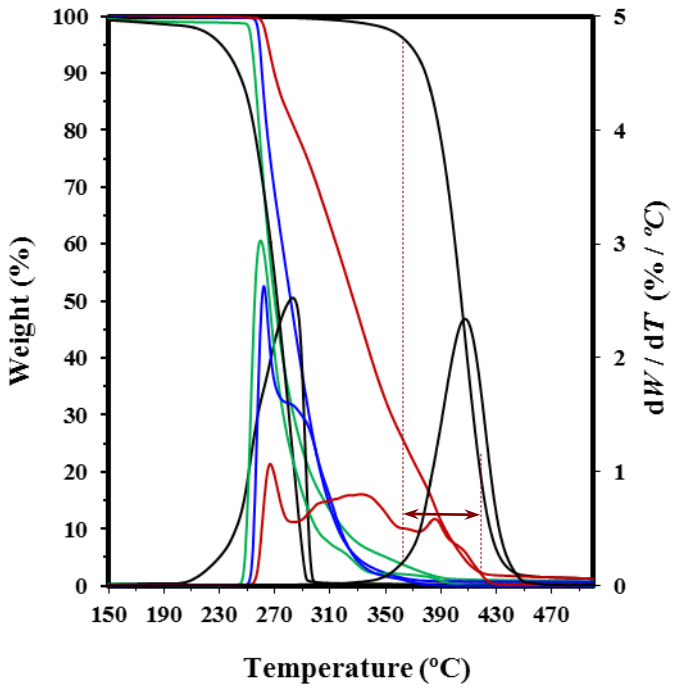

Figure 4.1.10 illustrates the Kissinger plots of all the samples. PCL had the highest activation energy (i.e., 171) whereas the slopes of the blends were similar and higher than that observed for PTMC. Specifically, the activation energy of the blends ranged between 137 and 121 kJ/mol, clearly higher values than that determined for the predominant decomposition step of PTMC (i.e., the second one). Note that a higher value was previously inferred for the first step and was in agreement with the higher energy calculated at low conversions by the Friedman and KAS methods, when non deconvoluted DTG profiles were analyzed (Figure 4.1.3).

Figure 4.1.10. Kissinger plots of the main degradation step of PTMC (*x*),[17] PCL (◊) and PCL/PTMC-*x* blends with *x* = 0.20 (□), 0.50 (Δ) and 0.80 (○).

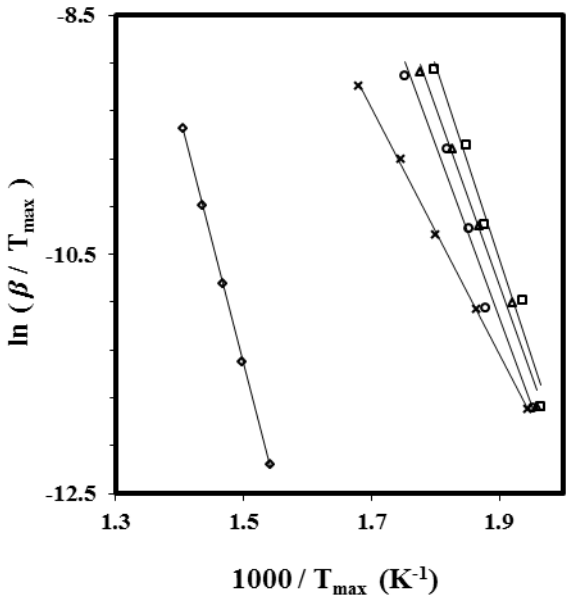

DTG curves of the first degradation step were obtained by deconvolution of the experimental profiles and used to determine the kinetic parameters. Figure 4.1.11 shows that activation energies calculated by the Friedman and KAS methods were constant for all conversions and rather comparable for the three studied blends. However, a slightly higher value was obtained for the sample with a higher ratio of PTMC, as occurred with the Kissinger analysis (Table 4.1.3).

Figure 4.1.11. Plots of the activation energy calculated by the KAS (full symbols) and Friedman (empty symbols) methods for the main degradation step poly(trimethylene carbonate) (*x*),[17] poly(ε-caprolactone) (◊) and the PCL/PTMC-*x* blends with *x* = 0.20 (□), 0.50 (Δ) and 0.80 (○). Blue (PTMC and PCL) and red (PCL/PTMC-*x*) dashed lines indicate the average activation energy over the conversion range where it can be considered practically constant.

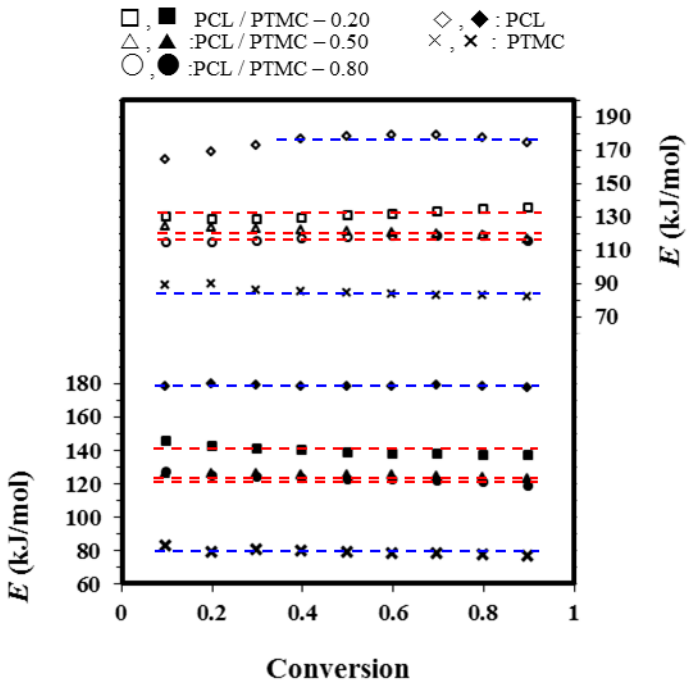

Table 4.1.2. Kinetic parameters determined for poly(trimethylene carbonate),[17] poly(ε-caprolactone) and PCL/PTMC-*x* blends.

Sample	Activation energy (kJ/mol)				Model	Frequency factor
	Kissinger	KAS	Friedman	Coats-Redfern[a]		ln (*A* / min^{-1})[a]
PTMC	83	85	75	72	A_3	14.60
PCL	171	179	177	170	$A_{3/2}$	28.98
PCL/PTMC-0.2	137	140	131	139	A_2	30.64
PCL/PTMC-0.5	125	125	121	115	A_3	24.79
PCL/PTMC-0.8	121	123	116	118	A_4	25.37

[a] *Values determined by considering all heating rates (i.e., 2, 5, 10, 20 and 40°C/min).*

The Coats-Redfern method was applied again to find the degradation mechanism associated with the first decomposition step. Table 4.1.4 summarizes the energies determined for representative heating rates, which clearly point to the Avrami mechanisms and made it possible to calculate the corresponding pre-exponential factors. Final values of the kinetic triplet associated with the first degradation step of the three blends are given in Table 4.1.3. Note that the exponent of the Avrami mechanisms increased (from 2 to 4) with increasing the PCL content, suggesting that the number of active nuclei for decomposition increased.

The complexity of the degradation process of the samples calls for a more detailed analysis but it seems to be beyond the scope of this work. However, we took ^{1}H NMR spectra (Figure 4.1.12) at the beginning of the thermal decomposition processes which reveal clear differences in the degradation of representative PLA/PTMC-0.50 and PCL/PTMC-0.20 blends from a chemical point of view. In the first case, the spectra of initial and degraded (weight loss of 30%) demonstrated that degradation mainly concerned to PLA samples since the ratio of lactide protons clearly decreased (i.e., the sample experimented a decrease of the lactide ratio from 50 to 27 wt-%). Lactide rings should be formed and released during decomposition, which may account for the hindrance to the characteristic unzipping mechanism of poly(trimethylene carbonate) if the rings had time to react with polymer end groups. In fact, stabilization of poly(trimethylene carbonate) was described for samples having protected terminal groups (e.g., samples with acetylated end groups).[37] A similar conclusion was drawn for polyglycolide and polytrimethylene carbonate blends.[17]

The evolution during degradation of the spectrum of the PCL/PTMC-0.20 sample is clearly different (Figure 4.1.12b) as new signals, together with a preferential release of trimethylene carbonate units (i.e., three PCL weight percentage increased from 20 to 28% for a total weight loss of 30%), were easily detected. Results suggest that the terminal trimethylene carbonate units were not protected by reaction with ε-caprolactone (note the difference in reactivity with the highly similar lactide or glycolide rings), thus facilitating unzipping depolymerization.

Table 4.1.4. Activation energies obtained by the Coats-Redfern method for the main degradation step of PCL (20 °C/min) and PCL/PTMC-*x* blends with *x* = 0.20 (40 °C/min), 0.50 (10 °C/min) and 0.80 (20 °C/min).[a]

	PCL		PCL/PTMC-0.8		PCL/PTMC-0.5		PCL/PTMC-0.2	
	E (kJ/mol)	*r*	*E* (kJ/mol)	*r*	*E* (kJ/mol)	*r*	*E* (kJ/mol)	*r*
Power	78.1	0.9801	164.3	0.9634	121.2	0.9130	93.6	0.9640
F_1	266.9	0.9991	483.8	0.9915	380.3	0.9668	283.0	0.9925
$A_{3/2}$	**174.0**	**0.9990**	319.5	0.9913	250.6	0.9660	185.6	0.9922
A_2	127.6	0.9990	237.3	0.9912	185.7	0.9652	**136.9**	**0.9919**
A_3	81.2	0.9989	155.2	0.9908	**120.8**	**0.9635**	88.2	0.9913
A_4	58.0	0.9988	**114.1**	**0.9904**	88.4	0.9618	63.8	0.9907
R_2	212.0	0.9937	403.6	0.9805	308.7	0.9451	235.6	0.9820
R_3	229.1	0.9961	428.7	0.9846	331.0	0.9530	250.4	0.9861
D_1	346.9	0.9839	684.8	0.9661	511.7	0.9209	402.2	0.9687
D_2	411.1	0.9911	772.5	0.9760	588.6	0.9385	458.3	0.9785
D_3	469.7	0.9963	866.5	0.9850	670.9	0.9541	510.1	0.9866
D_4	423.0	0.9929	798.0	0.9790	610.1	0.9432	469.5	0.9810
n=1.5	332.8	0.9997	579.2	0.9978	466.8	0.9822	339.2	0.9982
n=2	409.2	0.9972	689.1	0.9999	567.5	0.9918	403.7	1.0000
n=3	588.0	0.9889	944.6	0.9970	803.3	0.9992	553.5	0.9967
n=1.5 m=0.5	198.8	0.9971	340.0	0.9999	279.3	0.9915	197.2	1.0000
n=1.9 m=0.1	367.1	0.9972	619.3	0.9999	509.9	0.9917	362.4	1.0000

[a] *Selected activation energies are written in bold*

Figure 4.1.12. ^{1}H-NMR spectra showing distinctive signals of PLA/PTMC-*x* **(a)** and PCL-PTMC-*x* **(b)** blends before degradation and after weight losses of 30% (PLA/PTMC-0.50) and 30% (PCL-PTMC-0.20) (see insets).

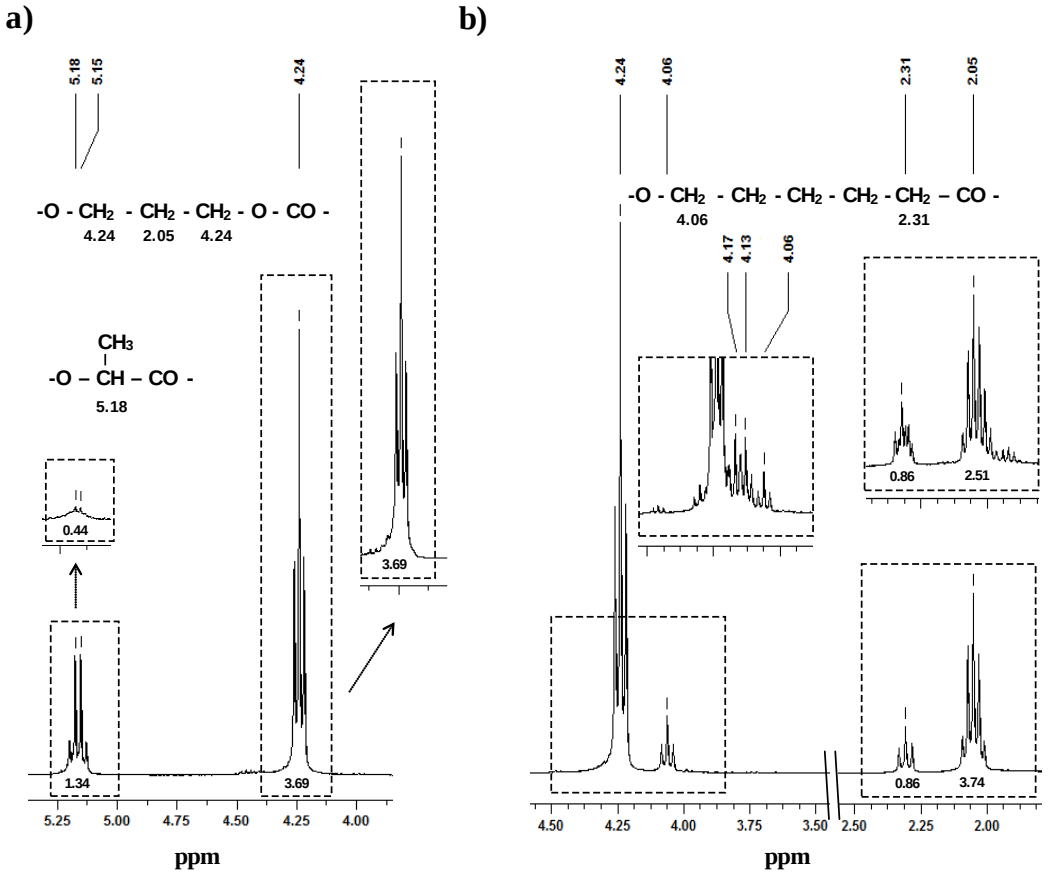

Finally, the degradation behavior of PCL was also evaluated considering the highly asymmetric DTG curves (Figure 4.1.9), which were again indicative of a complex mechanism. In this case, deconvolution was not performed because the first decomposition step was highly insignificant and the mathematical process was subject to the error associated with a not well defined peak. Figure 4.1.11 plots the activation energies deduced from the isoconversional KAS and Friedman methods, which appear rather constant for conversions higher than 0.2. Furthermore, a lower activation energy could be envisaged for the first step, when the evolution of the Friedman data is considered. Coats-Redfern kinetic analysis was performed using degradation data at conversions higher than 0.2. The values for a representative heating rate in Table 4.1.4 make it possible to assign an $A_{3/2}$ mechanism to the predominant decomposition process

of PCL, although the autocatalytic model (n = 1.5, m = 0.5) cannot be fully discarded. The frequency factor (ln (A / min^{-1}) = 28.98), and consequently the complete kinetic triplet, (E, A and $f(\alpha)$) were calculated using the selected model, as summarized in Table 4.1.3.

4.1.4. CONCLUSIONS

The degradation behavior of poly(trimethylene carbonate) changes substantially when this polymer is mixed with polylactide or poly(ε-caprolactone). Thus, the incorporation of PCL enhances the usually minor decomposition process associated with an unzipping depolymerization reaction occurring at the lower temperature range. By contrast, this process is practically suppressed and typical random chain scissions seem to be favored upon addition of PLA. In this case, thermal stabilization of PTMC is observed and the main decomposition process occurs at higher temperatures and the activation energy increases.

Decomposition of PLA and especially of PCL is favored when blending these polymers with the less thermally stable PTMC sample. In the case of PLA, a well-defined predominant process can be observed for blends with a low PTMC content.

Results clearly indicate that PLA/PTMC and PCL/PTMC blends have peculiar degradation processes which do not correspond to a mere superposition of the degradation processes associated with each constituent.

Thermal degradation of the samples proceeds by a complex process where different steps can be envisaged. Deconvolution of DTG curves makes it possible to distinguish the different decomposition steps and conduct a kinetic analysis for that corresponding to the main process. Activation energies of this step are practically independent of the degree of conversion, and therefore a single mechanism can be postulated, i.e., the Avrami model, whose exponent changes with the samples and the polymer ratio in the blends.

4.1.5. REFERENCES

1. Mecerreyes, D., Miller, R. D., Hedrick, J. L., Detrembleur, C. & Jerome, R. Ring-opening polymerization of 6-hydroxynon-8-enoic acid lactone: Novel biodegradable copolymers containing allyl pendent groups. *J. Polym. Sci. A Polym. Chem.* **38,** 870–875 (2000).

2. Holy, C. E., Fialkov, J. a, Davies, J. E. & Shoichet, M. S. Use of a biomimetic strategy to engineer bone. *J. Biomed. Mater. Res. A* **65,** 447–53 (2003).

3. Parrish, B., Breitenkamp, R. B. & Emrick, T. PEG- and peptide-grafted aliphatic polyesters by click chemistry. *J. Am. Chem. Soc.* **127,** 7404–10 (2005).

4. Noga, D. E. *et al.* Synthesis and modification of functional poly(lactide) copolymers: toward biofunctional materials. *Biomacromolecules* **9,** 2056–62 (2008).

5. Gilding, D. K. & Reed, A. M. Biodegradable polymers for use in surgery-polyglycolic-poly(lactic acid) homopolymers and copolymers. *Polymer (Guildf).* **2,** 1459–1464 (1979).

6. Middleton, J. C. & Tipton, A. J. Synthetic biodegradable polymers as medical devices. *Med. Plast. Biomater.* **5,** 30–39 (1998).

7. Albertsson, A.-C. & Varma, I. K. Recent developments in ring opening polymerization of lactones for biomedical applications. *Biomacromolecules* **4,** 1466–86 (2003).

8. Zurita, R., Puiggalí, J. & Rodríguez-Galán, A. Loading and release of ibuprofen in multi- and monofilament surgical sutures. *Macromol. Biosci.* **6,** 767–75 (2006).

9. Trimaille, T., Gurny, R. & Mo, M. Poly (hexyl-substituted lactides): Novel injectable hydrophobic drug delivery systems. *J. Biomed. Mater. Res. A* 55–65 (2006).

10. Albertsson, A. & Eklund, M. Influence of molecular structure on the degradation mechanism of degradable polymers *In Vitro* degradation of poly(trimethylene carbonate), poly(trimethylene carbonate-co-caprolactone), and poly(adipic anhydride). *J. Appl. Polym. Sci.* **57,** 87–103 (1995).

11. Matsuda, T., Kwon, I. K. & Kidoaki, S. Photocurable biodegradable liquid copolymers: synthesis of acrylate-end-capped trimethylene carbonate-based prepolymers, photocuring, and hydrolysis. *Biomacromolecules* **5,** 295–305 (2004).

12. Vandermeulen, G., Rouxhet, L., Arien, a, Brewster, M. E. & Préat, V. Encapsulation of amphotericin B in poly(ethylene glycol)-block-poly(epsilon-caprolactone-co-trimethylenecarbonate) polymeric micelles. *Int. J. Pharm.* **309,** 234–40 (2006).

13. Dinarvand, R., Alimorad, M. M., Amanlou, M. & Akbari, H. *In vitro* release of clomipramine HCl and buprenorphine HCl from poly adipic anhydride (PAA) and poly trimethylene carbonate (PTMC) blends. *J. Biomed. Mater. Res. A* **75,** 185–91 (2005).

14. Bezwada, R. S. *et al.* Monocryl suture, a new ultra-pliable absorbable monofilament suture. *Biomaterials* **16,** 1141–8 (1995).

15. Erneta, M. & Vhora, I. A. Aliphatic polyesters of trimethylene carbonate epsilon-caprolactone and glycolide. (1998).

16. Rodeheaver, G. T. *et al.* Biomechanical and clinical performance of a new synthetic monofilament absorbable suture. *J. Long. Term. Eff. Med. Implants* **6,** 181–198 (1996).

17. Díaz-Celorio, E., Franco, L., Márquez, Y., Rodríguez-Galán, A. & Puiggalí, J. Thermal degradation studies on homopolymers and copolymers based on trimethylene carbonate and glycolide units. *Thermochim. Acta* **528,** 23–31 (2012).

18. Lesnikovich, A. I. & Levchik, S. V. Isoparametric kinetic relations for chemical transformations in condensed substances (analytical survey). *J. Therm. Anal. Calorim.* **30,** 677–702 (1985).

19. Zou, H., Yi, C., Wang, L., Liu, H. & Xu, W. Thermal degradation of poly(lactic acid) measured by thermogravimetry coupled to Fourier transform infrared spectroscopy. *J. Therm. Anal. Calorim.* **97,** 929–935 (2009).

20. Zhou, Q. & Xanthos, M. Nanosize and microsize clay effects on the kinetics of the thermal degradation of polylactides. *Polym. Degrad. Stab.* **94,** 327–338 (2009).

21. Chrissafis, K. Detail kinetic analysis of the thermal decomposition of PLA with oxidized multi-walled carbon nanotubes. *Thermochim. Acta* **511,** 163–167 (2010).

22. Badía, J. D., Santoja-Blasco, L., Moriana, R. & Ribes-Greus, A. Thermal analysis applied to the characterization in soil of polylactide II. On th thermal stability and thermal decomposition kinetics. *Polym. Degrad. Stab.* **95,** 2192–2199 (2010).

23. Grause, G., Ishibashi, J., Kameda, T., Bhaskar, T. & Yoshioka, T. Kinetic studies of the decomposition of flame retardant containing high-impact polystyrene. *Polym. Degrad. Stab.* **95,** 1129–1137 (2010).

24. Persenaire, O., Alexandre, M., Degée, P. & Dubois, P. Mechanisms and kinetics of thermal degradation of poly(epsilon-caprolactone). *Biomacromolecules* **2,** 288–94 (2001).

25. Sivalingam, G. & Madras, G. Thermal degradation of poly(ε -caprolactone). *Polym. Degrad. Stab.* **80,** 11–16 (2003).

26. Kissinger, H. E. Reaction kinetics in differential thermal analysis. *Anal. Chem.* **29,** 1702–1706 (1957).

27. Akahira, T. & Sunose, T. Method of determining activation deterioration constant of electrical insulating materials. *Res. Rep. Chiba Inst. Technol.* **16,** 22–31 (1971).

28. Friedman, H. J. Kinetics of thermal degradation of char-forming plastics from thermogravimetry. *J. Polym. Sci. Part C Polym. Symp.* **6,** 183–195 (1964).

29. Flynn, J. H. & Wall, L. A. A quick, direct method for the determination of activation energy from thermogravimetric data. *Polym. Lett.* **4,** 323–328 (1966).

30. Sbirrazzouli, N., Girault, Y. & Elegant, L. Simulations for evaluation of kinetic methods in differential scanning calorimetry. 3. Peak maximum evolution methos and isoconversional methods. *Thermochim. Acta* **293,** 25–37 (1997).

31. Vyazovkin, S. & Sbirrazzouli, N. Isoconversional kinetic analysis of thermally stimulated processes in polymers. *Macromol. Rapid Commun.* **27,** 1515–1532 (2006).

32. Coats, A. W. & Redfern, J. P. Kinetic parameters from thermogravimetric data. *Nature* **201,** 68–69 (1964).

33. Phadnis, A. B. Determination of the kinetics and mechanism of a solid-state reaction-a simple approach. *Thermochim. Acta* **62,** 361–367 (1983).

34. Vyazovkin, S. & Dollimore, D. Linear and nonlinear procedures in isoconversional computations of the activation energy of nonisothermal reactions in solids. *J. Chem. Inf. Model.* **36,** 42–45 (1996).

35. Sánchez-Jiménez, P. E., Pérez-Maqueda, L. a., Perejón, A. & Criado, J. M. A new model for the kinetic analysis of thermal degradation of polymers driven by random scission. *Polym. Degrad. Stab.* **95,** 733–739 (2010).

36. Doyle, C. D. Kinetic analysis of thermogravimetric data. *J. Appl. Polym. Sci.* **5,** 285–292 (1961).

37. Mc Neill, J. C. & Rincon, A. Degradation studies of some polyesters and polycarbonates. 5. Poly(trimethylene carbonate). *Polym. Degrad. Stab.* **24,** 59–72 (1989).

4.2. Study on the hydrolytic degradation of the segmented GL-*b*-(GL-*co*-TMC-*co*-CL)-*b*-GL copolymer

The hydrolytic degradation of Monosyn®, a segmented copolymer derived from glycolide, trimethylene carbonate and ε-caprolactone, has been evaluated in buffered aqueous media at different pH and temperature. Degradation processes have been followed by considering mass loss and molecular weight profiles as well as the changes on ^{1}H-NMR and FTIR spectra, morphology and both calorimetric and mechanical properties during exposure to the selected media and temperature.

In all cases, the mass and molecular weight evolutions fitted with first order kinetic processes which were indicative of a random chain scission mechanism. Rate constants were found to strongly depend on temperature and pH. A slight deviation towards a backbiting mechanism was only found in the acid medium at long exposure times when degradation progresses through crystalline domains and recombination of ester groups were probable.

Amorphous and glycolide rich domains were more susceptible to the hydrolytic attack as revealed from mechanical assays and both spectroscopic and calorimetric data. Morphological changes occurring during degradation were highly dependent on pH and indeed different steps affecting the outer (longitudinal cracks) and inner (transversal cracks) parts of sutures could be distinguished. The high content on amorphous *soft segments* gave rise to well-defined circumferential cracks that affected the inner part of exposed sutures and were interpreted as a consequence of the hydrolytic attack to interlamellar regions.

4.2.1. INTRODUCTION

Nowadays the development of biodegradable polymers for their application in the biomedical field becomes one of the most interesting research topics. Polymers used as biomaterials must meet strict requirements depending on the intended use, and specifically bioabsorbable surgical sutures constitute an example of the difficulty to find an ideal material. In this case, polymers should be designed to accomplish a set of characteristics that involve physical and mechanical properties (e.g., tensile strength, Young modulus and capillarity), handling (e.g., pliability, knot tie-down and tissue drag), biocompatibility (e.g., absence of inflammatory reactions and wound infections) and biodegradability (e.g., biocompatibility of degradation products and adequate mass loss and tensile breaking strength profiles).

Since the commercialization of polyglycolide in 1970s as a bioabsorbable surgical suture different synthetic polymers and copolymers have been developed. These synthetic bioabsorbable materials have been specifically designed to loss their tensile strength within a reduced time period (i.e., 2-3 months). In general, copolymers of glycolide with different lactones and/or cyclic carbonates have been widely employed since they are able to cover the above indicated requirements.[1,2] These biodegradable polymers have been demonstrated to be ideal for orthopedic applications where a permanent implant is not desired.[3,4] Three-dimensional porous scaffolds for tissue engineering, controlled/sustained release drug delivery vehicles and osteoconductive materials are other well developed applications of these polymers in the biomedical field.[5,6] Morphological features have also been specifically considered and compared for random and segmented block copolymers[7] since morphology has a great influence on degradation and on drug release[8]. Structure and properties of bioabsorbable fibers have also been investigated during several industrial processing stages and *in vitro* degradation.[9]

Synthetic bioabsorbable sutures have been commercialized with different physical configurations: braided multifilament (e.g., polyglycolide and the copolymer made from 90% glycolide and 10% L-lactide known as Novosyn®) and monofilament forms. The latter has clear advantages like high resistance to harbor microorganisms and minimum tissue drag despite knot security and packaging memory may be disadvantageous.[10–12] The capillary capacity of suture materials should therefore be reduced and the use of capillary threads avoided as far as possible where there is a high infection risk.[13,14] Differences could also be found between multifilament sutures and for example knotting and handling

characteristics of the coated polyglycolic acid sutures were judged to be superior to the coated glycolide/lactide copolymer.[15]

Materials developed for bioabsorbable monofilament sutures correspond to homopolymers like poly(*p*-dioxanone) (PDS™ and Monoplus®), random copolymers like Caprosyn™ (a synthetic polyester composed of glycolide, ε-caprolactone, trimethylene carbonate and lactide) and segmented copolymers. In the first case, flexibility can be achieved by using a monomer that renders a lower ester group density and a lower frequency of hydrogen bonding interactions than the stiff polyglycolide. In the second case, flexibility is guaranteed by the random microstructure and the presence of flexible repeat units. However, the use of segmented copolymers seems ideal since composition and microstructure can be easily tuned to cover a wider range of properties. In general, these segmented copolymers are constituted by two polyglycolide *hard segments* and a middle *soft segment* derived from glycolide and other monomers (e.g., trimethylene carbonate, ε-caprolactone or *p*-dioxanone).[16–18] The specific characteristics of constitutive blocks can be combined and thus the *hard segments* could provide adequate tensile strength while the incorporation of middle *soft segments* improve flexibility and render good handling properties (e.g., pliability).

Maxon™ (Syneture) is one of the first monofilar synthetic sutures based on polyglycolide that has been commercialized.[19] Maxon™ is characterized by a slow degradation (about 7 months) and exhibits relatively high mechanical strength in comparison with other absorbable sutures. Chemical and physical aspects of the degradation of unoriented Maxon™ and its potential as a drug-release device have been evaluated.[20] In the same way, the rate at which monofilament absorbable sutures based on trimethylene carbonate lose their mechanical strength *in vivo* and specifically both *in vitro* and *in vivo* degradation behavior of Maxon™ have been reported.[21,22] Other interesting works concerning Maxon™ concern the effect of gamma irradiation and irradiation temperature on hydrolytic degradation,[23] the change on mechanical properties during hydrolytic degradation,[24] analysis of microstructure[25] and influence of degradation on crystallization kinetics.[26] Furthermore, it has been studied the influence on physical properties and degradability caused by small changes on microstructure (e.g., *hard*/*soft segment* ratio) and composition (i.e., glycolide and trimethylene carbonate content).[27] Monosyn® (B. Braun Surgical S.A.) is another monofilar suture that has been developed but in this case scarce studies concerning its degradation have been reported. The copolymer is synthesized following a classical two step procedure where firstly a *soft segment* is prepared by the ring-opening

polymerization of glycolide, trimethylene carbonate and ε-caprolactone and using a difunctional initiator. In a second phase soft segments with hydroxyl groups at each end are used to initiate the polymerization of glycolide and get the molecular structure depicted in Figure 4.2.1.

Figure 4.2.1. Chemical structure of GL-*b*-(GL-*co*-TMC-*co*-CL)-*b*-GL showing the *soft* and *hard segments*.

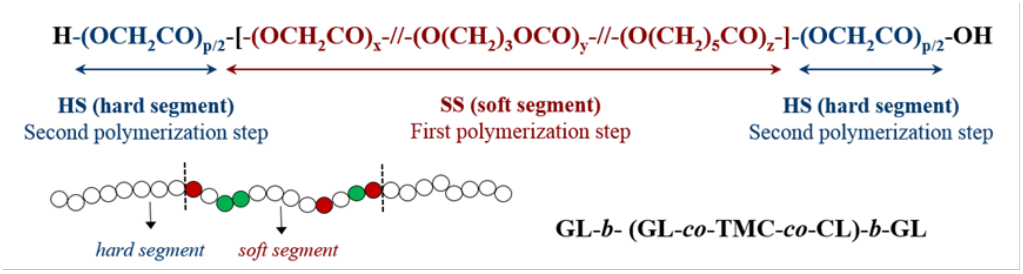

The middle *soft segment* of the commercial suture has 35 wt-%, 32.5 wt-% and 32.5 wt-% of glycolyl, trimethylene carbonyl and ε-caproyl unit, respectively, and constitutes a 43 wt-% of the total mass.[17] Respect to Maxon™ small changes concerning the glycolyl (72 respect to 67.5 wt-%) and *hard segment* (57 respect to 62 wt-%) contents are worth noting. It seems now interesting to investigate the hydrolytic degradation behaviour under different conditions (pH and temperature) of a material that has as a main distinctive feature the incorporation in the amorphous *soft segment* of a third component (i.e., ε–caprolactone) with hydrophobic and high flexible characteristics.

4.2.2. EXPERIMENTAL SECTION

4.2.2.1. Materials

Commercially available sutures of Monosyn® were kindly supplied by B. Braun Surgical S.A. The copolymer will be named as GL-*b*-(GL-*co*-TMC-*co*-CL)-*b*-GL in order to indicate its segmented nature and the components of each block (GL, TMC and CL for glycolide, trimethylene carbonate and ε-caprolactone, respectively). Weight and number average molecular weights of Monosyn® samples were in the 62,000-71,000 and 39,000 – 41,000 g/mol range, as determined by GPC for the different studied samples. Monofilaments of USP (United States Pharmacopoeia) sizes 1, 2/0 and 4/0 were employed in the degradation studies.

4.2.2.2. Hydrolytic degradation

In vitro hydrolytic degradation assays were carried out in a pH 7.4 phosphate buffer (Sörensen medium: 19.268 g of $Na_2HPO_4 \cdot 12 \cdot H_2O$ and 1.796 g of KH_2PO_4 in 1L of deionized water) at 37 ºC and 50 ºC, pH 10 carbonate/phosphate buffer (2.915 g of Na_2CO_3 and 1.890 g of KH_2PO_4 in 1L of distilled water) at 37 ºC and a pH 4 citrate/phosphate buffer (5.897 g of citric acid and 15.573 g of $Na_2HPO_4 \cdot 12 \cdot H_2O$ in 1 L of distilled water) at 37 ºC . Samples were kept under orbital shaking in bottles filled with 50 mL of the degradation medium and sodium azide (0.03 wt-%) to prevent microbial growth for selected exposure times. The samples were then thoroughly rinsed with distilled water, dried to constant weight under vacuum and stored over P_4O_{10} before analysis. Weight retention, molecular weight, changes in NMR and IR spectra as well as calorimetric and tensile properties were then evaluated. Degradation studies were performed in quintuplicated and the given data corresponded to the average values.

4.2.2.3. Measurements

Weight retention (W_r) of the specimens was determined by the percentage ratio of weight after degradation (W_d) to initial weight before degradation (W_0):

$$W_r = W_d / W_0 \times 100 \quad (1)$$

Hygroscopicity of samples was evaluated at 25 ºC by measuring the moisture sorption in samples exposed to 100% humidity.

Molecular weights were estimated by size exclusion chromatography (GPC) using a liquid chromatograph (Shimadzu, model LC-8A) equipped with an Empower computer program (Waters). A PL HFIP gel column (Polymer Lab) and a refractive index detector (Shimadzu RID-10A) were employed. The polymer was dissolved and eluted in 1,1,1,3,3,3-hexafluoroisopropanol containing CF_3COONa (0.05 M) at a flow rate of 1 mL/min (injected volume 100 µL, sample concentration 2.0 mg/mL). The number and weight average molecular weights were calculated using polymethyl methacrylate standards.

^{1}H-NMR spectra were acquired with a Bruker AMX-300 spectrometer operating at 300.1 MHz and 75.7 MHz, respectively. Chemical shifts were calibrated using tetramethylsilane

as an internal standard. Dried dimethyl sulfoxide-d_6 (DMSO) was used as the solvent at a temperature of 90-95 ºC to enhance solubility and resolution.

Calorimetric data were obtained by differential scanning calorimetry with a TA Instruments Q100 series with T_{zero} technology and equipped with a refrigerated cooling system (RCS). Experiments were conducted under a flow of dry nitrogen with a sample weight of approximately 5 mg and calibration was performed with indium. T_{zero} calibration required two experiments: the first was performed without samples while sapphire disks were used in the second.

Tensile properties of original and degraded samples were studied at room temperature by means of a universal tensile testing instrument Zwick Z 2.5 with a 100 N load cell equipped with a testXpert 8.1 program. Initial distance between jaws was 10 mm and the crosshead speed was 200 mm/min. The reported Young's modulus and ultimate tensile strength represented average values of at least five specimens.

Scanning electron microscopy (SEM) was employed to examine the morphology of sutures after different times of exposure to the selected degradation media. Carbon coating was accomplished with a Mitec k950 Sputter Coater (fitted with a film thickness monitor k150x). SEM micrographs were obtained with a Zeiss Neon 40 EsB instrument.

4.2.3. RESULTS AND DISCUSSION

4.2.3.1. Evaluation of hydrolytic degradation through weight retention measurements

Figure 4.2.2 shows the percentage of retained weight for different sized GL-*b*-(GL-*co*-TMC-*co*-CL)-*b*-GL sutures as a function of the exposure time in the distinct pH degradation media and/or at distinct temperatures. Experimental profiles point out a process that takes place according to at least two different steps. Firstly, there is a period defined by an induction time, t_d, where the sample weight remained practically constant and that corresponds to the time necessary for the diffusion of the aqueous media inside the fibers and the achievement of a sufficient hydrolysis of ester groups to render soluble fragments. The second step is characterized by a great weight loss ratio that gradually decreases by increasing the exposure time.

Degradation profiles clearly pointed out the enhanced degradation caused by the increment of temperature (i.e., Sörensen buffer at 50 ºC) and in a lesser extent, by the increment of pH (i.e., pH 10.0 basic medium at 37 ºC). An increase on temperature should obviously enhance the solubility of degradation products and facilitate also the diffusion of these products and water molecules through the polymer matrix if temperature becomes greater than the glass transition temperature of the material.

The profile obtained in the pH 4 medium suggests a slightly hindered degradation respect to the neutral condition. In fact, the cleavage of ester groups in an acidic medium is reported to be reversible and contrast with the irreversible alkaline hydrolysis. Despite recombination of polymer chain ends appears highly improbable in amorphous regions, it should be considered that recombination may be significant when polymer segments have restricted mobility as it is the case of breakages occurring in the crystalline lattice (i.e., the named cage effect).[28] Influence of pH on the degradation profiles has also been related to the destruction of hydrogen bonding interactions in a basic media.[29–31] Therefore, rigid and compact amorphous structures are expected in both neutral and acidic conditions, whereas more open and accessible amorphous phases should be attained in an alkaline media giving rise to a faster degradation.

Figure 4.2.2. Plots of weight retention versus exposure time to the different assayed hydrolytic degradation media for GL-*b*-(GL-*co*-TMC-*co*-CL)-*b*-GL sutures with the indicated USP sizes. Simulated curves (○) using first order equations are also plotted for the different degradation media.

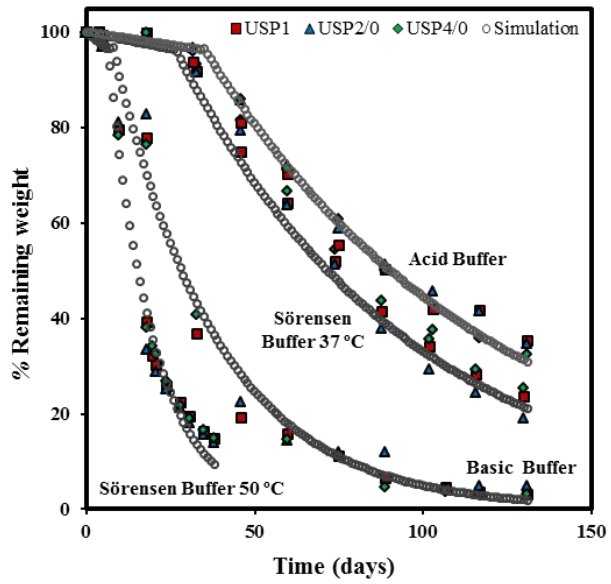

Degradation profiles obtained for the different USP sizes were highly similar (Figure 4.2.2) as expected when the bulk degradation process becomes independent of the polymer surface and specifically when the diffusion rate of water molecules into the polymer is greater than the hydrolysis reaction rate. In fact, hygroscopicity measurements indicated that water was quickly absorbed from an ambient medium at 100% humidity. The saturation level was reached after only 24 h of exposure and corresponded to a low value in the 1.2-0.9% range that indicated a moderate hydrophilicity.

The kinetics of the degradation process that occurred after the induction period was evaluated considering the general equation:

$$-\mathrm{d}m/\mathrm{d}t = K\,m^n \qquad (2)$$

where m is the mass at time t, K is the kinetic constant and n is the reaction order.

The plot of log $(-\mathrm{d}m/\mathrm{d}t)$ versus log m allowed calculating log K as the ordinate at the origin and n as the slope of the derived linear plot. Table 4.2.1 summarizes the K and n values together with the induction time determined for the different suture sizes and degradation media. Results clearly indicated that degradation followed always a first order kinetics, which means that degradation rate depended linearly on the amount of residual polymer. Kinetic constants ranged between 0.0116-0.0125 $days^{-1}$ (pH 4.0 buffer at 37 ºC) and 0.0733-0.0757 $days^{-1}$ (Sörensen medium at 50 ºC), and clearly expressed the great differences on the hydrolysis capability of the studied degradation media.

Theoretical values for weight retention can be calculated using the equation (3) derived from a first order reaction and the kinetic constant averaged over the experimental values obtained for the different USP sizes:

$$m = m_0 / \exp\left(K(t - t_d)\right) \qquad (3)$$

where m_0 is the mass at the induction time t_d.

Figure 4.2.2 demonstrated the good agreement between the simulated profiles and the experimental weight retention data.

Table 4.2.1. Kinetic parameters and correlation coefficients for the evolution of the retention weight of GL-*b*-(GL-*co*-TMC-*co*-CL)-*b*-GL sutures in the different studied degradation media.

	Sörensen 37 °C				Sörensen 50 °C				pH 4.0 buffer 37 °C				pH 10 buffer 37 °C			
Size	*n*	*K* ($days^{-1}$)	r^2	t_d (days)	*n*	*K* ($days^{-1}$)	r^2	t_d (days)	*n*	*K* ($days^{-1}$)	r^2	t_d (days)	*n*	*K* ($days^{-1}$)	r^2	t_d (days)
1	1.04	0.0144	0.9243	24	1.07	0.0741	0.9121	6	1.06	0.0116	0.9284	32	1.07	0.0324	0.8998	7
2/0	1.02	0.0160	0.8791	24	1.00	0.0733	0.9244	6	1.08	0.0118	0.9032	32	0.98	0.0318	0.8499	7
4/0	1.02	0.0134	0.8665	24	1.06	0.0757	0.9073	6	0.98	0.0125	0.9195	32	1.06	0.0334	0.9200	7

4.2.3.2. Evaluation of hydrolytic degradation through molecular weight measurements

The time evolution of GL-*b*-(GL-*co*-TMC-*co*-CL)-*b*-GL (USP size 1) molecular weight and its distribution during exposure to the different degradation media are shown in Figure 4.2.3.

Molecular weight profiles showed a rapid decrease during the first days of exposure until reaching an asymptotic value, which can be interpreted as a size solubility limit; that is, further degradation led to soluble fragments. The residual material should correspond to molecular fragments enriched on the more hydrophobic units (i.e., trimethylene carbonyl and caproyl residues) and/or molecules arranged in highly ordered crystalline domains.[32] Profile corresponding to degradation in the pH 4 medium is significantly different since a final step with a lower molecular weight decrease ratio can be detected (i.e., from 10 to 35 days of exposure). In this case, the typical two-stage bulk degradation process is evidenced with a fast degradation that began in the amorphous domains and a slow process that affects the crystalline domains that are highly susceptible as above indicated to recombination reactions. This degradation is probably initiated by hydrolysis of tie chains in the amorphous/crystal interface and progressed by a sequential propagation along the molecular chain into the interior of crystallites according to a one-dimensional stepwise hydrolytic fragmentation that lead to a different kinetic mechanism.

Polydispersity index profiles showed always a maximum value that reflects the accumulation of low molecular degradation products before their solubilization. In general, the high polydispersity indices attained suggest that small degradation compounds tend to remain in the polymer matrix probably because of lamellar confinement.

Figure 4.2.3. Plots of the variation in the weight average molecular weight **(a)** and polydispersity index **(b)** of a GL-*b*- (GL-*co*-TMC-*co*-CL)-*b*-GL suture (USP 1) during exposure to the different assayed degradation media.

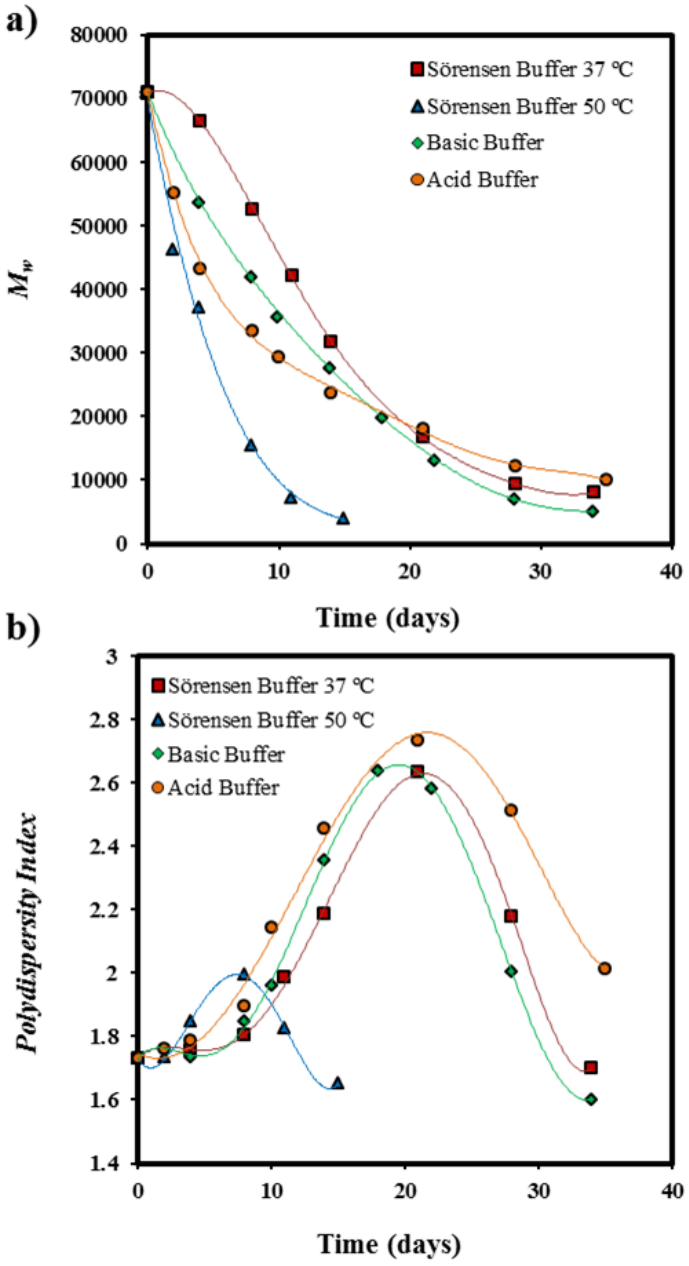

The degradation process during the earlier stages (i.e., with the greater molecular weight change) can be well explained considering on exponential relationship between molecular weight and degradation time as established for the hydrolytic bulk degradation of several polyesters constituted by glycolide units.[33,34] This relationship is consequence of a first order kinetic process that is in agreement with a random chain scission:

$$\ln M = \ln M_o - K t \quad (4)$$

$$t_{1/2} = \ln 2 / K \quad (5)$$

where M is the molecular weight, M_0 is the initial molecular weight, K is the apparent degradation rate and $t_{1/2}$ is the half degradation time. The weight-averaged molecular weight (M_w) was considered in the calculations since it decreased more slowly than the number-averaged value (M_n). Obviously the derived K and $t_{1/2}$ values should be lower and greater, respectively, respect to the parameters determined from the M_n values.

Table 4.2.2 summarizes the calculated K and $t_{1/2}$ parameters for different suture sizes and basic and neutral degradation media. The first one was determined from the slope of the fitting curve ($r^2 > 0.96$) between ln M_w and the exposure time. The degradation rate varied from a minimum value of 0.053 days^{-1} (Sörensen medium at 37 ºC) to a maximum value of 0.154 days^{-1} (Sörensen medium at 50 ºC) for the size USP 1, while the corresponding half degradation times ranged from 13 to 4.5 days.

It is interesting to note that the pH 4 degradation medium caused a rapid molecular weight decrease in the above indicated first step and therefore hydrolysis proceeded faster than expected from the remaining weight measurements. A worse fitting (i.e., a linear plot could only be determined at the beginning of degradation) was found in the acid medium considering a first order kinetics. In this case K and $t_{1/2}$ values for the size USP 1 where 0.094 days^{-1} and 7.4 days, respectively. It is worth noting that kinetic constants became clearly higher than calculated for the basic medium. It seems that degradation products were less soluble in the acid medium and that erroneous conclusions can be derived from a single kind of experiment (i.e., remaining weight measurements).

Table 4.2.2. Kinetic parameters for the evolution of the weight-averaged molecular weight of GL-*b*-(GL-*co*-TMC-*co*-CL)-*b*-GL sutures in the different studied degradation media.

Size	Sörensen 37 ºC		Sörensen 50 ºC		pH 10 buffer 37 ºC	
	K (days^{-1})	$t_{1/2}$ (days)	K (days^{-1})	$t_{1/2}$ (days)	K (days^{-1})	$t_{1/2}$ (days)
1	0.053	13	0.154	4.5	0.068	10.25
2/0	0.054	12.8	0.147	4.7	0.074	9.4
4/0	0.038	18.4	0.126	5.5	0.051	13.6

Figure 4.2.4 compares the simulated molecular weight profiles and the experimental data. It should be pointed out that only a disagreement was observed for the pH 4.0 medium at long exposure times. This observation may suggest a change of the hydrolysis mechanism from a quick random scission process to a slower chain-end-scission (backbiting) mechanism, which should be expected when degradation affects the crystalline domains and the medium favors the recombination of cleaved ester groups.

A slight influence on the diameter size on degradation was detected since only statically different values were observed for sutures with the lowest diameter (i.e., USP 4/0 that corresponds to a cross section area of 0.018-0.031 mm^2). In this case, degradation apparently proceeded slowly (i.e., lower and higher values for K and $t_{1/2}$, respectively), which is in disagreement with the analysis performed from the weight retention and also with the higher facility of water to completely penetrate inside sutures when their diameter decrease. Results point out that small fragments produced during degradation were more easily released from sutures with the lowest diameter and consequently a smaller decrease on the molecular weight of the remaining material was observed. This release effect was not so significant when the cross section area of the suture increased (e.g., 0.071-0.096 mm^2 (USP 2/0) and 0.126-0.195 mm^2 (USP 1)) since higher K values were determined.

Figure 4.2.4. (a) Simulated curves (empty symbols) using a first order equation for the variation of the weight average molecular weight of GL-*b*-(GL-*co*-TMC-*co*-CL)-*b*-GL sutures during exposure to the indicated media. Simulated curves for sutures with different USP sizes (red, blue and green for USP 1, USP 2/0 and USP 4/0, respectively) are also compared with experimental data (full symbols) for degradation in the basic medium**. (b)** Comparison between the experimental data for degradation in the acid medium of a suture with USP 1 size and the corresponding simulated profile for a first order kinetic process.

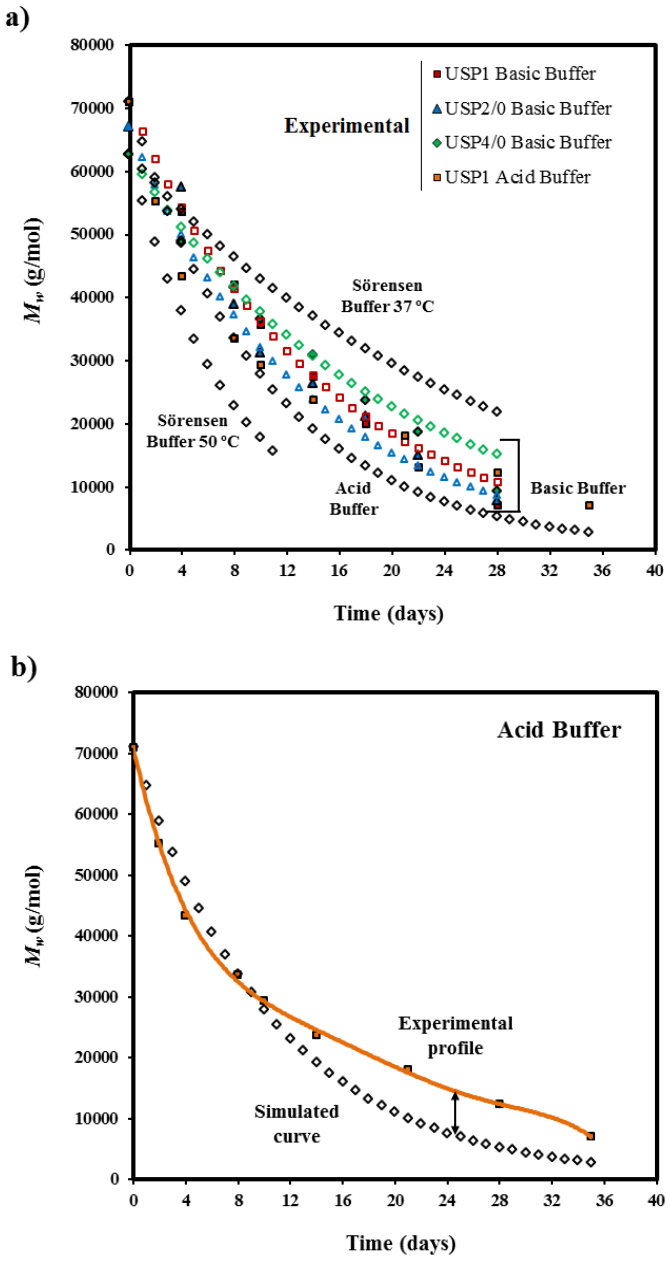

4.2.3.3. Changes on composition and microstructure during hydrolytic degradation

The ^{1}H-NMR spectra of the GL-*b*-(GL-*co*-TMC-*co*-CL)-*b*-GL sample show distinctive signals that can be used to determine molar composition and main microstructure features. A basic assignment is given in Figure 4.2.5. It should be pointed out the highly complex signal attributed to the glycoyl (G) protons that appeared from 4.83 to 4.59 ppm and indicated sequence sensitivity as well reported for similar bicomponent systems (i.e., poly(glycolide-*co*-trimethylene carbonate)[35] and poly(glycolide-*co*-ε-caprolactone)[36]). The strong signals between 4.83 and 4.78 ppm correspond to the middle glycolyl protons of G*G*G sequences and therefore their area can be used for a roughness estimation of glycoyl units belonging to the *hard segment* (% G_{HS}, equation 6). The spectrum clearly shows the presence of sequences indicative of transesterification reaction, which mainly occurred during the first polymerization step where a higher ratio of comonomers exists. Specifically, the four signals between 4.66 and 4.59 ppm could be assigned to TGT, TGCap, CapGT and CapGCap triads listed from down to highfield (T and Cap indicating trimethylene carbonyl and caproyl units, respectively). Note that these triads cannot be produced by direct ring opening copolymerization since the glycolide ring should lead to sequences having at least two consecutive glycolyl units. The intensity of signals allows estimating a percentage of transesterified sequences (% G_{trans}, equation 7).

^{1}H-NMR spectra shows also a complex signal between 4.20 and 4.06 ppm that corresponds to the overlapping of the α and β methylene protons of trimethylene carbonyl units and the ε methylene protons of caproyl units. In the same way the α-methylene protons of caproyl units showed sequence sensitivity and gave rise to the complex signal between 2.37 and 2.20 ppm. Therefore, the content of glycolyl (% G), trimethylene carbonyl (% TMC) and caproyl units (% Cap) was estimated though the signals at 4.83-4.59 ppm, 1.97 ppm (β-methylene protons of TMC) and 1.61 ppm (β and δ methylene protons of caproyl units) through equations 8, 9 and 10. The ^{1}H-NMR spectrum supports an amorphous character for the *soft segment* due to the multiple sequences produced by a practically random copolymerization of the three involved monomers and the existence of subsequent transesterification reactions.

$$\% G_{HS} = (A_{4.83\text{-}4.78} / A_{4.83\text{-}4.59}) \times 100 \quad (6)$$

$$\% G_{trans} = (A_{4.64\text{-}4.59} / (A_{4.83\text{-}4.59}) \times 100 \quad (7)$$

$$\% G = (A_{4.83\text{-}4.59} / (A_{4.83\text{-}4.59} + A_{1.97} + (A_{1.61}/2))) \times 100 \quad (8)$$

$$\% TMC = (A_{1.97} / (A_{4.83\text{-}4.59} + A_{1.97} + (A_{1.61}/2))) \times 100 \quad (9)$$

$$\% Cap = ((A_{1.61}/2) / (A_{4.83\text{-}4.59} + A_{1.97} + (A_{1.61}/2))) \times 100 \quad (10)$$

Figure 4.2.5. ^{1}H-NMR spectra of the initial GL-*b*-(GL-*co*-TMC-*co*-CL)-*b*-GL sample with labelling of the most distinctive sequences. Inset shows the specific transesterification sequences.

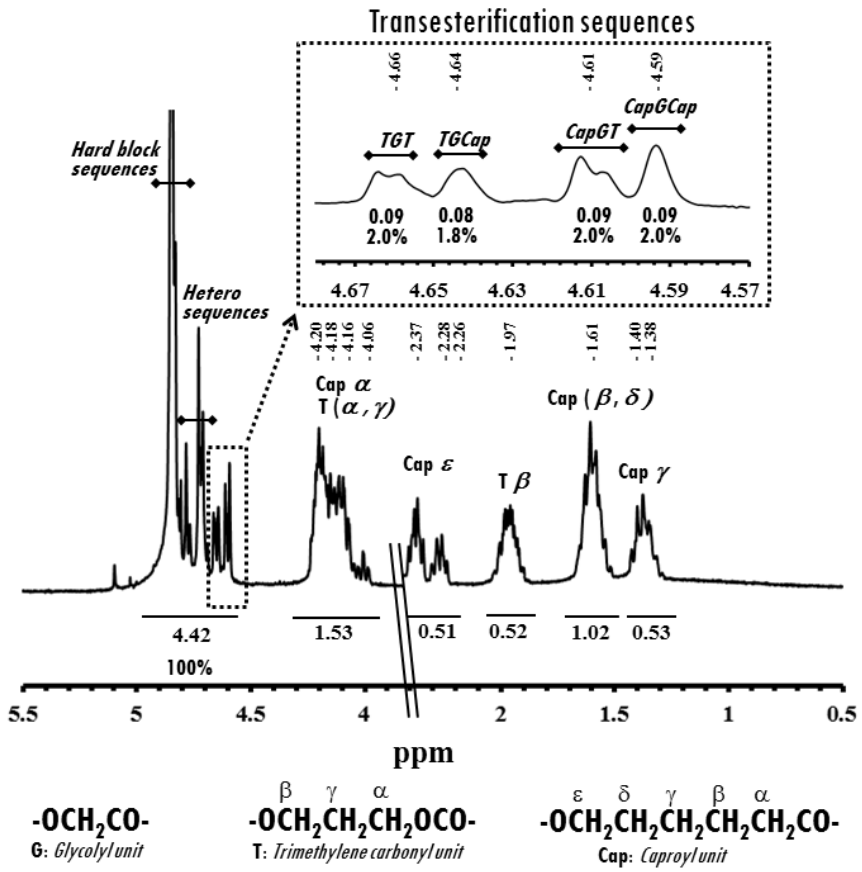

The ^{1}H-NMR spectra at advanced stages of degradation in selected media are shown in Figures 4.2.6a–4.2.6d. It can be envisaged that the spectra become significantly more complicated during degradation mainly because of the appearance of glycolyl terminal groups, and monomers, like glycolide and glycolic acid[25]. Spectra show a degradation

process with formation of -C*H*$_2$OH terminal groups at 4.10 ppm. Similarly, signals of glycolyl units vicinal to terminal carboxylic groups can be clearly distinguished (i.e., -C*H*$_2$CO-OCH$_2$COOH at 4.50-4.40 ppm and -OC*H*$_2$COOH at 4.76 ppm). Furthermore, glycolide rings can also be detected from the signal at 5.01 ppm that appears in the final stages of degradation, when the ratio of their precursor terminal groups is high.

Figure 4.2.6. ^{1}H-NMR spectra (region) of the GL-*b*-(GL-*co*-TMC-*co*-CL)-*b*-GL sample exposed to Sörensen buffer at 37 ºC for 88 days **(a)**, Sörensen buffer at 50 ºC for 35 days **(b)**, pH 4.0 buffer at 37 ºC for 88 days **(c)** and pH 10 basic buffer at 37 ºC for 60 days **(d).** Blue and black arrows indicate monomer and distinctive terminal group signals. For most degraded samples an inset (red box) is provided to shown terminal group signals at lower exposition times (i.e., 11, 28 days for Sörensen buffer at 50 ºC and the basic buffer at 37 ºC, respectively).

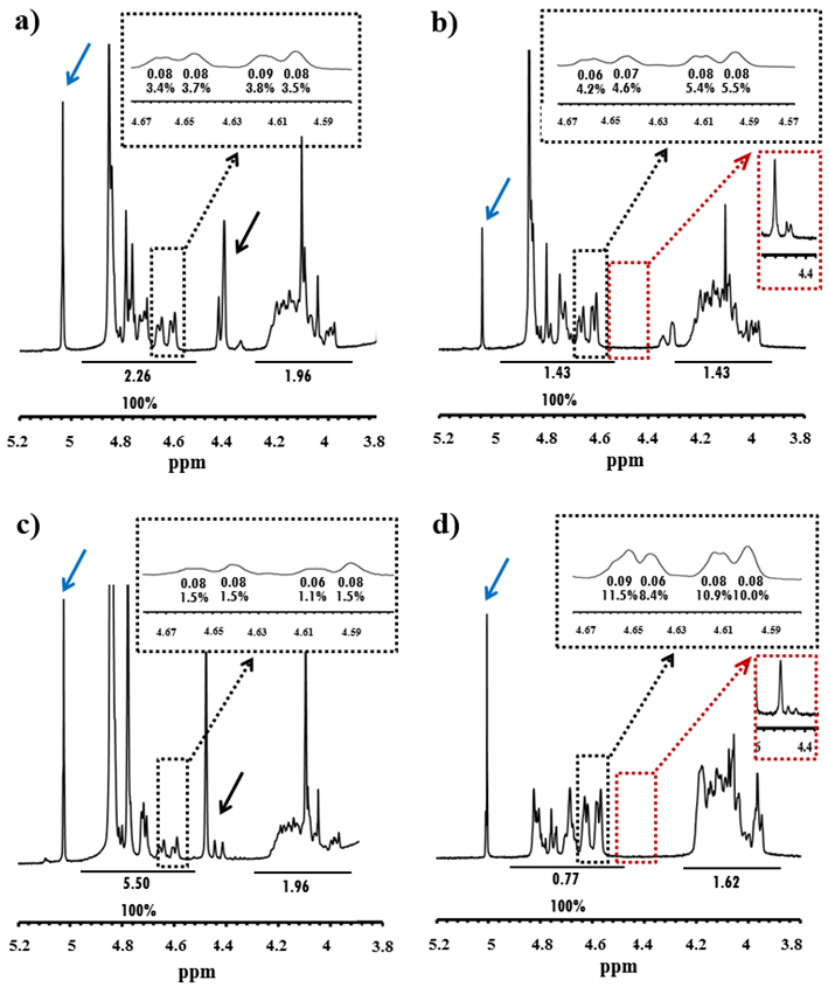

Figure 4.2.7 shows the change on composition, differentiating the glycolyl units belonging to the *hard* and *soft segments*, during exposure to the different degradation media. The results clearly point out that the ratio of *hard segments* always decreased as can be justified by the lower solubility of fragments coming from the more hydrophobic *soft segments*. Degradation should preferably take place in the amorphous domains but the generated fragments still remained in the sample due to their high insolubility. On the contrary, the fragments originated by the hydrolysis of *hard segments* were only constituted by the more hydrophilic glycolyl units and consequently were solubilized first.

Composition of the *soft segment* can be easily calculated by normalizing the above data as shown in Figure 4.2.7b. Results are interesting since demonstrated a correlation between the change of composition and the hydrophilicity of the involved units (i.e., a decrease, a slight increase and a significant increase were determined for glycolyl, trimethylene carbonyl and caproyl content, respectively).

Spectroscopic data obtained for the different degradation media shows that % G_{HS} is a good parameter to compare the hydrolysis rate. Thus, a decrease from 62% to 53% required 34, 18 and 116 days of exposure to the pH 10 basic buffer at 37 ºC, and the Sörensen buffer at 50 ºC and 37 ºC, respectively.

^{1}H-NMR spectra also indicated that transesterification sequences were scarcely susceptible to hydrolysis since their ratio increased during degradation (from an initial value of 7.2% to a 9-10% that was attained independently of the media when the weight loss was close to 50%).

Figure 4.2.7. (a) Variation of the molar content of ε-caproyl, trimethylene carbonyl and glycolyl units during exposure of GL-*b*- (GL-*co*-TMC-*co*-CL)-*b*-GL to a pH 10 basic buffer at 37 ºC (◊) and a Sörensen buffer at 50 ºC (Δ) and 37 ºC (□). Glycolyl units belonging to the *soft* and the *hard segment* have been differentiated. **(b)** Change in molar composition of the *soft segment* during exposure to a Sörensen buffer at 50 ºC (Δ) and 37 ºC (□) and a pH 10 basic buffer at 37 ºC (◊).

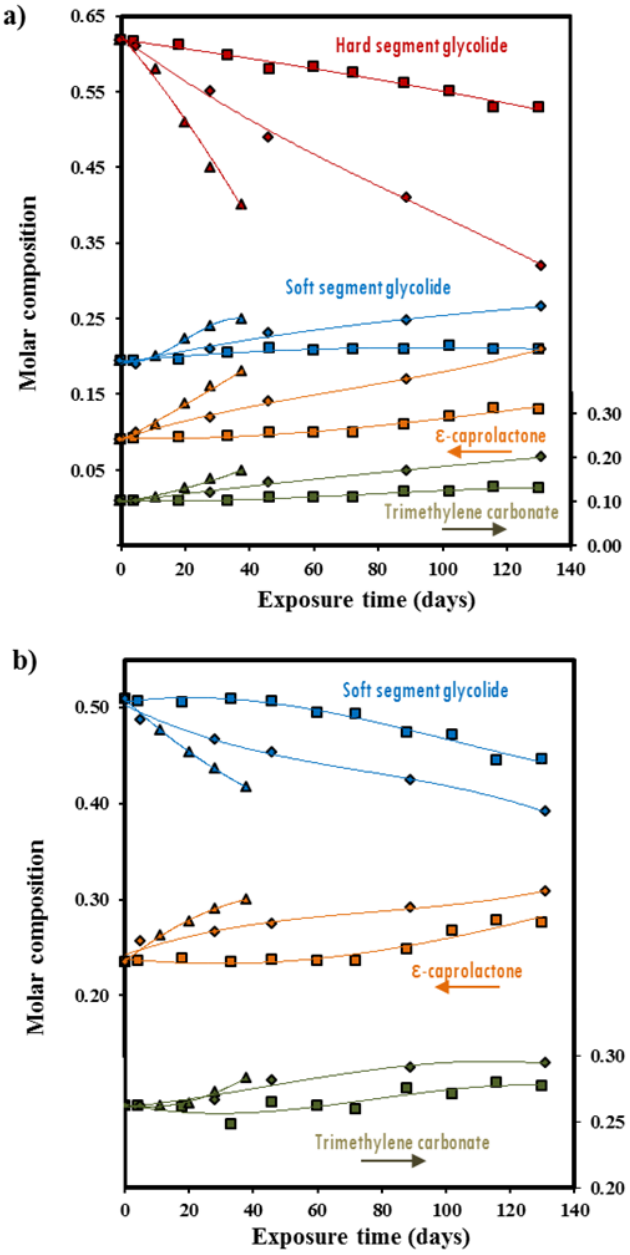

4.2.3.4. FTIR analysis of the hydrolytic degradation process

FTIR spectra are highly sensitive to the amorphous and crystalline character of samples and consequently can be used to verify the development of the crystalline phase during the degradation process. Figure 4.2.8 compares the transmission infrared spectra of GL-*b*-(GL-*co*-TMC-*co*-CL)-*b*-GL samples before and after exposure to the different media and conditions for a time that corresponds to a weight loss of approximately 40%.

Spectra are complicated since characteristic bands of glycolide, trimethylene carbonate and ε-caprolactone units are present. However, the 1800-750 cm^{-1} wavenumber region is informative since several bands associated to amorphous and crystalline polyglycolide appear well differentiated. Thus, crystalline domains were abundant in all samples since typical bands reported for the crystalline homopolymer,[27,37,38] such as those at 1414, 972, 902, 806 and 629 cm^{-1} could be well observed. On the contrary, bands associated to the polyglycolide amorphous phase (i.e., 1425, 1399 and 1250 cm^{-1}) could only be hardly distinguished in the initial samples as small shoulders. Normalized spectra considering the area of the band of the carbonyl group at 1740 cm^{-1} clearly show the increase and decrease of crystalline and amorphous bands during degradation.

As shown in Figure 4.2.8 bands at 1250, 972 and 902 cm^{-1} become the most representative to visualize this evolution. Respect to trimethylene carbonate units it should be indicated that relative intensity of typical bands at 1030 and 788 cm^{-1} clearly increased during degradation. It is significant the change on the relative areas of bands at 806 cm^{-1} (crystalline polyglycolide) and 788 cm^{-1} (trimethylene carbonate) which clearly demonstrated the enrichment on trimethylene carbonate units as degradation progressed.

Figure 4.2.8. FTIR spectra (region) of the GL-*b*-(GL-*co*-TMC-*co*-CL)-*b*-GL sample before (*) and after exposure to a Sörensen buffer at 37 ºC for 88 days (◊) and at 50 ºC for 35 days (□), a pH 4 acid buffer at 37 ºC for 88 days (Δ) and a pH 10 basic buffer at 37 ºC for 60 days (○). Dashed spectrum corresponds to a molten sample. Dashed circles point out bands at 806 and 788 cm^{-1} representative of crystalline polyglycolide and trimethylene carbonate units.

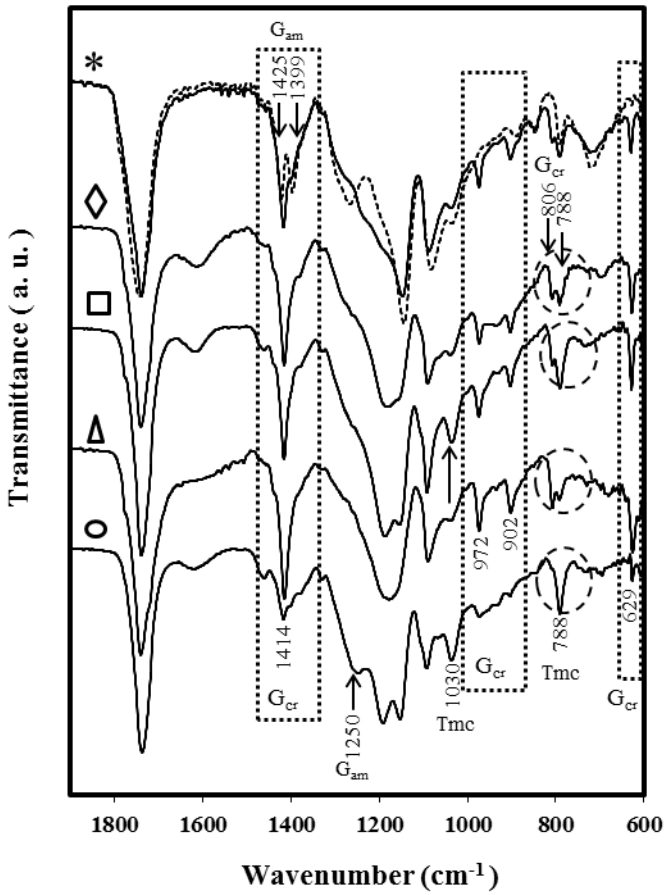

4.2.3.5. Influence of hydrolytic degradation on thermal properties

Figure 4.2.9a shows the different DSC traces obtained from heating/cooling runs performed with the initial GL-*b*-(GL-*co*-TMC-*co*-CL)-*b*-GL sample. These traces show always a predominant melting peak near 200 ºC that corresponds to the fusion of polyglycolide *hard segments*. In addition, the as-processed sample had a very small endothermic peak (ca., 4.1 J/g) near 100 ºC that could be associated to highly defective crystalline domains formed from small glycolide blocks of the *soft segment*.[27] Annealing conditions at which the fiber was submitted during processing make feasible this defective arrangement that was observed for all samples independently of their USP size.

Samples easily crystallized from both melt and glass state as revealed by the corresponding and well defined hot and cold crystallization peaks. Furthermore, the melting enthalpy, ΔH_m, was relatively high and allowed estimating a moderate relative degree of crystallinity, χ, when the heat of fusion for a 100% crystalline material (ΔH^0 = 191.1 J/g[39]) was considered.

It is also interesting to note that a single glass transition temperature was always observed as a consequence of the miscibility between *hard* and *soft segments*. This temperature was relatively high and close to 14 ºC due to the high glycolide content in the sample. In fact, reported T_g*s* for PCL, PGL and PTMC homopolymers were -60 ºC,[39] 35 - 40 ºC [40] and -18 ºC,[41] respectively.

Thermal properties clearly varied during hydrolytic degradation as shown in the DSC runs displayed in Figure 4.2.9b for a representative exposed sample and the evolution of the relative degree of crystallinity, crystallization temperature and glass transition temperature that are plotted in Figures 4.2.10a and 4.2.10b.

Figure 4.2.9. DSC traces obtained with a GL-*b*-(GL-*co*-TMC-*co*-CL)-*b*-GL suture (USP 1) before **(a)** and after exposure to a Sörensen buffer at 37 ºC for 88 days **(b)**. Traces correspond to the first heating run (i), the cooling run after keeping the sample in the melt state for 5 min (ii) and the heating run of a quenched sample from melt state (iii).

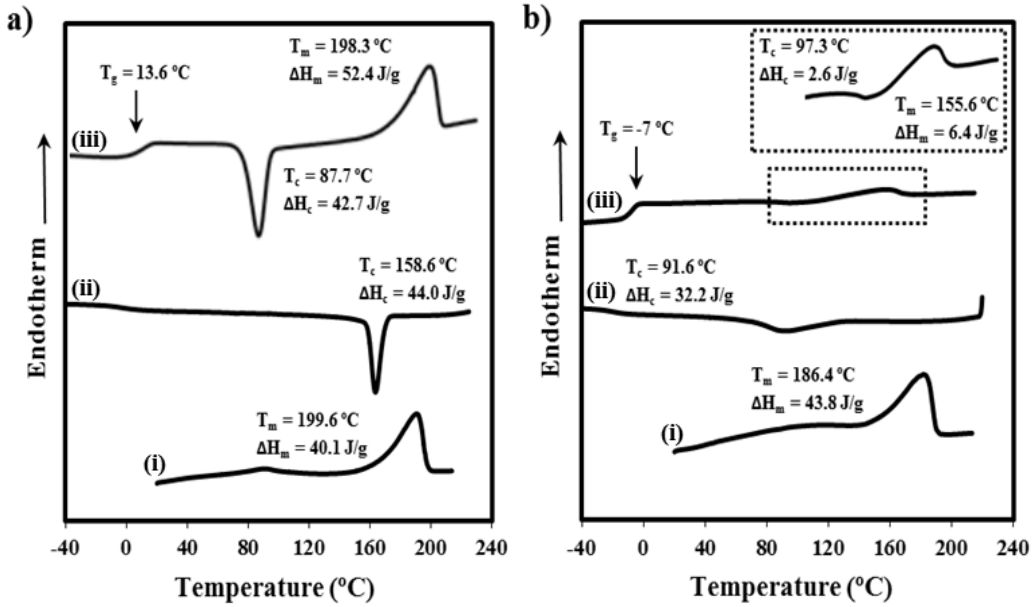

Main changes concern the minor melting peak around 100 ºC that disappeared after short exposure times (e.g., only 5 days were necessary for the less aggressive conditions: Sörensen buffer at 37 ºC). In fact, ^{1}H-NMR analysis demonstrated that the ratio of homoglycolide sequences starts to decrease since the beginning of exposure to the degradation media and consequently the hydrolytic attack seems to quickly affect the most defective crystals that give rise to the considered melting peak.

It is also highly relevant that melting temperature progressively decreased up to approximately 180 ºC as an evidence of an attack that affected also the crystalline domains even at the initial stages of degradation.

Figure 4.2.10. (a) Variation of the relative degree of crystallinity during exposure to the indicated degradation media and temperature for a GL-*b*-(GL-*co*-TMC-*co*-CL)-*b*-GL suture (USP 1). **(b)** Variation of the glass transition and crystallization temperatures during exposure to the indicated conditions for a GL-*b*-(GL-*co*-TMC-*co*-CL)-*b*-GL suture (USP 1).

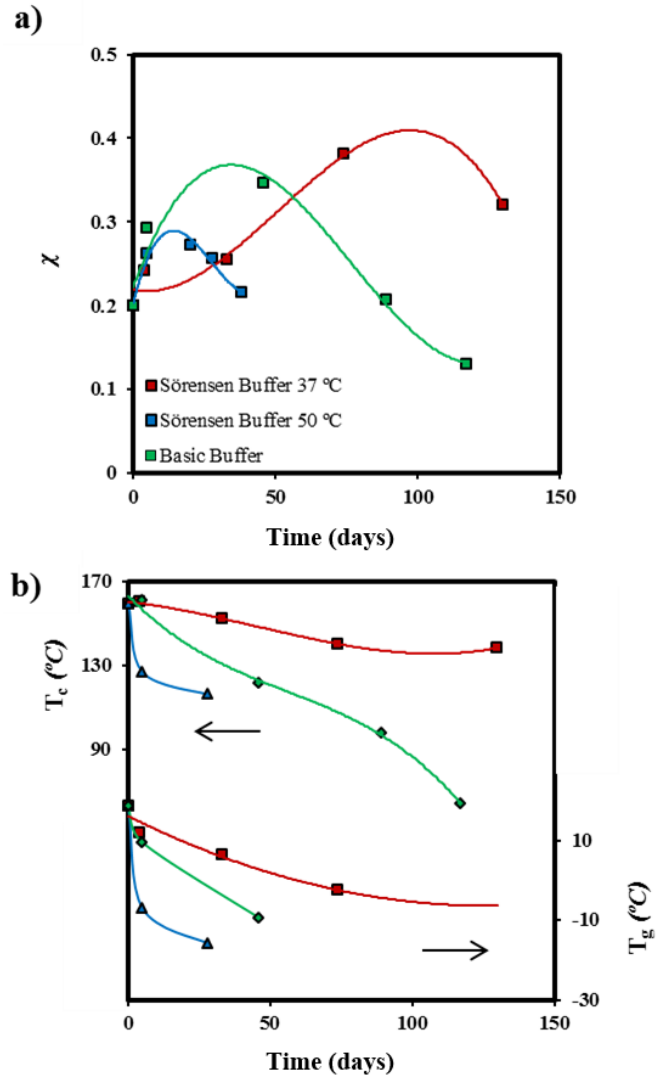

The melting enthalpy and consequently the relative degree of crystallinity showed an initial increase and a subsequent decrease. This feature is in agreement with a preferential attack of non-crystalline regions, which should be mainly constituted by the statistical *soft segments*. However, the higher values of crystallinity attained together with the NMR results that point also out a remarkable decrease on the *hard segment* content gives support to a previously postulated hypothesis based on the occurrence of secondary

crystallization.[42] In fact, the main-chain scissions produced during the earlier stages of hydrolysis diminished the entanglements between chains located in the amorphous region, increased the chain mobility and allowed a reorganization in a crystal phase.

The location of the melting enthalpy peak is also an indicator to compare the hydrolysis degradation rate caused by the different media (i.e., 36, 11 and 110 days of exposure to the pH 10 basic buffer at 37 ºC, and the Sörensen buffer at 50 ºC and 37 ºC, respectively). It is also interesting to remark the different degrees of crystallinity corresponding to the maxima, which increased as the aggressiveness of the media decreased. It seems that molecular reorganization has not enough time to be completed when degradation becomes faster since crystalline domains become also to degrade earlier.

Calorimetric data revealed also that hot and cold crystallizations were hindered as degradation progressed due to the formation of chain fragments with irregular sizes. Crystallization enthalpies clearly decreased but also the hot crystallization peak temperature showed a remarkable decrease (e.g., from 159 ºC to 64 ºC for the basic buffer) and became consequently a good parameter to follow degradation.

Finally, experimental observations indicated that the glass transition temperature progressively decreased (e.g., from 14 ºC to -16 ºC after 28 days of exposure to Sörensen buffer at 50 ºC) as a consequence of the molecular weight reduction, although the decrease of the glycolide content may also play a minor influence.

4.2.3.6. Morphological changes during hydrolytic degradation

Figure 4.2.11 shows the morphological changes occurring during the exposure of a GL-*b*-(GL-*co*-TMC-*co*-CL)-*b*-GL suture (USP size 1) in a Sörensen buffer at 50 ºC. Three steps can be clearly distinguished: a) Development of straight and parallel longitudinal cracks during the first 5 days of exposure (Figure 4.2.11a). The diameter of sutures had a decrease in this step as plotted in Figure 4.2.12. b) Removal of the outermost skin layer after approximately 10 days. The longitudinal cracks lead to a gradual formation of peeling layers (Figure 4.2.11b) that become progressively detached and lead to an additional reduction of the suture diameter (i.e., from 539 to 490 nm). The relatively high diameter of monofilament sutures allows differentiating an outer part from the core due to the temperature gradient that exist during the cooling process of the melt spun fiber. Note that the skin is exposed to ambient conditions and consequently crystallized faster and

experienced less shear stress during cooling from the molten stage than the core. In fact skin and core should differ of the degree of orientation achieved after solidification. c) Development of circumferential cracks (Figure 4.2.11c) with continuous reduction of the suture diameter (Figure 4.2.12). These cracks were regularly distributed (separation close to 60 μm) and lead with increasing exposure times to an accordion-shaped morphology and the formation of disks with a small thickness that ranged between 10 μm and 20 μm.

Morphology observations during exposure to a Sörensen medium at 37 ºC showed the same features with a logical delay on time caused by the lower degradation rate (i.e., 38 and 70 days to complete steps 1 and 2, respectively). Figure 4.2.11d shows specifically the suture at final stages of degradation. Note that the lateral surfaces of disks appear slightly rough as a consequence of a degradation that conducts to a continuous decrease of the diameter. It should be pointed out the smoother surface of basal faces of newly formed disk.

Figure 4.2.11. SEM micrographs showing the morphologic changes of a GL-*b*-(GL-*co*-TMC-*co*-CL)-*b*-GL suture (USP 1) during exposure for the indicated times to a Sörensen medium at 50 ºC **(a,b,c)** and 37 ºC **(d).**

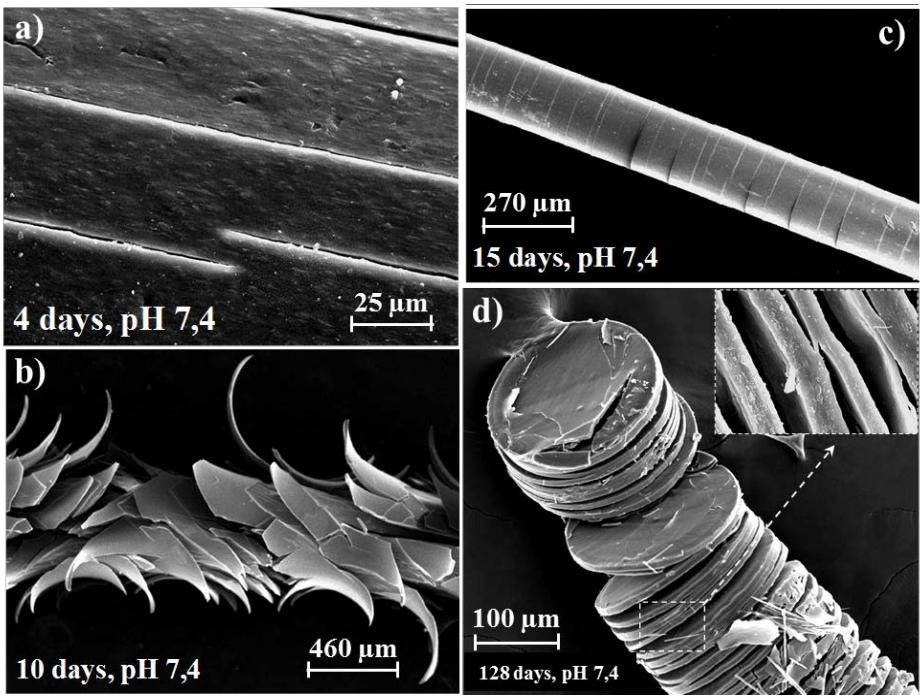

Figure 4.2.12. Variation of diameter of GL-*b*-(GL-*co*-TMC-*co*-CL)-*b*-GL sutures (USP 1) during exposure to a Sörensen buffer (1) and a pH 10 buffer (2) at 37 ºC, and to a Sörensen buffer at 50 ºC (3).

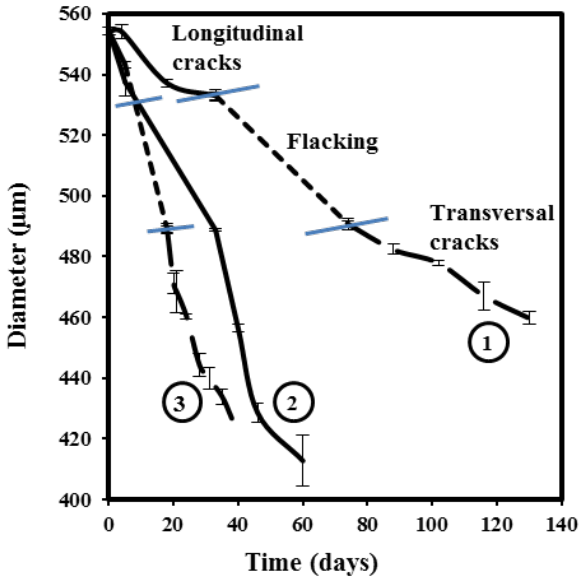

The indicated morphological changes should depend on the arrangement between crystalline and amorphous domains in the fiber. In this way, the *Swiss cheese* fibrous model postulated by Prevorsek[43] (Figure 4.2.13) can justify some experimental evidences. The model distinguishes between microfibrils and intermicrofibrillar noncrystalline domains characterized by a partial molecular orientation that could determine the final fiber properties. Microfibrils become constituted by high dense and ordered lamellar structures and amorphous interlamellar regions that alternate in the direction of the fiber. These interlamellar regions possess the lowest molecular orientation and density since are formed by molecular folds, tie chain segments between adjacent lamellar structures, and free chain ends. Furthermore, the middle *soft segment* of GL-*b*-(GL-*co*-TMC-*co*-CL)-*b*-GL should be excluded from lamellar crystalline structures and be incorporated in amorphous domains (e.g., the interlamellar region).

Figure 4.2.13. Scheme showing the development of alternate lamellar and amorphous interlamellar regions and interfibrillar amorphous domains. Two relatively disposition of crystalline blocks of adjacent microfibrils are considered to show the easier diffusion path (blue arrows) when blocks are placed at the same level. Red arrows shows the diffusion along the longitudinal direction through the interfibrillar amorphous domains. The inset illustrates the crystalline domain (1); the amorphous interlamellar regions (2); the presence of tie molecules (3), molecular folds (4) and free chain ends (5), and a *soft segment* (6).

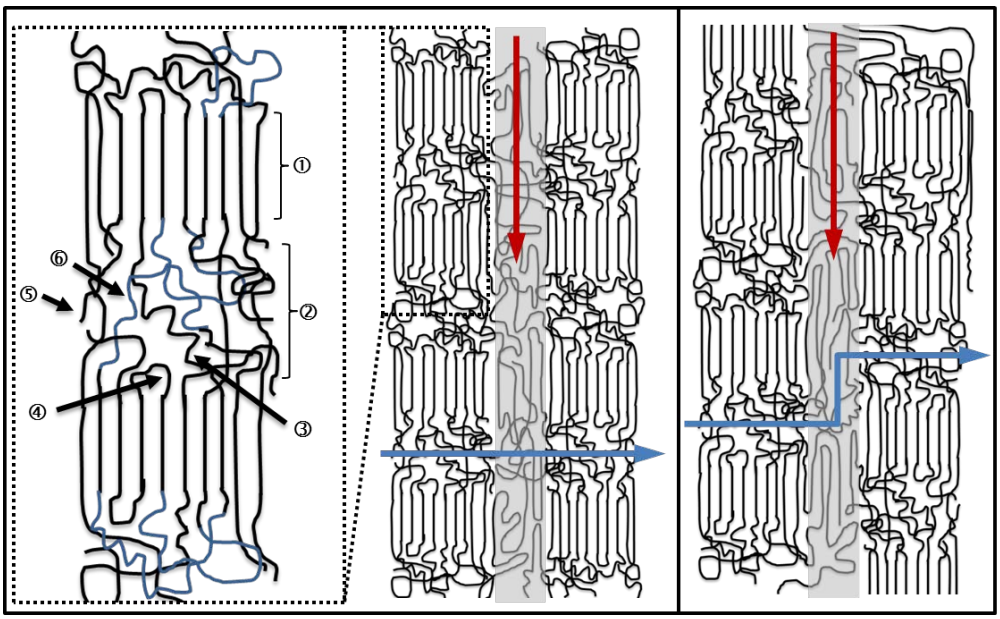

Hydrolysis could take place along the longitudinal and lateral fiber directions associated to amorphous interfibrillar and interlamellar regions, respectively, since crystalline domains should be more resistant to the diffusion of water molecules. Morphological changes occurring during degradation should logically depend on the prevailed direction and probably on the relatively disposition of crystalline blocks of adjacent microfibrils. Lateral diffusion should be hindered (i.e., diffusion channels are tortuous) when crystalline domains are disposed at different relatively levels and consequently longitudinal cracks should be preferentially developed (earlier degradation step). A less tortuous path and a favoured lateral diffusion should be expected when crystalline domains were arranged at a similar level (i.e., the amorphous domains of adjacent microfibrils are located at a common cross-sectional plane normal to the fiber axis), which probably will correspond to the suture core crystallized at a slower rate. In this way, microcracks formed during the third degradation step will continue to hydrolyze along the cross-sectional plane, where the

more open and less resistant amorphous regions are located. At the final stage, these circumferentially propagated cracks cut through the fiber and gave rise to smooth cross-sectional surfaces. Formation of thin disk morphologies is very clear for GL-*b*-(GL-*co*-TMC-*co*-CL)-*b*-GL probably as a consequence of the presence of an amorphous *soft segment* that is confined between two crystallizable polyglycolide *hard blocks*. Changes on the diffusion coefficient along longitudinal and lateral directions during degradation have been reported for *p*-polydioxanone sutures at temperatures of 40 and 50 ºC, being results in agreement with the above discussion.[44]

Mass loss during degradation should be related to the morphological changes and specifically the induction time where the sample weight remained practically constant corresponds to the time necessary to achieve the detachment of the outermost skin layer. The development of the circumferential cracks associated to the degradation of interlamellar amorphous regions occurred during the time period were the greater mass loss rate was detected.

Degradation in a basic medium seems to proceed in a different manner since in this case the first step was characterized by the formation of pores instead of longitudinal cracks (**Figure 4.2.14a**). Hence the diameter of the suture decreased progressively (**Figure 4.2.12**) and the detachment of a skin layer was not observed.

Cautions concerning interpretation of degradation process must however be taken into account since morphological observations are carried out with dried samples. Nevertheless, it should be pointed out that probably the different degradation process (i.e., disruption of hydrogen bonding interactions and irreversibility of ester bond cleavages) caused that hydrolysis along longitudinal and lateral directions were more similar and even some circumferential cracks could be developed in this stage. In the final step, the degradation of the amorphous interlamellar regions was predominant and gave rise to disk morphologies. However, these disks appear more irregular than those produced under the neutral medium due to the existence of longitudinal cracks (see arrow in **Figure 4.2.14b**)

Figure 4.2.14. SEM micrographs showing the morphologic changes of a GL-*b*-(GL-*co*-TMC-*co*-CL)-*b*-GL suture (USP 1) during exposure to a pH 10 basic buffer at 37 ºC.

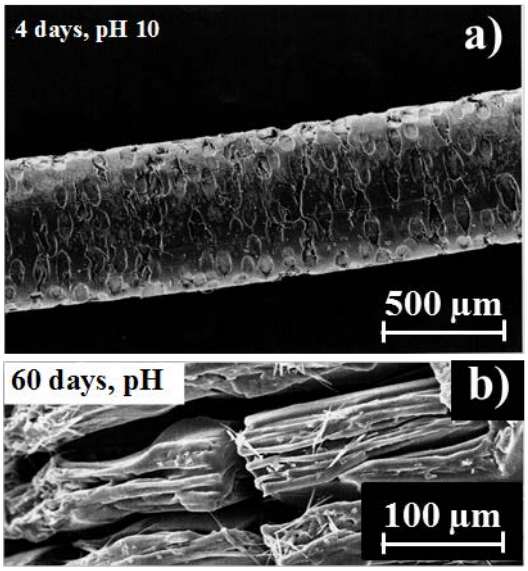

4.2.3.7. Changes on tensile properties during hydrolytic degradation

Figure 4.2.15 shows the evolution of Young modulus, and tensile strength during degradation under neutral and basic media. Mechanical properties were affected practically at the beginning of exposure in a similar way as molecular weights did. In fact, the maximum loss of tensile strength of samples degraded in the pH 7.4 media occurred at similar times than the maximum molecular weight loss, which was clearly differentiated from that associated to the maximum mass loss. In fact, tensile strength should decrease rapidly with the scission of tie molecules placed in the interlamellar amorphous regions, which obviously cannot produce a significant mass loss.

Figure 4.2.15. Variation of tensile strength at break (percentage, red curves) and Young modulus (percentage, blue curves) of a GL-*b*-(GL-*co*-TMC-*co*-CL)-*b*-GL suture (USP 1) during exposure to the indicated degradation media.

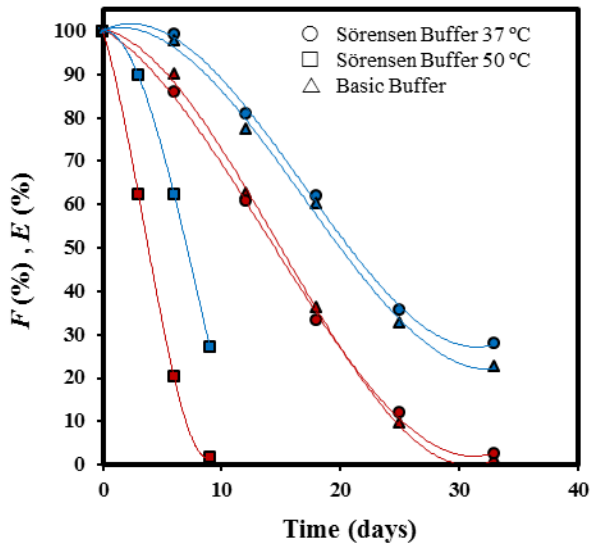

Hydrolysis is clearly enhanced by increasing temperatures and consequently the corresponding tensile strength curves become clearly differentiated. It is interesting to note the similar behaviour when degradation data from basic and neutral media are compared. It seems that the interlamellar amorphous regions are similarly hydrolyzed giving rise to a practically identical tensile strength evolution. This is not the case of crystalline regions where the cleavage of chains in the basic medium is irreversible and led to a higher molecular weight decrease respect to the pH 7.4 medium.

Young´s modulus measurements demonstrated that hydrolysis of crystalline regions took also place as previously determined from DSC and FTIR data. It is indeed possible to distinguish a first step where the modulus remained constant or had a minimum decrease when samples were exposed to media at 37 ºC. Hydrolysis at 50 ºC proceeded so quickly that the increase on the degree of crystallinity associated to the preferential attack to the amorphous domains could not be highlighted from modulus measurements. Figure 4.2.15 points also out that the basic media caused a higher modulus decrease since as above indicated the crystalline regions became more susceptible to the hydrolytic attack.

4.2.4. CONCLUSIONS

The study on the hydrolytic degradation of the segmented GL-*b*-(GL-*co*-TMC-*co*-CL)-*b*-GL commercial suture allows getting the following conclusions:

a) The evolution of the mass loss and molecular weight profiles during degradation in media differing on pH and/or temperature can be fitted to first order kinetic equations that are compatible with random scission mechanisms. This kinetics seems only to change when degradation occurs in acid media and after long exposure times. In this case, a backbiting process may dominate since degradation mainly affected the crystalline domains and recombination of cleaved ester groups could be significant. The diameter size of the suture had little influence on degradation processes although diffusion of degradation products caused an overestimation of the molecular weight when sutures with the lowest size were evaluated.

b) ^{1}H-NMR spectra revealed a preferential cleavage of glycolyl homosequences which mainly corresponded to amorphous domains as detected by FTIR spectroscopy. Sequences related to transesterification reactions were rather significant in the initial samples and were less susceptible to the hydrolytic degradation. Mechanical properties and DSC calorimetric data confirmed also that the degree of crystallinity was slightly increased during the first stages of degradation due to hydrolysis of amorphous domains but also probably for the occurrence of secondary crystallization. In any case, degradation of highly defective crystals related to glycolide units of the *soft segment* take also place at the initial degradation stages.

c) Morphology of degraded samples changed in a different way depending on the pH of the media. The highly differentiated amorphous domains caused by the presence of a high *soft segment* content allowed to distinguish the formation of longitudinal and circumferential cracks that affected the outer and inert part of sutures, respectively. These cracks may be associated to interfibrillar and interlamellar amorphous domains and a molecular diffusion that could be enhanced along longitudinal and lateral directions.

4.2.5. REFERENCES

1. Frazza, E. J. & Schmitt, E. E. A New absorbable suture. *J. Biomed. Mater. Res. Symp.* **1,** 43–58 (1971).

2. Chu, C. C. *Wound closure materials and devices*. (1997).

3. Middleton, J. C. & Tipton, A. J. Synthetic biodegradable polymers as medical devices. *Med. Device Diagnostic Ind. News Prod. Suppliers* 1–8 (1998).

4. Middleton, J. C. & Tipton, A. J. Synthetic biodegradable polymers as orthopedic devices. *Biomaterials* **21,** 2335–2346 (2000).

5. Nair, L. S. & Laurencin, C. T. Biodegradable polymers as biomaterials. *Prog. Polym. Sci.* **32,** 762–798 (2007).

6. Kokubo, S. *et al.* Long-term stability of bone tissues induced by an osteoinductive biomaterial, recombinant human bone morphogenetic protein-2 and a biodegradable carrier. *Biomaterials* **25,** 1795–1803 (2004).

7. Wang, Z. *et al.* Morphological development in absorbable poly (glycolide), copolymers during isothermal crystallization. *Polymer* **41,** 621–628 (2000).

8. Hurrell, S. & Cameron, R. E. The effect of initial polymer morphology on the degradation and drug release from polyglycolide. *Biomaterials* **23,** 2401–2409 (2002).

9. Fu, B. X. *et al.* A study of structure and property changes of biodegradable polyglycolide and poly(glycolide-co-lactide) fibers during processing and in vitro degradation. *Chinese J. Polym. Sci.* **21,** 159–167 (2003).

10. Homsy, C. A., Mcdonald, E. R. & Akers, W. W. Surgical suture-canine tissue interaction for six common suture types. *J. Biomed. Mater. Res.* **2,** 215–230 (1968).

11. Freeman, B. S., Homsy, C. A., Fissette, J. & Hardy, S. B. An analysis if suture withdrawal stress. *Surg. Gynecol. Obstet.* **131,** 441–449 (1970).

12. Casey, D. J. & Lewis, O. G. Absorbable and nonabsorbable sutures. In *Handb. Biomater. Eval. Sci. Tech. Clin. Test. Implant Mater.* (Editor, I. von R. A.) (Macmillan Publishing, 1986).

13. Blomstedt, B. & Ostenberg, B. Suture materials and wound infection. An experimental study. *Acta Chir. Scand.* **144,** 269–274 (1978).

14. Bennet, R. G. Selection of wound closure materials. *J. Am. Acad. Dermatol.* **18,** 619–637 (1988).

15. Rodeheaver, G. T., Ph, D., Thacker, J. G., Owen, J. & Edlich, R. F. Knotting and handling characteristics of coated synthetic absorbable sutures. *J. Surg. Res.* **35,** 525–530 (1983).

16. Katz, A. R., Mukherjee, D. P., Kaganov, A. L. & Gordon, S. A new synthetic monofilament absorbable suture made from polytrimethylene carbonate. *Surgery, Gynecol. Obstet.* **161,** 213–222 (1985).

17. Oberhoffner, S. & Planck, H. Surgical suture material from triblockterpolymer, its use in surgery and process for its preparation. EP 0835895. (2003).

18. Roby, M. S., Bennet, S. L. & Liu, E. K. Absorbable block copolymers and surgical articles fabricated thereform. U.S.Patent 5.403.347. (1995).

19. Bezwada, R. S. *et al.* Monocryl suture , a new ultra-pliable absorbable monofilament suture. *Biomaterials* **16,** 1141–1148 (1995).

20. Noorsal, K., Mantle, M. D., Gladden, L. F. & Cameron, R. E. Degradation and drug-release studies of a poly(glycolide-*co*-trimethylene carbonate) copolymer (Maxon). *J. Appl. Polym. Sci.* **95,** 475–486 (2005).

21. Walton, M. Strength retention of chromic gut and monofilament synthetic absorbable suture materials in joint tissues. *Clin. Orthop. Relat. Res.* **242,** 303–310 (1989).

22. Metz, S. A., Chegini, N. & Masterson, B. J. *In vivo* and *in vitro* degradation of monofilament absorbable sutures , PDS and Maxon. *Biomaterials* **11,** 41–45 (1990).

23. Chu, C. C., Zhang, L. & Coyne, L. D. Effect of gamma irradiation and irradiation temperature on hydrolytic degradation of synthetic absorbable sutures. *J. Appl. Polym. Sci.* **56,** 1275–1294 (1995).

24. Farrar, D. . & Gillson, R. Hydrolytic degradation of polyglyconate B: the relationship between degradation time, strength and molecular weight. *Biomaterials* **23,** 3905–3912 (2002).

25. Zurita, R., Franco, L., Puiggalí, J. & Rodríguez-Galán, A. The hydrolytic degradation of a segmented glycolide–trimethylene carbonate copolymer (Maxon™). *Polym. Degrad. Stab.* **92,** 975–985 (2007).

26. Díaz-Celorio, E., Franco, L., Rodríguez-Galán, A. & Puiggalí, J. Influence of degradation on the crystallization behaviour of a biodegradable segmented copolymer constituted by glycolide and trimethylene carbonate units. *Polym. Degrad. Stab.* **95,** 2376–2387 (2010).

27. Díaz-Celorio, E., Franco, L., Rodríguez-Galán, A. & Puiggalí, J. Synthesis of glycolide/trimethylene carbonate copolymers: Influence of microstructure on properties. *Eur. Polym. J.* **48,** 60–73 (2012).

28. Sharples, A. The hydrolysis of cellulose and its relation to structure. *Trans. Faraday Soc.* **53,** 1003–1013 (1957).

29. Gorham, S. D., Monsour, M. J. & Scott, R. The *in vitro* assessment of a collagen / Vicryl (Polyglactin) composite film together with candidate suture materials for use in urinary tract surgery. *Urol. Res.* **15,** 53–59 (1987).

30. Ginde, R. M. & Gupta, R. K. *In vitr*o chemical degradation of poly(glycolic acid) pellets and fibers. *J. Appl. Polym. Sci.* **33,** 2411–2429 (1987).

31. Bovey, F. A. & Winslow, F.H. Macromolecules: an introduction to polymer science, New York, Academic Press (1979).

32. Zong, X. *et al.* Structure and morphology changes in absorbable poly (glycolide) and poly (glycolide- co -lactide) during *in vitro* degradation. *Macromolecules* **32,** 8107–8114 (1999).

33. Wu, L. & Ding, J. Effects of porosity and pore size on in vitro degradation of three-dimensional porous poly(D,L-lactide-co-glycolide) scaffolds for tissue engineering. *J. Biomed. Mater. Res. A* **75,** 767–77 (2005).

34. Fernández, J., Larrañaga, A., Etxeberría, A. & Sarasua, J. R. Effects of chain microstructures and derived crystallization capability on hydrolytic degradation of poly(l-lactide/ ε-caprolactone) copolymers. *Polym. Degrad. Stab.* **98,** 481–489 (2012).

35. Zurita, R., Puiggalí, J., Franco, L. & Rodríguez-Galán, A. copolymerization of glycolide and trimethylene carbonate. *J. Polym. Sci. Part A Polym. Chem.* **44,** 993–1013 (2005).

36. Kasperczyk, J. Copolymerization of glycolide and ε-caprolactone , 1 Analysis of the copolymer microstructure by means of ^{1}H and ^{13}C NMR spectroscopy. *Macromol. Chem. Phys.* **910,** 903–910 (1999).

37. Kister, G., Cassanas, G. & Vert, M. Morphology of poly (glycolic acid) by IR and Raman spectroscopies. *Spectrochim. Acta Part A* **53,** 1399–1403 (1997).

38. Wang, H., Dong, J. H. U. A. & Qiu, K. U. N. Y. Synthesis and characterization of ABA-type block copolymer of poly (trimethylene carbonate) with poly (ethylene glycol): Bioerodible copolymer. *J. Polym. Sci. A Polym. Chem.* **36,** 695–702 (1998).

39. Brandrup, J., Immergut, E. H. & Grulke, E. A. *Polymer Handbook* (Interscience Publishers, 1999).

40. Starkweather, H. W., Avakian, P., Fontanella, J. J. & Wintersgill, M. C. Internal motions in polylactide and related polymers. *Macromolecules* **26,** 5084–5087 (1993).

41. Kim, J. & Lee, J. H. Preparation and chain-extension of P(LLA-*b*-TMC-*b*-LLA) triblock copolymers and their elastomeric properties. *Macromol. Res.* **10,** 54–59 (2002).

42. Chu, C. C. Hydrolytic degradation of polyglycolic acid: Tensile strength and crystallinity study. *J. Appl. Polym. Sci.* **26,** 1727–1734 (1981).

43. Prevorsek, D. C., Harget, P. J., Sharma, R. K. & Reimschuessel, A. C. Nylon 6 fibers: Changes in structure between moderate and high draw ratios. *J. Macromol. Sci. Part B* **8,** 127–156 (1973).

44. Lin, H. L., Chu, C. C. & Grubb, D. Hydrolytic degradation and morphologic study of poly-p-dioxanone. *J. Biomed. Mater. Res.* **27,** 153–66 (1993).

4.3. Influence of pH on morphology and structure during hydrolytic degradation of the segmented GL-*b*-(GL-*co*-TMC-*co*-CL)-*b*-GL copolymer

Hydrolytic degradation in media having a continuous variation of pH from 2 to 12 was studied for a copolymer having two polyglycolide hard blocks and a middle *soft segment* constituted by glycolide, trimethylene carbonate and ε-caprolactone units. The last units were susceptible to cross-linking reactions by γ irradiation that led to an increase of the molecular weight of the sample. Nevertheless, the susceptibility to hydrolytic degradation was enhanced respect to non-irradiated samples and consequently such samples were selected to analyze the degradation process through weight loss measurements and the evaluation of changes on molecular weight, morphology and SAXS patterns.

Results reflected the different hydrolytic mechanism that took place in acid and basic media and the different solubilization of the degradation products. Thus, degradation was faster and solubilization higher in the basic media. In this case fibers showed a high surface erosion and the formation of both, longitudinal and deep circumferential cracks that contrasted with the peeling process detected at intermediate pHs (from 6 to 8) and the absence of longitudinal cracks at low pHs.

SAXS measurements indicated that degradation was initiated through the hydrolysis of the irregular molecular folds placed on the amorphous interlamellar domains but also affected lamellar crystals at the last stages. Subsequent heating processes performed with degraded samples were fundamental to reveal the changes on microstructure that occurred during degradation and even the initial lamellar arrangement. In particular, the presence of interfibrillar domains and the disposition of lamellar domains at different levels along the fiber axis for a determined cross-section were evidenced.

4.3.1. INTRODUCTION

Sutures were the first commercial use of biodegradable polymers as orthopedic devices and by now its use has been extended to most surgical fields.[1] Nowadays, most of resorbable sutures are polyesters (homopolymers and copolymers) based on glycolide, lactide, trimethylene carbonate, ε-caprolactone and *p*-dioxanone units. These synthetic polymers, with hydrolyzable bonds in their main chain, provide clear advantages over natural polymers such as tailored properties and even predictable lot-to-lot uniformity. In fact, control over degradation rate and properties can be achieved by the appropriate selection of monomers, copolymer composition and copolymer architecture (e.g., blocky or random distributions). In this way, factors like hydrophilicity, crystallinity, chain stiffness and molecular weight can be easily controlled.[2]

Poly(glycolide), the first and simplest polyester employed as suture,[3] renders materials with high crystallinity, high melting and glass transition temperatures, high strength and Young modulus and high degradation rate. The polymer is commercialized as a braided material due to its high stiffness and consequently has some potential inconveniences associated to tissue drag, knot tie-down and risk of infection compared to monofilament sutures.[4–6] Flexible sutures threads that are processed in a monofilament form have been manufactured to avoid these problems. Some of them consist on glycolide/trimethylene carbonate copolymers (named as polyglyconates) and a segmented A-B-A architecture where A is a polyglycolide *hard block* and B a random *soft segment*. Maxon™ (Syneture) was one of the former monofilament synthetic suture based in glycolide that has been developed.[7] Therefore, detailed studies concerning synthesis, degradation, properties and crystallization have been performed on such copolymers as model materials for suture applications.[8–20]

Works about monofilament sutures having three (e.g., Monosyn®,[21] and Biosyn™ [22,23]) and four components (e.g., Caprosyn™ [24]) are more scarce despite the incorporation of additional monomers may lead to polymers with different properties and degradation behavior. Specifically, Monosyn® is the segmented GL-*b*-(GL-*co*-TMC-*co*-CL)-*b*-GL copolymer constituted by 72, 14 and 14 wt-% of glycolide, trimethylene carbonate and ε-caprolactone units, respectively. The material has a *soft segment* that represents the 43 wt-% of the sample and includes ε-caprolactone units. The high methylene content provided by them lead to a decrease on the degradation rate that may balance the opposite effect caused by the increase on the amorphous character.

Exposure to gamma rays is a process often employed for microbial decontamination of medical devices since this irradiation procedure is economically feasible for a large-scale terminal sterilization. Gamma irradiation is highly penetrating and ionizing events activate also numerous chemical reactions that can be useful to modify material properties. Basically, gamma irradiation may cause different effects on polymers: chain scission, crosslinking/grafting. The predominant process depends on the chemical nature of the polymer and the applied dose.[25]

Polyester sutures exposed to gamma irradiation can experiment both a chain scission through the ester moiety and a crosslinking that involves radicals formed on the carbon atoms of methylene groups of the main chain.[26] Both crosslinking and degradation may occur simultaneously (i.e., gas release and increase of molecular weight may be observed together), although usually one process predominates. Obviously, the effect of these reactions on material properties is clearly different. Crosslinking increases the molecular weight, lowers the mobility of molecules, reduces creep, raises the tensile strength and increases the hardness and brittleness. Radiation induced degradation, decreased the molecular weight as well as tensile, impact, shear strength and elongation at break.

The predominant effect of γ irradiation on polyglycolide is a chain scission that mainly leads to the unzipping of molecules and a faster loss of M_n than M_w.[3] Polyesters with a high number of methylene groups in the main chain are less susceptible to degradation since weakening of main chain bonds through ester resonance becomes less effective. Therefore, ε-caprolactone units belonging to the *soft segment* may be more susceptible to crosslinking than degradation. Note that segmented GL-*b*-(GL-*co*-TMC-*co*-CL)-*b*-GL could experiment a degradation through its *hard segments* and simultaneously a significant crosslinking through its *soft segments* that could give rise to an increase of the molecular weight. This is not the case of the bicomponent segmented copolymer GL-*b*-(GL-*co*-TMC)-*b*-GL, which chain scission events are still predominant during irradiation. Nevertheless, the molecular weight decrease was lower than that observed for polyglycolide suggesting that trimethylene carbonate units were also susceptible to crosslinking reactions.[27]

Molecular scission is expected to be more pronounced in the amorphous regions since recombination of formed radicals can be easier in the compact crystalline regions with immobile chain segments. Gamma irradiation should lead to a reduction of chain entanglement of polyglycolide segments in the amorphous phase and an open amorphous

structure that facilitates hydrolytic degradation.[27] In the same way, polymers could become more susceptible to enzymatic attack after altering their physical and chemical structures by gamma irradiation.[28]

Recent degradation studies on GL-*b*-(GL-*co*-TMC-*co*-CL)-*b*-GL revealed a complex process that could take place along longitudinal and lateral fiber directions depending on the degradation medium as also reported for other glycolide based sutures.[27,29] In all cases, disk morphologies were clearly detected in the last degradation stages, playing an important role the confinement of the amorphous *soft segment* between the two crystallizable polyglycolide hard blocks.[29] The present work insists on the morphological changes that took place during exposure of the gamma irradiated GL-*b*-(GL-*co*-TMC-*co*-CL)-*b*-GL copolymer that was selected for its higher susceptibility to hydrolysis and its segmented architecture. To this end, media with a gradual variation of pH from 2 to 12 were considered and the lamellar morphology analysed by means of small angle X-ray scattering (SAXS) of the exposed sutures before and after being submitted to a thermal annealing process that could enhance differences on the folding surfaces.

4.3.2. EXPERIMENTAL SECTION

4.3.2.1. Materials

Commercially available sutures of GL-*b*-(GL-*co*-TMC-*co*-CL)-*b*-GL (Monosyn™, USP 0) were kindly supplied by B. Braun Surgical, S.A. GL-*b*-(GL-*co*-TMC-*co*-CL)-*b*-GL samples were also exposed to a γ irradiation dosage above 25 kGry at temperature of 25 ºC (i.e., slightly higher than the glass transition temperature). The segmented microstructure was attained by a two-step synthesis (Figure 4.3.1) where firstly a random *soft segment* was prepared and then used as initiator for the ring opening polymerization of glycolide.

Figure 4.3.1. Two step synthesis of GL-*b*-(GL-*co*-TMC-*co*-CL)-*b*-GL showing the chemical structure of soft and hard segments.

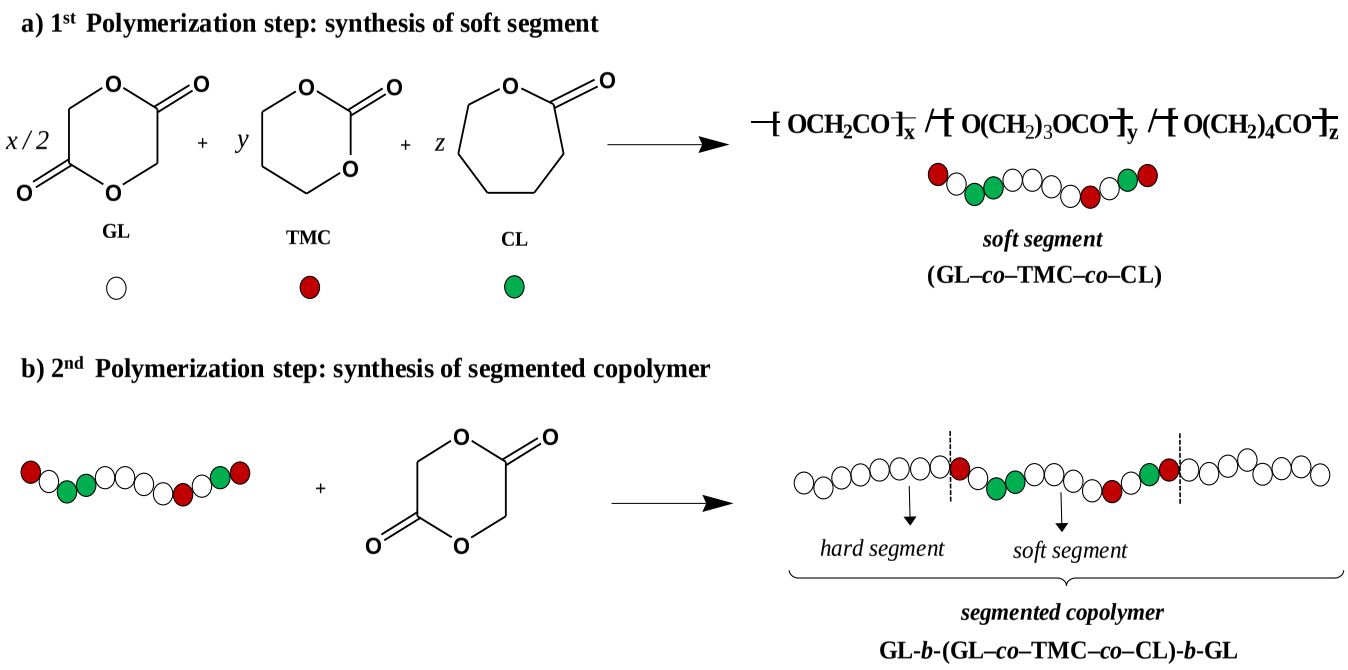

4.3.2.2. Hydrolytic degradation

In vitro hydrolytic degradation assays were carried out at physiological temperature of 37 ºC and in the pH range from 2 to 12 using the Universal buffer (citrate-phosphate-borate/HCl) solution.[30] This was prepared by mixing 20 mL of a stock solution with *x* mL of 0.1 M HCl and distilled water up to a volume of 100 mL. The stock solution (1 L) contained 100 mL of citric acid and 100 mL of phosphoric acid solution, each equivalent to 100 mL NaOH 1M, 3.54 g of boric acid and 343 mL of 1 M NaOH. pHs 2, 3, 4, 5, 6, 7, 8, 9, 10, 11 and 12 were attained with 74.4, 56.9, 50.7, 45.4 39.7, 32.9, 28.1, 24.0, 18.1, 14.7 and 1.3 mL (i.e., the *x* values) of the HCl solution, respectively.

Samples were kept under orbital shaking in bottles filled with 50 mL of the degradation medium and sodium azide (0.03 wt-%) to prevent microbial growth for selected exposure times. The samples were then thoroughly rinsed with distilled water, dried to constant weight under vacuum and stored over P_4O_{10} before analysis. Weight retention, molecular weight, calorimetric properties were then evaluated. Degradation studies were performed in quintuplicated and the given data corresponded to the average values.

4.3.2.3. Measurements

Weight retention (W_r) of the specimens was determined by the percentage ratio of weight after degradation (W_d) to initial weight before degradation (W_0):

$$W_r = W_d / W_0 \times 100 \quad (1)$$

Molecular weights were estimated by size exclusion chromatography (GPC) using a liquid chromatograph (Shimadzu, model LC-8A) equipped with an Empower computer program (Waters). A PL HFIP gel column (Polymer Lab) and a refractive index detector (Shimadzu RID-10A) were employed. The polymer was dissolved and eluted in 1,1,1,3,3,3-hexafluoroisopropanol containing CF_3COONa (0.05 M) at a flow rate of 1 mL/min (injected volume 100 µL, sample concentration 2.0 mg/mL). The number and weight average molecular weights were calculated using polymethyl methacrylate standards.

Calorimetric data were obtained by differential scanning calorimetry with a TA Instruments Q100 series with T_{zero} technology and equipped with a refrigerated cooling system (RCS). A first heating run (20 ºC/min) was performed to determine melting

temperature and enthalpy, whereas a cooling run (10 ºC/min) after keeping the sample in the melt state for three minutes to erase the thermal history was carried out to determine crystallization data. Experiments were conducted under a flow of dry nitrogen with a sample weight of approximately 5 mg and calibration was performed with indium. T_{zero} calibration required two experiments: the first was performed without samples while sapphire disks were used in the second.

Optical micrographs were taken with a Zeiss Axioskop 40 Pol light polarizing microscope equipped with a Zeiss AxiosCam MRC5 digital camera.

Scanning electron microscopy (SEM) was employed to examine the morphology of sutures after different times of exposure to the selected degradation media. Carbon coating was accomplished with a Mitec k950 Sputter Coater (fitted with a film thickness monitor k150x). SEM micrographs were obtained with a Zeiss Neon 40 EsB instrument.

Time resolved SAXS experiments were carried out at the NCD beamline (BL11) of the Alba synchrotron radiation light facility of Cerdanyola del Vallès (Catalunya). The beam was monochromatized to a wavelength of 0.1 nm. Polymer samples were confined between Kapton films and then held on a Linkam THMS600 hot stage with temperature control within ± 0.1 ºC. SAXS profiles were acquired during heating and cooling runs in time frames of 20 s and rates of 10 ºC/min. The SAXS detector was calibrated with diffractions of a standard of a silver behenate sample. The diffraction profiles were normalized to the beam intensity and corrected considering the empty sample background.

4.3.3. RESULTS AND DISCUSSION

4.3.3.1. Hydrolytic degradation in different pH media

Figure 4.3.2 shows the pH dependence of the degradation process evaluated through weight loss measurements during exposure to the different hydrolytic media. Degradation is characterized by sigmoidal curves with a short induction time, which is associated to the time required to render small soluble fragments able to diffuse from the fiber to the media, a period where an abrupt mass loss is observed and finally a period where degradation is slower due to the enrichment on more resistant fragments to the hydrolysis (e.g., crystalline regions). It is assumed that degradation initially occurs through random chain scissions that involved amorphous domains while a slower one-dimensional

stepwise hydrolytic fragmentation is characteristic of the last stages where crystalline regions are more abundant.[31]

Results show a clear trend where induction time regularly decreases and the second step becomes narrower as the pH of the media increases. Nevertheless, differences were more pronounced by small increases on basicity than on acidity. Note for example that a weight loss of 40% required 41 and 27 days when pH increased from 11 to 12, respectively, whereas 90 and 87 days were required for pHs of 2 and 3, respectively. Acid-catalyzed hydrolysis of esters is much slower at a given temperature than the alkali-catalyzed one giving rise also to a slower surface attack of the exposed samples.[32] It is well known that acid and alkaline hydrolysis take place through different mechanisms, being in the first case the process initiated by protonation of the single bonded oxygen of the ester group while in the second case the hydroxide ions attack the electron-deficient carbonyl carbons to form an intermediate anion.

Figure 4.3.2. Plot of remaining weight percentage versus exposure time to the different assayed hydrolytic degradation media for non-irradiated GL-*b*-(GL-*co*-TMC-*co*-CL)-*b*-GL samples. The inset shows a magnification for low pH media.

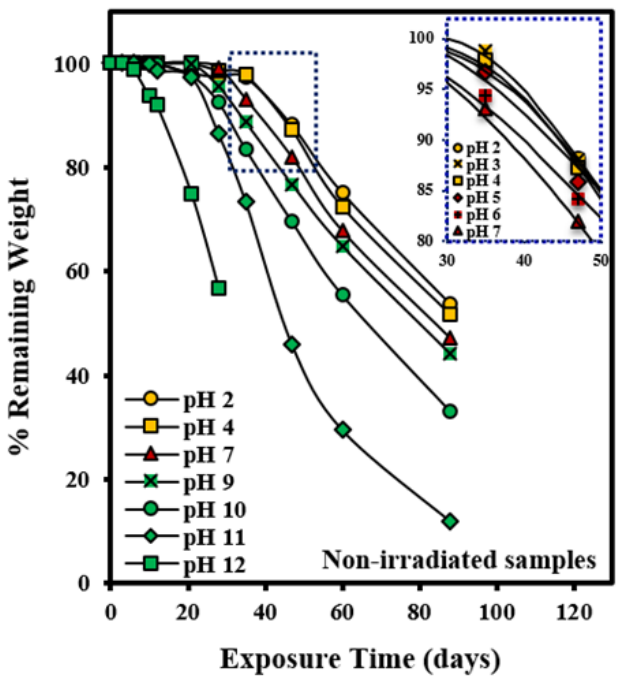

Figure 4.3.3a shows that degradation was clearly enhanced when samples were previously submitted to γ irradiation. Basically, main differences on degradation profiles of irradiated and non-irradiated samples at a given pH correspond to the induction time. This was more significant in acid media and therefore a weight loss of 40% required 27 and 20 days at pH 12 while 90 and 73 days at pH 2 for non-irradiated and γ irradiated samples (Figure 4.3.3b), respectively.

Figure 4.3.3. (a) Comparison between degradation of non-irradiated and γ irradiated GL-*b*-(GL-*co*-TMC-*co*-CL)-*b*-GL samples during exposure to different representative degradation media. **(b)** Plot of time required to get a weight loss of 40% for non-irradiated and γ irradiated GL-*b*-(GL-*co*-TMC-*co*-CL)-*b*-GL samples exposed to different pH media.

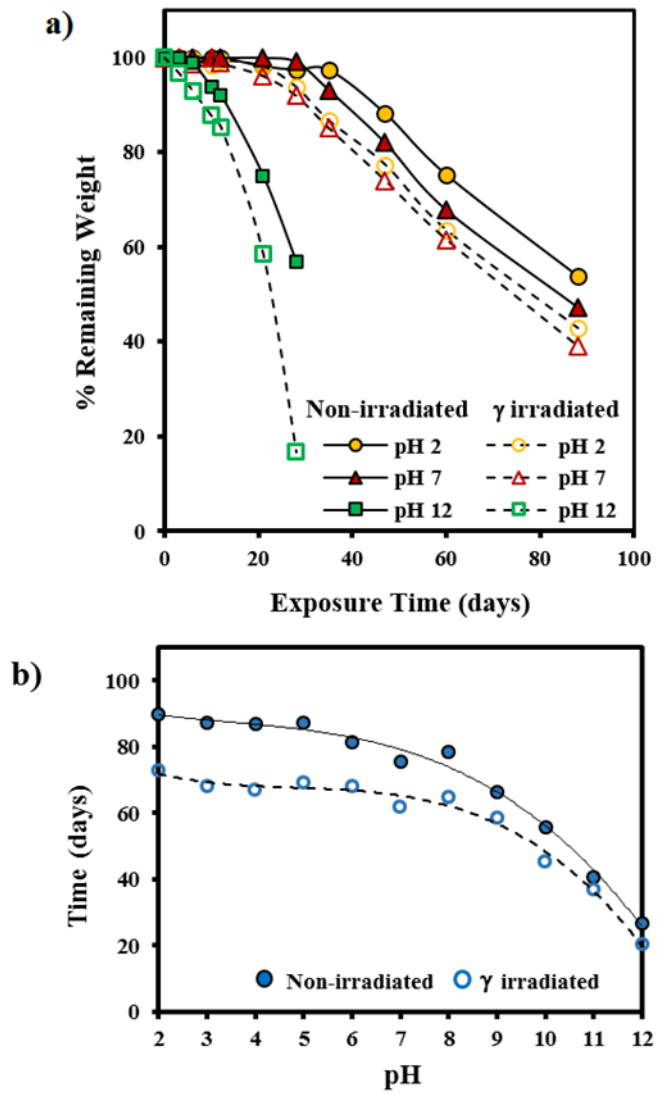

Figure 4.3.4 shows the changes on the pH of the medium during the degradation process. A decrease was observed for basic media as a consequence of the release of degradation products with an acid nature. Basically, curves were characterized by an initial region where pH is constant, followed by a narrow (e.g., pH 12) or wide (e.g., pH 9) region where a significant pH decrease was observed due to the moderate buffer capacity of the media. Finally, a region where pH became again practically constant was detected. Logically, the magnitude of the pH change decreased and the second region shifted to higher times as the initial pH of the medium decreased, a feature that is in agreement with previously indicated weight loss measurements. In fact, times corresponding to the maximum slope of pH (Figure 4.3.4) and weight loss curves (Figure 4.3.2) were similar. Comparison between pH curves of non-irradiated and γ irradiated samples demonstrated again the faster degradation of the second ones. Specifically, the maximum slope shifted for example from 30 to 23 days at pH 12 and from 48 to 30 days at pH 9.

Figure 4.3.4. pH evolution of representative degradation media during exposure of non-irradiated (solid lines) and γ irradiated (dashed lines) GL-*b*-(GL-*co*-TMC-*co*-CL)-*b*-GL samples.

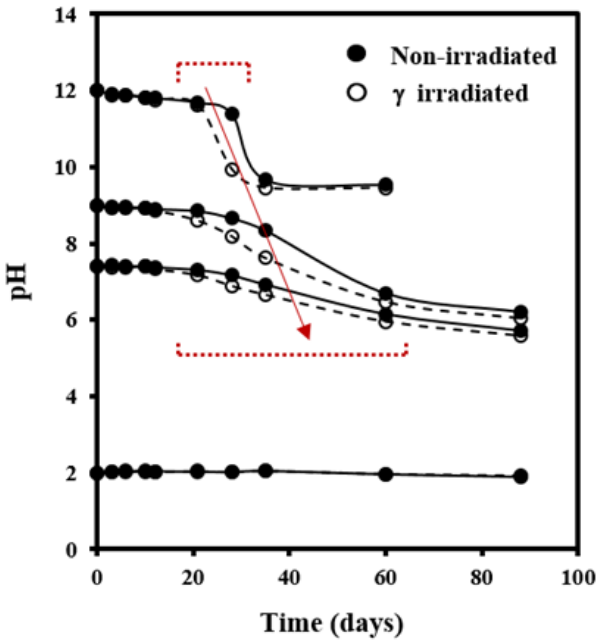

Evolution of weight average molecular weight of non-irradiated and irradiated samples during exposure at the two extreme pHs (i.e., 2 and 11) is shown in Figure 4.3.5. In this case curves were less influenced by the pH of the medium and were characterized by a rapid decrease during the first days of exposure until reaching a practically constant value at ca. 35 days. This can be interpreted as the minimum molecular size of insoluble degraded fragments. Note also that the initial molecular weight of the γ irradiated sample was the highest (i.e., 102,400 with respect to 90,700 g/mol), suggesting that crosslinking reactions were produced during irradiation.

Figure 4.3.5. Plots of the variation in the weight average molecular weight of a non-irradiated and a γ irradiated GL-*b*-(GL-*co*-TMC-*co*-CL)-*b*-GL sample during exposure to a pH 11 and pH 2 degradation media.

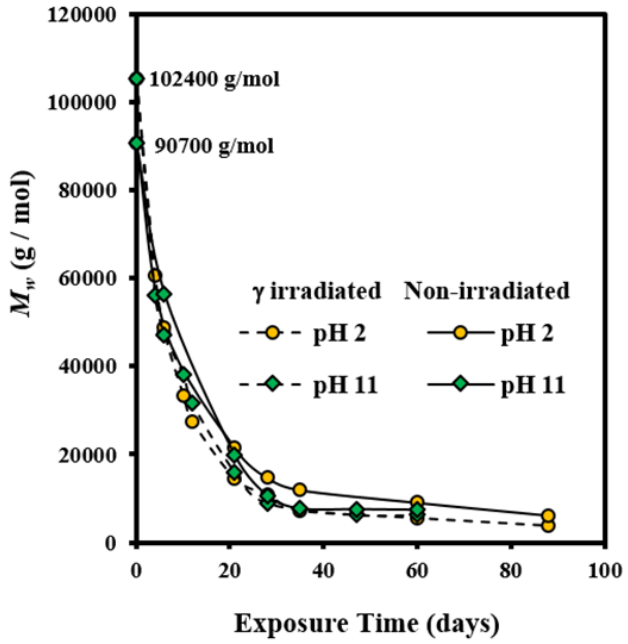

Figure 4.3.6 shows the relative M_w loss that allows comparing better the evolution for samples with different molecular size. It is clear that small differences could be found at the initial stages of degradation, being this enhanced for irradiated samples. The influence of pH is less clear but a faster decrease was observed at the beginning of exposure, probably as a consequence of the greater retention of small degraded molecules. Therefore, curves point out a variation on the degradation process that could obey a preferential degradation of the amorphous region at the beginning that is followed by a

slower degradation of the edge of crystallites.[33–35] In fact, the first step can be associated to a quick random chain scission mechanism that follows a first-order kinetic, irrespective of the chain length, whereas a slower chain-end-scission mechanism can be expected when degradation affects the crystalline domains.[29,36–39] Note in Figure 4.3.6 the differences between the experimental curve and the simulated one considering a theoretical first order equation.

Figure 4.3.6. Plots of the variation in the weight average molecular weight (percentage) of a non-irradiated and a γ irradiated GL-*b*-(GL-*co*-TMC-*co*-CL)-*b*-GL sample during the first steps of exposure to representative degradation media. For the sake of completeness simulated data for a degradation following a first order equation is also drawn (dashed line) for the γ irradiated sample exposed to pH 2.

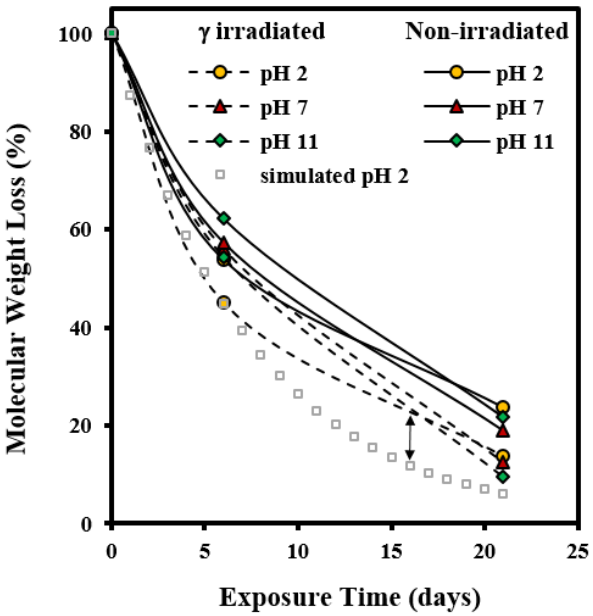

Figure 4.3.7 shows typical DSC scans obtained during heating and cooling experiments, which demonstrated that samples were semicrystalline and able to easily crystallize from the melt state.

Figure 4.3.7. DSC traces obtained with the original γ irradiated GL-*b*-(GL-*co*-TMC-*co*-CL)-*b*-GL sample. Traces correspond to the first heating run **(i)** and the cooling run after keeping the sample in the melt state for 3 min **(ii).**

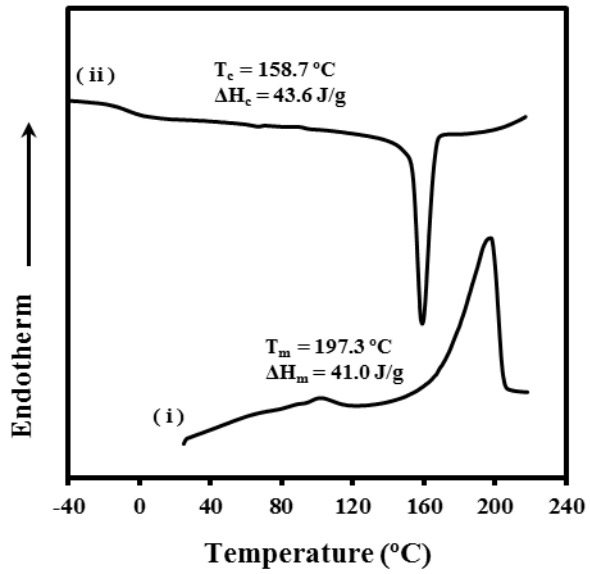

Changes on thermal properties point also out the time required to produce a significant degradation. Thus, melting temperature abruptly decreased as well as the crystallization temperature when the minimum molecular weight was attained as shown in Figure 4.3.8a for the degradation in the pH 7 representative medium. Therefore, lamellar crystals were sufficiently affected at the indicated degradation level to note a significant decrease on the melting temperature (e.g., from 200–198 °C to 191 °C). Furthermore, differences were also detected between irradiated and non-irradiated samples, specifically the abrupt temperature changes occurred at lower exposure when samples were irradiated (i.e., 28 with respect to 21 days). Nevertheless, the effect of degradation could be better detected through the major difficulty to crystallize for the degraded samples. In this way, crystallization temperature decreased from an initial value of 165–160 °C to temperatures of 130 and 110 °C for non-irradiated and irradiated samples, respectively. The larger variation observed in the second case confirms again the greater susceptibility to degradation of samples after being γ irradiated. Similar trends were observed from melting and crystallization enthalpies of degraded samples (Figure 4.3.8b). Thus, both enthalpies seem to reach a maximum value at the beginning of degradation as expected from a preferential attack to the amorphous region. Logically this maximum was observed at a lower exposure time when the γ irradiated samples was considered.

Figure 4.3.8. (a) Variation of melting and crystallization temperatures and **(b)** melting and crystallization enthalpies of non-irradiated and γ irradiated GL-*b*-(GL-*co*-TMC-*co*-CL)-*b*-GL samples during exposure time in a pH 7 buffer medium

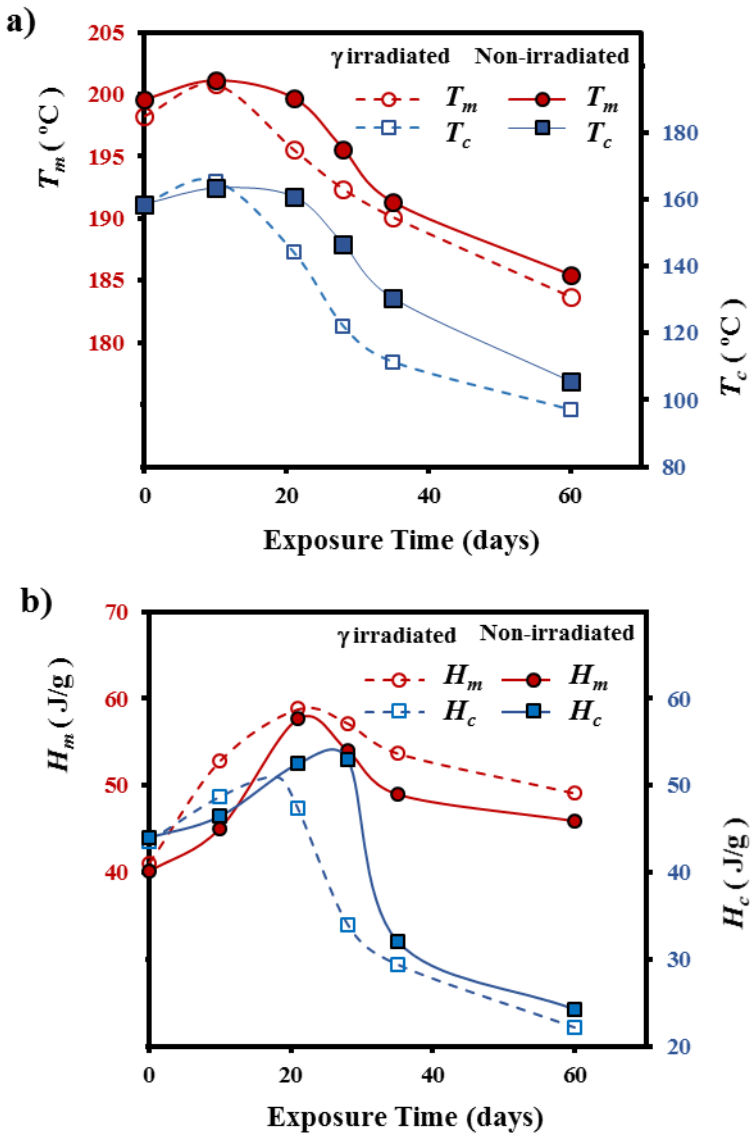

4.3.3.2. Morphological changes during hydrolytic degradation in different pH media

GL-*b*-(GL-*co*-TMC-*co*-CL)-*b*-GL oriented fibers exposed to a hydrolytic degradation process experiment complex morphological changes as a consequence of different factors:

a) Fibers are constituted by oriented lamellae and different amorphous regions which will be more susceptible to the hydrolysis process. In fact, oriented crystallites are embedded in an amorphous matrix, being possible to distinguish between interlamellar and interfibrillar amorphous regions (Figure 4.3.9a), according to previously postulated models.[40,41] The interlamellar domains alternate with lamellae in the direction of the fiber and possess the lowest molecular orientation and density since are formed by molecular folds, tie chain segments between adjacent lamellar structures, and free chain ends. Therefore, these domains appear to be the most susceptible to hydrolysis. On the contrary, the interfibrillar domains may have a partial orientation and correspond to the regions placed on lateral sides of lamellae arranged in a fibrillar way. Degradation may therefore follow two different pathways: longitudinal and transversal depending on whether the hydrolysis proceeds mainly through the interfibrillar or interlamellar regions, respectively.

b) The hydrolysis mechanism is different as previously indicated for acid and basic media. Differences not only concern to the kinetic mechanism but also the capability to solubilize degradation products. In this way, retention may be significant in both the interlamellar and interfibrillar regions when an acidic medium is employed and therefore lateral and longitudinal diffusion of water molecules could be hindered. On the contrary, rapid solubilization of degradation products may enhance the surface erosion of exposed fibers in a basic medium.

c) Morphology of fibers is not completely homogeneous due to a spinning process where the fiber surface is cooled faster than the core. Therefore, the shell layer should have different degree of molecular orientation and probably is constituted by a slightly different lamellar architecture (e.g., size of crystalline and amorphous domains).

Figure 4.3.9. (a) Scheme showing the presence of oriented lamellar crystals embedded in interlamellar (yellow) and interfibrillar (blue) amorphous domains. Blue and orange arrows indicate the attack able to generate longitudinal and circumferential cracks, respectively. **(b)** Schemes showing the distinctive morphological changes that occurred during heating of samples previously degraded in acidic, neutral and basic media. For the sake of completeness representative SAXS patterns taken during a heating scan are also shown.

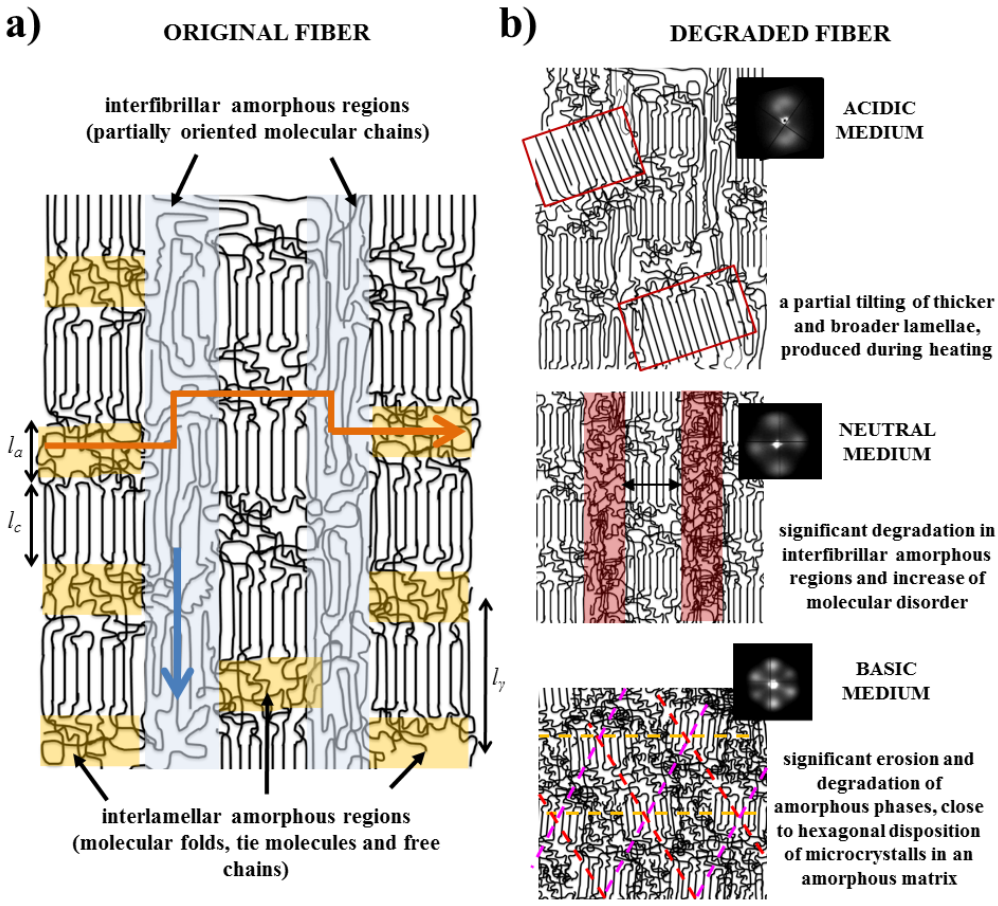

Morphological inspection of fibers exposed to different pH media revealed a continuous evolution with pH and logically with time as shown in Figures 4.3.10–4.3.12. Morphological changes were similar for non-irradiated and γ irradiated samples as shown in Figure 4.3.10 for a representative pH medium. However, in all cases changes proceeded faster when samples were exposed to irradiation in agreement with the above indicated accelerated degradation. Thus, longitudinal cracks and peeling were evident after exposure of the irradiated sample to a pH 7 medium for 21 and 35

days, respectively, whereas the non-irradiated fiber was practically unaltered after 21 days, being 35 and 47 days required to appreciate cracks and peeling. Some features can be highlighted according to the optical and SEM micrographs obtained at neutral (Figures 4.3.10 and 4.3.13), acidic (Figures 4.3.11 and 4.3.13) and basic (Figures 4.3.12 and 4.3.13) pHs:

Figure 4.3.10. Optical micrographs showing the morphological changes of non-irradiated and γ irradiated GL-*b*-(GL-*co*-TMC-*co*-CL)-*b*-GL samples during exposure for the indicated times to a pH 7 buffer medium at 37 ºC.

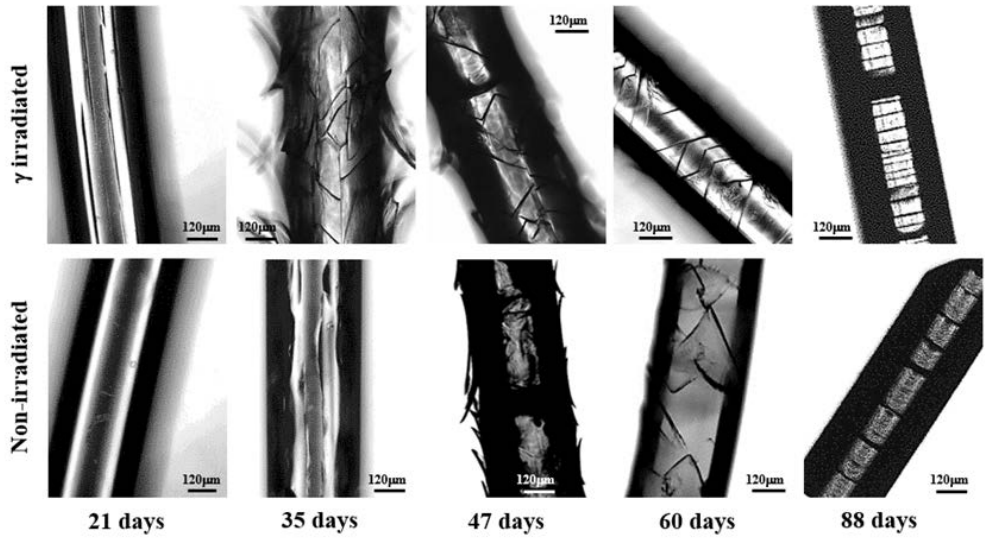

a) Degradation in a neutral pH proceeds through three well differentiated steps. The first one corresponds to the development of straight and longitudinal cracks that evolve through the detachment of the skin layer. Microcracks that propagate circumferentially around the fiber axis are characteristic of the second step although they initially contribute to the peeling out process of the outermost skin. In this step microcracks are irregularly distributed along the fiber and are not completely extended along the circumferential perimeter. In fact, optical micrographs show the presence of irregular cracks that appear inclined respect to the fiber axis. The last step is associated to the deeply propagation of the initiated circumferential cracks through the cross-sectional planes where interlamellar amorphous domains more susceptible to the hydrolysis exist. At the end of this step, regularly distributed discs perpendicular to the fiber axis are evident in the optical and SEM micrographs.

Figure 4.3.11. Optical micrographs showing the morphological changes of γ irradiated GL-*b*-(GL-*co*-TMC-*co*-CL)-*b*-GL samples during exposure for the indicated times to the indicated acidic media at 37 ºC.

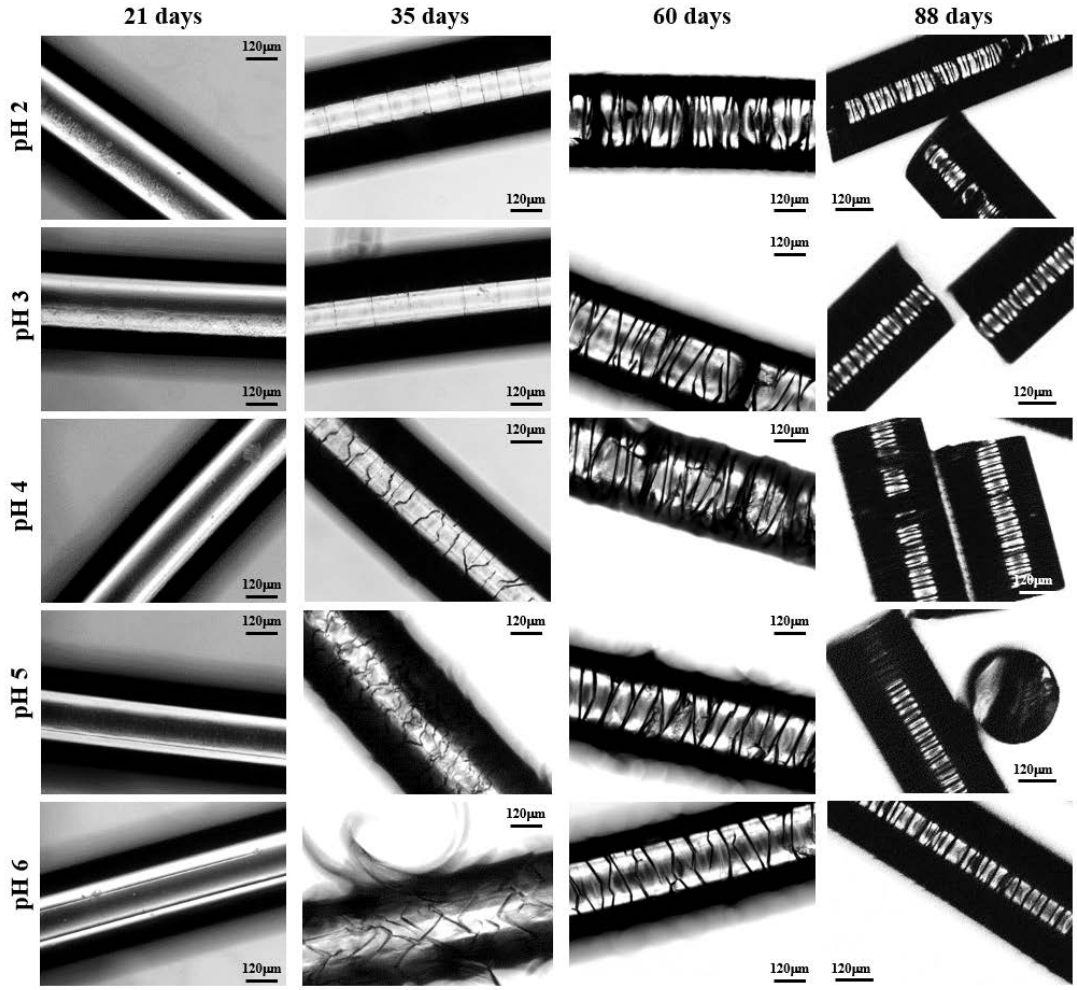

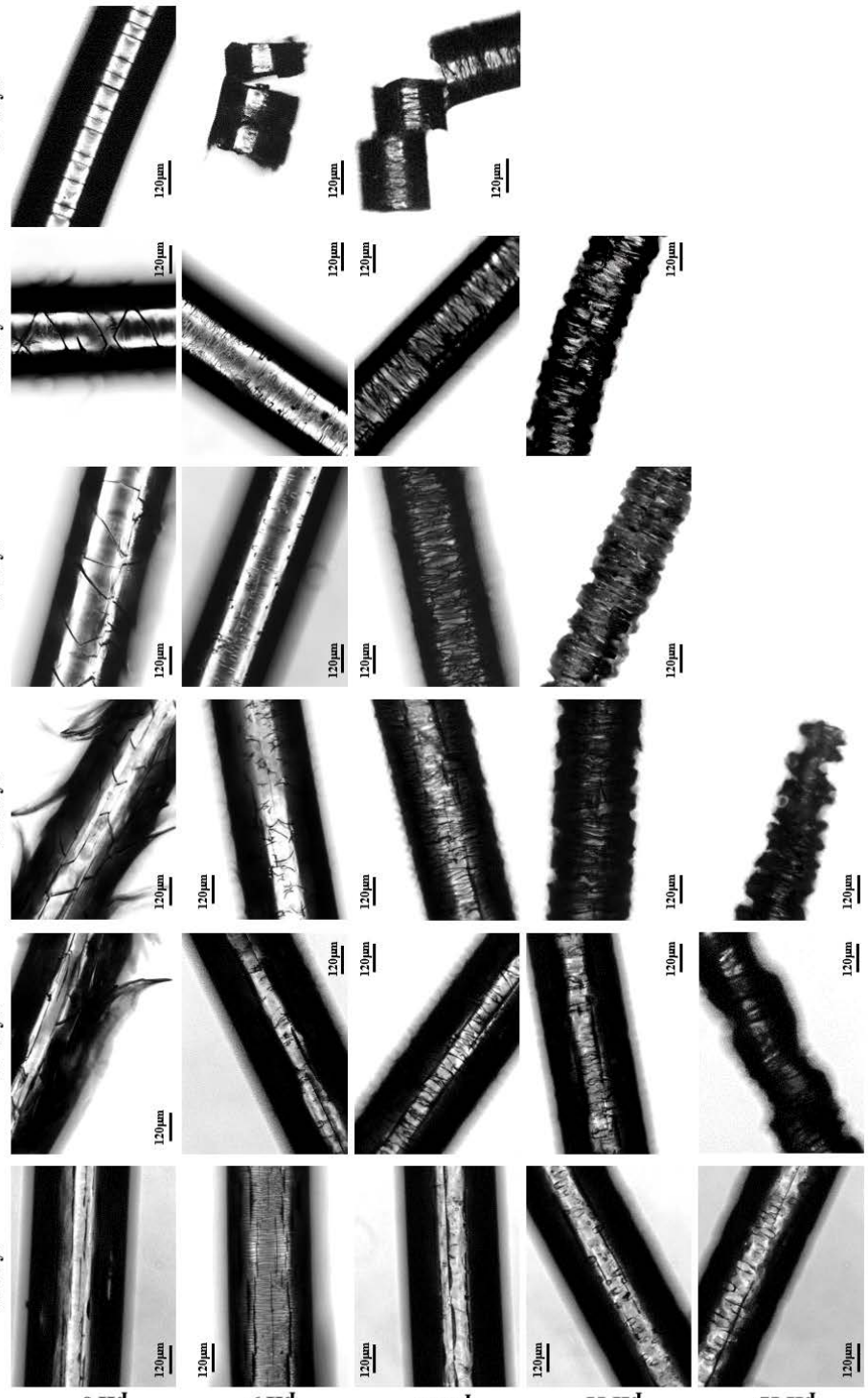

Figure 4.3.12 Optical micrographs showing the morphological changes of γ irradiated GL-*b*-(GL-*co*-TMC-*co*-CL)-*b*-GL samples during exposure for the indicated times to the indicated basic media at 37 °C.

b) Peeling was not observed when the pH of the degradation medium was lower than 6 and furthermore the formation of longitudinal cracks was clearly hindered in these acidic media (Figure 4.3.11). Logically, degradation became slower as the pH decreased and in fact unaltered surfaces were observed after 21 days of exposure even for the irradiated sample. Circumferential and highly spaced cracks perpendicular to the fiber axis were detected at the first stages of degradation in the most acidic media (pHs 2 and 3) whereas irregular and inclined cracks were observed in the optical microscopy images taken at pHs between 4 and 6. Nevertheless, SEM micrographs revealed that these cracks had a zig-zag appearance. In all cases, additional cracks appeared at longer exposures, giving rise to irregular fissures that ultimately lead to the thinner and regular discs that were perfectly oriented perpendicular to the fiber axis.

c) Degradation in basic media showed the formation of deep longitudinal cracks at the beginning of exposure that lead to peeling only when pH was lower than 9. Circumferential cracks were also observed at the earlier degradation steps together with a clear erosion of the fiber surface, which can already be detected in the irradiated samples exposed for only 21 days in a pH 10 medium. SEM micrographs revealed also the formation of such circumferential cracks and the resulting wrinkled fiber surface. In fact, degradation in the high basic media was peculiar since deep transversal cracks that led to narrow discs were practically formed at the beginning of exposure. Note also that the high solubilization of degradation products caused that the lineal and smooth fiber profile rapidly evolved towards highly tortuous surfaces.

Figure 4.3.13. SEM micrographs showing the morphological changes of a γ irradiated GL-*b*-(GL-*co*-TMC-*co*-CL)-*b*-GL sample during exposure to: **(a)** a pH 4 medium for 35 days (inset 55 days), **(b)** a pH 4 medium for 88 days (inset cross-section detail), **(c)** a pH 7 medium for 35 days (inset 21 days), **(d)** a pH 7 medium for 88 days, **(e)** a pH 10 medium for 35 days (insets 21 days and cross-section detail at 35 days) and **(f)** a pH 10 medium for 88 days (inset cross-section detail).

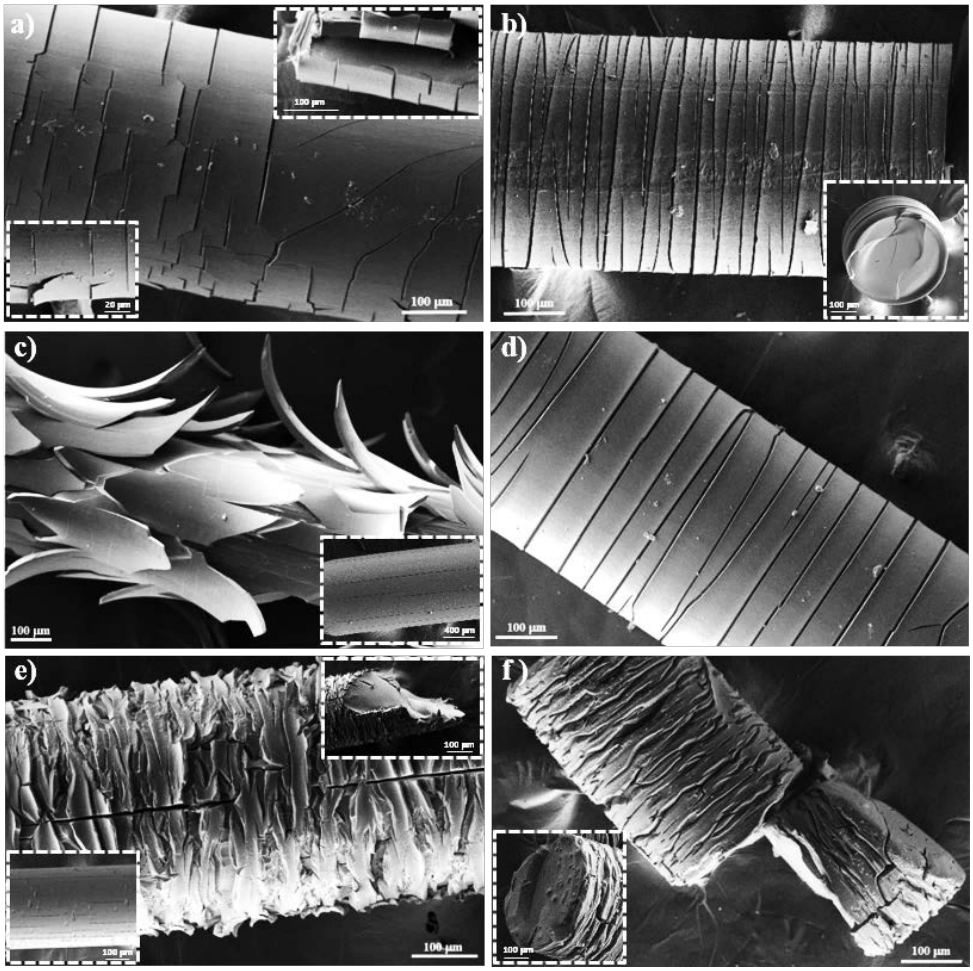

4.3.3.3. Changes on the lamellar parameters during hydrolytic degradation in different pH media

Lamellar structure of the non-irradiated and γ irradiated GL-*b*-(GL-*co*-TMC-*co*-CL)-*b*-GL samples gave rise to a strong meridional reflection in the SAXS pattern that corresponds to a L_B spacing close to 8.3-7.6 nm (e.g., Figure 4.3.14a for the γ irradiated sample). This high intensity suggests a large difference between the electronic density of amorphous and crystalline phases, which is in agreement with the tight packing of polyglycolide.[42] Slight differences on the degree of orientation can be detected, being in general lower after exposure to highly basic medium.

Both non-irradiated and γ irradiated samples exposed to the degradation media showed also the strong and oriented lamellar reflection (Figure 4.3.14 for representative γ irradiated samples) even when fibers began to lose their integrity. More interestingly the lamellar spacing clearly decreased in the advanced degradation stages from its initial value (e.g., 8.3 nm for the irradiated sample) to a spacing close to 5.40 nm that was reached just before the fiber integrity was lost (e.g., Figure 4.3.14a for fibers exposed to a pH 4 medium during 88 days). On the contrary, slight variations on the lamellar spacing were detected at all assayed pHs during the period associated to the molecular weight decrease (i.e., 0-35 days), namely just before to attain the asymptotic molecular weight (e.g., Figure 4.3.14a for irradiated fibers exposed to pHs 4, 7, 9 and 11, respectively). For example, a decrease from 8.3 to 7.7 nm was detected in this period at pH 4 (Figure 4.3.14a).

Characteristic lamellar parameters (i.e., long period, L_γ, amorphous layer thickness, l_a, and crystalline lamellar thickness, l_c) and crystallinity (i.e., crystallinity within the lamellar stacks, $X_c^{SAXS} = l_c / L_\gamma$) were determined by means of the normalized one-dimensional correlation function,[43] $\gamma(r)$:

$$\gamma(r) = \int_0^\infty q^2 I(q)\cos(qr)dq \; / \; \int_0^\infty q^2 I(q)dq \qquad (2)$$

where I is the intensity and q the scattering vector ($[4\pi/\lambda]$ sen θ).

SAXS data were collected within a limited angular range and consequently Vonk's model [44] and Porod's law were applied to perform extrapolations to low and high q values.

Correlation functions of representative degraded samples are displayed in Figure 4.3.14b, whereas the determined morphological parameters and crystallinities are summarized in Table 4.3.1.

Table 4.3.1. Morphological parameters of γ irradiated GL-*b*-(GL-*co*-TMC-*co*-CL)-*b*-GL samples during degradation in the indicated degradation media and exposure times.

pH	Time (days)	L_B (nm)	L_γ (nm)	l_c (nm)	l_a (nm)	X_c^{SAXS}
-	0	8.3	7.3	5.3	2.0	0.73
4	12	7.8	6.5	5.2	1.3	0.80
4	35	7.7	6.5	5.2	1.3	0.80
4	88	5.4	5.2	4.2	1.0	0.79
7	35	7.3	6.4	5.1	1.3	0.80
9	35	7.4	6.4	5.1	1.3	0.80
11	28	7.6	6.6	5.2	1.4	0.80

The one-dimensional correlation function is a relatively simple approximation and practicable method to derive the general structural differences of samples despite having some degree of orientation.[45] Additionally, it should be indicated that other methods have been developed to characterize more accurately samples with fiber symmetry (e.g., Chord Distribution Function [46,47]). The derived parameters indicate that degradation logically proceeded at the beginning of exposure through the molecular folds that constitute the interlamellar domains. Thus, l_c remained practically constant (i.e., 5.2-5.1 nm), whereas the amorphous layer thickness decreased from 2.0 to 1.3 nm (i.e., a reduction close to 35%). At the last stages of degradation the amorphous layer remained practically constant, being for example determined values close to 1.0 nm for l_a (i.e., a reduction close to 50%). At the same time the crystalline lamellar thickness started to decrease (i.e., a reduction of 21% corresponds to the observed change from 5.3 to 4.2 nm), which means that hydrolysis and depolymerisation affected the crystalline domains. In any case, the analysis demonstrates that the lamellar decrease was mainly caused by the disappearance of the amorphous layer as expected from a higher susceptibility to hydrolysis of the molecular folds placed on the lamellar surfaces.

Figure 4.3.14. (a) SAXS patterns of the initial γ irradiated GL-*b*-(GL-*co*-TMC-*co*-CL)-*b*-GL sample and after exposure to pH 4 for 12, 35 and 88 days, pH 7 for 35 days, pH 9 for 35 days and pH 11 for 28 days. Red arrows indicate the meridional fiber direction. **(b)** Comparison between correlation functions of γ irradiated GL-*b*-(GL-*co*-TMC-*co*-CL)-*b*-GL sample for: initial sample, after exposure to pH 4 for 12, 35 and 88 days.

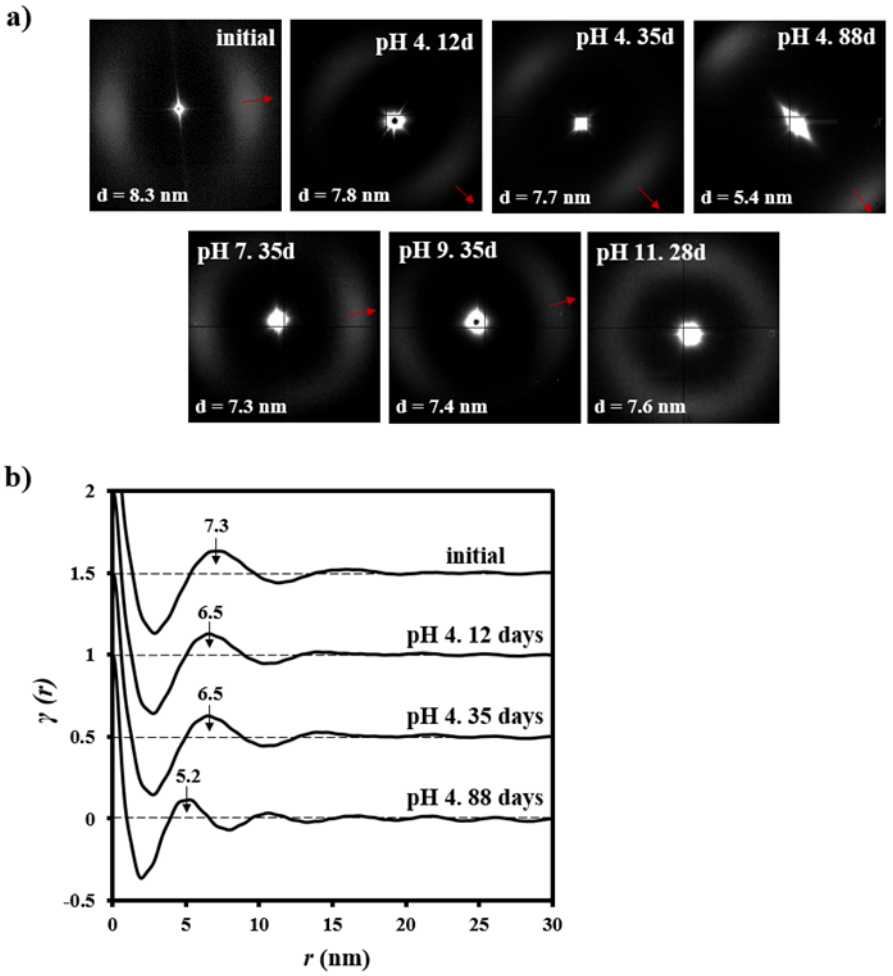

Correlation functions revealed also that initial samples had a broad distribution of the layer widths of the crystal phase since L_γ was higher than the long period determined from twice the value of the first minimum of the function (i.e., 5.6 nm respect to 7.3

nm). However, homogeneity increased during the first degradation step that involved the hydrolysis of the amorphous layer (e.g., 5.6 nm and 6.5 nm were determined for samples exposed for 12 and 35 days at the pH 4 medium). Logically, a wide distribution was again observed at the end when degradation affected the crystalline lamellar layers

4.3.3.4. Thermal annealing of degraded samples in different pH media: Repercussions on the lamellar morphology

The segmented polymer undergoes a lamellar reordering process on heating that causes an increase of the crystal thickness. Specifically, the irradiated sample had a change from an initial value of 8.3 nm to a spacing close to 20.8 nm that was attained just some degrees before fusion (Figure 4.3.15a). In addition, patterns also show how the corresponding arched reflections became highly oriented and adopted a circular shape, which evidenced an increase of the lamellar breadth and an irregular lamellar stacking.

Analysis of the correlation function (Figure 4.3.15b) demonstrates that the increase of the L_γ interlamellar spacing (from 7.3 nm to 16.8 nm) mainly corresponds to the regular increase of the crystalline lamellar thickness that changed from 5.3 nm to 13.8 nm, whereas a lower variation was found for the amorphous layer (i.e., from 2.0 to 3.0 nm). Nevertheless, the evolution of both spacing was proportional after achieving a temperature of 145 ºC and X_c^{SAXS} subsequently remained practically constant (i.e., close to 0.79-0.82).

Figure 4.3.15. (a) SAXS patterns of the initial γ irradiated GL-*b*-(GL-*co*-TMC-*co*-CL)-*b*-GL sample taken at representative temperatures during a heating run at 10 ºC/min (up). **(b)** Change on the correlation function during a heating run at 10 ºC/min of the initial γ irradiated GL-*b*-(GL-*co*-TMC-*co*-CL)-*b*-GL sample.

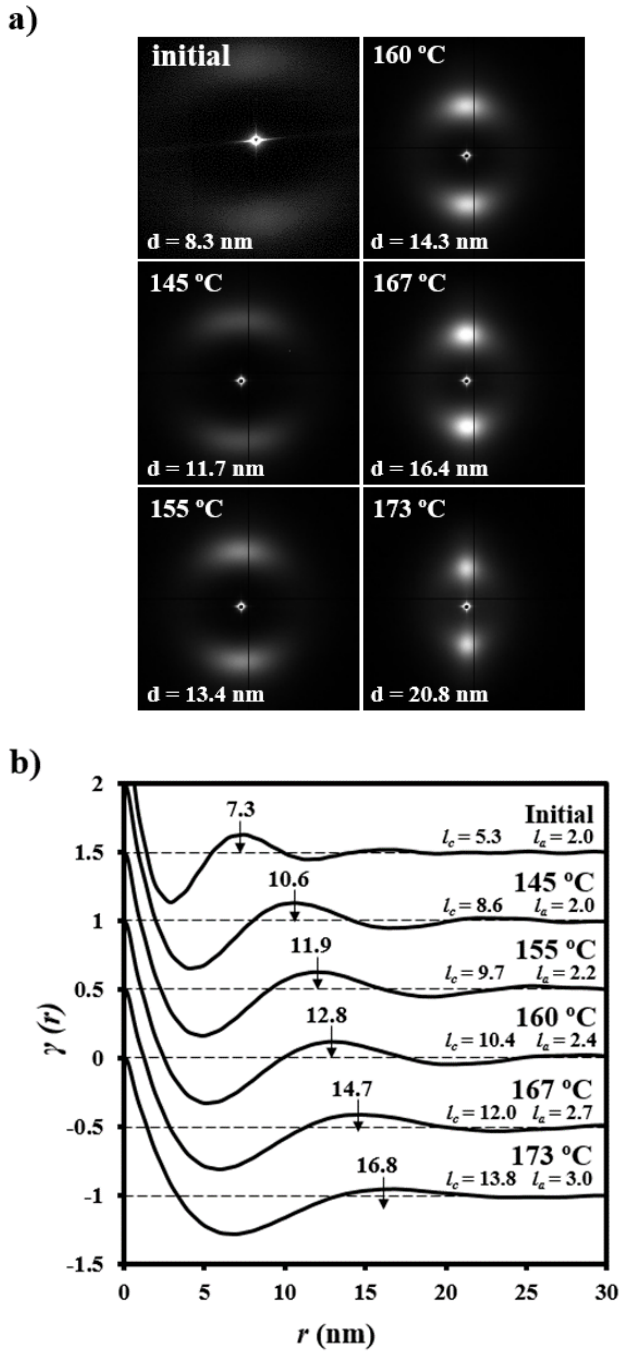

Lamellar microstructure is modified during hydrolytic degradation and consequently significant differences on the reordering process that occurs on heating should be expected not only respect the non-degraded sample but also between samples with different degree of degradation or exposed to different pH media. Figure 4.3.16 demonstrates the great differences on the evolution of SAXS patterns during heating for representative samples, being worthy of comment some observations that allow getting insight the initial fiber microstructure and how it was affected by degradation in the different media:

a) Samples degraded in acidic media basically showed the characteristic meridional reflections associated to the lamellar stacking. Firstly, these reflections had the previously indicated evolution when temperature was increased that led to an increase of both lamellar thickness and breadth. However, at the highest temperatures and especially for the most degraded samples (e.g., see patterns of samples degraded for 35 and 88 days), reflections were elongated in the meridional direction and extended towards the center of the pattern as presumable for a decrease of the crystalline domain size (i.e., the number of stacked lamellae). It is interesting to note that extrameridional reflections with a practically meridional orientation could also be detected during the heating of the less degraded samples (e.g., see arrow for the sample exposed for 12 days at pH 4). These spots suggest the sporadic formation and tilting of lamellae with a slightly greater thickness (i.e., 17.6 nm respect to 14.0 nm) that cannot be well accommodated in the surrounding and compact amorphous phase (Figure 4.3.9b). Note that solubilization of degradation products in the acidic medium was scarce at low exposure times.

b) An equatorial reflection is enhanced during heating of samples degraded at a neutral pH where the development of longitudinal cracks is characteristic. This reflection can be associated to the interfibrillar spacing (Figure 4.3.9b) which is greater than the interlamellar one (e.g., ca. 10.4 nm respect to ca. 12.3 nm as can be measured in the patterns shown in Figure 4.3.16). The regularity of interfibrillar domains was lost at the highest temperatures and consequently the corresponding reflection clearly disappeared before lamellar stacking was affected by partial fusion. Figure 4.3.16 also shows as equatorial reflections could still be detected at pH 9.

c) Patterns of samples exposed to basic pHs were more complicated since solubilization of degradation products allowed a greater readjustment/reorientation of constitutive lamellae. For example, the meridional reflection was splitted in the samples exposed to

pH 9, suggesting a slight tilting of lamellae according to opposite directions. Note that optical micrographs revealed the development of tortuous fiber morphologies during exposure to basic pHs (Figure 4.3.12). This lamellar tilting seems not appropriate to justify the regular six spot pattern detected at higher pH, being a plausible explanation the enhancement during degradation of a macrolattice arrangement where lamellar domains were disposed at different levels along the fiber axis as displayed in Figure 4.3.9.

Figure 4.3.16. SAXS patterns taken during a heating run at 10 ºC/min of γ irradiated GL-*b*-(GL-*co*-TMC-*co*-CL)-*b*-GL samples after being degraded in the indicated media and exposure times. Patterns in each row were acquired at increased temperatures from left to right. Red and blue arrows indicate the meridional and equatorial fiber directions.

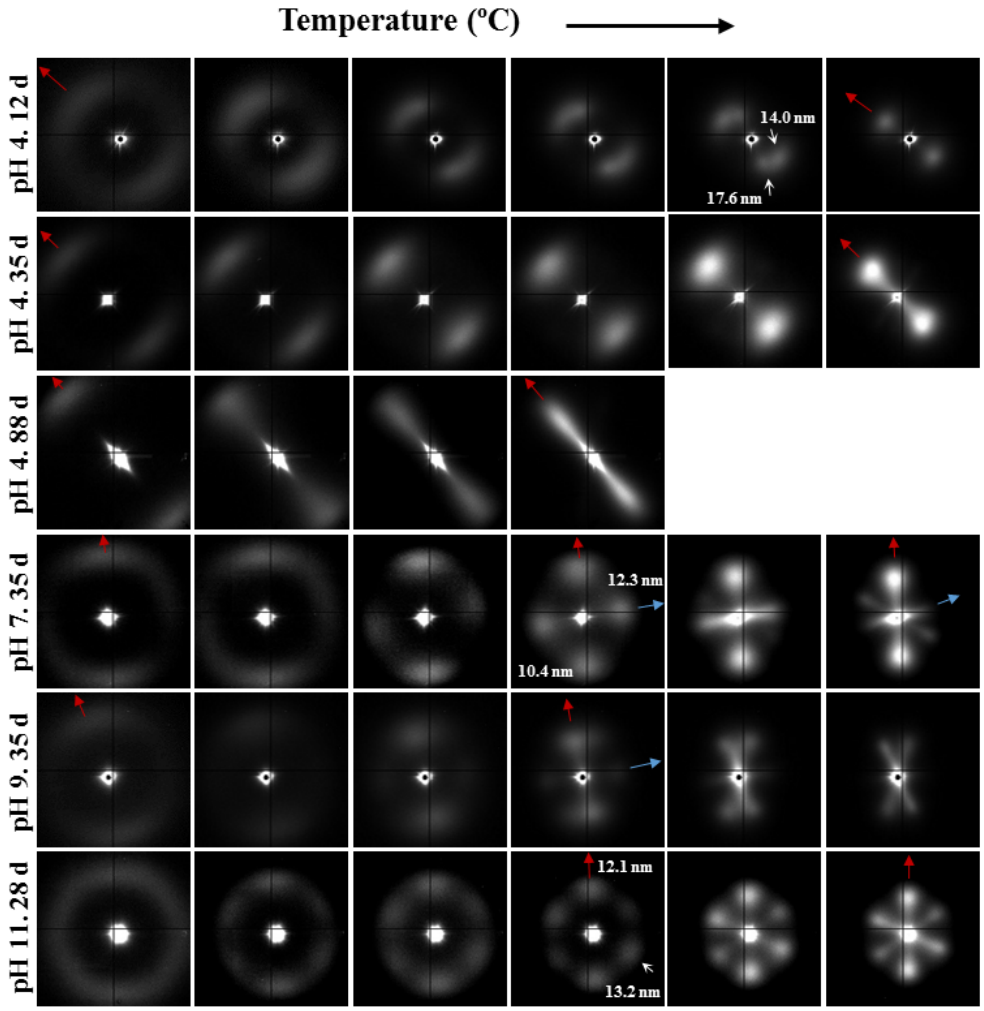

4.3.3.5. Change of lamellar parameters of degraded samples during subsequent non-isothermal crystallization and reheating processes

The complex lamellar structures obtained during the heating treatment of degraded fibers were not observed again after a non-isothermal crystallization from the melt state. Therefore, a homogeneous lamellar morphology was inferred for the spherulitic aggregates obtained by melt crystallization. A single and strong ring in the corresponding SAXS patterns (Figure 4.3.17a) was always detected, being also possible to get details of the lamellar stacking through the analysis of the well-defined correlation functions (Figure 4.3.17b). Nevertheless, small differences were detected between samples submitted at different degrees of degradation. The lamellar stacking of the non-degraded and γ irradiated GL-*b*-(GL-*co*-TMC-*co*-CL)-*b*-GL sample was characterized by L_B, L_γ, l_c and l_a values of 15.1, 12.8, 10.4 and 2.4 nm, respectively, which were clearly different from those observed for both the initial fiber and that submitted to the thermal annealing process. Specifically, long period L_γ was lower than attained after annealing (i.e., 12.8 nm with respect to 16.8 nm) as typical for a non-isothermal crystallization where lamellar insertion mechanism takes place at the ending stages due to the geometrical constraints imposed for the previously formed thicker lamellae. Note that in any case, l_c and l_a decreased in a proportional way giving rise to a similar X_c^{SAXS} crystallinity (i.e., 0.81).

Lamellar spacing clearly decreased with the degree of degradation, suggesting that the insertion mechanism was favoured. Note that L_B decreased to 10.9-10.6 nm and 8.6 nm for samples submitted to degradation for 28-35 days (i.e., the time required to reach the asymptotic molecular weight at a given pH) and 88 days, respectively. Note also that minimum changes were detected between samples exposed to different media but with similar degrees of degradation (e.g., pH 4 for 35 days and pH 11 for 28 days). The X_c^{SAXS} crystallinity of all these degraded samples was kept in the 0.81-0.80 range, obviously as a consequence of a proportional reduction of l_c and l_a. Therefore, the smaller and even more regular molecular fragments (i.e., those enriched on polyglycolide hard blocks) formed during degradation did not cause a significant variation of X_c^{SAXS} crystallinity.

Figure 4.3.17. SAXS patterns **(a)** and corresponding correlation functions **(b)** at the end of a cooling run performed at 10 ºC/min from the melt state of γ irradiated GL-*b*-(GL-*co*-TMC-*co*-CL)-*b*-GL samples before and after being degraded at pH 4 for 35 days, pH 11 for 28 days and pH 2 for 88 days.

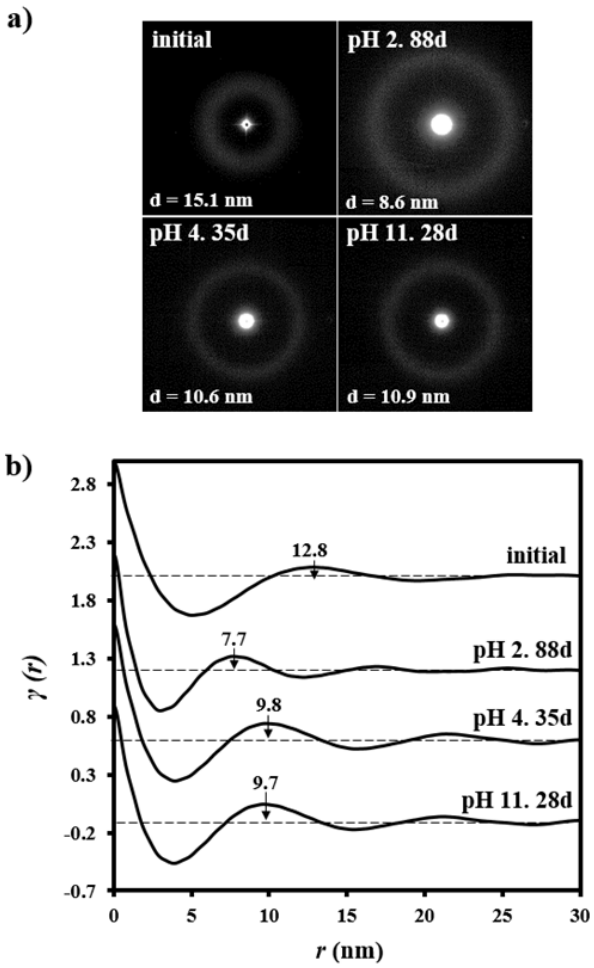

Subsequent heating runs demonstrated the capability of degraded polymers to experiment again reordering processes that led to a lamellar thickening (Figure 4.3.18 for a representative sample degraded at pH 9 for 35 days). Final long periods (L_γ) were lower than attained with the non-degraded polymers (e.g., 13.6 with respect to 16.8 nm) also in agreement with the lower spacing observed when non-isothermally crystallized samples were compared (Figure 4.3.17b). Correlation functions showed that both l_c and l_a values increased during the reordering process in such a way that X_c^{SAXS} was again practically

constant (i.e., 0.82) and comparable to that attained with the non-degraded sample. Figure 4.3.18 also highlighted the great difference between the lamellar structure of degraded fibers and that obtained after the thermal annealing of the corresponding melt crystallized spherulites. Thus, for example L_γ drastically changed from 6.4 to 13.6 nm.

Figure 4.3.18. SAXS patterns and correlation functions of a γ irradiated GL-*b*-(GL-*co*-TMC-*co*-CL)-*b*-GL sample degraded at pH 9 for 35 days that were obtained from sample directly extracted from the degradation medium and at different temperatures during a second heating run performed at 10 ºC/min. Red arrow indicate the fiber direction.

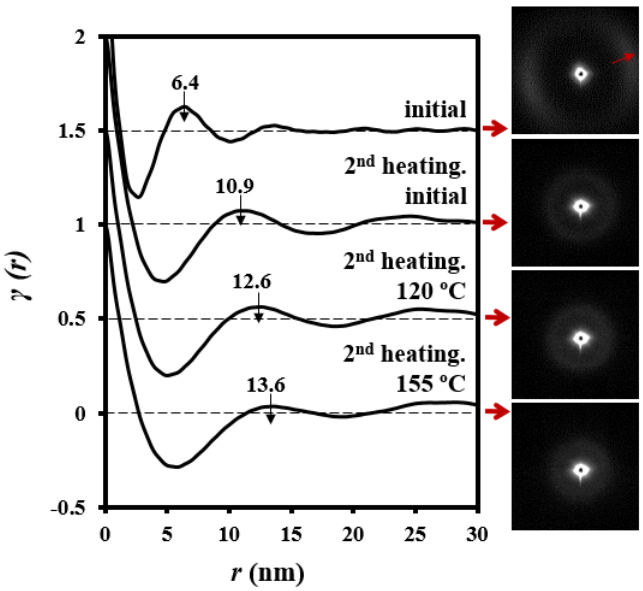

4.3.4. CONCLUSIONS

Hydrolytic degradation of the segmented GL-*b*-(GL-*co*-TMC-*co*-CL)-*b*-GL copolymers took place faster after being γ irradiated despite this treatment caused also cross-linking reactions and a slight increase of the initial molecular weight. Samples exposed to hydrolytic media experienced a quick decrease of the molecular weight until a constant value was reached but weight loss was still observed for longer exposure times. The gradual increase of the pH of the media caused also a progressive acceleration of degradation due to the greater solubilization of decomposition products and the modification of the hydrolysis mechanism.

Degraded fibers showed complex morphological changes that varied according to the pH of the medium. These changes involved the formation of longitudinal (at pHs equal or greater than 5) and circumferential (at all pHs) cracks and peeling (at pHs between 6 and 8).

Small angle X-ray scattering patterns of degraded samples indicated a fast hydrolysis of chains placed in the interlamellar domains followed by a continuous attack to the crystalline domains. Furthermore, the existence of interfibrillar amorphous domains was clearly highlighted during exposure to neutral and basic media, namely when formation of longitudinal cracks was enhanced.

Subsequent annealing processes performed with degraded fibers demonstrated the capability to experiment a reordering process that increased the lamellar thickness and also the lamellar breadth. Specifically, the evolution of patterns allowed detecting changes associated to lamellar tilting and structural features such as the presence of interfibrillar domains and the disposition of lamellar crystals at different levels along the fiber axis for a given cross-section.

Degraded samples were able to crystallize from the melt giving rise to aggregates with a lamellar structure that was clearly distinct than that observed in the initial fibers. Furthermore, differences were also detected between samples submitted at different levels of degradation. Specifically, lamelar thickness decreased when the hydrolytic attack was more aggressive as determined for both non-isothermally crystallized samples before and after a subsequent thermal annealing process.

4.3.5. REFERENCES

1. Middleton, J. C. & Tipton, A. J. Synthetic biodegradable polymers as orthopedic devices. *Biomaterials* **21**, 2335–2346 (2000).

2. Griffin Lewis, O. & Fabisial, W. Sutures. In *Kirk-Othmer encyclopedia of chemical technology* 4th Ed. Wiley, New York, USA (1997).

3. Gilding, D. K. & Reed, A. M. Biodegradable polymers for use in surgery-polyglycolic-poly(lactic acid) homopolymers and copolymers. *Polymer* **2**, 1459–1464 (1979).

4. Homsy, C. A., Mcdonald, E. R. & Akers, W. W. Surgical suture-canine tissue interaction for six common suture types. *J. Biomed. Mater. Res.* **2**, 215–230 (1968).

5. Blomstedt, B. & Ostenberg, B. Suture materials and wound infection. An experimental study. *Acta Chir. Scand.* **144**, 269–274 (1978).

6. Rodeheaver, G. T. *et al.* Knotting and handling characteristics of coated synthetic absorbable sutures. *J. Surg. Res.* **35**, 525–530 (1983).

7. Katz, A. R., Mukherjee, D. P., Kaganov, A. L. & Gordon, S. A new synthetic monofilament absorbable suture made from polytrimethylene carbonate. *Surgery, Gynecol. Obstet.* **161**, 213–222 (1985).

8. Zurita, R., Puiggalí, J., Franco, L. & Rodríguez-Galán, A. copolymerization of glycolide and trimethylene carbonate. *J. Polym. Sci. Part A Polym. Chem.* **44**, 993–1013 (2005).

9. Kasperczyk, J. Copolymerization of glycolide and ε -caprolactone , 1 Analysis of the copolymer microstructure by means of ^{1}H and ^{13}C-NMR spectroscopy. *Macromol. Chem. Phys.* **200**, 903–910 (1999).

10. Díaz-Celorio, E., Franco, L., Rodríguez-Galán, A. & Puiggalí, J. Synthesis of glycolide/trimethylene carbonate copolymers: Influence of microstructure on properties. *Eur. Polym. J.* **48**, 60–73 (2012).

11. Noorsal, K., Mantle, M. D., Gladden, L. F. & Cameron, R. E. Degradation and drug-release studies of a poly(glycolide-*co*-trimethylene carbonate) copolymer (Maxon). *J. Appl. Polym. Sci.* **95**, 475–486 (2005).

12. Díaz-Celorio, E., Franco, L., Rodríguez-Galán, A. & Puiggalí, J. Study on the hydrolytic degradation of glycolide/trimethylene carbonate copolymers having different microstructure and composition. *Polym. Degrad. Stab.* **98**, 133–143 (2013).

13. Freudenberg, S. *et al.* Biodegradation of absorbable sutures in body fluids and pH buffers. *Eur. Surg. Res.* **36**, 376–385 (2004).

14. Farrar, D. & Gillson, R. Hydrolytic degradation of polyglyconate B: the relationship between degradation time, strength and molecular weight. *Biomaterials* **23**, 3905–3912 (2002).

15. Ahmed, H. A. & Goldie, B. S. Comparison of the mechanical properties of polyglycolide-trimethylene carbonate (Maxon) and polydioxanone suture (PDSII) used for flexor tendon repair and active mobilization. *J. Hand Surg. Am.* **27B**, 329–332 (2002).

16. Mäkelä, P., Pohjonen, T., Törmalä, P., Waris, T. & Ashammakhi, N. Strength retention properties of self-reinforced poly L-lactide (SR-PLLA) sutures compared with polyglyconate (Maxon (R)) and polydioxanone (PDS) sutures. An in vitro study. Biomaterials **23**, 2587–2592 (2002).

17. Díaz-Celorio, E., Franco, L. & Puiggalí, J. Isothermal crystallization study on a biodegradable segmented copolymer constituted by glycolide and trimethylene carbonate units. *J. Appl. Polym. Sci.* **116**, 577–589 (2010).

18. Díaz-Celorio, E., Franco, L. & Puiggalí, J. Nonisothermal crystallization behavior of a biodegradable segmented copolymer constituted by glycolide and trimethylene carbonate units. *J. Appl. Polym. Sci.* **119**, 1548–1559 (2011).

19. Tomihata, K., Suzuki, M. & Ikada, Y. The pH dependence of monofilament sutures on hydrolytic degradation. J. Biomed. Mater. Res. **58**, 511–518 (2001).

20. Díaz-Celorio, E., Franco, L. & Puiggalí, J. Influence of microstructure on the crystallization of segmented copolymers constituted by glycolide and trimethylene carbonate units. *Express Polym. Lett.* **7**, 186–198 (2013).

21. Oberhoffner, S. & Planck, H. Surgical suture material from triblockterpolymer, its use in surgery and process for its preparation. EP 0835895 (2003).

22. Barber, F. A. Resorbable fixation devices: a product guide. *Orthop. Spec. Ed.* **4**, 1111–1117 (1998).

23. Roby, M. S., Bennet, S. L. & Liu, E. K. Absorbable block copolymers and surgical articles fabricated thereform. U.S.Patent 5.403.347. (1995).

24. Pineros-Fernández, A. *et al.* CAPROSYN*, Another major advance in synthetic monofilament absorbable suture. *J. Long. Term. Eff. Med. Implants* **14**, 359–368 (2004).

25. Martínez-Barrera, G. & Brostow, W. Fiber-reinforced polymer concrete: Property improvement by gamma irradiation. In *Gamma radiation effects on polymeric materials and its applications.* Barrera, C. Ed, Kerala, India 27–44 (2009).

26. D'Alelio, G. F., Haberli, R. & Pezdirtz, G. F. Effect of ionizing radiation on a series of saturated polyester. *J. Macromol. Sci. Chem.* **2**, 501-588 (1968).

27. Zhang, L., Loh, I. H. & Chu, C. C. A combined gamma irradiation and plasma deposition treatment to achieve that ideal degradation properties of synthetic absorbable polymers. *J. Biomed. Mater. Res.* **27**, 1425-1141 (1993).

28. Chu, C. C. & Williams, D. F. The effect of gamma irradiation on the enzymatic degradation of polyglycolic acid absorbable sutures. *J. Biomed. Mater. Res.* **17**, 1029–1040 (1983).

29. Márquez, Y., Franco, L., Turon, P., Rodríguez-Galán, A. & Puiggalí, J. Study on the hydrolytic degradation of the segmented GL-*b*-(GL-*co*-TMC-*co*-CL)-*b*-GL copolymer with application as monofilar surgical suture. *Polym. Degrad. Stab.* **98**, 2709-2721 (2013).

30. Theorell, T. & Stenhagen, E. Ein Universalpuffer fiir den pH-Bereich 2.0 bis 12.0. *Biochem. Z.* **299**, 416–419 (1939).

31. Lin, H. L., Chu, C. C. & Grubb, D. Hydrolytic degradation and morphologic study of poly-*p*-dioxanone. *J. Biomed. Mater. Res.* **27**, 153–166 (1993).

32. McIntyre, J. E. Polyester Fibres. In *Handbook of Fibre and Technology: Fibre Chemistry.* Eds. Lewin, M. & Pearce, E. M., Marcel Dekker Inc., New York, USA 1–73 (1998).

33. Li, S. M. Hydrolytic degradation characteristics of aliphatic polyesters derived from lactic and glycolic acids. *J. Biomed. Mater. Res. Part B Appl. Biomater.* **48B**, 342–353 (1999).

34. Fischer, E. W., Sterzel, H. J. & Wegner, G. Investigation of the structure of solution grown crystals of lactide copolymers by means of chemical reactions. *Kolloid Z Z Polym* **251**, 980–990 (1973).

35. Fredericks, R. J., Melveger, A. J. & Dolegiewtz, L. J. Morphological and structural changes in a copolymer of glycolide and lactide occuring as a result of hydrolysis. *J. Polym. Sci. Phys. Ed.* **22**, 57–66 (1984).

36. Wu, L. & Ding, J. Effects of porosity and pore size on *in vitro* degradation of three-dimensional porous poly(D,L-lactide-co-glycolide) scaffolds for tissue engineering. *J. Biomed. Mater. Res. A* **75**, 767–77 (2005).

37. Fernández, J., Larrañaga, A., Etxeberria, A. & Sarasua, J. R. Effects of chain microstructures and derived crystallization capability on hydrolytic degradation of poly(L-lactide/ε-caprolactone) copolymers. *Polym. Degrad. Stab.* **98**, 481–489 (2013).

38. Kulkarni, A., Reiche, J. & Lendlein, A. Hydrolytic degradation of poly(rac-lactide) an poly[(rac-lactide)-*co*-glycolide] at the air water interface. *Surf. Interface Anal.* **39**, 740–746 (2007).

39. Yoshioka, T., Kawazoe, N., Tateishi, T. & Chen, G. *In vitro* evaluation of biodegradation of poly(lactic-*co*-glycolic acid) sponges. *Biomaterials* **29**, 3438–3443 (2008).

40. Peterlin, A. Morphology and properties of crystalline polymers with fiber structure. *Text. Res. J.* **42**, 20 (1972).

41. Murthy, N. S., Reimschuessel, A. C. & Kramer, V. Changes in void content and free volume in fibers during heat setting and their influence on dye diffusion and mechanical properties. *J. Appl. Polym. Sci.* **40**, 249–262 (1990).

42. Chatani, Y., Suehiro, K., Okita, Y., Tadokoro, H. & Chujo, K. Structural studies of polyesters. I Crystal structure of polyglycolide. *Die Makromolekulare Chemie* **113**, 215–229 (1968).

43. Vonk, C. G. & Kortleve, G. X-ray small-angle scattering of bulk polyethylene. *Kolloid Z Z Polym* **220**, 19–24 (1967).

44. Vonk, C. G. A general computer program for the processing of small-angle X-ray scattering data. *J. Appl. Crystallogr.* **8**, 340–341 (1975).

45. Hsiao, B. S. & Verma, R. K. A novel approach to extract morphological variables in crystalline polymers from time-resolved SAXS measurements. *J. Synchrotron Radiat.* **5**, 23–29 (1998).

46. Stribeck, N. Extraction of domain strucure information from small angle scattering patterns of bulk materials. *J. Appl. Crystallogr.* **34**, 496–503 (2001).

47. Stribeck, N. & Fakirov, S. Three-dimensional chord distribution function SAXS analysis of the strained domain structure of a poly(ether ester) thermoplastic elastomer. *Macromolecules* **34**, 7758–7761 (2001).

5.

CRYSTALLIZATION STUDIES OF POLY(*p*-DIOXANONE) MONOFILAR SURGICAL SUTURE

5.1. Study of non-isothermal crystallization and analysis of morphological changes occurring during heating and cooling processes

Non-isothermal crystallization kinetic of polydioxanone (PDO), a polymer with well-established applications as bioabsorbible monofilar suture, was investigated by Avrami, Mo and isoconversional methodologies. Results showed Avrami exponents ranging in a relatively narrow range (i.e., between 3.76 and 2.77), which suggested a three-dimensional spherulitic growth and instantaneous nucleation at high cooling rates. The nucleation mechanism changed to sporadic at low rates, with both crystallization processes being detected in the DSC cooling traces. Formation of crystals was hindered as the material crystallized because of a decrease in the motion of molecular chains. Two secondary nucleation constants were derived from calorimetric data by applying the methodology proposed by Vyazovkin and Sbirrazzuoli through the estimation of effective activation energies. In fact, typical non-isothermal crystallization analysis based on the determination of crystal growth by optical microscopy allowed secondary nucleation constants of 3.07×10^5 K^2 and 1.42×10^5 K^2 to be estimated.

Microstructure of sutures was characterized by a stacking of lamellae perpendicularly oriented to the fiber axis and the presence of interlamellar and interfibrillar amorphous regions. The latter became enhanced during heating treatments due to loss of partial chain orientation and decrease of electronic density. Degradation under different pH media revealed different macroscopic morphologies and even a distinctive evolution of lamellar microstructure during subsequent heating treatments.

5.1.1. INTRODUCTION

Poly(*p*-dioxanone) (PDX or PDO) is a synthetic poly(ester-ether) with wide applications in the biomedical field due to its excellent properties (e.g., biodegradability, biocompatibility, bioabsorbability, softness and flexibility).[1] In relation to polyglycolide, i.e., the first polyester employed for biomedical applications, the chemical repeat unit of PDO has an ether bond and additional methylene groups that provide greater flexibility. In this way, PDO can be employed as a monofilar surgical suture, in contrast with the braided polyglycolide suture. PDO can be completely reabsorbed in a period close to 6 months, with no significant foreign body reaction being observed in the tissues surrounding the implant.

Several companies have commercialized PDO under different trademarks (e.g., PDS II and MonoPlus® by Ethicon and B. Braun Surgical S.A., respectively) as a long term surgical suture that appears as an ideal wound support for healing periods longer than 4 weeks. Other biomedical applications such as bone or tissue fixation devices, fasteners and drug delivery systems[2] should also be considered since the polymer can be easily injection-molded.

Isothermal crystallization of PDO has been extensively studied by different techniques including polarized optical microscopy and differential scanning calorimetry.[3–8] Changes in morphological parameters have also been evaluated by small-angle X-ray scattering.[9] Several works have been focused on the influence of degradation on morphology and isothermal crystallization behavior.[10–12]

Surprisingly, only few reports concern the crystalline structure of PDO and lead to some conflicting results. Thus, early studies pointed to an orthorhombic unit cell containing only two molecular segments with a tight pitch (i.e., the chain axis repeat was shortened by 52% compared to the expected value for an extended zig-zag conformation).[13] Subsequently, an orthorhombic unit cell with space group $P2_12_12_1$ and parameters a = 0.970 nm, b = 0.751 nm and c (chain axis) = 0.650 nm was postulated using X-ray and electron diffraction data.[14] The structural model was also supported by quantum mechanical calculations that indicated a chain periodicity given by a single residue with a TGT(-G)TT conformation and a unit cell containing four molecular segments. Crystals obtained from solution had a variable morphology (i.e., the acute apex angle of lozenge crystals varies with the crystallization conditions) that seems a consequence of the peculiar structure of PDO, where different folds for adjacent chain re-entry exists.[14]

It is well established that isothermal crystallization of PDO from the melt renders spherulites with a distinctive morphology depending on the crystallization temperature. Specifically, spherulites obtained at high temperature were double-ringed [3] whereas at low temperature they showed a negative birefringence and the typical Maltese cross. Isothermal crystallization kinetic studies linked the different morphologies to two crystallization regimes.[3] Ringed and negative birefringent spherulites were observed by evaporation of concentrated formic acid solutions. It was demonstrated that the *a* crystallographic axis of constitutive lamellae was oriented along the spherulite radius.[14]

Non-isothermal crystallization of PDO has been scarcely studied despite the fact that melt-processed samples (e.g., bioabsorbable surgical sutures) are obtained under non-isothermal conditions. However, some non-isothermal melt crystallization analyses have been performed from DSC data and by applying Ozawa[15] and Cazé[16] methodologies to evaluate Avrami exponents.[4] Values calculated by Ozawa were dependent on the temperature, whereas two different values of the Avrami exponent were determined depending on the cooling rate.[6] Non-isothermal cold crystallization has also been evaluated by calorimetric analysis[17] and Avrami,[18,19] Ozawa[15] and Tobin[20] methodologies. In this case, results suggested that the Avrami method was more effective in describing non-isothermal cold crystallization kinetics, with reported values of Avrami exponent in the 4.5-5.3 range.[17]

PDO has a limited use, for example, as blow processed films due to its low crystallization rate and melt strength, together with its high cost and relatively low thermal stability. Therefore, non-isothermal crystallization studies have mainly focused on blends of PDO with other polymers such as poly(vinyl alcohol) [21] and polylactide [22]. It is assumed that crystallization rate should be enhanced in blends. Thus, an improvement of properties and easier processing were determined.

The purpose of the present work is to perform a complete analysis of non-isothermal crystallization considering both the overall kinetic process from DSC data and crystal growth rates from optical microscopy data. Furthermore, morphological changes occurring during heating and cooling processes are analyzed by real time synchrotron experiments. Dynamic diffraction data from samples degraded under different pHs were useful in confirming a lamellar organization inside fibers. In this way, recent studies on degraded monofilament sutures constituted by polyglycolide hard blocks have highlighted a structural organization with interlamellar and interfibrillar domains.[23]

5.1.2. EXPERIMENTAL SECTION

5.1.2.1. Materials

Granulated PDO and processed PDO sutures (Monoplus®, USP 0) were kindly supplied by B. Braun Surgical, S.A. Number and weight average molecular weights determined by GPC were 112,800 and 250,000 for the granulated material and 103,000 and 226,300 for the commercial threads, respectively.

5.1.2.2. Measurements

Molecular weights were estimated by size exclusion chromatography (GPC) using a liquid chromatograph (Shimadzu, model LC-8A) equipped with an Empower computer program (Waters). A PL HFIP gel column (Polymer Lab) and a refractive index detector (Shimadzu RID-10A) were employed. The polymer was dissolved and eluted in 1,1,1,3,3,3-hexafluoroisopropanol containing CF_3COONa (0.05 M) at a flow rate of 1 mL/min (injected volume 100 µL, sample concentration 2.0 mg/mL). The number and weight average molecular weights were calculated using polymethyl methacrylate standards.

Calorimetric data were obtained by differential scanning calorimetry with a TA Instruments Q100 series with T_{zero} technology and equipped with a refrigerated cooling system (RCS). Experiments were conducted under a flow of dry nitrogen with a sample weight of approximately 5 mg and calibration was performed with indium. T_{zero} calibration required two experiments: the first was performed without samples while sapphire disks were used in the second. Thermal characterization was conducted following a protocol consisting in a heating run (3 °C/min), a cooling run (3 °C/min) after keeping the sample in the melt state for 5 min to wipe out the thermal history and a subsequent heating run (3 °C/min). Non-isothermal crystallization studies were performed by cooling the previously molten samples (5 min at 125 °C) at rates varying from 30 to 1 °C/min.

The spherulitic growth rate was determined by optical microscopy using a Zeiss Axioskop 40 Pol light polarizing microscope equipped with a Linkam temperature control system configured by a THMS 600 heating and freezing stage connected to a LNP 94 liquid nitrogen cooling system. Spherulites were grown from homogeneous thin films prepared from the melt. Small sections of these films were pressed or smeared between two cover slides and inserted into the hot stage, giving rise to samples with thicknesses close to 10

μm in all cases. Samples were kept at approximately 125 °C for 5 min to eliminate sample history effects. The radius of growing spherulites was monitored during crystallization with micrographs taken with a Zeiss AxiosCam MRC5 digital camera at appropriate time intervals. A first-order red tint plate was employed to determine the sign of spherulite birefringence under crossed polarizers.

In vitro hydrolytic degradation assays were carried out at a physiological temperature of 37 °C using a pH 7.4 phosphate buffer (Sörensen medium: 19.268 g of $Na_2HPO_4 \cdot 12H_2O$ and 1.796 g of KH_2PO_4 in 1L of deionized water) and a pH 11 from the Universal buffer (citrate-phosphate-borate/HCl) solution, mixing 20 mL of a stock solution with 14.7 mL of 0.1 M HCl and distilled water up to a volume of 100 mL. The stock solution (1 L) contained 100 mL of citric acid and 100 mL of phosphoric acid solution, each of which was equivalent to 100 mL NaOH 1M, 3.54 g of boric acid and 343 mL of 1 M NaOH. Samples were kept under orbital shaking in bottles filled with 50 mL of the degradation medium and sodium azide (0.03 wt-%) to prevent microbial growth for selected exposure times. The samples were then thoroughly rinsed with distilled water, dried to constant weight under vacuum and stored over P_4O_{10} before analysis. Finally, weight retention and molecular weight were then evaluated.

Time resolved SAXS experiments were conducted at the NCD beamline (BL11) of the Alba synchrotron radiation light facility of Cerdanyola del Vallès (Catalunya). The beam was monochromatized to a wavelength of 0.1 nm. Polymer samples were confined between Kapton films and then held on a Linkam THMS600 hot stage with temperature control within ± 0.1 ºC. SAXS profiles were acquired during heating and cooling runs in time frames of 20 s and rates of 10 ºC/min. The SAXS patterns were calibrated with diffractions of a standard of a silver behenate sample. The diffraction profiles were normalized to the beam intensity and corrected considering the empty sample background. The correlation function and corresponding parameters were calculated with the CORFUNC program for Fiber Diffraction / Non-Crystalline Diffraction provided by the Collaborative Computational Project 13.

5.1.3. RESULTS AND DISCUSSION

5.1.3.1. Melting and crystallization

Thermal behavior of PDO is rather complicated, as revealed by the DSC curves in Figure 5.1.1.

Figure 5.1.1. DSC traces corresponding to heating runs of commercial granulated PDO **(a)** and PDO suture **(d)**, the cooling run of the melted granulated PDO **(b)** and the subsequent heating run **(c)**. Glass transition can be detected in the magnification given in the inset in **(c)**. All scans were performed at a rate of 3 ºC/min.

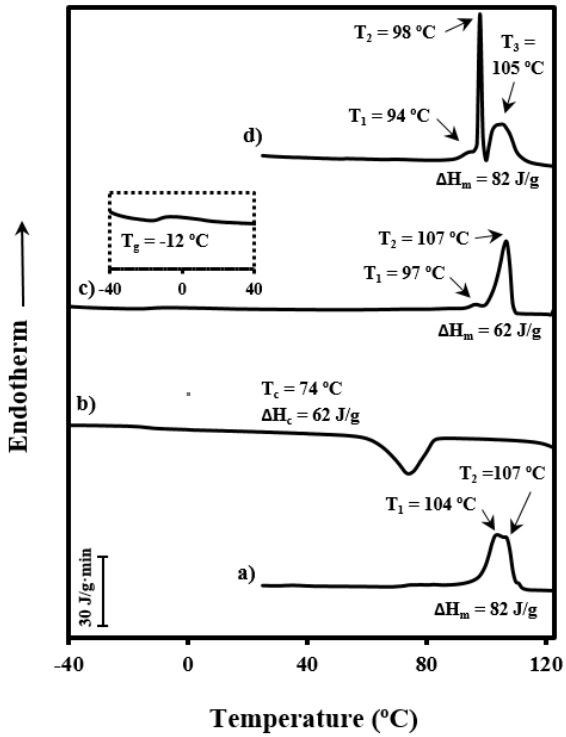

Heating traces are clearly different for commercial granulated samples crystallized from the melt and processed surgical sutures, demonstrating the significant influence of thermal treatments on melting behavior. Thus, two well-differentiated endothermic melting peaks at 97 ºC (small) and 107 ºC were observed when samples crystallized from the melt state at a rate of 3 ºC/min. These peaks have been largely discussed [6,7] and attributed to a typical lamellar reorganization process that leads to a lamellar thickening

during heating. Commercial granulated PDO showed that the high temperature peak was split into two equally intense peaks at 104 ºC and 107 ºC. Therefore, the population of thinner crystals was not present in the manufactured PDO form or at least were sufficiently energetically unstable to lead a complete recrystallization process on heating. Probably two populations of new crystals with practically the same thickness existed. The double peak appearing in the 104 ºC-107 ºC range was also detected in the heating run of the as-processed suture, but in this case the population of thinner crystals was highly stable and did not undergo a recrystallization process. Note the intense and narrow peak around 98 ºC, which in this case was observed as a consequence of an annealing process that was performed at high temperature which stabilized thinner lamellae.

Figure 5.1.2 shows the dynamic DSC exotherms obtained by cooling the melted samples at different rates. Crystallization peaks progressively shift to lower temperatures as the cooling rate increases, as expected, but peaks become broader. Two different crystallization processes seemed to occur at cooling rates equal or higher than 15 ºC/min, a feature that should be discussed on the basis of different nucleation mechanisms (i.e., instantaneous and sporadic at low and high temperatures, respectively).

Figure 5.1.2. Exothermic DSC traces performed at the indicated cooling rates. The dashed ellipse contains the high temperature crystallization peak detected at high cooling rates, whereas the dashed arrow indicates the evolution of the main crystallization peak.

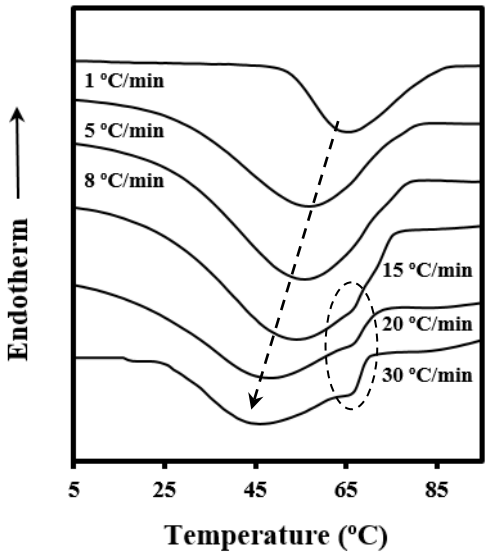

5.1.3.2. Non-isothermal kinetic analysis of poly(*p*-dioxanone) melt crystallization from DSC data

The process of crystallization under non-isothermal conditions is too complicated to be analyzed since crystallization from the melt takes place under different degrees of supercoolings, and therefore caution should be taken when interpreting experimental results.

Calorimetric data were used to determine the relative degree of crystallinity at any temperature, χ (T), for all cooling rates by the expression

$$\chi(T) = \frac{\int_{T_0}^{T_c} (dH_c / dT) dT}{\int_{T_0}^{T_\infty} (dH_c / dT) dT} \quad (1)$$

where dH_c is the enthalpy of crystallization released within an infinitesimal temperature range dT, T_0 denotes the initial crystallization temperature and T_c and T_∞ are the crystallization temperature at time t and after completion of the crystallization process, respectively. Thus, the denominator corresponds to the overall enthalpy of crystallization for specific heating/cooling conditions.

The relative degree of crystallinity was calculated as a function of time by the relationship:

$$(t - t_0) = (T_0 - T) / \phi \quad (2)$$

where T_0 is the temperature at which crystallization begins ($t = t_0$) and ϕ is the value of the cooling rate.

Figure 5.1.3 illustrates the variation of the time-dependent degree of crystallinity, $\chi (t - t_0)$, at different cooling rates, which allows a typical Avrami analysis to be performed [18] according to the equation:

$$1 - \chi(t - t_0) = \exp [-Z (t - t_0)^n] \quad (3)$$

where Z is the rate constant and n is the Avrami exponent. A normalized rate constant, $k = Z^{1/n}$, is however more useful for comparison since its dimension (time^{-1}) becomes independent of the Avrami exponent.

Figure 5.1.3. Time evolution of relative crystallinity at the indicated cooling rates for non-isothermal crystallization of PDO.

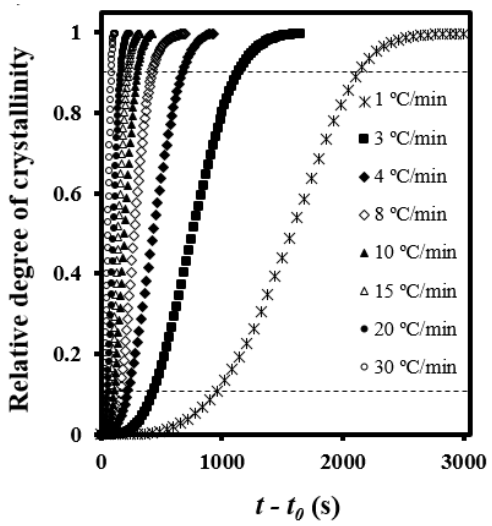

Figure 5.1.4 shows the plots of $\log\{-\ln[1-\chi(t-t_0)]\}$ versus $\log(t-t_0)$ at different cooling rates. A good linearity was observed between the relative degree of crystallinities of 0.10 and 0.90, that is, after formation of well-defined spherulitic morphologies and before occurrence of a secondary crystallization caused by the impingement of spherulites (see dashed lines in Figure 5.1.3).

Figure 5.1.4. Avrami analyses for non-isothermal crystallizations of PDO.

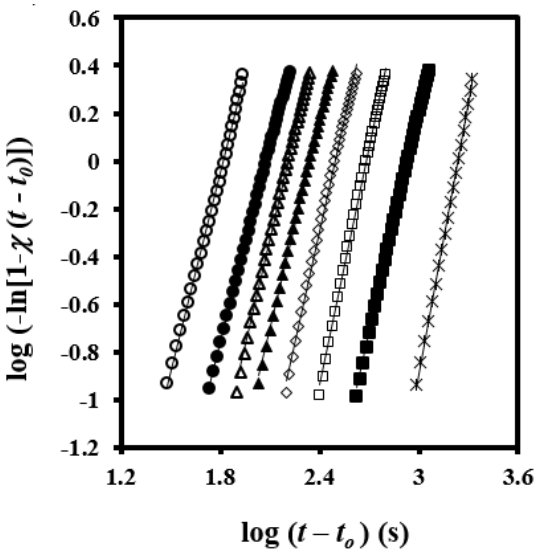

Table 5.1.1 summarizes the main kinetic parameters calculated by the Avrami analysis. As known from isothermal studies, the normalized rate constant was low (i.e., between 0.64 × 10^{-3} s^{-1} and 17.14 × 10^{-3} s^{-1}) and increased with the cooling rate. Avrami exponents showed a moderate variation (i.e., between 3.76 and 2.77), with the lowest values being determined for high cooling rates and the average value being close to 3.0. These exponents are lower than those previously reported by Zhang *et al.* [22] (i.e., 4.26-3.40) and in good agreement with those given by Andjelic *et al.* [4] for low crystallization rates (i.e., 3.0), although in this case a value of 1.1 was found for high crystallization rates. Isothermal crystallization studies also indicate slightly contradictory values. Thus, minimum changes with crystallization temperature were determined by Andjelic *et al.* (i.e., exponents varied between 2.22 and 2.62, with 2.5 being the average value),[4] but a systematic increase (i.e., from approximately 2 to 3.8) was also reported [6] for higher isothermal crystallization temperatures (i.e., from 30 to 80 ºC). The last behavior was interpreted as a consequence of a change from instantaneous to sporadic nucleation as T_c was increased.[6]

Table 5.1.1. Main non-isothermal crystallization kinetic parameters of PDO determined by DSC.

ϕ (ºC/min)	n	$Z(s^{-n})$	$k \times 10^3$ (s^{-1})	$\tau_{1/2}$ (s)	$(1/\tau_{1/2}) \times 10^3$ (s^{-1})	$(Z/\ln 2)^{1/n} \times 10^3$ (s^{-1})
1	3.76	6.79×10^{-13}	0.58	1574	0.64	0.64
3	3.11	7.90×10^{-10}	1.18	749	1.34	1.32
5	3.30	1.37×10^{-09}	2.06	428	2.34	2.31
8	3.10	1.83×10^{-08}	3.21	272	3.68	3.61
10	2.92	1.45×10^{-07}	4.55	192	5.21	5.16
15	2.97	2.76×10^{-07}	6.17	142	7.07	6.98
20	2.73	2.25×10^{-06}	8.60	104	9.65	9.83
30	2.77	9.12×10^{-06}	15.26	58	17.14	17.42

It is well stated that application of the Avrami equation under non-isothermal conditions merely corresponds to a mathematical fitting that allows appropriate values of the rate constant to be derived.[24–26] In this case, it should be pointed out that the determined exponents may even have a physical meaning since they suggest a three-dimensional

spherulitic growth and instantaneous nucleation, as postulated from the isothermal studies.[4,6] Furthermore, the sporadic nucleation detected at high isothermal crystallization temperatures[6] is in agreement with the increase of the exponent observed at low crystallization rates (i.e., 3.77 at 1 ^{o}C/min) and supports DSC evidence of the occurrence of two crystallization processes.

The values of the corresponding reciprocal crystallization half-times ($1/\tau_{1/2}$), calculated as the inverse of the difference between crystallization starting time and crystallization half time, are also given in Table 5.1.1. This parameter is a direct measure of the crystallization process, and could therefore be used to check the accuracy of Avrami analyses, as demonstrated by the excellent agreement with the theoretical kinetic value (i.e., $1/\tau_{1/2} = (Z/\ln 2)^{1/n}$). In conclusion, the deduced Avrami parameters are completely appropriate to simulate the non-isothermal crystallization process.

A kinetic equation that combines the Avrami [18] and Ozawa[15] expressions has been derived and applied in different non-isothermal studies [27]:

$$\log \phi = \log F(T) - a \log (t - t_0) \qquad (4)$$

where $F(T)$ is a kinetic parameter referring to the cooling rate which must be chosen at a unit crystallization time when the system reaches a certain crystallinity, and a is the ratio of apparent Avrami and Ozawa exponents.

A plot of $\log \phi$ versus $\log (t - t_0)$ yields a series of straight lines at a given value of $\chi(T)$ (Figure 5.1.5), which suggest the validity of the combined equation for this system. Kinetic parameters can be estimated by the intercept and slope of these lines. $F(T)$ has a definite physical implication since higher values correspond to slower crystallization rates. Results pointed out that $F(T)$ values increased with crystallinity (Table 5.1.2), which seems logical because motion of molecular chains becomes slower as the material crystallized and formation of new crystals was hindered. The values of a were almost constant between 0.91 and 0.98 and slightly increased with the relative degree of crystallinity.

Figure 5.1.5. Plots of log ϕ versus log $(t - t_0)$ for non-isothermal crystallization of PDO performed at the indicated crystallinities.

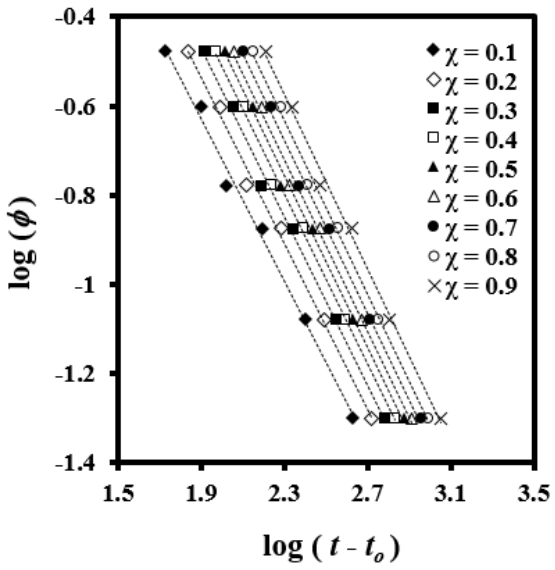

Table 5.1.2. Values of kinetic parameters at a given crystallinity estimated from the combined model [35] for non-isothermal crystallization of PDO.

$\chi(T)$	a	$F(T)$	r^2
0.1	0.91	12.67	0.993
0.2	0.93	16.98	0.995
0.3	0.94	20.79	0.996
0.4	0.95	24.27	0.996
0.5	0.96	27.64	0.996
0.6	0.96	31.12	0.996
0.7	0.97	35.04	0.995
0.8	0.98	41.51	0.995
0.9	0.98	48.11	0.993

The crystallization process has a non-Arrheniusian behavior and therefore a temperature-dependent *effective activation energy* needs to be defined. The value corresponding to a given degree of crystallinity, $E\chi$, can be determined by the Friedman isoconversional method [28]:

$$[d\chi / dt]\cdot\chi = A \exp(-E\chi / RT)\, f[\chi] \qquad (5)$$

where A is a preexponential factor and f $[\chi]$ is the crystallization model. Values of ln $[d\chi / dt]\cdot\chi$ at different temperatures and degrees of crystallization can be obtained from crystallization experiments performed at different cooling rates. In this way, the slopes of the linear plots of ln $[d\chi /dt]\cdot\chi$ versus $1/T$ (Figure 5.1.6a) allow $E\chi$ to be determined (Figure 5.1.6b). The temperature dependence of the *effective activation energy* (Figure 5.1.7) could finally be derived by considering also the average temperature associated with a given conversion (Figure 5.1.6b).

The *effective activation energy* was negative for crystallization experiments performed from the melt state and at low supercooling degrees (i.e., the temperature range where secondary nucleation plays a fundamental role) as shown in Figure 5.1.7. This energy increased progressively (i.e., the crystallization rate increased) as the temperature decreased, as discussed at length by Vyazovkin and Dranca,[29] reflecting the expected behavior for crystallizations performed at temperatures higher than those associated with the maximum crystallization rate.

Vyazovkin and Sbirrazzuoli proposed that crystallization parameters like the secondary nucleation constant should be derived through the effective activation energies [29–31]:

$$E(T) = -R\, d\ln G / d T^{-1} = U^*[T^2/(T-T_\infty)^2] + K_g R[(2\Delta T - T_m^0 f)/(\Delta T)\cdot 2f] \qquad (6)$$

where G is the crystal growth rate, U^* represents the activation energy characteristic of the transport of crystallizing segments across the liquid–crystal interface, T_∞ is the temperature below which such motion ceases, R is the gas constant, K_g is the secondary nucleation constant, ΔT is the degree of supercooling measured as $T_m^0 - T_c$ (where T_m^0 is the equilibrium melting temperature and T_c the crystallization temperature), and f is a correction factor accounting for the variation in the bulk melting enthalpy per unit volume with temperature ($f = 2T_c / (T_m^0 + T_c)$).

Figure 5.1.6. (a) Plots of ln [dχ/dt] χ versus 1/T for non-isothermal crystallization of PDO at the indicated cooling rates. Data corresponding to relative degrees of crystallinity of 0.8, 0.5 and 0.1 are represented by blue, green and red symbols, respectively. **(b)** Dependence of the activation energy of crystallization (●) and average temperature (○) on crystallinity.

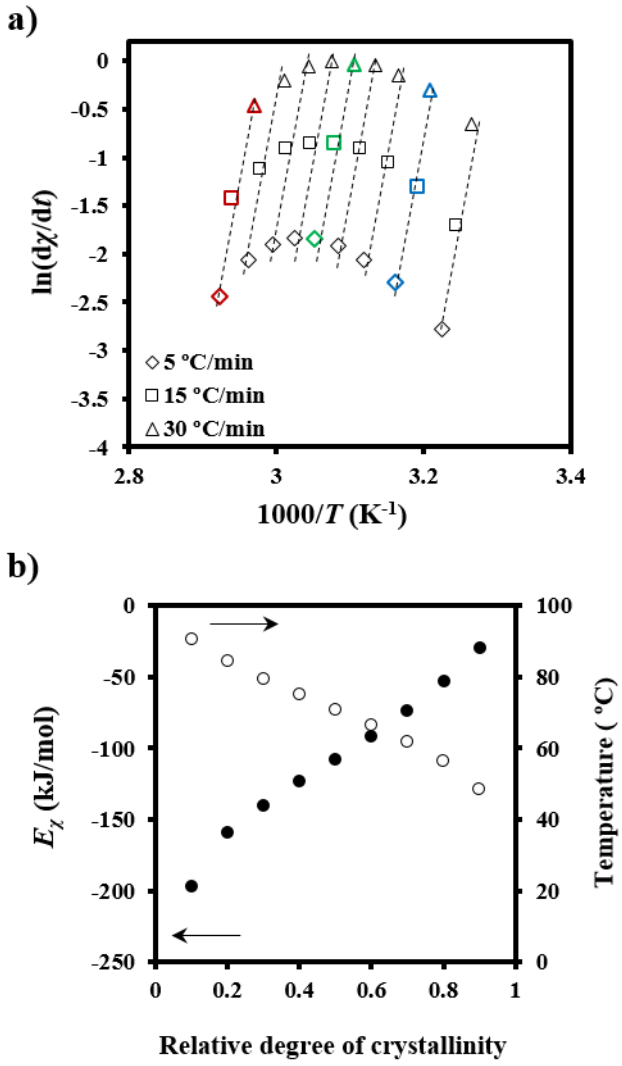

Figure 5.1.7 also compares the experimental $E\chi$-T plot with simulated ones using equation 6, U^* and T_∞ values of 1600 cal/mol and T_g-35 K, respectively (i.e., close to the universal values reported by Suzuki and Kovacs [32]), the equilibrium melting temperature of 127 ºC, as previously determined for PDO,[3] and representative K_g values. In fact, U^* and T_∞ have little influence on a temperature range that is far from the glass transition

temperature. The best fit between experimental and theoretical data was obtained considering two K_g parameters (i.e., 3.07×10^5 K^2 and 1.42×10^5 K^2), which are in agreement with the two crystallization regimes reported for PDO from isothermal crystallization experiments.[3] Note that the isoconversional analysis was able to detect the existence of several crystallization regimes and also to predict two maximum crystallization rates at temperatures of 45 ºC and 60 ºC as deduced from the temperatures for each simulated curve where the effective activation energy was zero.

Figure 5.1.7. Experimental $E\chi$ versus T plot and simulated curves according to equation 6. Arrows indicate the expected temperatures for the maximum crystallization rates (i.e., *effective activation energy* equal to zero).

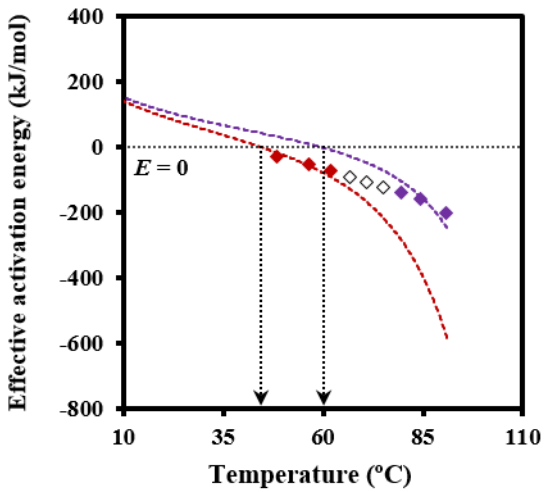

5.1.3.3. Non-isothermal kinetic analysis of poly(*p*-dioxanone) melt crystallization from optical microscopy data

Non-isothermal crystallization of PDO rendered double banded spherulites with progressively decreasing periodicity (Figure 5.1.8), which is in accordance with the continuous temperature decrease of a non-isothermal crystallization. In fact, morphologies obtained under isothermal conditions have been extensively studied,[3,5,6] and it was assumed that interband spacing decreased when crystallization temperature was lowered. Actually, two different banding periodicities could be detected where the broader bands had a negative birefringence. This kind of double bands with uneven spacings are characteristic of spherulites having a biaxial indicatrix twisted about the optic normal.[6,30,33]

PDO spherulites were also characterized by their big size, which led to poor nucleation and slow growth rate. Figure 5.1.8 also shows also that the number of active nuclei increased during cooling, and consequently size and morphology of spherulites were not identical. Logically smaller spherulites with a practically indistinguishable double band texture were formed at lower temperatures (see yellow arrows).

Figure 5.1.8. Optical micrograph of PDO spherulites formed during a non-isothermal crystallization from the melt state performed at a cooling rate of 20 ºC/min. Yellow arrows point to spherulites formed at low temperatures. Inset shows a micrograph taken with a first-order red tint plate to determine the birefringence sign.

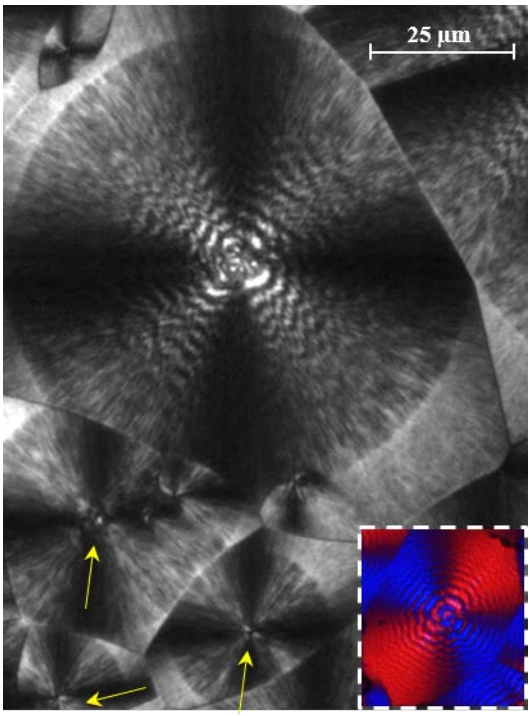

Spherulitic growth rates (G) were also determined for non-isothermal crystallization by measuring the change of the spherulite radius (R) with temperature (T) at a constant cooling/heating rate (dT/dt) [34,35]:

$$G = dR/dt = (dR/dT)(dT/dt) \quad (7)$$

Plots showing the variation of the spherulitic radius with crystallization temperature could be adjusted to third order equations with good regression coefficients (i.e., higher than

0.990) (Figure 5.1.9a). These coefficients were significantly better than those calculated for second order equations and remained constant for higher orders. Therefore, third order equations were employed to determine dR / dT as a function of the crystallization temperature. The corresponding crystal growth rate versus crystallization temperature curves are displayed in Figure 5.1.9b. Note that data were obtained at different cooling rates in order to maximize the crystallization temperature range where radii could be well measured.

Two bell-shaped curves with maximums of 45 ºC and 60 ºC reflected the temperature dependence of G, and therefore the existence of two crystallization regimes with different secondary nucleation constants. These were determined by the Lauritzen-Hoffman equation [36]:

$$G = G_0 \exp [-U^* / (R (T_c - T_\infty))] \times \exp [-K_g / (T_c (\Delta T) f)] \quad (8)$$

where G_0 is the constant pre-exponential factor and the other parameters as previously defined.

Figure 5.1.9c shows the linear plots obtained using U^* and T_∞ parameters of 1600 cal/mol and T_g – 35 K, respectively. It is clear that two crystallization regimes defined by secondary nucleation constants of 3.07×10^5 K^2 and 1.42×10^5 K^2 fits all the experimental data.

Furthermore, regimes III and II could be assumed since the experimental ratio between slopes (2.16) was close to the theoretical K_g^{III} / K_g^{II} value of 2. Figure 5.1.9c also shows that the two bell-shaped curves calculated by eq. 8, the estimated U^* and T_∞ parameters, and the deduced values of ln G_0 and K_g for each regime fit well with the experimental spherulitic growth data. The maximum growth rate was found in regime III and corresponded to a temperature of 45 °C. Our observations are in agreement with the same crystallization regimes determined from isothermal crystallization, although the nucleation constant becomes slightly higher than those previously reported (i.e., 2.49×10^5 K^2 and 1.19×10^5 K^2).[3] Note also that the deduced data support the results of the calorimetric study.

Figure 5.1.9. **(a)** Variation in spherulite radius with temperature during heating at the indicated rates. **(b)** Spherulitic growth rates determined by the equations deduced for the heating runs. Theoretical curves are also drawn (dashed lines) for comparative purposes. **(c)** Plot of ln $G + U^*/R(T_c - T_\infty)$ versus $1/T_c(\Delta T)f$ to determine the K_g secondary nucleation parameters of PDO.

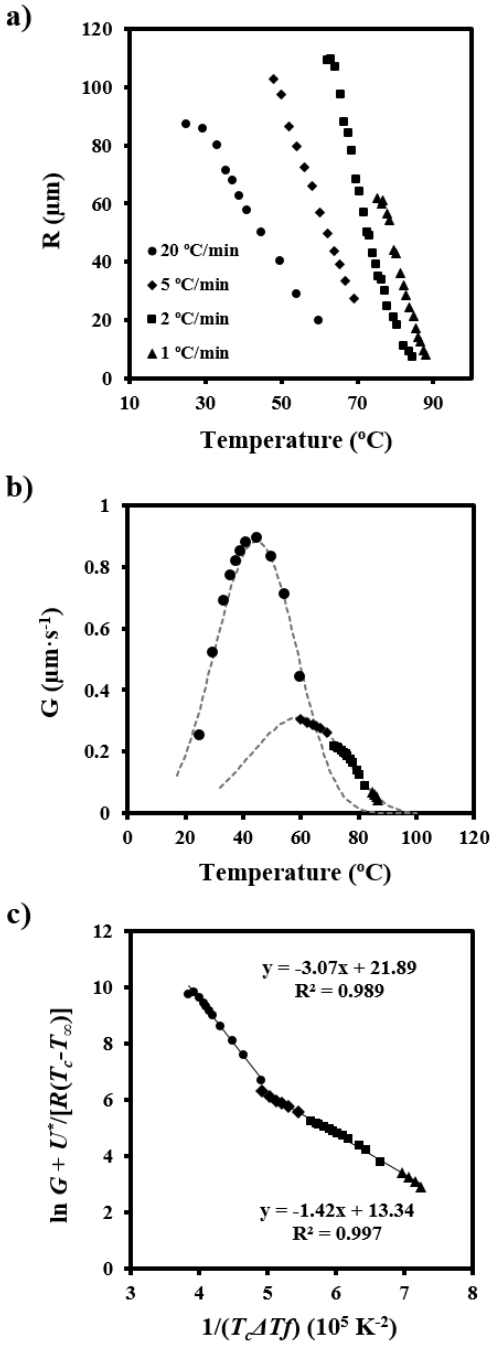

The fact that the crystallization rate is governed by two different processes makes it unfeasible to determine a single activation energy for the entire T_c range. Instead, an *effective activation energy* (E) dependent on T_c was evaluated by equation 9 [30]:

$$E = -R\, \mathrm{d} \ln G / \mathrm{d}T^{-1} = U^* T^2 / (T - T_\infty)^2 + K_g R [(T_m^0)^2 - T^2 - T_m^0 T] / [(T_m^0 - T)^2 T] \quad (9)$$

The calculated effective activation energies are plotted in Figure 5.1.10 and show a non-Arrhenius behavior, as expected. Different K_g values were used according to the crystallization regime. The *effective activation energy* is zero at the maximum crystallization rate for regimes III and II, which correspond to temperatures of 45 ºC and 60 ºC and agree again with those deduced by isoconversional analysis. In each case, positive values are found for temperatures lower than the corresponding maxima because the crystallization rate increases with increasing temperature, whereas negative values are determined for higher temperatures characterized by a decrease of the crystallization rate with increasing temperature.

Figure 5.1.10. Dependence of the *effective activation energy* on crystallization temperature for regimes II (■) and III (•). Extrapolated data for regimes II and III are indicated by dotted and dashed lines, respectively.

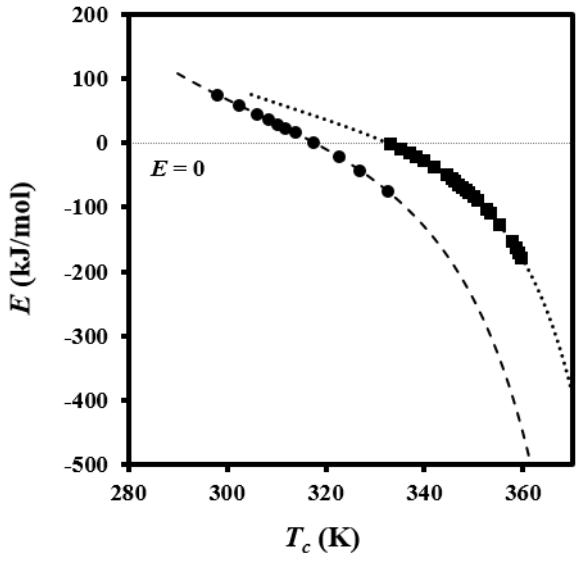

5.1.3.4. Evolution of morphologic parameters during heating

Figure 5.1.11 shows the evolution of the intensity of the peak detected in SAXS patterns during heating and cooling processes of the granulated PDO sample. In the first case, a recrystallization process that led to thicker lamellae can be deduced from the increase in SAXS peak intensity and its shift towards lower values of the scattering vector (q = [4π/λ] sen θ). In the second case, a shift of the peak once samples crystallized towards higher q values and a slight decrease in its intensity were observed. These features can be explained considering that a lamellar insertion mechanism took place at low temperatures together with a densification of the amorphous phase (i.e., a smaller difference between the density of amorphous and crystalline phases).

Figure 5.1.11. Variation of intensity ($I \cdot q^2$) and scattering vector on (q) of SAXS peaks observed in the diffraction profiles taken during heating (10 ºC/min) at room temperature (red) and during cooling (2 ºC/min) from the melt state (blue).

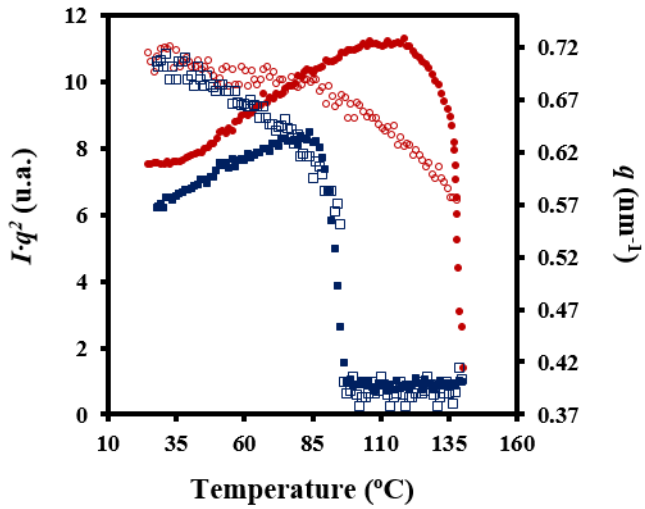

Characteristic lamellar parameters (i.e., long period, L_γ, amorphous layer thickness, l_a, and crystalline lamellar thickness, l_c) and crystallinity (i.e., crystallinity within the lamellar stacks, $X_c^{SAXS} = l_c / L_\gamma$) were determined by the normalized one-dimensional correlation function [33], γ(r):

$$\gamma(r) = \int_0^\infty q^2 I(q)\cos(qr)dq \;/\; \int_0^\infty q^2 I(q)dq \qquad (10)$$

where $I(q)$ is the intensity at each value of the scattering vector.

SAXS data were collected within a limited angular range, with application of Vonk's model [37] and Porod's law to perform extrapolations to low and high q values.

Figure 5.1.12 illustrates representative correlation functions obtained from patterns acquired during the heating of granulated PDO.

Figure 5.1.12. (a) SAXS patterns of a granulated PDO sample taken at 25 ºC and 102 ºC during a heating run performed at 10 ºC/min. **(b)** Change in the correlation function during the heating run. For the sake of completeness, the pattern and correlation function obtained at room temperature after cooling (10 ºC/min) a previously molten sample are also shown.

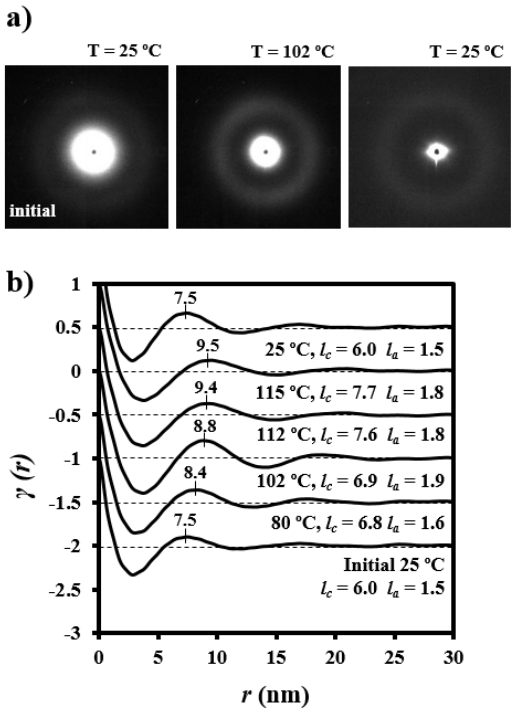

Lamellar thickening was due to the increase in crystalline lamellar thickness (i.e., from 6.0 nm to 7.7 nm) and amorphous layer thickness (i.e., from 1.5 nm to 1.8 nm). In this way, the reordering process led to minimum increase of the crystallinity within the lamellar stacks (i.e., from 0.80 to 0.81). However, it should be pointed out that the correlation function of

the sample heated up to 102 ºC (i.e., just before the first melting peak observed in the DSC trace) exhibited more defined peaks (see also the diffraction patterns in Figure 5.1.12) that were indicative of a high contrast between electronic densities of amorphous and crystalline phases. Basically, the amorphous phase became less dense, in agreement with the maximum value detected for l_a (i.e., 1.9 nm) and the minimum value of crystallinity (i.e., 0.78). Figure 5.1.12 also shows that morphological features were completely recovered after cooling the sample, and specifically the correlation functions and the X-ray diffraction pattern were identical to those obtained from the initial sample.

The evolution of SAXS patterns of a PDO thread on heating (Figure 5.1.13) was very different because they reflect the microstructure of the processed sample.

Figure 5.1.13. (a) SAXS patterns of a PDO suture taken at representative temperatures during a heating run at 10 ºC/min. **(b)** Correlation function of diffraction patterns corresponding to: the initial suture, a suture heated (10 ºC/min) just before melting and a melt crystallized (cooling rate of 10 ºC/min) suture at room temperature.

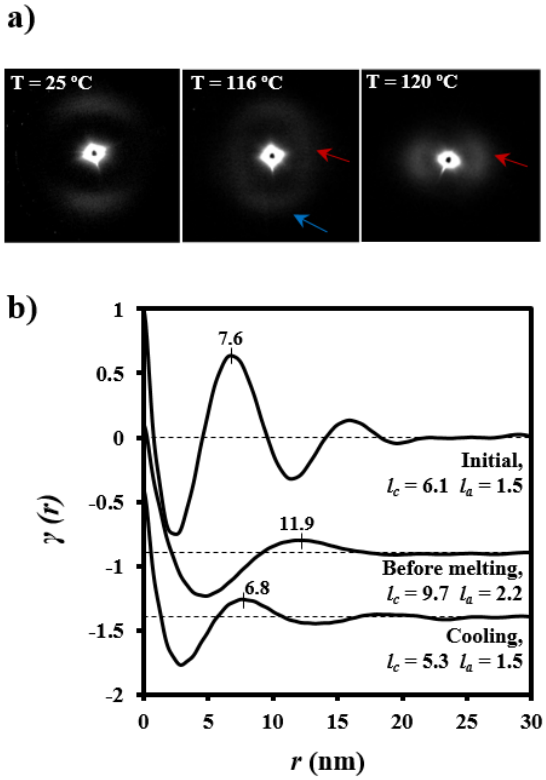

Some observations can be made:

a) The initial pattern was characterized by a meridional reflection that indicates a stacking of lamellae perpendicularly oriented to the fiber axis. Peaks observed in the corresponding correlation function were highly prominent, suggesting a tie molecular arrangement in the dense crystalline phase. However, l_a and l_c values (6.1 nm and 1.5 nm) were close to those determined for the granulated sample.

b) As the temperature was increased, the interlamellar reflection decreased in intensity while a new perpendicular reflection appeared and progressively increased in intensity. This new equatorial reflection could be associated with the existence of interfibrillar amorphous domains that correspond to the regions placed on lateral sides of lamellae. Note that molecular chains in these domains may have had a partial orientation at the beginning of the heating (i.e., the as-processed thread) but became more randomly distributed as temperature was increased. Therefore, a decrease in electronic density of the amorphous phase and an enhancement of the intensity of the SAXS reflection were derived. The correlation function of the interfibrillar reflection observed in the pattern taken just before fusion gave l_a and l_c values (i.e., 9.7 nm and 2.2 nm, respectively), which were clearly different from those determined for the interlamellar reflection. In any case, X_c^{SAXS} was again close to 0.81.

c) The pattern and correlation function of the sample after being cooled to room temperature from the melt state were similar to those determined from the initial sample and indicated a similar lamellar organization. Nevertheless, a slight decrease of l_c was detected (i.e., 5.3 nm as opposed to 6.1 nm) as well as a decrease of crystallinity within lamellar stacks (i.e., 0.78 as opposed to 0.80), in agreement with the lack of an annealing process for the melt crystallized sample.

5.1.3.5. Evolution of morphologic parameters during melt crystallization

Figure 5.1.14 illustrates the correlation functions from patterns taken during the cooling run (2 ºC/min) of a melted PDO sample. It is clear that L_γ, l_a, and l_c decreased progressively and had similar values (7.6 nm, 1.5 nm and 6.1 nm) to those observed for the initial granulated PDO sample. The decrease in lamellar thickness can be due to the lower value expected when crystallization temperature decreases and also to a lamellar insertion mechanism (i.e., formation of thinner lamellar crystals between loosely stacked primary lamellae). Similar results were obtained at different cooling rates, but it is remarkable that

morphological parameters were practically identical at room temperature, as shown in Figure 5.1.12 for the sample cooled at 10 ºC/min.

Figure 5.1.14. Correlation functions of patterns obtained at the indicated temperatures during the cooling run (2 ºC/min) from the melt state. The correlation function of the pattern obtained at room temperature after cooling at 10 ºC/min is also shown for comparative purposes.

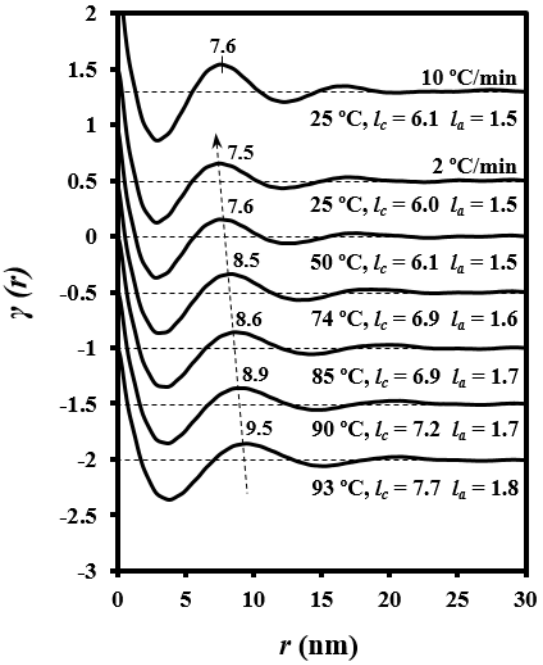

Note that crystallization took place at lower temperatures when the cooling rate was increased and consequently lower lamellar thicknesses should be expected. Therefore, the invariance observed for l_c suggests a counterbalance effect derived from the enhanced insertion mechanism (i.e., decrease of the lamellar thickness) when cooling rate was decreased.

5.1.3.6. Changes in microstructure of degraded samples during heating

Insights on the crystalline microstructure of sutures can be obtained following the evolution of SAXS patterns of degraded samples during a subsequent heating process.[23] To this end, PDO sutures were exposed to hydrolytic degradation media at pHs 7 and 11 and a 37 ºC for 36 days to analyze samples with clear differences in their degree of hydrolysis.

Specifically, M_w values of 117,700 g/mol and 83,800 g/mol were determined after exposure to pHs 7 and 11, respectively. Weight losses were close to 3% (pH 7) and 11% (pH 11). Micrographs in Figures 5.1.15 and 5.1.16 reveal the greater morphological changes occurred under basic conditions and specifically the appearance of deep transversal cracks that led to narrow disks and tortuous suture surfaces (Figure 5.1.15). This degradation can be interpreted as a consequence of greater hydrolysis of interlamellar amorphous regions, which are depleted and dissolved in the medium.[11]

Figure 5.1.15. SAXS patterns taken at representative temperatures of 25 ºC **(a)**, 102 ºC **(b)** and 107 ºC **(c)** during a heating run at 10 ºC/min of a PDO suture previously degraded in a pH 11 hydrolytic medium for 36 days. The pattern obtained at room temperature after cooling (10 ºC/min) and the optical micrograph of the degraded suture are shown in **(d)** and **(e)**, respectively.

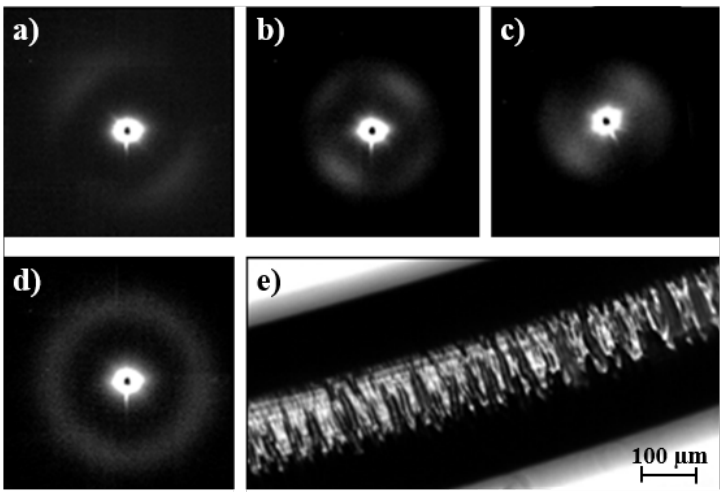

Morphology of sutures exposed to the neutral pH for a relatively short time is quite different because in this case smoother surfaces and numerous longitudinal cracks formed (Figure 5.1.16). In fact, it has been reported that, when hydrated, interfibrillar amorphous regions swell more easily than interlamellar amorphous regions.[12] Note that the latter are constituted by tie chains, which connect the lamellae in each fibril whereas fewer tie chains are expected to connect adjacent fibrils. Thus, water diffusion and formation of longitudinal cracks seems to be favored.

Figure 5.1.16. SAXS patterns taken at representative temperatures of 25 ºC **(a)**, 102 ºC **(b)** and 112 ºC **(c)** during a heating run at 10 ºC/min of a PDO suture previously degraded in a pH 7 hydrolytic medium for 36 days. The pattern obtained at room temperature after cooling (10 ºC/min) and the optical micrograph of the degraded suture are shown in **(d)** and **(e)**, respectively.

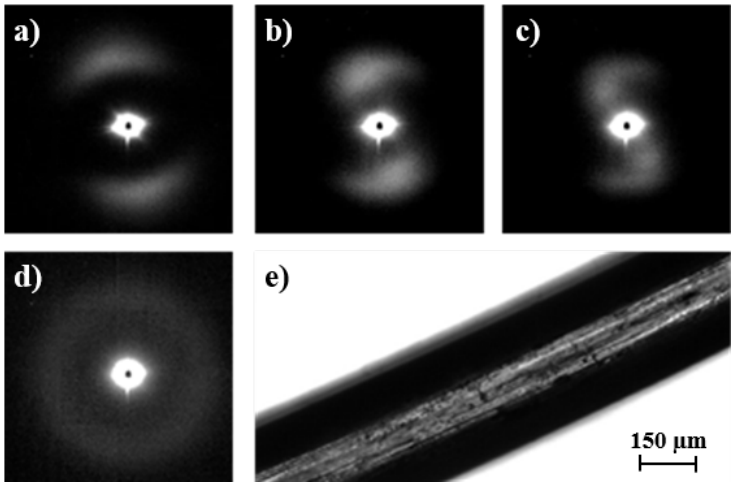

SAXS patterns of degraded samples showed a slight decrease of meridional interlamellar spacing, L_B, because of the more compact structure achieved after scissions of chains belonging to the amorphous regions. Therefore, the initial spacing of 9.6 nm decreased to 9.2 nm and 9.3 nm after 36 days of degradation in basic and neutral pHs, respectively. Analysis of correlation functions (not shown) indicated that l_c and l_a values decreased from 6.1 nm and 1.5 nm, respectively, to 5.3 nm and 1.3 nm for the basic pH. Logically, SAXS crystallinity increased during degradation since the main change occurred in the amorphous layer.

Lamellar crystals in degraded samples were able to recrystallize and even reorient during subsequent heating runs in an easier way than that observed for the initial suture. The increased freedom resulting from scission of tie chains belonging to interfibrillar and interlamellar amorphous regions should play a fundamental role. Diffraction patterns during a subsequent heating showed clear differences between highly and scarcely degraded samples. Thus, in the first case, an increase in lamellar thickness, together with the appearance of an intense equatorial reflection associated with the interfibrillar spacing previous to the disappearance of the meridional reflection, was observed. Specifically, L_B values of 13.2 nm and 11.7 nm were determined at temperatures close to

fusion (i.e., 102 ºC). This behavior was similar to that observed for the initial suture taking into account the differences in spacings and intensities of reflections. Logically, greater spacings and intensities were detected for degraded samples as a consequence, in the first case, of an enhanced reorganization when tie interconnecting chains were cleaved and, in the second case, of a higher contrast between amorphous/crystalline regions.

Figure 5.1.16 reveals a different evolution when samples were degraded in the pH 7 medium because the great thickening of lamellae was hindered due to a still compact chain packing (note that weight loss was minimal). Therefore, the thickened lamellae (L_B = 11.4 nm) tilted with respect to the fiber axis gave rise to a second reflection. Breadth of reorganized crystals was also clearly increased, as could be deduced from the observed spot like reflections. Finally, Figures 5.1.15 and 5.1.16 show the reversibility of the thermal process for degraded samples since the diffraction patterns obtained after cooling to room temperature are identical to those obtained from the initial sample before any thermal treatment.

5.1.4. CONCLUSIONS

PDO showed complex melting and crystallization peaks because of a typical lamellar thickening process and the existence of different nucleation mechanisms, respectively. Calorimetric analysis of non-isothermal crystallization showed an increase of the Avrami exponent at low cooling rates, which could be associated with a homogeneous nucleation process instead of the instantaneous nucleation observed at high rates. Isoconversional analyses from non-isothermal calorimetric data revealed the existence of two crystallization regimes, demonstrating the suitability of this methodology. These regimes were well characterized by optical microscopy observations, and the non-isothermal crystallization results were in relatively good agreement with those previously reported from isothermal studies.

Real time SAXS profiles taken during heating and cooling processes showed the occurrence of a lamellar reordering and a lamellar insertion mechanism that led to an increase and a decrease in lamellar thickness, respectively. SAXS patterns taking during heating of samples degraded under neutral and basic pHs had a different evolution that revealed the existence of interlamellar and interfibrillar amorphous domains.

5.1.5. REFERENCES

1. Yang, K. J., Wang, X. L. & Wang, Y. Z. Poly(*p*-dioxanone) and its copolymers. *J. Macromol. Sci. Part C Polym. Rev.* **C42,** 373–398 (2002).

2. Li, X. W., Xiao, J., Li, X. Y., Xiong, C. D. & Deng, X. M. Preparation of biodegradable PLA-PEG copolymer microspheres with micron sizes. *Polym. Mater. Sci. Eng. Div.* **14,** 20–22 (1998).

3. Sabino, M. A., Feijoo, J. L. & Müller, A. J. Crystallisation and morphology poly(*p*-dioxanone). *Macromol. Chem. Phys.* **201,** 2687–2698 (2000).

4. Andjelic, S. *et al.* Crystallization study on absorbable poly(*p*-dioxanone) polymers by differential scanning calorimetry. *J. Appl. Polym. Sci.* **79,** 742–759 (2001).

5. Andjelic, D., Jamiolkowski, D., McDivitt, J., Fisher, J. & Zhou, J. Spherulitic growth rates and morphology of absorbable poly(*p*-dioxanone) homopolymer and its copolymer by hot-stage optical microscopy. *J. Polym. Sci. Part B Polym. Phys.* **39,** 3073–3089 (2001).

6. Sabino, M. A., Ronca, G. & Müller, A. J. Heterogeneous nucleation and self-nucleation of poly(*p*-dioxanone). *J. Mater. Sci.* **35,** 5071–5084 (2000).

7. Pezzin, A. P. T., Alberda van Ekenstein, G. O. R. & Duek, E. A. R. Melt behavior, crystallinity and morphology of poly(*p*-dioxanone). *Polymer* **42,** 8303–8306 (2001).

8. Yang, K. K., Wang, X. L., Wang, Y. Z. & Huang, H. X. Effects on molecular weights of bioabsorbable poly(*p*-dioxanone) on its crystallization behavior. *J. Appl. Polym. Sci.* **100,** 2331–2335 (2006).

9. Andjelic, S. *et al.* Time-resolved crystallization study of absorbable polymers by synchrotron small-angle X-ray scattering. *J. Polym. Sci. Part B Polym. Phys.* **39,** 153–167 (2001).

10. Sabino, M. A., Feijoo, J. L. & Müller, A. J. Crystallisation and morphology of neat and degraded poly(*p*-dioxanone). *Polym. Degrad. Stab.* **73,** 541–547 (2001).

11. Sabino, M. A., Albuerne, J., Müller, A. J., Brisson, J. & Prud'homme, R. E. Influence of in vitro hydrolytic degradation on the morphology and crystallization behavior of poly(*p*-dioxanone). *Biomacromolecules* **5,** 358–370 (2004).

12. Ooi, C. P. & Cameron, R. E. The hydrolytic degradation of polydioxanone (PDS II) sutures. Part II: Micromechanisms of deformation. *J. Biomed. Mater. Res. (Appl. Biomater.)* **63,** 291–298 (2002).

13. Furuhashi, Y. *et al.* X-ray and electron diffraction study of poly(*p*-dioxanone). *Macromol. Rapid Commun.* **25,** 1943–1947 (2004).

14. Gestí, S., Lotz, B., Casas, M. T., Alemán, C. & Puiggalí, J. Morphology and structure of poly(*p*-dioxanone). *Eur. Polym. J.* **43,** 4662–4674 (2007).

15. Ozawa, T. Kinetics of non-isothermal crystallization. *Polymer* **12,** 150–158 (1971).

16. Cazé, C., Devaux, E., Crespy, A. & Cavrot, J. P. A new method to determine the Avrami exponent by DSC studies of non-isothermal crystallization from the molten state. *Polymer* **38,** 497–502 (1997).

17. Zeng, J. B., Srinivansan, M., Li, S. L., Narayan, R. & Wang, Y.-Z. Non isothermal and isothermal cold crystallization behaviors of biodegradable poly(*p*-dioxanone). *Ind. Eng. Chem. Res.* **50,** 4471–4477 (2011).

18. Avrami, M. Kinetics of phase change. I General Theory. *J. Chem. Phys.* **7,** 1103–1112 (1939).

19. Cebe, P. Non-isothermal crystallization of poly(etheretherketone) aromatic polymer composite. *Polym. Compos.* **9,** 271–279 (1988).

20. Tobin, M. C. Theory of phase transition kinetics with growth site impingement. I. Homogeneous nucleation. *J. Polym. Sci. Part B Polym. Phys.* **12,** 399–406 (1974).

21. Zhou, Z. X. *et al.* Thermal properties and non-isothermal crystallization behavior of biodegradable poly(*p*-dioxanone)/poly(vinyl alcohol) blends. *Polym. Int.* **55,** 383–390 (2006).

22. Zhang, X., Bai, W., Chen, D., Xiong, C. & Pang, X. Nonisothermal crystallization behaviour of poly(*p*-dioxanone) and poly(*L*-lactic acid) blends. *Bull. Mater. Sci.* **38,** 517–523 (2015).

23. Márquez, Y., Martínez, J. C., Turon, P., Franco, L. & Puiggalí, J. Influence of pH on morphology and structure during hydrolytic degradation of the segmented GL-*b*-[GL-*co*-TMC-*co*-CL]-*b*-GL copolymer. *Fibers* **3,** 348–372 (2016).

24. Schultz, J. M. *Polymer crystallization the development of crystalline order in thermoplastic polymers.* (ACS/Oxford University Press, 2001).

25. López, L. C. & Wilkes, G. L. Non-isothermal crystallization kinetics of poly(*p*-phenylene suphide). *Polymer* **30,** 882–887 (1989).

26. Privalko, V. P., Kawai, T. & Lipatov, Y. S. Crystallization of filled Nylon 6. III Non-isothermal crystallization. *Colloid. Polym. Sci.* **257,** 1042–1048 (1979).

27. Liu, T. X., Mo, Z. S., Wang, S. G. & Zhang, H. F. Nonisothermal melt and cold crystallization kinetics of poly(aryl ether ether ketone ketone). *Polym. Eng. Sci.* **37,** 568–575 (1997).

28. Friedman, H. J. Kinetics of thermal degradation of char-forming plastics from thermogravimetry. *J. Polym. Sci. Part C Polym. Symp.* **6,** 183–195 (1964).

29. Vyazovkin, S. & Dranca, I. Isoconversional analysis of combined melt and glass crystallization data. *Macromol. Chem. Phys.* **207,** 20–25 (2006).

30. Vyazovkin, S. & Sbirrazzouli, N. Isoconversional approach to evaluating the Hoffman-Lauritzen parameters (U* and K_g) from overall rates of nonisothermal melt crystallization. *Macromol. Rapid Commun.* **25,** 733–738 (2004).

31. Vyazovkin, S., Stone, J. & Sbirrazzouli, N. Hoffman-Lauritzen parameters for non-isothermal crystallization of poly(ethylene terephthalate) and poly(ethylene oxide) melts. *J. Therm. Anal. Calorim.* **80,** 177–180 (2005).

32. Suzuki, T. & Kovacs, A. J. Temperature dependence of spherulitic growth rate of isotactic polystyrene. A critical comparison with the kinetic theory of surface nucleation. *Polym. J.* **1,** 82–100 (1970).

33. Vonk, C. G. & Kortleve, G. X-ray small-angle scattering of bulk polyethylene. *Kolloid Z Z Polym* **220,** 19–24 (1967).

34. Di Lorenzo, M. L., Cimmino, S. & Silvestre, C. Nonisothermal crystallization of isotactic polypropylene blended with poly (α -pinene). 2 . Growth rates. *Macromolecules* **33,** 3828–3832 (2000).

35. Di Lorenzo, L. M. Determination of spherulite growth rates of poly (*L*-lactic acid) using combined isothermal and non-isothermal procedures. *Polymer* **42,** 9441–9446 (2001).

36. Lauritzen, J. I. & Hoffman, J. D. Extension of theory of growth of chain-folded polymer crystals to large undercoolings. *J. Appl. Phys.* **44,** 4340–4352 (1973).

37. Vonk, C. G. A general computer program for the processing of small-angle X-ray scattering data. *J. Appl. Crystallogr.* **8,** 340–341 (1975).

6.

INCORPORATION OF DRUGS INTO GL–*b*–(GL–*co*–TMC–*co*–CL)–*b*–GL MONOFILAR SURGICAL SUTURE

6.1 Incorporation of antimicrobial drugs: biguanide compounds

A new biodegradable coating was developed for bioabsorbable monofilament sutures. Specifically, a random copolymer having 35 wt-% and 65 wt-% of lactide and trimethylene carbonate units showed appropriate flexibility, stickiness and degradation rate, as well as capability to produce a complete and uniform coating. Monofilament sutures of glycolide-*b*-(glycolide-*co*-trimethylene carbonate-*co*-ε-caprolactone)-*b*-glycolide were loaded with chlorhexidine (CHX) and poly(hexamethylene biguanide) (PHMB) to explore the possibility to achieve antimicrobial activity without adverse cytotoxic effects. To this end, two processes based on single drug adsorption onto the suture surface and incorporation into the coating copolymer were used and subsequently evaluated. Although the second process could be considered more complex, clear benefits were observed in terms of drug loading efficiency, antimicrobial effect and even biocompatibility. In general, drugs could be loaded in an amount leading to a clear bacteriostatic effect for both Gram-negative and Gram-positive bacteria without causing significant cytotoxicity. Release profiles of PHMB and CHX were clearly different. Specifically, adsorption of the drug onto the fiber surface which prevented complete release was detected for PHMB. This polymer had advantages derived from its high molecular size, which hindered penetration into cells, thus resulting in lower cytotoxicity. Furthermore, bacterial growth kinetics measurements and bacterial adhesion assays showed greater effectiveness of this polymer.

6.1.1 INTRODUCTION

Adhesion and proliferation of bacteria on the surface of materials are responsible for severe health problems. Microorganisms can survive on appropriate materials for long periods of time, especially in hospital environments, developing biofilms that could be involved in most chronic infections,[1,2] hence the current demand of bacteriostatic, antiseptic and bactericidal agents to prevent bacterial survival and biofilm formation.[3–5] Nowadays, 23% of surgical site infections[6] are caused by Gram-positive *Staphylococcus aureus* bacteria. Specifically, its drug-resistant strain becomes highly dangerous[7] since it could lead to patient mortality and high costs for society.[8]

Typical bactericidal agents such as triclosan (TCS), chlorhexidine (CHX) and poly(hexamethylene biguanide) (PHMB) [9] have been employed to prevent bacterial infection. However, other natural agents like bacteriophages[10] can be considered, as well as industrial and clinical agents such as silver[11], quaternary ammonium groups[12], hydantoin compounds[13], and tetracycline antibiotics[14].

CHX (1,1′-hexamethylene-bis-5-(4-chlorophenyl)biguanide) (Figure 6.1.1) has a high activity towards microorganisms[15] as a consequence of the presence of secondary amines that can be protonated, and therefore positively charged under normal pH conditions.[16] Thus, CHX affects the stability of bacterial membranes since it can attach to their negatively loaded (anionic) phospholipids. Furthermore, it has been claimed that CHX may display an anti-inflammatory effect on neutrophil toxic products.[17] PHMB is a cationic oligomer having an average of 7–13 biguanide groups spaced by flexible hexamethylene segments (Figure 6.1.1). The high number of biguanide groups lead to a high effectiveness against microorganisms[18], although chemical characterization is hindered by the high dispersion of oligomer sizes.

Sutures penetrate through the protective skin and can come in contact with microorganisms that grow in subcutaneous tissues such as hair follicles. Microorganisms can therefore attach to the suture surface, allowing biofilm formation and acting as a niche for subsequent infections.[19–21] Moreover, the risk of infection can be increased by an inflammatory response caused by the suture. These problems are very important for sensitive and risk applications like sutures securing a central venous catheter.[21]

Currently, the most commonly used antimicrobial surgical suture is Coated Vicryl Plus Antibacterial Suture, a multifilament suture constituted by a copolymer having 90 wt-% of glycolide and 10 wt-% of L-lactide and TCS deposited on its surface to take profit of its capability to inhibit the colonization of a broad spectrum of bacteria.[22] Nevertheless, the incorporation of other bactericides is strongly recommended for the following reasons: a) The increasing resistance of bacteria to TCS caused by its massive use,[23] and b) Safety issues concerning the bioaccumulation of TCS and its negative effect on immune and reproductive functions.[24] In this way, coating formulations based on an amphiphilic polymer, poly[(aminoethyl methacrylate)-co-(butyl methacrylate)] (PAMBM), have been proposed due to its higher antimicrobial activity at lower concentrations than that detected for TCS loaded samples.[25]

CHX has been considered as alternative to TCS; specifically, coatings based on fatty acids (i.e., chlorhexidine laurate and chlorhexidine palmitate) were evaluated using Vicryl Plus as a reference multifilament suture.[26] High antimicrobial efficacy was demonstrated for up to 5 days while acceptable cytotoxic levels were determined for 11 μg/cm drug content.

Figure 6.1.1. Chemical structures of GL-*b*-(GL-*co*-TMC-*co*-CL)-*b*-GL (Monosyn®), the coating poly(LA-*co*-TMC) copolymer and the selected CHX and PHMB bactericides.

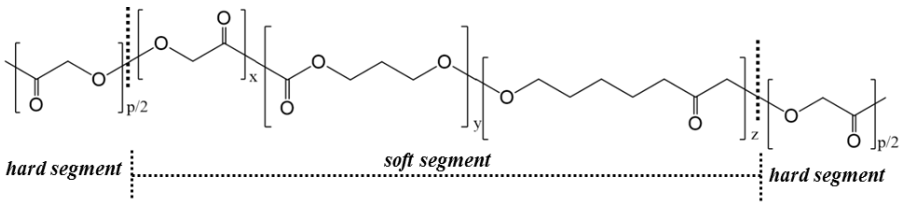

GL – *b* - (GL – *co* - TMC – *co* - CL) – *b* – GL

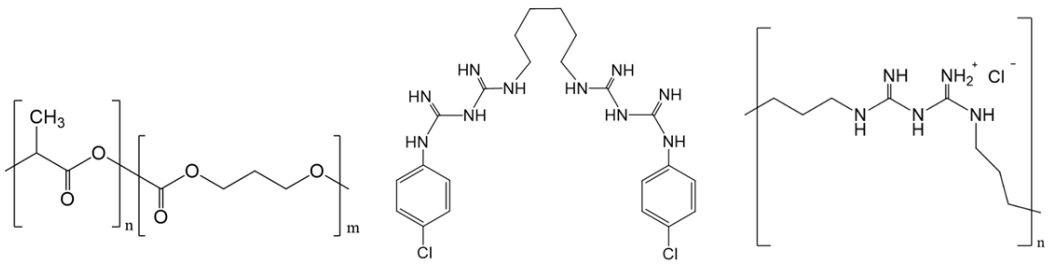

Poly(LA-*co*-TMC) **CHX** **PHMB**

The use of coatings is essential for multifilament sutures since they have a lubricant effect and can diminish tissue drag and risk of infection caused by capillarity.[27,28] These problems are not found when monofilament sutures are employed but the use of a coating may be still highly interesting if a drug is incorporated. This is studied in the present work using Monosyn® (i.e., glycolide-*b*-(glycolide-*co*-trimethylene carbonate-*co*-ε-caprolactone)-*b*-glycolide (Figure 6.1.1) abbreviated as GL-*b*-(GL-*co*-TMC-*co*-CL)-*b*-GL)[29] as a monofilament suture and CHX and PHMB as examples of bactericidal drugs with low and relatively high molecular weights, respectively. In addition, a new coating constituted by lactide and trimethylene carbonate (Figure 6.1.1) (abbreviated as poly(LA-*co*-TMC)) was developed according to the interest of this kind of copolymers for different biomedical applications.[30–33] Composition was selected to obtain a material with a sticky nature and a low degradation rate.

6.1.2 EXPERIMENTAL SECTION

6.1.2.1 Materials

Lactide, trimethylene carbonate and $Sn(Oct)_2$ were purchased from Sigma-Aldrich. Commercially available sutures of GL-*b*-(GL-*co*-TMC-*co*-CL)-*b*-GL (Monosyn®, USP 0 and diameter 0.35-0.399 mm) were kindly supplied by B. Braun Surgical, S.A. This triblock copolymer was constituted by 72, 14 and 14 wt-% of glycolide, trimethylene carbonate and ε-caprolactone units, respectively. The material had a middle *soft segment* that represents the 43 wt-% of the sample. Weight average molecular weight was 90,700 g/mol.

All solvents, chlorhexidine (CHX), 3-(4,5-dimethylthiazol-2-yl)-2,5-diphenyl-2H-tetrazolium bromide (MTT) and cell culture labware were purchased from Sigma-Aldrich. Cosmocil® (polyhexamethylene biguanide hydrochloride, PHMB) was kindly provided by B. Braun Surgical S.A.

The microbial culture was prepared with reagents and labware from Scharlau. *Escherichia coli* CECT 101 and *Staphylococcus epidermidis* CECT 245 bacterial strains were obtained from Spanish Collection of Type Culture. African green monkey kidney fibroblast-like (COS-7) and epithelial-like (VERO) cells were purchased from American Type Culture Collection.

6.1.2.2 Polymerization

Synthesis of the coating copolymer was carried out in tubes previously silanized with a silanization solution type I (Sigma-Aldrich) to prevent chemical reaction between the monomers and the OH groups contained in the glass. Silanization was performed during 30 min and then tubes were washed three times with anhydrous methanol and dried for 24 hours in a preheated oven at 120 °C. Copolymers with different ratios of lactide and trimethylene carbonate were synthesized in order to select the composition with better properties to be used as a coating.

Specifically, the selected poly(LA-*co*-TMC) copolymer having a theoretical 35 wt-% of lactide units was synthesized by bulk ring-opening polymerization of the appropriate mixture of lactide (LA) and trimethylene carbonate (TMC) for 48 h at 130 ºC under nitrogen atmosphere. $Sn(Oct)_2$ (0.1 mol /L solution in dry toluene) was used as a catalyst and the monomer/initiator (M/I) ratio was equal to 1,000. This relatively low ratio should enhance polycondensation and transesterification reactions and lead to a polymer with a random microstructure and in relatively short reaction time. When polymerization was completed, the tube was cooled to room-temperature and the resulting copolymer was dissolved in chloroform and precipitated in methanol. The recovered material was washed several times with methanol, dried in vacuum.

6.1.2.3 Measurements

Infrared absorption spectra were recorded in the 4000-600 cm^{-1} range with a Fourier Transform FTIR 4100 Jasco spectrometer equipped with a Specac model MKII Golden Gate attenuated total reflection (ATR) cell.

^{1}H-NMR spectra were recorded with a Bruker AMX-300 spectrometer operating at 300.1 MHz. Chemical shifts were calibrated using tetramethylsilane as the internal standard and $CDCl_3$ ($\delta(^1H)$ = 7.26 ppm) and deuterated DMSO ($\delta(^1H)$ = 2.50 ppm) as solvents.

Calorimetric data were obtained by differential scanning calorimetry with a TA Instruments Q100 series with T_{zero} technology and equipped with a refrigerated cooling system (RCS). Experiments were conducted under a flow of dry nitrogen at a heating rate of 20 ºC/min with a sample weight of approximately 5 mg. Calibration was performed with indium.

6.1.2.4 Degradation studies

Prismatic pieces (1 × 1.5 × 0.02 cm^3) were employed for hydrolytic degradation while films (0.5 × 0.5 × 0.2 cm^3) were employed for enzymatic degradation in order to enhance the surface/bulk ratio. To this end, polymer samples (0.4 g) were heated at 100 ºC (i.e., clearly above its glass transition temperature) for 12 min by means of a hydraulic press equipped with heating plates and a temperature controller (Graseby Specac). Pressure was progressively increased from 1 to 4 bar. Samples were recovered after cooling the mold or the film to room temperature. Films were subsequently cut to the desired size.

In vitro hydrolytic degradation assays were carried in a deionized water at 37 ºC, 50 ºC and 70 ºC. Samples were kept under orbital shaking in tubes filled with 8 mL of the degradation medium and sodium azide (0.03 wt-%) to prevent microbial growth for selected exposure times. The samples were then thoroughly rinsed with distilled water, dried to constant weight under vacuum and stored over P_4O_{10} before analysis. Degradation studies were performed in triplicated and the given data corresponded to the average values.

Weight retention (W_r) of the specimens was determined by the percentage ratio of weight after degradation (W_d) to initial weight before degradation (W_0):

$$W_r = W_d / W_0 \times 100 \quad (1)$$

Molecular weights were estimated by size exclusion chromatography (GPC) using a liquid chromatograph (Shimadzu, model LC-8A) equipped with an Empower computer program (Waters). A PL HFIP gel column (Polymer Lab) and a refractive index detector (Shimadzu RID-10A) were employed. The polymer was dissolved and eluted in 1,1,1,3,3,3-hexafluoroisopropanol containing CF_3COONa (0.05 M) at a flow rate of 1 mL/min (injected volume 100 µL, sample concentration 2.0 mg/mL). The number and weight average molecular weights were calculated using polymethyl methacrylate standards.

The enzymatic studies were carried out with a porcine lipase (30–90 U/mg) medium and using four replicates. All samples were exposed to 1 mL of pH 7.4 phosphate buffer containing the enzyme alongside with sodium azide (0.03 *w/v*-%). Solutions were renewed every 48 h to prevent enzymatic activity loss. Samples were extracted, washed and dried as indicated before.

6.1.2.5 Incorporation of CHX and PHMB onto uncoated and coated sutures

GL-*b*-(GL-*co*-TMC-*co*-CL)-*b*-GL monofilaments (5 cm length) were immersed (during 5 s) in ethanol or methanol solutions containing different percentages of CHX (0.1-15 *w/v*-%) or PHMB (0.1-6 *w/v*-%), respectively. After drying in hot air sutures were immersed in an ethyl acetate bath containing 3 *w/v*-% of poly(LA-*co*-TMC) when coated samples were required. Monofilaments were finally dried and stored under vacuum.

The total amount of drug loaded was determined by dissolution of the suture and the drug in 1,1,1,3,3,3-hexafluoroisopropanol, precipitation of polymers by addition of ethanol and finally by absorbance measurements by UV spectroscopy of the resulting solution using a Shimadzu 3600 spectrometer. Calibration curves were obtained by plotting the absorbance measured at 261 and 236 nm versus CHX and PHMB concentrations, respectively.

6.1.2.6 Release experiments

Controlled release measurements were performed with 5 cm length pieces of uncoated and coated sutures. These pieces were incubated at 37 °C in an orbital shaker at 80 rpm in tubes of 10 mL for 1 week. A 3:7 *v/v* mixture of PBS buffer and ethanol was employed as release media, although some experiments were also carried out in an ethanol medium. Drug concentration was evaluated by UV spectroscopy as above indicated. Samples were withdrawn from the release medium at predetermined time intervals. The volume was kept constant by the addition of fresh medium. All drug release tests were carried out using three replicates and the results were averaged.

6.1.2.7 Antimicrobial test

E. coli and *S. epidermidis* bacteria were selected to evaluate the antimicrobial effect of CHX and PHMB loaded sutures. The bacteria were previously grown aerobically to exponential phase in broth culture (5 g/L beef extract, 5 g/L NaCl, 10 g/L tryptone, pH 7.2).

Growth experiments were performed on a 24-well culture plate. 5 pieces of 1 cm length of uncoated and coated sutures were placed into each well. Then, 2 mL of broth culture containing 10^3 CFU was seeded on the suture samples. The cultures were incubated at 37 °C and agitated at 80-100 rpm. Aliquots of 100 µL were taken at predetermined time

intervals for absorbance measurement at 650 nm in a plate reader. Thus, turbidity was directly related to bacterial growth.

Bacterial adhesion onto sutures was also determined. The culture media were aspirated after incubation and the material washed once with distilled water. Then, 0.5 mL of sterile 0.01 M sodium thiosulfate was added to each well and after that the sutures were removed. After the addition of 1 mL of broth culture, the plate was incubated at 37 °C and agitated at 80-100 rpm for 24 h. The bacterial number was determined as above indicated. All assays were conducted in quadruplicate and the values averaged.

Regarding the qualitatively method, around 5 cm length pieces of loaded and unloaded sutures were placed into the agar diffusion plate and, seeded with 10^4 CFU/mL of both bacteria separately. The culture medium was prepared with 10.6 g of Brilliant Green Agar (BGA. Scharlau) or 7.9 g of Violet Red Bill Dextrose Agar (VRBDA, Scharlau) dissolved in 200 mL of Milli-Q water and sterilized at 121 ºC for 30 min in an autoclave. Plates were filled with 15 mL of medium and kept at rest to solidify the medium at room temperature. Inhibition halos images were taken after incubation of samples with bacteria for 24 h at 37 ºC.

6.1.2.8 Cell adhesion and proliferation assays

Studies were performed with fibroblast-like COS-7 cells and epithelial Vero cells. In all cases, cells were cultured in Dulbecco's Modified Eagle Medium (DMEM) as previously reported.[34]

Five pieces of 1 cm length of uncoated and coated sutures were placed and fixed in each well of a 24-well culture plate with a small drop of silicone (Silbione® MED ADH 4300 RTV, Bluestar Silicones). This plate was then sterilized by UV-radiation in a laminar flux cabinet for 15 min. For the cell adhesion and proliferation assays, aliquots of 50–100 µL containing 2×10^5 cells were seeded onto the samples in each well and incubated for 24 h (adhesion assay) or 96 h (proliferation assay).

Samples were evaluated by the standard adhesion and proliferation method.[34] The used procedure is based on a simple modification of the ISO10993-5:2009 standard test that describes the appropriate methodology to assess the *in vitro* cytotoxicity of medical devices. This test is designed to determine the *in vitro* biological response of mammalian

cells using appropriate biological parameters. According to this ISO standard, devices are placed in one of three categories based on the expected contact with the patient: a) Limited (≤24 h), b) Prolonged (>24 h and ≤30 days) and c) Permanent (>30 days). In our case, the assay was performed according to both, limited and prolonged categories. The study was carried out using four replicates and the results were averaged. Samples with adhered and grown cells on the samples were fixed with 2.5 *w/v*-% formaldehyde at 4 °C overnight. They were subsequently dehydrated and processed for observation of cell morphology.

Scanning electron microscopy (SEM) was employed to examine the morphology of coated and uncoated sutures as well as the morphology of adhered cells onto them. Carbon coating was accomplished with a Mitec k950 Sputter Coater (fitted with a film thickness monitor k150x. SEM micrographs were obtained with a Zeiss Neon 40 EsB instrument.

6.1.2.9 Statistical analysis

Values were averaged and graphically represented, together with their respective standard deviations. Statistical analysis was performed by one-way ANOVA test to compare the means of all groups, and then Tukey's test was applied to determine a statistically significant difference between two groups. The test confidence level was set at 95% ($p < 0.05$).

6.1.3 RESULTS AND DISCUSSION

6.1.3.1 Synthesis and characterization of the coating poly(LA-*co*-TMC) copolymer

The copolymer that exhibited better coating properties was that having a lactide content of 30-35 wt-%. Other compositions rendered coatings that were too rigid and easily detached from the suture surface (e.g., 50 wt-% of lactide) or too sticky for proper handling of the suture (e.g., 20 wt-% of lactide).

A reaction temperature of 130 ºC was enough to guarantee complete conversion of monomers in a reasonable time and avoid thermal degradation. The progress of the reaction could be easily followed from ^{1}H-NMR spectra taken from aliquots of the reaction mixture at regular time intervals. Thus, spectra recorded at the beginning of

copolymerization showed signals of unreacted lactide (5.43 and 1.22 ppm) and trimethylene carbonate (4.43 and 1.98 ppm) monomers, which can be easily distinguished from those corresponding to units incorporated into the polymer chain (5.25–4.95 and 1.61–1.52 ppm for methine and methyl protons of lactic acid units (L); 4.20–4.10 ppm for the α- and γ-methylene protons and 2.10–1.90 ppm for the β-methylene protons of trimethylene carbonate units (TMC)) (Figure 6.1.2). Lactide reacted faster, and consequently polymerization time was determined by the achievement of a complete conversion of trimethylene carbonate, as shown in the spectrum of Figure 6.1.2.[35]

The areas of peaks at 5.20–4.90 ppm and 4.20–4.10 ppm were used to determine the final composition of lactide units:

$$LA\ (wt\text{-}\%) = A_{5.20-4.90} \times 72 \,/\, [(A_{5.20-4.90} \times 72) + (A_{4.20-4.10} \times 102\ /4)] \qquad (2)$$

where 72 and 102 are the molecular weights of lactyl and trimethyl carbonyl units, respectively.

Values were slightly lower than the theoretical monomer feed ratio due to a practically negligible sublimation of lactide. Thus, 32-34 wt-% was determined when the feed ratio corresponded to 35 wt-%.

Sequence sensitivity was found for methine and methyl protons, and consequently information of chain microstructure could be derived, as previously reported.[36]

The proton spectrum showed an intense multiplet at around 5.18 ppm, which was attributed to LLL and TmcLL triads, together with a quintuplet around 5.03 ppm caused by the overlapping of quadruplets associated with LLTmc and TmcLTmc triads. In addition, doublets corresponding to the LL and TmcL sequences could be detected at around 1.60 and 1.53 ppm, respectively, in agreement with the reported dyad sensitivity of CH_3 protons. Note that the upfield dyad has a clearly higher intensity, indicating a high ratio of TmcLTmc sequences in the copolymer. This triad results from transesterification reactions inside the lactidyl units and should be favored by temperature, time and catalysts.

Figure 6.1.2. ^{1}H-NMR spectrum of the coating copolymer with indication of peaks associated with trimethylene carbonate (T) and acid lactic (L) units as labelled in the chemical formula. Small arrow points to the presence of a minor amount of trimethylene carbonate monomer for samples taken at a reaction time slightly shorter than that corresponding to a complete conversion.

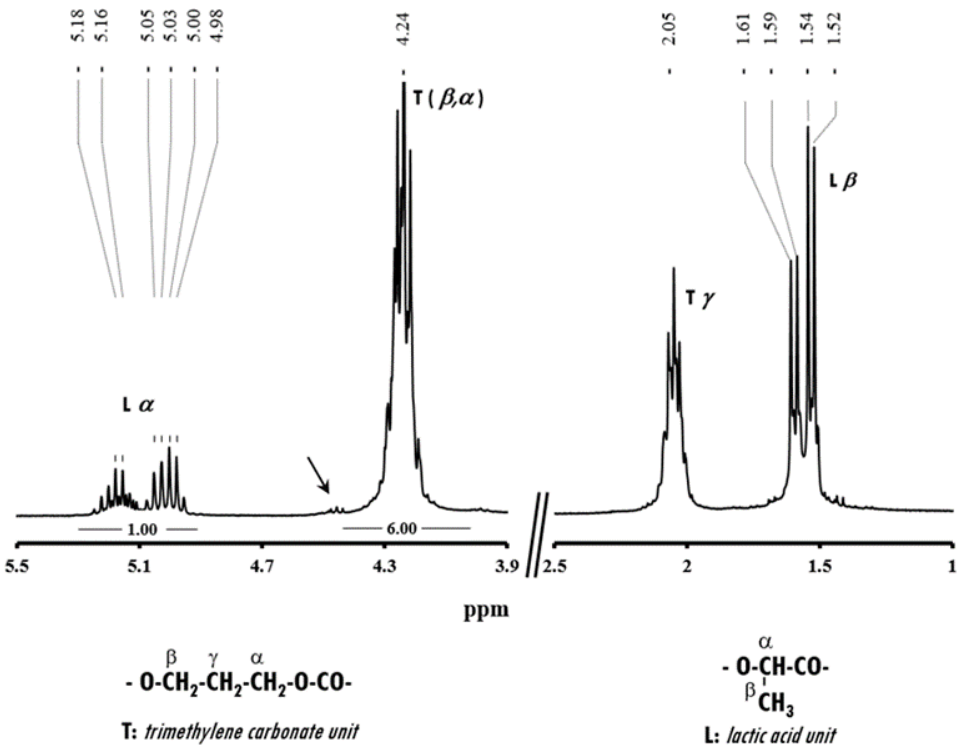

The copolymer was obtained with a weight average molecular weight of 145,000 g/mol and a polydispersity index of 2.3. The FTIR spectrum was in full agreement with the expected chemical constitution, displaying the characteristic common bands of both homopolymers (e.g., carbonyl group at 1735–1745 cm^{-1}) as well as those only associated with polylactide or polytrimethylene carbonate (Figure 6.1.3).[37,38] The main peculiar difference, which may be a consequence of molecular interactions, is the decrease of the 1080 cm^{-1} band (i.e., symmetric C-O-C stretching) that usually appears with higher intensity in the PLA homopolymer.

Figure 6.1.3. FTIR spectra (2050-650 cm^{-1}) of PLA, PTMC and the synthesized copolymer. Characteristic peaks of PLA and PTMC are indicated by red and green dashed lines, respectively, whereas common peaks are indicated by the blue dashed lines.

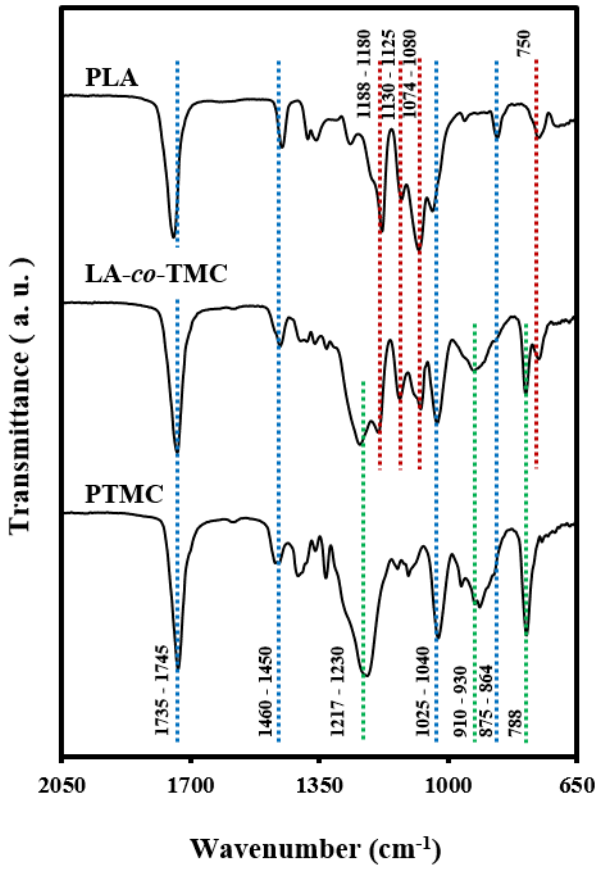

The DSC calorimetric trace (Figure 6.1.4) revealed the amorphous character of the copolymer since only a glass transition temperature of -20 ºC could be detected. This temperature was close to that reported for poly(trimethylene carbonate) (i.e., -25 ºC [39] and -32 ºC [40]) and far from the value of 60 ºC for polylactide, as could be expected from the chemical composition. Thermal behavior was clearly different from that of the polymer matrix, which showed a glass transition temperature of -14 ºC and great ability to crystallize from the glassy state, giving rise to polyglycolide crystalline entities with a melting point close to 198 ºC (Figure 6.1.4).

Figure 6.1.4. DSC heating traces of GL-*b*-(GL-*co*-TMC-*co*-CL)-*b*-GL (down) and the coating copolymer (up).

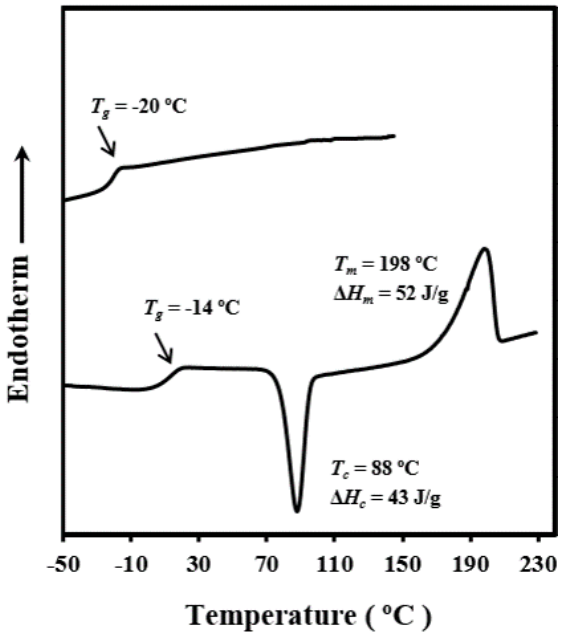

The copolymer was hydrolytically and enzymatically degradable, as could be inferred from both, the sample weight (Figure 6.1.5) and molecular weight losses (Figure 6.1.6) observed during exposure to the different degradation media. Thus, three phases were observed for the pH 7.4 medium under the accelerated condition provided by a temperature of 70 ºC. Initially, the sample weight decreased very slowly, and approximately 24 days were required to produce a loss of 9%. After this period, a very fast weight loss was observed as degradation after the previous step was sufficiently advanced to render a high proportion of soluble molecular fragments. Specifically, weight loss increased from 9% to 83% between days 24 and 34. The third step was again slow because it involved highly insoluble and crystalline low molecular weight residues. Only the first step was detected up to 83 days, when degradation was performed at 50 ºC; in particular, a loss of 18% was determined. Practically no weight loss was detected at the physiological temperature of 37 ºC at the maximum exposure time (i.e., 83 days). A low susceptibility to enzymatic degradation was also found since a weight loss of only 7% was determined after 61 days of exposure.

Figure 6.1.5. Remaining weight percentage of poly(LA-*co*-TMC) coating sample exposed to a pH 7.4 hydrolytic degradation medium at 70 ºC (▲), 50 ºC (■) and 37 ºC (●) and a porcine pancreatic lipase enzymatic medium (◊).

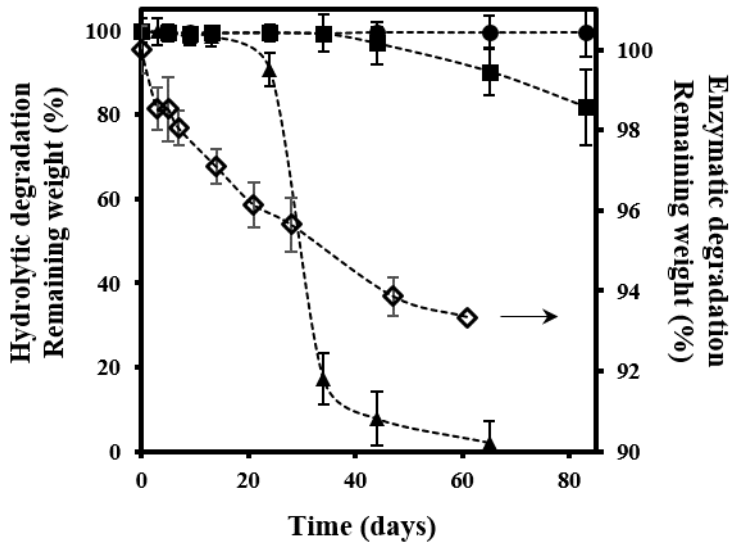

Molecular weight changes were very useful to verify the progress of degradation. Thus, a steady decrease was observed in a first degradation step for hydrolytic degradation at the three test temperatures. This step followed a first-order kinetic which could be associated with a random chain scission mechanism. Obviously, the kinetic constant decreased with temperature. In a second step, the molecular weight reached a practically constant value that can be interpreted as the minimum molecular size of insoluble degraded fragments. Thus, a molecular weight of 3,000 g/mol was attained after 24 days of exposure to the medium at 70 ºC, whereas 65 days were required to achieve a constant molecular weight of 7,100 g/mol at a temperature of 50 ºC. Note that this molecular weight was slightly higher than that observed at 70 ºC due to the different solvent capability.

The evolution of the polydispersity index (inset of Figure 6.1.6) was also useful to follow the degradation process since it reached a maximum value at the end of the first degradation step. After this period, samples became more homogeneous due to solubilization of small fragments and degradation of high molecular weight chains.

Figure 6.1.6. Changes in the weight average molecular weight of poly(LA-*co*-TMC) coating sample exposed to a pH 7.4 hydrolytic degradation medium at 70 ºC (▲), 50 ºC (■) and 37 ºC (●). Changes in the polydispersity index during accelerated degradation are shown in the inset.

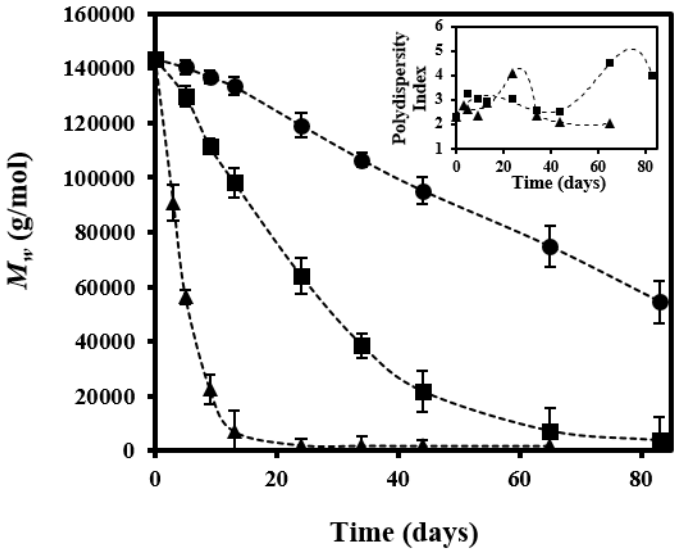

6.1.3.2 CHX and PHMB loading of sutures

The selected drugs (CHX and PHMB) had a hydrophilic character that contrasted with the hydrophobicity of the selected coating copolymer. Therefore, a relatively volatile and economical common solvent could not be used for the copolymer and the drugs. Ethyl acetate, ethanol and methanol were selected for coating and loading baths containing poly(LA-*co*-TMC), CHX and PHMB, respectively. Thus, the drug loading process involved two steps: incorporation of CHX or PHMB and coating, if necessary.

Immersion time (5 s), drying method (hot air stream) and copolymer concentration (3 *w/v*-%) were optimized to obtain the most economical and fastest process, as well as completely coated and uniform sutures. For example, Figure 6.1.7a shows that a higher copolymer concentration (e.g., 10 *w/v*-%) leads to formation of some aggregates on the monofilament surface. Drug particles can be detected on the suture surface after the first immersion, with these non-homogeneities being clearer for PHMB (Figure 6.1.7b).

Nevertheless, uniform surfaces were achieved after incorporation of the coating, as shown in **Figure 6.1.7c**.

Figure 6.1.7. Scanning electron micrographs of a monofilament of the GL-*b*-(GL-*co*-TMC-*co*-CL)-*b*-GL suture with the following treatments: **(a)** coating by immersion for 5 s in an ethyl acetate bath containing 10 *w/v*-% of poly(LA-*co*-TMC), **(b)** immersion in a methanol bath containing 3 *w/v*-% of PHMB and **(c)** a first immersion in a methanol bath containing 3 *w/v*-% of PHMB and then in an ethyl acetate bath containing 3 *w/v*-% of poly(LA-*co*-TMC) (c).

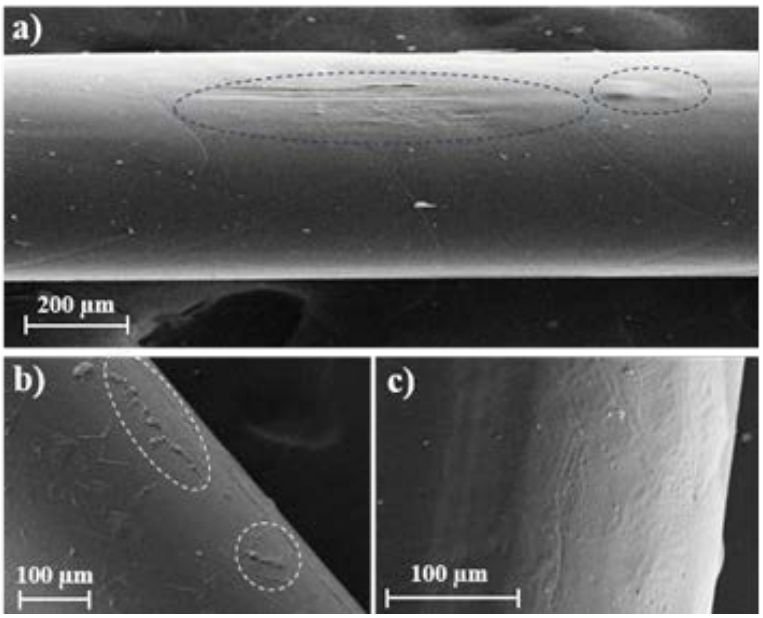

Good correlation was observed between the drug concentration in the alcohol bath and the amount of loaded drug referred to the suture unit length (**Figure 6.1.8**). The slope of linear plots was 1.12 and 1.13 for CHX and PHMB, respectively, where 0.98-0.99 was the value of the determination coefficient (r^2). These similar slopes indicated that the amount of incorporated drug was independent of its nature, as could be expected from the high chemical similarity of both biguanide compounds and the fact that the loaded amount should be mainly determined by the suture surface (i.e., diameter of the suture or USP number).[33]

Figure 6.1.8. Plot of the amount of chlorhexidine (●) and PHMB (■) incorporated into the GL-*b*-(GL-*co*-TMC-*co*-CL)-*b*-GL suture (drug weight/suture length) versus drug concentration of ethanol and methanol baths. Results are given for solutions with (solid lines) and without (dashed lines) poly(LA-*co*-TMC).

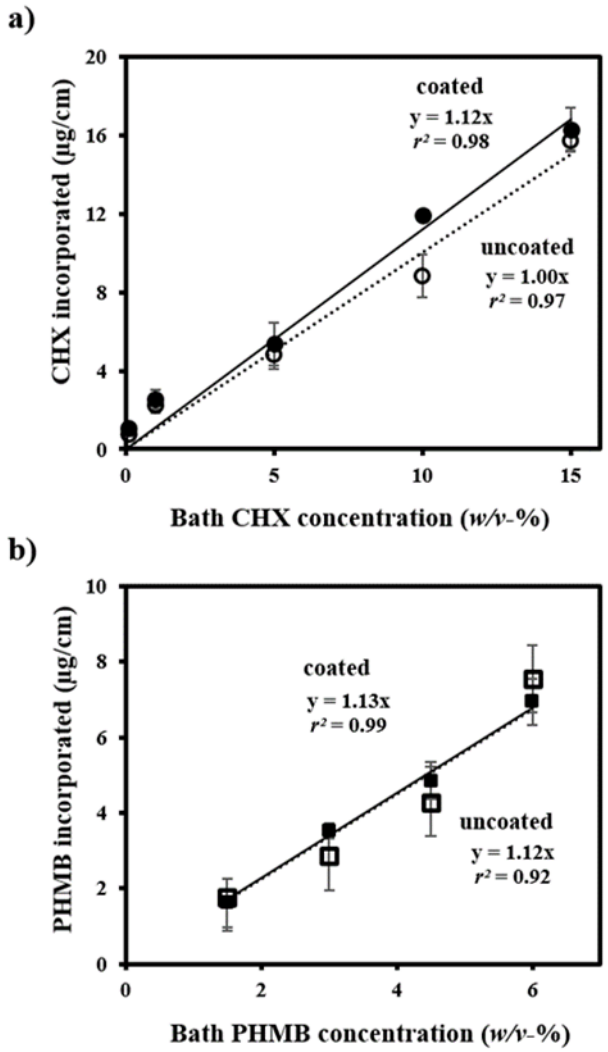

For the sake of completeness, Figure 6.1.8 also shows the correlation for uncoated samples (i.e., when the drug was merely absorbed on the fiber surface after the first bath). In this case, the determination coefficient decreased, and specifically a value of 0.92 was determined for PHMB. It seems that the relatively high deviation from a perfect linear plot is due to an easy desorption during the manipulation of a suture lacking the protective

coating. Note also that in the case of CHX the slope decreased to 1.00, suggesting again some loss of the absorbed drug during manipulation. It is, however, important to emphasize the protective effect of the selected coating, together with the fact that drugs loaded in the first bath remained adsorbed on the suture during the coating step due to their complete insolubility in the ethyl acetate bath. It should also be pointed out that the amount of loaded drug was even greater (CHX in Figure 6.1.8a) when the coating was employed even though the process required an additional bath.

6.1.3.3 CHX and PHMB release from sutures

The release of PHMB and CHX was studied using a medium consisting of a 3:7 *v/v* mixture of PBS buffer and ethanol since it was a better solvent for the selected drugs than a typical nutrient serum medium. Figure 6.1.9a compares PHMB release percentages for uncoated and coated sutures at given drug load (i.e., ~ 6.8 μg/cm). Results clearly demonstrated the effectiveness of the coating to suppress the burst effect. In fact, 83% of the drug was released from the uncoated suture in only 5 min, while a decrease to 5% was determined when poly(LA-*co* -TMC) was used as a coating. In this case, total release was achieved after 1 h of exposure. The release was enhanced when 100% ethanol was used, with complete release being achieved after 45 min. Nevertheless, even in this case the coating was appropriate to suppress the burst effect.

The release of CHX was faster, as shown by comparing the samples loaded with a similar amount of PHMB and CHX in Figure 6.1.9a. It can also be seen that CHX was not completely released. Thus, a small amount of the drug was effectively adsorbed in the suture (i.e., 16% (Figure 6.1.9b) for the sample loaded with ~ 5.6 μg/cm, which means a value close to 0.9 μg/cm).

Figure 6.1.9b illustrates the change in the release profiles for samples loaded with different amounts of CHX. All profiles showed a fast release step with a slope that slightly increased with concentration and a different percentage of retained drug (i.e., a plateau level was detected). This percentage always corresponded to an adsorption around 0.9 μg/cm. Thus, it was an intrinsic characteristic of physicochemical interactions that could be established between CHX and the polymer matrix. Note that the plateau observed in the release curves could not be associated with a solubility problem since samples loaded with a higher amount of CHX should have lower release percentages.

Figure 6.1.9. (a) PHMB release percentages in PBS-EtOH 30:70 medium for uncoated (○) and coated (●) sutures. For the sake of completeness, data for an EtOH medium are also plotted (▲) for the coated suture as well as the CHX release percentage plot in PBS-EtOH 30:70 medium for the coated suture (■). Samples were obtained from baths containing 6 *w/v*-% and 5 *w/v*-% of PHMB and CHX, respectively. **(b)** CHX release percentages in a PBS-EtOH 30:70 medium for coated sutures loaded in baths with 15 *w/v*-% (♦), 10 *w/v*-% (●), 5 *w/v*-% (■) and 1 *w/v*-% (▲) of CHX. For the sake of completeness, data for an uncoated suture coming from a bath containing 5 *w/v*-% (□) of CHX are also plotted.

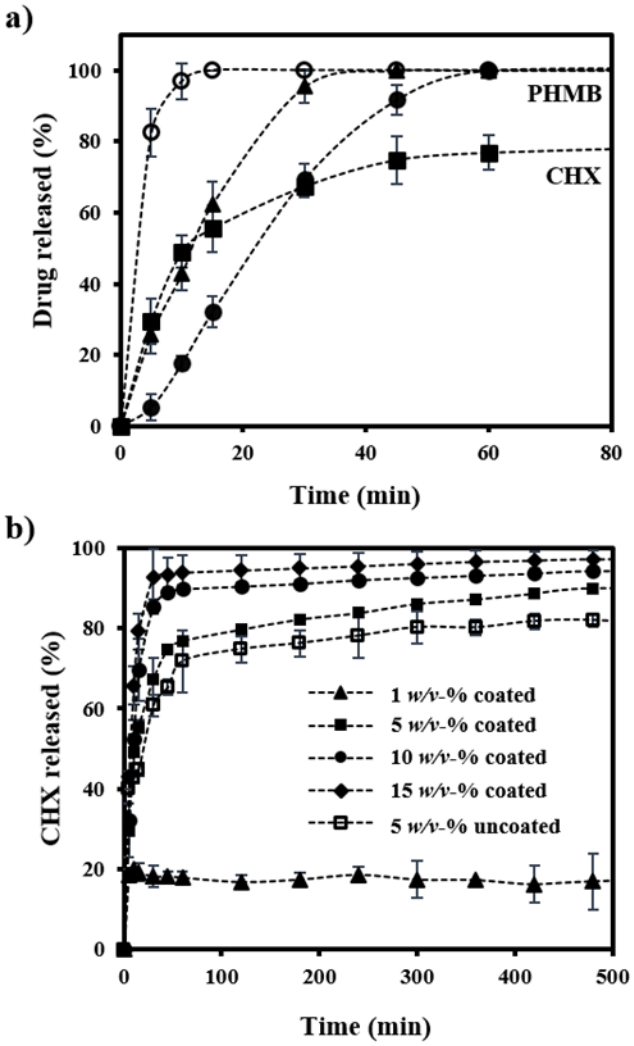

For the sake of completeness, Figure 6.1.9b also plots the release profile of an uncoated suture. This sample incorporated approximately 5 μg/cm of CHX, according to the loading relationship of Figure 6.1.8, and consequently, the observed release percentage of 82% indicated that again 0.9 μg/cm of CHX remained adsorbed on the suture surface. Therefore, the coating is not relevant for retaining the amount of CHX corresponding to the plateau, which should be mainly due to interactions with GL-*b*-(GL-*co*-TMC-*co*-CL)-*b*-GL.

6.1.3.4 Antimicrobial effect of CHX and PHMB loaded sutures

The antimicrobial effect of CHX and PHMB loaded sutures was quantitatively evaluated following the growth kinetics of Gram-negative (*E.coli*) and Gram-positive (*S. epidermidis*) bacteria.

Figure 6.1.10 shows that, for both types of bacteria, bacterial growth on the coated suture was always similar to that of the control. This growth was characterized by a lag or latency phase for a period of 4 h followed by a typical exponential growth (log phase). Therefore, the results showed that the coated suture was highly susceptible to bacterial infection. For this reason, it seemed interesting to incorporate CHX or PHMB to suppress this effect.

Sutures loaded in baths with a drug concentration of 0.1 *w/v*-% (equivalent to a load of 0.112 μg/cm and 0.113 μg/cm for CHX and PHMB, respectively) did not have any growth inhibitory effect. In fact, concentrations of 0.3 *w/v*-% and 1 *w/v*-% were required for PHMB and CHX, respectively, to lead to a bacteriostatic effect. This effect was characterized by an increased duration of the lag phase up to 10 h and a subsequent linear growth instead of the typical exponential growth. The observed linear relationship basically indicates that bacterial growth increases as the drug is consumed. The bacteriostatic effect was found for PHMB and CHX concentrations in the baths of 1.5 *w/v*-% and 5 *w/v*-% or higher, respectively. In these cases, the latency phase was around 30 h and the maximum growth after 48 h of culture was 20%. A completely inhibitory effect required a minimum CHX and PHMB concentration of 10 *w/v*-% and 3 *w/v*-%, respectively, which means a load of 11.2 μg/cm and 3.4 μg/cm.

Figure 6.1.10. Growth curves of *E. coli* **(a,c)** and *S. epidermidis* **(b,d)** on culture plate as positive control (□), coated suture as blank (○) and poly(LA-*co*-TMC) coated sutures (dashed lines) loaded in baths with the indicated *w/v*-% of CHX **(a,b)** and PHMB **(c,d)**. For the sake of completeness, data for uncoated sutures loaded from selected baths are also plotted (solid lines).

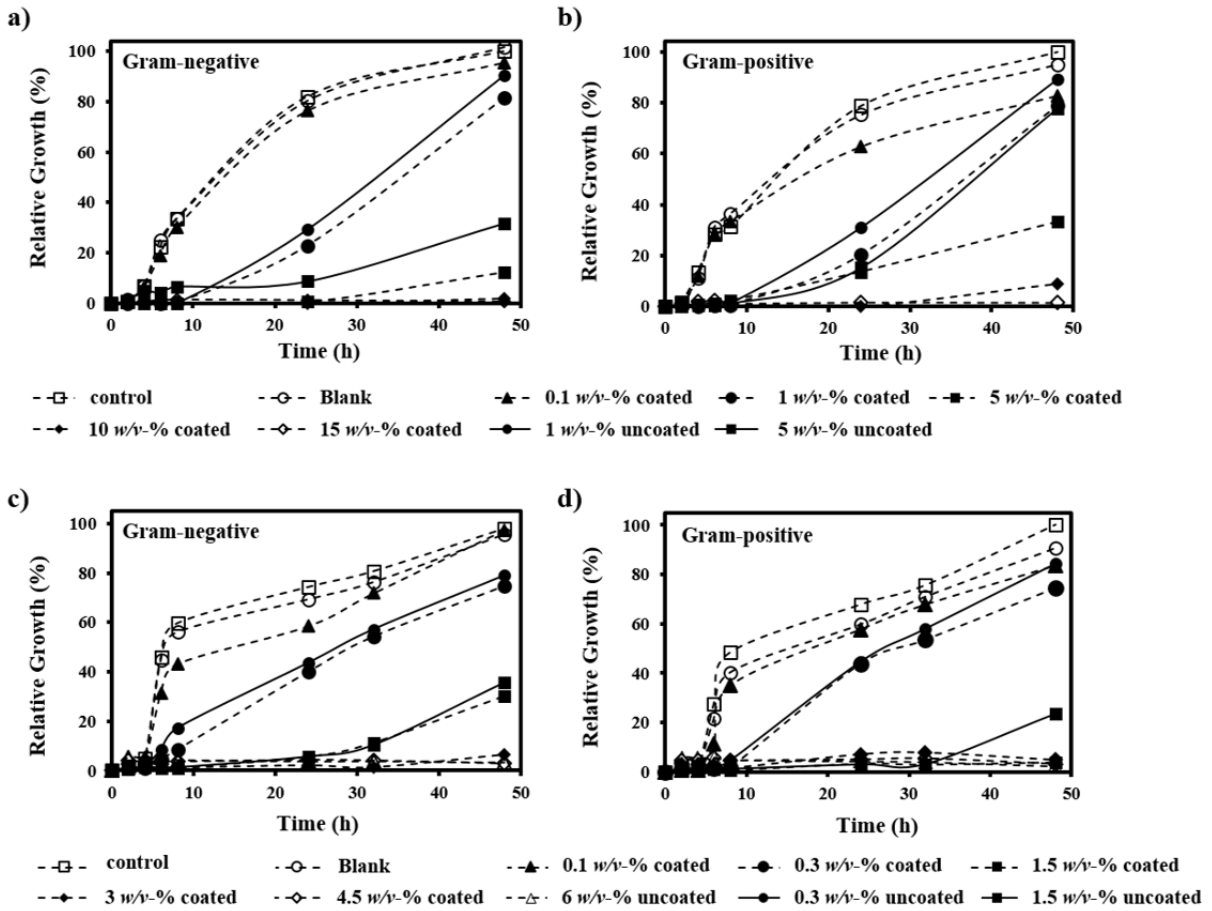

The behavior of uncoated CHX and PHMB loaded sutures was similar for some representative samples (i.e., sutures loaded with the amount corresponding to a bacteriostatic effect), as shown in Figure 6.1.10. In fact, a lower inhibition with respect to coated sutures can be explained considering that the amount of drug loaded in the bath was lower than expected (Figure 6.1.8), especially in the case of CHX.

Evaluation of bacterial adhesion was carried out as another antimicrobial control for the new materials (Figure 6.1.11). Results demonstrated a dose-dependent effect for both Gram-negative and Gram-positive bacteria. Therefore, adhesion was not inhibited for sutures coming from baths containing 0.1 *w/v*-% of drugs, while partial adhesion in the 40%-60% range was found for sutures coming from baths containing 5 *w/v*-% and 0.3-1.5 *w/v*-% of CHX and PHMB, respectively. Finally, complete inhibition was observed for the high doses corresponding to baths containing 10-15 *w/v*-% and 3-6 *w/v*-% of CHX and PHMB. Inhibition was higher for coated than uncoated sutures because of higher drug loading efficiency (Figure 6.1.8).

Figure 6.1.11. Adhesion of *E. coli* **(a,c)**, and *S. epidermidis* **(b,d)** bacteria on uncoated (gray bars) and poly(LA-*co*-TMC) coated (grid bars) sutures loaded in baths with the indicated concentrations of CHX **(a,b)** and PHMB **(c,d)**. Data concerning the culture plate as positive control and the coated and uncoated sutures as blank are also provided.

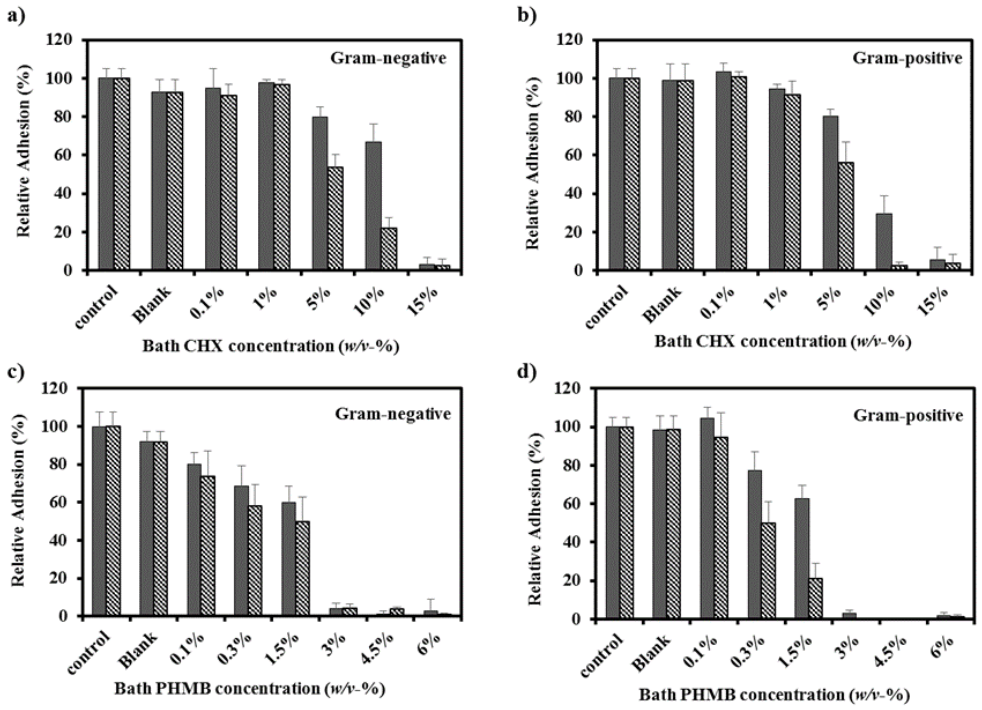

The above results could also be qualitatively observed in the Agar tests by measurement of the inhibition halos around sutures (Figure 6.1.12). These halos are a consequence of the bactericidal activity which affects both inhibition of bacterial growth and bacterial adhesion on the suture. It should be considered that this test misestimates the effect produced by cationic antimicrobial compounds since they have a limited diffusion in the lipophilic agar medium. Nevertheless, results clearly showed that CHX and PHMB have a preferential effect against Gram-positive bacteria, which exhibited clearly greater inhibition halos than the Gram-negative medium.

Figure 6.1.12. Agar tests showing the inhibition zone of *E. coli* and *S. epidermidis* bacteria caused by uncoated and poly(LA-*co*-TMC) coated sutures loaded in baths with the indicated CHX and PHMB concentrations.

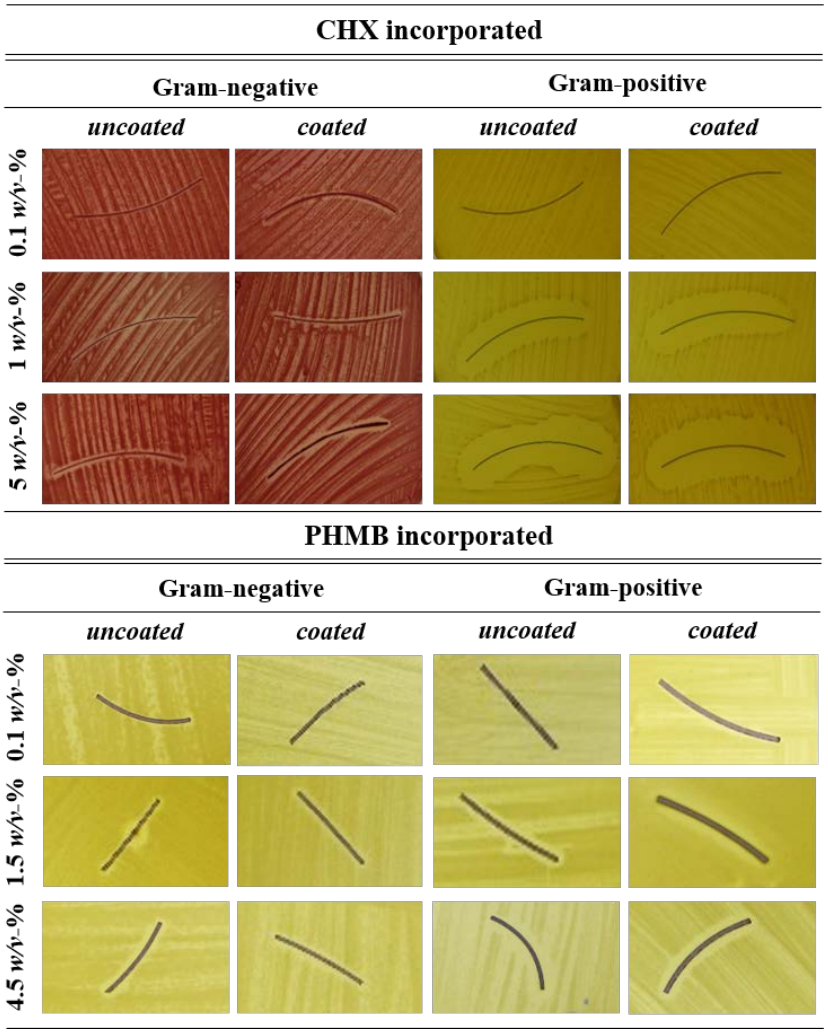

Differences in activity against Gram-positive bacteria between CHX and PHMB were reflected by the greater inhibition halos of CHX, probably caused by easy diffusion of lower molecular sizes through the agar medium. Note that an opposite behavior can be deduced from growth kinetic measurements, a feature that can be explained by a high diffusion rate for the lower molecular weight drug. Finally, the behavior of coated and uncoated sutures was always similar. This demonstrates that the selected coating did not hinder drug diffusion from the suture to the medium, which was independent of drug size (small and big for CHX and PHMB, respectively).

6.1.3.5 Cytotoxicity of CHX and PHMB loaded sutures

Fibroblast-like and epithelial-like cell lines were employed to evaluate the cytotoxicity of drug loaded sutures by cell adhesion and cell proliferation events after 24 and 96 h of culture, respectively (Figure 6.1.13).

Adhesion of both cell lines was reduced in the 40% - 60% range when sutures were loaded with the amount of CHX that rendered a bactericidal effect and even for the lowest load leading to a bacteriostatic effect. Cell proliferation assays were more useful to discriminate between the different loads. Thus, samples coming from baths having 5 *w/v*-% or higher percentages of CHX reduced cell viability drastically, whereas those loaded from a bath with 1 *w/v*-% allowed a cell growth similar to that observed for the control and the unloaded suture (Figures 6.1.13e and 6.1.13f).

On the other hand, the incorporation of PHMB reduced cell adhesion in the 20%-40% range for both types of cell lines, which was practically independent of the amount of loaded drug (Figures 6.1.13c and 6.1.13d). Furthermore, bactericidal and bacteriostatic doses of PHMB caused a decrease close to 60% in the cell proliferation assays (Figures 6.1.13g and 6.1.13h). Differences with CHX results demonstrated that the molecular size of biguanide compounds had adverse effects on cell growth, as can be expected from differences in the ability to penetrate into the cells. The results indicated that the use of coated sutures favored cell adhesion and proliferation, as can be clearly seen in Figures 6.1.13d and 6.1.13g.

Figure 6.1.13. Adhesion **(a–d)** and proliferation **(e–h)** of Vero **(a,c,e,g)** and COS-7 **(b,f,d,h)** cells on uncoated (gray bars) and poly(LA-*co*-TMC) (grid bars) coated sutures loaded in baths with the indicated concentrations of CHX **(a,b,e,f)** and PHMB **(c,d,g,h)**. Data concerning the culture plate as positive control are also provided.

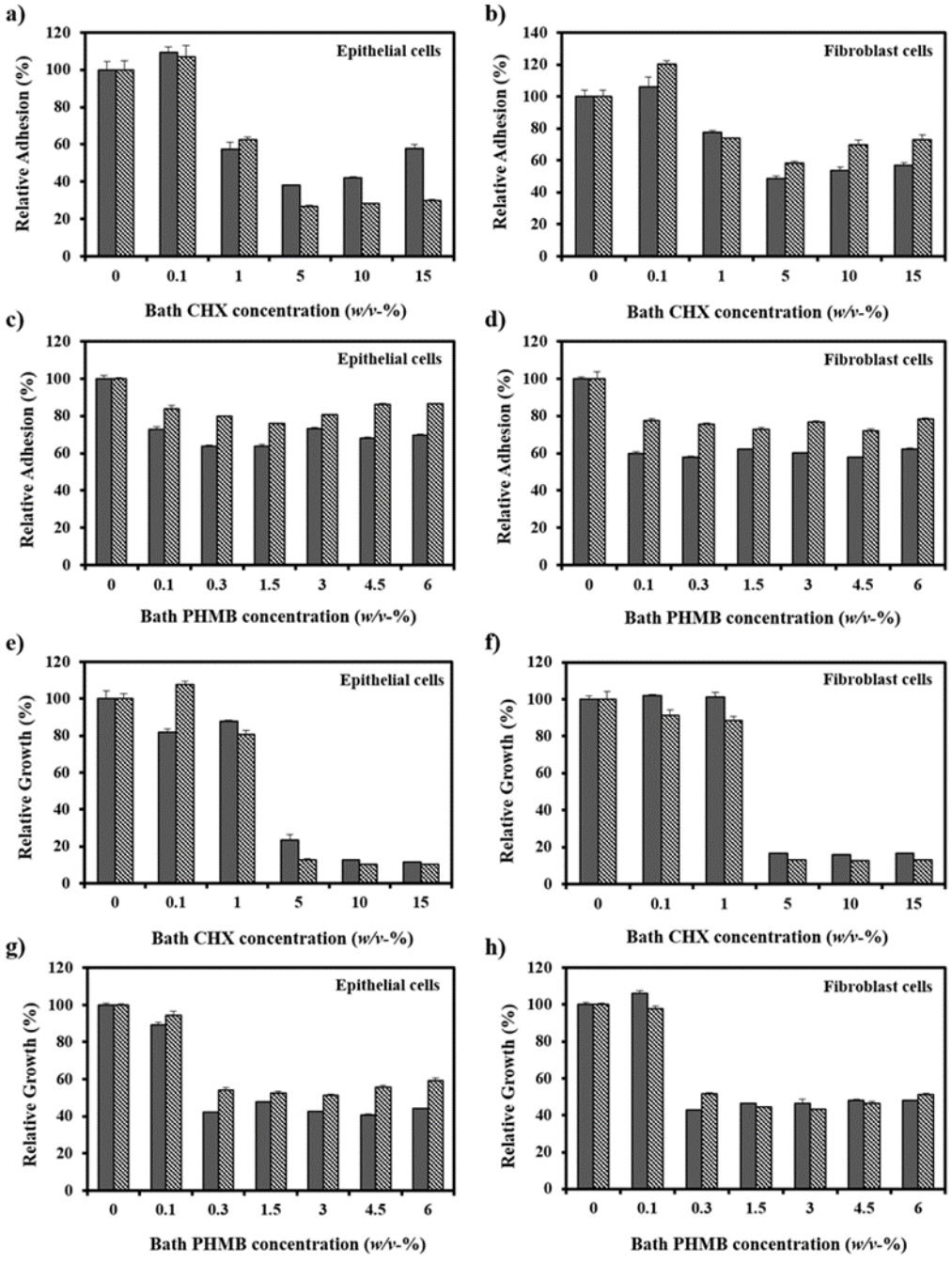

Micrographs in Figure 6.1.14 show the morphology of epithelial-like and fibroblast-like cells adhered to drug loaded sutures. In general, epithelial like cells appear widely extended, forming clusters while fibroblast-like cells appear as single, extended, well distributed cells.

Figure 6.1.14. SEM micrographs of Vero **(a,b)** and COS-7 **(c)** cell growth on poly(LA-*co*-TMC) coated sutures loaded in baths with CHX **(a,b)** and PHMB **(c)** concentrations of 1 *w/v*-% and 1.5 *w/v*-%, respectively.

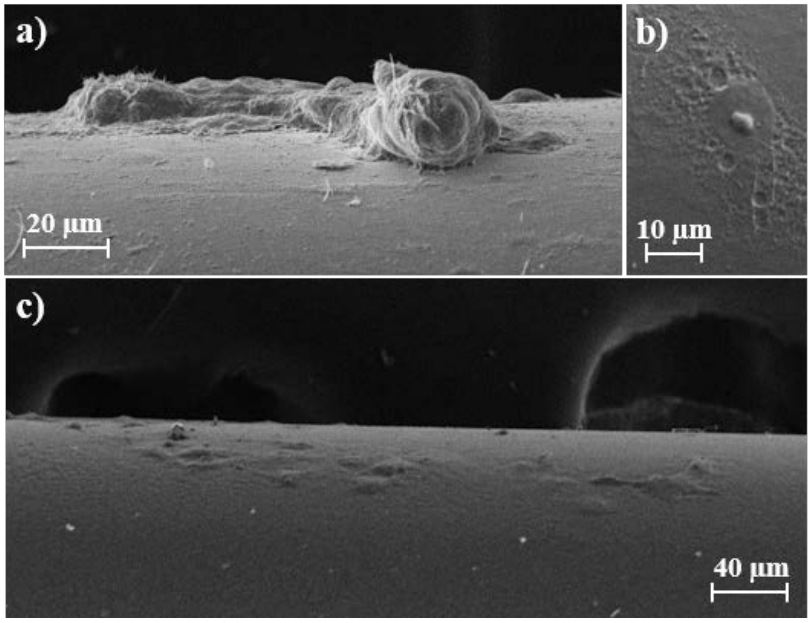

6.1.4 CONCLUSIONS

A random copolymer prepared by ring opening polymerization of 35 wt-% of lactide and 65 wt-% of trimethylene carbonate showed appropriate characteristics to be used as a coating of monofilament sutures such as the GL-*b*-(GL-*co*-TMC-*co*-CL)-*b*-GL three block copolymer. The new coating was characterized by a T_g close to -20 ºC, a low degradation rate at room temperature in a pH 7.4 medium, and a solubility in organic media enabling a consistent and homogeneous coating to be obtained by immersion of sutures in an ethyl acetate bath.

Antimicrobial drugs such as CHX and PHMB can be directly adsorbed on the suture surface or loaded into the suture by a two-step procedure involving a subsequent coating. The second method showed advantages in terms of loading efficiency as drugs were more protected against detachment caused by handling. Furthermore, the coating was essential to avoid a complete burst effect in the case of PHMB. CHX was released according to a first relatively fast step and at a rate slightly dependent on the amount of loaded drug. However, in all cases an amount close to 0.9 μg/cm was retained on the suture surface, probably as a consequence of good interactions with the polymer matrix. The selected drugs exhibited a dose-dependent antimicrobial activity, and it was possible to distinguish between bacteriostatic and bactericidal activity. Bacterial growth kinetics and bacterial adhesion measurements indicated greater activity of PHMB against Gram-positive bacteria when samples with similar loaded weights of CHX and PHMB were compared. Incorporation of the coating was not essential in terms of bactericidal activity if the effect of lower drug loading efficiency was discarded.

Cell adhesion and cell proliferation assays demonstrated the potential cytotoxicity of sutures having high doses of CHX and PHMB and that those with a clear bacteriostatic effect (i.e., inhibition of bacterial growth for a period between 10 h–30 h) could fortunately be considered biocompatible. The presence of the coating copolymer was more beneficial to reduce cytotoxicity, especially when the higher molecular weight PHMB was employed since the molecular size influenced the rate of diffusion towards cells.

In summary, sutures loaded with biguanide derivatives such as CHX and PHMB exhibited a clear preventive effect against bacterial infection or colonization while allowing cell adhesion and proliferation in regenerated tissues.

6.1.5 REFERENCES

1. Davies, D. Understanding biofilm resistance to antibacterial agents. *Nat. Rev. Drug Discov.* 2, 114–22 (2003).

2. Sun, G. Prevention of hospital and community acquired infections by using antibacterial textiles and clothing. In *Polymeric materials with antimicrobial activity* (eds. Muñoz-Bonilla, A., Cerrada, M. L. & Fernández-García, M.) 139–154 (RSC Polymer Chemistry Series, 2014).

3. Costerton, J. W., Stewart, P. S. & Greenberg, E. P. Bacterial bofilms: a common cause of persistent infections. *Science* (80-.). 284, 1318–1322 (1999).

4. Chen, L., Bromberg, L., Hatton, T. A. & Rutledge, G. C. Electrospun cellulose acetate fibers containing chlorhexidine as a bactericide. *Polymer.* 49, 1266–1275 (2008).

5. Del Valle, L. J., Franco, L., Katsarava, R. & Puiggalí, J. Electrospun biodegradable polymers loaded with bactericide agents. *AIMS Mater. Sci.* 3, 52-87 (2016).

6. Lenz, A. M., Fairweather, M. & Cheadle, W. G. Resistance profiles in surgical-site infection. *Future Microbiol.* 3, 453–462 (2008).

7. Deleo, F. R., Deleo, F. R., Chambers, H. F. & Chambers, H. F. Reemergence of antibiotic-resistant *Staphylococcus-aureus* in the genomics era. *J. Clin. Invest.* 119, 2464-2474 (2009).

8. Broex, E. C. J., van Asselt, A. D. I., Bruggeman, C. A. & van Tiel, F. H. Surgical site infections: how high are the costs? *J. Hosp. Infect.* 72, 193–201 (2009).

9. Danese, P. N. Antibiofilm approaches: Prevention of catheter colonization. *Chem. Biol.* 9, 873–880 (2002).

10. Abedon, S. T., Kuhl, S. J., Blasdel, B. G. & Kutter, E. M. Phage treatment of human infections. Bacteriophage 1, 66–85 (2011).

11. Melaiye, A. *et al.* Silver(I)-imidazole cyclophane gem-diol complexes encapsulated by electrospun tecophilic nanofibers: Formation of nanosilver particles and antimicrobial activity. *J. Am. Chem. Soc.* 127, 2285–2291 (2005).

12. Baley, G. J., Peck, G. E. & Banker, G. S. Bactericidal properties of quaternary ammonium compounds in dispersed systems. *J. Pharm. Sci.* 66, 696–699 (1977).

13. Ortenzio, L. F. & Stuart, L. S. The behavior of chlorine-bearing organic compounds in the AOAC available chlorine gemicidal equivalent concentration test. *J. Assoc. Off. Ana. Chem.* 42, 630–633 (1959).

14. Chopra, I. & Roberts, M. Tetracycline antibiotics : Mode of action, applications, molecular biology, and epidemiology of bacterial resistance. *Microbiol. Mol. Biol. Rev.* 65, 232–260 (2001).

15. Leikin, J. B. & Paloucek, F. P. Chlorhexidine Gluconate. In *Poisoning and Toxicology Handbook* 183–184 (Informa, 2008).

16. Green, J.-B. D., Fulghum, T. & Nordhaus, M. A. Immobilized antimicrobial agents: A critical perspective. In *Science against microbial pathogens: communicating current research and technological advances* (ed. A., M.-V.) 84–98 (2011).

17. Montecucco, F. *et al.* Chlorhexidine prevents hypochlorous acid-induced inactivation of 1-antitrypsin. *Clin. Exp. Pharmacol. Physiol.* 36, 72–77 (2009).

18. Kaehn, K. Polihexanide: A safe and highly effective biocide. *Skin Pharmacol. Physiol.* 23, 7–16 (2010).

19. Katz, S., Izhar, M. & Mirelman, D. Bacterial adherence to surgical sutures. A possible factor in suture induced infection. *Ann. Surg.* 194, 35–41 (1981).

20. Donlan, R. M., Costerton, J. W., Donlan, R. M. & Costerton, J. W. Biofilms : Survival mechanisms of clinically relevant microorganisms. *Clin. Microbiol.* 15, 167–193 (2002).

21. Karpanen, T. J. *et al.* Clinical evaluation of a chlorhexidine intravascular catheter gel dressing on short-term central venous catheters. *Am. J. Infect. Control* 1–7 (2015)

22. Storch, M. L., Rothenburger, S. J. & Jacinto, G. Experimental efficacy study of coated VICRYL plus antibacterial suture in guinea pigs challenged with *Staphylococcus aureus*. *Surg. Infect.*. 5, 281–8 (2004).

23. Yazdankhah, S. P. *et al.* Triclosan and antimicrobial resistance in bacteria: an overview. *Microb. Drug Resist.* 12, 83–90 (2006).

24. Rees Clayton, E. M., Todd, M., Dowd, J. B. & Aiello, A. E. The impact of bisphenol A and triclosan on immune parameters in the U.S. population, NHANES 2003-2006. *Environ. Health Perspect.* 119, 390–396 (2011).

25. Li, Y. *et al.* New bactericidal surgical suture coating. *Langmuir* 28, 12134–12139 (2012).

26. Obermeier, A. *et al.* Novel high efficient coatings for anti-microbial surgical sutures using chlorhexidine in fatty acid slow-release carrier systems. *PLoS One* 9, (2014).

27. Homsy, C. A., Mcdonald, E. R. & Akers, W. W. Surgical suture-canine tissue interaction for six common suture types. *J. Biomed. Mater. Res.* 2, 215–230 (1968).

28. Hirshman, H. P., Schurman, D. J. & Kajiyama, G. Penetration of *Staphylococcus aureus* into sutured wounds. *J. Orthopaed. Res.* 2, 269–271 (1984).

29. Oberhoffner, S. & Planck, H. Surgical suture material from triblockterpolymer, its use in surgery and process for its preparation. EP 0835895. (1996).

30. Södergård, A. & Stolt, M. Properties of lactic acid based polymers and their correlation with composition. *Prog. Polym. Sci.* 27, 1123–1163 (2002).

31. Grijpma, D. W., Hou, Q. & Feijen, J. Preparation of biodegradable networks by photo-crosslinking lactide, e-caprolactone and trimethylene carbonate-based oligomers functionalized with fumaric acid monoethyl ester. *Biomaterials* 26, 2795–2802 (2005).

32. Cai, J., Zhu, J. C. & Yang, S. L. Surface biodegradable copolymers – poly(D,L-lactide-*co*-1-methyl-1,3-trimethylene carbonate) and Poly(D,L-lactide-*co*-2,2-dimethylene carbonate): Preparation, characterization and biodegradation characteristics *in vivo*. *Polymer.* 39, 4409–4415 (1998).

33. Zurita, R., Puiggalí, J. & Rodríguez-Galán, A. Triclosan release from coated polyglycolide threads. *Macromol. Biosci.* 6, 58–69 (2006).

34. Llorens, E., Del Valle, L. J., Díaz, A., Casas, M. T. & Puiggalí, J. Polylactide nanofibers loaded with vitamin B6 and polyphenols as bioactive platform for tissue engineering. *Macromol. Res.* 21, 775–787 (2013).

35. Franco, L., Bedorin, S. & Puiggalí, J. Comparative thermal degradation studies on glycolide/trimethylene carbonate and lactide/trimethylene carbonate copolymers. *J. Appl. Polym. Sci.* 104, 3539–3553 (2007).

36. Draney, D. R. & Jarrett, P. K. *Polym. Prepr. (Am. Chem. Soc., Div. Polym. Chem.)* 31, 137 (1990).

37. Kister, G., Cassanas, G. & Vert, M. Effects of morphology, conformation and configuration on the IR and Raman spectra of various poly(lactic acid)s. *Polymer.* 39, 267–273 (1998).

38. Wang, H., Dong, J. H. & Qiu, K. Y. Synthesis and characterization of ABA-type block copolymer of poly (trimethylene carbonate) with poly (ethylene glycol): Bioerodible copolymer. *J. Polym. Sci: A Polym. Chem.* 36, 695–702 (1998).

39. Kim, J. & Lee, J. H. Preparation and chain-extension of P(LLA- *b* -TMC- *b* -LLA) triblock copolymers and their elastomeric properties. *Macromol. Res.* 10, 54–59 (2002).

40. Sanson, C., Le Meins, J.-F., Schatz, C., Soum, A. & Lecommandoux, S. Temperature responsive poly(trimethylene carbonate)-*block*-poly(L-glutamic acid) copolymer: polymersomes fusion and fission. *Soft Matter* 6, 1722 (2010).

6.2 Incorporation of chloramphenicol and captopril

Incorporation of chloramphenicol and captopril to coated and uncoated monofilament sutures was evaluated, as well as the derived bactericide and wound healing effects. To this end, a commercially available suture and an amorphous random copolymer constituted by trimethylene carbonate and lactide units were considered. The suture had a segmented architecture based on polyglycolide hard blocks and a soft block constituted by glycolide, trimethylene carbonate and ε-caprolactone units. Chloramphenicol was better loaded when the coating copolymer was employed due to its protective effect whereas captopril showed an opposite behavior due to its partial solubilization during the immersion in the coating bath. Interestingly, the release behavior was very different for the two studied drugs since a significant retention of chloramphenicol was always detected, suggesting the establishment of interactions between drug and copolymers. On the other hand, delivery of captopril showed a typical dose dependent behavior. Biocompatibility of the two drugs was evaluated considering epithelial-like and fibroblast-like cells. Bactericide effect of chloramphenicol against Gram-negative and Gram-positive bacteria was demonstrate at a dose that was non toxic for the different assayed cells. An accelerating wound healing effect of captopril was also demonstrated for early events. In this case, the use of a coating copolymer was fundamental to avoid cytotoxic effects on highly loaded sutures.

6.2.1 INTRODUCTION

Regeneration of incised tissue after surgery is favored and accelerated by employing appropriate suturing materials. These have great advantages as low cost, flexibility, resistance to traction and torsion, ease of sterilization, biocompatibility and degradability if required. However, potential problems related to tissue irritation, inflammatory response, and risk of infection should be taken into account and avoided while the wound healing process should be facilitated. The use of lubricant coatings is well-established. Now efforts are focused on the incorporation of compounds with a specific pharmacological activity (e.g., anti-inflammatory, bactericide or wound healing).

One of the major threats to patients is hospital-acquired infection (i.e., nosocomial infections). In fact, medical devices and products introduced into the bodies (e.g., catheters, drainage tubes and even surgical sutures) may have problems derived from biofilm formation. Therefore, it is highly important to guarantee antimicrobial properties by adding directly bactericides or bacteriostatic agents to the material or to a protective coating.

Triclosan-coated sutures have been developed as a strategy for reduction of surgical-site infections (SSIs). Among commercialized monofilament sutures incorporating triclosan, PDS® and Monocryl Plus®, i.e., polydioxanone and the segmented block copolymer constituted by glycolide and ε-caprolactone, are worth mentioning. A systematic review involving 13 randomized controlled trials (RCT) totaling 3,568 surgical patients supported the clinical effectiveness of triclosan loaded sutures in the prevention of SSIs.[1] On the other hand, no other previous studies indicated a prophylactic effect against SSIs.[2] In fact, antimicrobial activity seems to depend on different factors like length of skin incision, extent of wound contamination, and coincidence with other diseases susceptible to infections, (e.g., diabetes).[3] The widespread use of triclosan (e.g., detergents, soaps, cosmetics) has given rise to triclosan-resistant bacteria, which may limit its application in the near future.

As a result of this, other bactericide agents like chlorhexidine[4], silver[5] and AgNPs[6] have already been proposed for incorporation into suture coatings. However, no studies have focused on the application of antibiotics like chloramphenicol.

Chloramphenicol (CHO) is an antimicrobial inhibitor of ribosome function. Specifically, it inhibits peptide bond formation by binding to a peptidyl transferase enzyme on the 50S subunit of the bacterial ribosome. This prevents transfer of amino acids to growing peptide chains, ultimately inhibiting protein formation is completely. The antibiotic shows broad-spectrum effectiveness against rickettsiae, Gram-positive and Gram-negative bacteria and certain spirochetes. Topical formulations of chloramphenicol are FDA approved ointments for treatment of bacterial conjunctivitis and have also been considered for use in sutured wounds as prophylaxis for infection. Several studies on the clinical significance of CHO in reducing the rate of infection have been carried out but results are still not clear.[7,8] Some problems of this antibiotic are related to the limitation on the amount that can be topically applied to avoid systemic toxicity. On the other hand, chloramphenicol does not have any adverse effect on wound healing since the fibroblast system is less sensitive to it than other types of tissues.[9]

Different compounds are currently employed to enhance wound healing properties, including natural products such as monoterpenes[10] and synthetic compounds like captopril[11] and enapril [12].

Captopril (CAP) is an inhibitor of the angiotensin converting enzyme (ACE), which increased the level of bradykinin by preventing its breakdown and also enhances prostaglandin synthesis which, in turn, promotes wound healing (i.e., the restoration of the continuity of living tissue). Following cutaneous injury, fibroblasts migrate to the site of trauma and produce collagen fibers that increase the tensile strength of the scar and could even, unfortunately, promote the formation of hypertrophic scar and keloid. Captopril also avoids these problems associated with wound healing and combines this property with antioxidant activity, an anti-inflammatory effect and a free radical scavenging potential, which benefit the wound healing process.

The main goal of the present work is to prepare monofilament bioabsorbable sutures incorporating CHO and CAP. Specifically, the segmented copolymer glycolide-*b*-(glycolide-*co*-trimethylene carbonate-*co*-ε-caprolactone)-*b*-glycolide[13] (**Figure 6.2.1**) (abbreviated as GL-*b*-(GL-*co*-TMC-*co*-CL)-*b*-GL) and commercialized under the trademark Monosyn® is considered as an example of a commercial monofilament suture. Therefore, CHO and CAP load, release, pharmacological response (e.g., bactericide activity and enhancement of cell growth) and biocompatibility are evaluated by also considering the potential advantage of employing a coating polymer. In this sense, a random copolymer constituted by 35 wt-%

of lactide units and 65 wt-% of trimethylene carbonate units is evaluated because of its appropriate properties (e.g., sticky nature, low glass transition temperature, biocompatibility and adequate degradation rate, see 6.1.2.2 and 6.1.3.1.

Figure 6.2.1. Chemical structures of GL-*b*-(GL-*co*-TMC-*co*-CL)-*b*-GL (Monosyn®), the coating poly(LA-*co*-TMC) copolymer and the selected CHO antibiotic and CAP wound healing agent.

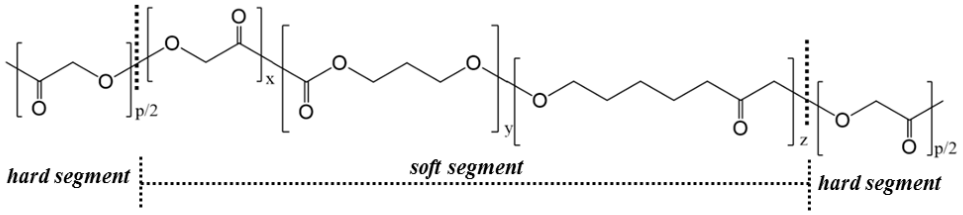

GL – *b* - (GL – *co* - TMC – *co* - CL) – *b* – GL

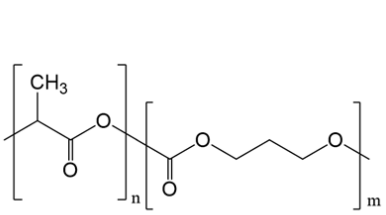

Poly(LA-*co*-TMC)

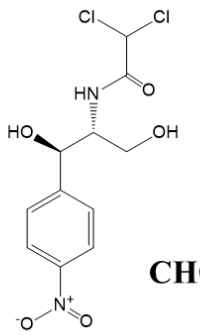

CHO

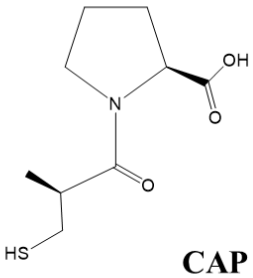

CAP

6.2.2 EXPERIMENTAL SECTION

6.2.2.1 Materials

Commercially available sutures of GL-*b*-(GL-*co*-TMC-*co*-CL)-*b*-GL (Monosyn®, USP 0 and diameter 0.35-0.399 mm) were kindly supplied by B. Braun Surgical, S.A. This triblock copolymer was constituted by 72, 14 and 14 wt-% of glycolide, trimethylene carbonate and ε-caprolactone units, respectively. The material had a middle *soft segment* representing 43 wt-% of the sample. Weight average molecular weight was 90,700 g/mol.

All solvents, chloramphenicol (CHO), captopril (CAP), 3-(4,5-dimethylthiazol-2-yl)-2,5-diphenyl-2H-tetrazolium bromide (MTT) and cell culture labware were purchased from Sigma-Aldrich (Spain).

The microbial culture was prepared with reagents and labware from Scharlab. *Escherichia coli* CECT 101 and *Staphylococcus epidermidis* CECT 245 bacterial strains were obtained from Spanish Collection of Type Culture. African green monkey kidney fibroblast (COS-7) and epithelial (VERO) cells were purchased from American Type Culture Collection.

6.2.2.2 Incorporation of CHO and CAP into uncoated and coated sutures

GL-*b*-(GL-*co*-TMC-*co*-CL)-*b*-GL monofilaments (5 cm in length) were immersed in ethyl acetate or ethanol solutions containing different percentages of CHO (0.1-5 *w/v*-%) or CAP (0.1-15 *w/v*-%), respectively for 5 s. In the case of coated sutures, different methodologies were employed due to the different solubilities of CHO and CAP. In the first case, the suture was immersed in a single ethyl acetate bath containing the required amount of CHO and 3 *w/v*-% of poly(LA-*co*-TMC). In the second case, CAP was loaded as previously indicated from the ethanol solution, and the suture was subsequently dried in a hot air stream and finally immersed in an ethyl acetate bath containing 3 *w/v*-% of poly(LA-*co*-TMC). In both cases, monofilaments were finally dried and stored under vacuum.

The total amount of loaded drug was determined by dissolution of the suture and the drug in 1,1,1,3,3,3-hexafluoroisopropanol and precipitation of polymers by addition of ethanol. Finally, absorbance was measured by UV spectroscopy of the resulting solution using a Shimadzu 3600 spectrometer. Calibration curves were obtained by plotting the absorbance measured at 276 and 202 nm versus CHO and CAP concentrations, respectively.

6.2.2.3 Release experiments

Controlled release measurements were performed with 5 cm long pieces of uncoated and coated sutures. These pieces were incubated at 37 °C in an orbital shaker at 80 rpm in tubes of 10 mL for 1 week. A 3:7 *v/v* mixture of PBS buffer and ethanol was employed as release medium, although some experiments were carried out in an ethanol medium. Drug concentration was evaluated by UV spectroscopy, as above indicated. Samples were

withdrawn from the release medium at predetermined time intervals. Volume was kept constant by addition of fresh medium. All drug release tests were conducted using three replicates and the results were averaged.

6.2.2.4 Antimicrobial test

E. coli and *S. epidermidis* bacteria were selected to evaluate the antimicrobial effect of CHO loaded sutures. The bacteria were previously grown aerobically to exponential phase in broth culture (5 g/L yeast extract, 5 g/L NaCl, 10 g/L tryptone, pH 7.2).

Growth experiments were performed on a 24-well culture plate. Five pieces of 1 cm in length of uncoated and coated sutures were placed into each well. Then, 2 mL of broth culture containing 10^3 CFU was seeded in the wells containing the suture samples. The cultures were incubated at 37 °C and agitated at 80-100 rpm. Aliquots of 100 µL were taken at predetermined time intervals for absorbance measurement at 650 nm in a microplate reader. Thus, turbidity was directly related to bacterial growth.

Bacterial adhesion to sutures was also determined. The culture media were aspirated after incubation and the material was washed once with distilled water. Then, 0.5 mL of sterile 0.01 M sodium thiosulfate was added to each well, and then the sutures were removed. After addition of 1 mL of broth culture, the plate was incubated at 37 °C and agitated at 80-100 rpm for 24 h. The bacterial number was determined as above indicated. All assays were conducted in quadruplicate and the values were averaged.

Regarding the qualitatively method, around 5 cm long pieces of loaded and unloaded sutures were placed onto an agar diffusion plate and seeded separately with 10^4 CFU/mL of each bacteria. The culture medium was prepared with 37 g of Brain Heart Infusion Broth and 15 g Bacto™ Agar (Scharlau) dissolved in 1 L of Milli-Q water and sterilized in an autoclave at 121 ºC for 30 min. Plates were filled with 15 mL of medium and kept at rest at room temperature to allow solidification of the medium. Inhibition halos images were taken after incubation of samples with bacteria at 37 ºC for 24 h.

6.2.2.5 Cell adhesion and proliferation assays

Studies were performed with fibroblast (COS-7) cells and epithelial (Vero) cells. In all cases, cells were cultured in Dulbecco's Modified Eagle Medium (DMEM), as previously reported.[14]

Five pieces of 1 cm in length of uncoated and coated sutures were placed and fixed in each well of a 24-well culture plate with a small drop of silicone (Silbione® MED ADH 4300 RTV, Bluestar Silicones). This plate was then sterilized by UV-radiation in a laminar flux cabinet for 15 min. For cell adhesion assays, aliquots of 50–100 μL containing 5×10^4 and 2×10^5 cells for CAP and CHO, respectively, were seeded onto the thread samples in each well and incubated for 24 h (adhesion assay). For cell proliferation assays, the same aliquot volume but containing lower cell concentration than for adhesion experiments (i.e., 2×10^4 and 1×10^5 cells for CAP and CHO, respectively) were seeded and incubated for 96 h.

Samples were evaluated by the standard adhesion and proliferation method.[14] The procedure is based on a simple modification of the ISO10993-5:2009 standard test, which describes the appropriate methodology to assess *in vitro* cytotoxicity of medical devices. This test is designed to determine the *in vitro* biological response of mammalian cells using appropriate biological parameters. According to this ISO standard, devices fall into one of three categories based on expected contact with the patient: a) Limited (≤24 h), b) Prolonged (>24 h and ≤30 days) and c) Permanent (>30 days). In our case, the assay was performed according to the limited and prolonged categories and using four replicates. The results were averaged. Samples with adhered and grown cells were fixed with 2.5 *w/v*-% formaldehyde at 4 °C overnight. They were subsequently dehydrated and processed for observation of cell morphology.

Scanning electron microscopy (SEM) was used to examine the morphology of coated and uncoated sutures, as well as that of adhered cells. Carbon coating was accomplished with a Mitec k950 Sputter Coater (fitted with a film thickness monitor k150x). SEM micrographs were obtained with a Zeiss Neon 40 EsB instrument.

6.2.2.6 Wound healing activity of captopril loaded sutures

An *in vitro* wound closure model was employed to evaluate the effect of CAP on cell migration. A confluent monolayer of epithelial (Vero) cells was obtained after 48 h of culture of 1 mL of DMEM medium containing 10^5 cells seeded in each well. Subsequently, a linear defect was made in the monolayers with a sterilized propylene tip (diameter of 0.2 mm) and the layer was rinsed with PBS to remove cells damaged during wound formation. Then, 1 mL of medium was added to each well, together with 1 cm long coated and uncoated sutures (5 samples for each assay) previously loaded with CAP (from 5 *w/v*-% and 15 *w/v*-% baths). Non-loaded sutures (both coated and uncoated samples) were used as controls. The rate of closure was monitored using an invert light microscopy and taking microphotographs every 24 h at the same magnification. The free area between cells was determined by fitting it to a rectangular geometry. The evolution of closure over time was determined as:

$$WC\ (\%) = (A_0 - A_t)\ /A_0 \times 100 \qquad (1)$$

where A_t and A_0 correspond to the areas evaluated at times t and 0, respectively.

6.2.2.7 Statistical analysis

Values were averaged and graphically represented together with their respective standard deviations. Statistical analysis was performed by one-way ANOVA test to compare the means of all groups, and then Tukey's test was applied to determine a statistically significant difference between two groups. The test confidence level was set at 95% ($p < 0.05$).

6.2.3 RESULTS AND DISCUSSION

6.2.3.1 Load and release of chloramphenicol

CHO loading was performed by direct immersion of sutures in ethyl acetate baths containing different percentages of CHO for uncoated sutures. Poly(LA-*co*-TMC) was also incorporated into the bath when a coated sample was prepared.

Immersion time (5 s), drying method (hot air stream) and copolymer concentration (3 *w/v*-%) were optimized to obtain the most economical and fastest process, as well as completely coated and uniform sutures. Figure 6.2.2 shows that uniform surface textures were obtained for both, uncoated and coated sutures incorporating CHO.

Figure 6.2.2. Scanning electron micrographs of a GL-*b*-(GL-*co*-TMC-*co*-CL)-*b*-GL monofilament suture after immersion in an ethyl acetate bath containing 3.5 *w/v*-% of CHO **(a)** and also 3 *w/v*-% of poly(LA-*co*-TMC) **(b)**.

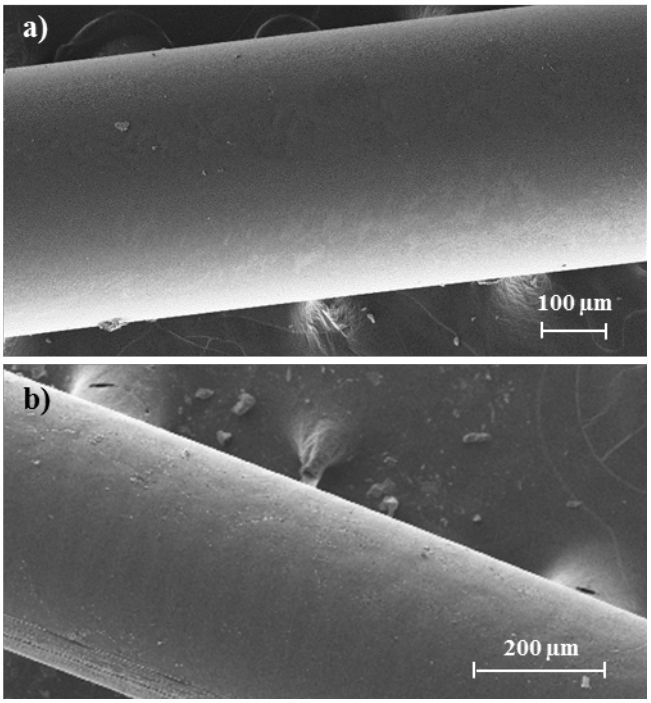

Figure 6.2.3a shows the relatively good correlation between CHO concentration in the ethyl acetate bath and the amount of loaded drug referred to the suture unit length. The slope of this linear plot is 0.65, but the determination coefficient (r^2) is relatively low (i.e., 0.86) due to higher load observed when CHO concentration in the bath is low. It seems that CHO had some difficulty in perfectly adhered to the copolymer surface, and consequently the drug appeared well retained only when the load was low.

The use of a preventive coating led to an increase in the amount of loaded drug, as shown by the higher value of the slope of the linear plot (i.e., 0.94 in front of 0.65). In this case, the determination coefficient was improved and increased up to 0.98. It is clear that the drug could not be detached as a consequence of manipulation and poor adhesion of the suture. The amount of loaded drug was similar for coated and uncoated sutures only when the drug concentration in the bath was low (1 *w/v*-%), suggesting that desorption problems were not significant in this case. It should also be pointed out that final loading efficiency seems to be higher for the coated sutures due to an effective protective effect against subsequent manipulation.

CHO delivery was evaluated using a release medium consisting of a 3:7 *v/v* mixture of PBS buffer and ethanol since the latter was a better solvent for CHO than a typical nutrient serum medium. Therefore, results served to determine the effect of load concentration and use of a protective coating employing a medium that should accelerate the release, and that consequently make differences observed in the CHO delivery more significant.

Figure 6.2.3b compares CHO release percentages for uncoated and coated sutures at two differentiated drug loads (i.e., ~1 μg/cm and 3.2-4.7 μg/cm). Results showed release profiles characterized by a burst effect, a sustained release between 5 and 60 min and a final plateau associated with retention of a significant drug percentage on the suture. The values of the retained percentage is the main difference between the studied samples, and therefore merit attention.

Figure 6.2.3. (a) Plot of the amount of chloramphenicol (●,○) incorporated into the GL-*b*-(GL-*co*-TMC-*co*-CL)-*b*-GL suture (drug weight/suture length) versus drug concentration of ethyl acetate baths. Results are given for solutions with (solid lines) and without (dashed lines) poly(LA-*co*-TMC). **(b)** CHO release percentages in 3:7 *v/v* mixture of PBS buffer and ethanol (dashed lines) for uncoated (□,○) and coated (■, ●) sutures. For the sake of completeness, data for an EtOH medium are also plotted (solid lines) Samples were obtained from baths containing 5 *w/v*-% (full symbols) and 1 *w/v*-% (empty symbols) of CHO.

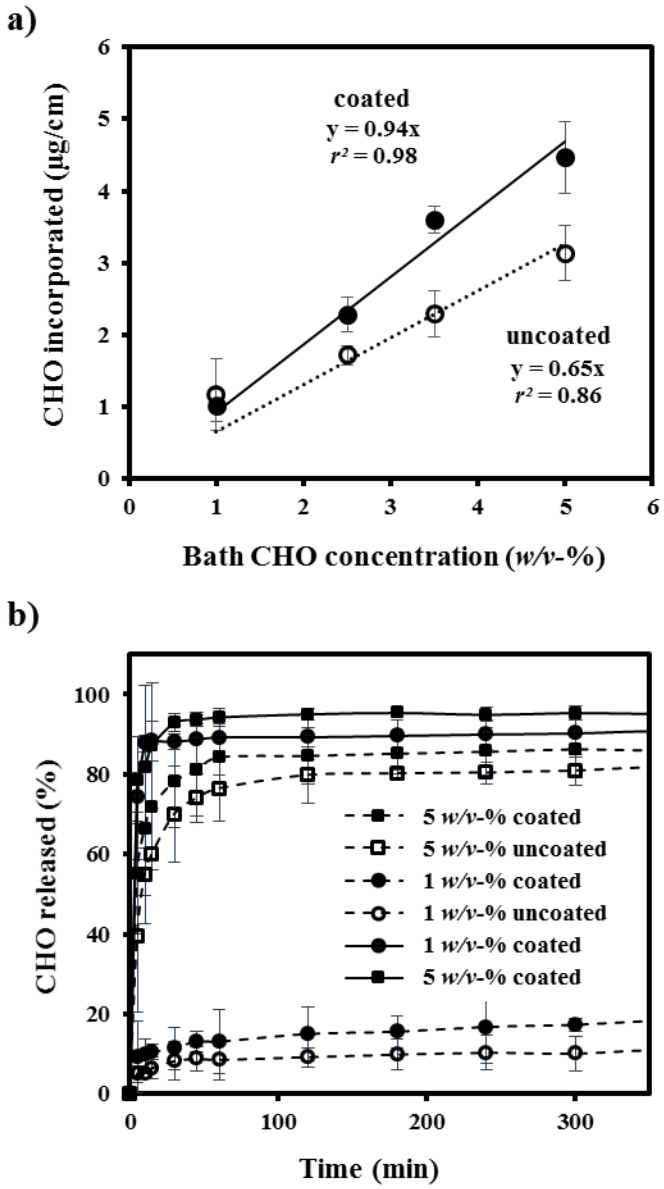

The coated suture loaded from a bath containing 5 *w/v*-% of CHO retained 15% of the loaded drug, which is equivalent to 0.7 μg/cm considering the relationship defined by a slope of 0.94 (**Figure 6.2.3a**). The retained percentage increased up to 80% when the suture was loaded from a 1 *w/v*-% bath. However, it is interesting to note that this percentage also corresponds again to a retention close to 0.7 μg/cm. This retention seems an intrinsic characteristic caused by the physicochemical interactions that could be established between CHO and the polymer matrix. It is significant that the observed plateau is not a consequence of limited drug solubility (i.e., saturation of the medium) since lower release percentages should, in this case, be found for higher amounts of loaded drug.

Coating had a minimum effect on release since the behavior of uncoated samples was practically similar. Although the plateau was always found at a lower release percentage than the related coated samples, it should be taken into account that the effective drug load was different (see the different slopes of the plots in **Figure 6.2.3a**). Thus, the uncoated suture coming from a 5 *w/v*-% bath was loaded with 3.25 μg/cm and a release of 80% was detected. This value indicates only a slightly lower drug retention (i.e., 0.65 μg/cm becomes rather similar to the value found for coated sutures and suggests only a minor protective effect of the coating copolymer). Similar conclusions can be obtained when the release of the sample coming from the 1 *w/v*-% bath is evaluated, since in this case CHO retentions close to 0.7 μg/cm were again deduced taking into account either the slope of the linear plot of the loading process (**Figure 6.2.3a**) or the experimental drug load. Note that, at this small load percentage, the experimental data deviated from linearity, as above explained.

For the sake of completeness, **Figure 6.2.3b** shows the release from coated sutures in an ethanol medium, which causes a greater swelling of both the coating and the suture and where CHO is more soluble. In this case, it is evident that the coating is still able to retain a certain drug percentage that corresponds to 0.23 μg/cm and 0.09 μg/cm for samples coming from 5 *w/v*-% and 1 *w/v*-% drug loaded baths, respectively. However, the amount of retained drug is clearly different and increases according to the amount of loaded drug (i.e., 4.7 μg/cm and 0.94 μg/cm) instead of representing a constant value that could be related to a physicochemical adsorption.

6.2.3.2 Antimicrobial effect of chloramphenicol loaded sutures

The antimicrobial effect of CHO loaded sutures was quantitatively evaluated following the growth kinetics of Gram-negative (*E.coli*) and Gram-positive (*S. epidermidis*) bacteria as displayed in Figure 6.2.4. It is clear that the unloaded suture is highly susceptible to the bacterial infection since bacterial growth becomes similar to that of the control. Specifically, a latency phase that extends over a period of 4 h followed by an exponential growth (log phase) was characteristic.

A very low decrease in bacterial proliferation was detected for both uncoated and coated sutures loaded from baths containing only 0.1 *w/v*-% (i.e., close to 0.094 μg/cm). Nevertheless, the growing curve was characterized by an identical latency phase and an exponential growth phase. Uncoated sutures loaded with 0.7 μg/cm displayed a bacteriostatic effect against Gram-positive bacteria, with the latency phase increasing up to 8 h and a subsequent linear growth instead of the typical exponential growth phase. In contrast, complete inhibition was determined for coated sutures coming from baths having the same drug concentration. This feature may be related to the higher effective load deduced from the slopes in Figure 6.2.3. It should also be pointed out that the 1 *w/v*-% concentration (i.e., a load of 0.94 μg/cm) was sufficient to render a completely inhibitory effect against Gram-negative bacteria, independently of using a coated or an uncoated (not shown) suture. On the contrary, this concentration rendered a practically inhibitory effect against Gram-positive bacteria only when the coated suture was employed. Higher concentrations were logically completely effective against both Gram-positive and Gram-negative bacteria.

Figure 6.2.5 shows the evaluation of bacterial adhesion to the new materials as a different way to control the antimicrobial effect. Results demonstrated a dose-dependent response for Gram-positive bacteria since relative adhesion decreased to 20% (uncoated) and 30% (coated) for samples having the highest CHO content. In contrast, the decrease of relative adhesion was practically constant (i.e., between 40% and 55%) for Gram-negative bacteria, independently of the amount of loaded CHO provided it exceeded 2.35 μg/cm. Differences between coated and uncoated sutures were not highly significant for either kind of bacteria, especially considering the different effects caused by the higher CHO load for coated sutures when drug concentration of the loading baths was the same and the more difficult diffusion of the drug when the suture was coated.

Figure 6.2.4. Growth curves of *E. coli* **(a)** and *S. epidermidis* **(b)** on culture plate as positive control (□), coated suture as blank (○) and poly(LA-*co*-TMC) coated sutures loaded in baths with the indicated *w/v*-% of CHO. For the sake of completeness, data for uncoated sutures loaded from selected baths are also plotted (solid lines).

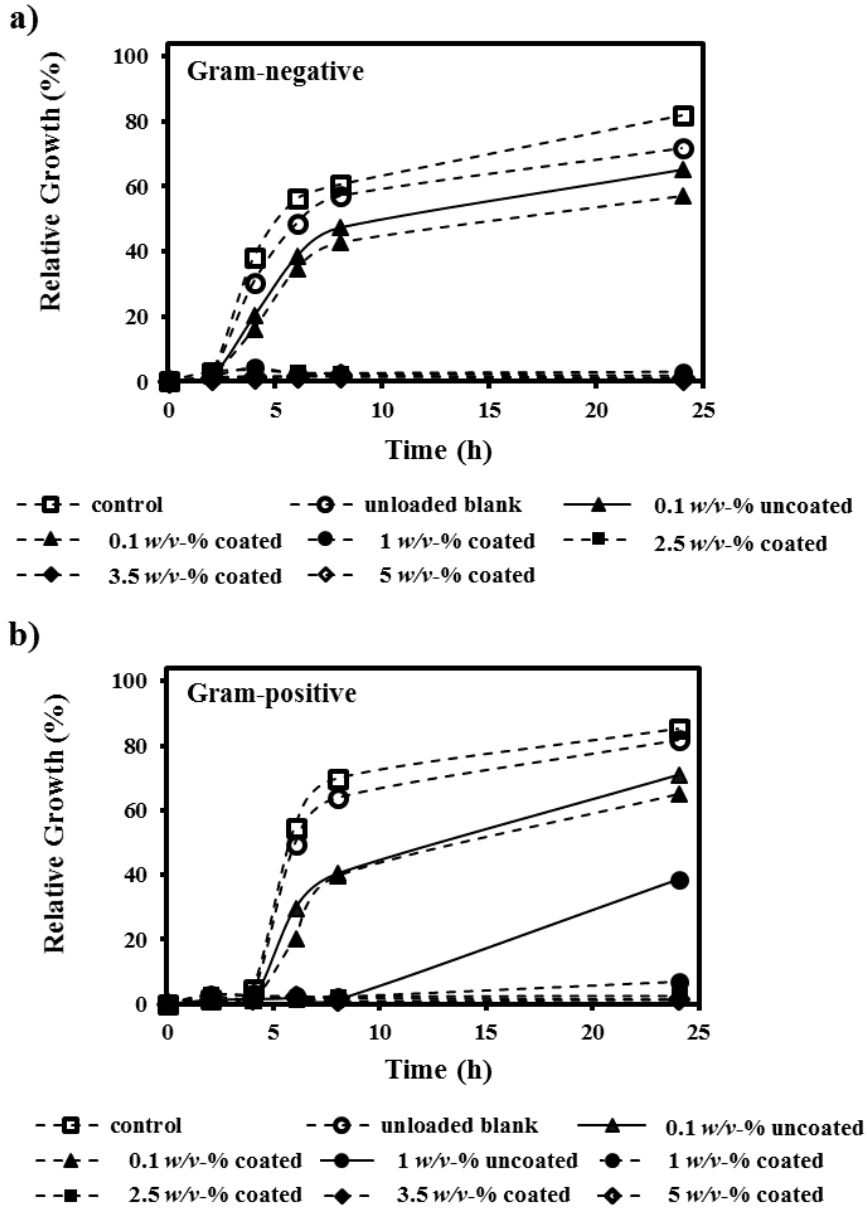

Figure 6.2.5. Adhesion of *E. coli* **(a)** and *S. epidermidis* **(b)** bacteria to uncoated (gray bars) and poly(LA-*co*-TMC) coated (grid bars) sutures loaded in baths with the indicated CHO concentrations. Data concerning the culture plate as positive control and the unloaded coated and uncoated sutures as blanks are also provided.

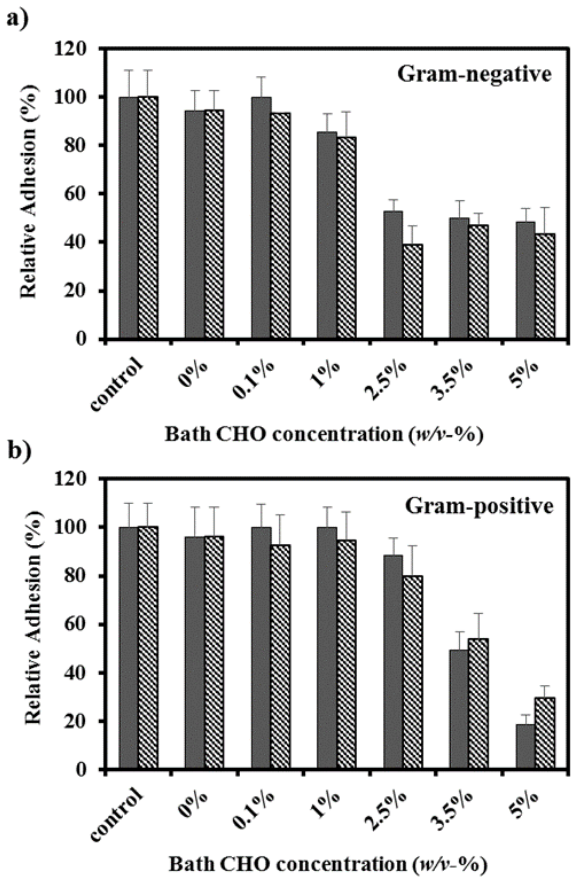

Bactericide effect can also be qualitatively observed in the Agar tests by measurement of the inhibition halos around sutures as shown in Figure 6.2.6. Results point out the following issues: a) Halos logically increased with the amount of loaded drug (i.e., see halos in each vertical raw), b) The effect caused for a given load and preparation method (i.e., coated and uncoated suture) is similar for Gram-positive and Gram-negative bacteria, c) Inhibition halos appear larger for the coated suture when compared with the equivalent uncoated one. The selected coating does not seem to hinder CHO diffusion from the suture to the medium but caution must be taken because of the higher amount of drug that is loaded from a fixed bath concentration.

Figure 6.2.6. Agar tests showing the inhibition zone of *E. coli* and *S. epidermidis* bacteria caused by uncoated and poly(LA-*co*-TMC) coated sutures loaded in baths with the indicated CHO concentrations.

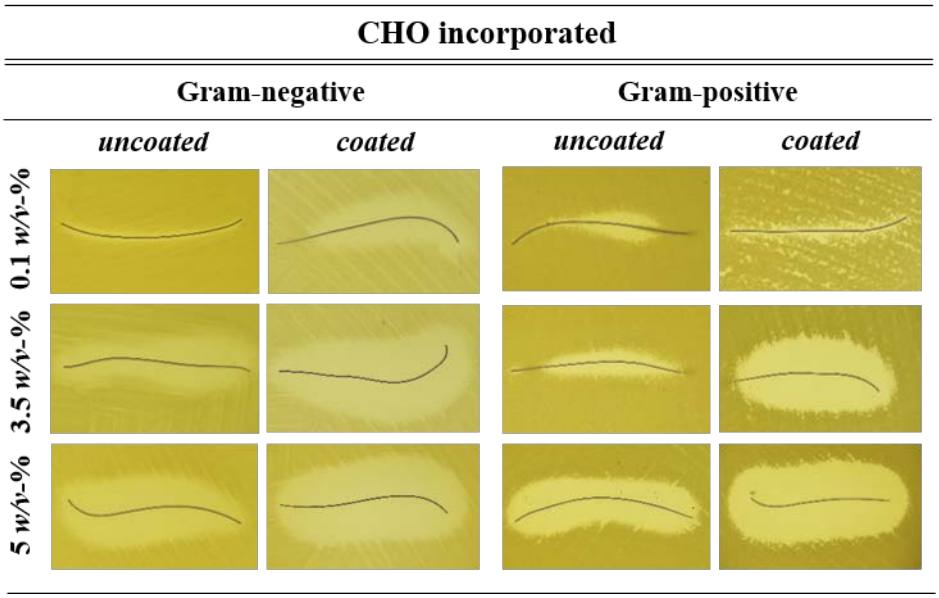

6.2.3.3 Cytotoxicity of CHO loaded sutures

Figure 6.2.7 shows the results of cell adhesion and cell proliferation events determined for epithelial-like and fibroblast-like cell lines after 24 and 96 h of culture, respectively.

Adhesion of epithelial-like cells was only significantly reduced at the highest load (i.e., samples coming from 5 *w/v*-% bath), with the maximum decrease close to 32% for the coated suture and 40% for the uncoated one (Figure 6.2.7a). Probably, release of chloramphenicol was hindered by the coating copolymer. Thus, it was possible to justify higher cell adhesion despite the slightly higher drug load. However, it is important to point out that proliferation assays demonstrated that cell colonization took place, and specifically percentages similar to the control were attained for the most problematic uncoated suture (Figure 6.2.7c). Fibroblast-like cells were less sensitive to toxic effects because epithelial-like cells require a great surface to adhered to through their basal domains, and consequently can be more affected by adverse surfaces. Therefore, adhesion of fibroblast-like cells decreased only to 20% in the most adverse case (i.e., the maximum

CHO load), while a similar behavior to that of the control was determined for all the other loads (Figure 6.2.7b). Proliferation assays indicate that cell growth was completely recovered for the coated suture even when an initial decrease in cell adhesion was detected (Figure 6.2.7d).

Figure 6.2.7. Adhesion to **(a,b)** and proliferation **(c,d)** of Vero **(a,c)** and COS-7 **(b,d)** cells in uncoated (gray bars) and poly(LA-*co*-TMC) (grid bars) coated sutures loaded in baths with the indicated CHO concentrations. Data concerning the culture plate as positive control are also provided.

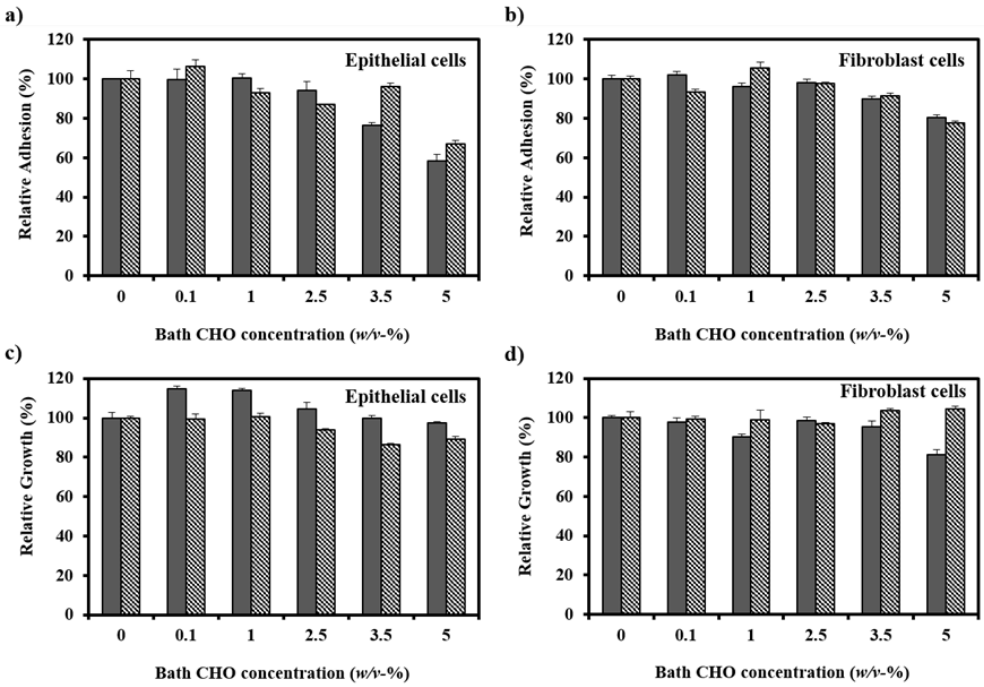

Micrographs in Figure 6.2.8 show the morphology of fibroblast-like and epithelial-like cells adhered to both uncoated and coated sutures loaded from 3.5 *w/v*-% baths. In general, epithelial-like cells appear widely extended, forming clusters (Figure 6.2.8c and 6.2.8d) while fibroblast-like cells appear as single, extended and well-distributed cells (Figures 6.2.8a and 6.2.8b) after adhesion and proliferation assays and independently of the use of a coating polymer (Figures 6.2.8a and 6.2.8b).

Figure 6.2.8. SEM micrographs of COS-7 **(a,b)** and Vero **(c,d)** cells growth on uncoated **(b)** and poly(LA-*co*-TMC) coated **(a,c,d)** sutures loaded in baths with CHO concentration of 3.5 *w/v*-%. Figures correspond to adhesion **(a–c)** and proliferation **(d)** assays.

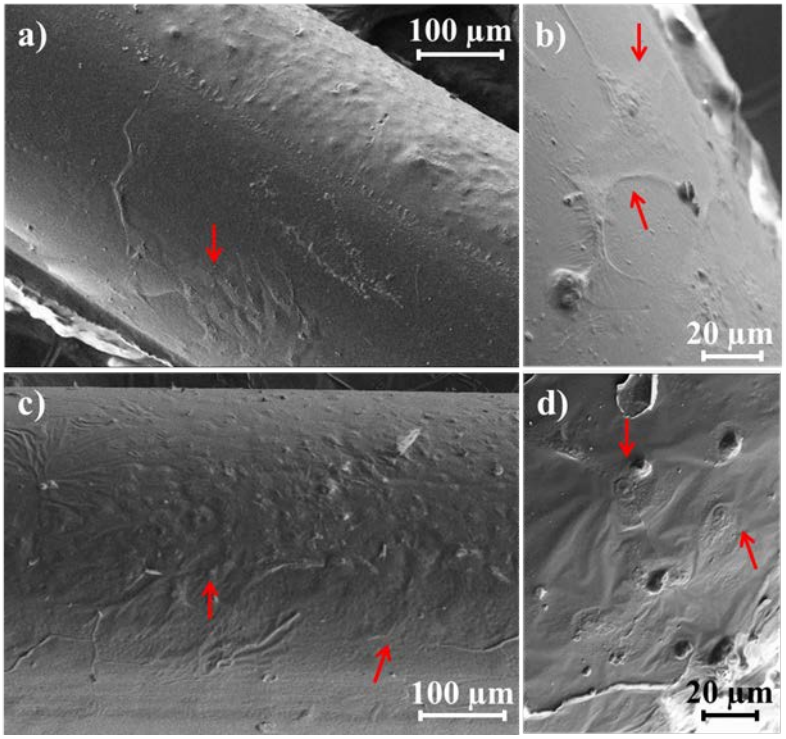

6.2.3.4 Load and release of captopril into/from sutures

Figure 6.2.9 correlates the amount of CAP loaded into uncoated and coated sutures following the above two-step protocol. Good determination coefficients were again found between the amount of loaded drug and its concentration in the ethanol bath (i.e., 0.96-0.98). Slopes were clearly lower than those determined for CHO (i.e., 0.41-0.15 as opposed to 0.94-0.65), suggesting poorer affinity between CAP and the suture. In contrast with CHO results, the load was clearly lower for the coated samples, a feature that can be explained by a partial solubilization of CAP when the suture was immersed in the ethyl acetate coating bath. In fact, ethyl acetate has been proposed for crystallization of CAP because it is sparingly soluble at 25 ºC but has a moderate solubility at 60 ºC.[15]

Figure 6.2.9. Plot of the amount of captopril (●,○) incorporated into the GL-*b*-(GL-*co*-TMC-*co*-CL)-*b*-GL suture (drug weight/suture length) versus drug concentration of ethanol baths. Results are given for solutions with (solid lines) and without (dashed lines) poly(LA-*co*-TMC).

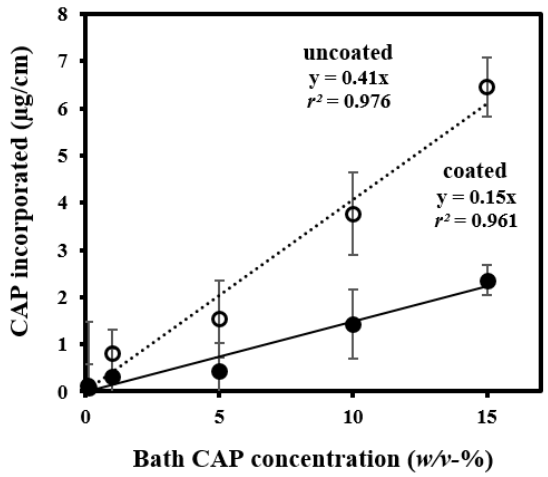

Figure 6.2.10a compares the release percentages of CAP in the 3:7 *v/v* mixture of PBS/EtOH medium from uncoated sutures loaded from baths having different drug percentages. It is clear that the burst effect decreased for lower amounts of loaded drug and even a sustained release was found from samples coming from 1 *w/v*-% and 0.1 *w/v*-% baths. The high burst effect clearly indicated that the amount of retained drug was small, and even measurements performed at plateau levels indicated irregular adsorption (i.e., 0.61 μg/cm, 0.73 μg/cm and 0.92 μg/cm when samples were loaded from baths having 15 *w/v*-%, 10 *w/v*-% and 5 *w/v*-% CAP concentrations). This feature contrast with the constant value observed for CHO loaded samples, where better interactions between drug and the copolymer suture should be established. The completely different behavior of scarcely loaded samples, where the percentage of released drug was lower than 30% and did not achieve a constant value even after 4500 min of exposure, is also highly significant. The slower release suggests that important interactions can be established between CAP and the suture surface for low doses. The amount of retained drug after this period (0.26 μg/cm) was nevertheless clearly lower than that observed for highly loaded samples despite the fact that the drug was clearly detached from these samples (burst effect). When ethanol was employed as the delivery medium, the release percentage of samples coming from 1 *w/v*-% and 0.1 *w/v*-% baths increased respect to the PBS/ethanol

medium, but a sustained release was still observed (i.e., the plateau was still not achieved after 4500 min of exposure) despite higher solubility of the drug in this medium.

Figure 6.2.10. CAP release percentages in 3:7 *v/v* mixture of PBS buffer and ethanol (solid lines) for uncoated sutures loaded from the indicated CAP concentrations in the loading bath. For the sake of completeness, data for an EtOH medium and two selected concentrations are also plotted (dashed lines).

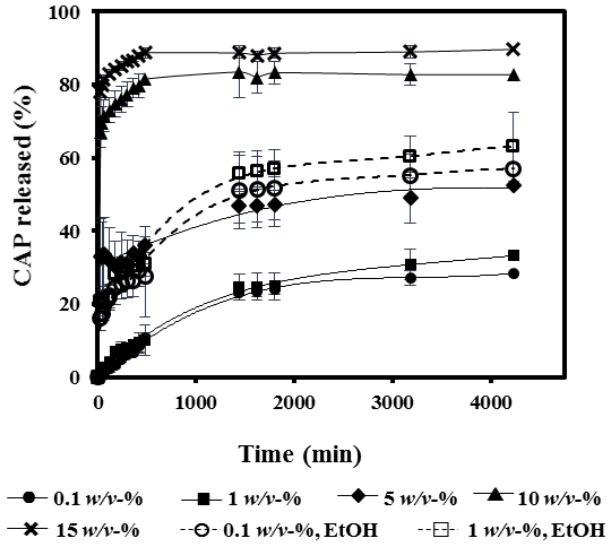

Figure 6.2.11 compares the release behavior of coated sutures. In this case, it is clear that the coating reduces the burst effect and that the released percentage decreased with the amount of loaded drug. Results are logical when amounts of released drug from a determined suture are compared. Values of 0.22 μg and 0.04 μg are determined after 4500 min of exposure for the most and least loaded suture, respectively, which agree with a diffusion driven process. The plot in Figure 6.2.11 also shows that a sustained release was detected when ethanol was employed despite its higher solubilizing power and even its ability to swell the coating and favor drug diffusion. Logically, comparison between sutures coming from the same bath concentration (i.e., 10 *w/v*-%, Figure 6.2.11) demonstrated the higher release attained in the ethanol medium.

Figure 6.2.11. CAP release percentages in 3:7 *v/v* mixture of PBS buffer and ethanol (solid lines) for coated sutures loaded from the indicated CAP concentrations in the loading bath. For the sake of completeness, data for an EtOH medium and a selected concentration are also plotted (dashed lines).

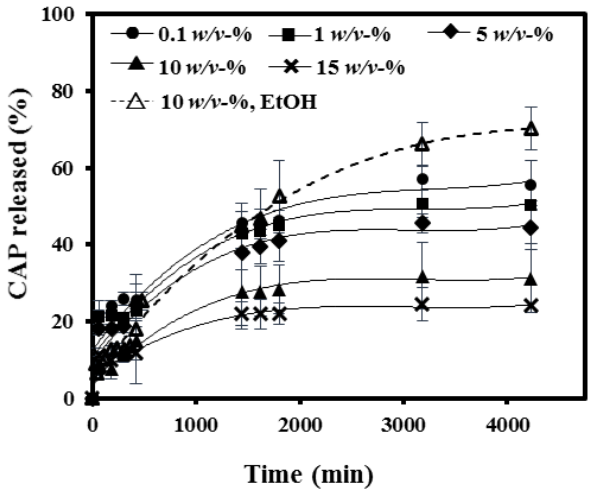

6.2.3.5 Cytotoxicity of CAP loaded sutures

Figure 6.2.12 compares proliferation and adhesion of epithelial-like and fibroblast-like cells to uncoated and coated sutures loaded with different amounts of CAP. Both assays showed a decrease of cell viability when the amount of incorporated CAP increased. Toxicity was highly dependent on the presence of the coating copolymer, probably as a consequence of the lower drug load when samples came from baths having the same drug concentration and mainly of the delayed release caused by the indicated equilibrium conditions attained for the distribution of the drug in the coating and the external medium. In any case, certain recovery of cell growth was detected for uncoated samples in long events (i.e., proliferation assays) performed with highly loaded samples. Certain cytotoxicity was detected for both kinds of cells when uncoated samples initially loaded with a high amount of CAP were tested. Thus, relative growth of epithelial-like and fibroblasts-like cells decreased to 40% and 22%, respectively. Results in Figure 6.2.12 point out that cytotoxicity was not significant when uncoated samples were loaded with 2.05 μg/cm and 0.41 μg/cm of CAP for epithelial-like and fibroblast-like cells, respectively. In contrast, coated samples could be loaded with 2.25 μg/cm and 1.5 μg/cm of CAP for epithelial-like and fibroblast-like cells, respectively.

Figure 6.2.12. Adhesion to **(a,b)** and proliferation **(c,d)** of Vero **(a,c)** and COS-7 **(b,d)** cells in uncoated (blue bars) and poly(LA-*co*-TMC) (grid bars) coated sutures loaded in baths with the indicated CAP concentrations. Data concerning the culture plate as positive control are also provided.

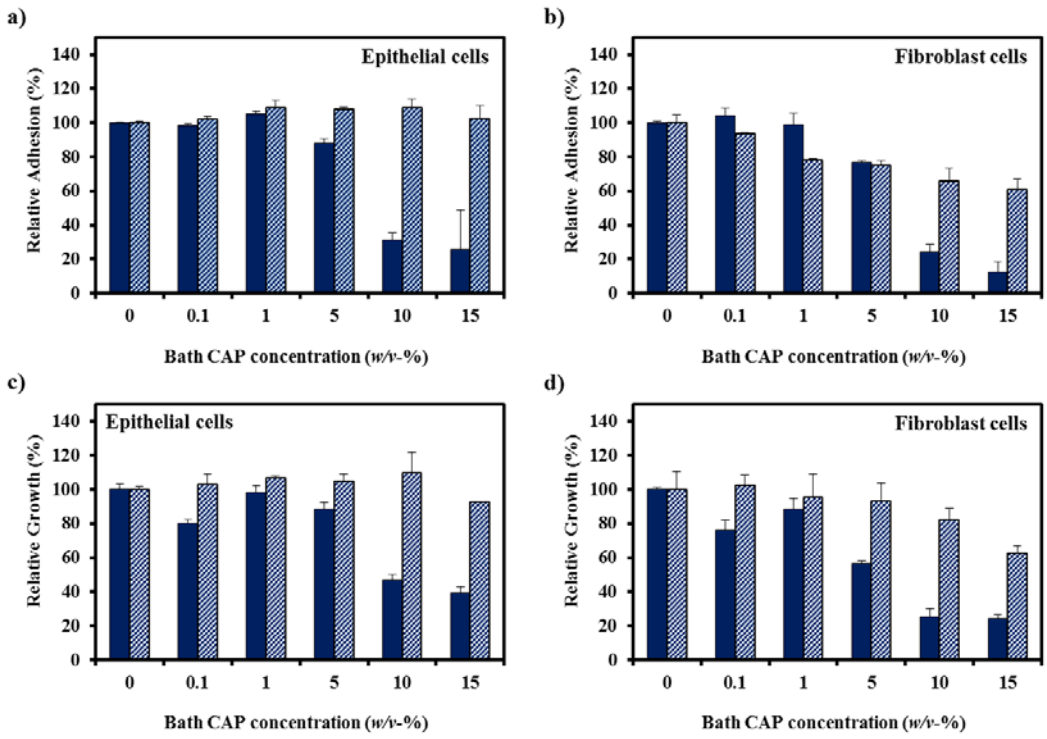

SEM micrographs of cells adhered to the coated sutures loaded from 5 *w/v*-% CAP bath are shown in Figure 6.2.13. Both epithelial-like and fibroblasts-like cells exhibited good cell adhesion characteristics. Cytoplasmic extensions can be observed as lamellipodia for Vero cell line, i.e., epithelial-like cells (Figure 6.2.13a), while for COS-7 cell line, i.e., fibroblast-like cells, cytoplasmic extensions of filopodia type were found for cells adhered to the suture surface (Figure 6.2.13b). In both kinds of cells, attachment and spreading on uncoated and poly(LA-*co*-TMC) coated sutures, loaded with CAP showed clear evidences of biocompatibility.

Figure 6.2.13. SEM micrographs of Vero **(a)** and COS-7 **(b)** cells growth on poly(LA-*co*-TMC) coated sutures loaded from a 5 *w/v*-% CAP bath.

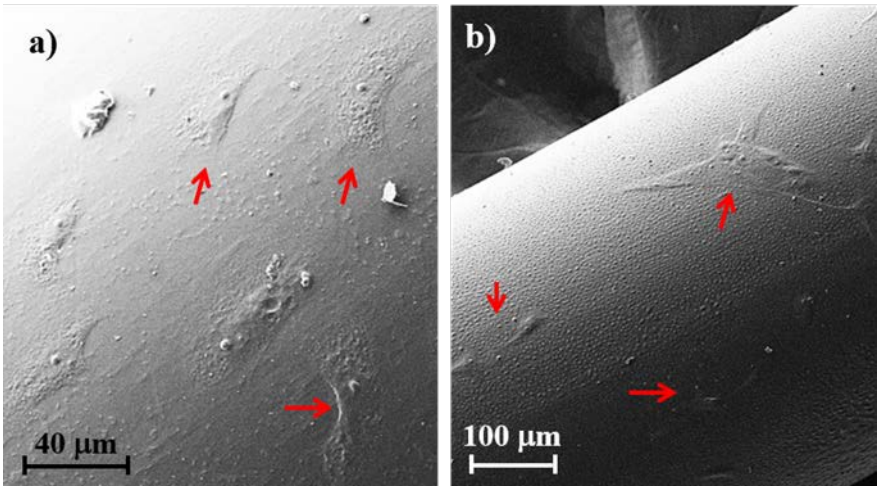

6.2.3.6 Wound healing effect of CAP loaded sutures

The *in vitro* wound healing effect was only evaluated for samples coming from 5 *w/v*-% and 15 *w/v*-% baths since, as indicated in the previous section, the resulting samples showed high and low biocompatibility, respectively. Note also that differences in biocompatibility were enhanced for uncoated sutures due to their higher effective load.

Wound healing was clearly favored in the most highly loaded samples (i.e., coming from the 15 *w/v*-% bath) as shown in Figure 6.2.14. Specifically, WC percentages of 40% and 24% were determined for coated and uncoated sutures, respectively, after 21 h of exposure. These percentages decreased to 28% (coated) and 15% (uncoated) for samples coming from the 5 *w/v*-% bath. These percentages are close to those obtained for unloaded controls (28% and 13% for coated and uncoated samples, respectively). After, 45 h of exposure, WC percentages were in the 60%-54% range for all conditions. Results demonstrate the accelerating effect of CAP on wound healing for early events (i.e., 21 h). Moreover, high CAP concentration may have a different effect on the surface of sutures (i.e., a clear cytotoxicity was determined) and on the surrounding cell monolayer (i.e., negative effects were minimized due to the decrease in CAP concentration since it depends on the diffusion process).

Figure 6.2.14. Optical micrographs of epithelial-like cell growth in linear defects made in a cell monolayer when sutures were incorporated in the broth medium. Results are given after 0 days **(a1,b1,c1,d1,e1** and **f1)** and 21 h **(a2,b2,c2,d2,e2** and **f2)** of exposure for unloaded and uncoated **(a1,a2)** sutures, unloaded and coated **(b1,b2)** sutures, uncoated sutures loaded from a *5 w/v-%* bath **(c1,c2)**, coated sutures loaded from 5 *w/v-%* bath **(d1,d2)**, uncoated sutures loaded from a 15 *w/v-%* bath **(e1,e2)** and coated sutures loaded from 15 *w/v-%* bath **(f1,f2)**.

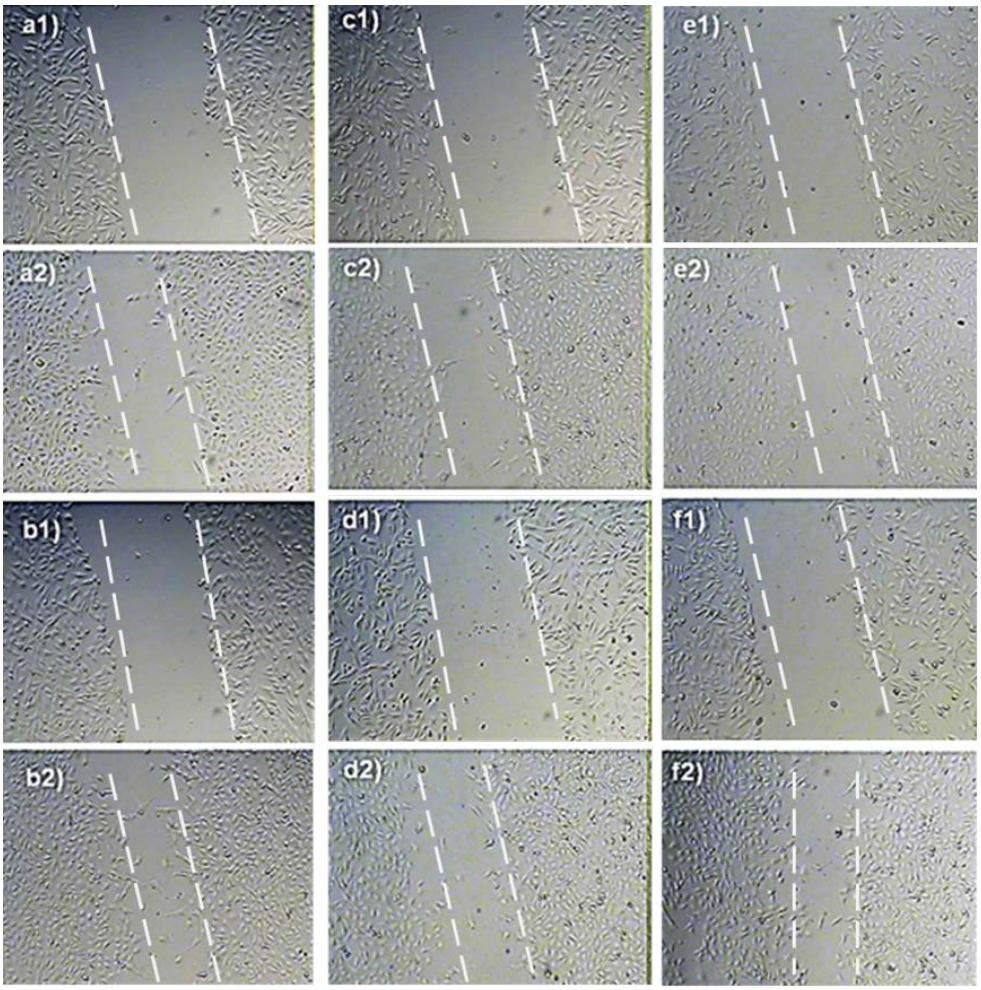

The beneficial wound healing effect increased with the amount of loaded drug (i.e., 15 *w/v-%* versus 5 *w/v-%* baths) and depended on the presence of the coating polymer. Specifically, wound healing improved when coated sutures were employed, which

may be related to a slower drug release that favors cell colonization on the suture material and decreases the cytotoxic effect around the suture.

6.2.4 CONCLUSIONS

CHO can be easily loaded onto the surface of GL-*b*-(GL-*co*-TMC-*co*-CL)-*b*-GL monofilament sutures after their immersion in ethyl acetate solutions containing the drug. A linear relationship was found between drug concentration in the bath and the amount of CHO incorporated into the suture. Fitting was better for coated sutures due to the protective effect against drug detachment. CHO release was characterized by a constant amount of CHO that was retained in uncoated and coated sutures, which suggests the establishment of good intermolecular interactions between the drug and involved copolymers. A complete inhibitory effect against Gram-negative and Gram-positive bacteria was determined for uncoated and coated sutures loaded from baths having 5 *w/v*-% of CHO, whereas lower concentrations rendered less effective materials against Gram-positive bacteria when uncoated samples were evaluated. Adhesion of Gram-positive bacteria was significantly lower than adhesion of Gram-negative ones at the maximum CHO load. Cell proliferation assays demonstrated effective cell colonization (for both epithelial-like and fibroblast-like cells), even at the maximum assayed CHO load, giving rise to a significant decrease in the cell adhesion. In any case, cell adhesion and proliferation results demonstrated a lack of cytotoxicity for samples loaded with the CHO amount capable of rendering a clear bactericide effect.

CAP loading was more problematic when sutures were immersed into a second coating bath as a consequence of a partial solubilization of the previously loaded drug. The coating was highly effective to suppress the burst effect and to render a sustained release, which had in this case a typical diffusion behavior (i.e., the amount of delivered drug increased with the amount of loaded drug). Adhesion and proliferation of fibroblast-like and epithelial-like cells decreased significantly for uncoated sutures loaded from baths having CAP concentrations higher than 5 *w/v*-%, whereas the use of a coating copolymer was fundamental to avoid any cytotoxic response. Furthermore, wound healing was clearly improved for early events when coated sutures were employed.

6.2.5 REFERENCES

1. Edmiston, C. E., Daoud, F. C. & Leaper, D. Is there any evidence-based argument for embracing an antimicrobial (triclosan)-coated suture technology to reduce the risk for surgical site infections? A meta-analysis. *Surgery* **154,** 89–100 (2013).

2. Diener, M. K. *et al.* Effectiveness of triclosan-coated PDS Plus versus uncoated PDS II sutures for prevention of surgical site infection after abdominal wall closure: the randomised controlled. PROUD trial. *Lancet.* **384,** 142–152 (2014).

3. Nakamura, T. *et al.* Triclosan-coated sutures reduce the incidence of wound infections and the costs after colorectal surgery: a randomized controlled trial. *Surgery* **153,** 576–583 (2013).

4. Obermeier, A. *et al.* Novel high efficient coatings for anti-microbial surgical sutures using chlorhexidine in fatty acid slow-release carrier systems. *PLoS One* **9,** (2014).

5. Blaker, J. J., Nazhar, S. N. & Boccaccini, A. R. Development and characterization of silver-doped bioactive glass-coated sutures for tissue engineering and wound healing applications. *Biomaterials* **25,** 1319–1329 (2004).

6. Zhang, S. W., Liu, X. L., Wang, H. L., Peng, J. & Wong, K. K. Y. Silver nanoparticle-coated suture effectively reduces inflammation and improves mechanical strength at intestinal anastomosis in mice. *J. Pediatr. Surg.* **49,** 606–613 (2014).

7. Chan, M., Fong, P. & Stern, C. Chloramphenicol wound infection prophylaxis. *Calif. Pharm. Fall* 56–58 (2009).

8. Heal, C. F. *et al.* Does single application of topical chloramphenicol to high risk sutured wounds reduce incidence of wound infection after minor surgery? Prospective randomised placebo controlled double blind trial. *BMJ* **338,** 2812 (2009).

9. Bloom, G. P. & Grillo, H. C. The influence of tetracycline and chloramphenicol on the healing of cutaneous wounds. *J. Surg. Res.* **10,** 1–5 (1970).

10. Barreto, R. S. S. *et al.* A systematic review of the wound-healing effects of monoterpenes and iridoid derivatives. *Molecules* **19,** 846–862 (2014).

11. Qiu, J. G. *et al.* Wound healing: captopril, an angiogenesis inhibitor, an Staphylococcus aureus peptidoglycan. *J. Surg. Res.* **92,** 177–185 (2000).

12. Iannello, S., Milazzo, P., Bordorano, F. & Belfiore, F. Low-dose enalapril in the treatment of surgical cutaneous hypertrophic scar and keloid: two case reports and literature review. *MedGenMed* **8,** 60 (2006).

13. Oberhoffner, S. & Planck, H. Surgical suture material from triblockterpolymer, its use in surgery and process for its preparation. EP 0835895. (1996).

14. Llorens, E., Del Valle, L. J., Díaz, A., Casas, M. T. & Puiggalí, J. Polylactide nanofibers loaded with vitamin B6 and polyphenols as bioactive platform for tissue engineering. *Macromol. Res.* **21,** 775–787 (2013).

15. Wang, J., Gao, L. & Liu, Y. Solubility of captopril in 2-propanol, acetone, acetonitrile, methyl acetate, ethyl acetate, and butyl acetate. *J. Chem. Eng. Data* **55,** 966–967 (2010).

7.

REINFORCED POLYMERIC MATRIX BY MEANS OF ELECTROSPINNING

7.1. Poly(ε-caprolactone) films reinforced with chlorhexidine loaded electrospun polylactide microfibers

Poly(ε-caprolactone) (PCL) films reinforced with polylactide (PLA) microfibers were prepared by two different methodologies: a) melt pressing of an electrospun PLA mat between two PCL films, and b) melt pressing of a co-electrospun mat composed of PLA microfibers and PCL nanofibers. Electrospinning conditions were optimized for each polymer to obtain films loaded with 10, 20 and 30 wt-% of PLA. Thermal and mechanical properties varied depending on the preparation method. Thus, PLA crystallinity was higher when films were obtained by the co-electrospinning process, as revealed from DSC and synchrotron X-ray diffraction data since cold crystallization of the highly oriented PLA microfibers was favored in the subsequent heating run when they were in a close contact with PCL nanofibers. Samples obtained from co-electrospinning also showed higher mechanical properties (e.g., Young modulus) with increasing PLA loading. In this case, fracture surfaces showed significant interactions between fibers and the PCL matrix and reduced fiber pull-out.

All fabrics were also loaded with chlorhexidine (CHX) as a hydrophilic bactericide agent. A delayed release was observed when the drug was only loaded into the electrospun PLA microfibers, and diffusion varied with the method of preparation. In all cases, samples had a clear bactericide effect against Gram positive and Gram negative bacteria. Nevertheless, the protective effect slightly lower when CHX was only loaded in the reinforcing PLA microfibers.

7.1.1. INTRODUCTION

Electrospinning is a technique that allows fibers having from a nanometric to a micrometric diameter from a wide range of polymeric materials and for multiple applications mainly in the biomedical field when biodegradable and biocompatible polymers are involved.[1–11] In fact, the derived mats can mimic the extracellular matrix, be used with some advantages in tissue regeneration, encapsulate drugs for local and sustained release, and allow surface modification and development of nanosensors.[12]

The advantage of the technique is also linked to its great versatility and high simplicity. Basically, this electrostatic technique only involves the use of a high voltage field to charge the surface of a polymer solution droplet that is held at the end of a capillary tube, in such a way that a liquid jet is ejected towards a grounded target (collector) placed at a fixed distance. The success of the process mainly depends on solution properties (i.e., polymer concentration, nature of the solvent, conductivity and viscosity of the solution) and operational parameters (i.e., diameter of the needle, applied voltage, tip-collector distance and flow rate).[3,5–8]

Electrospun micro/nanofibers can also be used as reinforcing materials for biodegradable matrices with low mechanical properties.[13–17] This feature appears highly interesting when these weak matrices must be loaded with pharmacological agents since the incorporated drugs usually lead to a significant loss of material properties. It has been demonstrated that this approximation is useful. Specifically, reinforced and drug loaded composites were prepared by a melt compression technique.[16] Thus, a fibrous mat of the hard polymer (e.g., PLA) was placed between two sheets of the soft polymer (e.g., PCL) that would become the matrix after molding at a temperature higher than its melting point and lower than that of the electrospun fibers (Figure 7.1.1a). Similar reinforced laminates based on non-degradable materials have also been studied. It was demonstrated that electrospun fibers can effectively increase the impact properties of composites because of the good load distribution behavior of fibers and the absence of interleaves that could alter the thickness of the composites.[17]

Chlorhexidine (1,1′-hexamethylene-bis-5-(4-chlorophenyl) biguanide, CHX) has an antibacterial activity due to the presence of biguanide secondary amines that can be protonated under physiological pH conditions.[18] That is why scaffolds incorporating CHX have received great attention.[19–21] In this work, we consider the possibility of achieving a

delayed release by embedding mats constituted by drug loaded microfibers into a biodegradable polymeric matrix. Results are compared with those obtained from direct incorporation of the drug into the polymer matrix and into both the matrix and the electrospun mat. Note that the hydrophilic character of CHX should lead to a practically immediate release in aqueous media, which is beneficial when a rapid effect is desired, but it may also be interesting to have a drug reservoir to prevent future contaminations. CHX was selected as a drug model with the worst conditions for a delayed release (e.g., high diffusivity due to its low molecular size, high affinity towards aqueous release media and low affinity towards hydrophobic matrices and reinforcements), with the expected effect probably being clearer when high molecular weight hydrophobic drugs were employed.

An alternative fabric method to obtain matrices reinforced with electrospun fibers consists in the use of a dual electrospinning system as depicted in Figure 7.1.1b. Fibers of each constitutive polymer are deposited in a common rotatory collector after being generated by independent jets ejected from needles facing each other and separated by the collector. In this way, disturbing effects from the two electrically charged jets should be minimized while high fiber mixing efficiency should be expected. The co-electrospun fibrous mat is subsequently molded at an intermediate temperature between those of the melting point of each polymer (i.e., just some degrees above the melting point of PCL). This process seems ideal to obtain a perfect addition of electrospun fibers into the matrix of the soft polymer since molding is performed with a mat where fibers of each polymer are in close contact and well mixed, as displayed for example in Figure 7.1.1c. After the cooling process, a solid, homogeneous and reinforced laminate is obtained (Figure 7.1.1d).

Reinforcement of polymer matrices by either of the indicated methods requires a sufficient difference in the melting temperatures of the two selected biodegradable polymers. Therefore, we considered poly(ε-caprolactone), which has a melting point close to 60 ºC, as the polymer matrix and polylactide with a melting point higher than 150 ºC as the reinforcing fiber. Note that this model system is similar from a calorimetric point of view, to other combinations that involve polymers widely employed as wound closure materials. Polydioxanone (T_f : 115 ºC) - polyglycolide (T_f : 225 ºC) or polydioxanone – polyglyconate (T_f : 215 ºC) are significant examples that open potential applications in the field of sutures by adding reinforcement nanofibers, which counteracts the loss of properties caused by incorporation of pharmacological agents.

Figure 7.1.1. Schematic representation of procedures applied to obtain PCL pieces reinforced with PLA microfibers: **(a)** Molding a PLA electrospun fibrous mat between PCL sheets, and **(b)** using a co-electrospun fibrous mat constituted by PLA and PCL obtained by means of a common rotatory collector. The resulting mat before fusion of PCL and the molded piece are shown in **(c)** and **(d)**, respectively.

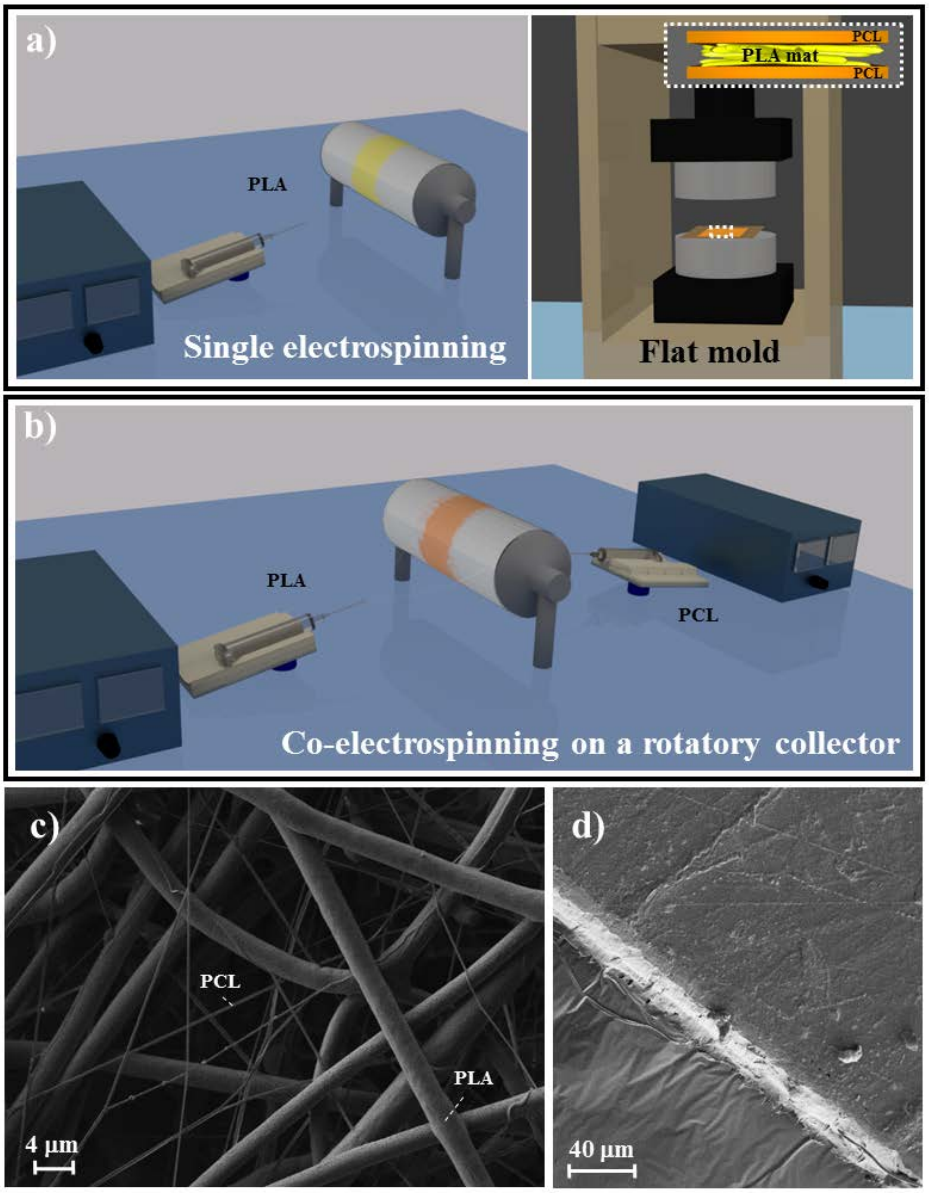

7.1.2. EXPERIMENTAL SECTION

7.1.2.1. Materials

A commercial PLA from Natureworks® with 95.8 wt-% of L-lactic isomer content was used (PLA 2002D grade). According to the manufacturer, PLA 2002D is a transparent solid with a density of 1.24 g/cc. Its calorimetric and mechanical properties are defined by a glass transition temperature (T_g) of 58 ºC, a melting point (T_m) of 153 ºC, a tensile modulus (E) of 3500 MPa, a tensile strength (σ) of 53-60 MPa and a tensile elongation (γ) of 6%. Number and weight average molecular weights and polydispersity index determined by GPC were 98,100 g/mol, 181,000 g/mol and 1.85, respectively.[22]

PCL (M_w: 65,000 g/mol) and chlorhexidine (CHX) were purchased from Sigma-Aldrich. The bacterial strains *Escherichia coli* CECT 101 and *Staphylococcus epidermidis* CECT 231 were obtained from the Spanish Type Culture Collection.

7.1.2.2. Measurements

^{1}H-NMR spectra were recorded with a Bruker AMX-300 spectrometer operating at 300.1 MHz. Chemical shifts were calibrated using tetramethylsilane as the internal standard and $CDCl_3$ $\delta(^1H)$ = 7.26 ppm and deuterated DMSO $\delta(^1H)$ = 2.50 ppm as solvents.

Calorimetric data were obtained by differential scanning calorimetry with a TA Instruments Q100 series with T_{zero} technology and equipped with a refrigerated cooling system (RCS). Experiments were conducted under a flow of dry nitrogen with a sample weight of approximately 5 mg and calibration was performed with indium. A four run protocol was employed in all cases to characterize the samples: first, a heating run at 20 ºC/min up to 190 ºC, second, a cooling run at 10 ºC/min up to -50 ºC after keeping the sample in the melt state for 5 min to wipe off the thermal history of the sample, third, a second heating run at 20 ºC/min and finally a third heating run performed at 20 ºC/min with the sample quenched up to -50 ºC from the melt state at the maximum cooling rate allowed by the equipment.

Optical micrographs were taken with a Zeiss Axioskop 40 Pol light polarizing microscope equipped with a Zeiss AxiosCam MRC5 digital camera.

Scanning electron microscopy (SEM) was used to examine the morphology of electrospun fibers and fracture surfaces. Carbon coating was accomplished with a Mitec k950 Sputter Coater (fitted with a film thickness monitor k150x). SEM micrographs were obtained with a Zeiss Neon 40 EsB instrument.

Mechanical properties were determined with a Zwick Z2.5/TN1S testing machine in stress-strain tests carried out at a deformation rate of 10 mm/min. Measurements were performed on rectangular samples (30 x 5 x 0.35 mm^3) cut from melt-pressed pieces. The mechanical parameters were averaged from a minimum of six measurements for each polymer sample.

Time resolved WAXD experiments were conducted at the NCD beamline (BL11) of the Alba synchrotron radiation light facility of Cerdanyola del Vallès (Catalunya). The beam was monochromatized to a wavelength of 0.1 nm. Polymer samples were confined between Kapton films and then held on a Linkam HFSX-350-CAP hot stage with temperature control within ± 0.1 ºC. WAXD profiles were acquired during heating and cooling runs in time frames of 20 s and rates of 10 ºC/min. The WAXD detector was calibrated with diffractions of a standard of a Cr_2O_3 sample. The diffraction profiles were normalized to the beam intensity and corrected considering the empty sample background.

7.1.2.3. Preparation of reinforced PCL films by co-electrospinning

A dual electrospinning system was used to prepare scaffolds constituted by a mixture of PCL and PLA microfibers, as depicted in Figure 7.1.1b. Samples will be denoted by the indicated experimental procedure (i.e., C for co-electrospinning) and the polylactide wt-% (i.e., C-PLA/PCL-30, C-PLA/PCL-20 and C-PLA/PCL-10 correspond to blends with 30, 20 and 10 wt-% of PLA, respectively). Electrospun fibers were collected on a rotary grounded collector operating at 30 rpm and at a variable distance (6-25 cm) from two equidistant needle tips (inside diameter of 0.84 mm) at room temperature. The needles were placed facing each other in order to minimize disturbing effects between the two electrically charged jets of PLA and PCL solutions. The voltage was varied between 15 and 30 kV and applied to the collector using two high-voltage suppliers (Gamma High Voltage Research, ES30-5W). Polymer solutions were delivered via two KDS100 infusion syringe pumps to control the flow rate (from 3.5 to 15 $mL \cdot h^{-1}$). Flow rates for each polymer solution were adjusted to obtain the desired polymer composition in the final fibrous matrix. All electrospinning experiments were carried out at room temperature.

Unloaded and CHX loaded electrospun fibers were prepared using optimized parameters (i.e., needle-collector distance, voltage and flow rates) and solvent conditions (i.e., solvent ratio, and polymer and drug concentrations). Electrospinning of PLA was carried out using an acetone-$CHCl_3$ (1:2, *v:v*) mixture with a polymer concentration of 10 wt-%, whereas PCL was electrospun in an EtOH-$CHCl_3$ (1:2, *v:v*) mixture and at a concentration of 22 wt-%. The CHX content of the electrospinning solutions was adjusted to obtain PLA and/or PCL electrospun fibers loaded with 0.5 wt-% of the drug. The insolubility of CHX in the acetone-$CHCl_3$ (1:2, *v:v*) mixture required the use a ternary mixture for the electrospinning of CHX loaded PLA by adding a 10 *v*-% of dimethylsulfoxide where CHX was initially dissolved.

Reinforced films were prepared by pressing (Manual Hydraulic Press, Specac) several rectangular sections (4 × 6 cm^2) of the appropriate co-electrospun mat until obtaining total weight of 400 mg. These mats were placed into a flat mold of the same internal dimensions that was covered with Teflon sheets to avoid polymer adhesion to the mold. Samples were heated at 15 ºC above the melting point of PCL (i.e., 60 ºC) for 12 min and using heating plates and a temperature controller. Pressure was progressively increased from 1 to 4 bar. Polymer films with a thickness close to 150 μm were recovered after cooling the mold to room temperature.

7.1.2.4. Preparation of reinforced PCL films by single electrospinning of PLA

Mats of unloaded and CHX loaded PLA electrospun microfibers were prepared as above indicated but using only one syringe. PCL films were prepared by pressing 350 mg of the polymer at a temperature of 75 ºC, as above mentioned. In order to obtain the reinforced matrices, electrospun PLA mats were cut into rectangular pieces (4 × 6 cm^2) and placed between two molded PCL films. Final PLA concentrations of 10, 20 and 30 wt-%, were obtained by adding PLA mats until reaching weights close to 78, 175 or 300 mg. After melt pressing as above indicated, reinforced films with thicknesses between 250 and 310 μm were obtained. Samples will be denoted as PLA/PCL-*x* where *x* is the theoretical weight percentage of PLA. PCL films prepared by solvent casting were used when CHX was also incorporated into PCL. In this case, the same solvent selected for electrospinning of PCL was used.

7.1.2.5. Drug release

Drug release experiments were performed in triplicate with square pieces prepared by both methodologies (total weight 10-25 mg). Samples were introduced in Falkon tubes with 40 mL of a mixture of Sorensen's buffer (pH 7.4) with ethanol 70 % (*v/v*). The released drug concentration was determined with a UV-3600 spectrometer (Shimadzu) by absorbance measurements at a wavelength of 260 nm, which corresponds to the maximum of the absorbance profile. Calibration curves were prepared using different stock solutions of the assayed CHX drug in the two different release media and relating the measured absorbance at 260 nm to the concentration. 1 mL of sample was taken from each tube at predetermined times and replaced with fresh medium. The presented results are an average value of the replicates.

Encapsulation efficiency was calculated by measuring the amount of drug incorporated into the scaffold by UV-vis absorbance measurements at a wavelength of 260 nm. When release finished, the loaded sample was dissolved in chloroform. CHX was separated by centrifugation after the precipitation of polymers by the addition of ethanol (final concentration chloroform – ethanol mixture: 5:95 *v.v*).

7.1.2.6. Antimicrobial test assays

Antimicrobial tests were performed to determine the bacteriostatic effect of the loaded drug. Thus, adhesion and growth assays of both *Escherichia coli* (*E. coli*) and *Staphylococcus epidermidis* (*S. epidermidis*) were performed on the PCL reinforced films using 24-well culture plates. Bacterial inhibition was quantitatively and qualitatively evaluated. In the first case, 0.05 mL of sample was taken every two hours for 8 h and final samples after 24 h and 48 h. Absorbance was measured in a microplate reader at 650 nm to determine bacterial growth. Regarding the qualitatively method, around 5 mg of loaded and unloaded samples was placed onto an Agar diffusion plate and seeded separately with 10^4 CFU/mL of each bacteria. The culture medium was prepared with 10.6 g of Brilliant Green Agar (BGA. Scharlau) dissolved in 200 mL of Milli-Q water and sterilized in an autoclave at 121 ºC for 30 min. Plates were filled with 15 mL of medium and kept at rest at room temperature to allow solidification of the medium. Inhibition halos images were taken after incubation of samples with bacteria at 37 ºC for 24 h.

For bacterial adhesion test, the culture medium was aspirated after the proliferation measurements and the material was washed three times with distilled water. Then, 0.5 mL of sterile 0.01 M sodium thiosulfate was added to each well to detach bacteria adhered on the surface of the sample. Then, plates were shaken at 100 rpm for 1 h. Finally, the polymeric samples were removed and 500 μL of culture medium was added to the wells and incubated at 37 ºC and 100 rpm for 24 h. Absorbance was measured in a microplate reader at 650 nm when culture medium was added and also after 24 h. Each sample was analyzed in quadruplicate and the results averaged. To determine variance and significant difference of the samples, a one-way ANOVA test and a *t*-test with a 95% ($p < 0.05$) confidence level were performed.

7.1.3. RESULTS AND DISCUSSION

7.1.3.1. Reinforced PCL films derived from co-electrospun PLA and PCL micro/nanofibers

The electrospinning conditions selected to obtain PLA microfibers and PCL nanofibers are summarized in Table 7.1.1. Dimensions of PCL fibers were chosen in the nanometric scale to facilitate the subsequent melting process. Specifically, a high voltage and a solvent less volatile than that employed for PLA were selected, which allowed thinner fibers to be obtained because the stretching process became longer. Note that flow rates for PLA and PCL solutions had to be changed in order to obtain the desired mat composition. Obviously, flow rates increased and decreased for PLA and PCL, respectively, as the PLA wt-% of the final mat was increased.

Table 7.1.1. Selected parameters for PLA and PCL to get co-electrospun mats of the indicated compositions. Diameter of fibers are also indicated.

	PLA				PCL			
PLA:PCL (wt:wt)	Flow ($mL \cdot h^{-1}$)	Distance (cm)	Voltage (kV)	Diameter (μm)	Flow ($mL \cdot h^{-1}$)	Distance (cm)	Voltage (kV)	Diameter (nm)
10:90	3.7	6	15	1.8 ± 0.2	15	8	23	175 ± 35
20:80	6.7	7	15	1.4 ± 0.2	12	8	30	235 ± 30
30:70	10.0	7	15	1.4 ± 0.2	10.5	8	30	220 ± 30

Homogeneous and continuous PLA and PCL fibers were attained under all selected conditions, as shown in Figure 7.1.2.

Figure 7.1.2. SEM micrographs showing PLA **(a,b,c)** and PCL **(d,e,f)** electrospun fibers prepared under the conditions selected to obtain fibrous mats containing 10 **(a,d)**, 20 **(b,e)** and 30 wt-% of PLA **(c,f)**.

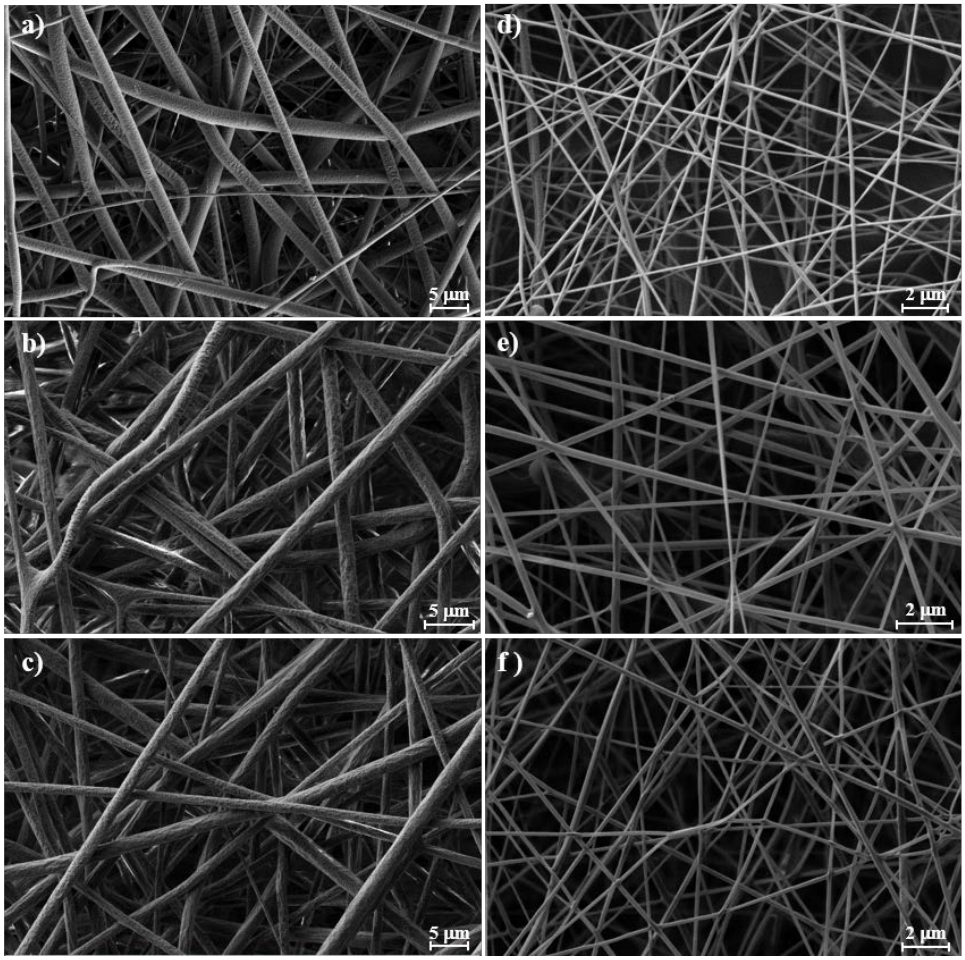

The diameter sizes always had a monomodal distribution (Figure 7.1.3) (average diameters are also summarized in Table 7.1.1.) The most striking feature for PLA and PCL fibers is that the average diameter tends to increase when the flow rate decreases. Nevertheless, it should be pointed out that the voltage was increased for electrospinning of PCL when the flow rate decreased, which should lead to a compensatory effect since a larger pendant

drop was formed and a higher diameter was favored. In the case of PCL, the tip-collector distance was kept constant, whereas for PLA it was slightly increased when the flow rate increased, with a slight decrease in the diameter being also observed. On the other hand, some authors have reported that above a limiting value of the flow rate, the fiber diameter tends to decrease.[23]

Figure 7.1.3. Diameter distribution curves of PLA **(a,b,c)** and PCL **(d,e,f)** electrospun fibers prepared under the conditions selected to obtain fibrous mats containing 10 **(a,d)**, 20 **(b,e)** and 30 wt-% of PLA **(c,f).**

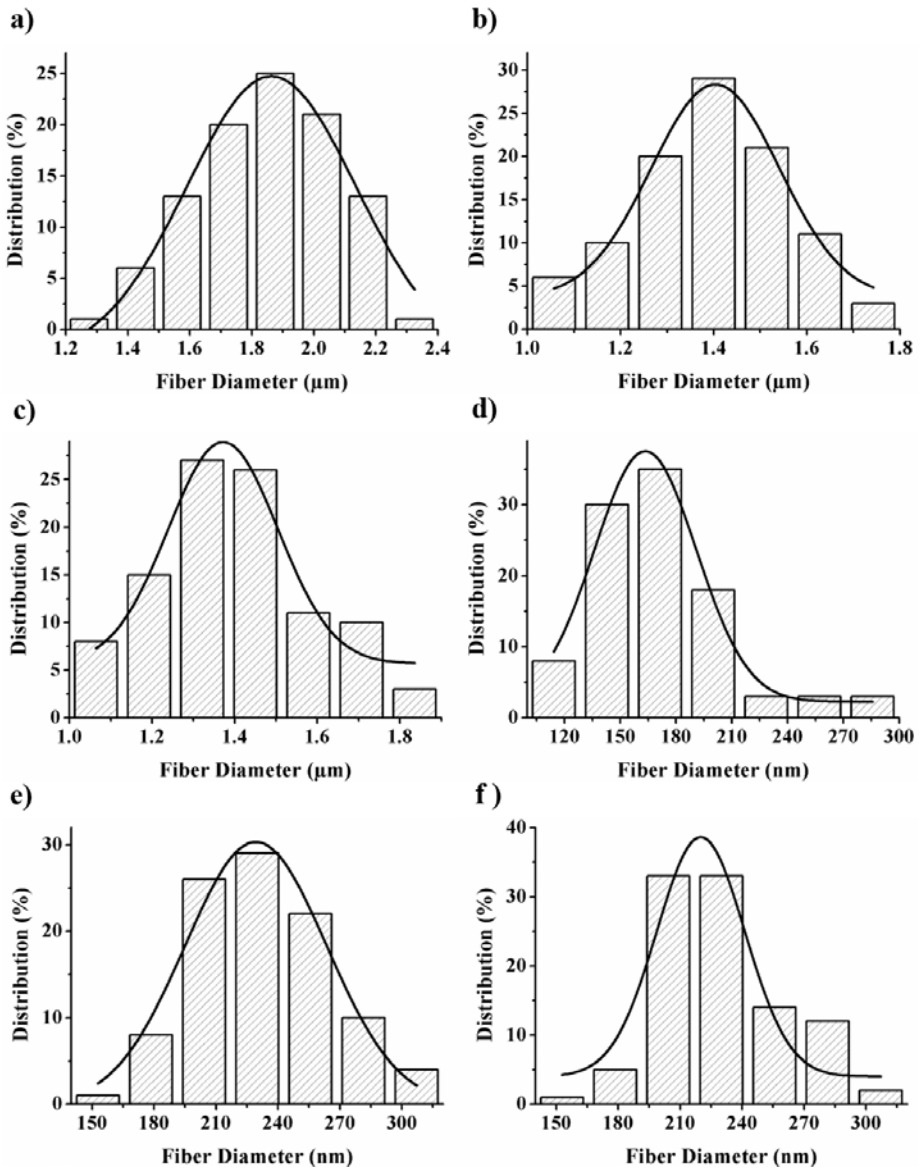

Texture of PCL and PLA electrospun fibers could also be clearly differentiated. Thus, a smooth surface was characteristic of thin PCL fibers, whereas the presence of longitudinal striations and more frequently a porous surface were characteristics of PLA microfibers.

Figure 7.1.4 shows representative SEM micrographs of co-electrospun mats with the 10 and 20 wt-% compositions. They revealed the difference in ratio between PLA and PCL fibers and a well-mixed distribution. Note that both kinds of fibers can be easily distinguished because of their different diameter size and texture. The insets of Figure 7.1.4 clearly show the presence of striations and pores in the PLA microfibers.

Figure 7.1.4. SEM micrographs showing the fibrous mats of co-electrospun samples containing PLA theoretical weight percentages of 10 **(a)** and 20 **(b)**. Details of the surface textures are shown in the corresponding high magnification insets.

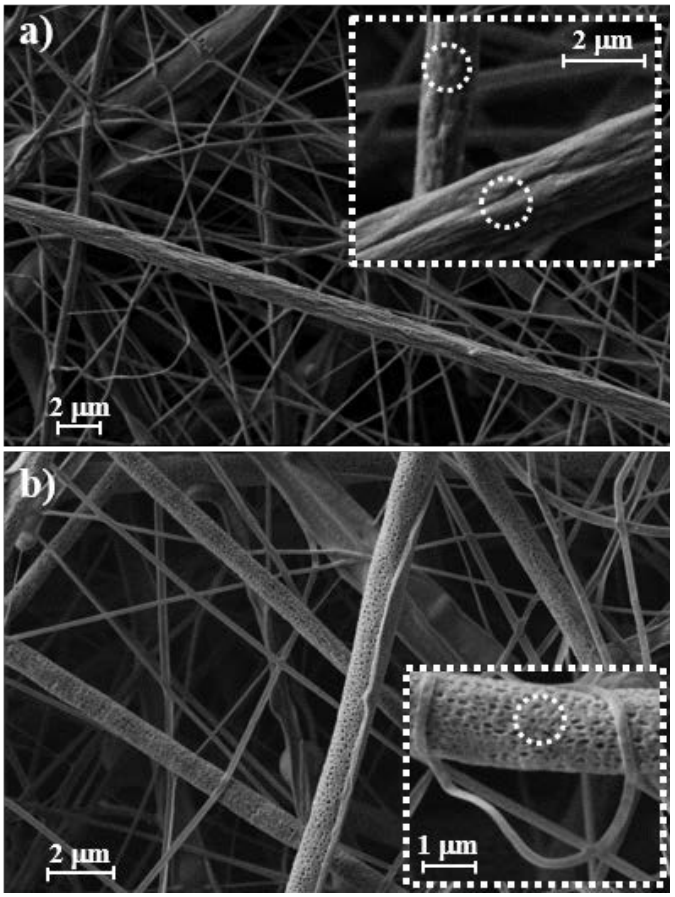

A representative ^{1}H-NMR spectrum of a co-electrospun mat is shown in Figure 7.1.5. The area of the typical quadruplet associated with the CH group of PLA (5.22-5.10 ppm) and the area of the triplet associated with the CH_2-O group of PCL (4.15-4.00 ppm) were used to estimate the composition of the scaffold according to equation 1:

$$\text{PLA (wt-\%)} = (A_{5.22\text{-}5.10} \times 72.1) / [(A_{5.22\text{-}5.10} \times 72.1) + (0.5 \times A_{4.15\text{-}4.00} \times 114.1)] \quad (1)$$

where 72.1 and 114.1 are the molecular weights of lactide and ε-caprolactone units, respectively.

Figure 7.1.5. ^{1}H-NMR spectra of the PLA/PCL co-electrospun sample containing 30 wt-% of PLA. Assignment of signals, as well as the areas of main peaks is indicated.

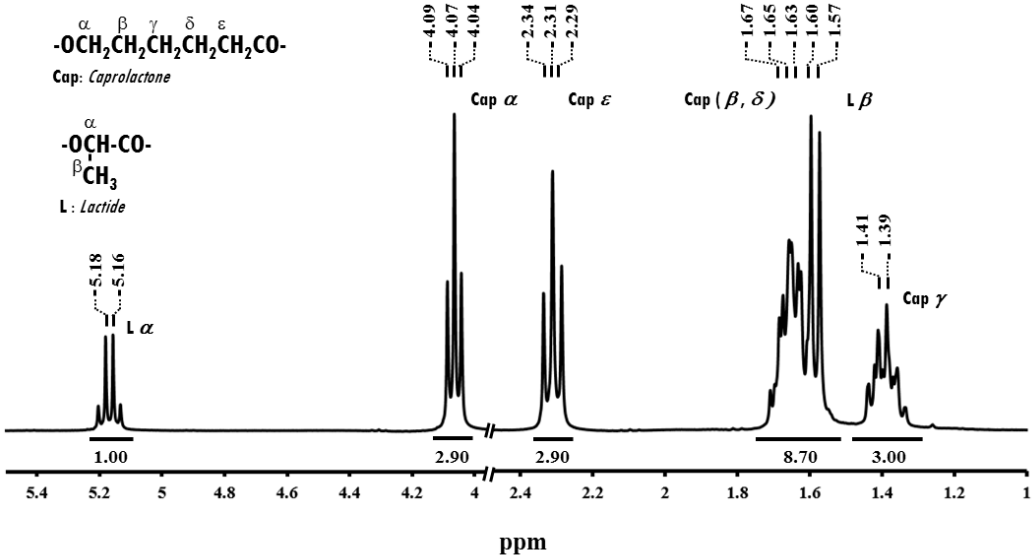

Table 7.1.2 compares the theoretical composition of the electrospun mats and the experimental values that correspond to an average of seven samples taken at regular intervals along the diagonal of the rectangular mat. In all cases, a relatively good agreement was observed, demonstrating that flow rates were properly chosen and that a homogeneous distribution was achieved by dual electrospinning and the use of a rotatory collector.

Table 7.1.2. Theoretical and experimental compositions of reinforced samples prepared by co-electrospinning and single electrospinning.

Samples	Theoretical Composition PLA:PCL (wt:wt)	Experimental Composition PLA:PCL (wt:wt)
Reinforced films by co-electrospinning	10:90	8.7 (± 1.9):91.3 (± 1.9)
	20:80	18.4 (± 2.9):81.6 (± 2.8)
	30:70	29.8 (± 3.8):70.2 (± 3.8)
Reinforced films by single electrospinning	10:90	11.3 (± 1.8):88.7 (± 1.8)
	20:80	19.8 (± 3.7):80.2 (± 3.7)
	30:70	29.4 (± 4.7):70.6 (± 4.7)

7.1.3.2. PCL films reinforced with electrospun PLA microfibers

PLA was electrospun using the same parameters selected for the dual electrospinning process (Table 7.1.1). Namely, they were varied according to the final composition since it was preferable to use PLA microfibers completely comparable (size and morphology) with those attained by co-electrospinning process. ^{1}H-NMR spectra were employed as above indicated to determine the composition of molded samples. Again, a good agreement was observed between theoretical and experimental values (Table 7.1.2), which means that there was a negligible loss of the lower viscosity PCL sample through the mold walls.

7.1.3.3. Thermal properties of PCL films reinforced with PLA

Calorimetric data of samples differing in composition and preparation methodology are summarized in Table 7.1.3.

Table 7.1.3. Calorimetric data of reinforced samples with different composition and processed according to the two proposed methodologies.

Sample	1st Heating				Cooling		2nd Heating						3rd Heating					
	PCL		PLA		PCL		PCL		PLA				PCL		PLA			
	T_f (°C)	ΔH_f (J/g)	T_f(°C)	ΔH_f (J/g)	T_c (°C)	ΔH_c (J/g)	T_f (°C)	ΔH_f (J/g)	T_f (°C)	ΔH_f (J/g)	T_c (°C)	ΔH_c (J/g)	T_f (°C)	ΔH_f (J/g)	T_f (°C)	ΔH_f (J/g)	T_c(°C)	ΔH_c (J/g)
PLA/PCL-10	59.8	79.1	165.7	1.1	26.4	67.0	56.0	68.1	-	-	-	-	56.7	66.1	-	-	-	-
PLA/PCL-20	56.2	72.9	164.7	0.8	27.8	63.6	57.2	62.0	-	-	-	-	57.2	60.8	-	-	-	-
PLA/PCL-30	59.8	64.8	165.3	2.39	30.9	56.6	56.0	55.6	164.7	1.2	-	-	55.4	57.4	164.4	1.6	-	-
C-PLA/PCL-10	61.6	75.3	166.4	4.5	28.9	58.6	56.1	59.8	165.2	5.6	133.3	3.8	55.5	57.4	164.9	4.7	135.0	4.7
C-PLA/PCL-20	61.8	68.9	165.6	6.7	28.4	51.8	56.5	52.0	165.6	3.7	131.0	2.9	56.6	51.5	165.4	3.1	133.7	2.8
C-PLA/PCL-30	62.0	59.7	166.4	8.7	27.0	46.8	56.9	43.5	165.8	7.4	128.2	6.1	56.9	42.1	165.9	7.0	129.9	5.9

These data correspond to the four run protocol shown in Figure 7.1.6 for a representative reinforced sample that allows thermal behavior in terms of fusion and crystallization to be determined from the melt and glassy state.

Figure 7.1.6. DSC scans performed with the reinforced sample prepared by molding a co-electrospun mat containing 30 wt-% of PLA: **(a)** first heating run, **(b)** cooling run after keeping the sample at 190 ºC for 5 min, **(c)** second heating run performed with the above cooled sample and **(d)** third heating run performed with a sample cooled at the maximum rate allowed by the equipment from 190 ºC to -50 ºC.

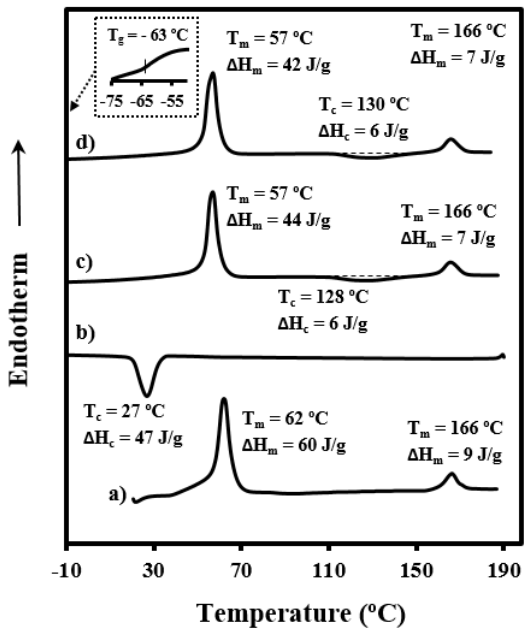

The following observations can be made:

a) A clear melting peak associated with the PCL matrix can always been detected in the 55-62 ºC temperature interval in DSC traces of the as-processed samples. The enthalpy is close to 83-86 J/g and 87-92 J/g (referred to the weight of PCL) for samples prepared by dual and single electrospinning, respectively. These values correspond to high crystallinities that are close to 60% and 63% when a value of 142 J/g for a 100% crystalline sample is considered.[24] Differences are not highly significant but suggest a better distribution of PLA fibers within the molten PCL phase that slightly hindered the crystallization process in films prepared by co-electrospinning.

b) Interestingly, melting enthalpy and crystallinity associated with PCL clearly decreased in the second and third heating runs (i.e., up to 43-55%, with the lower values being determined for samples prepared by co-electrospinning). Note that these values correspond to samples crystallized in a different way since in this case PLA was completely melted, whereas PLA fibers were always present in the crystallization of the molded samples.

c) All reinforced samples showed a small peak between 165 and 167 ºC associated with the fusion of PLA fibers. It is clear that the electrospinning process favored alignment of PLA chains, giving rise to a significant crystallization during molding process of samples prepared by co-electrospinning. Thus, crystallinities between 29% and 45% could be estimated considering a melting enthalpy of 93.1 J/g for a 100% crystalline PLA sample[25]. Good contact between PCL and PLA, together with an enhanced cold-crystallization process during the heating performed in the mold was observed. On the contrary, cold crystallization was less favored when samples were prepared by intercalation of PLA mats between PCL films. In this case, crystallinities of PLA were in the 8-11% range.

d) Cooling runs only showed the crystallization peak of PCL, with PLA remaining in the amorphous state. Note that PLA crystallizes with difficulty from the melt state because chains are not aligned, as is typical in an electrospinning process.

e) Cold crystallization peaks of PLA were observed during the second and third heating runs of samples prepared by dual electrospinning but not for those prepared by single electrospinning. It seems that during the heating scan the better distribution of PLA within the molten PCL phase facilitated its crystallization.

f) Glass transition of PCL was detected at around -63 ºC for all quenched samples, but that corresponding to PLA could not be observed because of the overlapping with the PCL melting peak.

7.1.3.4. Structure and morphology of PCL films reinforced with PLA

X-ray diffraction patterns of reinforced films exhibited the characteristic reflections of PCL, as shown in Figure 7.1.7 for the samples enriched in PLA. Thus, four Bragg peaks at 0.415, 0.404, 0.375 and 0.367 nm, which corresponded to the (110), (111), (200) and (201) reflections of PCL,[26,27] were clearly observed. In addition, the film prepared from co-electrospinning (Figure 7.1.7a) showed PLA reflections at 0.542 and 0.472 nm, which correspond to the (200)+(110) and (203) reflections of the α-form of polylactide.[28,29] It is interesting to note that PLA reflections could not be detected in the co-electrospun scaffold (Figure 7.1.7b), indicating that PLA crystallized during the molding process, as postulated in the previous section. In fact, time resolved diffraction profiles taken during the heating process (Figure 7.1.8) of co-electrospun scaffolds demonstrated that cold crystallization of PLA took place once the PCL nanofibers were completely melted.

PLA reflections were absent in the diffraction patterns of reinforced films prepared by single electrospinning of PLA (Figure 7.1.7c). Thus, cold crystallization was not significant during molding when fibers were directly deposited between the two PCL films.

Figure 7.1.7. WAXD profiles ($q = [4\pi/\lambda] \sin(\theta) = 2\pi/d$, where θ is the scattering angle and d the Bragg spacing) and corresponding 2D-patterns (insets) obtained from final C-PLA/PCL-30 reinforced films **(a)**, C-PLA/PCL-30 fibrous mat before performing the molding process **(b)** and PLA/PCL-30 reinforced films **(c)**. Spacings of main reflections are indicated in nanometers.

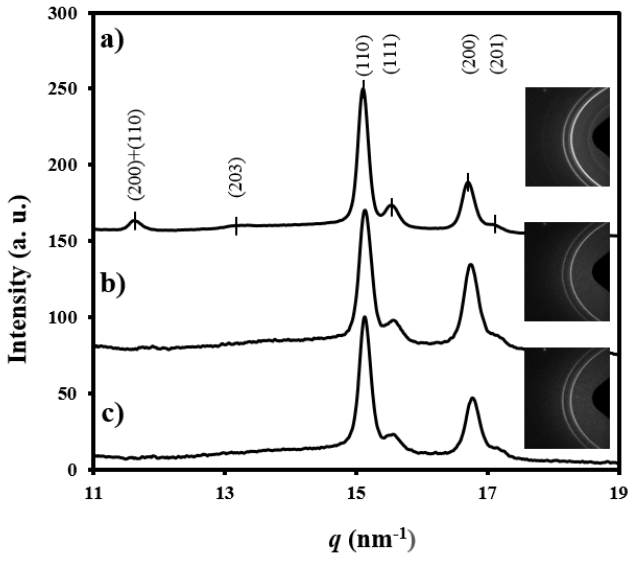

Figure 7.1.8. Three-dimensional WAXD profiles taken during a heating scan (10 ºC/min) of a fibrous mat constituted by 30 wt-% of PLA microfibers and 70 wt-% of PCL nanofibers.

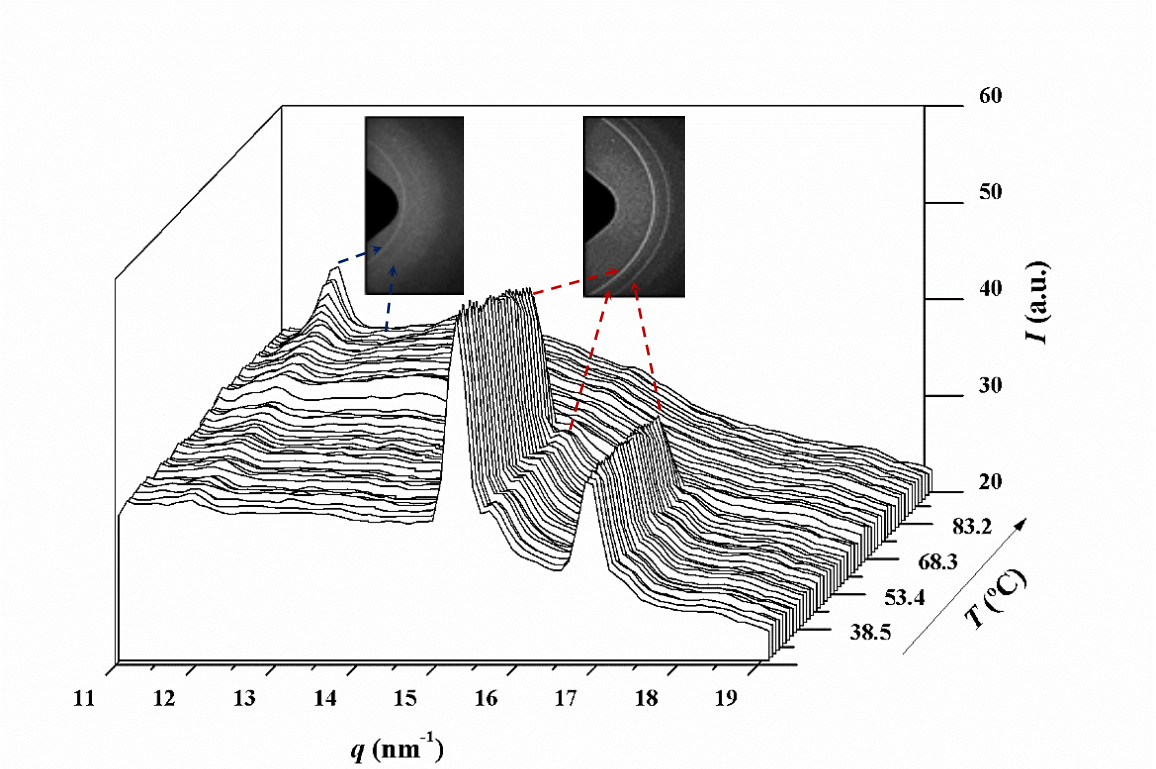

Figure 7.1.9 shows polarizing optical micrographs of co-electrospun scaffolds taken at different temperatures. At the high molding temperature, PLA microfibers appear unaltered inside the amorphous background corresponding to PCL (Figure 7.1.9a). This polymer began to crystallize at temperatures close to 50 ºC (Figure 7.1.9b) and gave rise to well-developed PCL fibrillar spherulites with a typical negative birefringence at room temperature (Figure 7.1.9c). Micrographs of thin films reveal an average spherulite diameter close 40-50 μm, with PLA microfibers randomly dispersed and integrated inside the crystallized spherulites (Figure 7.1.9d). Microfibers showed a slight birefringence that is indicative of a certain degree of orientation of PLA chains.

Figure 7.1.9. Polarizing optical micrographs showing PLA microfibers embedded in a melted PCL sample **(a)**, and spherulitic morphologies obtained after cooling to 50 ºC **(b)** and room temperature **(c,d)**. Micrographs **(b)**, **(c)** and **(d)** were taken with a red tint plate. A thinner film was used to show spherulites in **(d)** more clearly.

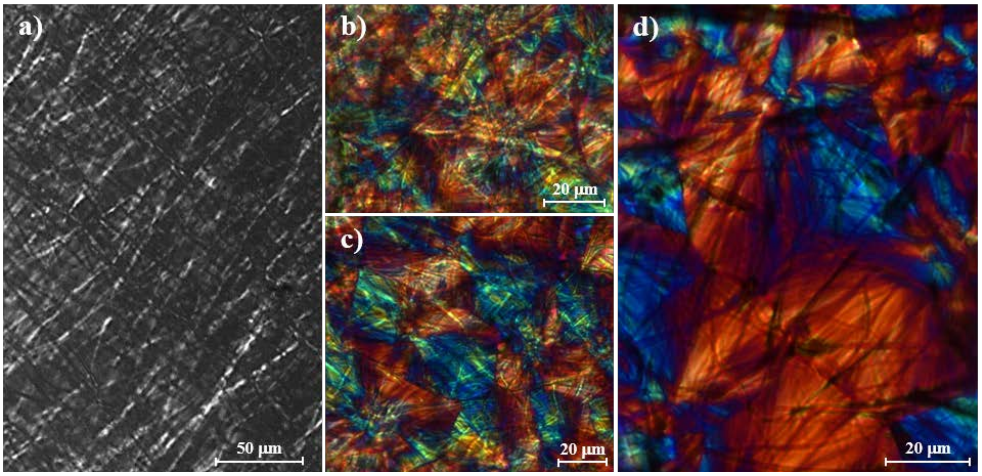

7.1.3.5. Mechanical properties of PCL films reinforced with PLA

Several works have addressed the reinforcing effect of electrospun fibers,[13,14,30] which may be higher than that of conventional reinforcements due to their high surface contact area with the polymeric matrix. Moreover, the porous PLA scaffold may favor the attainment of an interpenetrating structure, a feature that is logically enhanced by the co-electrospinning set up. The use of microfibers is also justified by recent works indicating that nanofibers clearly reduced the porosity of the scaffold and hindered the achievement of optimal interactions with the melted polyester after performing the molding process.[16] Table 7.1.4 summarizes the increase of elastic modulus and maximum stress with incorporation of PLA microfibers in the PCL matrix as an evidence of an interlocking mechanism.[14,30] Data also indicate that the presence of stretched polymer chains in the electrospun fibers leads to a decrease in tensile deformation compared to that of the bulk PCL matrix.[30,31]

Table 7.1.4. Mechanical properties of PCL films with and without reinforcing PLA fibers.

Sample	*E* (MPa)	Maximum stress (MPa)	Strain (%)
PCL film	159 (± 7)	15 (± 3)	150 (± 14)
PLA/PCL-10	251 (± 9)	21 (± 1)	19 (± 3)
PLA/PCL-20	313 (± 6)	23 (± 1)	20 (± 6)
PLA/PCL-20 CHX[a]	262 (± 6)	19 (± 4)	20 (± 4)
PLA/PCL-30	361 (± 8)	24 (± 3)	32 (± 7)
C-PLA/PCL-10	278 (± 14)	18 (± 3)	13 (± 6)
C-PLA/PCL-20	401 (± 12)	20 (± 2)	14 (± 5)
C-PLA/PCL-20 CHX[a]	390 (± 14)	19 (± 4)	12 (± 3)
C-PLA/PCL-30	428 (± 9)	26 (± 6)	18 (± 3)

[a] *Samples with CHX loaded into PLA microfibers.*

Figure 7.1.10 compares stress-strain curves for representative samples showing that the indicated changes caused by the incorporation of PLA fibers.

Figure 7.1.10. Stress-strain curves of PCL and samples prepared by co-electrospinning and containing 10 and 30 wt-% of PLA.

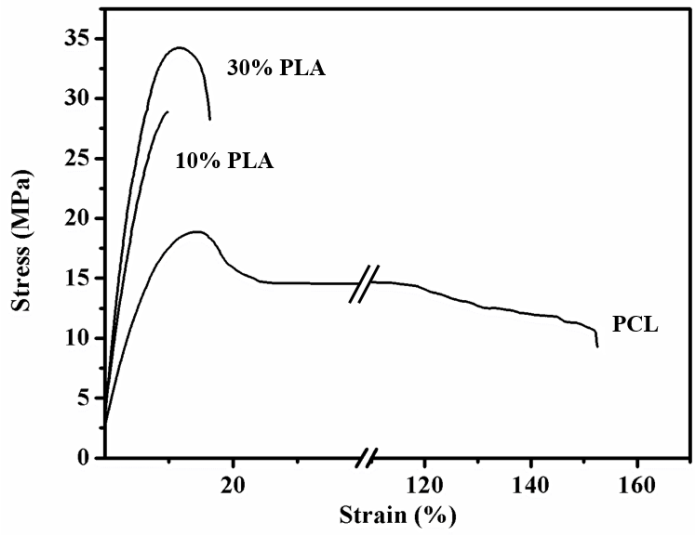

Figure 7.1.11 compared the evolution of the Young modulus with the percentage of incorporated PLA fibers. It is clear that preparation method of the reinforced films results in a different behavior. Specifically, a higher increase is detected for samples prepared by co-electrospinning because of better interlocking with the PCL matrix.

Figure 7.1.11. Evolution of the Young modulus with the PLA microfibers content according to the two used preparation methods: co-electrospinning (blue circles), and molding an electrospun PLA fibrous mat between PCL films (orange rhombus).

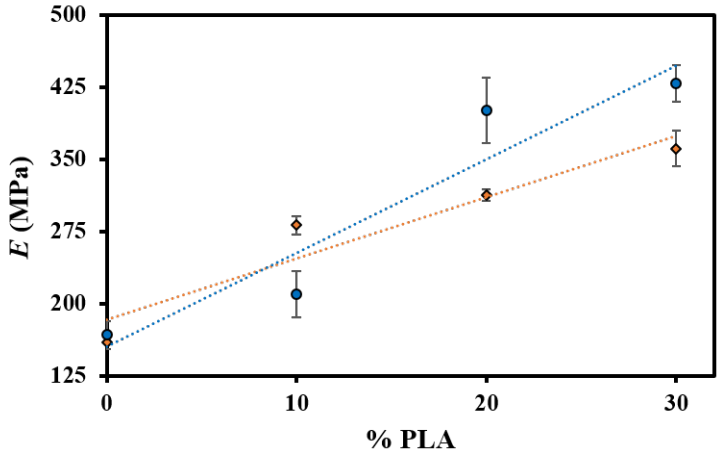

Figure 7.1.12 illustrates the fracture surface of samples prepared by the two different methodologies. Pull-out, good dispersion and alignment of fibers after breaking is clear in contrast with their random orientation in the initial scaffold. Mechanical properties are the result of several factors that show the evolution of damage under the applied stress: matrix cracking, matrix deformation, fiber fracture, pull-out fiber and debonding.[32,33] Matrix deformation and pull-out of fibers are more significant for samples prepared by single electrospinning suggesting weaker interactions between PLA fibers and the PCL matrix and leading to higher strain and even a worse modulus compared with samples prepared by co-electrospinning. Nevertheless, it should be also considered that in the last case crystallinity of PLA is slightly higher, also contributing to a higher modulus. Figure 7.1.12a also shows that the film surface is highly porous near the fracture, which reveals the internal presence of PLA fibers and logically the deformation of the thin external PCL surface.

Figure 7.1.12. SEM micrographs showing the fracture surface of PCL samples reinforced with PLA microfibers prepared from co-electrospun mats **(a,b)** and molding between PCL films **(c,d).** Low **(a,c)** and high magnification images **(b,d)** are provided together with specific details (insets).

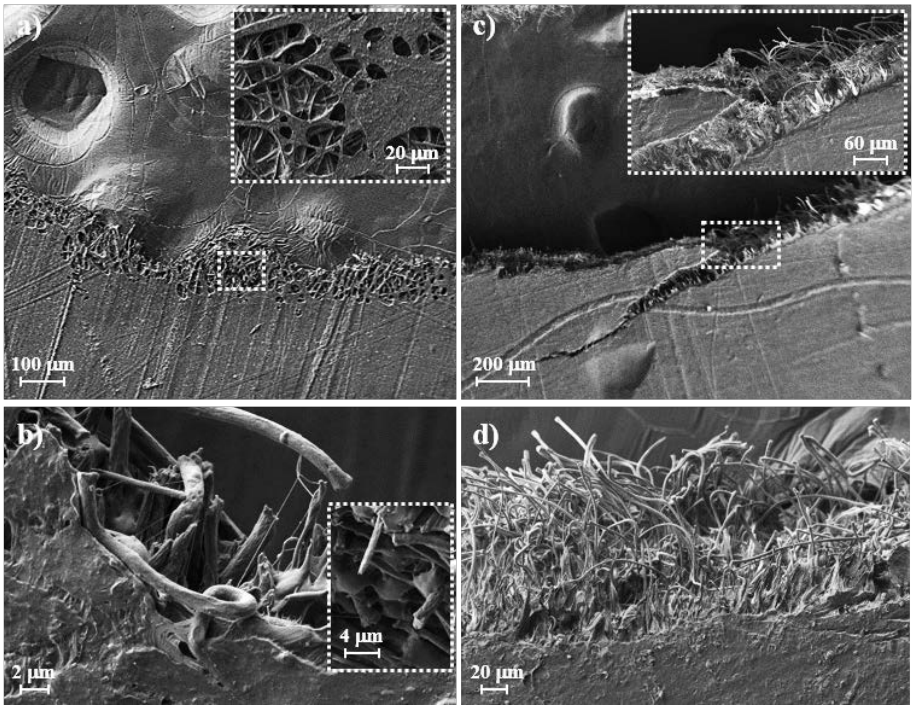

7.1.3.6. CHX load and release from PCL films reinforced with PLA

Electrospinning conditions were varied for two reasons. First, because the electrospinning solvent was modified by addition of dimethylsulfoxide to the acetone-$CHCl_3$ mixture in order to allow dissolution of CHX. Second, because the voltage for PCL had to be reduced from 30 to 22.5 kV when flow rates under 15 mL/min were required. In all cases, homogeneous fibers with similar characteristics to those obtained from unloaded samples were attained. Specifically, no significant differences between diameters of loaded and unloaded PLA microfibers were determined (i.e., diameters varied in the 1.2-1.7 µm range). Table 7.1.4 shows that the mechanical properties of CHX loaded samples follow the above trends. A slight decrease of the modulus and the tensile strength compared to the related unloaded samples is always observed, but it is clear that these values are still higher than those found for unloaded PCL films.

CHX release was evaluated for samples prepared by single and dual electrospinning as well by loading of the drug into one (PLA or PCL) or both polymers, as shown in Figure 7.1.13.

Figure 7.1.13. Scheme showing the three different ways to load the CHX drug into the samples obtained by molding the PLA electrospun mat between PCL sheets **(a–c)** and by co-electrospinning process **(d–f)** (i.e., into PLA fibers **(a,d)**, into PCL **(b,e)** and into both, PCL and PLA **(c,f)**).

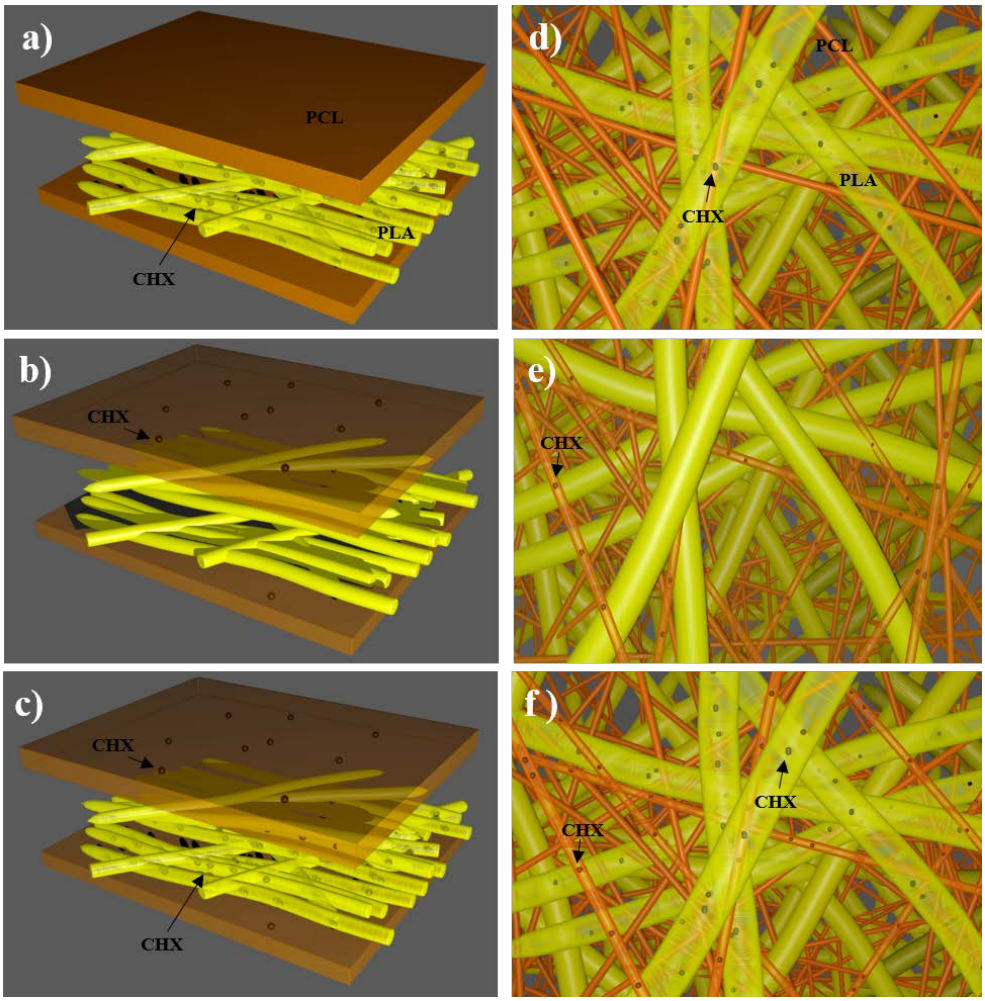

Typical release profiles can be seen in Figure 7.1.14 for representative C-PLA/PCL-20 and PLA/PCL-20 samples. Note that samples with slightly different PLA ratios behave similarly (i.e., from 10 to 30 wt-%).

Figure 7.1.14. CHX release profiles of PCL matrices containing a theoretical PLA weight percentage of 20 %. Empty symbols correspond to samples prepared from co-electrospun mats, whereas full symbols correspond to the sample prepared by molding the PLA electrospun mat between two PCL sheets.

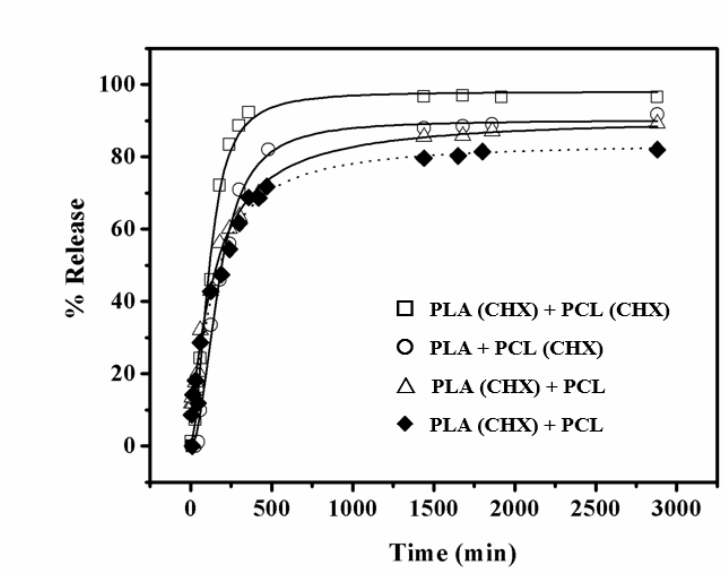

Main release data are summarized in Table 7.1.5. Some relevant observations can be made:

a) Release was always characterized by a fast step that could be fitted (i.e., the regression coefficient was always higher than 0.97) with a typical Higuchi equation initially conceived for planar geometries [34,35]:

$$M_t / M_0 = k_H t^{(1/2)} \quad (2)$$

where k_H is the Higuchi release constant, M_t is the percentage of drug released at time t, and M_0 is the maximum percentage of released drug.

b) Higuchi constant was lower when only PLA electrospun fibers were loaded with CHX since the drug diffusion pathway was increased compared to samples with the drug loaded into the PCL matrix. In the same sense, release was faster for samples prepared by co-electrospinning since PLA fibers were better distributed/mixed inside the PCL matrix, and consequently the pathway was reduced.

c) In all cases, a slight percentage of the loaded drug was effectively encapsulated into the reinforced films at least during an exposure to the release medium of up to 3000 h. This retention was significant (i.e., 15% and 11%) for samples having only CHX loaded into the PLA microfibers. Logically, the lower retention was found for samples prepared by co-electrospinning.

d) Significant differences in the time required to reach the maximum release were detected when only CHX was loaded into the PLA microfibers. Thus, 1500-1800 min was determined for these samples, whereas this period decreased to 400-550 min when PCL was also loaded.

Table 7.1.5. Release data corresponding to the different loaded samples.[a]

Sample	Polymer where CHX was loaded	k_H ($h^{-0.5}$)	CHX released[b] (%)	t_{97}[c] (min)
C-PLA/PCL	PLA	0.39	89	1500
C-PLA/PCL	PCL	0.46	91	550
C-PLA/PCL	PLA + PCL	0.47	95	400
PLA/PCL	PLA	0.28	85	1800
PLA/PCL	PCL	0.47	95	500
PLA/PCL	PLA + PCL	0.48	97	400

[a] *Values are averaged over the three compositions since no significant differences were found between them.*
[b] *Percentage delivered after 3000 minutes of exposure to the release medium.*
[c] *Time required to achieve a release of 97% with respect to the value achieved after 3000 minutes of exposure to the release medium.*

7.1.3.7. Antibacterial activity of PCL films reinforced with PLA and loaded with CHX

Bacterial growth inhibition of *E. coli* and *S. epidermidis* is shown in Figures 7.1.15a and 7.1.15b, respectively. The behavior of unloaded samples prepared by co-electrospinning and single electrospinning displayed against the selected Gram positive and Gram negative bacteria was similarto that of the control. Typical curves with a lag phase (approximately 4

h), a log phase indicative of exponential growth (up to 8-9 h of culture) and a final stationary phase beyond 24 h were observed. On the contrary, all samples loaded with CHX showed a complete inhibition of bacterial growth, with the exception of samples where CHX was loaded in the PLA microfibers only. In any case, the worst situation (*S. epidermidis*) corresponded to a maximum bacterial growth of only 5% with respect to the control, and could therefore be considered insignificant. The result, however, clearly indicates the greater difficulty of CHX to diffuse in this fabric configuration.

Figure 7.1.15. Relative growth of *E. coli* **(a)** and *S. epidermidis* **(b)** on control, unloaded and CHX loaded samples containing 20 wt-% of PLA microfibers. Reinforced polymer samples were prepared by co-electrospinning.

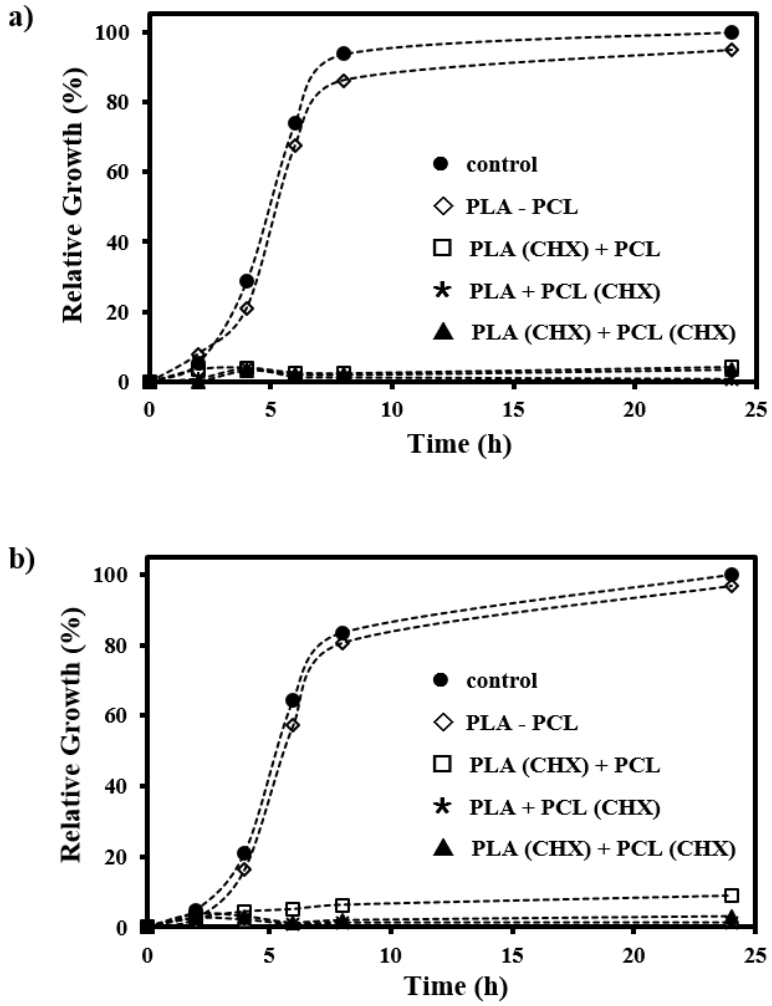

Similar qualitative results were obtained from the observation of inhibition halos (Figure 7.1.16). It is clear that CHX loaded in the PLA microfibers only diffused without problem trhough the PCL layers. It should be pointed out that inhibition halos were always homogeneous around the films plates, indicating a good distribution of the drug during the preparation method. Finally, Figure 7.1.16 indicates that the size of the halos varied according to the polymer where CHX was loaded, decreasing in the order: PCL+PLA > PCL > PLA. On the other hand, halos were highly similar for the two preparation methods (i.e., single and dual electrospinning) were compared.

Figure 7.1.16. Images showing the inhibition halos on agar plates seeded with *E. coli* and *S. epidermidis* for unloaded and CHX loaded samples and prepared from co-electrospun mats and by molding the electrospun PLA mat between two PCL sheets. Results of the different ways of incorporating the bactericide drug are also shown.

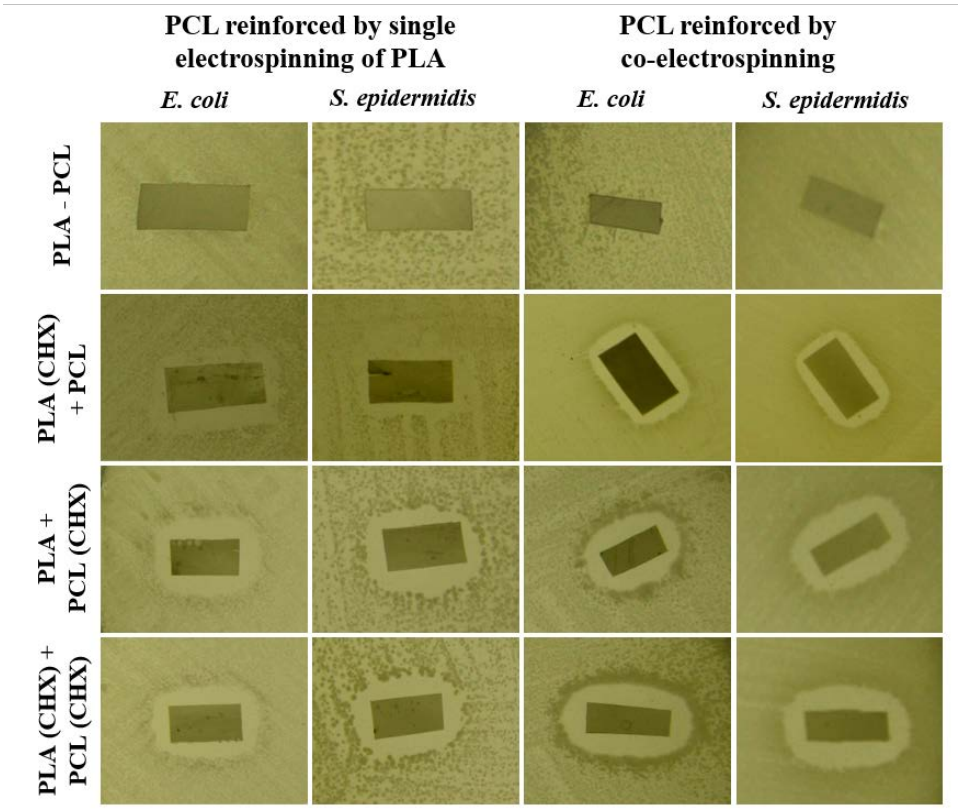

Figure 7.1.17 shows the results of bacterial adhesion after 24 h of incubation in broth culture medium. Note that measurements indicated residual bactericide activity after a previous inhibition of 24 h.

Figure 7.1.17. Results of bacterial adhesion assays performed on 10 **(a,c)** and 20 wt-% **(b,d)** PLA reinforced samples prepared by co-electrospun PLA and PCL fibers **(a,b)** and by molding a PLA fibrous mat between two PCL films **(c,d).**

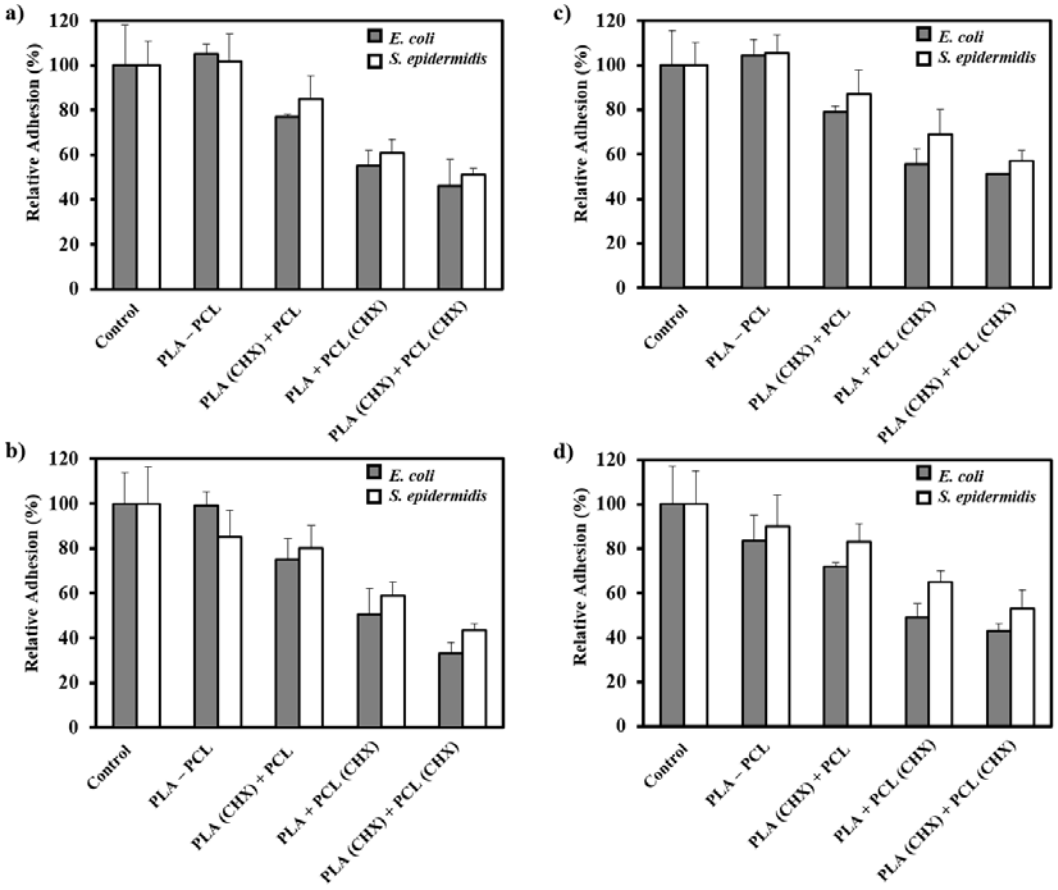

It is clear that unloaded specimens are highly susceptible to be colonized by both kinds of bacteria, whereas a different sensitivity of loaded films towards bacteria was observe. The highest infection rate (ca. 80%) was found when CHX was incorporated in the reinforcing microfibers of PLA only, intermediate infection rate when only the PCL matrix was loaded

(ca. 60%) and the lowest when CHX was loaded into both polymers (ca. 40%). In general, CHX was found to be most effective against *S. epidermidis*, but no significant differences were detected according to the preparation method (single or dual electrospinning) and even according to the ratio of PLA microfibers incorporated into the PCL matrix.

7.1.4. CONCLUSIONS

PCL films reinforced with PLA microfibers can be effectively prepared by a co-electrospun procedure that rendered clear advantages in terms of crystallinity and mechanical properties compared to typical molding of PLA microfibers between films of the PCL matrix. The proposed procedure improved interaction between PLA fibers and the PCL matrix, with cold crystallization of PLA being favored during the molding process.

The incorporation of PLA microfibers can compensate the loss of mechanical properties caused by the incorporation of small drugs into PCL matrices and even improve the final performance of the material.

The co-electrospinning procedure allowed bactericide agents like chlorhexidine to be easily loaded into both polymers. However, a slower release rate and a high retention were observed when the drug was only loaded into the PLA fibers. Slight differences were again detected between the two preparation methods; specifically, the films prepared by co-electrospinning showed a faster release. A bactericide effect against Gram positive and Gram negative bacteria was demonstrated for all CHX loaded samples despite the high susceptibility of both polymers to be colonized. Antibacterial activity was still highly significant under the worst release conditions (i.e., samples prepared by single electrospinning and loaded only into the PLA fibers).

7.1.5. REFERENCES

1. Reneker, D. H. & Chun, I. Nanometre diameter fibres of polymer, produced by electrospinning. *Nanotechnology* **7,** 219–223 (1996).

2. Reneker, D. H., Yarin, A. L., Fong, H. & Koombhongse, S. Bending instability of electrically charged liquid jets of polymer solutions in electrospinning. *J. Appl. Phys.* **87,** 4531–4547 (2000).

3. Frenot, A. & Chronakis, I. S. Polymer nanofibers assembled by electrospinning. *Curr. Opin. Colloid Interface Sci.* **8,** 64–75 (2003).

4. Dzenis, Y. Spinning continuous fibers for nanotechnology. *Science* **304,** 1917–1919 (2004).

5. Li, D. & Xia, Y. Electrospinning of nanofibers: Reinventing the wheel? *Adv. Mater.* **16,** 1151–1170 (2004).

6. Jayaraman, K., Kotaki, M., Zhang, Y., Mo, X. & Ramakrishna, S. Recent advances in polymer nanofibers. *J. Nanosci. Nanotechnol.* **4,** 52–65 (2004).

7. Dhakate, S. R., Singla, B., Uppal, M. & Mathur, R. B. Effect of processing parameters on morphology and thermal properties of polycarbonate nanofibers. *Adv. Materals Lett.* **1,** 200–204 (2010).

8. Sharma, S. Ferroelectric nanofibers: Principle, processing and applications. *Adv. Materals Lett.* **4,** 522–533 (2013).

9. Dersch, R., Steinhart, M., Boudriot, U., Greiner, A. & Wendorff, J. H. Nanoprocessing of polymers: Applications in medicine, sensors, catalysis, photonics. *Polym. Adv. Technol.* **16,** 276–282 (2005).

10. Chronakis, I. S. Novel composites and nanoceramics based on polymer nanofibers using electrospinning process - A review. *J. Mater. Process. Technol.* **167,** 283–293 (2005).

11. Deitzel, J. M., Kleinmeyer, J., Harris, D. & Tan, N. C. B. The effect of processing variables on the morphology of electrospun nanofibers and textiles. *Polymer* **42,** 261–272 (2001).

12. Tiwari, A., Terada, D., Yoshikawa, C. & Kobayashi, H. An enzyme-free highly glucose -specific assay using self-assembled aminobenzene boronic acid upon polyelectrolytes electrospun nanofibers-mat. *Talanta* **82,** 1725–1732 (2010).

13. Bergshoef, M. M. & Vancso, G. J. Transparent nanocomposites with ultrathin electrospun nylon-4,6 fiber reinforcement. *Adv. Mater.* **11,** 1362–1365 (1999).

14. Fong, H. Electrospun nylon 6 nanofiber reinforced BIS-GMA/TEGDMA dental restorative composite resins. *Polymer* **45,** 2427–2432 (2004).

15. Pinho, E. D., Martins, A., Araújo, J. V., Reis, R. L. & Neves, N. M. Degradable particulate composite reinforced with nanofibres for biomedical applications. *Biomaterialia* **5,** 1104–1114 (2009).

16. Del Valle, L. J., Díaz, A., Royo, M. & Rodríguez-Galán, A. Biodegradable polyesters reinforced with triclosan loaded polylactide micro/nanofibers: Properties, release and biocompatibility. *eXPRESS Polym. Lett.* **6,** 266–282 (2012).

17. Molnár, K., Kostáková, E. & Mészáros, L. The effect of needleless electrospun nanofibrous interleaves on mechanical properties of carbon fabrics/epoxy laminates. *eXPRESS Polym. Lett.* **8,** 62–72 (2014).

18. Green, J.-B. D., Fulghum, T. & Nordhaus, M. A. Immobilized antimicrobial agents: A critical perspective. In *Science against microbial pathogens: communicating current research and technological advances* (ed.Méndez-Vilas, A.) 84–98 (2011).

19. Chen, L., Bromberg, L., Hatton, T. A. & Rutledge, G. C. Electrospun cellulose acetate fibers containing chlorhexidine as a bactericide. *Polymer* **49,** 1266–1275 (2008).

20. Del Valle, L. J., Roa, M., Díaz, A., Casas, M. T. & Puiggalí, J. Electrospun nanofibers of a degradable poly(ester amide). Scaffolds loaded with antimicrobial agents. *J. Polym. Res.* **19,** 9792–9805 (2012).

21. Fernandes, J. G. *et al.* PHB-PEO electrospun fiber membranes containing chlorhexidine for drug delivery applications. *Polym. Test.* **34,** 64–71 (2014).

22. Cailloux, J. *et al.* Sheets of branched poly(lactic acid) obtained by one step reactive extrusion calendering process: Melt rheology analysis. *eXPRESS Polym. Lett.* **7,** 304–318 (2013).

23. Barua, B. & Saha, M. C. Investigation on jet stability, fiber diameter, and tensile properties of electrospun polyacrylonitrile nanofibrous yarns. *J. Appl. Polym. Sci.* **132,** 41918 (2015).

24. Wunderlich, B. *Crystal melting. Macromolecular Physics* **3,** (Academic Press, 1980).

25. Fischer, E. W., Sterzel, H. J. & Wegner, G. Investigation of the structure of solution grown crystals of lactide copolymers by means of chemical reactions. *Kolloid Z Z Polym* **251,** 980–990 (1973).

26. Chatani, Y., Okita, Y., Tadokoro, H. & Yamashita, Y. Structural studies of polyesters. III Crystal structure of poly(ε-caprolactone). *Polym. J.* **1,** 555–562 (1970).

27. Iwata, T. & Doi, Y. Morphology and enzymatic degradation of poly(ε-caprolactone) single crystals: does a polymer single crystal consist on micro-crystals? *Polym. Int.* **51,** 852–858 (2002).

28. De Santis, P. & Kovacs, A. J. Molecular conformation of poly(S-lactic acid). *Biopolymers* **6,** 299–306 (1968).

29. Hoogsteem, W., Postema, A. R., Pennings, A. J., Brinke, G. T. & Zugenmaier, P. Crystal structure, conformation and morphology of solution-spun poly(L-lactide) fibers. *Macromolecules* **23,** 634–642 (1990).

30. Baji, A., Mai, Y.-W., Wong, S.-C., Abtahi, M. & Chen, P. Electrospinning of polymer nanofibers: Effects on oriented morphology, structures and tensile properties. *Compos. Sci. Technol.* **70,** 703–718 (2010).

31. Lu, J.-W. *et al.* High-elongation fiber mats by electrospinning of polyoxymethylene. *Macromolecules* **41,** 3762–3764 (2008).

32. Kroll, L. & Hufenbach, W. A physically based failure criterion for laminated composites. *Mech. Compos. Mater.* **35,** 277–284 (1999).

33. Brauer, D. S., Rüssel, C., Vogt, S., Weisser, J. & Schnabelrauch, M. Degradable phosphate glass fiber reinforced polymer matrices: Mechanical properties and cell response. *J. Mater. Sci. Mater. Med.* **19,** 121–127 (2008).

34. Higuchi, T. Mechanism of sustained-action medication. Theoretical analysis of rate of release of solid drugs dispersed in solid matrices. *J. Pharm. Sci.* **52,** 1145–1149 (1963).

35. Baker, R. W. *Controlled release of biologically active agents.* (John Wiley & Sons, 1987).

7.2. Tunable drug loading and reinforcement of poly(ε-caprolactone) films by electrospun nanofibers of glycolide segmented copolymers

Electrospinning of a segmented copolymer having polyglycolide *hard segments* was successfully performed from 1,1,1,3,3,3-hexafluoroisopropanol solutions. A bactericide agent such as chlorhexidine (CHX) was also effectively loaded during the electrospinning process, rendering nanofibers with smaller diameter due to the change of solvent conductivity. New fabrics based on the molding of alternate layers of poly(ε-caprolactone) (PCL) films and the electrospun scaffolds of the segmented copolymer were prepared. The thermal molding process rendered a PCL matrix homogeneously reinforced with nanofibers that could compensate the loss of mechanical properties when CHX was incorporated.

The release of CHX was evaluated in different media being observed a different behavior depending on the layer where the drug was incorporated. Therefore, systems with an immediate bacteriostatic effect could be obtained as well as systems with a potential long term antimicrobial effect. Growth inhibition and adhesion assays demonstrate the fast bactericide effect of samples having the CHX drug loaded in the outer layers of the multilayered system.

7.2.1. INTRODUCTION

Electrospun nanofibers appear as ideal systems to be employed as reinforcing materials due to their anisotropy and high surface/volume ratio. In addition, these nanofibers can also be employed for the encapsulation of drugs due to the ease of loading provided by the electrospinning process. In general, mechanical properties of a polymer matrix worsen when drugs are incorporated. Thus, compensate this effect using appropriate reinforcing agents seems interesting. Furthermore, a tunable release can be obtained by selecting the composition of the nanofibers as well as the place where the drug is loaded (e.g., slow and fast releases should be expected when drugs were incorporated into the matrix or into the filler, respectively). Different works about the use of electrospun micro/nanofibers as fillers have currently been performed, being demonstrated the improvement of mechanical properties of derived composites.[1–5] In this sense, a good distribution of fibers and the absence of interleaves are meaningful factors that must be taken into account.[5]

Drug release behavior can be modified by varying the composition of the encapsulating system. For example, a tuned release of a model drug such as triclosan can be achieved by employing electrospun fibers prepared from different mixtures of polylactide and poly(ε-caprolactone).[6] In the same sense, a similar effect can be attained from copolymers with different compositions, being probably poly(lactic acid-*co*-glycolic acid) (PLGA) the most widely studied system. Nevertheless, it also seems highly interesting to consider the use of segmented copolymers because they could provide better properties than the indicated random copolymers. Furthermore, it is possible to get a great control on the final mechanical performance by modifying the ratio between the stiff *hard blocks* and the flexible *soft blocks*, which characterize the segmented architecture.[7]

Poly(ε-caprolactone) (PCL) is a biodegradable and biocompatible polymer with an easy processing, which has wide applications in tissue engineering, drug delivery and packaging.[8–10] Nevertheless, it also has important disadvantages such as poor barrier properties, low melting temperature and low modulus, which limit their applications. Therefore, PCL appears as an ideal matrix for loading biodegradable and biocompatible nanofillers in order to improve mechanical properties and extend the range of application as a drug delivery system.

Although electrospun fibers of polyglycolide (PGA) appear as ideal fillers due to their relatively high degradation rate and high tensile modulus, it should be considered that PGA

has a high hydrophilic character, which contrast with the hydrophobicity of PCL. A lack of surface adhesion between PCL and PGA homopolymers is expected, and consequently a poor benefit on mechanical properties should be derived. The use of electrospun fibers produced from PCL and PGA mixtures have been considered a good alternative to improve adhesion and make feasible the load transfer from the PCL matrix to the stronger fiber reinforcement.[11] Specifically, it was determined that incorporation of 40 wt-% of fibers constituted by equivalent weights of PCL and PGA allowed to increase the yield strength.

The present work has as a main objective the evaluation of the possibilities of using segmented polymers as reinforcing materials. To this end, GL-*b*-(GL-*co*-TMC-*co*-CL)-*b*- GL (Figure 7.2.1a) has been selected since it is a commercial bioabsorbable suture (Monosyn®) with high crystallinity, good mechanical properties and biodegradability.[12–15] The material has a relatively hydrophobic *soft segment* that represents the 43 wt-% of the sample and includes ε-caprolactone units together with glycolide and trimethylene carbonate units.[16]

Polyglycolide electrospun nanofibers can be prepared from 8 wt-% solutions in HFIP, being the average fiber diameter of 310 nm, and ranging the diameter distribution between 50 and 650 nm.[17] However, scarce works are available about the electrospinning of polyglycolide despite its wide application in the biomedical field, a situation that can be extrapolated to copolymers with a segmented architecture.

Multilayer system is a new approach to obtain reinforced matrices. Different layers combining polymeric films and electrospun scaffolds allow tailoring mechanical properties and drug release when a pharmacological agent is incorporated at different layers. The present work is focused on a specific system constituted by five layers, three of poly(ε-caprolactone) films and two of electrospun GL-*b*-(GL-*co*-TMC-*co*-LA)-*b*-GL mats (Figure 7.2.1b). Furthermore, the possibility of using this kind of systems for achieving a controlled drug release is evaluated using a hydrophilic drug. This is expected to be quickly delivered from a hydrophobic matrix to a hydrophilic media. For this reason, it represents a good model to evaluate the loading capacity from different configurations to obtain a delayed release.

CHX (1,1′-hexamethylene-bis-5-(4-chlorophenyl)biguanide) (Figure 7.2.1a) is a hydrophilic drug with high interest due to its high activity towards microorganisms.[18] CHX affects the stability of bacterial membranes because of the capacity of its protonated

secondary amines to be attached to negatively loaded (anionic) phospholipids of the membranes.[19]

Figure 7.2.1. (a) Chemical structures of GL-*b*-(GL-*co*-TMC-*co*-CL)-*b*-GL (Monosyn®) and the selected CHX hydrophilic drug. **(b)** Schematic representation showing the distribution of layers and the different CHX loading configurations.

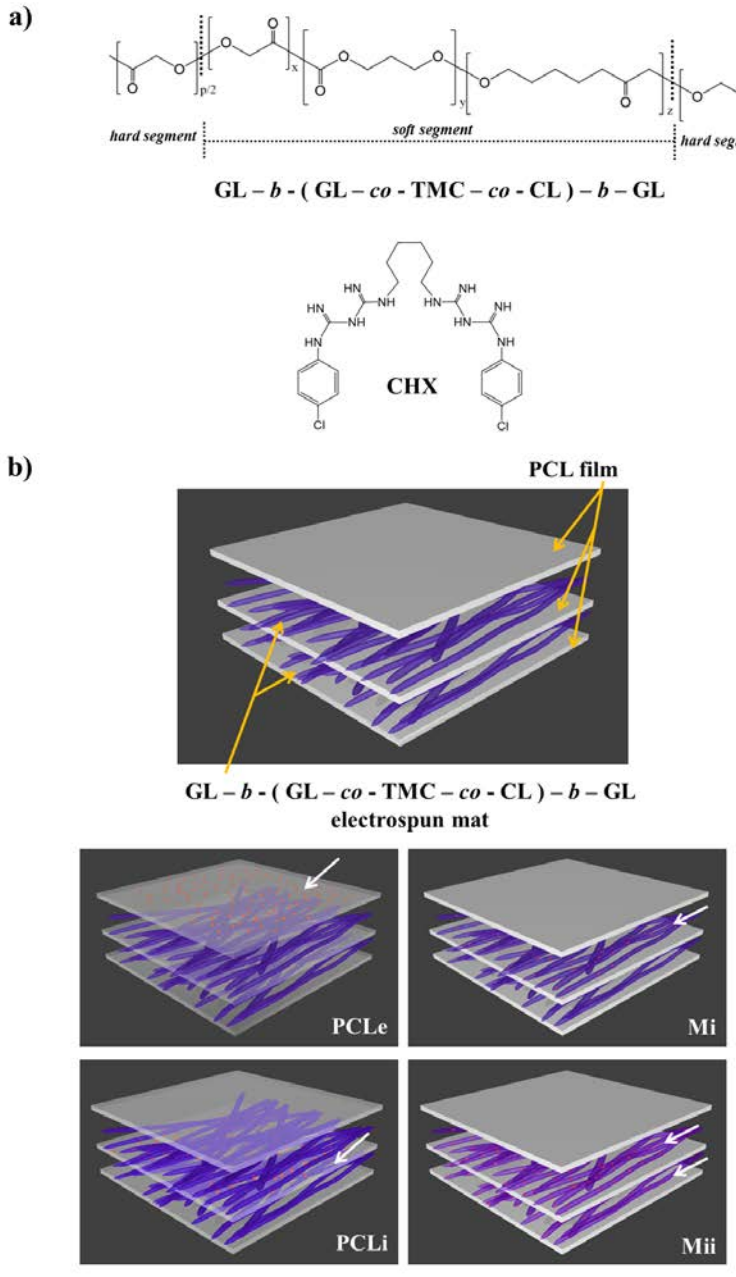

7.2.2. EXPERIMENTAL SECTION

7.2.2.1. Materials

Commercially available violet sutures of GL-*b*- (GL-*co*-TMC-*co*-CL)-*b*-GL (Monosyn®, USP 0) with a weight average of 90,700 g/mol were kindly supplied by B. Braun Surgical, S.A. Poly(ε-caprolactone) (PCL) (Mw: 65000 g/mol) and chlorhexidine diacetate (CHX) were purchased from Sigma-Aldrich as well as phosphate buffered saline (PBS-Dulbecco's Phosphate Buffer Saline).

Solvents (i.e., ethanol absolute and methanol) were purchased from Scharlab and 1,1,1,3,3,3-hexafluoroisopropanol (HFIP) from Apollo Scientific.

Reagents and labware for microbial culture were obtained from Scharlab. The bacterial strains *Escherichia coli* CECT 101 and *Staphylococcus aureus* CECT 245 were obtained from the Spanish Type Culture Collection

7.2.2.2. Measurements

Tensile properties of 1 x 2 cm^2 samples of PCL films, electrospun mats and the resulting matrices were analized at room temperature and humidity by a universal tensile testing instrument Zwick Z2.5/TN1S with a 100 N load cell equipped with a testXpert 8.1 program. Thickness of specimens depended on the preparation method (0.2, 0.05 and 0.7 mm for films, electrospun mats and melt pressed matrices, respectively). Initial distance between clamps was 10 mm and the crosshead speed was 10 mm/min. The reported Young's modulus and tensile strength were averaged values of at least five specimens.

Scanning electron microscopy (SEM) was used to examine the morphology of electrospun fibers and fracture surfaces. Carbon coating was accomplished with a Mitec k950 Sputter Coater fitted with a film thickness monitor k150x. SEM micrographs were obtained with a Zeiss Neon 40 EsB instrument.

Thermal degradation was determined at a heating rate of 10 ºC/min with around 5 mg of samples in a Q50 thermogravimetric analyzer of TA Instruments under a flow of dry nitrogen and in the temperature range from 50 to 600 ºC.

7.2.2.3. Electrospinning of GL-*b*-(GL-*co*-TMC-*co*-CL)-*b*-GL

Electrospinning of GL-*b*-(GL-*co*-TMC-*co*-CL)-*b*-GL was carried out in HFIP with a polymer concentration of 10 *w/v*-%. CHX loaded samples were obtained by adding a 0.5 *w/w*-% of the drug in the electrospinning solution.

Electrospun fibers were collected on a rotary grounded collector operating at 30 rpm and at a variable distance (10-15 cm) at room temperature. The voltage was applied to the collector using a high-voltage supplier (Gamma High Voltage Research, ES30-5W) and varied between 10 and 30 kV. Polymer solution was ejected by a KDS100 infusion syringe pumps to control the flow rate (from 3.5 to 10 mL h^{-1}).

Unloaded and CHX loaded electrospun fibers were prepared using optimized parameters (i.e., needle-collector distance, voltage and flow rates) and solvent conditions (i.e., solvent and polymer concentration).

7.2.2.4. Preparation of loaded and unloaded PCL films

PCL films were prepared by pressing 0.7 g of PCL in a 4 x 6 cm^2 mold that was heated at 15 ºC above the melting point of PCL (i.e., 60 ºC) for 8 min with a pressure progressively increasing from 1 to 2 bars. A hydraulic press, heated platens and a temperature controller were employed. Mold and polymer were covered with Teflon sheets in order to avoid polymer adhesion to the mold. PCL films with a thickness close to 200 μm were recovered after cooling the mold to room temperature.

CHX was incorporated by solvent casting. Specifically, 0.7 g of PCL and 3.5 mg of CHX (i.e., 0.5 *w/w*-%) were dissolved in 10 mL of an ethanol/chloroform 1:2 (*v/v*) mixture and the resulting solution was kept at rest at room temperature to allow evaporation of the solvent. The obtained films were cut in small pieces and melt pressed as above explained. Smooth films with a similar thickness (i.e., 220 μm) were obtained.

7.2.2.5. Preparation of multilayered matrices

PCL films and GL-*b*-(GL-*co*-TMC-*co*-CL)-*b*-GL electrospun mats were assembled in an alternating way to obtain a system constituted by five layers, as shown in Figure 7.2.1b. The two outers and the middle sheets corresponded specifically to PCL films. The assembly

was introduced in a 1 x 2 x 0.5 cm^3 mold and heated at 75 ºC for 15 min. The resulting matrices had a thickness close to 700 µm.

Different combinations of CHX loaded and unloaded layers were evaluated. These correspond to the loading of CHX in one of the outer layers (PCLe), in the inner PCL layer (PCLi), in one electrospun mat (M(i)) and the two electrospun mats (M(ii)).

7.2.2.6. Drug release

Drug release experiments were performed with 1 × 1 cm^2 square pieces (thickness close to 0.7 mm) representative of each drug loading configuration. These pieces were incubated at 37 ºC in an orbital shaker at 80 rpm in tubes of 10 mL for 1 week. A 3:7 *v/v* mixture of PBS buffer and ethanol was employed as release media, although some experiments were also carried out in an ethanol medium for all configurations and in only PBS when CHX was incorporated in the outer layer of PCL (PCLe). Samples were withdrawn from the release medium at predetermined time intervals and the drug concentration was evaluated by UV spectroscopy using a Shimadzu 3600 spectrometer. Thus, the absorbance was measured at a wavelength of 260 nm.

Calibration curves were prepared using different stock solutions of the assayed CHX drug in the different release media and relating the measured absorbance with the concentration. The volume of the release medium was kept constant during the experiments by the addition of fresh medium. All drug release tests were carried out using three replicates and the results were averaged.

Encapsulation efficiency was calculated by measuring the amount of drug incorporated into the scaffold by UV-vis absorbance measurements at a wavelength of 260 nm. To this end, samples were dissolved in 0.5 mL of HFIP and subsequently the polymer was precipitated by addition of ethanol (0.5 mL). CHX was separated by centrifugation, being dissolved in the solvent phase.

7.2.2.7. Antimicrobial test assays

E. coli and *S. aureus* bacteria were selected to evaluate the antimicrobial activity of CHX loaded matrices. The bacteria were previously grown aerobically to exponential phase in broth culture (5 g/L yeast extract, 5 g/L NaCl, 10 g/L tryptone, pH 7.2).

Growth experiments were performed on a 24-well culture plate. The different kinds of CHX loaded samples (1x1 cm^2 and thickness close to 0.7 mm) were placed into each well and an unloaded sample was used as a blank. Then, 2 mL of broth culture containing 10^3 CFU were added to the samples. The cultures were incubated at 37 ºC and agitated at 80 rpm. Aliquots of 100 µL were taken at predetermined time intervals for absorbance measurement at 650 nm in a microplate reader (every 2 h for 8 h, and after 12, 24 and 48 h from the starting time). Thus, turbidity was directly related to bacterial growth and represented as relative growth considering the maximum bacterial growth in the absence of any polymeric matrix (control).

Bacterial adhesion onto matrices samples was also determined. After growth experiments had finished, the culture media were aspirated and the material was washed three times with distilled water. Then, 0.5 mL of sterile 0.01 M sodium thiosulfate was added to each well to detach the adhered bacteria. After 1 h in agitation (100 rpm) at 37 ºC, samples were removed and 1 mL of broth culture was added in each well. Just after filling the plate with fresh broth culture, the first sample was taken to measure as a time 0 for adhesion assay. Then, plates were incubated at 37 ºC and 100 rpm for 24 h. The bacterial number was determined as above indicated. All assays were conducted in quadruplicate and the values averaged.

Regarding a qualitatively evaluation, the different pieces (1×1×0.07 cm^3) of CHX loaded samples and an unloaded one, which was used as a blank, were placed into an agar diffusion plate and seeded separately with 10^4 CFU/mL of each bacteria. The culture medium was prepared with 18.5 g Brain Heart Infusion broth, 7.5 g Bacto™ Agar in 1 L of Milli-Q water and sterilized in an autoclave at 121 ºC for 30 min. Plates were filled with 15 mL of medium and kept at rest at room temperature to allow solidification of the medium. Inhibition halos images were taken after incubation of samples with bacteria at 37 ºC for 24 h.

7.2.3. RESULTS AND DISCUSSION

7.2.3.1. Electrospinning of CHX loaded and unloaded GL-*b*-(GL-*co*-TMC-*co*-CL)-*b*-GL nanofibers

The low solubility of polymers having significant polyglycolide blocks limited the selection of an appropriate solvent for the electrospinning process to HFIP. A polymer concentration

around 10 wt-% was found adequate to obtain nanofibers, as previously described for polyglycolide (i.e., 8 wt-% in a HFIP solution).[17] The needle-collector distance had a limited influence in the fiber morphology, and specifically distances between 12 and 15 cm allowed getting continuous and well-formed nanofibers in most of the assayed conditions. Lower values did not guarantee a complete solvent evaporation while at higher distance the population of narrower fibers increased.

The most significant problem to obtain appropriate fiber morphology concerned the formation of a great proportion of irregular beads and even the disruption of the electrospun nanofibers. Table 7.2.1 summarizes some representative experiments, which indicate a beneficial effect when the applied voltage increased and the flow rate decreased. It is well-known that the stretching process is enhanced at high voltages[20] whereas the decrease in the flow rate leads to low fiber diameters.[21] Solvents cannot be uniformly and completely evaporated at high flow rates leading to the formation of abundant beads and even a merging of fibers into a web.[22] The selected conditions corresponded to a voltage of 25 kV, a flow rate of 3.5 mL/h and a needle-collector distance of 12 cm. Small variations lead to defective morphologies for a higher flow rate and lower applied voltages (Table 7.2.1).

Table 7.2.1. Morphology of unloaded and CHX loaded electrospun GL-*b*-(GL-*co*-TMC-*co*-CL)-*b*-GL samples depending on processing parameters (voltage, flow rate and needle-collector distance).

Voltage (kV)	Flow ($mL \cdot h^{-1}$)	Distance (cm)	Results
			Electrospun fibers
12.5	5	12.5	Many beads
15	5	15	Some beads
15	8	15	Some beads
15	3.5	12	Few beads
20	3.5	12	Few beads
25	**3.5**	**12**	**No beads**
			Electrospun fibers with CHX
25	3.5	12	Many beads
20	3.5	12	More beads. Disruption of fiber
20	7	12	Less beads but many fibers merging into a web
20	5	12	Many beads
25	**5**	**12**	**No beads**

SEM micrographs at different magnifications (Figures 7.2.2a, 7.2.2b and 7.2.2c) show that highly uniform and continuous nanofibers with smooth surfaces can be obtained under the selected processing conditions. Figure 7.2.3a shows wide diameter distribution curve (i.e., from 200 to 900 nm) that follows a unimodal distribution. Most of fibers have a diameter around 410 nm, being the average diameter 500 nm and the standard deviation 118 nm.

Characteristics of the solution were drastically modified when the ionic CHX compound was added since logically the electrical conductivity of the solution was modified. It is well established that an increase of solution conductivity tends to decrease fiber diameter due to the increase in electrical charge carried by the jet and thus the resulting tensile force in the presence of an electric field.[23] Processing conditions were also modified (Table 7.2.1) in order to avoid fiber disruption and formation of droplets at low flow rates. In any case, continuous and homogeneous nanofibers (Figures 7.2.2d, 7.2.2e and 7.2.2f) could be obtained at 5 mL/h and keeping the applied voltage (i.e., 25 kV) and the needle-collector distance (i.e., 12 cm).

Figure 7.2.2. SEM micrographs showing unloaded **(a,b,c)** and CHX loaded **(d,e,f)** GL-*b*-(GL-*co*-TMC-*co*-CL)-*b*-GL electrospun nanofibers at different magnifications. Nanofibers were obtained in both cases under the optimized conditions.

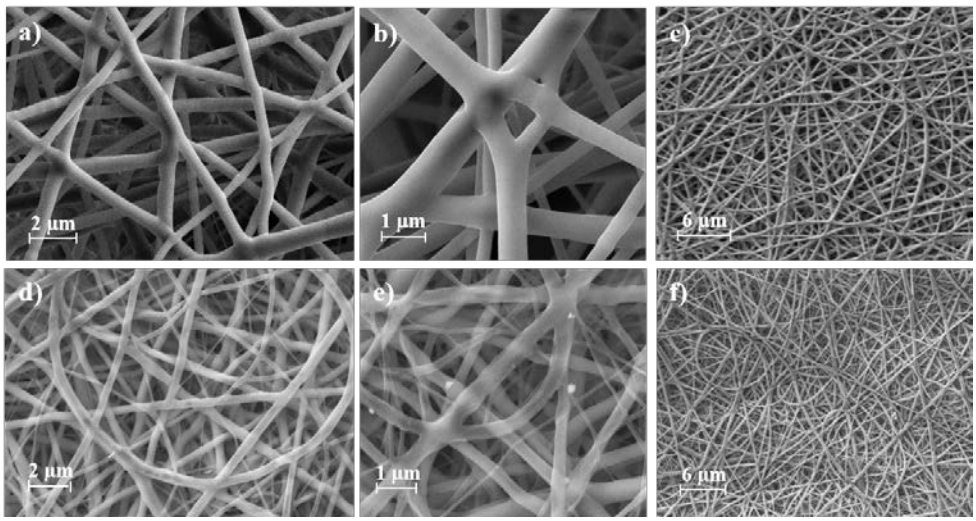

High magnification SEM images (Figure 7.2.2e) revealed a smooth fiber surface but also the presence of some very small crystals that could be attributed to CHX. Micrographs also

showed the presence of two fiber populations, which could also be deduced from the diameter distribution (Figure 7.2.3b). The most abundant population corresponds to an average diameter of 150 nm and a standard deviation of 38 nm, whereas values of 320 nm and 90 nm characterize the second one. In any case, the maximum diameter was close to 600 nm, a value significantly lower than that determined for the unloaded fibers (i.e., 900 nm).

Figure 7.2.3. Diameter distribution curves of unloaded **(a)** and CHX loaded **(b)** GL-*b*-(GL-*co*-TMC-*co*-CL)-*b*-GL electrospun nanofibers obtained in both cases under the optimized conditions.

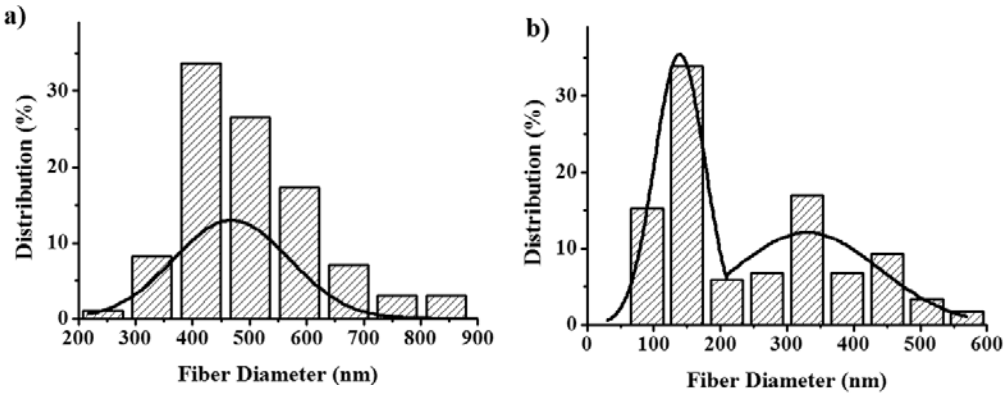

7.2.3.2. Preparation of multilayered PCL matrices containing GL-*b*-(GL-*co*-TMC-*co*-CL)-*b*-GL nanofibers

The thermal molding process allowed obtaining a successful integration of nanofibers in the PCL matrix. In fact, only some edges of the molded pieces revealed the five-layered configuration, as shown in Figure 7.2.4a, probably because of a deficient pressure in the borders of the mold. Nevertheless, comparison of Figures 7.2.4b and 7.2.4c demonstrates the capability of PCL to flow through the electrospun scaffolds, as a consequence of its moderate viscosity at the molding temperature and the porosity of the scaffold. Figure 7.2.4b shows the initial morphology where a scaffold appears surrounded by two PCL films whereas Figure 7.2.4c shows as the different layers cannot be distinguished in the inner sections of the piece after performing the molding process. The presence of fibers relatively well distributed in the matrix can be envisaged in high magnification images (see arrows in the inset of Figure 7.2.4c). In any case, the fracture surfaces of molded

pieces obtained after cracking them in liquid nitrogen indicated a homogeneous appearance that was similar to that observed for the initial PCL films (see inset in Figure 7.2.4c).

Figure 7.2.4. SEM micrographs showing the lateral edge of the final multilayered matrix **(a)**, the assembly of an electrospun mat between two PCL films before performing the melt pressing process **(b)** and a lateral view of the inner part of the matrix after being cracked in liquid nitrogen **(c)**. The insets show a magnification where nanofibers can be distinguished, pointed by the red arrows, and a section of the PCL film.

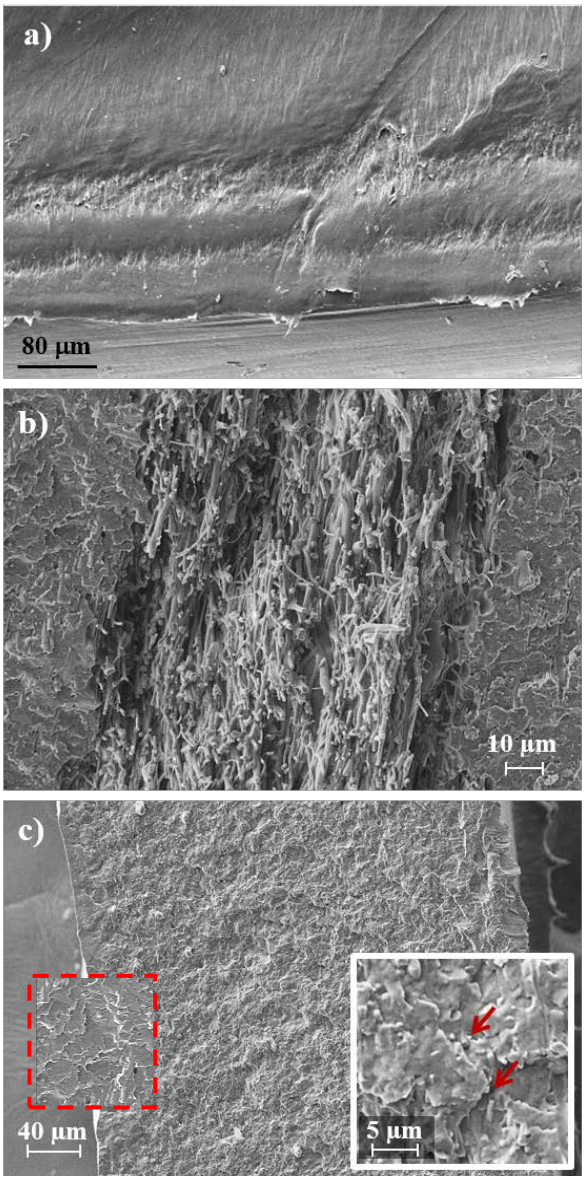

7.2.3.3. Thermal degradation of multilayered matrices

TG and DTG curves (Figure 7.2.5) demonstrated the high thermal stability of the multilayered matrices, which had an onset degradation temperature of 250 ºC and decomposed according to two steps with DTG peak temperatures at 350 ºC and 410 ºC. These degradation processes were in full agreement with those observed for the nanofibrous scaffold (i.e., single peak at 350 ºC) and the PCL film (i.e., single peak at 410 ºC), being lower the weight loss associated to the first step due to the lower content of nanofibers (i.e., 15 wt-%) in the matrix.

Figure 7.2.5. TGA (a) and DTGA (b) curves for the indicated representative samples.

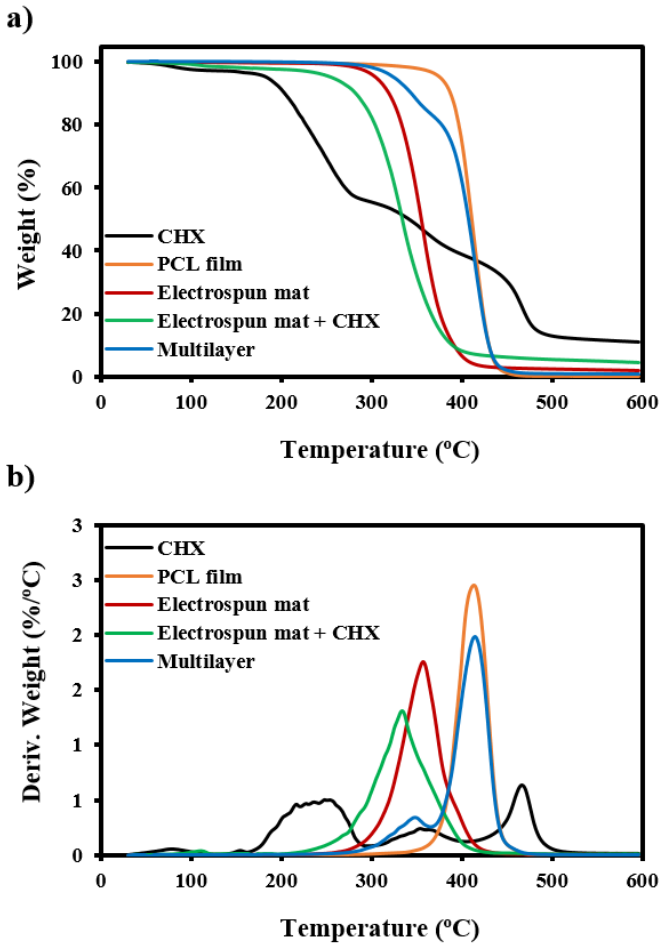

It is clear that the multilayered sample could be prepared without any evidence of thermal degradation because nanofibers were obtained by electrospinning at room temperature and the molding process was performed at a temperature far away of the beginning of decomposition due to the low melting temperature of PCL.

However, TG and DTG curves of CHX showed a relatively low stability that could affect the processing of multilayered matrices. Specifically, CHX had a complex three step degradation process with an onset degradation temperature of 175 ºC and DTG peak temperatures of 250 ºC, 355 ºC and 466 ºC. Incorporation of CHX in the electrospun scaffold had a remarkable influence on its onset degradation temperature that decreased to 200 ºC despite the low amount of loaded drug. Furthermore, the temperature of the single DTG peak decreased from 355 ºC to 330 ºC. In addition, a char yield close to 4% was detected in the corresponding DTG curve in agreement with the high residue observed in the degradation of the CHX drug due to its high aromatic content. Although the processing was still not problematic in our case, the result is interesting since it points out that cautions should be taken into account when other polymers with a higher melting point (e.g., polylactide) were selected as a matrix.

7.2.3.4. Mechanical properties of multilayered matrices

Representative stress-strain curves of the different fabrics are shown in Figure 7.2.6.

Figure 7.2.6. Stress-strain curves of unloaded (dashed green line) and CHX loaded electrospun mats of GL-*b*-(GL-*co*-TMC-*co*-CL)-*b*-GL (solid green line), unloaded (dashed red line) and CHX loaded (solid red line) PCL films, unloaded (dashed orange line) and loaded (solid orange line) multilayered matrices.

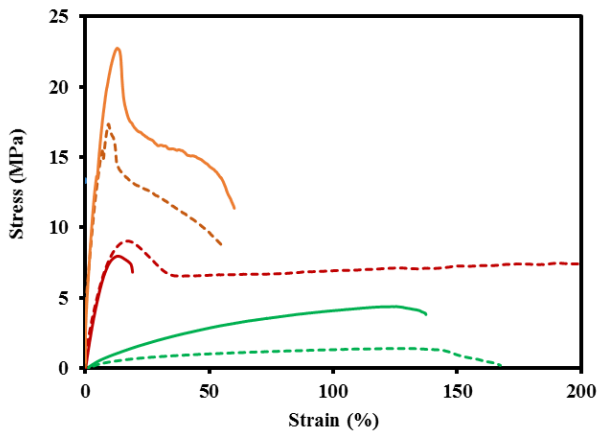

Some points deserve attention:

a) Unloaded scaffolds have a low Young modulus (i.e., 20 MPa) as expected for an electrospun sample. This modulus is limited because of the slippage between the nonwoven fibers. The final deformation becomes close to 170% and the maximum stress around 2 MPa. This value clearly increased (i.e., 5 MPa) when the scaffold was loaded with CHX while modulus and final strain were similar. The observed differences can be explained considering that the incorporation of CHX had a great influence on the fiber morphology and specifically a significant reduction on the fiber diameter was derived.

b) PCL films showed a typical behavior characterized by a high elastic modulus (i.e., 180 MPa) due to the high crystallinity of PCL, a maximum stress of 10 MPa at the necking point and then a plastic region until a final deformation higher than 200% (i.e., 660% not shown). These properties changed drastically when CHX was incorporated even for a low percentage as 0.5 wt-%. Thus, the maximum stress decreased to 8 MPa and the deformation to 20%. Crystallization was also slightly hindered and consequently the modulus decreased to 150 MPa.

c) The unloaded multilayered matrix showed a slight increase of the Young modulus compared to that found for the PCL film (i.e., from 180 MPa to 220 MPa) as a consequence of the incorporation of nanofibers. Moreover, an increase on the maximum stress (i.e., 14 MPa) was observed demonstrating a reinforcing effect and therefore the existence of relative good interactions between the matrix and the nanofibers. The elongation at break (i.e., 55%) decreased compared to the matrix due to the stiff nature of the added fibers. It should be emphasized that multilayered matrices having CHX loaded in the nanofibers showed improved properties (235 MPa, 20 MPa and 60% for the Young modulus, the maximum stress and the final deformation, respectively) since the nanofiber diameters decreased as above indicated. The most important conclusion is that these loaded multilayered samples displayed clearly better properties than PCL films having a similar drug load.

7.2.3.5. CHX release from multilayered matrices

The release behavior was firstly studied in an ethanol medium since it had a great capability to swell the polymer matrix and favor the release of the drug. Furthermore, ethanol is also a good solvent for the selected CHX drug. In this way, results on ethanol

appear useful to highlight the ability of the different layers to retain the drug, if it is the case.

Figure 7.2.7a shows a practically immediate release when the drug was loaded in the outer PCL layer, being achieved a complete delivery only after 35 h of exposure. The release was also fast when the inner PCL layer was loaded, although in this case more than 100 h were required to get a relative release percentage of 98%. Basically, the difference between loading CHX in the outer and the inner PCL films is a consequence of the variation of the diffusion path of the drug.

On the contrary, a highly significant different behavior was observed when the drug was incorporated into the scaffolds. Logically, the increased retention could not just be a consequence of an increased diffusion path and therefore it should be considered that CHX could establish better interactions with the hydrophilic PGA rich copolymer than with the hydrophobic PCL. Interestingly, Figure 7.2.7 also demonstrates that different release profiles were attained depending on whether the drug was incorporated in one or both scaffolds. Thus, in the first case the release was 90% after 100 h of exposure, while in the second case only was 80% after the same period. The increased amount of nanofibers clearly hindered the release of the drug since it had more chance to interact with them. Note that an opposite result should be expected attending the higher drug concentration inside the matrix when both scaffolds were loaded.

Release of CHX in an aqueous PBS medium was insignificant, even when the drug was loaded in the outer PCL layer (i.e., 15% after 100 h). It is clear that water was not able to swell the hydrophobic polymer properly to facilitate drug diffusion. Differences with the other loaded matrices were logically not relevant. Figure 7.2.7b points also out that the release behavior can be tuned in function of the ethanol/water ratio of the release medium. Specifically, the system with CHX loaded in both scaffold layers reflected the highest sensitivity with respect to a decrease of the ethanol content from 100% to 70%. Note that the release percentage decreased from 80% to 70% after 100 h of exposure.

Figure 7.2.7. CHX release percentages in EtOH **(a)** and PBS-EtOH 30:70 **(b)** media from the different loading configurations of the multilayered matrix. For the sake of completeness, data in a PBS medium are also plotted (solid line) for the configuration where CHX is loaded in the outer PCL films (PCLe).

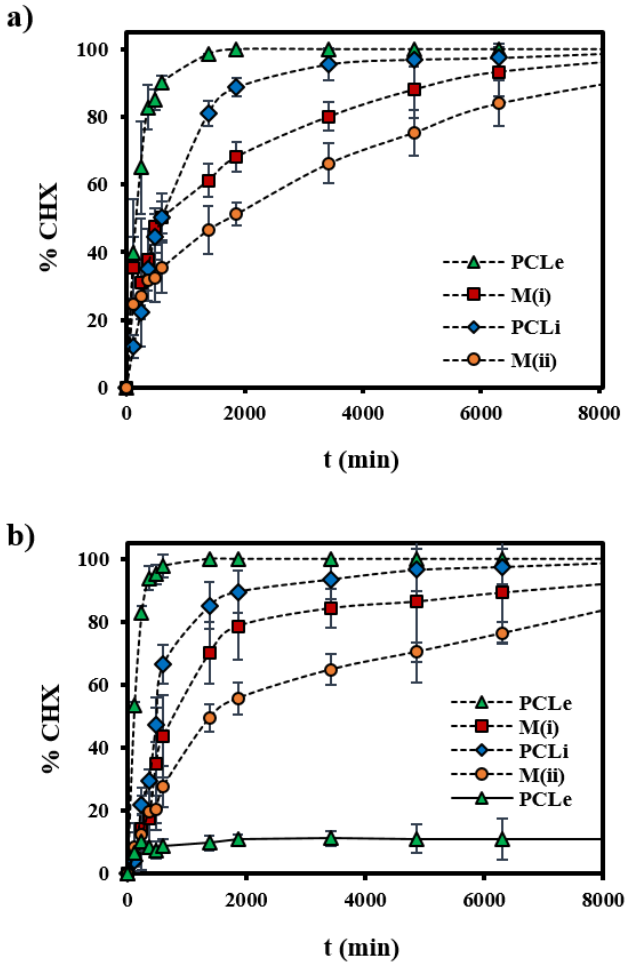

7.2.3.6. Antibacterial properties of CHX loaded multilayered matrices

Bactericide effect of the different CHX loaded matrices was qualitatively evaluated through Agar tests by measurement of the inhibition halos around the different multilayered fabrics. Results point out that halos were only significant for PCLe samples, independently of the type of bacterium (Figure 7.2.8). Logically, samples loaded with CHX in the nanofibers did not show a bactericide activity in these short time events. Also these

results are consistent with the slow release of the drug from this type of multilayered matrices, which could ensure long-term antibacterial effect.

Figure 7.2.8. Images showing the inhibition halos on Agar plates seeded with *E. coli* and *S. aureus* bacteria caused by multilayered matrices loaded in the outer PCL film and the electrospun mat. The images of blanks (unloaded matrices) are also provided.

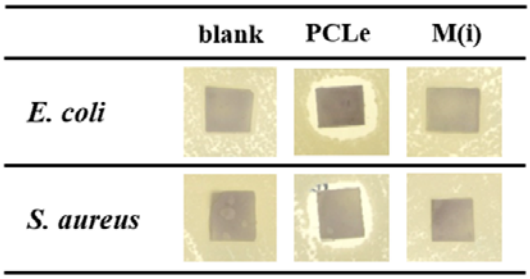

The antimicrobial effect was also quantitatively evaluated following the growth kinetics of Gram negative (*E. coli*) and Gram positive (*S. aureus*) bacteria, as displayed in Figures 7.2.9a and 7.2.9b.

It is clear that the unloaded matrix (named blank in the Figure 7.2.9) is highly susceptible to bacterial infection, with a latency phase that occurs over a period of 4 h, then an exponential growth (log) phase with growth velocity ($t_{½}$) of 0.125 h^{-1} and finally it reaches a maximum growth near 100%. Thus, these characteristics of growth were similar to the control or bacterial growth in the absence of polymeric matrix. A significant decrease in bacterial proliferation was only detected when CHX was loaded in the outer PCL film (PCLe), being in this case the growth curve characterized by a latency phase extends over 6 h and an exponential growth phase with velocity of 0.095 and 0.083 h^{-1} for *E.coli* and *S.aureus*, respectively. However, in both bacteria the maximum growth corresponded around of 80%, and it demonstrated that this kind of matrix have an inhibitory activity of 20%.

Figure 7.2.9. Growth curves of *E. coli* **(a)** and *S. aureus* **(b)** on the different CHX loaded multilayered matrices and the unloaded one as blank.

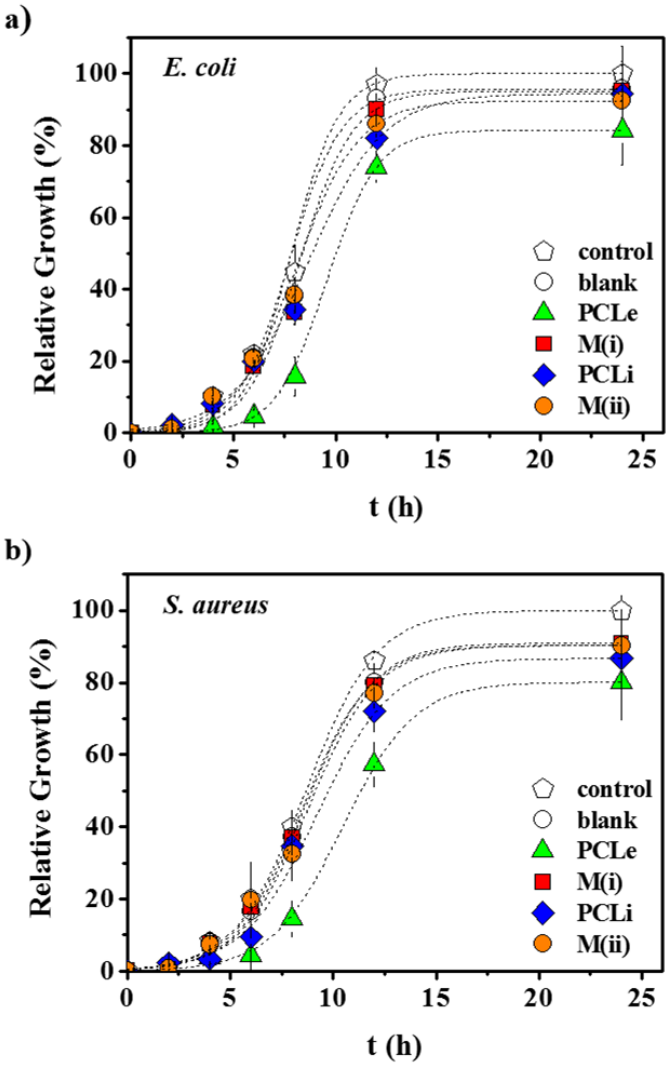

Results indicate that an immediate bacteriostatic effect could be attained by incorporating the drug in the outer layers but it is also interesting the possibility to have a reservoir of drug for long term events. In this sense, it is clear that the loading of CHX in the inner electrospun scaffolds gave rise a greater drug release after more than 83 h (i.e., after the drug from PCL was completely released). Note that growth inhibition during the period of 8 to 24 h was slightly higher for the PCLi multilayered matrix than for the unloaded blank and even for the M(ii) sample (i.e., note the decrease of the growth velocity ($t_{1/2}$=0.1h^{-1}) in the curve for *S. aureus* bacterium).

In fact, bacterial adhesion tests (Figure 7.2.10) demonstrated that PCLe was the only loaded matrix with a clear effect in bacterial adhesion for short term assay (24 h) and that *S. aureus* was the most sensitive bacteria to the effect of CHX. Thus, the adhesion was 90 % and 85 % compared to the control for *E. coli* and *S. aureus*, respectively.

Figure 7.2.10. Adhesion of *E. coli* (gray bars), and *S. aureus* (grid bars) bacteria on the different CHX loaded multilayered matrices. Data concerning the culture plate as positive control and loaded matrix as blank are also provided.

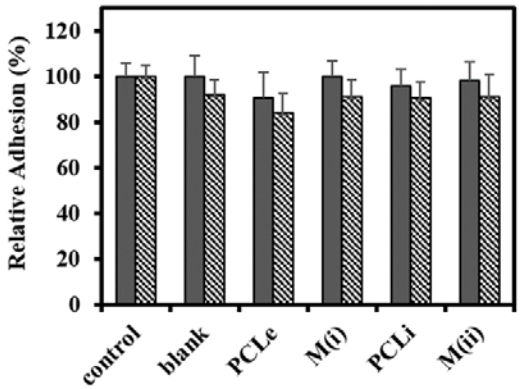

7.2.4. CONCLUSIONS

Segmented copolymers having 57 wt-% of polyglycolide *hard segments* and *soft segments* constituted by glycolide, trimethylene carbonate and ε-caprolactone units can be successfully electrospun from HFIP diluted solutions. Continuous and uniform nanofibers with an average diameter of 500 nm and a smooth texture were attained using voltage, flow rate and needle-collector distance of 25 kV, 3.5 mL/h and 12 cm, respectively. The increase of flow rate and the decrease of the voltage had a great repercussion on the fiber morphology and specifically bead formation was clearly enhanced.

Electrospinning allowed obtaining fibers loaded with a bactericide drug such as chlorhexidine, although processing parameters should be modified due to the increase in the electrical conductivity of the solution. In this case, a bimodal diameter distribution was achieved, being 150 and 320 nm the mean diameters of the two populations.

Molding of a five layer assembly of alternate PCL films and electrospun scaffolds gave rise to a PCL matrix reinforced with well distributed nanofibers. Probably favorable interaction were established between the matrix and the soft segments containing ε-caprolactone. Mechanical properties of loaded multilayered matrices revealed that the presence of nanofibers could compensate the decrease of mechanical performance when PCL was loaded with CHX.

Drug release experiments revealed that the multilayered system was able to guarantee a fast release of CHX when it was loaded in the outer PCL layers, whereas a delayed release could be achieved when CHX was loaded into the nanofibers due to the good interactions that could be established between the drug and the hydrophilic polyglycolide component. This tunable release behavior appears highly interesting to get a short and long term bactericide effect as demonstrated by growth inhibition.

REFERENCES

1. Bergshoef, M. M. & Vancso, G. J. Transparent nanocomposites with ultrathin electrospun nylon-4,6 fiber reinforcement. *Adv. Mater.* **11,** 1362–1365 (1999).

2. Fong, H. Electrospun nylon 6 nanofiber reinforced BIS-GMA/TEGDMA dental restorative composite resins. *Polymer.* **45,** 2427–2432 (2004).

3. Pinho, E. D., Martins, A., Araújo, J. V., Reis, R. L. & Neves, N. M. Degradable particulate composite reinforced with nanofibres for biomedical applications. *Biomaterialia* **5,** 1104–1114 (2009).

4. Del Valle, L. J., Díaz, A., Royo, M. & Rodríguez-Galán, A. Biodegradable polyesters reinforced with triclosan loaded polylactide micro/nanofibers: Properties, release and biocompatibility. *eXPRESS Polym. Lett.* **6,** 266–282 (2012).

5. Molnár, K., Kostáková, E. & Mészáros, L. The effect of needleless electrospun nanofibrous interleaves on mechanical properties of carbon fabrics/epoxy laminates. *eXPRESS Polym. Lett.* **8,** 62–72 (2014).

6. Del Valle, L. J. *et al.* Electrospinning of polylactide and polycaprolactone mixtures for preparation of materials with tunable drug release properties. *J. Polym. Res.* **18,** 1903–1917 (2011).

7. Díaz-Celorio, E., Franco, L., Rodríguez-Galán, A. & Puiggalí, J. Synthesis of glycolide/trimethylene carbonate copolymers: Influence of microstructure on properties. *Eur. Polym. J.* **48,** 60–73 (2012).

8. Mkhabela, V. J. & Ray, S. S. Poly(ε -caprolactone) nanocomposite scaffolds for tissue engineering: A brief overview. *J. Nanosci. Nanotechnol.* **14,** 535–545 (2014).

9. Dash, T. K. & Konkimalla, V. B. Poly(ε-caprolactone) based formulations for drug delivery and tissue engineering: A review. *J. Control. Release* **158,** 15–33 (2012).

10. Ikada, Y. & Tsuji, H. Biodegradable polyesters for medical and ecological applications. *Rapid Commun.* **21,** (2000).

11. Spearman, S. S., Rivero, I. V. & Abidi, N. Influence of polycaprolactone/polyglycolide blended electrospun fibers on the morphology and mechanical properties of polycaprolactone. *J. Appl. Polym. Sci.* **131,** 40224 (2014).

12. Márquez, Y. *et al.* Spherulitic morphologies of the triblock poly(GL)-*b*-poly(GL-*co*-TMC-*co*-CL)-*b*-poly(GL) copolymer: Isothermal and non-isothermal crystallization studies. *Eur. Polym. J.* **73,** 222–236 (2015).

13. Márquez, Y., Martínez, J. C., Turon, P., Franco, L. & Puiggalí, J. Influence of pH on morphology and structure during hydrolytic degradation of the segmented GL-*b*-[GL-*co*-TMC-*co*-CL]-*b*-GL copolymer. *Fibers* **3,** 348–372 (2016).

14. Márquez, Y., Franco, L., Turon, P. & Puiggalí, J. Isothermal and non-isothermal crystallization kinetics of a polyglycolide copolymer having a tricomponent middle soft segment. *Thermochim. Acta* **585,** 71–80 (2014).

15. Márquez, Y., Franco, L., Turon, P., Rodríguez-Galán, A. & Puiggalí, J. Study on the hydrolytic degradation of the segmented GL-*b*-[GL-*co*-TMC-*co*-CL]-*b*-GL copolymer with application as monofilar surgical suture. *Polymer Degradation and Stability* (2013).

16. Oberhoffner, S. & Planck, H. Surgical suture material from triblockterpolymer, its use in surgery and process for its preparation. EP 0835895. (1996).

17. You, Y., Min, B. M., Lee, S. J., Lee, T. S. & Park, W. H. *In vitro* degradation behavior of electrospun polyglycolide, polylactide, and poly(lactide-*co*-glycolide). *J. Appl. Polym. Sci.* **95,** 193–200 (2004).

18. Leikin, J. B. & Paloucek, F. P. in *Poisoning and Toxicology Handbook* 183–184 (Informa, 2008).

19. Green, J.-B. D., Fulghum, T. & Nordhaus, M. A. in *Science against microbial pathogens: communicating current research and technological advances* (ed. A., M.-V.) 84–98 (2011).

20. Shenoy, S., Bates, W., Frisch, H. & Wnek, G. Role of chain entanglements on fiber formation during electrospinning of polymer solutions good solvent, non-specific polymer-polymer interaction limit. *Polymer.* **46,** 3372–3384 (2005).

21. Zong, X. *et al.* Structure and process relationship of electrospun bioabsorbable nanofiber membranes. *Polymer.* **43,** 4403–4412 (2002).

22. Yuan, X., Zhang, Y., Dong, C. & Sheng, J. Morphology of ultrafine polysulfone fibers prepared by electrospinning. *Polym. Int.* **53,** 1704–1710 (2004).

23. Angammana, C. J. & Jayaram, S. H. Analysis of the effects of solution conductivity on electrospinning process and fiber morphology. *IEEE Trans. Ind. Appl.* **47,** 1109–1117 (2011).

CONCLUSIONS

The main conclusions derived from this Thesis can be summarized as follows.

Crystallization studies of GL-*b*-(GL-*co*-TMC-*co*-CL)-*b*-GL monofilar surgical suture

Isothermal and non-isothermal crystallization kinetics by means of Differential Scanning Calorimetry.

- Incorporation of a 43 wt-% of amorphous GL-*co*-TMC-*co*-CL *soft segment* into the polyglycolide molecular chain caused a small depression on the melting point and had a major influence on the glass transition temperature.
- The equilibrium melting temperature of the sample (219 ºC) became lower than that reported for the polyglycolide homopolymer and segmented polyglycolide copolymers having a lower *soft segment* content.
- Isothermal crystallization of GL-*b*-(GL-*co*-TMC-*co*-CL)-*b*-GL from the melt state took place according to a heterogeneous nucleation and a spherulitic growth. Maximum overall crystallization rate was estimated to occur at 131 ºC according to the Lauritzen-Hoffman treatment.
- Ozawa and Avrami combined analysis for non-isothermal crystallization from the melt state pointed out that the motion of molecular chains became slower as the material crystallized. The method reported by Cazé gave an average value for the Avrami exponent that was in close agreement with that deduced from isothermal.
- A secondary nucleation constant close to 1.90×10^5 K^2 and a temperature of 127.5 ºC for the maximum crystallization rate could be estimated from non-isothermal experiments following an isoconversional analysis.

Spherulitic morphologies: Isothermal and non-isothermal crystallization studies

- Crystallization of segmented copolymers having polyglycolide *hard segments* is influenced by the constitution of the amorphous *soft segment*. Thus, significant differences on secondary nucleation constant and lamellar morphology were found between copolymers displaying similar properties but having *soft segments* with three or two components
- *Hard* and *soft segments* of GL-*b*-(GL-*co*-TMC-*co*-CL)-*b*-GL were compatible/miscible and on crystallization gave rise to spherulites with a positive birefringence from the melt and the glass state.

- Spherulites obtained under low supercoolings had a flower-like appearance and were mainly constituted by flat-on lamellae. Isothermal and non-isothermal kinetic analyses indicated heterogeneous nucleation and three-dimensional growth which tended to be two-dimensional for isothermal crystallizations under low supercooling.
- Crystallization was characterized by a rather low primary nucleation density and crystal growth rate.
- Lauritzen and Hoffman analysis demonstrated a single crystallization regime defined by a secondary nucleation constant (K_g = 2.88×10^5 K^2 - 2.42×10^5 K^2 for isothermal and non-isothermal crystallization, respectively) higher than that determined for related segmented copolymers with a slightly lower *soft segment* content. Statistical blocks constituted by three repeat units played a significant role in hindering primary nucleation and proper arrangement of polyglycolide *hard segments* over crystal growth surfaces.
- Similar lamellar morphologies were attained by crystallization from the melt state or from thermal treatment of oriented fibers, being characteristic lamellar insertion and lamellar thickening processes, respectively.
- Final morphologies are defined by a crystallinity within the lamellar stacks of 0.82 and a crystalline thickness of 8.6-9.0 nm that contrast with values of 0.74-0.83 and 10.0 nm found for the bicomponent system when was processed in a similar form.

Degradation studies of GL-*b*-(GL-*co*-TMC-*co*-CL)-*b*-GL monofilar surgical suture

Thermal degradation studies of poly(trimethylene carbonate) blends with poly(ε-caprolactone) and others polyesters

- The degradation behavior of poly(trimethylene carbonate) changes substantially when this polymer is mixed with polylactide or poly(ε-caprolactone).
- The incorporation of PCL enhances the usually minor decomposition process associated with an unzipping depolymerization reaction occurring at the lower temperature range.
- By contrast, upon addition of PLA a typical random chain scissions seems to be favored. In this case, thermal stabilization of PTMC is observed and the main decomposition process occurs at higher temperatures and the activation energy increases.

- Decomposition of PLA and especially of PCL is favored when blending these polymers with the less thermally stable PTMC sample. In the case of PLA, a well-defined predominant process can be observed for blends with a low PTMC content.
- PLA/PTMC and PCL/PTMC blends have peculiar degradation processes which do not correspond to a mere superposition of the degradation processes associated with each constituent.
- Deconvolution of DTG curves made it possible to distinguish the different decomposition steps of the complex degradation process. Activation energies of the main step of degradation are practically independent of the degree of conversion, and therefore a single mechanism can be postulated.

Study on the hydrolytic degradation of the segmented GL-b -(GL-co -TMC-co -CL)-b –GL copolymer

- First order kinetic equations, that are compatible with random scission mechanisms, can be fitted for the evolution of the mass loss and molecular weight profiles during degradation in media differing on pH and/or temperature.
- This kinetics seems only to change when degradation occurs in acid media and after long exposure times. In this case, a backbiting process may dominate since degradation mainly affected the crystalline domains and recombination of cleaved ester groups could be significant.
- The diameter size of the suture has little influence on degradation processes although diffusion of degradation products caused an overestimation of the molecular weight when sutures with the lowest size were evaluated.
- A preferential cleavage of glycolyl homosequences which mainly corresponded to amorphous domains, as detected by FTIR spectroscopy, was revealed by ^{1}H-NMR spectra. Sequences related to transesterification reactions were rather significant in the initial samples and were less susceptible to the hydrolytic degradation.
- Mechanical properties and DSC calorimetric data confirmed also that the degree of crystallinity was slightly increased during the first stages of degradation due to hydrolysis of amorphous domains but also probably for the occurrence of secondary crystallization. In any case, degradation of highly defective crystals related to glycolide units of the soft segment take also place at the initial degradation stages.

- Morphology of degraded samples changed in a different way depending on the pH of the media.
- Longitudinal and circumferential cracks that affected the outer and inert part of sutures, respectively were distinguished. These cracks may be associated to interfibrillar and interlamellar amorphous domains and a molecular diffusion that could be enhanced along longitudinal and lateral directions.

Influence of pH on morphology and structure during hydrolytic degradation of the segmented GL-b -(GL-co -TMC-co -CL)-b –GL copolymer

- Hydrolytic degradation of the copolymer took place faster after being γ irradiated despite this treatment caused also cross-linking reactions and a slight increase of the initial molecular weight.
- Samples exposed to hydrolytic media experienced a quick decrease of the molecular weight until a constant value was reached but weight loss was still observed for longer exposure times.
- The gradual increase of the pH of the media caused also a progressive acceleration of degradation due to the greater solubilization of decomposition products and the modification of the hydrolysis mechanism.
- Degraded fibers showed complex morphological changes that varied according to the pH of the medium. Formation of longitudinal (at pHs equal or greater than 5) and circumferential (at all pHs) cracks and peeling (at pHs between 6 and 8) was found.
- Small angle X-ray scattering patterns of degraded samples indicated a fast hydrolysis of chains placed in the interlamellar domains followed by a continuous attack to the crystalline domains.
- The existence of interfibrillar amorphous domains was clearly highlighted during exposure to neutral and basic media, namely when formation of longitudinal cracks was enhanced.
- A reordering process, that increased the lamellar thickness and also the lamellar breadth, took place when a subsequent annealing process was performed with degraded fibers. Specifically, the evolution of patterns allowed detecting changes associated to lamellar tilting and structural features such as the presence of interfibrillar domains and the disposition of lamellar crystals at different levels along the fiber axis for a given cross-section.

- Degraded samples were able to crystallize from the melt giving rise to aggregates with a lamellar structure that was clearly distinct than that observed in the initial fibers.
- Lamelar thickness decreased when the hydrolytic attack was more aggressive as determined for both, non-isothermally crystallized samples before and after a subsequent thermal annealing process.

Crystallization studies of poly (*p*-dioxanone) monofilar surgical suture

Study of non-isothermal crystallization and analysis of morphological changes occurring during heating and cooling processes

- PDO showed complex melting and crystallization peaks because of a typical lamellar thickening process and the existence of different nucleation mechanisms, respectively.
- An increase of the Avrami exponent at low cooling rates, which could be associated with a homogeneous nucleation process instead of the instantaneous nucleation observed at high rates, was determined by calorimetric analysis of non-isothermal crystallization.
- Isoconversional analyses from non-isothermal calorimetric data revealed the existence of two crystallization regimes. These regimes were well characterized by optical microscopy observations, and the non-isothermal crystallization results were in relatively good agreement with those previously reported from isothermal studies.
- Real time SAXS profiles taken during heating and cooling processes showed the occurrence of a lamellar reordering and a lamellar insertion mechanism that led to an increase and a decrease in lamellar thickness, respectively.
- SAXS patterns taking during heating of samples degraded under neutral and basic pHs had a different evolution that revealed the existence of interlamellar and interfibrillar amorphous domains.

Incorporation of drugs into GL-*b*-(GL-*co*-TMC-*co*-CL)-*b*-GL monofilar surgical suture

Incorporation of antimicrobial drugs: biguanide compounds (CHX and PHMB)

- A random copolymer, prepared by ring opening polymerization, of 35 wt-% of lactide and 65 wt-% of trimethylene carbonate showed appropriate characteristics to be used as a coating of this monofilament suture.
- The new coating was characterized by a T_g close to -20 ºC, a low degradation rate at room temperature in a pH 7.4 medium, and a solubility in organic media enabling a consistent and homogeneous coating to be obtained by immersion of sutures in an ethyl acetate bath.
- Antimicrobial drugs such as CHX and PHMB can be directly adsorbed on the suture surface or loaded into the suture by a two-step procedure involving a subsequent coating.
- Two-step procedure showed advantages in terms of loading efficiency as drugs were more protected against detachment caused by handling. Furthermore, the coating was essential to avoid a complete burst effect in the case of PHMB.
- CHX was released according to a first relatively fast step and at a rate slightly dependent on the amount of loaded drug. However, in all cases an amount close to 0.9 μg/cm was retained on the suture surface, probably as a consequence of good interactions with the polymer matrix.
- The selected drugs exhibited a dose-dependent antimicrobial activity, and it was possible to distinguish between bacteriostatic and bactericidal activity. Bacterial growth kinetics and bacterial adhesion measurements indicated greater activity of PHMB against Gram-positive bacteria when samples with similar loaded weights of CHX and PHMB were compared. Incorporation of the coating was not essential in terms of bactericidal activity if the effect of lower drug loading efficiency was discarded.
- Cell adhesion and cell proliferation assays demonstrated the potential cytotoxicity of sutures having high doses of CHX and PHMB and that those with a clear bacteriostatic effect (i.e., inhibition of bacterial growth for a period between 10 h–30 h) could fortunately be considered biocompatible.
- The presence of the coating copolymer was more beneficial to reduce cytotoxicity, especially when the higher molecular weight PHMB was employed since the molecular size influenced the rate of diffusion towards cells.

Incorporation of chloramphenicol (CHO) and captopril (CAP)

- CHO can be easily loaded onto the surface of GL-*b*-(GL-*co*-TMC-*co*-CL)-*b*-GL monofilament sutures after their immersion in ethyl acetate solutions containing the drug.
- A linear relationship was found between drug concentration in the bath and the amount of CHO incorporated into the suture. Fitting was better for coated sutures due to the protective effect against drug detachment.
- CHO release was characterized by a constant amount of CHO that was retained in uncoated and coated sutures, which suggests the establishment of good intermolecular interactions between the drug and involved copolymers.
- A complete inhibitory effect against Gram-negative and Gram-positive bacteria was determined for uncoated and coated sutures loaded from baths having 5 *w/v-%* of CHO, whereas lower concentrations rendered less effective materials against Gram-positive bacteria when uncoated samples were evaluated. Adhesion of Gram-positive bacteria was significantly lower than adhesion of Gram-negative ones at the maximum CHO load.
- Cell proliferation assays demonstrated effective cell colonization (for both epithelial-like and fibroblast-like cells), even at the maximum assayed CHO load, giving rise to a significant decrease in the cell adhesion. In any case, cell adhesion and proliferation results demonstrated a lack of cytotoxicity for samples loaded with the CHO amount capable of rendering a clear bactericide effect.
- CAP loading was more problematic when sutures were immersed into a second coating bath as a consequence of a partial solubilization of the previously loaded drug. The coating was highly effective to suppress the burst effect and to render a sustained release.
- Adhesion and proliferation of fibroblast-like and epithelial-like cells decreased significantly for uncoated sutures loaded from baths having CAP concentrations higher than 5 *w/v-%*.
- The use of a coating copolymer was fundamental to avoid any cytotoxic response. Furthermore, wound healing was clearly improved for early events when coated sutures were employed.

Reinforced polymeric matrix by means of electrospinning

Poly(ε-caprolactone) films reinforced with chlorhexidine loaded electrospun polylactide microfibers

- PCL films reinforced with PLA microfibers can be effectively prepared by a co-electrospun procedure that rendered clear advantages in terms of crystallinity and mechanical properties compared to typical molding of PLA microfibers between films of the PCL matrix.
- The co-electrospinning method improved the interaction between PLA fibers and the PCL matrix, with the cold crystallization of PLA being favored during the molding process.
- The loss of mechanical properties due to the incorporation of small drugs into polymeric matrix can be compensated by incorporation of PLA microfibers, improving the final performance of the material.
- The procedure allowed bactericide agents like chlorhexidine to be easily loaded into both polymers, PLA and PCL. However, a slower release rate and a high retention were observed when the drug was only loaded into the PLA fibers.
- Slight differences were again detected between the two preparation methods; specifically, the films prepared by co-electrospinning those that showed a faster release.
- Antibacterial activity against Gram positive and Gram negative bacteria was demonstrated for all samples with CHX, even under the worst case condition (i.e., samples prepared by single electrospinning and loaded only into the PLA fibers).

Tunable drug loading and reinforcement of poly(ε-caprolactone) films by electrospun nanofibers of glycolide segmented copolymer.

- Segmented copolymers can be successfully electrospun from HFIP diluted solutions. Continuous and uniform nanofibers with a smooth texture were obtained.
- The increase of flow rate and the decrease of the voltage had a great repercussion on the fiber morphology and specifically bead formation was clearly enhanced.

- Electrospinning allowed obtaining fibers loaded with a bactericide drug such as chlorhexidine, although processing parameters should be modified due to the increase in the electrical conductivity of the solution.
- Molding of a five layer assembly of alternate PCL films and electrospun scaffolds gave rise to a PCL matrix reinforced with well distributed nanofibers. Probably favorable interaction were established between the matrix and the soft segments containing ε-caprolactone.
- Mechanical properties of loaded multilayered matrices revealed that the presence of nanofibers could compensate the decrease of mechanical performance when PCL was loaded with CHX.
- Drug release experiments revealed that the multilayered system was able to guarantee a fast release of CHX when it was loaded in the outer PCL layers, whereas a delayed release could be achieved when CHX was loaded into the nanofibers. This tunable release behavior appears highly interesting to get a short and long term bactericide effect as demonstrated by growth inhibition.